

in Neuroendovascular Therapy

Neurovascular
Malformation Solutions

Ischemic Stroke and
Carotid Artery Disease Solutions

For more information or a product demonstration,
contact your local MicroVention representative:



MicroVention, Inc.
Worldwide Headquarters
1311 Valencia Avenue
Tustin, CA 92780 USA
MicroVention UK Limited
MicroVention Europe, S.A.R.L.
MicroVention Deutschland GmbH

PH +1.714.247.8000

PH +44 (0) 191 258 6777

PH +33 (1) 39 21 77 46

PH +49 211 210 798-0

BARRICADE™ COIL SYSTEM

COILS THAT PERFORM

Cost Analysis of Cerebral Aneurysms Treated with the Barricade Coil System, A Retrospective Review

22 Patients Treated ♦ 114 Total Barricade Coils Used ♦ 8.2mm Mean Aneurysm Size

RIGHT PERICALLOSAL ANEURYSM

LEFT ICA TERMINUS ANEURYSM



PRE-TREATMENT

POST-TREATMENT

PRE-TREATMENT

POST-TREATMENT

“ I have successfully treated a wide range of aneurysms with the Barricade Coil System. I am impressed with the overall performance of the coils and the realized cost savings.”

-Yince Loh, M.D.

COILS THAT SAVE \$

\$110,000*
SAVED

Images and data courtesy of Yince Loh, M.D., Seattle, WA

* Estimated savings in this case, data on file.

The Barricade Coil System is intended for the endovascular embolization of intracranial aneurysms and other neurovascular abnormalities such as arteriovenous malformations and arteriovenous fistulae. The System is also intended for vascular occlusion of blood vessels within the neurovascular system to permanently obstruct blood flow to an aneurysm or other vascular malformation and for arterial and venous embolizations in the peripheral vasculature. Refer to the instructions for use for complete product information.

18 TECHNOLOGY DRIVE #169, IRVINE CA 92618 | p: 949.788.1443 | f: 949.788.1444
WWW.BLOCKADEMEDICAL.COM

MKTG-050 Rev. A



Smooth and stable.

Target Detachable Coils deliver consistently smooth deployment and exceptional microcatheter stability. Designed to work seamlessly together for framing, filling and finishing. Target Coils deliver the high performance you demand.

For more information, please visit www.strykerneurovascular.com/Target or contact your local Stryker Neurovascular sales representative.



Target®
DETACHABLE COILS

The Foundation of the ASNR Symposium 2017: *Discovery and Didactics* April 22-23, 2017

ASNR 55th Annual Meeting: *Diagnosis and Delivery* April 24-27, 2017



Long Beach Convention & Entertainment Center
© Long Beach Convention & Visitors Bureau

Jacqueline A. Bello, MD, FACR
ASNR 2017 Program Chair/President-Elect

*Programming developed in cooperation with and
appreciation of the...*

American Society of Functional Neuroradiology (ASFNR)
Kirk M. Welker, MD

American Society of Head and Neck Radiology (ASHNR)
Rebecca S. Cornelius, MD, FACR

American Society of Pediatric Neuroradiology (ASPNR)
Susan Palasis, MD

American Society of Spine Radiology (ASSR)
Joshua A. Hirsch, MD, FACR, FSIR

Society of NeuroInterventional Surgery (SNIS)
Blaise W. Baxter, MD

**American Society of Neuroradiology (ASNR)
Health Policy Committee**
Robert M. Barr, MD, FACR

Computer Sciences & Informatics (CSI) Committee
John L. Go, MD, FACR

Research Scientist Committee
Dikoma C. Shungu, PhD and Timothy, P.L. Roberts, PhD

**The International Hydrocephalus Imaging Working Group
(IHIWG)/CSF Flow Group**
William G. Bradley, Jr., MD, PhD, Harold L. Rekate, MD
and Bryn A. Martin, PhD



ASNR 55th Annual Meeting

c/o American Society of Neuroradiology
800 Enterprise Drive, Suite 205 • Oak Brook, Illinois 60523-4216
Phone: 630-574-0220 • Fax: 630 574-0661 • www.asnr.org/2017



ASFNR ASHNR ASPNR ASSR SNIS

THE FOUNDATION OF THE ASNR



Come to the beach! Please join us in Long Beach, California, April 22-27, 2017, for the 55th Annual Meeting of the ASNR. Known for its 5.5 miles of Pacific Ocean waterfront, this southern California beach resort boasts a blend of city sophistication and seaside serenity. ASNR is delighted to provide a “4D” focus for this meeting, as depicted by our meeting logo: **Discovery and Didactics** for The Foundation of the ASNR Symposium 2017: **Diagnosis and Delivery** for the ensuing Annual Meeting Program.

Centered on Discovery and Didactics, the symposium will feature sessions on “What’s New?” in the role neuroimaging plays defining CNS disease mechanisms and how to best prepare for “What’s Next?” for our subspecialty in terms of training, teaching, and leading the process of lifelong learning. The annual meeting programming will address best practices in Diagnosis and Delivery, as we strive to provide value, promote quality in better health and care and consider cost. Our discussions will consider how to navigate the changing landscape of healthcare reform and reimbursement as subspecialists in a field that is changing at an equally “fast forward” pace!



Hyatt Regency Long Beach
© Hyatt Regency Long Beach



Westin Long Beach
© The Westin Long Beach



AMA Preferred Provider Offers and Services



AMA Preferred Provider Offers and Services

Special offers that fit you and your practice's needs.

Which savings would benefit you the most? Discounts on pharmaceuticals, medical supplies and equipment? Or on travel, practice financing, and financial and insurance services? Now physicians can save in all of these professional and personal categories and more through the AMA Preferred Provider Offers and Services program.

Please activate your 2016 AMA membership by calling **(800) 262-3211** or visit **ama-assn.org/go/join**.



* Subsidiary of the American Medical Association.



American Society of Head & Neck Radiology

Comprehensive Head and Neck Imaging: 50 Years of Progress

September 7 - 11, 2016

Hyatt Regency Washington on Capitol Hill
Washington, D.C.

29.25 AMA PRA Category 1 Credit(s)TM

Four sessions of the meeting program will be submitted for SAM qualification.

**Hands-on US and US-Guided Biopsy Seminar
Saturday, September 10, 2016**

Separate Registration Required
Registration is Limited to 20 Attendees Per Session.

Not accredited for AMA PRA Category 1 Credit(s)TM

Please contact Educational Symposia at 813-806-1000 or ASHNR@edusymp.com or visit www.ASHNR.org for additional information.

AXS Catalyst™ Distal Access Catheter

See package insert for complete indications, complications, warnings, and instructions for use.

INTENDED USE/INDICATIONS FOR USE

The AXS Catalyst Distal Access Catheter is indicated for use in facilitating the insertion and guidance of appropriately sized interventional devices into a selected blood vessel in the peripheral and neurovascular systems. The AXS Catalyst Distal Access Catheter is also indicated for use as a conduit for retrieval devices.

CONTRAINDICATIONS

None known.

ADVERSE EVENTS

Potential adverse events associated with the use of catheters or with the endovascular procedures include, but are not limited to: access site complications, allergic reaction, aneurysm perforation, aneurysm rupture, death, embolism (air, foreign body, plaque, thrombus), hematoma, hemorrhage, infection, ischemia, neurological deficits, pseudoaneurysm, stroke, transient ischemic attack, vasospasm, vessel dissection, vessel occlusion, vessel perforation, vessel rupture, and vessel thrombosis.

WARNING

Contents supplied sterile using an ethylene oxide (EO) process. Do not use if sterile barrier is damaged. If damage is found, call your Stryker Neurovascular representative. For single use only. Do not reuse, reprocess or resterilize. Reuse, reprocessing or resterilization may compromise the structural integrity of the device and/or lead to device failure which, in turn, may result in patient injury, illness or death. Reuse, reprocessing or resterilization may also create a risk of contamination of the device and/or cause patient infection or cross-infection, including, but not limited to, the transmission of infectious disease(s) from one patient to another.

Contamination of the device may lead to injury, illness or death of the patient. After use, dispose of product and packaging in accordance with hospital, administrative and/or local government policy.

- Limited testing has been performed with solutions such as contrast media, and saline. The use of these catheters for delivery of solutions other than the types that have been tested for compatibility is not recommended.
- Not intended for use with power injectors.
- If flow through catheter becomes restricted, do not attempt to clear catheter lumen by infusion. Doing so may cause catheter damage or patient injury. Remove and replace catheter.

- Never advance or withdraw an intravascular device against resistance until the cause of the resistance is determined by fluoroscopy. Movement of the device against resistance could dislodge a clot, perforate a vessel wall, or damage the device.

PRECAUTIONS

- Carefully inspect all devices prior to use. Verify size, length, and condition are suitable for the specific procedure. Do not use a device that has been damaged in any way. Damaged device may cause complications.
- To control the proper introduction, movement, positioning and removal of the catheter within the vascular system, users should employ standard clinical angiographic and fluoroscopic practices and techniques throughout the interventional procedure.
- Use the product prior to the "Use By" date printed on the label.
- To prevent thrombus formation and contrast media crystal formation, maintain a constant infusion of appropriate flush solution through catheter lumen.
- Torquing the catheter may cause damage which could result in kinking or separation of the catheter shaft.

Trevo® XP ProVue Retrievers

See package insert for complete indications, complications, warnings, and instructions for use.

INDICATIONS FOR USE

The Trevo Retriever is intended to restore blood flow in the neurovasculature by removing thrombus in patients experiencing ischemic stroke within 8 hours of symptom onset. Patients who are ineligible for intravenous tissue plasminogen activator (IV t-PA) or who fail IV t-PA therapy are candidates for treatment.

COMPLICATIONS

Procedures requiring percutaneous catheter introduction should not be attempted by physicians unfamiliar with possible complications which may occur during or after the procedure. Possible complications include, but are not limited to, the following: air embolism; hematoma or hemorrhage at puncture site; infection; distal embolization; pain/headache; vessel spasm, thrombosis, dissection, or perforation; emboli; acute occlusion; ischemia; intracranial hemorrhage; false aneurysm formation; neurological deficits including stroke; and death.

COMPATIBILITY

3x20mm retrievers are compatible with Trevo® Pro 14 Microcatheters (REF 90231) and Trevo® Pro 18 Microcatheters (REF 90238). 4x20mm retrievers are compatible with Trevo® Pro 18

Microcatheters (REF 90238). 4x30mm retrievers are compatible with Excelsior® XT-27® Microcatheters (150cm x 6cm straight REF 275081) and Trevo® Pro 18 Microcatheters (REF 90238). 6x25mm Retrievers are compatible with Excelsior® XT-27® Microcatheters (150cm x 6cm straight REF 275081). Compatibility of the Retriever with other microcatheters has not been established. Performance of the Retriever device may be impacted if a different microcatheter is used. Balloon Guide Catheters (such as Merci® Balloon Guide Catheter and FlowGate® Balloon Guide Catheter) are recommended for use during thrombus removal procedures. Retrievers are compatible with the Abbott Vascular DOC® Guide Wire Extension (REF Z2260).

Retrievers are compatible with Boston Scientific RHV (Ref 421242).

WARNINGS

- Contents supplied STERILE, using an ethylene oxide (EO) process. Nonpyrogenic.
- To reduce risk of vessel damage, adhere to the following recommendations:
 - Take care to appropriately size Retriever to vessel diameter at intended site of deployment.
 - Do not perform more than six (6) retrieval attempts in same vessel using Retriever devices.
 - Maintain Retriever position in vessel when removing or exchanging Microcatheter.
- To reduce risk of kinking/fracture, adhere to the following recommendations:
 - Immediately after unsheathing Retriever, position Microcatheter tip marker just proximal to shaped section. Maintain Microcatheter tip marker just proximal to shaped section of Retriever during manipulation and withdrawal.
 - Do not rotate or torque Retriever.
 - Use caution when passing Retriever through stented arteries.
- Do not resterilize and reuse. Structural integrity and/or function may be impaired by reuse or cleaning.
- The Retriever is a delicate instrument and should be handled carefully. Before use and when possible during procedure, inspect device carefully for damage. Do not use a device that shows signs of damage. Damage may prevent device from functioning and may cause complications.
- Do not advance or withdraw Retriever against resistance or significant vasospasm. Moving or torquing device against resistance or significant vasospasm may result in damage to vessel or device. Assess cause of resistance

using fluoroscopy and if needed resheath the device to withdraw.

- If Retriever is difficult to withdraw from the vessel, do not torque Retriever. Advance Microcatheter distally, gently pull Retriever back into Microcatheter, and remove Retriever and Microcatheter as a unit. If undue resistance is met when withdrawing the Retriever into the Microcatheter, consider extending the Retriever using the Abbott Vascular DOC guidewire extension (REF Z2260) so that the Microcatheter can be exchanged for a larger diameter catheter such as a DAC® catheter. Gently withdraw the Retriever into the larger diameter catheter.
- Administer anti-coagulation and anti-platelet medications per standard institutional guidelines.

PRECAUTIONS

- Prescription only – device restricted to use by or on order of a physician.
- Store in cool, dry, dark place.
- Do not use open or damaged packages.
- Use by "Use By" date.
- Exposure to temperatures above 54°C (130°F) may damage device and accessories. Do not autoclave.
- Do not expose Retriever to solvents.
- Use Retriever in conjunction with fluoroscopic visualization and proper anti-coagulation agents.
- To prevent thrombus formation and contrast media crystal formation, maintain a constant infusion of appropriate flush solution between guide catheter and Microcatheter and between Microcatheter and Retriever or guidewire.
- Do not attach a torque device to the shaped proximal end of DOC® Compatible Retriever. Damage may occur, preventing ability to attach DOC® Guide Wire Extension.



Stryker Neurovascular
47900 Bayside Parkway
Fremont, CA 94538

strykerneurovascular.com

Date of Release: MAY/2016

EX_EN_US

Copyright © 2016 Stryker
NV00020190_AA

Target® Detachable Coil

See package insert for complete indications, contraindications, warnings and instructions for use.

INTENDED USE / INDICATIONS FOR USE

Target Detachable Coils are intended to endovascularly obstruct or occlude blood flow in vascular abnormalities of the neurovascular and peripheral vessels.

Target Detachable Coils are indicated for endovascular embolization of:

- Intracranial aneurysms
- Other neurovascular abnormalities such as arteriovenous malformations and arteriovenous fistulae
- Arterial and venous embolizations in the peripheral vasculature

CONTRAINDICATIONS

None known.

POTENTIAL ADVERSE EVENTS

Potential complications include, but are not limited to: allergic reaction, aneurysm perforation and rupture, arrhythmia, death, edema, embolus, headache, hemorrhage, infection, ischemia, neurological/intracranial sequelae, post-embolization syndrome (fever, increased white blood cell count, discomfort), TIA/stroke, vasospasm, vessel occlusion or closure, vessel perforation, dissection, trauma or damage, vessel rupture, vessel thrombosis. Other procedural complications including but not limited to: anesthetic and contrast media risks, hypotension, hypertension, access site complications.

WARNINGS

- Contents supplied STERILE using an ethylene oxide (EO) process. Do not use if sterile barrier is damaged. If damage is found, call your Stryker Neurovascular representative.
- For single use only. Do not reuse, reprocess or resterilize. Reuse, reprocessing or resterilization may compromise the structural integrity of the device and/or lead to device failure which, in turn, may result in patient injury, illness or death. Reuse, reprocessing or resterilization may also create a risk of contamination of the device and/or cause patient infection or cross-infection, including, but not limited to, the transmission of infectious disease(s) from one patient to another. Contamination of the device may lead to injury, illness or death of the patient.

- After use, dispose of product and packaging in accordance with hospital, administrative and/or local government policy.

• This device should only be used by physicians who have received appropriate training in interventional neuroradiology or interventional radiology and preclinical training on the use of this device as established by Stryker Neurovascular.

- Patients with hypersensitivity to 316LVM stainless steel may suffer an allergic reaction to this implant.
- MR temperature testing was not conducted in peripheral vasculature, arteriovenous malformations or fistulae models.
- The safety and performance characteristics of the Target Detachable Coil System (Target Detachable Coils, InZone Detachment Systems, delivery systems and accessories) have not been demonstrated with other manufacturer's devices (whether coils, coil delivery devices, coil detachment systems, catheters, guidewires, and/or other accessories). Due to the potential incompatibility of non Stryker Neurovascular devices with the Target Detachable Coil System, the use of other manufacturer's device(s) with the Target Detachable Coil System is not recommended.
- To reduce risk of coil migration, the diameter of the first and second coil should never be less than the width of the ostium.
- In order to achieve optimal performance of the Target Detachable Coil System and to reduce the risk of thromboembolic complications, it is critical that a continuous infusion of appropriate flush solution be maintained between a) the femoral sheath and guiding catheter, b) the 2-tip microcatheter and guiding catheters, and c) the 2-tip microcatheter and Stryker Neurovascular guidewire and delivery wire. Continuous flush also reduces the potential for thrombus formation on, and crystallization of infusate around, the detachment zone of the Target Detachable Coil.
- Do not use the product after the "Use By" date specified on the package.
- Reuse of the flush port/dispenser coil or use with any coil other than the original coil may result in contamination of, or damage to, the coil.
- Utilization of damaged coils may affect coil delivery to, and stability inside, the vessel or aneurysm, possibly resulting in coil migration and/or stretching.
- The fluoro-saver marker is designed for use with a Rotating Hemostatic Valve (RHV). If used without an RHV, the distal end of the coil may be beyond the alignment

marker when the fluoro-saver marker reaches the microcatheter hub.

- If the fluoro-saver marker is not visible, do not advance the coil without fluoroscopy.
- Do not rotate delivery wire during or after delivery of the coil. Rotating the Target Detachable Coil delivery wire may result in a stretched coil or premature detachment of the coil from the delivery wire, which could result in coil migration.
- Verify there is no coil loop protrusion into the parent vessel after coil placement and prior to coil detachment. Coil loop protrusion after coil placement may result in thromboembolic events if the coil is detached.
- Verify there is no movement of the coil after coil placement and prior to coil detachment. Movement of the coil after coil placement may indicate that the coil could migrate once it is detached.
- Failure to properly close the RHV compression fitting over the delivery wire before attaching the InZone® Detachment System could result in coil movement, aneurysm rupture or vessel perforation.
- Verify repeatedly that the distal shaft of the catheter is not under stress before detaching the Target Detachable Coil. Axial compression or tension forces could be stored in the 2-tip microcatheter causing the tip to move during coil delivery. Microcatheter tip movement could cause the aneurysm or vessel to rupture.
- Advancing the delivery wire beyond the microcatheter tip once the coil has been detached involves risk of aneurysm or vessel perforation.
- The long term effect of this product on extravascular tissues has not been established so care should be taken to retain this device in the intravascular space.

Damaged delivery wires may cause detachment failures, vessel injury or unpredictable distal tip response during coil deployment. If a delivery wire is damaged at any point during the procedure, do not attempt to straighten or otherwise repair it. Do not proceed with deployment or detachment. Remove the entire coil and replace with undamaged product.

- After use, dispose of product and packaging in accordance with hospital, administrative and/or local government policy.

CAUTIONS / PRECAUTIONS

- Federal Law (USA) restricts this device to sale by or on the order of a physician.
- Besides the number of InZone Detachment System units needed to complete the case, there must be an extra

InZone Detachment System unit as back up.

- Removing the delivery wire without grasping the introducer sheath and delivery wire together may result in the detachable coil sliding out of the introducer sheath.
- Failure to remove the introducer sheath after inserting the delivery wire into the RHV of the microcatheter will interrupt normal infusion of flush solution and allow back flow of blood into the microcatheter.
- Some low level overhead light near or adjacent to the patient is required to visualize the fluoro-saver marker; monitor light alone will not allow sufficient visualization of the fluoro-saver marker.
- Advance and retract the Target Detachable Coil carefully and smoothly without excessive force. If unusual friction is noticed, slowly withdraw the Target Detachable Coil and examine for damage. If damage is present, remove and use a new Target Detachable Coil. If friction or resistance is still noted, carefully remove the Target Detachable Coil and microcatheter and examine the microcatheter for damage.
- If it is necessary to reposition the Target Detachable Coil, verify under fluoroscopy that the coil moves with a one-to-one motion. If the coil does not move with a one-to-one motion or movement is difficult, the coil may have stretched and could possibly migrate or break. Gently remove both the coil and microcatheter and replace with new devices.
- Increased detachment times may occur when:
 - Other embolic agents are present.
 - Delivery wire and microcatheter markers are not properly aligned.
 - Thrombus is present on the coil detachment zone.
- Do not use detachment systems other than the InZone Detachment System.
- Increased detachment times may occur when delivery wire and microcatheter markers are not properly aligned.
- Do not use detachment systems other than the InZone Detachment System.



Stryker Neurovascular
47900 Bayside Parkway
Fremont, CA 94538

strykerneurovascular.com

Date of Release: MAR/2016

EX_EN_US

Copyright © 2016 Stryker
NV00018669_AA



Aneurysm
Therapy Solutions

A 360-Degree Approach to Performance Based Solutions

microvention.com

MICROVENTION is a registered trademark of MicroVention, Inc. Scientific and clinical data related to this document are on file at MicroVention, Inc. Refer to Instructions for Use for additional information. Federal (USA) law restricts this device for sale by or on the order of a physician.
© 2016 MicroVention, Inc. 08/16

Take on tortuosity.

The **AXS Catalyst™ Distal Access Catheter** family is designed for easy navigation in challenging cases.



AXS Catalyst 6

DISTAL ACCESS CATHETER

for rapid revascularization with
Trepo[®] XP ProVue Retriever

AXS Catalyst 5

DISTAL ACCESS CATHETER

for flow diversion support

ACCLINO[®] flex Stent



Not for sale within the territory of the United States

HIGH FLEXIBILITY

- For microcatheters with 0.017" ID (Ø 3.5 and 4.5 mm) and 0.021" ID (Ø 6.5 mm)
- Repositionable up to 90 %

AJNR

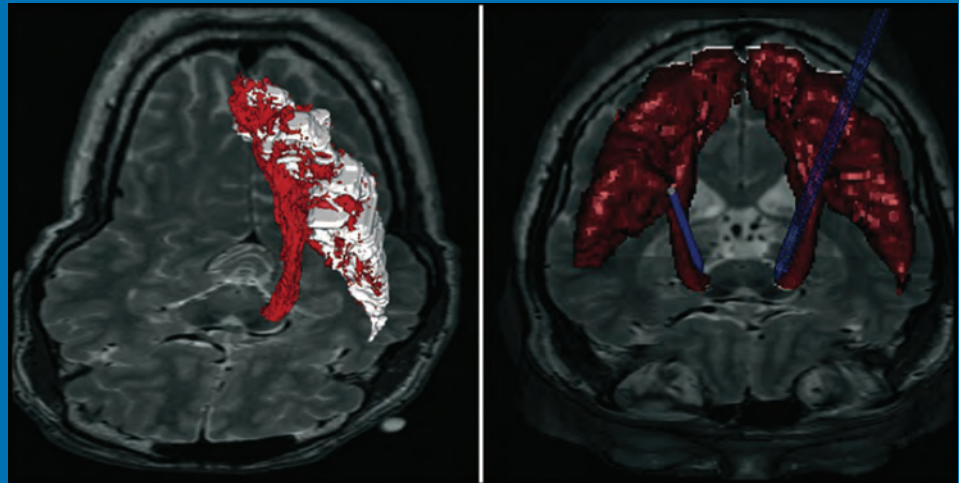
AMERICAN JOURNAL OF NEURORADIOLOGY

AUGUST 2016
VOLUME 37
NUMBER 8
WWW.AJNR.ORG

THE JOURNAL OF DIAGNOSTIC AND
INTERVENTIONAL NEURORADIOLOGY

Validation of DTI tractography
Comparison of sequences to visualize spinal cord MS
Imaging of neurovascular compression syndromes

Official Journal ASNR • ASFNR • ASHNR • ASPNR • ASSR



AJNR

AMERICAN JOURNAL OF NEURORADIOLOGY

AUGUST 2016
VOLUME 37
NUMBER 8
WWW.AJNR.ORG

Publication Preview at www.ajnr.org features articles released in advance of print. Visit www.ajnrblog.org to comment on AJNR content and chat with colleagues and AJNR's News Digest at <http://ajnrndigest.org> to read the stories behind the latest research in neuroimaging.

1383 **PERSPECTIVES** *B. Thomas*

REVIEW ARTICLE



1384 **Imaging of Neurovascular Compression Syndromes: Trigeminal Neuralgia, Hemifacial Spasm, Vestibular Paroxysmia, and Glossopharyngeal Neuralgia** *S. Haller, et al.*

ADULT BRAIN
HEAD & NECK

GENERAL CONTENTS



1393 **Multimodal CT Imaging: Time to Treatment and Outcomes in the IMS III Trial** *A. Vagal, et al.*

ADULT BRAIN

1399 **Performance of CT ASPECTS and Collateral Score in Risk Stratification: Can Target Perfusion Profiles Be Predicted without Perfusion Imaging?** *S. Dehkharghani, et al.*

ADULT BRAIN



1405 **MR Imaging in Spinocerebellar Ataxias: A Systematic Review** *A. Klaes, et al.*

ADULT BRAIN

1413 **Geometric Parameter Analysis of Ruptured and Unruptured Aneurysms in Patients with Symmetric Bilateral Intracranial Aneurysms: A Multicenter CT Angiography Study** *Z.-Q. Huang, et al.*

ADULT BRAIN
INTERVENTIONAL



1418 **MRI Appearance of Intracerebral Iodinated Contrast Agents: Is It Possible to Distinguish Extravasated Contrast Agent from Hemorrhage?** *O. Nikoubashman, et al.*

ADULT BRAIN
INTERVENTIONAL



1422 **Prevalence of Intracranial Aneurysms in Patients with Connective Tissue Diseases: A Retrospective Study** *S.T. Kim, et al.*

ADULT BRAIN



1427 **T1 Signal-Intensity Increase in the Dentate Nucleus after Multiple Exposures to Gadodiamide: Intraindividual Comparison between 2 Commonly Used Sequences** *J. Ramalho, et al.*

ADULT BRAIN



1432 **Characteristics of Diffusional Kurtosis in Chronic Ischemia of Adult Moyamoya Disease: Comparing Diffusional Kurtosis and Diffusion Tensor Imaging** *K. Kazumata, et al.*

ADULT BRAIN



1440 **Improved Leakage Correction for Single-Echo Dynamic Susceptibility Contrast Perfusion MRI Estimates of Relative Cerebral Blood Volume in High-Grade Gliomas by Accounting for Bidirectional Contrast Agent Exchange** *K. Leu, et al.*

ADULT BRAIN
FUNCTIONAL

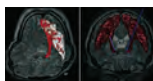


1447 **Lesion Heterogeneity on High-Field Susceptibility MRI Is Associated with Multiple Sclerosis Severity** *D.M. Harrison, et al.*

ADULT BRAIN

AJNR (Am J Neuroradiol ISSN 0195-6108) is a journal published monthly, owned and published by the American Society of Neuroradiology (ASNR), 800 Enterprise Drive, Suite 205, Oak Brook, IL 60523. Annual dues for the ASNR include \$170.00 for journal subscription. The journal is printed by Cadmus Journal Services, 5457 Twin Knolls Road, Suite 200, Columbia, MD 21045; Periodicals postage paid at Oak Brook, IL and additional mailing offices. Printed in the U.S.A. POSTMASTER: Please send address changes to American Journal of Neuroradiology, P.O. Box 3000, Denville, NJ 07834, U.S.A. Subscription rates: nonmember \$380 (\$450 foreign) print and online, \$305 online only; institutions \$440 (\$510 foreign) print and basic online, \$875 (\$940 foreign) print and extended online, \$365 online only (basic), extended online \$790; single copies are \$35 each (\$40 foreign). Indexed by PubMed/Medline, BIOSIS Previews, Current Contents (Clinical Medicine and Life Sciences), EMBASE, Google Scholar, HighWire Press, Q-Sensei, RefSeek, Science Citation Index, and SCI Expanded. Copyright © American Society of Neuroradiology.

-    1454 **Cortical Perfusion Alteration in Normal-Appearing Gray Matter Is Most Sensitive to Disease Progression in Relapsing-Remitting Multiple Sclerosis** *S.-P. Hojjat, et al.* **ADULT BRAIN**
-    1462 **A Diffusion Tensor Imaging Study on White Matter Abnormalities in Patients with Type 2 Diabetes Using Tract-Based Spatial Statistics** *Y. Xiong, et al.* **ADULT BRAIN**
-   1470 **Electrophysiologic Validation of Diffusion Tensor Imaging Tractography during Deep Brain Stimulation Surgery** *V.A. Coenen, et al.* **ADULT BRAIN**
- 1479 **Neurovascular Manifestations of Hereditary Hemorrhagic Telangiectasia: A Consecutive Series of 376 Patients during 15 Years** *W. Brinjikji, et al.* **ADULT BRAIN
INTERVENTIONAL
PEDIATRICS**
-  1487 **Reduced Myelin Water in the White Matter Tracts of Patients with Niemann-Pick Disease Type C** *J. Davies-Thompson, et al.* **ADULT BRAIN
PEDIATRICS**
-  1490 **Fate of Coiled Aneurysms with Minor Recanalization at 6 Months: Rate of Progression to Further Recanalization and Related Risk Factors** *J.P. Jeon, et al.* **INTERVENTIONAL
ADULT BRAIN**
-  1496 **Prediction of Carotid Intraplaque Hemorrhage Using Adventitial Calcification and Plaque Thickness on CTA** *L.B. Eisenmenger, et al.* **EXTRACRANIAL
VASCULAR**
- 1504 **Do Radiologists Report the TNM Staging in Radiology Reports for Head and Neck Cancers? A National Survey Study** *B. Ko, et al.* **HEAD & NECK**
-  1510 **Reduced Field-of-View Diffusion Tensor Imaging of the Optic Nerve in Retinitis Pigmentosa at 3T** *Y. Zhang, et al.* **HEAD & NECK
ADULT BRAIN
FUNCTIONAL**
- 1516 **A New Ultrasound Marker for Bedside Monitoring of Preterm Brain Growth** *J.A. Roelants, et al.* **PEDIATRICS**
-  1523 **MR Imaging of the Pituitary Gland and Postsphenoid Ossification in Fetal Specimens** *T.M. Mehemed, et al.* **PEDIATRICS**
-  1528 **Quiet T1-Weighted Pointwise Encoding Time Reduction with Radial Acquisition for Assessing Myelination in the Pediatric Brain** *N. Aida, et al.* **PEDIATRICS**
- 1535 **Cranial Ultrasonography in Infantile Encephalitic Beriberi: A Useful First-Line Imaging Tool for Screening and Diagnosis in Suspected Cases** *N.A. Wani, et al.* **PEDIATRICS**
- 1541 **Spectrum of Clinical and Associated MR Imaging Findings in Children with Olfactory Anomalies** *T.N. Booth, et al.* **PEDIATRICS
HEAD & NECK**
-  1549 **Reduction of Oxygen-Induced CSF Hyperintensity on FLAIR MR Images in Sedated Children: Usefulness of Magnetization-Prepared FLAIR Imaging** *H.-K. Jeong, et al.* **PEDIATRICS**
-  1556 **Effect of the Suboccipital Musculature on Symptom Severity and Recovery after Mild Traumatic Brain Injury** *S. Fakhran, et al.* **SPINE
ADULT BRAIN**
-  1561 **Evaluation of Focal Cervical Spinal Cord Lesions in Multiple Sclerosis: Comparison of White Matter–Suppressed T1 Inversion Recovery Sequence versus Conventional STIR and Proton Density–Weighted Turbo Spin-Echo Sequences** *D.K. Sundarakumar, et al.* **SPINE**
- 1567 **SAPHO Syndrome: Imaging Findings of Vertebral Involvement** *A.M. McGauvran, et al.* **SPINE**



Left image shows a 3D rendition of the left corticospinal tract depicted as a DICOM hull structure. Right image shows the transferred DICOM structure within the planning software. Blue represents the tested electrode positions.

BOOK REVIEWS *R.M. Quencer, Section Editor*

Please visit www.ajnrblog.org to read and comment on Book Reviews.

-  Indicates Editor's Choices selection
-  Indicates Fellows' Journal Club selection
-  Indicates open access to non-subscribers at www.ajnr.org
-  Indicates article with supplemental on-line table
-  Indicates article with supplemental on-line photo
-  Indicates article with supplemental on-line video
-  Evidence-Based Medicine Level 1
-  Evidence-Based Medicine Level 2

Official Journal:

American Society of Neuroradiology
American Society of Functional Neuroradiology
American Society of Head and Neck Radiology
American Society of Pediatric Neuroradiology
American Society of Spine Radiology

EDITOR-IN-CHIEF

Jeffrey S. Ross, MD

Professor of Radiology, Department of Radiology,
Mayo Clinic College of Medicine, Phoenix, AZ

SENIOR EDITORS

Harry J. Cloft, MD, PhD

Professor of Radiology and Neurosurgery,
Department of Radiology, Mayo Clinic College of
Medicine, Rochester, MN

Thierry A.G.M. Huisman, MD

Professor of Radiology, Pediatrics, Neurology, and
Neurosurgery, Chairman, Department of Imaging
and Imaging Science, Johns Hopkins Bayview,
Director, Pediatric Radiology and Pediatric
Neuroradiology, Johns Hopkins Hospital,
Baltimore, MD

C.D. Phillips, MD, FACR

Professor of Radiology, Weill Cornell Medical
College, Director of Head and Neck Imaging,
New York-Presbyterian Hospital, New York, NY

Pamela W. Schaefer, MD

Clinical Director of MRI and Associate Director of
Neuroradiology, Massachusetts General Hospital,
Boston, Massachusetts, Associate Professor,
Radiology, Harvard Medical School, Cambridge, MA

Charles M. Strother, MD

Professor of Radiology, Emeritus, University of
Wisconsin, Madison, WI

Jody Tanabe, MD

Professor of Radiology and Psychiatry,
Chief of Neuroradiology,
University of Colorado, Denver, CO

STATISTICAL SENIOR EDITOR

Bryan A. Comstock, MS

Senior Biostatistician,
Department of Biostatistics,
University of Washington, Seattle, WA

EDITORIAL BOARD

Ashley H. Aiken, *Atlanta, GA*
Lea M. Alhilali, *Phoenix, AZ*
John D. Barr, *Dallas, TX*
Ari Blitz, *Baltimore, MD*
Barton F. Branstetter IV, *Pittsburgh, PA*
Jonathan L. Brisman, *Lake Success, NY*
Julie Bykowski, *San Diego, CA*
Keith Cauley, *Danville, PA*
Asim F. Choudhri, *Memphis, TN*
Alessandro Cianfoni, *Lugano, Switzerland*
J. Matthew Debnam, *Houston, TX*
Seena Dehkharghani, *New York, NY*
Colin Derdeyn, *Iowa City, IA*
Rahul S. Desikan, *San Francisco, CA*
Yonghong Ding, *Rochester, MN*
Clifford J. Eskey, *Hanover, NH*
Saeed Fakhran, *Phoenix, AZ*
Massimo Filippi, *Milan, Italy*
Allan J. Fox, *Toronto, Ontario, Canada*
Wende N. Gibbs, *Los Angeles, CA*
Christine M. Glastonbury, *San Francisco, CA*
John L. Go, *Los Angeles, CA*
Allison Grayev, *Madison, WI*
Brent Griffith, *Detroit, MI*
Wan-Yuo Guo, *Taipei, Taiwan*
Ajay Gupta, *New York, NY*
Rakesh K. Gupta, *Lucknow, India*
Lotfi Hacein-Bey, *Sacramento, CA*
Christopher P. Hess, *San Francisco, CA*
Andrei Holodny, *New York, NY*
Benjamin Huang, *Chapel Hill, NC*
George J. Hunter, *Boston, MA*
Mahesh V. Jayaraman, *Providence, RI*
Valerie Jewells, *Chapel Hill, NC*
Christof Karmonik, *Houston, TX*
Timothy J. Kaufmann, *Rochester, MN*
Hillary R. Kelly, *Boston, MA*
Toshibumi Kinoshita, *Akita, Japan*
Kenneth F. Layton, *Dallas, TX*
Michael M. Lell, *Nürnberg, Germany*
Michael Lev, *Boston, MA*
Karl-Olof Lovblad, *Geneva, Switzerland*
Franklin A. Marden, *Chicago, IL*
M. Gisele Matheus, *Charleston, SC*
Joseph C. McGowan, *Merion Station, PA*
Stephan Meckel, *Freiburg, Germany*
Christopher J. Moran, *St. Louis, MO*
Takahisa Mori, *Kamakura City, Japan*
Suresh Mukherji, *Ann Arbor, MI*
Amanda Murphy, *Toronto, Ontario, Canada*
Alexander J. Nemeth, *Chicago, IL*
Sasan Partovi, *Cleveland, OH*
Laurent Pierot, *Reims, France*
Jay J. Pillai, *Baltimore, MD*
Whitney B. Pope, *Los Angeles, CA*

Andrea Poretti, *Baltimore, MD*
M. Judith Donovan Post, *Miami, FL*
Tina Young Poussaint, *Boston, MA*
Joana Ramalho, *Lisbon, Portugal*
Otto Rapalino, *Boston, MA*
Álex Rovira-Cañellas, *Barcelona, Spain*
Paul M. Ruggieri, *Cleveland, OH*
Zoran Rumboldt, *Rijeka, Croatia*
Amit M. Saindane, *Atlanta, GA*
Erin Simon Schwartz, *Philadelphia, PA*
Lubdha M. Shah, *Salt Lake City, UT*
Aseem Sharma, *St. Louis, MO*
J. Keith Smith, *Chapel Hill, NC*
Maria Vittoria Spampinato, *Charleston, SC*
Gordon K. Sze, *New Haven, CT*
Krishnamoorthy Thamburaj, *Hershey, PA*
Cheng Hong Toh, *Taipei, Taiwan*
Thomas A. Tomsick, *Cincinnati, OH*
Aquila S. Turk, *Charleston, SC*
Willem Jan van Rooij, *Tilburg, Netherlands*
Arastoo Vossough, *Philadelphia, PA*
Elysa Widjaja, *Toronto, Ontario, Canada*
Max Wintermark, *Stanford, CA*
Ronald L. Wolf, *Philadelphia, PA*
Kei Yamada, *Kyoto, Japan*
Carlos Zamora, *Chapel Hill, NC*

EDITORIAL FELLOW

Daniel S. Chow, *San Francisco, CA*

SPECIAL CONSULTANTS TO THE EDITOR

AJNR Blog Editor

Neil Lall, *Denver, CO*

Case of the Month Editor

Nicholas Stence, *Aurora, CO*

Case of the Week Editors

Juan Pablo Cruz, *Santiago, Chile*
Sapna Rawal, *Toronto, Ontario, Canada*

Classic Case Editor

Sandy Cheng-Yu Chen, *Taipei, Taiwan*

Facebook Editor

Peter Yi Shen, *Sacramento, CA*

Health Care and Socioeconomics Editor

Pina C. Sanelli, *New York, NY*

Physics Editor

Greg Zaharchuk, *Stanford, CA*

Podcast Editor

Yvonne Lui, *New York, NY*

Twitter Editor

Ryan Fitzgerald, *Little Rock, AR*

YOUNG PROFESSIONALS ADVISORY COMMITTEE

Asim K. Bag, *Birmingham, AL*
Anna E. Nidecker, *Sacramento, CA*
Peter Yi Shen, *Sacramento, CA*

Founding Editor
Juan M. Taveras

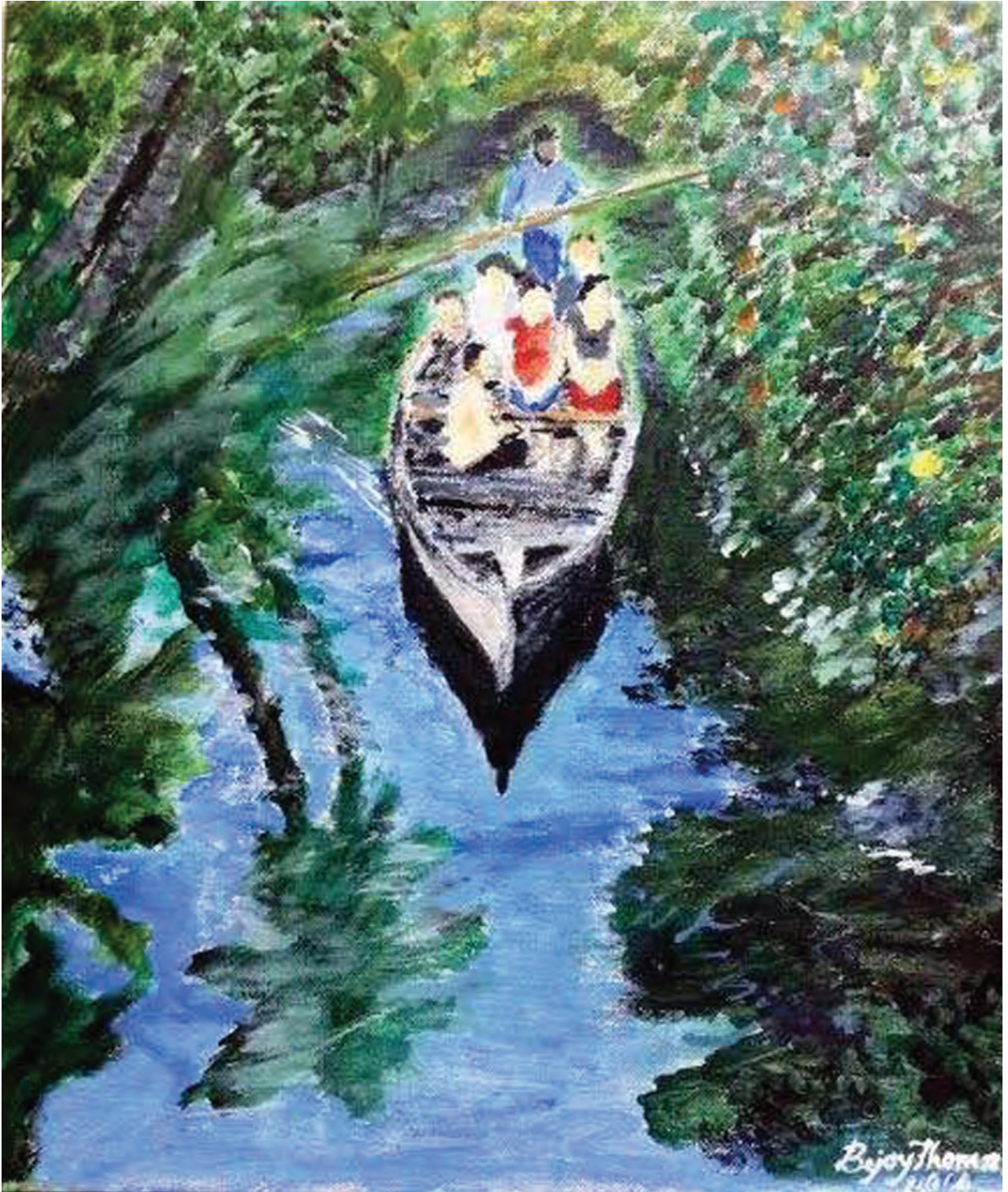
Editors Emeriti
Mauricio Castillo, Robert I. Grossman,
Michael S. Huckman, Robert M. Quencer

Managing Editor
Karen Halm

Assistant Managing Editor
Laura Wilhelm

Executive Director, ASNR
James B. Gantenberg

Director of Communications, ASNR
Angelo Artemakis



Title: Backwater Cruise in God's Own Country. Acrylic on canvas, 15" × 12". More of Dr. Thomas' work can be viewed at <http://bejoythomas.weebly.com/>.

Bejoy Thomas, MD, DNB, PDCC, Trivandrum, Kerala, India

Imaging of Neurovascular Compression Syndromes: Trigeminal Neuralgia, Hemifacial Spasm, Vestibular Paroxysmia, and Glossopharyngeal Neuralgia

 S. Haller,  L. Etienne,  E. Kövari,  A.D. Varoquaux,  H. Urbach, and  M. Becker



ABSTRACT

SUMMARY: Neurovascular compression syndromes are usually caused by arteries that directly contact the cisternal portion of a cranial nerve. Not all cases of neurovascular contact are clinically symptomatic. The transition zone between the central and peripheral myelin is the most vulnerable region for symptomatic neurovascular compression syndromes. Trigeminal neuralgia (cranial nerve V) has an incidence of 4–20/100,000, a transition zone of 4 mm, with symptomatic neurovascular compression typically proximal. Hemifacial spasm (cranial nerve VII) has an incidence of 1/100,000, a transition zone of 2.5 mm, with symptomatic neurovascular compression typically proximal. Vestibular paroxysmia (cranial nerve VIII) has an unknown incidence, a transition zone of 11 mm, with symptomatic neurovascular compression typically at the internal auditory canal. Glossopharyngeal neuralgia (cranial nerve IX) has an incidence of 0.5/100,000, a transition zone of 1.5 mm, with symptomatic neurovascular compression typically proximal. The transition zone overlaps the root entry zone close to the brain stem in cranial nerves V, VII, and IX, yet it is more distal and does not overlap the root entry zone in cranial nerve VIII. Although symptomatic neurovascular compression syndromes may also occur if the neurovascular contact is outside the transition zone, symptomatic neurovascular compression syndromes are more common if the neurovascular contact occurs at the transition zone or central myelin section, in particular when associated with nerve displacement and atrophy.

ABBREVIATIONS: AICA = anterior inferior cerebellar artery; CN = cranial nerve; GN = glossopharyngeal neuralgia; HFS = hemifacial spasm; NVC = neurovascular compression; NVCS = neurovascular compression syndrome; REZ = root entry/exit zone; TN = trigeminal neuralgia; TZ = transition zone

Neurovascular compression syndrome (NVCS) is defined as a direct contact with mechanical irritation of cranial nerves (CNs) by blood vessels.^{1–5} The most common neurovascular compression syndromes are trigeminal neuralgia (TN; compression of CN V), hemifacial spasm (HFS; CN VII), vestibulocochlear neuralgia (CN VIII), and glossopharyngeal neuralgia (GN; CN IX). Because neurovascular contacts are frequent imaging findings in asymptomatic patients, several factors will determine whether a neurovascular contact may become symptomatic. First, arteries are more likely to cause symptomatic NVCS than veins,

presumably due to the higher pressure and pulsatility.^{5,6} Second, the anatomic location of the neurovascular contact can also be a relevant factor.

Cranial nerves are surrounded by a myelin sheath, which provides insulating and metabolic support for the axon. Oligodendrocytes form the myelin in the central nervous system, whereas Schwann cells form the myelin in the peripheral nervous system. The transition zone (TZ) between central and peripheral myelin⁷ is an anatomic area with increased mechanical vulnerability, which is of particular interest in the context of symptomatic NVCS.⁸ Skinner⁹ already demonstrated in 1931 that the length and location of the TZ varies between cranial nerves, with CN VIII having a long and distal TZ in comparison with CNs V, VII, and IX. The term “root entry/exit zone” (REZ) is often used in the context of NVCS.¹⁰ In some publications, the term “REZ” is used as a synonym for TZ, whereas in other publications, the term “REZ” is used to define the portion of the nerve that includes the TZ, the central myelin root portion, and the adjacent brain stem surface¹¹; the 2 terms should, therefore, not be used interchangeably.⁸ The TZ appears to be the more relevant and vulnerable anatomic structure, and it is not always located in the same position as the REZ. For example, in the vestibulocochlear nerve (CN

From the Faculty of Medicine (S.H.), University of Geneva, Geneva, Switzerland; Centre de Diagnostique Radiologique de Carouge (S.H.), Carouge, Switzerland; Departments of Surgical Sciences and Radiology (S.H.), Uppsala University, Uppsala, Sweden; Department of Neuroradiology (S.H., H.U.), University Hospital Freiburg, Germany; Departments of Radiology (L.E., M.B.) and Psychiatry (E.K.), Geneva University Hospitals, Geneva, Switzerland; and Department of Radiology (A.D.V.), University Hospital La Timone, Marseille, France.

Please address correspondence to Sven Haller, MD, MSc, Affidea Centre de Diagnostique Radiologique de Carouge, Clos de la Fonderie 1, 1227 Carouge, Switzerland; e-mail: sven.haller@me.com

 Indicates open access to non-subscribers at www.ajnr.org

 Indicates article with supplemental on-line video.

<http://dx.doi.org/10.3174/ajnr.A4683>

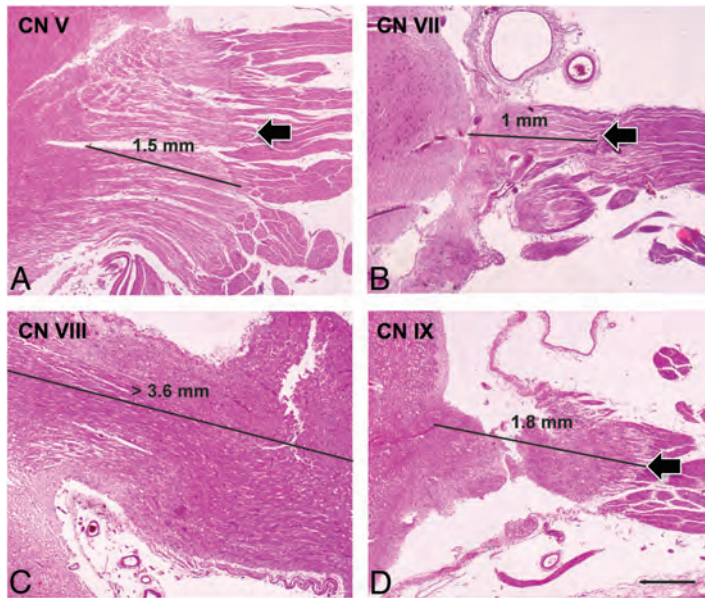


FIG 1. Histologic images of the transition zone of the trigeminal (CN V, A), facial (CN VII, B), vestibulocochlear (CN VIII, C), and glossopharyngeal (CN IX, D) nerves. Note the very distal TZ of CN VIII, which is beyond the field that can be analyzed with the current methodology compared with CNs V, VII, and IX (hematoxylin-eosin, scale bar on D = 0.5 mm).

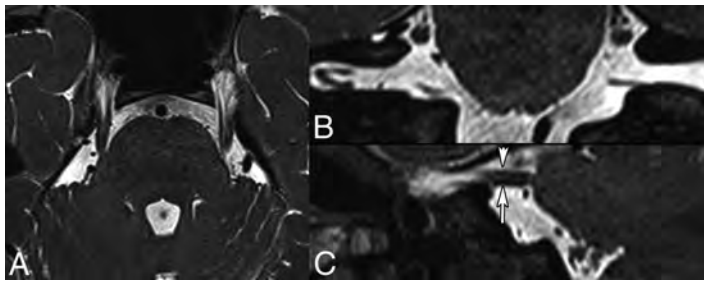


FIG 2. Normal anatomy of the cisternal segment of CN V obtained at 3T. Axial 0.6-mm thin-section (A), coronal (B), and sagittal (C) 2D reconstructions (same thickness) from a 3D T2-weighted balanced steady-state free precession sequence. Note that multiple individual nerve fibers can be identified in both cisternal CN Vs. The *short arrow* in C points to the motor root of the left CN V, while the *long arrow* points to the sensory root.

VIII), the TZ is clearly distal to the REZ. In the current article, we, therefore, focus on the TZ.

Exact anatomic knowledge of the position and morphology of the TZ is of fundamental importance for the interpretation of neuroimaging findings in suspected NVCS (Fig 1). This review highlights current evidence regarding the TZ and implications for imaging. We also provide illustrative cases of normal anatomy and histologic sections from postmortem specimens for the understanding of the etiology of NVCS, as well as surgically proven cases of NVCS involving CNs V, VII, VIII, and IX.

Imaging Recommendations

The combination of high-resolution 3D T2-weighted imaging with 3D time-of-flight angiography and 3D T1-weighted gadolinium-enhanced sequences is considered the standard of reference for the detection of neurovascular compression (NVC).¹²⁻¹⁶ This combination can successfully guide neurosurgical treatment and may predict treatment response.¹⁷⁻¹⁹ A variety of high-resolution 3D heavily T2-weighted sequences is currently available, includ-

ing CISS; FIESTA; balanced steady-state free precession; driven equilibrium and radiofrequency reset pulse; and sampling perfection with application-optimized contrasts by using different flip angle evolution (SPACE sequence; Siemens, Erlangen, Germany), providing accurate visualization of the cisternal portion of the involved CN. Multiplanar oblique reconstructions and fusion of 3D T2-weighted sequences with corresponding TOF images or 3D T1-weighted gadolinium-enhanced images are very useful in the preoperative context. More recently, diffusion tensor imaging with tractography has been increasingly used, mainly in trigeminal neuralgia.^{15,20,21}

Trigeminal Nerve (CN V)

Anatomic Considerations. CN V is a mixed nerve responsible for the sensory innervation of the face and motor functions of the masticatory muscles and tensor veli palatine muscle. It has 3 main branches: the ophthalmic (V1), the maxillary (V2), and the mandibular (V3) nerve. These 3 branches join the Gasserian ganglion in the Meckel cave. The Gasserian ganglion transmits the sensory information to the brain stem via the cisternal portion (Figs 2 and 3). NVCS occurs at the cisternal portion. The cisternal portion measures between 8 and 15 mm in length, and the zone with central myelin (distance from brain stem to the TZ) is shorter on the medial

side of the nerve (1.13 mm) than on its lateral side (2.47 mm).⁸ A histologic study in fresh cadavers has shown that the TZ measures about 2 mm in length and the most distal part of the TZ is at 4.19 ± 0.81 mm away from the brain stem (Fig 1 and Table 1).¹¹ The reported volume of the normal cisternal CN V measured on 3T MR imaging *in vivo* is $77.4\text{--}78$ mm³ in men and $66.1\text{--}66.4$ mm³ in women, with no statistically significant difference found between the left and right.²² With current MR imaging technology, it is also possible to visualize 1 (51.2%), 2 (37.5%) or even 3 (11.2%) small motor roots that typically emerge from the pons anterosuperomedially to the entry point of the large sensory root (Fig 2).¹³

Trigeminal Neuralgia. The most common cause of trigeminal neuralgia is NVCS; however, other etiologies, such as neoplastic, inflammatory, and infectious conditions or trauma, may exist as well. Patients with “classic” or “idiopathic” TN have recurrent episodes of stabbing pain in the territory of V1 or V2. The pain is triggered by mild stimulation of a small area of the face (“trigger zone”) by everyday activities, such as brushing teeth, shaving, eat-

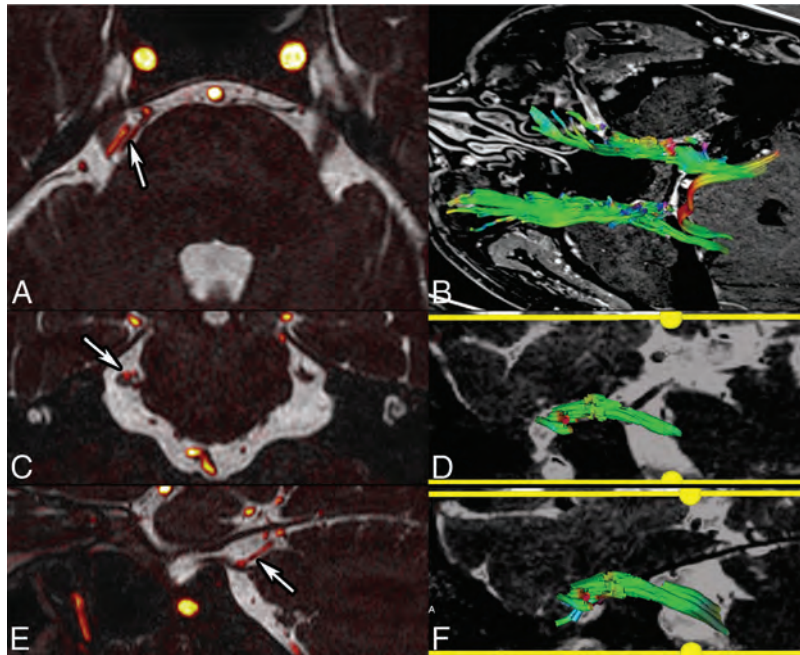


FIG 3. NVCS in a 55-year-old woman with right TN. Fusion of CISS (0.6-mm sections) and TOF angiography sequences (A, axial; C, coronal; E, sagittal) show contact between the duplicated superior cerebellar artery and the superior portion of the cisternal CN V (arrows). Tractography reconstruction from DTI (B, superior view; D, right CN V; F, left CN V) shows a slightly diminished number of fibers on the right, as opposed to the left. Fiber color-coding is the following: antero-posterior = green; left-right = red; craniocaudal = blue. Fractional anisotropy measurements show diminished values on the right.

Table 1: Cisternal length and transition zone of cranial nerves V, VII, VIII, and IX^a

	Cisternal Length	TZ
CN V: trigeminal nerve	8–15 mm ^b	1.13 mm (medial) ^b
	13.11 ± 1.12 mm (range, 11.9–15.2 mm) ^c	2.47 mm (lateral) ^b
CN VII: facial nerve	Motor root, 2–20 mm ^d	4.19 ± 0.81 mm ^c
	17.93 ± 2.29 mm (range, 14.8–20.9 mm) ^c	2.86 ± 1.19 mm ^c
	9.9 ± 3.03 mm (range, 4.78–20.13 mm) lateral side ^e	1.9 ± 1.14 ^e
CN VIII: vestibulocochlear nerve	16.48 ± 1.78 mm (range, 14.2–19.2 mm) ^f	11.50 ± 1.56 mm ^f
CN IX: glossopharyngeal nerve	16.36 ± 2.53 mm (range, 14.2–19.9 mm) ^c	1.51 ± 0.39 mm ^c

^a Values are mean ± standard deviation in mm (and range in mm).

^b Peker et al.⁸

^c Guclu et al.¹¹

^d Yousry et al.¹³

^e Tomii et al.⁴⁶

^f Guclu et al.⁵³

Table 2: Incidence of symptomatic neurovascular compression syndromes

	NVCS	Incidence
CN V	Trigeminal neuralgia	4.3/100,000 ^a
		4–20/100,000 ^b
CN VII	Hemifacial spasm	0.77/100,000 ^c
CN VIII	Vestibular paroxysmia	–
CN IX	Glossopharyngeal neuralgia	0.062/100,000 ^d
		0.2–0.7/100,000 ^b

^a Katusic et al.²⁴

^b Manzoni and Torelli.²⁵

^c Auger and Whisnant.⁴⁹

^d Spurling and Grantham.⁵⁸

ing, or applying makeup. Typically, no neurologic deficits are clinically evident. Between attacks, most patients are usually pain-free. However, the longer the TN lasts, the more intense the pain becomes and the more frequent the attacks are. When patients

present a steady component or mild sensory loss between the attacks, the term “atypical TN” is used.²³ The overall prevalence of TN is estimated to be in the range of 4–20/100,000,^{24,25} and women are affected more often than men (Table 2).^{25,26} Although rare, pediatric cases have been described as well.²³

NVCS of CN V is usually caused by a neighboring elongated superior cerebellar artery coming from above (Fig 3 and On-line Video) or by an anterior inferior cerebellar artery (AICA) coming from below,¹¹ with the superior cerebellar artery being more common (88% alone or in association) than the AICA (≤25%).⁵ Both the superior cerebellar artery and AICA usually compress the nerve in its superomedial portion (60%) (Fig 3).⁵ Less often, CN V is compressed by the basilar and vertebral arteries,^{15,16} by a saccular aneurysm, a persistent trigeminal artery, an arteriovenous malformation,^{27,28} or a petrous vein (Figs 4 and 5). A small cerebellopontine angle cistern appears to predispose to NVCS.²⁹ Histologically, in patients with TN, the cisternal CN V shows focal demyelination in the region of vascular compression.^{8,23,30,31} TN has been reported to be more frequent in proximal (<3 mm) than in distal NVC.³² According to Peker et al,⁸ the TZ of CN V is <2.5 mm away from the brain stem, while according to Guclu et al,¹¹ the TZ is at approximately 4.19 ± 0.81 mm away. Therefore, the proposed practical cutoff of 3 mm for the location of the TZ with respect to the nerve entry/exit is a reasonable compromise. It is certainly an oversimplification to assume that NVCS can occur only at the TZ because

nerve compression has been described in the proximal cisternal, midcisternal, and juxtapetrous nerve segments.¹⁷ Furthermore, in a series of 579 patients with TN,⁵ NVCS was found to be equally frequent in the proximal and in the mid-third cisternal CN, while it was clearly less frequent in the Meckel cave.⁵

In most patients with classic TN, surgical decompression of the CN V root produces immediate intraoperative improvement in nerve conduction and rapid symptom relief (Fig 4). This phenomenon is thought to reflect the reversal of a compression-induced conduction block in larger myelinated fibers outside the region of demyelination.²³ Immediate postoperative pain relief is between 87% and 98%. Approximately 80% of patients with microvascular decompression are symptom-free 1 year after the procedure; however, 8–10 years later, this percentage decreases to 58%–68%.^{33,34} Immediate postoperative remission is an independent predictive factor for good long-term outcome after mi-

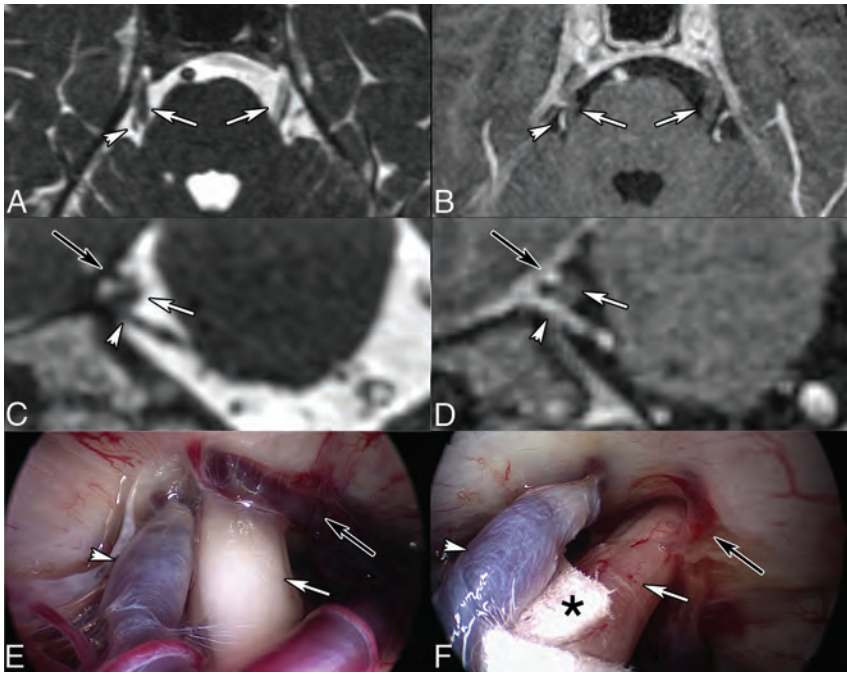


FIG 4. Right TN in a 45-year-old man caused by venous compression. Axial (A) and coronal (C) 2D reconstruction from CISS (0.7-mm thin sections). Contrast-enhanced 3D T1-weighted reconstructed images (0.9 mm) in the axial (B) and coronal (D) planes. Intraoperative views before (E) and after (F) the operation. MR imaging shows bifocal CN V (white arrows) compression by the Dandy vein (white short arrows) and by a transverse pontine vein (black arrows), respectively. Teflon (Dupont, Wilmington, Delaware) (asterisk, F) was interposed between CN V (white arrow, F) and the Dandy vein (white arrowhead, F). The transverse pontine vein was coagulated (black arrow, F). Intraoperative images are courtesy of Dr Arnaud Deveze, MD, Department of Ear, Nose and Throat Surgery, University Hospital, Hôpital Nord, Marseille, France.

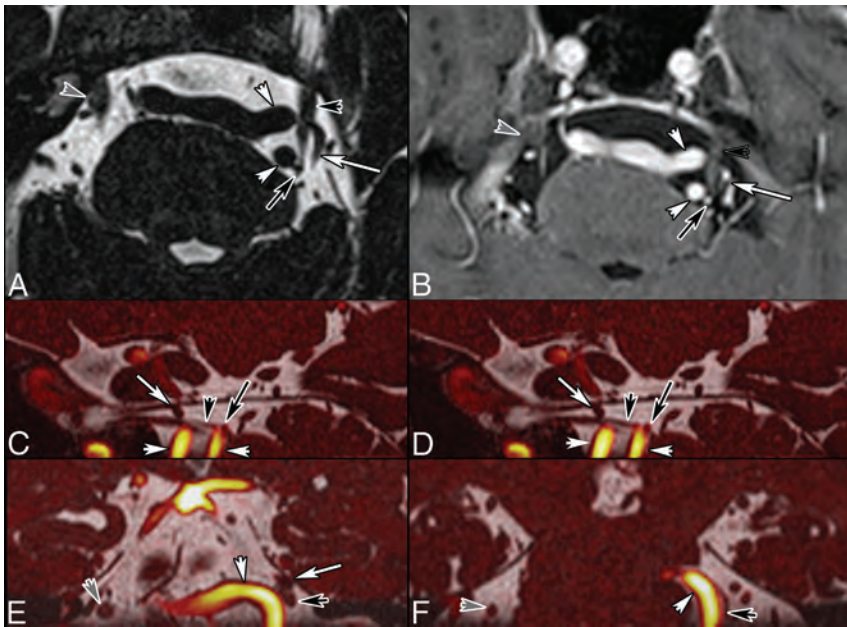


FIG 5. NVCS in a 70-year-old man with left TN. Axial T2-weighted image (A, 0.5 mm). Contrast-enhanced T1-weighted image (B, 0.5 mm). Fusion of 3D T2 and TOF angiography sequences (C and D, sagittal; E and F, coronal sections). Note contact between the tortuous vertebral arteries (white arrowheads), the left AICA (black arrows), the superior cerebellar artery (white arrows), and the cisternal left CN V (black arrowheads). Note that the TZ of CN V is thinned, while the more distal portion of CN V close to the Meckel cave has a normal rounded shape. Gray arrowhead points to the right CN V.

crovascular decompression.³⁴ Before considering microvascular decompression, patients usually undergo pharmacologic treatment with carbamazepine, oxcarbazepine, or, in selected cases, baclofen, gabapentin, and other anti-convulsants. Further treatment options in TN include stereotactic radiosurgery (also called “gamma knife”), which is increasingly performed, especially in elderly patients.

Neurovascular contacts due to vessel juxtaposition along CN V also occur in a non-negligible percentage of asymptomatic subjects (31.9% of control subjects and 48.9% on the contralateral asymptomatic side in patients with TN).³⁵ In a combined MR imaging and specimen study, the superior cerebellar artery and AICA had contact with the sensory CN V root in 45.5% of all MR imaging examinations and in 42.9% of specimens.¹³ Asymptomatic contact is more common more distal to the brain stem (3.85 ± 2.69 mm), compared with symptomatic NVC, which is typically proximal (0.94 ± 1.27 mm).³² A cutoff value of 3 mm from the brain stem has been proposed because TN symptoms occur in 83.1% (103/124) of cases with neurovascular contact at a distance of <3 mm, but only in 19.6% (9/46) of patients with a distance of >3 mm.³²

Similar results were found by other authors: Neurovascular contact occurred in the proximal part (REZ in this study) in 76% of symptomatic and 17% of asymptomatic nerves.³⁶ These observations indicate that proximal NVCs are more likely symptomatic than distal NVCs, yet the pure presence or absence of an NVC is insufficient to accurately predict symptomatic NVCs. Consequently, additional parameters may determine whether a neurovascular contact is symptomatic. Tash et al³⁷ assessed 85 asymptomatic patients and found 30% of 170 CN Vs with a neurovascular contact in the REZ, but only 2% of these asymptomatic cases had a deformity of the nerve. Correspondingly, the presence of nerve displacement by the vessel or focal atrophy was observed more commonly in symptomatic (52%) compared with asymptomatic (9%) nerves.³⁶

Atrophy of CN V in patients with classic TN has been observed intra-

operatively and at MR imaging (Fig 4).^{29,38-41} Erbay et al³⁹ found that the nerve diameter and cross-sectional area were 20% and 28% smaller on the symptomatic side compared with the asymptomatic side. Horínek et al⁴⁰ found that the volume of the affected nerve was, on average, 28% smaller than that of the unaffected nerve; however, only 7 of the 18 patients with TN were diagnosed

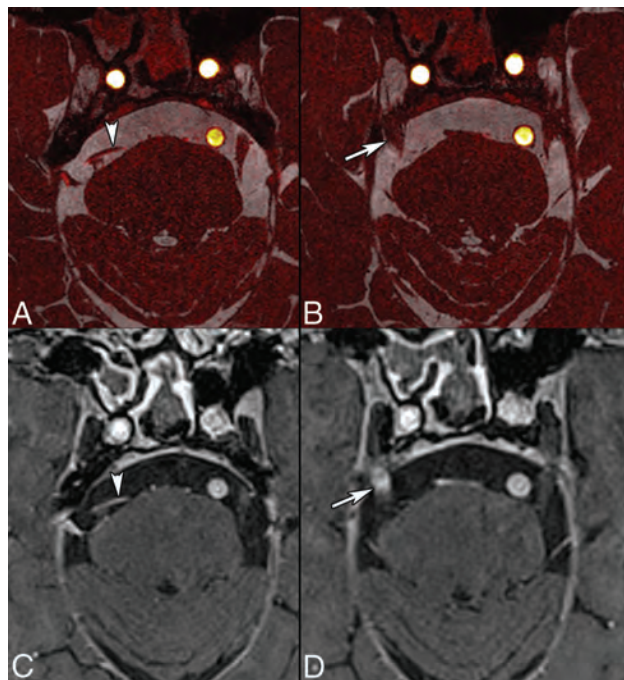


FIG 6. TN in an 81-year-old man treated with stereotactic radiosurgery. Axial images (0.5 mm) obtained by fusion of CISS and TOF angiography sequences (A and B) and contrast-enhanced 3D T1-weighted volumetric interpolated brain examination (C and D, 0.6 mm) show NVCS caused by the superior cerebellar artery (arrowheads). There is contrast enhancement of the right CN V at the stereotactic radiosurgery site (arrow, D). Contrast enhancement on follow-up examinations disappeared gradually.

with nerve atrophy on the basis of MR imaging volumetry. Although CN V atrophy can be observed in TN, the low sensitivity of this finding does not warrant its routine use for the diagnosis of trigeminal NVCS. Nevertheless, according to Antonini et al, in 2014,³⁶ nerve atrophy and displacement are highly specific (97%) signs with good negative (82%–87%) and positive (81%–86%) predictive values. In summary, anatomic abnormalities such as deformity and atrophy of the cisternal CN V and a small cerebellopontine angle cistern are more frequent in symptomatic NVCS and—whenever present—should be used as additional diagnostic signs.

DTI in severe TN may reveal a loss of anisotropy due to tissue damage associated with demyelination.^{20,39,42,43} A reduction of fractional anisotropy, increase in radial diffusivity and apparent diffusion coefficient, and a trend toward increased mean diffusivity can be observed in NVCS. Furthermore, reversibility of an abnormally low fractional anisotropy has been reported after successful microvascular decompression.²⁰ DTI metrics also appear to correlate with clinical parameters, such as disease duration and the visual analog scale of pain.⁴² Therefore, it has been suggested that correlation between fractional anisotropy reduction and the visual analog scale suggests fractional anisotropy as a potential objective MR imaging biomarker to correlate with clinical severity.⁴² However, these observations have not been confirmed by other authors and, therefore, require further investigation.⁴⁴

MR imaging can also be used to assess padding or other morphologic and functional changes after microvascular decompression⁴⁵ or stereotactic radiosurgery (gamma knife) for TN. After stereotactic radiosurgery, the affected nerve may show focal contrast enhancement (Fig 6), and gradual decrease of nerve volume occurs with time. Park et al²⁹ found CN V atrophy of the affected side in 96% of patients with TN treated by stereotactic radiosurgery, with a mean reduction in CN V volume of 39%.

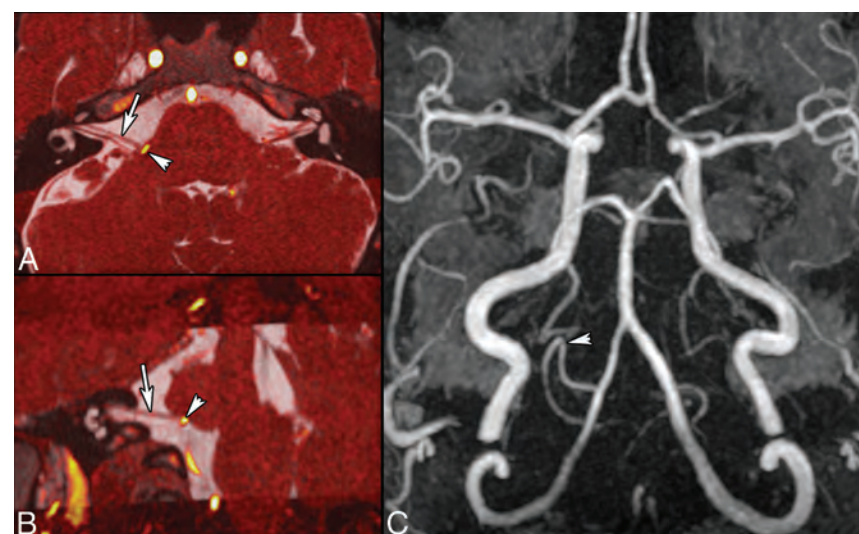


FIG 7. HFS caused by a posterior inferior cerebellar artery (PICA) loop in a 54-year-old man. Axial oblique (A) and coronal oblique (B) reformatted images obtained by fusion of CISS (0.6 mm) and TOF angiography sequences show NVC of CN VII (arrows, A and B) by the PICA at the presumed TZ (arrowhead). 3D MIP reconstruction of the TOF sequence (C) shows a PICA loop on the right, responsible for HFS. Findings were confirmed surgically.

Facial Nerve (CN VII)

Anatomy. CN VII is a mixed nerve, which essentially controls the muscles of facial expression, transmits taste sensations from the anterior two-thirds of the tongue, and supplies parasympathetic fibers to the nasal mucosa, submandibular, sublingual, and lacrimal glands. The motor component is of particular relevance in the context of the current review. CN VII exits the brain stem as a single entity forming the cisternal segment (Fig 1). Analogous to CN V, most cases of NVCS also occur in the cisternal segment. According to one study,¹¹ the length of the cisternal segment was 17.93 ± 2.29 mm (range, 14.8–20.9 mm). In another study,⁴⁶ the TZ was described at 1.9 mm from the nerve entry/exit into the brain stem, which is about one-tenth of its cisternal

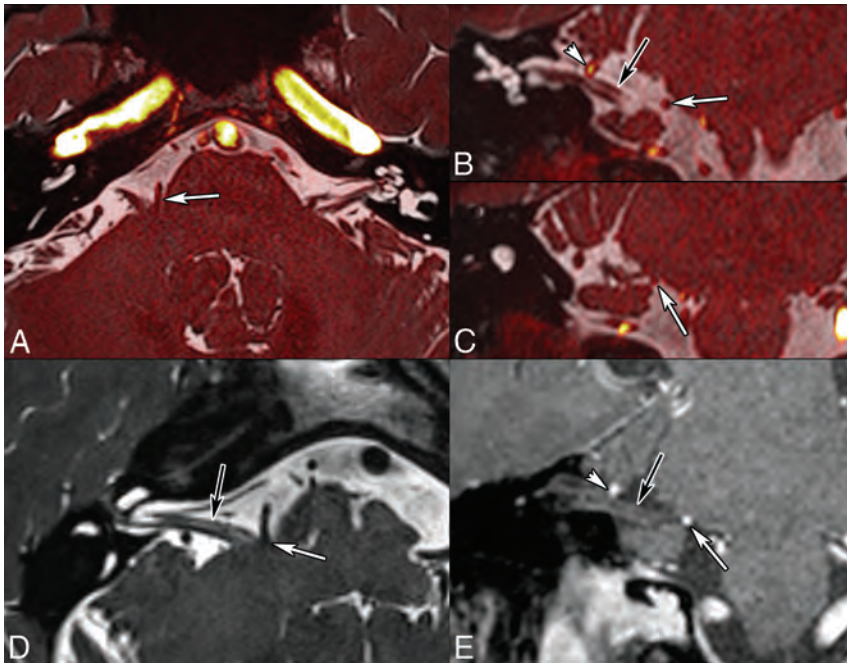


FIG 8. Right HFS caused by an AICA loop in a 60-year-old man. Fusion of 3D T2 and TOF angiography sequences (0.6-mm thin sections; A, axial; B and C, coronal sections). Axial oblique reformatted T2-weighted image along the cisternal CN VII (D). Coronal oblique reformatted contrast-enhanced T1-weighted image (E). Note contact between an AICA loop and the presumed TZ of CN VII (white arrows), which is slightly indented. There is a second contact between the AICA and the more distal CN VII (arrowheads). Black arrows point to CN VII. NVCS due to the AICA loop impinging on the TZ was confirmed surgically. After the operation, symptoms disappeared.

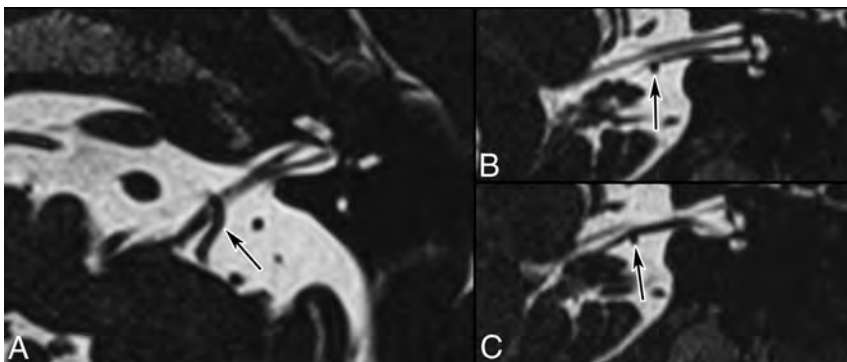


FIG 9. NVC in a 70-year-old man with tinnitus and vertigo. A, Axial oblique reformatted T2-weighted image (0.5 mm). Coronal oblique T2-weighted images (0.5 mm; B, anterior section; C, posterior section). Note the tortuous AICA (arrows) displacing and indenting the cochlear nerve (B) and the vestibular nerve (C). Brain and temporal bone MR imaging and high-resolution temporal bone CT findings were otherwise normal.

length.⁴⁷ Another study reported that the most distal part of the TZ is 2.86 mm away from the brain stem.¹¹ By interpolating these data, we can estimate the length of the TZ to be about 0.96 mm (range, 2.86–1.9 mm). Similar to CN V, the medial portion of the TZ is also shorter than the lateral portion.^{46,47}

Hemifacial Spasm. Hemifacial spasm is characterized by unilateral, intermittent contractions of the muscles of facial expression, typically beginning in the orbicularis oculi and spreading to the other muscles.⁴⁸ Primary HFS is triggered by NVC, whereas secondary HFS comprises all other causes of CN VII damage. HFS has an incidence of 0.77/10,000.⁴⁹ The AICA (43%) is the most common vessel causing NVC (Figs 7 and 8), followed by the pos-

terior inferior cerebellar artery (31%) and vertebral artery (23%).⁶ NVCS can occur either at the REZ (10%–96% depending on study),^{50,51} adjacent cisternal segment (up to 64%),⁶ TZ (22%), or other cisternal portions (3%).⁶ According to Dou et al,⁵² attrition of the neurovascular interface yields action potentials from the demyelinated facial nerves and therefore causes HFS symptoms. As shown by Sindou et al,⁵¹ microvascular decompression is highly effective in HFS and symptoms disappear after an operation in 90%–95% of cases; however, recurrence is seen in up to 25% of patients. In the long term, 75%–85% of patients remain symptom-free.

Vestibulocochlear Nerve (CN VIII)

Anatomic Considerations. CN VIII is a sensory nerve carrying information from the spiral auditory organ (cochlear nerve) and the labyrinth (vestibular nerve) to the brain stem. It has a long cisternal segment, which extends from the brain stem to the internal acoustic meatus (total distance = 14.2–19.2 mm).⁵³ The distance of the most distal part of the TZ from the brain stem has been measured at 9.28–13.84 mm (Fig 1). Most acoustic schwannomas originate from the internal auditory canal or its porus area,⁴⁷ which is colocalized with the TZ. Consequently, it was postulated that acoustic schwannomas might originate from the glio-Schwannian junction.⁵³ The alternative hypothesis is that the origin of many acoustic schwannomas is the ganglion of Scarpa, which is also colocalized in this region.⁵⁴

NVC of CN VIII (Vestibular Paroxysmia). In contrast to the clearly established NVCS of CN V and VII, NVCS of CN

VIII is more controversial.⁵⁵ The site of NVC can vary between 0.0 and 10.2 mm from the brain stem, and in most cases (75%), the AICA is the compressing vessel.⁵⁶ The recording of action potentials of the cochlear nerve during microvascular decompression has demonstrated that the site of NVC correlates well with clinical symptoms.⁵⁵ Ryu et al⁵⁵ have shown that vertigo appears to be associated with vascular compression of the rostroventral nerve (vestibular nerve), while tinnitus appears to be associated with compression of the caudal surface (cochlear nerve) of the nerve (Fig 9). In patients with both vertigo and tinnitus, the authors found compression of both the vestibular and cochlear nerves.⁵⁵

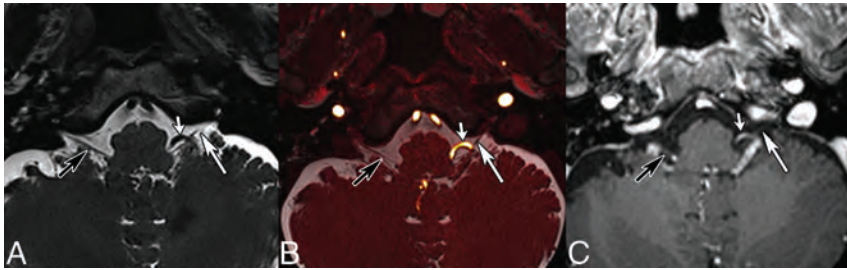


FIG 10. GN caused by a tortuous vertebral artery in a 64-year-old man. Axial T2-weighted (A), fused T2-weighted and TOF (B) images, and contrast-enhanced 3D T1 gradient recalled-echo image (C) show displacement and contact between CN IX (long arrows) and a tortuous vertebral artery (short arrows). Note that in B, 2 contact points are seen, 1 proximal and 1 more distal. Black arrows point to the contralateral IX–X nerve complex. Findings were confirmed surgically.

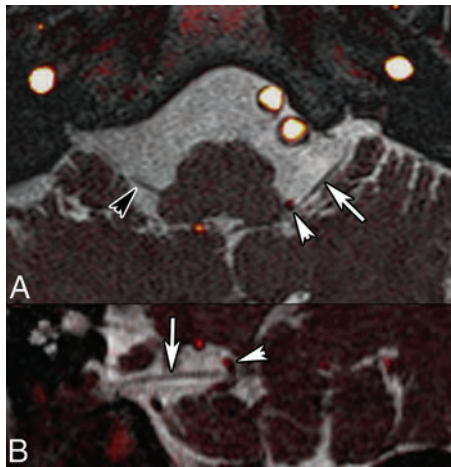


FIG 11. Left invalidating GN caused by a posterior inferior cerebellar artery (PICA) loop in an 80-year-old otherwise healthy female patient. Fusion of 3D T2 and TOF angiography sequences (A, axial; B, coronal oblique) reveals displacement of CN IX (white arrows) and contact between the TZ of CN IX and the left PICA (arrowheads). Right CN IX is indicated by a black arrowhead.

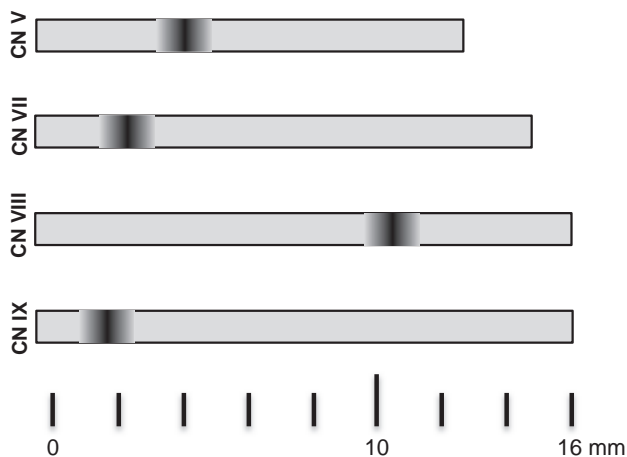


FIG 12. Schematic illustration of the cisternal length and location of the transition zone for CN V, VII, VIII, and IX.

Glossopharyngeal Nerve (CN IX)

Anatomy. CN IX is a mixed sensory, motor, and parasympathetic nerve. Sensory information comes from the posterior tongue and oropharyngeal and ear region, while chemo- and baroreceptor

input comes from the carotid body and carotid sinuses. The motor component supplies the stylopharyngeal muscle and the secretomotor fibers of the ipsilateral parotid gland. As opposed to CN V and VII, CN IX exits as 3–5 rootlets, which later unite to form the cisternal CN IX. The length of CN IX from the medulla oblongata to the jugular foramen varies between 14.2 and 19.9 mm (mean, 16.36 ± 2.53 mm).¹¹ The TZ is located at 1.51 ± 0.39 mm¹¹ and has a typical cone shape (Fig 1).⁹

Glossopharyngeal Neuralgia. Glossopharyngeal neuralgia is characterized by severe paroxysmal episodes of pain localized in the posterior tongue, tonsil, throat, or external ear canal. The pain is similar to that experienced by patients with TN and can be triggered by eating, swallowing, and speaking.⁵⁷ Life-threatening complications due to cardiac instability, syncope, and convulsions are well-documented. The overall incidence of GN appears to be considerably lower than that of TN and is estimated at 0.2–0.7 cases per 100,000 person-years²⁵ and 0.062/100,000 (Fig 7).⁵⁸ However, some authors believe that the true incidence of GN may be higher due to lack of awareness of the disease and difficulties in diagnosis. In general, GN is caused by NVC, while in a minority of cases, trauma, neoplasms, infection, or an elongated styloid process (Eagle syndrome) can be identified. Because symptoms are not always straightforward, imaging is usually performed to exclude a neoplasm in the pharynx or larynx or to look for an elongated styloid process. Analogous to CN V and VII, in patients with GN caused by NVCS, MR imaging allows precise assessment of the relationship between CN IX and the conflicting artery in the supraolivary fossa (Figs 10 and 11). GN caused by NVC occurs almost exclusively (95%) in the proximal REZ,⁵⁹ which overlaps the proximal location of the TZ of 1.51 ± 0.39 mm.¹¹ The posterior inferior cerebellar artery and, less frequently, the AICA are responsible for nerve compression.^{60,61} The low incidence of GN in comparison with CN V and CN VII is probably related to the proximal position of the TZ and the short central myelin portion in CN IX.^{10,11}

CONCLUSIONS

TZ length and location vary between cranial nerves (Fig 12). While the TZ is close to the brain stem and overlaps the REZ in CN V, VII, and IX, it is longer, located more distally, and does not overlap the REZ in CN VIII.⁹ Although symptomatic NVCS can occur outside the TZ, most NVCSs are seen at the TZ. MR imaging with high-resolution heavily T2-weighted sequences and angiography sequences plays a major role in the identification of the compressing vessel, its precise location, and ruling out other causes of pain that may mimic NVCS. DTI with tractography is a potential biomarker in TN.

Disclosures: Sven Haller—UNRELATED: Grants/Grants Pending: Swiss National Science Foundation.* Comments: project on real-time fMRI neurofeedback. *Money paid to the institution.

REFERENCES

1. Dandy WE. Concerning the cause of trigeminal neuralgia. *Am J Surg* 1934;24:447–55 CrossRef
2. Gardner WJ, Miklos MV. Response of trigeminal neuralgia to decompression of sensory root: discussion of cause of trigeminal neuralgia. *J Am Med Assoc* 1959;170:1773–76 CrossRef Medline
3. Gardner WJ. Concerning the mechanism of trigeminal neuralgia and hemifacial spasm. *J Neurosurg* 1962;19:947–58 CrossRef Medline
4. Jannetta PJ. Arterial compression of the trigeminal nerve at the pons in patients with trigeminal neuralgia. *J Neurosurg* 1967;26(suppl):159–62 CrossRef Medline
5. Sindou M, Howeydi T, Acevedo G. Anatomical observations during microvascular decompression for idiopathic trigeminal neuralgia (with correlations between topography of pain and site of the neurovascular conflict): prospective study in a series of 579 patients. *Acta Neurochir (Wien)* 2002;144:1–12; discussion 12–13 CrossRef Medline
6. Campos-Benitez M, Kaufmann AM. Neurovascular compression findings in hemifacial spasm. *J Neurosurg* 2008;109:416–20 CrossRef Medline
7. Tarlov IM. Structure of the nerve root, I: nature of the junction between the central and the peripheral nervous system. *Arch Neuropsych* 1937;37:555–83 CrossRef
8. Peker S, Kurtkaya O, Uzün I, et al. Microanatomy of the central myelin-peripheral myelin transition zone of the trigeminal nerve. *Neurosurgery* 2006;59:354–59; discussion 354–59 CrossRef Medline
9. Skinner H. Some histologic features of the cranial nerves. *Arch Neuropsych* 1931;25:356–72 CrossRef
10. De Ridder D, Møller A, Verlooy J, et al. Is the root entry/exit zone important in microvascular compression syndromes? *Neurosurgery* 2002;51:427–33; discussion 433–34 CrossRef Medline
11. Guclu B, Sindou M, Meyronet D, et al. Cranial nerve vascular compression syndromes of the trigeminal, facial and vago-glossopharyngeal nerves: comparative anatomical study of the central myelin portion and transitional zone—correlations with incidences of corresponding hyperactive dysfunctional syndromes. *Acta Neurochir (Wien)* 2011;153:2365–75 CrossRef Medline
12. Leal PR, Froment JC, Sindou M. MRI sequences for detection of neurovascular conflicts in patients with trigeminal neuralgia and predictive value for characterization of the conflict (particularly degree of vascular compression) [in French]. *Neurochirurgie* 2010;56:43–49 CrossRef Medline
13. Yousry I, Moriggl B, Holtmannspöetter M, et al. Detailed anatomy of the motor and sensory roots of the trigeminal nerve and their neurovascular relationships: a magnetic resonance imaging study. *J Neurosurg* 2004;101:427–34 CrossRef Medline
14. Leal PR, Hermier M, Souza MA, et al. Visualization of vascular compression of the trigeminal nerve with high-resolution 3T MRI: a prospective study comparing preoperative imaging analysis to surgical findings in 40 consecutive patients who underwent microvascular decompression for trigeminal neuralgia. *Neurosurgery* 2011;69:15–25; discussion 26 CrossRef Medline
15. Becker M, Kohler R, Vargas MI, et al. Pathology of the trigeminal nerve. *Neuroimaging Clin N Am* 2008;18:283–307, x CrossRef Medline
16. Borges A, Casselman J. Imaging the trigeminal nerve. *Eur J Radiol* 2010;74:323–40 CrossRef Medline
17. Leal PR, Hermier M, Froment JC, et al. Preoperative demonstration of the neurovascular compression characteristics with special emphasis on the degree of compression, using high-resolution magnetic resonance imaging: a prospective study, with comparison to surgical findings, in 100 consecutive patients who underwent microvascular decompression for trigeminal neuralgia. *Acta Neurochir (Wien)* 2010;152:817–25 CrossRef Medline
18. Leal PR, Froment JC, Sindou M. Predictive value of MRI for detecting and characterizing vascular compression in cranial nerve hyperactivity syndromes (trigeminal and facial nerves) [in French]. *Neurochirurgie* 2009;55:174–80 CrossRef Medline
19. Naraghi R, Tanrikulu L, Troeschler-Weber R, et al. Classification of neurovascular compression in typical hemifacial spasm: three-dimensional visualization of the facial and the vestibulocochlear nerves. *J Neurosurg* 2007;107:1154–63 CrossRef Medline
20. Herweh C, Kress B, Rasche D, et al. Loss of anisotropy in trigeminal neuralgia revealed by diffusion tensor imaging. *Neurology* 2007;68:776–78 CrossRef Medline
21. Lutz J, Linn J, Mehrkens JH, et al. Trigeminal neuralgia due to neurovascular compression: high-spatial-resolution diffusion-tensor imaging reveals microstructural neural changes. *Radiology* 2011;258:524–30 CrossRef Medline
22. Yildiz E, Yolcu S. Volume of the cisternal portion of the trigeminal nerve: a study with 3.0-Tesla constructive-interference-in-steady-state imaging of healthy subjects. *J Neurological Sci (Turkish)* 2015;32:106–14
23. Love S, Coakham HB. Trigeminal neuralgia: pathology and pathogenesis. *Brain* 2001;124:2347–60 CrossRef Medline
24. Katusic S, Beard CM, Bergstralh E, et al. Incidence and clinical features of trigeminal neuralgia, Rochester, Minnesota, 1945–1984. *Ann Neurol* 1990;27:89–95 CrossRef Medline
25. Manzoni GC, Torelli P. Epidemiology of typical and atypical craniofacial neuralgias. *Neurol Sci* 2005;26(suppl 2):s65–67 CrossRef Medline
26. Maarbjerg S, Gozalov A, Olesen J, et al. Trigeminal neuralgia: a prospective systematic study of clinical characteristics in 158 patients. *Headache* 2014;54:1574–82 CrossRef Medline
27. de Bondt BJ, Stokroos R, Casselman J. Persistent trigeminal artery associated with trigeminal neuralgia: hypothesis of neurovascular compression. *Neuroradiology* 2007;49:23–26 CrossRef Medline
28. Garcia-Pastor C, López-González F, Revuelta R, et al. Trigeminal neuralgia secondary to arteriovenous malformations of the posterior fossa. *Surg Neurol* 2006;66:207–11; discussion 211 CrossRef Medline
29. Park SH, Hwang SK, Lee SH, et al. Nerve atrophy and a small cerebellopontine angle cistern in patients with trigeminal neuralgia. *J Neurosurg* 2009;110:633–37 CrossRef Medline
30. Brisman R, Khandji AG, Mooij RB. Trigeminal nerve-blood vessel relationship as revealed by high-resolution magnetic resonance imaging and its effect on pain relief after gamma knife radiosurgery for trigeminal neuralgia. *Neurosurgery* 2002;50:1261–66; discussion 1266–67 Medline
31. Devor M, Govrin-Lippmann R, Rappaport ZH. Mechanism of trigeminal neuralgia: an ultrastructural analysis of trigeminal root specimens obtained during microvascular decompression surgery. *J Neurosurg* 2002;96:532–43 CrossRef Medline
32. Suzuki M, Yoshino N, Shimada M, et al. Trigeminal neuralgia: differences in magnetic resonance imaging characteristics of neurovascular compression between symptomatic and asymptomatic nerves. *Oral Surg Oral Med Oral Pathol Oral Radiol* 2015;119:113–18 CrossRef Medline
33. Sindou M, Leston J, Howeydi T, et al. Micro-vascular decompression for primary trigeminal neuralgia (typical or atypical): long-term effectiveness on pain—prospective study with survival analysis in a consecutive series of 362 patients. *Acta Neurochir (Wien)* 2006;148:1235–45; discussion 1245 CrossRef Medline
34. Oesman C, Mooij JJ. Long-term follow-up of microvascular decompression for trigeminal neuralgia. *Skull Base* 2011;21:313–22 CrossRef Medline
35. Chun-Cheng Q, Qing-Shi Z, Ji-Qing Z, et al. A single-blinded pilot study assessing neurovascular contact by using high-resolution MR imaging in patients with trigeminal neuralgia. *Eur J Radiol* 2009;69:459–63 CrossRef Medline
36. Antonini G, Di Pasquale A, Cruccu G, et al. Magnetic resonance imaging contribution for diagnosing symptomatic neurovascular contact in classical trigeminal neuralgia: a blinded case-control study and meta-analysis. *Pain* 2014;155:1464–71 CrossRef Medline

37. Tash RR, Sze G, Leslie DR. **Trigeminal neuralgia: MR imaging features.** *Radiology* 1989;172:767–70 CrossRef Medline
38. Bederson JB, Wilson CB. **Evaluation of microvascular decompression and partial sensory rhizotomy in 252 cases of trigeminal neuralgia.** *J Neurosurg* 1989;71:359–67 CrossRef Medline
39. Erbay SH, Bhadelia RA, O'Callaghan M, et al. **Nerve atrophy in severe trigeminal neuralgia: noninvasive confirmation at MR imaging—initial experience.** *Radiology* 2006;238:689–92 CrossRef Medline
40. Horínek D, Brezová V, Nimsky C, et al. **The MRI volumetry of the posterior fossa and its substructures in trigeminal neuralgia: a validated study.** *Acta Neurochir (Wien)* 2009;151:669–75 CrossRef Medline
41. Kress B, Schindler M, Rasche D, et al. **MRI volumetry for the preoperative diagnosis of trigeminal neuralgia.** *Eur Radiol* 2005;15:1344–48 CrossRef Medline
42. Liu Y, Li J, Butzkueven H, et al. **Microstructural abnormalities in the trigeminal nerves of patients with trigeminal neuralgia revealed by multiple diffusion metrics.** *Eur J Radiol* 2013;82:783–86 CrossRef Medline
43. Leal PR, Roch JA, Hermier M, et al. **Structural abnormalities of the trigeminal root revealed by diffusion tensor imaging in patients with trigeminal neuralgia caused by neurovascular compression: a prospective, double-blind, controlled study.** *Pain* 2011;152:2357–64 CrossRef Medline
44. Wilcox SL, Gustin SM, Eykman EN, et al. **Trigeminal nerve anatomy in neuropathic and non-neuropathic orofacial pain patients.** *J Pain* 2013;14:865–72 CrossRef Medline
45. Prieto R, Pascual JM, Yus M, et al. **Trigeminal neuralgia: assessment of neurovascular decompression by 3D fast imaging employing steady-state acquisition and 3D time of flight multiple overlapping thin slab acquisition magnetic resonance imaging.** *Surg Neurol Int* 2012;3:50 CrossRef Medline
46. Tomii M, Onoue H, Yasue M, et al. **Microscopic measurement of the facial nerve root exit zone from central glial myelin to peripheral Schwann cell myelin.** *J Neurosurg* 2003;99:121–24 CrossRef Medline
47. Skinner HA. **The origin of acoustic nerve tumours.** *Br J Surg* 1929;16:440–63 CrossRef
48. Kong DS, Park K. **Hemifacial spasm: a neurosurgical perspective.** *J Korean Neurosurg Soc* 2007;42:355–62 CrossRef Medline
49. Auger RG, Whisnant JP. **Hemifacial spasm in Rochester and Olmsted County, Minnesota, 1960 to 1984.** *Arch Neurol* 1990;47:1233–34 CrossRef Medline
50. Sindou MP. **Microvascular decompression for primary hemifacial spasm. Importance of intraoperative neurophysiological monitoring.** *Acta Neurochir (Wien)* 2005;147:1019–26; discussion 1026 CrossRef Medline
51. Sindou M, Keravel Y. **Neurosurgical treatment of primary hemifacial spasm with microvascular decompression [in French].** *Neurochirurgie* 2009;55:236–47 CrossRef Medline
52. Dou NN, Zhong J, Zhou QM, et al. **The mechanism of hemifacial spasm: a new understanding of the offending artery.** *Neurol Res* 2015;37:184–88 CrossRef Medline
53. Guclu B, Sindou M, Meyronet D, et al. **Anatomical study of the central myelin portion and transitional zone of the vestibulocochlear nerve.** *Acta Neurochir (Wien)* 2012;154:2277–83; discussion 2283 CrossRef Medline
54. Pirsig W, Eckermeier L, Mueller D. **As to the origin of vestibular schwannomas.** In: House WF, Luetje CM, eds. *Acoustic Tumors*. Vol 1. Baltimore: University Park Press; 1979:52–55
55. Ryu H, Yamamoto S, Sugiyama K, et al. **Neurovascular compression syndrome of the eighth cranial nerve: can the site of compression explain the symptoms?** *Acta Neurochir (Wien)* 1999;141:495–501 CrossRef Medline
56. Best C, Gawehn J, Krämer HH, et al. **MRI and neurophysiology in vestibular paroxysmia: contradiction and correlation.** *J Neurol Neurosurg Psychiatry* 2013;84:1349–56 CrossRef Medline
57. Laha RK, Jannetta PJ. **Glossopharyngeal neuralgia.** *J Neurosurg* 1977;47:316–20 CrossRef Medline
58. Spurling RG, Grantham EG. **Glossopharyngeal neuralgia.** *South Med J* 1942;35:509–12
59. Sindou M, Keravel Y. **Neurosurgical treatment of vago-glossopharyngeal neuralgia [in French].** *Neurochirurgie* 2009;55:231–35 CrossRef Medline
60. Alafaci C, Granata F, Cutugno M, et al. **Glossopharyngeal neuralgia caused by a complex neurovascular conflict: case report and review of the literature.** *Surg Neurol Int* 2015;6:19 CrossRef Medline
61. Hiwatashi A, Matsushima T, Yoshiura T, et al. **MRI of glossopharyngeal neuralgia caused by neurovascular compression.** *AJR Am J Roentgenol* 2008;191:578–81 CrossRef Medline

Multimodal CT Imaging: Time to Treatment and Outcomes in the IMS III Trial

 A. Vagal,  L.D. Foster,  B. Menon,  A. Livorine,  J. Shi,  E. Qazi,  S.D. Yeatts,  A.M. Demchuk,  M.D. Hill,  T.A. Tomsick, and  M. Goyal



ABSTRACT

BACKGROUND AND PURPOSE: The importance of time in acute stroke is well-established. Using the Interventional Management of Stroke III trial data, we explored the effect of multimodal imaging (CT perfusion and/or CT angiography) versus noncontrast CT alone on time to treatment and outcomes.

MATERIALS AND METHODS: We examined 3 groups: 1) subjects with baseline CTP and CTA (CTP+CTA), 2) subjects with baseline CTA without CTP (CTA), and 3) subjects with noncontrast head CT alone. The demographics, treatment time intervals, and clinical outcomes in these groups were studied.

RESULTS: Of 656 subjects enrolled in the Interventional Management of Stroke III trial, 90 (13.7%) received CTP and CTA, 216 (32.9%) received CTA (without CTP), and 342 (52.1%) received NCCT alone. Median times for the CTP+CTA, CTA, and NCCT groups were as follows: stroke onset to IV tPA (120.5 versus 117.5 versus 120 minutes; $P = .5762$), IV tPA to groin puncture (77.5 versus 81 versus 91 minutes; $P = .0043$), groin puncture to endovascular therapy start (30 versus 38 versus 44 minutes; $P = .0001$), and endovascular therapy start to end (63 versus 46 versus 74 minutes; $P < .0001$). Compared with NCCT, the CTA group had better outcomes in the endovascular arm (OR, 2.12; 95% CI, 1.36–3.31; adjusted for age, NIHSS score, and time from onset to IV tPA). The CTP+CTA group did not have better outcomes compared with the NCCT group.

CONCLUSIONS: Use of CTA with or without CTP did not delay IV tPA or endovascular therapy compared with NCCT in the Interventional Management of Stroke III trial.

ABBREVIATIONS: ED = emergency department; EVT = endovascular therapy; IMS III = Interventional Management of Stroke III trial

The importance of time is well-established in acute ischemic stroke. Ample evidence suggests that the benefit of treatment decreases with increasing time to treatment in intravenous and

endovascular therapy (EVT).^{1–3} It is critical to minimize time delays in stroke treatment workflow components, including imaging time delays. However, imaging protocols vary by institution, and there is no nationally or internationally recognized standard imaging protocol for evaluating patients with acute stroke.

Multimodal imaging, including CT angiography, CT perfusion, or MR angiography and MR perfusion may provide useful information on arterial occlusion, collateral flow, and tissue viability. On the contrary, these imaging techniques may also delay initiation of revascularization therapies. Recent endovascular stroke trials (Multicenter Randomized CLinical trial of Endovascular treatment for Acute ischemic stroke in the Netherlands [MR CLEAN],⁴ Endovascular Treatment for Small Core and Proximal Occlusion Ischemic Stroke [ESCAPE],⁵ Extending the Time for Thrombolysis in Emergency Neurological Deficits–Intra-Arterial [EXTEND-IA],⁶ Solitaire With the Intention For Thrombectomy as Primary Endovascular Treatment [SWIFT PRIME],⁷ Endovascular Revascularization With Solitaire Device Versus Best Medical Therapy in Anterior Circulation Stroke Within 8 Hours [REVAS-

Received October 14, 2015; accepted after revision January 22, 2016.

From the Department of Radiology (A.V., A.L., J.S., T.A.T.), University of Cincinnati Medical Center, Cincinnati, Ohio; Department of Public Health Sciences (L.D.F., S.D.Y.), Medical University of South Carolina, Charleston, South Carolina; and Departments of Neurology (A.M.D., M.D.H.) and Radiology (B.M., E.Q., M.G.), University of Calgary, Calgary Alberta, Canada.

A.V. was funded by the Clinical and Translational Science Awards 8 ULI TR000077-05 CT2 Award, the Imaging Core Lab, A Study of the Efficacy and Safety of Activase (Alteplase) in Patients With Mild Stroke (PRISMS) Trial, and Genentech. S.D.Y. was funded by the National Institutes of Health/National Institute of Neurological Disorders and Stroke (U01 NS052220). B.M. was funded by the Canadian Institute of Health Research, Heart and Stroke Foundation, and Alberta Innovates Health Solutions.

Paper previously presented at: International Stroke Conference, February 10–13, 2015; Nashville, Tennessee.

Please address correspondence to Achala Vagal, MD, MS, Department of Radiology, University of Cincinnati Medical Center, 234 Goodman St, Cincinnati, OH 45267; e-mail: Achala.Vagal@uchealth.com

 Indicates open access to non-subscribers at www.ajnr.org

<http://dx.doi.org/10.3174/ajnr.A4751>

Table 1: Demographic characteristics

	CTP+CTA (n = 90)	CTA (n = 216)	NCCT (n = 342)	P Value
Age (median) (IQR)	69 (59–75)	70 (58–77)	68 (57–76)	.6719
Male (No.) (%)	47 (52.2)	116 (53.7)	171 (50)	.6885
Black/African American/African Canadian (No.) (%)	12 (13.3)	13 (6)	44 (12.9)	.0258
Hispanic or Latino (No.) (%)	4 (4.4)	7 (3.2)	12 (3.5)	.8727
Baseline NIHSS score ^a (median) (IQR)	17 (13–20)	16 (13–20)	17 (13–21)	.5262
ASPECTS 8–10 ^b (No.) (%)	51 (57.3)	126 (58.9)	197 (58.3)	.9679
Treatment arm				.4006
IV tPA only (No.) (%)	29 (32.2)	66 (30.6)	123 (36)	
Endovascular (No.) (%)	61 (67.8)	150 (69.4)	219 (64)	
Received endovascular treatment (No.) (%)	49 (80.3)	123 (82.0)	161 (73.5)	.1349

Note:—IQR indicates interquartile range.

^a Two subjects have missing data (CTP+CTA, *n* = 1; CTA, *n* = 1).

^b Denominators for percentages do not include subjects with missing data (CTP+CTA, *n* = 1; CTA, *n* = 2; NCCT, *n* = 4).

CAT],⁸ Assess the Penumbra System in the Treatment of Acute Stroke [THERAPY],⁹ and Trial and Cost Effectiveness Evaluation of Intra-arterial Thrombectomy in Acute Ischemic Stroke [THRACE]¹⁰ demonstrating the benefit of endovascular therapy have used supplementary imaging, in addition to noncontrast CT, for patient selection. It is therefore imperative to understand whether additional imaging causes delays in the initiation of treatment of patients with acute ischemic stroke.

The Interventional Management of Stroke III (IMS III) trial was a phase III randomized trial of endovascular treatment after intravenous tPA versus IV tPA alone.¹¹ Multimodal imaging was available in a subgroup of patients at the discretion of the enrolling site. Our objective was to explore the effect of multimodal imaging: CTP+CTA or CTA (without CTP) versus NCCT on time to treatment and outcomes in the IMS III trial.

MATERIALS AND METHODS

Study Population

IMS III was a multicenter, phase III, randomized, open-label clinical trial testing the approach of IV tPA followed by endovascular treatment, compared with standard IV tPA alone, determined by the primary outcome of a modified Rankin Scale score of 0–2 at 90 days. Details of the design, methodology, and outcomes of the IMS III trial have been published.¹¹

A noncontrast head CT was the only required baseline imaging. Additional imaging, including CTP and/or CTA, was not a prerequisite for entry or patient selection in the IMS III trial. However CTA or CTP was performed at a few study sites at their discretion.

Imaging Subgroups

The analysis consisted of 3 subgroups based on baseline imaging: 1) subjects with baseline CTP and CTA (CTP+CTA), 2) subjects with CTA (without a concurrent CTP study), and 3) subjects without CTA or CTP (noncontrast head CT alone). The baseline demographics, time intervals, and outcomes in these 3 groups were studied.

Time Intervals

The following intervals were calculated for all subjects: 1) stroke onset to emergency department (ED) arrival, 2) ED arrival to start of imaging, and 3) start of imaging to IV tPA initiation.

Additional time intervals were calculated for the endovascular treatment arm: 1) IV tPA initiation to groin puncture, 2) groin puncture to the start of EVT, and 3) the duration of EVT (for subjects who received endovascular treatment).

Baseline imaging time was defined as the time of the first imaging performed. EVT initiation was defined as the start of intra-arterial tPA/balloon occlusion/thrombus aspiration or the first deployment of the device, depending on the type of endovascular therapy administered. Similarly, the EVT end time was defined as the time of the last deployment, time of last thrombus aspiration attempt, or time of the end of intra-arterial infusion.

Statistical Analysis

Because the time intervals described above did not follow a normal distribution, descriptive statistics are reported as median (interquartile range). Normality was assessed graphically via histogram and quantile-quantile plot. The Hodges-Lehmann estimator of location shift was used to calculate differences, with confidence intervals, in time intervals between groups. To compare the 3 groups (CTP+CTA versus CTA versus NCCT), we used the Kruskal-Wallis test for continuous variables and the χ^2 test for categorical variables. The primary clinical outcome (mRS 0–2 at 90 days) was analyzed via a logistic regression model to estimate adjusted odds ratios. The linearity in the log assumption was confirmed for continuous covariates. All tests were conducted at the .05 level of significance. If there was a significant association, pair-wise comparison was also performed between the CTP+CTA and CTA groups. Because this analysis is exploratory, *P* values were not adjusted for multiple testing. Because the endovascular group was of particular interest in light of recent trial results, separate models were created to estimate odds ratios by treatment. Statistical analysis was performed in SAS, Version 9.3T (SAS Institute, Cary, North Carolina).

RESULTS

Population Demographics

Of 656 subjects enrolled in the IMS III trial, 90 (13.7%) received CTP and CTA, 216 (32.9%) received CTA (without CTP), and 342 (52.1%) did not receive CTP or CTA (NCCT). Eight subjects with CTP performed without CTA were excluded from the analysis to increase the homogeneity within groups. Demographic characteristics are provided in Table 1.

Time Intervals

The time intervals for the 3 imaging groups are provided in Table 2. The use of CTP or CTA imaging did not cause delays in IV tPA (Fig 1) or endovascular treatment (Fig 2). Time from the start of imaging to IV tPA initiation was shorter in the CTP+CTA and CTA groups, compared with NCCT (6 minutes [95% CI, 1–11 minutes] and 8 minutes [95% CI, 4–12 minutes] shorter, respec-

Table 2: Time intervals for the 3 imaging groups

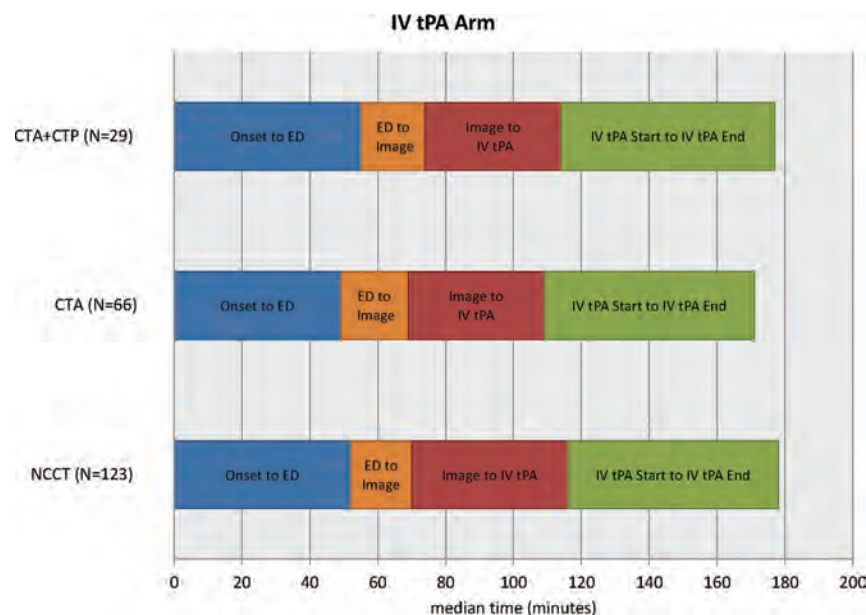
Time (min) (Median) (IQR)	CTP+CTA (n = 90)	CTA (n = 216)	NCCT (n = 342)	P Value
Onset to ED arrival	55.5 ^a (41–80)	51 (38–69)	48 (33–67)	.0216
ED arrival to start of imaging	19.5 (14–26)	21 ^a (14–28)	18 (10–25)	.0016
Imaging start to IV tPA initiation	40 ^a (29–54)	38 (24–51)	47 (33–64)	.0001
Onset to IV tPA initiation	120.5 (100–160)	117.5 (96–145)	120 (97–145)	.5762
ED to IV tPA initiation	62 (50–75)	59.5 (47–77)	65.5 (49–86)	.1554
IV tPA start to groin puncture ^b	77.5 (58.5–105.5)	81 ^a (65–96)	91 (66–115)	.0043
Imaging to groin puncture ^b	124 ^a (97–155.5)	119 ^a (95–140)	142 (115–170.5)	<.0001
ED to groin puncture ^b	146.5 (118.5–182.5)	144 ^a (120–167)	160 (132–191)	.0008
Groin puncture to EVT start ^c	30 ^a (26–45)	38 ^a (25–56)	44 (34–60)	.0001
EVT start to EVT finish ^c	63 (20–115)	46 ^a (14–83)	74 (42–119)	<.0001

Note.—IQR indicates interquartile range.

^a Significant pair-wise difference between the imaging subgroup and the NCCT group.

^b Applicable only to subjects with groin puncture: CTP + CTA (n = 60), CTA (n = 150), NCCT (n = 210).

^c Applicable only to subjects who received endovascular therapy with non-missing start time: CTP + CTA (n = 49), CTA (n = 117), NCCT (n = 159).

**FIG 1.** Time intervals of 3 imaging subgroups in the IV tPA treatment arm.

tively). Door to IV tPA initiation was not significantly different among groups. Time from baseline imaging to puncture was shorter in the CTP+CTA and CTA groups compared with NCCT (17 minutes [95% CI, 4–29 minutes] and 22 minutes [95% CI, 14–30 minutes] shorter, respectively). Groin puncture to EVT start was faster in the CTP+CTA and CTA groups, compared with the NCCT group (12 minutes [95% CI, 7–18 minutes] and 7 minutes [95% CI, 2–12 minutes] faster, respectively). EVT duration was 26 minutes (95% CI 14–37) faster in the CTA compared with the NCCT group, though the CTP+CTA and NCCT groups were not significantly different. Total ED arrival to puncture time was shorter in the CTP+CTA and CTA groups compared with the NCCT group (14 minutes [95% CI, 0–27 minutes] and 17 minutes [95% CI, 8–26 minutes] shorter, respectively).

There were no significant pair-wise time interval differences between the CTP + CTA and CTA groups. The rate of mother ship enrollment (direct admit of patient to tertiary stroke center) differed by subgroup: 97% in CTP+CTA group, 94% in CTA group, and 77% in NCCT group. When transfer subjects were removed, no statistical difference remained among groups for the time from onset to

IV tPA bolus ($P = .5568$). Times from imaging to groin puncture and groin puncture to the start of EVT were still shorter in the CTP+CTA and CTA populations ($P = .0088$ and $P = .0006$, respectively).

The high-enrolling sites (defined as sites that enrolled >6 subjects) were identified because these are usually high-volume, experienced stroke centers and tend to have established systems of care with streamlined workflows. There was no difference in the proportion of subjects from high-enrolling sites by imaging subgroups (85% CTP+CTA, 88% CTA, 86% NCCT; χ^2 , $P = .7947$). The sites were grouped by the ability to perform CTP, defined as having at least 1 subject in the CTP+CTA group, and we compared time to treatment and outcome. There were no significant differences between CTP sites and non-CTP sites in time from ED to IV tPA initiation, time from ED to groin puncture, or 90-day mRS of 0–2 (Table 3).

Outcomes

In the IV tPA treatment arm, there was not a significant difference in good clinical outcome in the 3 imaging subgroups (34.5% in CTP+CTA versus 40.9% in CTA versus 38.2% in NCCT; $P = .8338$). In the endovascular arm, more good outcomes were observed with CTA (39.3% in CTP+CTA versus 52.0% in CTA versus 33.8% in NCCT; $P = .0022$). In the endovascular arm, subjects with CTA had about twice the odds of good clinical outcome compared with subjects with NCCT, after adjustment for

age, NIHSS strata, and time from onset to IV tPA initiation (adjusted OR, 2.12; 95% CI, 1.36–3.31; Table 4).

DISCUSSION

The principal finding of our study is that additional imaging, including CT angiography with or without CT perfusion, did not delay treatment times compared with noncontrast CT in the IMS III trial. In fact, the imaging algorithms of NCCT + CTP + CTA or NCCT + CTA are possible with faster treatment times than NCCT alone.

The guiding principle of stroke therapy is rapid treatment because potential benefits and less adverse events are greatest with earlier reperfusion. Recently, multiple acute stroke trials have demonstrated that endovascular therapy improves functional outcomes in subjects with major arterial occlusions compared with standard therapy, including IV tPA.^{4–10} These trials included CTA and/or CTP imaging techniques to identify patients who would be likely to benefit from endovascular therapy. The MR CLEAN and REVASCAT trials used CTA to identify proximal vessel occlusion; ESCAPE evaluated vessel occlusion and collat-

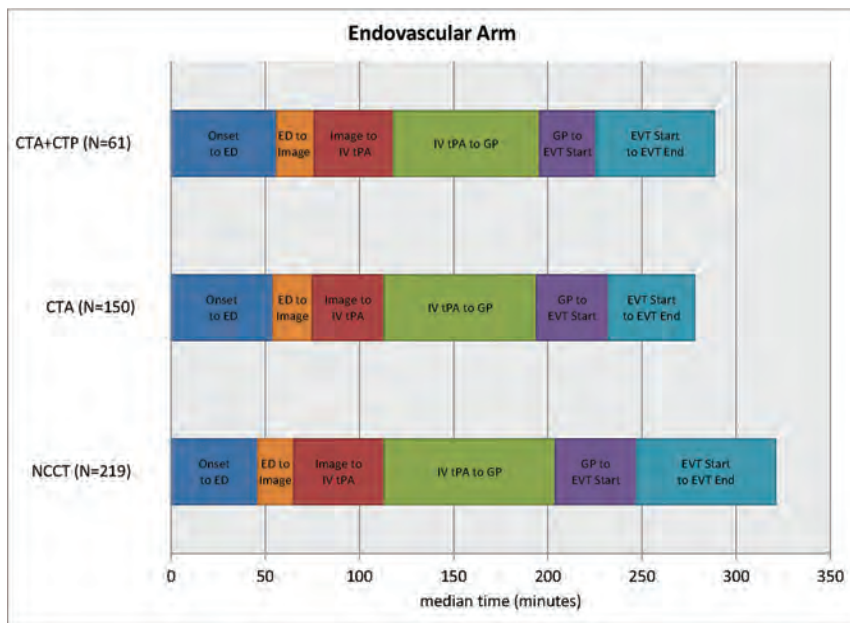


FIG 2. Time intervals of 3 imaging subgroups in the endovascular treatment arm.

Table 3: Time intervals and outcome for CTP and non-CTP sites

	CTP Sites ^a (20 Sites/266 Subjects)	Non-CTP Sites (38 Sites/382 Subjects)
ED to IV tPA initiation ^b (median) (IQR)	63 (47.5–76)	63 (49–87)
ED to groin puncture ^c (median)	145 (122.5–176)	157 (128–185)
90-Day mRS 0–2 (No.) (%)	114 (42.9%)	146 (38.2%)

Note:—IQR indicates interquartile range.

^a Sites that performed at least 1 baseline CTP.

^b Two subjects were missing from the CTP sites; 4 subjects were missing from the non-CTP sites.

^c Applicable only to subjects with groin puncture: 172 subjects from the CTP sites, 249 subjects from the non-CTP sites.

Table 4: Logistic regression for outcome (mRS 0–2 at 90 days) by treatment category

	Unadjusted OR (95% CI)	Adjusted ^a OR (95% CI)
Endovascular		
CTP+CTA vs NCCT	1.27 (0.71–2.28); <i>P</i> = .4218	1.32 (0.71–2.44); <i>P</i> = .3765
CTA vs NCCT	2.12 (1.39–3.25); <i>P</i> = .0005	2.12 (1.36–3.31); <i>P</i> = .0010
CTA vs CTP +CTA	1.67 (0.91–3.06); <i>P</i> = .0968	1.60 (0.85–3.03); <i>P</i> = .1444
IV tPA only		
CTP+CTA vs NCCT	0.85 (0.37–2.06); <i>P</i> = .7093	0.93 (0.38–2.29); <i>P</i> = .8708
CTA vs NCCT	1.12 (0.61–2.06); <i>P</i> = .7172	1.29 (0.66–2.49); <i>P</i> = .4557
CTA vs CTP +CTA	1.32 (0.53–3.27); <i>P</i> = .5547	1.39 (0.53–3.62); <i>P</i> = .5053

^a Adjusted for age, NIHSS score, and onset to IV treatment time.

eral circulation by using multiphase CTA; EXTEND-IA used CTA and CTP with automated perfusion processing; and the SWIFT PRIME study started with CTA/CTP or MRA/MR perfusion but amended the imaging protocol to a CT/CTA/MRA strategy to accommodate more sites. Multimodal imaging selection in these trials may lead to a paradigm shift in the use of imaging in acute ischemic stroke work-up. Investigation of workflow while using these imaging algorithms is even more important in the current era.

The strength of our study is that we have analyzed time to treatment with 3 different imaging paradigms in the setting of a large, randomized multicenter acute stroke trial (IMS III). The recent endovascular stroke trials selected patients on the basis of additional imaging, including CTA, multiphase CTA, or CTP. These trials do not have a control NCCT-alone group for similar workflow comparisons, as we have in our study. Our results sup-

port the findings of these trials by suggesting benefits with the use of CTA with or without CTP in the work-up of patients with ischemic stroke.

We found that the CTA group of subjects was associated with better clinical outcome in the endovascular arm, likely a marker of faster treatment times among more advanced stroke centers. In a previous analysis by using data from the IMS III trial, we found that the odds of favorable outcome in subjects with baseline CTA were higher.^{12,13} In this study, we have further explored this group by adding CTP to the imaging analysis. In a prior study involving a multicenter, prospective, single-arm thrombectomy trial, our group demonstrated that multimodal CT-based imaging did not affect workflow.³ Our results are consistent with a single-center experience in which change in acute stroke imaging protocol to include multimodal CT did not delay administration of IV tPA.¹⁴ Our findings differed from those in a retrospective, multi-institutional study, in which advanced imaging was associated with delays in endovascular treatment without added benefit in outcomes.¹⁵ However, there are considerable differences between the 2 studies. The study by Sheth et al¹⁵ was a retrospective analysis of both CT and MR imaging, which included only subjects with endovascular treatment; perfusion imaging was used for decision-making, and the study did not address the vascular imaging times and time to IV tPA.

Most surprising, in our study, the NCCT group had longer treatment times, including imaging to IV tPA initiation and imaging to endovascular treatment times. This may be multifactorial.

A CTA study can be advantageous for endovascular therapy planning, adding valuable information regarding the presence or absence of large-vessel occlusion, the exact site of the occlusion, anatomic details of the vessels, and the presence of atherosclerotic plaque, and as a result, CTA can potentially reduce procedural time.¹³ In addition, institution-specific practice and workflow patterns may translate into faster treatments. Experienced, high-volume stroke centers may have parallel processes in place, whereby the treatment decisions are made in the CT console, including administration of IV tPA (if appropriate) after NCCT.¹⁶ A workflow that offers IV tPA administration in parallel to imaging and rapid activation of the interventional team has the potential to reduce treatment times.

Perfusion may provide information regarding tissue viability. However, in our analysis the addition of CTP did not add an

outcome benefit compared with CTA alone. Potential reasons for this observation include the following: 1) CTP was not always used for treatment decisions; 2) there is marked variability in CTP postprocessing, and its ability to reliably identify nonviable tissue likely varies substantially across centers; and 3) there is a high potential for selection bias, and patients who underwent additional CTP imaging may have had different baseline characteristics from those who did not.

Limitations

Our study has several important limitations, including the heterogeneity of imaging protocols in the IMS III centers. Our data did not address the institutional variables affecting workflow, which is critical in understanding the differences in time parameters. Institutional practice variability due not only to the large number of participating IMS III centers (58 centers) but also changes in practice during the trial (2006–2012) confound analysis of center-specific practice patterns. Institution-specific data on workflow details around IV tPA administration, neurointervention team activation, and time taken for study consent were not available. We also acknowledge that other unmeasured variables, including general-versus-local anesthesia and complete-versus-focused angiograms, can influence the time intervals.

It is likely that multimodal imaging (CTA and/or CTP) did not necessarily lead to faster treatment but was simply performed in centers that were generally faster. High-volume stroke centers that perform CTA and CTP routinely may have expedited workflows leading to shorter times to revascularization. The recent ESCAPE trial had aggressive time targets (median time from imaging to first reperfusion of 84 minutes), and most of subjects were enrolled at endovascular centers that successfully implemented well-organized workflow and imaging processes.⁵

Although CTA and CTP can be performed quickly with the new-generation scanners (median time to perform CTP+CTA and CTA was 9 and 5 minutes, respectively, in our study), data postprocessing and interpretation and decision-making to activate endovascular teams can cause time delays, and we could not analyze this step of the workflow. Ideally, the image processing and interpretation should be performed in parallel with other workflow steps rather than being a sequential flow, to minimize delays.

Another limitation of our study is that it is unclear whether CTA/CTP imaging was used for treatment decisions with potential impact on outcomes, particularly in the endovascular arm, though as per the study protocol, advanced imaging was not used for treatment decisions. We acknowledge that there are constraints in the data that particularly limit what can be said about the role and importance of CTP. The key ones are the relatively small number of patients who underwent CTP and the lack of information about how the CTP data were processed or used in the study.

We did not analyze the MR imaging–based paradigms due to a very small number of subjects who underwent baseline MR imaging in IMS III. Although MR imaging has obvious diagnostic advantages, it can cause delays in treatment compared with CT-based paradigms.^{3,17,18} Finally, this is a post hoc analysis and additional confounding factors and baseline differences may

account for the differences in outcome, thus limiting the generalizability of our results. The outcome differences should be viewed with caution and in the context of limitations of a post hoc analysis.

CONCLUSIONS

Use of CTA with or without CTP did not delay IV tPA thrombolysis or endovascular therapy compared with NCCT in the IMS III trial. Efficient institutional protocols and expedited workflows to allow rapid neuroimaging for patient selection without delaying treatment are very relevant in the current landscape.

Disclosures: Achala Vagal—RELATED: Grant: Clinical and Translational Science Awards 8 UL1 TR000077-05,* Genentech,* Comments: research grant: Clinical and Translational Science Awards KL2 Career Award; research grant: Imaging Core Lab, PRISMS trial, Genentech. Lydia D. Foster—RELATED: Grant: National Institute of Neurological Disorders and Stroke (IMS U01 NS077304).* Sharon D. Yeatts—RELATED: Grant: National Institutes of Health/National Institute of Neurological Disorders and Stroke (U01 NS052220),* Comments: Statistics and Data Coordination Center for IMS III: unblinded statistician; UNRELATED: Consultancy: Genentech, Comments: PRISMS Trial Steering Committee member. Andrew M. Demchuk—RELATED: Grant: National Institutes of Health/National Institute of Neurological Disorders and Stroke,* Comments: National Institutes of Health funded the Calgary CT Core Laboratory for the IMS-III trial; UNRELATED: Payment for Lectures (including service on Speakers Bureaus): Medtronic, Comments: honorarium for Continuing Medical Education lectures. Michael D. Hill—RELATED: Grant: National Institutes of Health/National Institute of Neurological Disorders and Stroke*; UNRELATED: Consultancy: Merck, Comments: paid Adjudication Committee for outcomes assessment in clinical trials; Grants/Grants Pending: Covidien,* Comments: grant for the ESCAPE trial; Stock/Stock Options: Calgary Scientific (stock ownership, imaging company). Thomas A. Tomsick—RELATED: Grant: National Institute of Neurological Disorders and Stroke,* Comments: Angiography Core Lab. Interventional Co-Principal Investigator; UNRELATED: Expert Testimony: Multiple legal entities. Mayank Goyal—RELATED: Grant: Covidien,* Comments: partial funding of ESCAPE trial through an unrestricted grant to University of Calgary; Consulting Fee or Honorarium: Covidien, Stryker, Comments: speaking engagement on acute stroke, design and conduct of SWIFT PRIME trial; Other: GE Healthcare, Comments: licensing agreement regarding further development of systems of stroke diagnosis.*Money paid to the institution.

REFERENCES

1. Khatri P, Yeatts SD, Mazighi M, et al; IMS III Trialists. **Time to angiographic reperfusion and clinical outcome after acute ischaemic stroke: an analysis of data from the Interventional Management of Stroke (IMS III) phase 3 trial.** *Lancet Neurol* 2014;13:567–74 CrossRef Medline
2. Lees KR, Bluhmki E, von Kummer R, et al. **Time to treatment with intravenous alteplase and outcome in stroke: an updated pooled analysis of ECASS, ATLANTIS, NINDS, and EPITHET trials.** *Lancet* 2010;375:1695–703 CrossRef Medline
3. Menon BK, Almekhlafi MA, Pereira VM, et al; STAR Study Investigators. **Optimal workflow and process-based performance measures for endovascular therapy in acute ischemic stroke: analysis of the Solitaire FR thrombectomy for acute revascularization study.** *Stroke* 2014;45:2024–29 CrossRef Medline
4. Berkhemer OA, Fransen PS, Beumer D, et al. **A randomized trial of intraarterial treatment for acute ischemic stroke.** *N Engl J Med* 2015; 372:11–20 CrossRef Medline
5. Goyal M, Demchuk AM, Menon BK, et al; ESCAPE Trial Investigators. **Randomized assessment of rapid endovascular treatment of ischemic stroke.** *N Engl J Med* 2015;372:1019–30 CrossRef Medline
6. Campbell BC, Mitchell PJ, Kleinig TJ, et al; EXTEND-IA Investigators. **Endovascular therapy for ischemic stroke with perfusion-imaging selection.** *N Engl J Med* 2015;372:1009–18 CrossRef Medline
7. Saver JL, Goyal M, Bonafe A, et al. **Stent-retriever thrombectomy**

- after intravenous tPA vs. tPA alone in stroke. *N Engl J Med* 2015;372:2285–95 CrossRef Medline
8. Jovin TG, Chamorro A, Cobo E, et al; REVASCAT Trial Investigators. **Thrombectomy within 8 hours after symptom onset in ischemic stroke.** *N Engl J Med* 2015;372:2296–306 CrossRef Medline
 9. Mocco J, Zaidat O, von Kummer R, et al. **Results of the THEPAPY trial.** In: *Proceedings of the European Stroke Organisation*, Glasgow, UK. April 17–19, 2015
 10. Bracard S GF, Ducrocq X. **THRACE study: intermediate analysis results.** In: *Proceedings of the European Stroke Organisation*, Glasgow, UK. April 17–19, 2015
 11. Broderick JP, Palesch YY, Demchuk AM, et al; Interventional Management of Stroke (IMS) III Investigators. **Endovascular therapy after intravenous tPA versus tPA alone for stroke.** *N Engl J Med* 2013;368:893–903 CrossRef Medline
 12. Demchuk AM, Goyal M, Yeatts SD, et al; IMS III Investigators. **Recanalization and clinical outcome of occlusion sites at baseline CT angiography in the Interventional Management of Stroke III trial.** *Radiology* 2014;273:202–10 CrossRef Medline
 13. Goyal M, Almekhlafi MA, Fan L, et al. **Evaluation of interval times from onset to reperfusion in patients undergoing endovascular therapy in the Interventional Management of Stroke III trial.** *Circulation* 2014;130:265–72 CrossRef Medline
 14. Salottolo KM, Fanale CV, Leonard KA, et al. **Multimodal imaging does not delay intravenous thrombolytic therapy in acute stroke.** *AJNR Am J Neuroradiol* 2011;32:864–68 CrossRef Medline
 15. Sheth KN, Terry JB, Nogueira RG, et al. **Advanced modality imaging evaluation in acute ischemic stroke may lead to delayed endovascular reperfusion therapy without improvement in clinical outcomes.** *J Neurointerv Surg* 2013;5(suppl 1):i62–65 CrossRef Medline
 16. Goyal M, Menon BK, Hill MD, et al. **Consistently achieving computed tomography to endovascular recanalization <90 minutes: solutions and innovations.** *Stroke* 2014;45:e252–56 CrossRef Medline
 17. Yoo SH, Kwon SU, Lee DH, et al. **Comparison between MRI screening and CT-plus-MRI screening for thrombolysis within 3 h of ischemic stroke.** *J Neurol Sci* 2010;294:119–23 CrossRef Medline
 18. Chalela JA, Kidwell CS, Nentwich LM, et al. **Magnetic resonance imaging and computed tomography in emergency assessment of patients with suspected acute stroke: a prospective comparison.** *Lancet* 2007;369:293–98 CrossRef Medline

Performance of CT ASPECTS and Collateral Score in Risk Stratification: Can Target Perfusion Profiles Be Predicted without Perfusion Imaging?

S. Dehkharghani, R. Bammer, M. Straka, M. Bowen, J.W. Allen, S. Rangaraju, J. Kang, T. Gleason, C. Brasher, and F. Nahab

ABSTRACT

BACKGROUND AND PURPOSE: Endovascular trials suggest that revascularization benefits a subset of acute ischemic stroke patients with large-artery occlusion and small-core infarct volumes. The objective of our study was to identify thresholds of noncontrast CT-ASPECTS and collateral scores on CT angiography that best predict ischemic core volume thresholds quantified by CT perfusion among patients with acute ischemic stroke.

MATERIALS AND METHODS: Fifty-four patients with acute ischemic stroke (<12 hours) and MCA/intracranial ICA occlusion underwent NCCT/CTP during their initial evaluation. CTP analysis was performed on a user-independent platform (RAPid processing of Perfusion and Diffusion), computing core infarct (defined as CBF of <30% normal). A target mismatch profile consisting of infarction core of ≤ 50 mL was selected to define candidates with acute ischemic stroke likely to benefit from revascularization.

RESULTS: NCCT-ASPECTS of ≥ 9 with a CTA collateral score of 3 had 100% specificity for identifying patients with a CBF core volume of ≤ 50 mL. NCCT-ASPECTS of ≤ 6 had 100% specificity for identifying patients with a CBF core volume of > 50 mL. In our cohort, 44 (81%) patients had an NCCT-ASPECTS of ≥ 9 , a CTA collateral score of 3, or an NCCT-ASPECTS of ≤ 6 .

CONCLUSIONS: Using an NCCT-ASPECTS of ≥ 9 or a CTA collateral score of 3 best predicts CBF core volume infarct of ≤ 50 mL, while an NCCT-ASPECTS of ≤ 6 best predicts a CBF core volume infarct of > 50 mL. Together these thresholds suggest that a specific population of patients with acute ischemic stroke not meeting such profiles may benefit most from CTP imaging to determine candidacy for revascularization.

ABBREVIATIONS: AIS = acute ischemic stroke; RAPID = RAPid processing of Perfusion and Diffusion

Revascularization aims to prevent progression of ischemic injury in acute ischemic stroke (AIS).¹⁻⁴ Recent success in trials of endovascular AIS therapy, while restoring motivation for acute stroke intervention, has left the subject of an optimal patient-selection paradigm largely unaddressed.⁵⁻⁸ While the primary goals in this setting include timely revascularization, the relative merits of expedited triage versus identification of target imaging profiles remain the subject of ongoing inquiry.

Contemporary guidelines on AIS management, therefore, remain inconclusive as to the role of multimodal imaging selection.⁹

We recently reported the benefits of a high-speed computing tool for CT perfusion analysis over qualitative approaches to imaging triage for prognostication among patients with anterior circulation AIS.¹⁰ The findings therein suggested that a user- and vendor-independent computational tool may outperform purely qualitative approaches in outcome prediction. Similar implementations of this tool in recent, prospective endovascular trials suggested strong results as an approach to patient selection; however, the relative contribution of CTP-based selection criteria, among other trial-specific features, remains uncertain in light of the overall favorable outcomes reported across disparate trial designs.⁵⁻⁸

The objective of our study was to identify thresholds of NCCT-ASPECTS and collateral score on CT angiography that best predict ischemic core volume thresholds quantified by CTP among patients with AIS.

Received November 20, 2015; accepted after revision January 10, 2016.

From the Departments of Radiology and Imaging Sciences (S.D., M.B., J.W.A., T.G.) and Neurology (S.D., J.W.A., S.R., C.B., F.N.), Emory University Hospital, Atlanta, Georgia; Department of Radiology (R.B.), Stanford University Hospital, Stanford, California; Institut für Radiologie und Nuklearmedizin (M.S.), Kantonsspital Winterthur, Winterthur, Switzerland; and Department of Biostatistics (J.K.), University of Michigan, Ann Arbor, Michigan.

Please address correspondence to Seena Dehkharghani, MD, Department of Radiology and Imaging Sciences and Neurology, Neuroradiology Division; Attention: Mary Davis, Department of Radiology and Imaging Sciences, Emory University Hospital, 1364 Clifton Rd NE, Atlanta, GA 30322; e-mail: Seena.Dehkharghani@Emory.edu

<http://dx.doi.org/10.3174/ajnr.A4727>

MATERIALS AND METHODS

The population examined was previously studied in a report of the relative predictive value of quantitative and qualitative acute stroke imaging analysis in prognostication and clinical outcome prediction.¹⁰ Briefly, 62 continuous patients (36 women; median age, 70 years; range, 33–94 years) with AIS (<12 hours) and MCA or intracranial ICA occlusion were identified from a prospectively collected, single-institution stroke registry and radiologic informatics query of 815 patients with ischemic stroke, spanning February 1, 2011, to December 31, 2013, with Emory University Hospital review board approval. All patients were evaluated initially by a dedicated vascular neurologist in the emergency setting, with initiation of institutional stroke protocol facilitating expedited triage, imaging, interpretation, and treatment when appropriate. All patients underwent comprehensive stroke imaging at presentation, including NCCT, CTA, and CTP. Patients were included in the analysis on the basis of successful completion of the imaging protocol, absence of motion or other artifacts rendering imaging nondiagnostic, and the absence of large hemorrhages such as parenchymal hematomas (types 1 and 2) potentially confounding final infarction measurement. Exclusion criteria were an inability to undergo multimodal CT, a history of renal failure, and patient age younger than 18 years. A subset of patients received intravenous and/or intra-arterial thrombolytic therapy as per institutional protocol and at the discretion of the treating vascular neurologist and neurointerventionalist.

Imaging Protocol

All patients underwent an institutional stroke imaging protocol including NCCT, CTP, and CTA. CT was performed on a 40-mm, 64–detector row clinical system (LightSpeed VCT; GE Healthcare, Milwaukee, Wisconsin). Helical NCCT (120 kV[peak], 100–350 auto-mAs) was performed from the foramen magnum through the vertex at 5.0-mm section thickness. In the absence of visible intracranial hemorrhage during real-time evaluation by a radiologist and stroke neurologist, 2 contiguous CTP slabs were obtained for 8-cm combined coverage of the supratentorial brain, obtained at 5-mm sections per slab. Cine mode acquisition (80 kVp, 100 mAs) permitting high-temporal-resolution (1-second sampling interval) dynamic bolus passage imaging was performed following the administration of 35 mL of iodinated contrast (iopamidol, Isovue 370; Bracco Diagnostics, Princeton, New Jersey), power injected at 5 mL/s through an 18-ga or larger antecubital IV access. Contrast administration was followed by a 25-mL saline flush at the same rate. For both slabs, the same acquisition and injection protocol was used (ie, a total of 70 mL of iodine was used for CTP). Last, helical CTA (120 kVp, 200–350 auto-mAs) was performed from the carina to the vertex (section thickness/interval, 0.625/0.375 mm) following IV administration of 70 mL of iodinated contrast injected at 5 mL/s and followed by a 25-mL saline flush.

Follow-up imaging in all patients included brain MR imaging for documentation of final infarct size within 3 days of CTP, performed on a 3T (Tim Trio; Siemens, Erlangen, Germany) clinical whole-body system with local signal reception by a dedicated 12-channel head coil. All images were transferred to a separate workstation for analysis (Mac Pro; Apple, Cupertino, California) by

using a third-party DICOM viewer (OsiriX Imaging Software; <http://www.osirix-viewer.com>). The details of the postprocessing pipeline were reported previously.¹⁰

Imaging Analysis

NCCT-ASPECTS. ASPECTSs were assigned by 2 experienced vascular neurologists (S.R., F.N.) blinded to all other imaging and clinical outcomes. ASPECTS uses a 10-point visual inspection scale estimating ischemic burden in the supratentorial brain as detailed previously by Barber et al.¹¹

CTA Collateral Score. A CTA-derived collateral vessel-scoring methodology was used as detailed previously.^{10,12} Briefly, 2 experienced neuroradiologists, both with subspecialty certification and experienced in stroke and neurovascular imaging, assigned CTA collateral scores using a visual inspection methodology to quantify surface leptomeningeal collaterals in response to proximal arterial compromise, compared with the contralateral side.¹² The neuroradiologists assigned scores blinded to clinical and outcomes data and all other imaging.^{13,14} A collateral score was assigned by using an ordinal, visual grading system estimating collateral flow, scored 0–3 as follows: Collateral flow was assigned a score of zero for absent surface vasculature, 1 for >0 but ≤50% vasculature, 2 for >50 but <100% vasculature, and 3 for normal or supranormal surface vasculature of the MCA territory. CTA analysis was performed by using 20-mm axial sliding maximum intensity projection and 0.625-mm axial source images and orthogonal and curved multiplanar reformats as needed.

CT Perfusion. All perfusion imaging was postprocessed by using a custom, noncommercial version of a vendor-independent software platform (RAPID) provided by Stanford University.¹⁵ RAPID is an automated computational tool designed for timely analysis of CTP data as used recently in the stroke trial setting.^{3–5,7} Details of the perfusion postprocessing pipeline were discussed previously.^{10,15} Briefly, following preprocessing steps correcting rigid-body motion, arterial input function selection is performed and deconvolved from the voxel time-attenuation course using a delay-insensitive algorithm for isolation of the tissue residue function. The time to maximum of the tissue residue function is determined on a voxelwise basis, and time-to-maximum maps are incrementally thresholded between 4 and 10 seconds at 2-second intervals with penumbral maps overlaid on the source CTP data.^{10,15}

Cerebral blood flow maps expressed in milliliters/100 g/minute were computed as outlined elsewhere. Relative CBF maps have been used in the stroke trial setting as estimates of irreversibly infarcted (core) tissues by using thresholds of relative CBF of <30% contralateral normal tissues.¹⁶ Parametric maps were automatically generated and overlaid on source images for review purposes.

Statistical Analysis

The range, mean, and median values of relative CBF–derived infarction core were determined across ASPECTS levels and for dichotomized ASPECTS of ≥7. A linear regression model was fitted with relative CBF core volume as an outcome, creating dummy variables for covariate NCCT-ASPECTS in regression analysis;

Table 1: Patient characteristics^a

Characteristics	
Admission NIHSS	15 (16)
Time of onset/last known healthy to imaging (min)	210 (252)
IV tPA (No.) (%)	23 (43)
Endovascular treatment (No.) (%)	9 (17)
IA tPA	3
Thrombectomy	6
NCCT-ASPECTS	9 (1)
Final infarction volume (mL)	37 (96)

Note:—IA indicates intra-arterial.

^aData are reported as median (interquartile range) unless otherwise noted.

ANOVA analysis was performed on the fitted linear regression, and an *F*-test was applied. Because the NCCT-ASPECTS was considered a dummy variable in the regression and ANOVA analyses, the Kendall τ correlation was used to test the strength of the correlation. Given the previously high interreader correlation for the NCCT-ASPECTS of ≥ 7 (0.93) in our study population, all variables were assessed as the unweighted mean of combined reader scores for qualitative variables.¹⁰

An operationally defined CTP profile predicting favorable outcome was assigned as prescribed in a recently reported, prospective endovascular therapy trial.⁵ Specifically, a target mismatch profile consisting of an infarction core of ≤ 50 mL was selected as the target relative CBF infarction core volume determined across NCCT-ASPECTS and at a dichotomized NCCT-ASPECTS of ≥ 7 . The 50 mL threshold was selected as a reference volume as reported by the investigators of the recent Solitaire With the Intention for Thrombectomy as Primary Endovascular Treatment (SWIFT PRIME) trial and as used in the recent development of a benchmarking software environment for quality control in stroke perfusion imaging.^{5,17} The Fisher exact test was further applied to determine the association of ASPECTS of ≥ 7 and infarction core of ≤ 50 mL. A prediction error model for correct classification of patients as having greater or less than 50 mL CBF infarction core was determined across NCCT-ASPECTS and at a dichotomized ASPECTS of ≥ 7 . Sensitivity, specificity, and positive and negative predictive values for various thresholds of ASPECTS and collateral scores were calculated and reported.

Statistical analysis was performed in R statistical and computing software (<http://www.r-project.org/>).

RESULTS

Sixty-two patients (36 women; median age, 70 years; range, 33–94 years) with AIS (<12 hours) and MCA or intracranial ICA occlusion constituted the study population as previously reported. Incomplete or degraded imaging necessitated exclusion of 8 patients, leaving 54 patients for analysis. An ICA or M1 occlusion was present in 41 (76%) patients, with proximal M2 segment occlusion in the remainder. No patients had bilateral arterial occlusions.

As shown in Table 1, the median NIHSS score at admission was 15 (interquartile range, 16); the mean duration from the time of onset/last known healthy to imaging was 210 minutes. Twenty-three (43%) patients received IV tPA, and 9 (17%) underwent endovascular treatment with intra-arterial tPA ($n = 3$) or thrombectomy ($n = 6$). The median NCCT-ASPECTS was 9 (interquar-

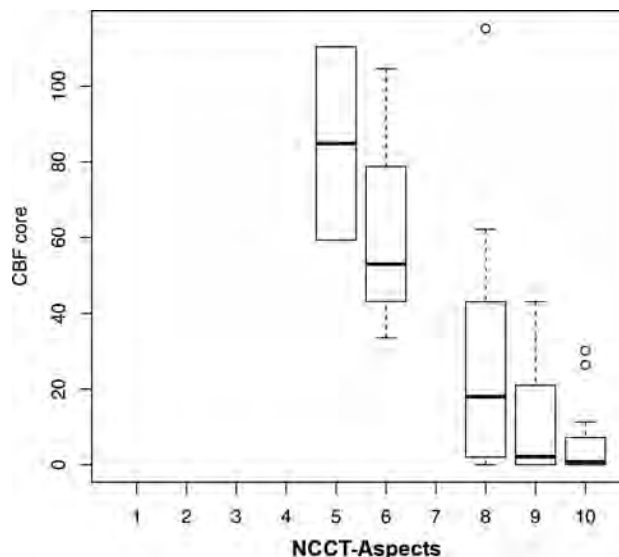


FIG 1. Computed ischemic core volumes by using relative CBF thresholded at <30% contralateral normal tissues. Boxplots illustrate the range and distribution of ischemic core values across NCCT-ASPECTS values for the entire study population. An ASPECTS of 7 represented a null dataset following averaging of 2 blinded readers (see text). Notably, no patients with NCCT-ASPECTS of ≤ 5 were encountered within the study population. Values are shown as median (line), interquartile range (box), 10th/90th percentile (bars), and outliers (circles).

tile range, 1). Median final infarction volume as measured by MR imaging was 37 (interquartile range, 96) mL.

While a significant association was detected between CBF core estimates and NCCT-ASPECTS (Kendall τ correlation, -0.51 ; $P < .01$), large variability was found across 2-reader mean ASPECTS values (Fig 1). For example, across patients with an NCCT-ASPECTS of 8, the CBF core volume ranged from 0 to 115 mL with a median of 23 mL (interquartile range, 42 mL). Ranges of core volume increased further at lower ASPECTS. Table 2 presents sensitivity, specificity, negative predictive values, and positive predictive values of the candidate predictors, NCCT-ASPECTS and collateral scores. For the analysis of dichotomized ASPECTS of ≥ 7 , the CBF core volume ranged from 0 to 115 mL with a median of 4 mL (interquartile range, 15 mL). An NCCT-ASPECTS of ≥ 9 had 100% specificity (95% CI, 60–100) for identifying patients with CBF core volume of ≤ 50 mL, while an NCCT-ASPECTS of ≤ 6 had 100% specificity (95% CI, 90%–100%) for identifying patients with a CBF core volume of > 50 mL. The prediction error model for correct identification of infarction core of ≤ 50 mL among ASPECTS of ≥ 7 demonstrated significant associations but low specificity relative to a CBF core of ≤ 50 mL (prediction error, 9%; $P = .025$; sensitivity, 0.98; specificity, 0.50; negative predictive value, 0.80; positive predictive value, 0.92).

Our cohort included 28 patients with a collateral score of 1, 10 patients with a score of 2, and 15 patients with a score of 3. A collateral score of 3 on CTA had 100% specificity (95% CI, 47%–99%) but only 33% sensitivity (95% CI, 20%–49%) for identifying patients with AIS with a CBF core volume of ≤ 50 mL. A collateral score of ≤ 1 had an 88% sensitivity (95% CI, 47%–99%) and a 53% specificity (95% CI, 38%–68%) for identifying patients with AIS with a CBF core volume of > 50 mL. The collateral

score demonstrated a significant association with CBF ischemic core volumes ($P < .01$).

DISCUSSION

Our study found significant variability in CBF core volumes among patients with AIS with similar NCCT-ASPECTS, we identified thresholds of NCCT-ASPECTS of ≥ 9 and collateral scores of 3 with high specificity for finding patients with AIS with core volumes considered ideal for revascularization. We also found that NCCT-ASPECTS of ≤ 6 had a high specificity for identifying patients with AIS with core volumes that made them suboptimal candidates for revascularization.

Recent successful AIS trials have used disparate methodologies for patient selection. These have differed primarily in their use of either fast but potentially insensitive methodologies (eg, NCCT-ASPECTS) versus more rigorous approaches to estimating tissue viability with CTP, permitting operational tissue classification,

segmentation, and volume measures.^{3,4,7,18} These specific factors have been emphasized as targets for optimization and general requirements in the stroke-research setting in recent expert consensus.¹⁹ NCCT-ASPECTS aims to qualitatively identify early ischemic changes modulated by ischemic bulk water shifts (ie, edema). The speed and nearly invariable access to NCCT-ASPECTS are clearly advantageous; however, reproducibility and interrater agreement are reportedly variable.^{11,20-22} The insensitivity of NCCT to initial water shifts, primarily those from the interstitial to the intracellular compartment preceding progressive vasogenic edema, may preclude accurate estimation of neuronal injury in the very early aftermath of infarction.^{14,20-23} NCCT-ASPECTS may furthermore be limited by its tendency to cluster largely variable volumes of injury across its coarsely changing scale, as illustrated in Fig 2, in which identical NCCT-ASPECTS between 2 subjects can belie considerable differences in the actual volume of injury. Such challenges may underlie existing

reports of greater agreement and predictive accuracy for CTP in comparison with NCCT-ASPECTS.^{13,14,24,25} Notwithstanding these features, we previously reported a high interrater agreement in the assignment of dichotomized ASPECTS of >7 , despite more marginal agreement across all ASPECTSs.

We selected an infarction core threshold of 50 mL as a reference volume against which NCCT-ASPECTS and collateral scores were studied, as reported by the investigators of the recent SWIFT PRIME trial.⁵ The 50-mL threshold has furthermore been pro-

Table 2: Accuracy of NCCT-ASPECTS and collateral score in prediction of CBF infarction core of ≤ 50 mL

Threshold	Sensitivity	Specificity	PPV	NPV
NCCT-ASPECTS (CBF core volume ≤ 50 mL)				
≥ 4	100	0	84.9	—
≥ 5	100	25	88.2	100
≥ 6	100	37.5	90.0	100
≥ 7	97.8	50	91.7	80.2
≥ 8	91.1	62.5	93.2	55.5
≥ 9	68.9	100	100	36.4
≥ 10	26.7	100	100	19.5
Collateral score (CBF core volume ≤ 50 mL)				
≥ 0	100	0	84.9	—
≥ 1	53.3	87.5	96.0	25.0
≥ 2	33.3	100	100	21.0
≥ 3	0	100	—	15.1

Note:—PPV indicates positive predictive value; NPV, negative predictive value; —, non-value.

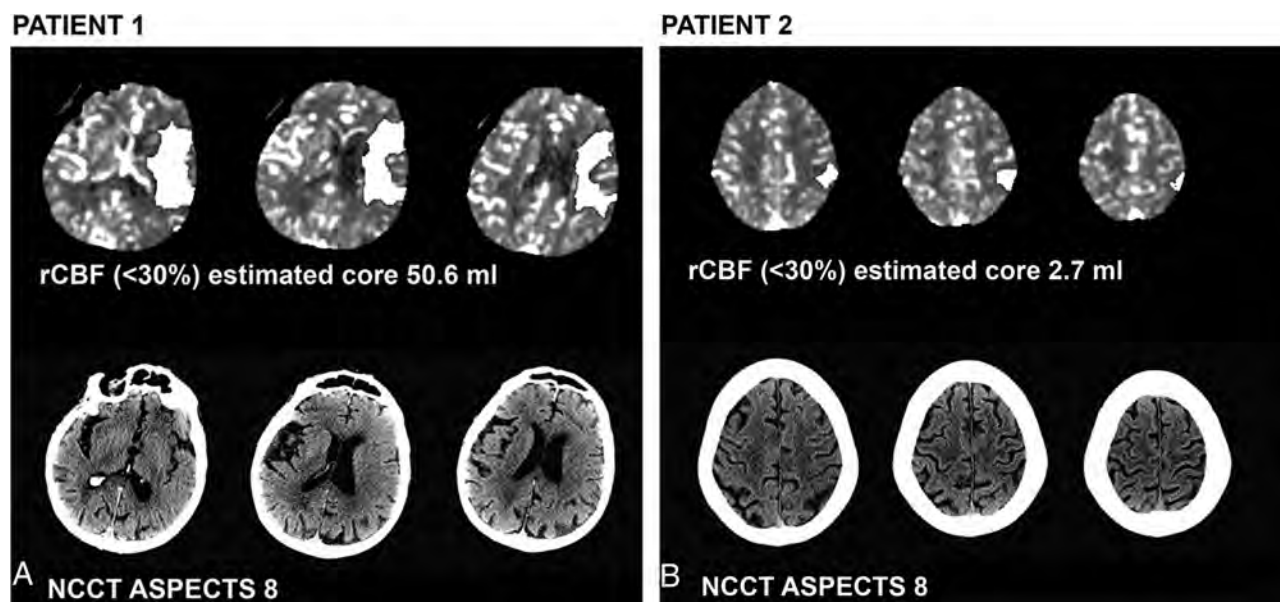


FIG 2. CT perfusion ischemic core estimates and complementary NCCT-ASPECTS in 2 patients (A and B). Selected images from panels of RAPID-derived CBF core maps (white overlays) and NCCT-ASPECTS in 2 subjects, both with an ASPECTS of 8. Large differences in the estimated volume of irreversible ischemic core are noted despite high ASPECTS in both patients presenting with acute stroke-like symptoms. Patient 1 is an 83-year-old woman (NIHSS score = 29) with NCCT-ASPECTS hypoattenuation suspected within the anterior left insular region and lateral lentiform; Patient 2 is an 83-year-old man (NIHSS = 28) with NCCT-ASPECTS abnormality suspected within the lateral perirolandic parietal lobe and the lateral temporal lobe (not shown). rCBF indicates relative CBF.

posed in the development of a recently reported benchmarking tool derived from pooled, prospectively acquired stroke trial data to test the accuracy of perfusion-processing software for future trial use.¹⁷ We thus propose that this threshold is relevant and reflective of current viewpoints in stroke imaging. Specifically with regard to such CTP selection criteria in AIS trials, we observed large ranges and variability in CBF infarction core volumes across ASPECTS.⁵

Within this population, the CTA collateral score demonstrated a strong statistical association with CTP ischemic core volumes, but low sensitivity and specificity for threshold infarction prediction. While these findings could reflect statistical limitations related to sample size, we hypothesize that collateral score and other static measures of surface vascularity may be unable to capture the dynamic nature of collateral enhancement, while also lacking in their ability to identify the truly nutritive capacity of surface vessels. Recent advances in CT angiography, particularly the development of timing-invariant CTA derived from CTP dynamic bolus-passage source data, offer some promise in mitigating the timing sensitivity of standard CTA in identifying collateral vessels.²⁶

We acknowledge several study limitations, particularly those inherent in the retrospective nature of the analysis. Heterogeneity in the study cohort precluded subselection of treated-versus-untreated patients. However, we contend that bias related to treatment selection had a negligible impact on the study conclusions because the primary aim of our study was to examine the variability between contemporaneously acquired imaging triage strategies. The qualitative parameters in this study were generated from 2 independent, experienced readers, in whom variability may bias results; however, as previously reported, interreader agreement was high across variables in this study population.¹⁰ The relative standard in this study, against which the qualitative variables were compared, was the RAPID software environment. While other such software solutions are available, we recently reported the strengths of the RAPID tool as a fully automated, user- and vendor-independent means of semi-quantitative perfusion analysis. As a semi-quantitative CTP computing tool, RAPID has been shown to perform well, matching or exceeding the accuracy of similar software environments relative to a ground truth digital perfusion phantom in a recent study, and the use of similar iterations of the RAPID tool in recent multicenter trials may further support the generalizability of our findings.^{3,4,5,7,27}

Patient selection criteria likely modulate success in achieving a favorable clinical response following revascularization in acute ischemic stroke. The era of contemporary revascularization technologies now permits timely and dependable restoration of flow in most cases; however, optimal identification of a target population for treatment remains critical, and the ideal selection strategy remains inconclusively established. These findings suggest that readily available and expedited approaches to selection such as ASPECTS correlate with commonly used perfusion parameters but may lack sensitivity to inform accurate and quantitative estimations of core volumes.

CONCLUSIONS

Using an NCCT-ASPECTS of ≥ 9 or a CTA collateral score of 3 best predicts a CBF core volume infarct of ≤ 50 mL, while an NCCT-ASPECTS of ≤ 6 best predicts a CBF core volume infarct of > 50 mL. Together these thresholds suggest that a specific population of patients with AIS not meeting such profiles may benefit most from CT perfusion to determine their candidacy for revascularization.

Disclosures: Matus Straka—UNRELATED: Employment: iSchemaView; Stock/Stock Options: iSchemaView. Srikanth Rangaraju—UNRELATED: Grants/Grants Pending: National Institutes of Health,* Comments: Dr Rangaraju is a trainee under the National Institute of Neurological Disorders and Stroke T32 training grant (2T32 NS 007480-15, Principal Investigator, Allan I. Levey). *Money paid to the institution.

REFERENCES

1. Saver JL, Jahan R, Levy EI, et al. **Solitaire flow restoration device versus the Merci retriever in patients with acute ischaemic stroke (SWIFT): a randomised, parallel-group, non-inferiority trial.** *Lancet* 2012;380:1241–49 CrossRef Medline
2. Nogueira RG, Lutsep HL, Gupta R, et al. **Trevo versus Merci retrievers for thrombectomy revascularisation of large vessel occlusions in acute ischaemic stroke (TREVO 2): a randomised trial.** *Lancet* 2012;380:1231–40 CrossRef Medline
3. Lansberg MG, Straka M, Kemp S, et al; DEFUSE 2 study investigators. **MRI profile and response to endovascular reperfusion after stroke (DEFUSE 2): a prospective cohort study.** *Lancet Neurol* 2012;11: 860–67 CrossRef Medline
4. Albers GW, Thijs VN, Wechsler L, et al; DEFUSE Investigators. **Magnetic resonance imaging profiles predict clinical response to early reperfusion: the diffusion and perfusion imaging evaluation for understanding stroke evolution (DEFUSE) study.** *Ann Neurol* 2006; 60:508–17 CrossRef Medline
5. Saver JL, Goyal M, Bonafe A, et al; SWIFT PRIME Investigators. **Stent-retriever thrombectomy after intravenous t-PA vs. t-PA alone in stroke.** *N Engl J Med* 2015;372:2285–95 CrossRef Medline
6. Goyal M, Demchuk AM, Menon BK, et al; ESCAPE Trial Investigators. **Randomized assessment of rapid endovascular treatment of ischemic stroke.** *N Engl J Med* 2015;372:1019–30 CrossRef Medline
7. Campbell BC, Mitchell PJ, Kleinig TJ, et al; EXTEND-IA Investigators. **Endovascular therapy for ischemic stroke with perfusion-imaging selection.** *N Engl J Med* 2015;372:1009–18 CrossRef Medline
8. Berkhemer OA, Fransen PS, Beumer D, et al. **A randomized trial of intraarterial treatment for acute ischemic stroke.** *N Engl J Med* 2015; 372:11–20 CrossRef Medline
9. Powers WJ, Derdeyn CP, Biller J, et al; American Heart Association Stroke Council. **2015 American Heart Association/American Stroke Association Focused Update of the 2013 Guidelines for the Early Management of Patients With Acute Ischemic Stroke Regarding Endovascular Treatment: A Guideline for Healthcare Professionals From the American Heart Association/American Stroke Association.** *Stroke* 2015;46:3020–35 CrossRef Medline
10. Dehkharghani S, Bammer R, Straka M, et al. **Performance and predictive value of a user-independent platform for CT perfusion analysis: threshold-derived automated systems outperform examiner-driven approaches in outcome prediction of acute ischemic stroke.** *AJNR Am J Neuroradiol* 2015;36:1419–25 CrossRef Medline
11. Barber PA, Demchuk AM, Zhang J, et al. **Validity and reliability of a quantitative computed tomography score in predicting outcome of hyperacute stroke before thrombolytic therapy: ASPECTS Study Group—Alberta Stroke Programme Early CT Score.** *Lancet* 2000; 355:1670–74 CrossRef Medline
12. Tan IY, Demchuk AM, Hopyan J, et al. **CT angiography clot burden score and collateral score: correlation with clinical and radiologic outcomes in acute middle cerebral artery infarct.** *AJNR Am J Neuroradiol* 2009;30:525–31 CrossRef Medline

13. Sillanpaa N, Saarinen JT, Rusanen H, et al. **The clot burden score, the Boston Acute Stroke Imaging Scale, the cerebral blood volume ASPECTS, and two novel imaging parameters in the prediction of clinical outcome of ischemic stroke patients receiving intravenous thrombolytic therapy.** *Neuroradiology* 2012;54:663–72 CrossRef Medline
14. Sillanpaa N, Saarinen JT, Rusanen H, et al. **CT perfusion ASPECTS in the evaluation of acute ischemic stroke: thrombolytic therapy perspective.** *Cerebrovasc Dis Extra* 2011;1:6–16 CrossRef Medline
15. Straka M, Albers GW, Bammer R. **Real-time diffusion-perfusion mismatch analysis in acute stroke.** *J Magn Reson Imaging* 2010;32:1024–37 CrossRef Medline
16. Campbell BC, Christensen S, Levi CR, et al. **Cerebral blood flow is the optimal CT perfusion parameter for assessing infarct core.** *Stroke* 2011;42:3435–40 CrossRef Medline
17. Cereda CW, Christensen S, Campbell BC, et al. **A benchmarking tool to evaluate computer tomography perfusion infarct core predictions against a DWI standard.** *J Cereb Blood Flow Metab* 2015 Oct 19. [Epub ahead of print] CrossRef Medline
18. Davis SM, Donnan GA, Parsons MW, et al; EPITHET Investigators. **Effects of alteplase beyond 3 h after stroke in the Echoplanar Imaging Thrombolytic Evaluation Trial (EPITHET): a placebo-controlled randomised trial.** *Lancet Neurol* 2008;7:299–309 CrossRef Medline
19. Wintermark M, Albers GW, Broderick JP, et al. **Acute stroke imaging research roadmap II.** *Stroke* 2013;44:2628–39 CrossRef Medline
20. Weir NU, Pexman JH, Hill MD, et al. **How well does ASPECTS predict the outcome of acute stroke treated with IV tPA?** *Neurology* 2006;67:516–18 CrossRef Medline
21. Puetz V, Dzialowski I, Hill MD, et al. **The Alberta Stroke Program Early CT Score in clinical practice: what have we learned?** *Int J Stroke* 2009;4:354–64 CrossRef Medline
22. Dzialowski I, Hill MD, Coutts SB, et al. **Extent of early ischemic changes on computed tomography (CT) before thrombolysis: prognostic value of the Alberta Stroke Program Early CT Score in ECASS II.** *Stroke* 2006;37:973–78 CrossRef Medline
23. Aviv RI, Mandelcorn J, Chakraborty S, et al. **Alberta Stroke Program Early CT Scoring of CT perfusion in early stroke visualization and assessment.** *AJNR Am J Neuroradiol* 2007;28:1975–80 CrossRef Medline
24. Lin K, Rapalino O, Law M, et al. **Accuracy of the Alberta Stroke Program Early CT Score during the first 3 hours of middle cerebral artery stroke: comparison of noncontrast CT, CT angiography source images, and CT perfusion.** *AJNR Am J Neuroradiol* 2008;29:931–36 CrossRef Medline
25. van Seeters T, Biessels GJ, Niesten JM, et al; Dust Investigators. **Reliability of visual assessment of non-contrast CT, CT angiography source images and CT perfusion in patients with suspected ischemic stroke.** *PLoS One* 2013;8:e75615 CrossRef Medline
26. Smit EJ, Vonken EJ, van der Schaaf IC, et al. **Timing-invariant reconstruction for deriving high-quality CT angiographic data from cerebral CT perfusion data.** *Radiology* 2012;263:216–25 CrossRef Medline
27. Kudo K, Christensen S, Sasaki M, et al; Stroke Imaging Repository (STIR) Investigators. **Accuracy and reliability assessment of CT and MR perfusion analysis software using a digital phantom.** *Radiology* 2013;267:201–11 CrossRef Medline

MR Imaging in Spinocerebellar Ataxias: A Systematic Review

 A. Klaes,  E. Reckziegel,  M.C. Franca Jr,  T.J.R. Rezende,  L.M. Vedolin,  L.B. Jardim, and  J.A. Saute



ABSTRACT

BACKGROUND AND PURPOSE: Polyglutamine expansion spinocerebellar ataxias are autosomal dominant slowly progressive neurodegenerative diseases with no current treatment. MR imaging is the best-studied surrogate biomarker candidate for polyglutamine expansion spinocerebellar ataxias, though with conflicting results. We aimed to review quantitative central nervous system MR imaging technique findings in patients with polyglutamine expansion spinocerebellar ataxias and correlations with well-established clinical and molecular disease markers.

MATERIALS AND METHODS: We searched MEDLINE, LILACS, and Cochrane data bases of clinical trials between January 1995 and January 2016, for quantitative MR imaging volumetric approaches, MR spectroscopy, diffusion tensor imaging, or other quantitative techniques, comparing patients with polyglutamine expansion spinocerebellar ataxias (SCAs) with controls. Pertinent details for each study regarding participants, imaging methods, and results were extracted.

RESULTS: After reviewing the 706 results, 18 studies were suitable for inclusion: 2 studies in SCA1, 1 in SCA2, 15 in SCA3, 1 in SCA7, 1 in SCA1 and SCA6 presymptomatic carriers, and none in SCA17 and dentatorubropallidoluysian atrophy. Cerebellar hemispheres and vermis, whole brain stem, midbrain, pons, medulla oblongata, cervical spine, striatum, and thalamus presented significant atrophy in SCA3. The caudate, putamen and whole brain stem presented similar sensitivity to change compared with ataxia scales after 2 years of follow-up in a single prospective study in SCA3. MR spectroscopy and DTI showed abnormalities only in cross-sectional studies in SCA3. Results from single studies in other polyglutamine expansion spinocerebellar ataxias should be replicated in different cohorts.

CONCLUSIONS: Additional cross-sectional and prospective volumetric analysis, MR spectroscopy, and DTI studies are necessary in polyglutamine expansion spinocerebellar ataxias. The properties of preclinical disease biomarkers (presymptomatic) of MR imaging should be targeted in future studies.

ABBREVIATIONS: AD = axial diffusivity; CAG = cytosine-adenine-guanine; CAG_{exp} = CAG repeat length on the expanded allele; DRPLA = dentatorubropallidoluysian atrophy; FA = fractional anisotropy; Glu = glutamate; ICARS = International Cooperative Ataxia Rating Scale; MJD = Machado-Joseph disease; PolyQ = polyglutamine repeats; RD = radial diffusivity; SARA = Scale for the Assessment and Rating of Ataxia; SCA = spinocerebellar ataxia; SRM = standardized response mean; VBM = voxel-based morphometry

Spinocerebellar ataxias (SCAs) are autosomal dominant disorders clinically characterized by symptoms resulting from cerebellum and cerebellar interconnection neurodegeneration. SCA due to expansions of coding cytosine-adenine-guanine (CAG) repeats (PolyQ) such as SCA1, SCA2, SCA3/Machado-Joseph dis-

ease (MJD), SCA6, SCA7, SCA17, and dentatorubropallidoluysian atrophy (DRPLA) are the most frequent forms.^{1,2} Similar to other PolyQ diseases, these disorders manifest above a threshold of CAG repeats that varies depending on the gene.¹

Ataxia is often accompanied by extracerebellar findings, such as pyramidal and extrapyramidal signs, oculomotor abnormali-

Received November 25, 2015; accepted after revision January 22, 2016.

From the Departments of Radiology (A.K., L.M.V.) and Medical Genetics Services (E.R., L.B.J., J.A.M.S.), Hospital de Clínicas de Porto Alegre, Porto Alegre, Brazil; Departments of Neurology (M.C.F., T.J.R.R.) and Cosmic Rays and Chronology (T.J.R.R.), Universidade Estadual de Campinas, Campinas, Brazil; and Department of Internal Medicine (L.M.V., L.B.J.) and Postgraduate Program in Medicine: Medical Sciences (L.B.J.), Universidade Federal do Rio Grande do Sul, Porto Alegre, Brazil.

A.K., E.R., L.M.V., L.B.J., and J.A.M.S. participated in the conception and design of the study. A.K., E.R., M.C.F., T.J.R.R., and J.A.M.S. participated in research project execution. A.K., E.R., and J.A.M.S. contributed to the interpretation of data, and wrote the first draft. All authors reviewed the manuscript.

Full articles were obtained by CAPES and the Brazilian Ministry of Education publications portal (www.periodicos.capes.gov.br). E.R. was supported by CNPq. We received financial support from Fundo de Incentivo à Pesquisa e Eventos, Hospital de Clínicas de Porto Alegre.

Please address correspondence to Jonas Alex Morales Saute, MD, PhD, Medical Genetics Service, Hospital de Clínicas de Porto Alegre, Rua Ramiro Barcelos 2350; 90.035-903, Porto Alegre, Brazil; e-mail: jsaute@hcpa.edu.br

 Indicates article with supplemental on-line appendix and tables.

<http://dx.doi.org/10.3174/ajnr.A4760>

ties, and peripheral neuropathy.^{1,3} Sleep, cognitive, and psychiatric symptoms are also frequent in PolyQ-SCA, possibly due to a more widespread CNS degeneration.^{4,5}

Natural history studies with well-validated SCA scales, such as the Scale for the Assessment and Rating of Ataxia (SARA)⁶ and the Neurologic Examination Score for Spinocerebellar Ataxia⁷ were concordant with both the very slow disease progression⁸⁻¹⁰ and the necessity for large sample sizes to test disease-modifying therapies in future randomized clinical trials.⁸⁻¹³ Surrogate biomarkers could hasten randomized clinical trials and drug discoveries for SCA. The number of biomarkers evaluated so far is small, and neuroimaging, particularly MR imaging, is the best-evaluated candidate.¹⁴

Many studies evaluated brain MR imaging in SCA, some with conflicting results. Most evaluated a small number of patients with a high risk of bias. Although different methodologies were applied with multiple qualitative and quantitative approaches, it is still unknown which technique and which region is best-suited for a reliable biomarker for future randomized clinical trials in a given PolyQ-SCA. So far, no systematic review has been published on the subject, to our knowledge.

We aimed to perform a systematic review of the studies that evaluated central nervous system quantitative MR imaging techniques in patients with PolyQ-SCA, to assess the correlations of reported findings with well-established clinical and molecular disease markers and to evaluate the reported sensitivity to change of the findings, when available.

MATERIALS AND METHODS

Search Criteria and Strategy

The objective and search strategy were established by using the Population, Intervention, Comparator, Outcome format. We searched MEDLINE, LILACS, and Cochrane data bases of clinical trials between January 1995 and January 10, 2016. We restricted the results to humans; no language restrictions were adopted. Population, Intervention, Comparator, Outcome-specific search terms regarding the population (“spinocerebellar ataxia,” “autosomal dominant cerebellar ataxia”) were combined with intervention-of-interest keywords (“MR imaging,” “NMR,” “spectroscopy,” “volumetry,” “morphometry,” “gray matter atrophy,” “regional atrophy,” “white matter atrophy,” “DTI,” “tractography,” “diffusion tensor”). After performing the search, we also performed manual citation review to ensure that all relevant studies were found. The review process followed the Preferred Reporting Items for Systematic Reviews and Meta-Analyses guidelines.¹⁵ For the complete search strategy, see the On-line Appendix.

Study Selection

To be included, a given study should meet at least 1 criterion from each of the following: 1) study design: systematic review, randomized clinical trial, cohort, case-control or case series; 2) population: symptomatic individuals with a molecular diagnosis of a PolyQ-SCA (SCA1, SCA2, SCA3/MJD, SCA6, SCA7, SCA17, and DRPLA) or asymptomatic carriers of PolyQ-SCA mutation; and 3) intervention: CNS MR imaging with ≥ 1.5 T field; image processing by using volumetric analysis, MR spectroscopy, diffusion tensor imaging, tractography, or other MR imaging quantitative

techniques. In addition, at least 1 of the following data points regarding the subjects, age, age at disease onset, CAG repeat length on the expanded allele (CAG_{exp}), or scores obtained from a validated ataxia scale should be reported. We excluded studies with the following characteristics: 1) study design: case reports or reviews, other than systematic; 2) population: absence of a healthy control group or < 20 individuals per group or representing < 5 different families (when informed); and 3) intervention: qualitative CNS MR imaging analysis or neuroimaging studies other than MR imaging. Prospective studies with ≥ 15 individuals and studies on presymptomatic individuals with ≥ 10 subjects were accepted, though the conclusions of studies with < 20 individuals per group were considered of limited value.

Data Extraction

Two independent reviewers performed the search (A.K., E.R.). Before performing data extraction, we established a consensus of eligible articles between reviewers and a separate assessor (J.A.M.S.). For data extraction, we considered author, year, country, study design and medical scenario, population, sample size, outcomes, MR imaging acquisition and postprocessing, MR imaging main findings, clinical molecular correlations, and study limitations. Comparisons of MR imaging findings among different SCAs, qualitative findings, and diagnostic properties of MR imaging for SCAs were not analyzed.

RESULTS

Seven hundred six articles were retrieved on the basis of the title/abstract data base search; 698 on MEDLINE, 4 on LILACS, and 4 at the Cochrane Library. Eighteen studies (case-control and prospective cohorts) were included for critical evidence evaluation based on our eligibility criteria. See Fig 1 for the study-selection procedures and the On-line Appendix for the complete search strategy.

Study Characteristics and Risk of Bias within Studies

For main descriptive data of included studies, see On-line Tables 1–4.

Results of Individual Studies

Eighteen studies were selected for this review: 2 including SCA1, 1 including SCA2, 15 including SCA3/MJD, 1 including patients with SCA7, and 1 study including presymptomatic carriers of SCA1 and SCA6 mutations. No eligible studies were found for SCA17 and DRPLA. On-line Table 1 summarizes the results of volumetric analysis, spectroscopy, DTI, and other methods for infratentorial regions, and On-line Table 2 gives the results for supratentorial regions. Although we found significant bias in most studies (selection and measurement bias being the most frequent), in general these findings did not limit the overall results, considering the relative consistency of findings across studies (On-line Tables 3–6).

Only 2 studies evaluated prospectively MR imaging changes in patients with SCA.^{16,17} Both studies assessed volumetric analysis, and 1 of them assessed MR spectroscopy changes with time.¹⁶

Volumetric studies used voxel-based morphometry (VBM) and surface-based analysis. VBM analysis, implemented in differ-

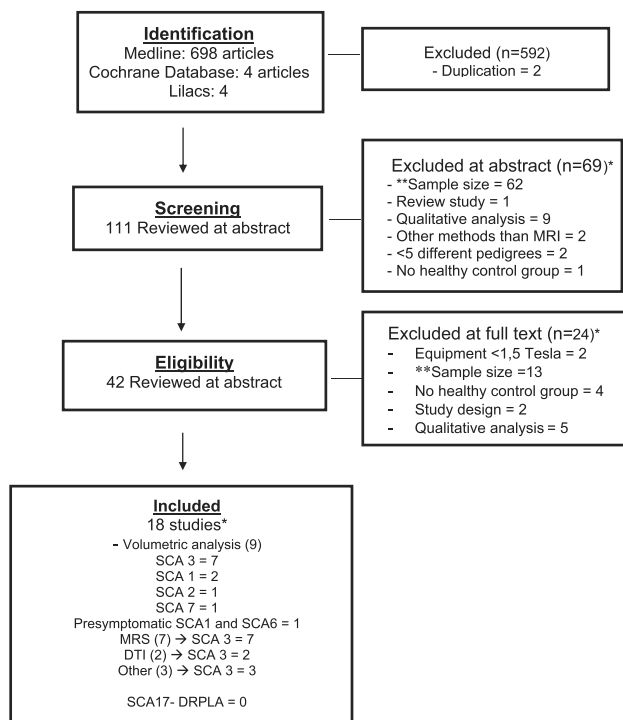


FIG 1. Flow diagram outlining the selection procedure. The *asterisk* indicates that the total number of studies is lower than the sum of individual studies because some studies were excluded for ≥ 2 reasons and some studies evaluated >1 SCA subtype. *Double asterisks* indicate sample size exclusion criteria: <20 individuals per group for cross-sectional studies, <15 individuals for prospective studies, and <10 individuals per group for studies in presymptomatic individuals.

ent versions of the SPM software (SPM2, SPM5, and SPM8; tools; <http://www.fil.ion.ucl.ac.uk/spm/software/spm8>), varied among selected studies, which used ROIs or VOI analysis and/or whole-brain volume analysis with standardization maps. Seven studies used ROI or VOI^{16,18-23} analysis (2 with manual outlining), and 8 studies performed whole brain analysis (5 automated²⁴⁻²⁸ and 3 semiautomated^{17,29,30} processing). One study performed both manual and automated morphometric measurement of the thalamus.³¹ Surface-based analysis with the FSL Toolbox (<http://fsl.fmrib.ox.ac.uk/fsl/fslwiki/Randomise>) and FreeSurfer (<http://surfer.nmr.mgh.harvard.edu>) were used in 2 articles. All spectroscopic studies were performed by using single-voxel protocols.

SCA1

MR Imaging Volumetric Studies. A single study evaluated quantitative volumetric changes in SCA1, comprising 48 patients with SCA1, 24 patients with SCA3/MJD, and 32 controls in a multicenter study.²⁹

Infratentorial Regions. The authors reported gray matter volume loss in the cerebellar hemispheres, vermis, and whole brain stem and white matter loss in the whole brain stem, midbrain, pons, middle cerebellar peduncles, and cerebellar hemispheres on VBM analysis. Semiautomated volume analysis showed similar results with whole brain stem, pons, and medulla oblongata atrophy. Results of the SARA and Unified Huntington's Disease Rating Scale, which both increase with disease severity, correlated inversely with whole brain stem ($R = -0.447, P < .001; R =$

$-0.376, P < .01$, respectively) and pons volumes ($R = -0.531, P < .001; R = -0.438, P < .001$; respectively).²⁹

Supratentorial Structures. Gray matter volume losses were found in the caudate nucleus and temporal lobes on VBM and in the putamen on semiautomated analysis. No significant correlations of supratentorial volumes with clinical or molecular data were reported.²⁹

Prospective Studies. Reetz et al¹⁷ prospectively evaluated 37 patients with SCA1 and 19 with SCA3/MJD during approximately 2 years. On VBM analysis, patients with SCA1 showed significant decline in gray matter in the whole brain stem, left anterior and posterior cerebellum, and the right putamen and pallidum. The length of the expanded CAG repeat allele correlated with cerebellum ($R = -0.48, P < .005$) and pons ($R = -0.47, P < .005$) volume loss in SCA1.¹⁷ On semiautomated analysis, significant atrophy progression was found in the whole brain stem, pons, putamen, left caudate, and left cerebellar hemisphere. The length of the expanded CAG repeat allele correlated with left ($R = -0.370, P < .05$) and right ($R = 0.380, P < .05$) cerebellum volume loss. When we compared patients with SCA1 and SCA3/MJD regarding CNS atrophy progression, SCA1 showed an increased rate of volume loss in the whole brain stem, left cerebellar hemisphere, and putamen.¹⁷

Presymptomatic Individuals. A single study evaluated MR imaging volumetric analysis in presymptomatic individuals, the Ataxia Study Group study of individuals at Risk for SCA1, SCA2, SCA3, SCA6, SCA7 (RISCA).³⁰ This was a multicenter observational European study, in which 50 presymptomatic individual carriers of a PolyQ-SCA mutation and 33 noncarrier controls underwent MR imaging in 8 centers. Carriers and noncarriers were grouped for evaluation in 26 carriers and 13 noncarriers for SCA1 mutations, 4 carriers and 8 noncarriers for SCA2 mutations, 9 carriers and 6 noncarriers for SCA3/MJD mutations, and 11 carriers and 6 noncarriers for SCA6 mutations. According to our criteria, only SCA1 and SCA6 data (pooled controls) were reviewed.

The mean estimated time from onset for SCA1 carriers was -11 years (-14 to -8), the mean age was 26 years, and 23 (88%) were women. The VBM results showed gray matter loss in the medulla oblongata extending to the pons and in lobule IX of the cerebellum in SCA1 carriers. On semiautomated analysis, no differences were seen between carriers and noncarriers, even when pooling the noncarrier individuals in a common control group ($n = 33$). The MR imaging volumes did not correlate with time from onset in any genotype.³⁰

SCA2

MR Imaging Volumetric Studies. A single study evaluated quantitative volumetric changes in 20 patients with SCA2 and 20 healthy matched controls.¹⁸

Infratentorial and Supratentorial Regions. The authors reported symmetric gray matter volume loss in the cerebellar vermis and hemispheres, with sparing of vermian lobules I, II, and X and of hemispheric lobules I, II, and crus II, on VBM analysis. White matter volume loss was depicted in the peridentate regions, middle cerebellar peduncles, dorsal portion of the pons, and the su-

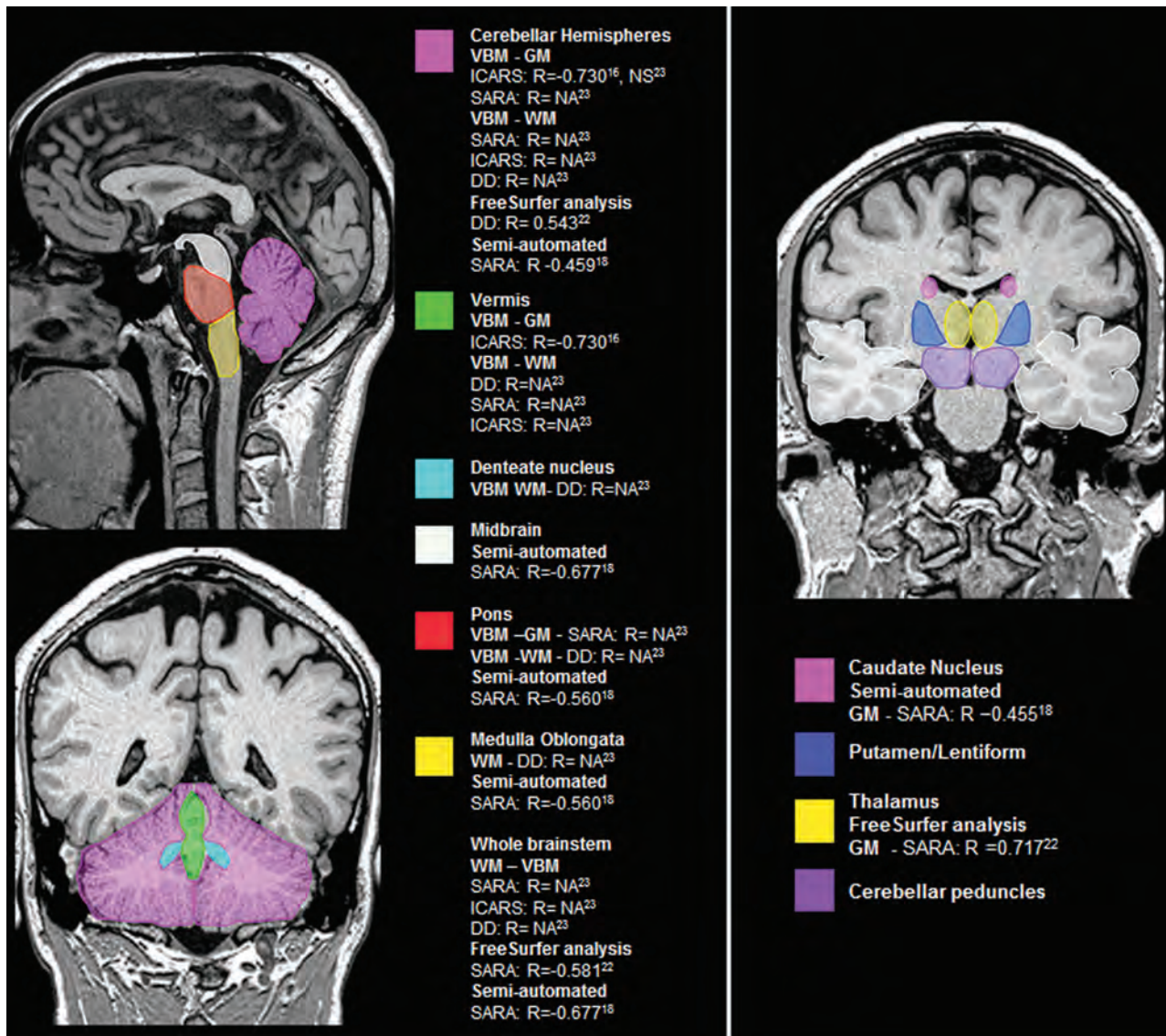


FIG 2. Main encephalic regions with volume loss and its clinical and molecular correlations in SCA3/MJD. DD indicates disease duration; NA, not available; NS, not significant.

perforial portion of the cerebral peduncles.¹⁸ International Cooperative Ataxia Rating Scale (ICARS) correlated inversely with average cerebellar gray matter volume ($R = -0.53$) and average white matter volume of the peridentate regions, middle cerebellar peduncles, dorsal pons, and cerebral peduncles ($R = -0.54$), and it correlated directly with CSF volume in the posterior cranial fossa ($R = 0.45$). The P values for correlation analysis were not given. No gray or white matter volume losses were observed in the cerebral hemispheres of patients with SCA2.

SCA3/MJD

MR Imaging Volumetric Studies. Six studies evaluated volumetric changes in patients with SCA3/MJD and control individuals, 4 with VBM, 1 with FreeSurfer analysis,^{16,29,30,32,33} and 3 with semiautomated analysis,^{29,31,34} comprising a total of 246 patients with SCA3/MJD evaluated. Five of the 6 cross-sectional studies were performed by the same group in a single center in Brazil.^{16,31-34}

Infratentorial Structures. All 4 studies that analyzed cerebellar volume with VBM and FreeSurfer found significant atrophy for the total cerebellum or cerebellar hemispheres^{16,29,32,33}; 3 studies also reported vermian atrophy.^{16,29,33} One study reported dentate nucleus atrophy,³³ while another study reported no differences in this region.²⁹ Two studies reported cerebellar peduncle atrophy.^{29,33} Four studies reported whole brain stem atrophy,^{16,29,32,33} and 3 studies, pontine atrophy.^{16,32,33} Two studies reported midbrain^{16,29} and medulla oblongata atrophy,^{16,33} while 1 study found no differences for midbrain³³ and 1, for medulla oblongata volumes.²⁹

Semiautomated volume analysis from a single study²⁹ showed results similar to those of the overall VBM analysis with atrophy in the total cerebellum, cerebellar hemispheres and vermian, whole brain stem, midbrain, pons, and medulla oblongata.

Both cerebellar and brain stem structures presented significant correlation with SARA,^{29,32,33} ICARS,^{16,33} disease duration,^{32,33} and CAG repeat expansions length (On-line Table 1 and Fig 2).¹⁶

A single study evaluated semiautomated cervical spine volumetric analysis and found significant atrophy in SCA3/MJD, which correlated with longer disease duration.³⁴

Supratentorial Regions: Subcortical Nuclei. Regarding automated gray matter analysis, 2 studies found caudate nucleus and putamen, internal globus pallidum, or lentiform atrophy in SCA3/MJD,^{16,32} while 1 study found no differences.²⁹ Three studies found thalamic atrophy,^{16,31,32} while a single study did not.²⁹ One of these studies reported a significant inverse correlation of left thalamus volume with SARA,³² while the other 3 studies reported no significant correlations with clinical or molecular data.^{16,29,31} Regarding semiautomated volumetric analysis, a single study found caudate and putamen atrophy, with an inverse correlation of caudate atrophy with SARA scores,²⁹ and a single study found thalamic atrophy, with no significant correlations with clinical or molecular data (On-line Table 1 and Fig 2).³¹

Supratentorial Regions: Cerebral Hemispheres. Three cross-sectional studies evaluated cerebral hemispheres with VBM and cortical thickness.^{16,29,32} Two studies found significant atrophy of the temporal, frontal, parietal, occipital, and/or limbic lobes/gyri. Two studies found significant correlation of some of these regions with disease duration,^{16,32} one with SARA³² and the other with ICARS.¹⁶ One study reported significant correlation of these regions with CAG repeat expansions length,¹⁶ while the other 2 did not.^{29,32} Regarding semiautomated volumetric analysis, a single study found temporal lobe atrophy in SCA3/MJD without significant correlations with clinical and molecular features (On-line Table 1).²⁹

Prospective Studies. In the study by Reetz et al,¹⁷ the main effect in gray matter changes on VBM after 2 years of follow-up in the SCA3/MJD group ($n = 19$) was restricted to the bilateral putamen and pallidum. Thirty patients with SCA3/MJD were also prospectively assessed in a Brazilian study.¹⁶ No losses of gray matter and white matter densities on VBM analysis were seen after 12.5 months.¹⁶ On semiautomated volumetric analysis, Reetz et al¹⁷ found significant atrophy progression in the whole brain stem, pons, putamen, and left caudate in SCA3/MJD, with no correlations with CAG_{exp}.

MR Spectroscopy. All 6 included MR spectroscopy studies evaluated only patients with SCA3/MJD, comprising 235 individuals.^{19–22,25,26} Many of the studies evaluated different ROIs, which made it difficult to pool data.

Infratentorial Structures. Five studies evaluated MR spectroscopy of infratentorial regions in SCA3/MJD^{10–22}; all of them evaluated cerebellar structures, and only 1 evaluated the brain stem (see On-line Table 1 for the main findings).¹⁹

The *N*-acetylaspartate/creatinine ratio was evaluated in 4 studies with ROIs in the cerebellar hemispheres/cortex,^{20–22} all with reduced NAA/Cr ratios; 2 of them had inverse correlations with SARA scores.^{21,22} NAA/Cr ratio with ROIs in the cerebellar vermis was evaluated in 3 studies, all with reduced ratios,^{20–22} 2 of them with inverse correlations with SARA scores.^{21,22} NAA/Cr ratio with ROI in dentate nucleus and cerebellar peduncles was evaluated in a single study. Both regions showed reduced NAA/Cr ratio with a direct correlation with SARA scores for both regions, a direct correlation with disease duration in the dentate nucleus,

and an inverse correlation with age at onset in the cerebellar peduncles.²⁰ A single study evaluated the NAA + *N*-acetyl-aspartyl-glutamate/total Cr ratio in the left cerebellar white matter of patients with SCA3/MJD and found reduced ratios.²⁶ Reduced NAA levels in the cerebellar vermis and pons, with a strong inverse correlation between SARA scores and NAA levels in the pons, were reported in a single study.¹⁹ Two studies evaluated the NAA/choline ratio^{20,21}; NAA/Cho ratio was reduced in the cerebellar vermis in both studies, but one reported a direct²⁰ and the other an inverse correlation²¹ with SARA. One study found reduced NAA/Cho ratio in the cerebellar hemispheres, with an inverse correlation with SARA scores and a direct correlation with disease duration,²¹ while the other found no differences.²⁰ No differences of NAA/Cho ratio were found in the dentate nucleus.²⁰

Two studies evaluated the Cho/Cr ratio^{20,22}; one study discovered a NAA/Cho ratio reduction in the cerebellar vermis, with no significant clinical or molecular correlations²² and the other found no differences for the cerebellar vermis, cortex, dentate nucleus, or cerebellar peduncles.²⁰ One study evaluated the glutamate (Glu)/total Cr ratio in the left cerebellar white matter and found reductions in SCA3/MJD, but with no correlations with motor clinical or molecular data.²⁶ One study evaluated MR spectroscopy Glu levels and found reductions in the cerebellar vermis and pons, with no significant clinical or molecular correlations.¹⁹ MR spectroscopy Cr and myo-inositol levels were both increased in the cerebellar vermis and pons of patients with SCA3/MJD in a single study, with a direct correlation of myo-inositol with SARA in the pons.¹⁸ Other metabolites were assessed in the same study, with no differences from controls.¹⁹

Supratentorial Structures. A single study evaluated MR spectroscopy in the corpus callosum and found reduced NAA/Cr ratio and normal Cho/Cr ratios in patients with SCA3/MJD, with no significant clinical or molecular correlations.²⁵

Prospective Studies. D'Abreu et al¹⁶ assessed MR spectroscopy in 19 patients with SCA3/MJD after 12.5 months. No difference in the NAA/Cr ratio in the superior posterior region of the left hemisphere was found.

Diffusion Tensor Imaging. Only 1 study evaluated DTI in SCA3/MJD, comprising 38 patients.²⁴ We excluded the DTI data in the study by Lopes et al²⁶ after contacting the study authors, because there was an overlap of patients and findings with the study by Guimarães et al.²⁴ This study reported reduced fractional anisotropy (FA) in the bilateral cerebellum, including the dentate and other nuclei and cerebellar peduncles, and in the brain stem, including the midbrain and pons. Increased axial diffusivity (AD) and radial diffusivity (RD) were seen in different cerebellar and brain stem regions, while mean diffusivity did not differ from that in controls. AD also increased in the thalamus, and RD increased in the thalamus, frontal and parietal lobes, and corpus callosum. The only significant correlation of DTI parameters with FA was in the pons, with disease duration a direct correlation.²⁴

Other Quantitative MR Imaging Evaluations. Three studies evaluated other quantitative MR imaging methods: relaxometry²⁴ (38 patients with SCA/MJD), perfusion²³ (22 symptomatic patients and 16 presymptomatic SCA3/MJD mutation carriers), and frac-

tal dimension analysis²⁷ (48 patients with SCA3/MJD). Only MR imaging fractal analysis of the cerebellum and cerebral regions showed significant correlations with disease duration and SARA (See On-line-Table 6 for detailed results for other method studies).²⁷

SCA6

MR Imaging Volumetric Studies: Presymptomatic Individuals. RISA was the only study included that evaluated individuals with SCA6.³⁰ Eleven presymptomatic SCA6 carriers (6 women), with a mean estimated time from onset of -20 years (-23 to -16) (mean age, 46 years), were studied. VBM and semiautomated analysis results showed no differences between SCA6 mutation carriers and noncarriers.

SCA7

MR Imaging Volumetric Studies. A single study evaluated quantitative semiautomated volumetric changes in 24 patients with SCA7 and age-matched controls.²⁸

Infratentorial and Supratentorial Regions. Hernandez-Castillo²⁸ reported the largest volume losses in the right anterior cerebellum and left posterior cerebellum. Right anterior cerebellum culmen ($R = -0.817, P < .05$) and posterior tonsil ($R = -0.740, P < .05$), and left anterior cerebellum culmen ($R = -0.759, P < .05$) and posterior cerebellum semilunar ($R = -0.640, P < .05$) showed significant inverse correlations with SARA scores. No brain stem volume loss was reported.¹³ Gray matter atrophy was also seen in the cuneus, precuneus, pre/post central gyri, inferior frontal gyrus, and temporal lobes. Right ($R = -0.742, P < .05$) and left ($R = -0.799, P < .05$) precentral and inferior frontal gyri ($R = -0.72, P < .05$) volumes inversely correlated with SARA scores. No volume loss was reported for subcortical nuclei.²⁸

DISCUSSION

This is the first systematic review on quantitative MR imaging findings of PolyQ-SCA. Although the number of MR imaging studies published for these disorders in the past 10 years is quite large, the small sample sizes and qualitative analysis of the findings limited the validity of most study results. We adopted a critical evaluation approach,³⁵ which aimed to include studies that met a predetermined threshold of quality, to define our eligibility criteria. Our most restrictive criterion was related to study sample size. A threshold of sample size was selected (exclusion criteria: <20 individuals per group for cross-sectional studies, <15 individuals for prospective studies, and <10 individuals per group for studies in presymptomatic individuals) because no sample size estimation with study power definition was provided in the studies found.

Recent studies in neuroimaging applied different techniques such as manual segmentation, voxel-based morphometry, spectroscopy, and DTI. In fact, most studies described in this review performed volumetric estimations and objective evaluations as in DTI or in spectroscopy. We will now discuss the current knowledge on MR imaging quantitative techniques for PolyQ-SCAs and potential areas for future research, considering these instruments as potential surrogate outcomes for future clinical trials.

MR Volumetric Analysis SCA1

When we consider the available data, whole brain stem, pons, putamen, caudate, and cerebellar hemisphere atrophy seem to be the best target regions as surrogate outcomes in SCA1.^{17,29} The standardized response mean (SRM = mean score change/SD of the score change; an effect size index used to enable the comparison among different instruments) of region-specific volume loss on MR imaging was similar or even larger than that of clinical scales. The 2-year SRM of volume loss was -1.6 for whole brain stem, -1.5 for the pons, -1.3 for the putamen, -1.2 for the caudate, and -0.7 for the cerebellum in SCA1, which are similar or even higher than the SRM of SARA, which was 1.2. Of note, SRM values of >0.8 are considered large changes with time.^{8,11,17}

MR Volumetric Analysis, MR Spectroscopy, and DTI in SCA3/MJD

SCA3/MJD was by far the most studied PolyQ-SCA with MR imaging. SCA3/MJD studies generally presented larger sample sizes and lower risks of selection bias. Regarding volumetric studies, cerebellar hemispheres and vermis, whole brain stem, midbrain, pons, medulla oblongata, cervical spine, caudate and putamen nuclei, and thalamus seem to be the best target regions as surrogate outcomes in SCA3/MJD according to cross-sectional studies.^{16,29,24,32,33} In the study by Schulz et al,²⁹ the stepwise inclusion of the pons and medulla oblongata together explained 53% of the variance in SARA in a linear regression model, and in another study, the cross-sectional area of the cervical spine explained 49.1% of SARA scores in a regression model built with disease duration and cerebellar volume.⁹ Some minor differences in the results across studies might be related to technical differences between semiautomated and automated analyses and differences between VBM and surface analysis (FreeSurfer).³⁵⁻³⁷ Although several volumetric analyses have been published, the use of at least 3 technical approaches, the heterogeneity of comparisons with independent variables (CAG_{exp}, disease duration, ataxia scales, and so forth), and the way data are presented in VBM studies prevented any data meta-analysis.

On a prospective study, the main gray matter changes in the SCA3/MJD group were in the whole brain stem, pons, putamen, and caudate.¹⁷ The 2-year SRMs of region-specific volume loss on MR imaging were -1.1 for the whole brain stem, -0.9 for the pons, -1.5 for the putamen, and -1.6 for the caudate in SCA3/MJD, which is similar or even higher than the 1.4 SRM of SARA.¹⁷ Another study did not find gray matter and white matter density losses on VBM analysis in 30 patients with SCA3/MJD after 12.5 months.¹⁶ This finding could be explained by both shorter follow-up and statistical differences regarding processing of VBM (an unbiased analysis, corrected for many different comparisons) and semiautomated volumetric analysis (fewer target regions), with semiautomated volumetric analysis apparently presenting greater study power for longitudinal studies.

A single prospective study evaluated MR spectroscopy with the ROI over the superior posterior region of the left hemisphere during 1 year and failed to show differences in metabolite ratios.¹⁶ It will be important to report the differences with time of structures and metabolites with relevant alterations on cross-sectional studies as NAA/Cr, NAA/Cho and Glu/Cr ratios, NAA, Glu, Cr,

and myo-inositol levels of the cerebellar hemispheres/cortices, vermis, and pons.^{19–22}

Given the available data, DTI may not yet be considered a potential surrogate biomarker for SCA3/MJD. Although differences in FA, AD, and RD were seen for the infratentorial and supratentorial regions, the significance in relation to well-known clinical and molecular parameters is not defined, with a possible relevance related to nonmotor findings of the disorder.²⁴

Multimodal Approach in SCA3/MJD

None of the eligible studies directly compared the findings of different quantitative MR imaging modalities or tried to put together their information (structural and functional). The results of studies with volumetric analysis, MR spectroscopy, and DTI in SCA3/MJD found abnormalities in similar infratentorial regions (the cerebellum and brain stem). Comparison of data across MR imaging modalities was not possible for supratentorial regions because of the following: 1) the results of studies on volumetric analysis were heterogeneous, 2) only metabolites in the corpus callosum were evaluated with MR spectroscopy, and 3) DTI results were based on a single study.

Other PolyQ-SCAs

We reviewed single studies that performed MR imaging volumetric analysis in SCA2 and SCA7.^{18,24} Although infratentorial gray and white matter volume loss that correlated with ICARS scores were found for SCA2¹⁸ and different cerebellar region and supratentorial structure (frontal, parietal, temporal, and occipital lobes) atrophies that correlated with SARA scores were found for SCA7,²⁸ these results must be replicated by confirmatory cross-sectional studies, and the role of the discovered patterns of atrophy as disease surrogate biomarkers should be tested in prospective studies. Only a single study performed MR volumetric analysis in a small sample of presymptomatic individuals with SCA6 and showed no brain atrophy.³⁰ Neither studies on symptomatic patients with SCA6, SCA17, and DRPLA nor studies with quantitative methods other than volumetric analysis, except for SCA3/MJD, were eligible.

CONCLUSIONS

There is a need for further cross-sectional MR imaging volumetric analysis, MR spectroscopy, and DTI studies for SCA1, SCA2, SCA6, SCA7, SCA17, and DRPLA to better define which techniques and regions are the best candidates for surrogate end points to be further tested in prospective studies. MR imaging fractal²⁷ and multimodal approach analysis also deserves further study in PolyQ-SCA. These studies will probably need to be collaborative initiatives to obtain larger sample sizes that may allow an adequate interpretation and validity of findings.

Further prospective studies will be necessary for defining the best surrogate biomarker outcomes for all PolyQ-SCA. The only publication with promising results collected prospectively and published so far¹⁷ must be seen as a discovery study. The results need to be replicated by independent cohorts of patients with SCA1 and SCA3/MJD. Moreover, the scarcity of cross-sectional and prospective studies in presymptomatic individuals might explain the present lack of preclinical disease markers for PolyQ-

SCA. For instance, in a recent clinical trial, creatine was given to presymptomatic at-risk individuals for Huntington disease,³⁸ and the main trial efficacy outcomes were MR imaging cortical and striatum atrophy at 6 and 18 months after therapy. The authors found significant differences between groups, favoring creatine. Although the clinical relevance of the findings is still unknown, this study raises the possibility of including individuals presymptomatic for PolyQ disorders in clinical trials, irrespective of their carrier status, and of using MR imaging volumetric analysis as a surrogate end point of the disease process before the commencement of clinical manifestations. Such study design should be pursued for PolyQ-SCA in the future.

The study of supratentorial structures other than subcortical nuclei may have a more relevant and yet-not-well-explored relation with nonmotor and nonataxic motor manifestations of PolyQ-SCA and deserves further exploration. Other MR imaging methods, such as surface analysis techniques (such as FreeSurfer), have been shown to be more sensitive for evaluating supratentorial gray matter, especially for their ability to analyze the folds and surface compared with VBM.^{39,40}

Disclosures: Laura Bannach Jardim—UNRELATED: Grants/Grants Pending: Pfizer Brazil, CNPq 478057/2012, FAPERGS 1209–2551/13–4, CNPq 402968/2012–3, CAPES 061–15, Comments: donation (Pfizer) to help maintain www.redeneurogenetica.ufrgs.br; Travel/Accommodations/Meeting Expenses Unrelated to Activities Listed: Machado-Joseph Disease Foundation, Australia, Comments: travel expenses to attend the International Machado-Joseph Disease Meeting, 2015.

REFERENCES

1. Durr A. **Autosomal dominant cerebellar ataxias: polyglutamine expansions and beyond.** *Lancet Neurol* 2010;9:885–94 CrossRef Medline
2. Ruano L, Melo C, Silva MC, et al. **The global epidemiology of hereditary ataxia and spastic paraplegia: a systematic review of prevalence studies.** *Neuroepidemiology* 2014;42:174–83 CrossRef Medline
3. Bird TD. **Hereditary ataxia overview.** 1998 October 28. Updated 2015 June 11. In: Pagon RA, National Human Genome Research Institute; National Library of Medicine; University of Washington; National Center for Biotechnology Information; National Institutes of Health. *GeneReviews*. Seattle: University of Washington; 1993
4. Pedrosa JL, França MC Jr, Braga-Neto P, et al. **Nonmotor and extracerebellar features in Machado-Joseph disease: a review.** *Mov Disord* 2013;28:1200–08 CrossRef Medline
5. Rüb U, Schöls L, Paulson H, et al. **Clinical features, neurogenetics and neuropathology of the polyglutamine spinocerebellar ataxias type 1, 2, 3, 6 and 7.** *Prog Neurobiol* 2013;104:38–66 CrossRef Medline
6. Schmitz-Hübsch T, du Montcel ST, Baliko L, et al. **Scale for the assessment and rating of ataxia: development of a new clinical scale.** *Neurology* 2006;66:1717–20 CrossRef Medline
7. Kieling C, Rieder CRM, Silva ACF, et al. **A neurological examination score for the assessment of spinocerebellar ataxia 3 (SCA3).** *Eur J Neurol* 2008;15:371–76 CrossRef Medline
8. Schmitz-Hübsch T, Fimmers R, Rakowicz M, et al. **Responsiveness of different rating instruments in spinocerebellar ataxia patients.** *Neurology* 2010;74:678–84 CrossRef Medline
9. Jardim LB, Hauser L, Kieling C, et al. **Progression rate of neurological deficits in a 10-year cohort of SCA3 patients.** *Cerebellum* 2010; 9:419–28 CrossRef Medline
10. Jacobi H, Bauer P, Giunti P, et al. **The natural history of spinocerebellar ataxia type 1, 2, 3, and 6: a 2-year follow-up study.** *Neurology* 2011;77:1035–41 CrossRef Medline
11. Saute JA, Donis KC, Serrano-Munuera C, et al; Iberoamerican Multidisciplinary Network for the Study of Movement Disorders (RIB-

- ERMOV) Study Group. **Ataxia rating scales: psychometric profiles, natural history and their application in clinical trials.** *Cerebellum* 2012;11:488–504 CrossRef Medline
12. Saute JA, de Castilhos RM, Monte TL, et al. **A randomized, phase 2 clinical trial of lithium carbonate in Machado-Joseph disease.** *Mov Disord* 2014;29:568–73 CrossRef Medline
 13. Saute JA, Rieder CR, Castilhos RM, et al. **Planning future clinical trials in Machado Joseph disease: lessons from a phase 2 trial.** *J Neurol Sci* 2015;358:72–76 CrossRef Medline
 14. Saute JA, Jardim LB. **Machado Joseph disease: current clinical, genetic and therapeutic issues.** *Expert Opin Orphan Drug* 2015;5: 517–35 CrossRef
 15. Moher D, Liberati A, Tetzlaff J, et al; PRISMA Group. **Preferred reporting items for systematic reviews and meta-analyses: the PRISMA statement.** *PLoS Med* 2009;6:e1000097 CrossRef Medline
 16. D'Abreu A, França MC Jr, Yasuda CL, et al. **Neocortical atrophy in Machado-Joseph disease: a longitudinal neuroimaging study.** *J Neuroimaging* 2012;22:285–91 CrossRef Medline
 17. Reetz K, Costa AS, Mirzazade S, et al; Ataxia Study Group Investigators. **Genotype-specific patterns of atrophy progression are more sensitive than clinical decline in SCA1, SCA3 and SCA6.** *Brain* 2013; 136:905–17 CrossRef Medline
 18. Della Nave R, Ginestroni A, Tessa C, et al. **Brain structural damage in spinocerebellar ataxia type: a voxel-based morphometry study.** *Mov Disord* 2008;23:899–903 CrossRef Medline
 19. Adanyeguh IM, Henry PG, Nguyen TM, et al. **In vivo neurometabolic profiling in patients with spinocerebellar ataxia types 1, 2, 3, and 7.** *Mov Disord* 2015;30:662–70 CrossRef Medline
 20. Lei L, Liao Y, Liao W, et al. **Magnetic resonance spectroscopy of the cerebellum in patients with spinocerebellar ataxia type 3/Machado-Joseph disease.** *Zhong Nan Da Xue Xue Bao Yi Xue Ban* 2011;36: 511–19 CrossRef Medline
 21. Lirng JF, Wang PS, Chen HC, et al. **Differences between spinocerebellar ataxias and multiple system atrophy-cerebellar type on proton magnetic resonance spectroscopy.** *PLoS One* 2012;7:e47925 CrossRef Medline
 22. Wang PS, Chen HC, Wu HM, et al. **Association between proton magnetic resonance spectroscopy measurements and CAG repeat number in patients with spinocerebellar ataxias 2, 3, or 6.** *PLoS One* 2012;7:e47479 CrossRef Medline
 23. Xing W, Wang XY, Liao XX, et al. **Spin labeling artery method perfusion MRI study of SPG4 and SCA3/MJD.** *Magn Reson Imaging* 2014;32:1330–34 CrossRef Medline
 24. Guimarães RP, D'Abreu A, Yasuda CL, et al. **A multimodal evaluation of microstructural white matter damage in spinocerebellar ataxia type 3.** *Mov Disord* 2013;28:1125–32 CrossRef Medline
 25. D'Abreu A, França M Jr, Appenzeller S, et al. **Axonal dysfunction in the deep white matter in Machado-Joseph disease.** *J Neuroimaging* 2009;19:9–12 CrossRef Medline
 26. Lopes TM, D'Abreu A, França MC Jr, et al. **Widespread neuronal damage and cognitive dysfunction in spinocerebellar ataxia type 3.** *J Neurol* 2013;260:2370–79 CrossRef Medline
 27. Wang TY, Jao CW, Soong BW, et al. **Change in the cortical complexity of spinocerebellar ataxia type 3 appears earlier than clinical symptoms.** *PLoS One* 2015;10:e0118828 CrossRef Medline
 28. Hernandez-Castillo CR, Galvez V, Diaz R, et al. **Specific cerebellar and cortical degeneration correlates with ataxia severity in spinocerebellar ataxia type 7.** *Brain Imaging Behav* 2015 Apr 28. [Epub ahead of print] Medline
 29. Schulz JB, Borkert J, Wolf S, et al. **Visualization, quantification and correlation of brain atrophy with clinical symptoms in spinocerebellar ataxia types 1, 3 and 6.** *Neuroimage* 2010;49:158–68 CrossRef Medline
 30. Jacobi H, Reetz K, du Montcel ST, et al. **Biological and clinical characteristics of individuals at risk for spinocerebellar ataxia types 1, 2, 3, and 6 in the longitudinal RISCA study: analysis of baseline data.** *Lancet Neurol* 2013;12:650–58 CrossRef Medline
 31. D'Abreu A, França MC Jr, Yasuda CL, et al. **Thalamic volume and dystonia in Machado-Joseph disease.** *J Neuroimaging* 2011;21: e91–93 CrossRef Medline
 32. de Rezende TJ, D'Abreu A, Guimarães RP, et al. **Cerebral cortex involvement in Machado-Joseph disease.** *Eur J Neurol* 2015;22:277–83, e23–24 CrossRef Medline
 33. Fahl CN, Branco LM, Bergo FP, et al. **Spinal cord damage in Machado-Joseph disease.** *Cerebellum* 2015;14:128–32 CrossRef Medline
 34. Lam RW, Kennedy SH. **Using metaanalysis to evaluate evidence: practical tips and traps.** *Can J Psychiatry* 2005;50:167–74 Medline
 35. Greeve DN. **An absolute beginner's guide to surface- and voxel-based morphometric analysis.** *Proc Intl Soc Mag Reson Med* 2011;19. <http://cds.ismrm.org/protected/11MPProceedings/files/ISMRM2011-8410.pdf>. Accessed April 7, 2016
 36. Grimm O, Pohlack S, Cacciaglia R, et L. **Amygdalar and hippocampal volume: a comparison between manual segmentation, FreeSurfer and VBM.** *J Neurosci Methods* 2015;253:254–61 CrossRef Medline
 37. Nordenskjöld R, Malmberg F, Larsson EM, et al. **Intracranial volume estimated with commonly used methods could introduce bias in studies including brain volume measurements.** *Neuroimage* 2013; 83:355–60 CrossRef Medline
 38. Rosas HD, Doros G, Gevorkian S, et al. **PRECREST: a phase II prevention and biomarker trial of creatine in at-risk Huntington disease.** *Neurology* 2014;82:850–57 CrossRef Medline
 39. Hutton C, Draganski B, Ashburner J, et al. **A comparison between voxel-based cortical thickness and voxel-based morphometry in normal aging.** *Neuroimage* 2009;48:371–80 CrossRef Medline
 40. Hansen TI, Brezova V, Eikenes L, et al. **How does the accuracy of intracranial volume measurements affect normalized brain volumes? Sample size estimates based on 966 subjects from the HUNT MRI Cohort.** *AJNR Am J Neuroradiol* 2015;36:1450–56 CrossRef Medline
 41. Desikan RS, Ségonne F, Fischl B, et al. **An automated labeling system for subdividing the human cerebral cortex on MRI scans into gyral based regions of interest.** *Neuroimage* 2006;31:968–80 CrossRef Medline
 42. Schmahmann JD, Doyon J, McDonald D, et al. **Three-dimensional MRI atlas of the human cerebellum in proportional stereotaxic space.** *NeuroImage* 1999;10:233–60 CrossRef Medline

Geometric Parameter Analysis of Ruptured and Unruptured Aneurysms in Patients with Symmetric Bilateral Intracranial Aneurysms: A Multicenter CT Angiography Study

Z.-Q. Huang, Z.-H. Meng, Z.-J. Hou, S.-Q. Huang, J.-N. Chen, H. Yu, L.-J. Feng, Q.-J. Wang, P.-A. Li, and Z.-B. Wen

ABSTRACT

BACKGROUND AND PURPOSE: Previous studies of geometric and morphologic parameters of intracranial aneurysms have been conducted to determine rupture risk, which remains incompletely defined due to patient-specific risk factors, such as sex, hypertension, and age. To this end, we compared characteristics of ruptured and unruptured aneurysms in the same patients with symmetric bilateral intracranial aneurysms.

MATERIALS AND METHODS: Between January 2008 and March 2014, 2361 patients with 2674 aneurysms were diagnosed by CT angiography or surgical findings at 4 medical centers. Geometric and morphologic parameters examined for symmetric bilateral intracranial aneurysms comprised aneurysm wall regularity, size, neck width, aspect ratio, size ratio, neck-to-parent artery ratio, and area ratio. Univariate and multivariate statistical analyses were performed to determine independent risk factors for rupture.

RESULTS: Sixty-three patients (48 women, 15 men; mean age, 62.5 ± 9.8 years) with symmetric bilateral aneurysms were eligible for the study and were included. The most frequent aneurysm location was the posterior communicating artery. Univariate analysis disclosed that aneurysm size, aspect ratio, size ratio, area ratio, and irregular wall differed between patients with ruptured and unruptured aneurysms. Multivariate analysis indicated that aspect ratio of ≥ 1.6 (adjusted OR, 9.521; 95% CI, 2.182–41.535), area ratio of ≥ 1.5 (adjusted OR, 4.089; 95% CI, 1.247–13.406), and irregular shape (adjusted OR, 10.443; 95% CI 3.394–32.135) were significant predictive factors for aneurysm rupture after adjustment for aneurysm size.

CONCLUSIONS: An aspect ratio of ≥ 1.6 , area ratio of ≥ 1.5 , and irregular wall are associated with aneurysm rupture independent of aneurysm size and patient characteristics. These characteristics alone can help in distinguishing ruptured bilateral intracranial aneurysms from unruptured ones.

ABBREVIATIONS: A_2 = area of parent artery within the neck; A_1 = aneurysm area; AR = aspect ratio; SR = size ratio

Unruptured intracranial aneurysms are common lesions with a prevalence of 3%–7%.^{1,2} Aneurysm rupture is the primary cause of subarachnoid hemorrhage, leading to high morbidity and mortality. Meanwhile, prophylactic treatment of unruptured

intracranial aneurysms is also associated with risks.^{3,4} Therefore, identification of the risk factors for aneurysm rupture is essential for both risk assessment and treatment.

Previous research on geometric parameters, including aspect ratio (AR), size ratio (SR), and aneurysm flow angles, has shown their association with aneurysm rupture.^{5–7} However, conclusions are confounded by patient-specific characteristics, such as hypertension, age, and history of subarachnoid hemorrhage from another aneurysm which, along with geographic region, have been identified as risk factors for aneurysm rupture.^{8–10} Hence, aneurysm-related factors need to be analyzed by comparing the aneurysm characteristics of ruptured and unruptured aneurysms in the same individual to identify risk factors in a case-control design. We conducted a multicenter, retrospective cohort study of intracranial aneurysms in the Chinese population. The objectives of the article were to elucidate the morphologic and geometric parameters that discriminate intracranial aneurysm rupture status in the same patient with symmetric bilateral intracranial aneurysms.

Received October 29, 2015; accepted after revision January 28, 2016.

From the Medical Image Center (Z.-Q.H., H.Y., L.-J.F., Z.-B.W.) and Department of Neurosurgery (Q.-J.W.), Zhujiang Hospital, Southern Medical University, Guangzhou, Guangdong Province, China; Medical Image Center (Z.-Q.H., Z.-H.M., J.-N.C.) and Department of Neurosurgery (P.-A.L.), Yuebei People's Hospital, Shantou University Medical College, Shantou, Guangdong Province, China; Department of Radiology (Z.-J.H.), The Second Affiliated Hospital of Guangzhou Medical University, Guangzhou, Guangdong Province, China; and Department of Radiology (S.-Q.H.), Sun Yat-Sen Memorial Hospital, Sun Yat-Sen University, Guangzhou, Guangdong Province, China.

This work was supported by the Shaoguan Science and Technology department (grant No. 2013 CX/K200).

Please address correspondence to Z.-B. Wen, MD, Image Diagnosis Center, Zhujiang Hospital, 253, Industrial Road, Haizhu District, Guangzhou, Guangdong Province, China; e-mail: zhibowen@163.com

<http://dx.doi.org/10.3174/ajnr.A4764>

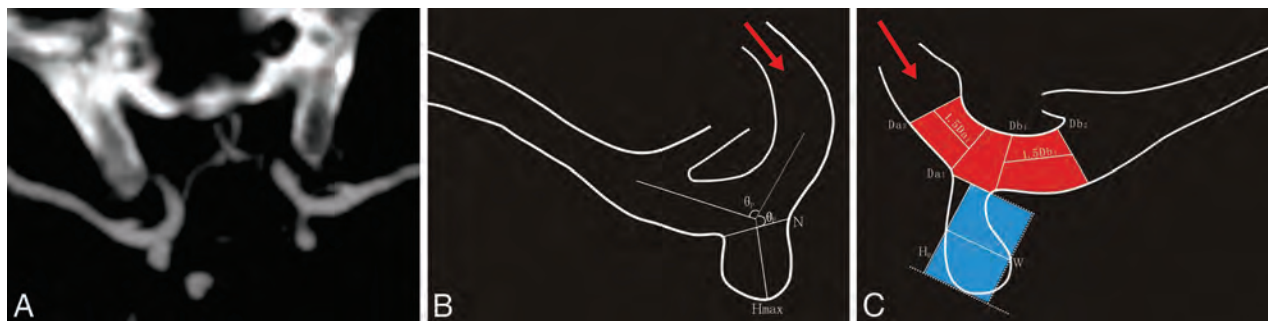


FIG 1. Methodology of morphologic and geometric parameter measurements. *A*, CT angiography shows maximum intensity projection with a 10-mm section thickness, under $\times 4$ magnification and a standardized window setting, of symmetric bilateral intracranial aneurysms at the internal carotid artery. *B*, The angle maximum aneurysm height (H_{max}) and neck width measurements are schematically shown. *C*, Area ratio measurements. The area ratio was defined as the area of the aneurysm to the parent artery in the neck plane. The area of the aneurysm (area with blue) is $\pi \times H_p \times W$, and the area of the parent artery within the neck (area with red) is $\pi \times D_v \times N$. The red arrow indicates blood flow direction.

MATERIALS AND METHODS

Patient Selection and Data Collection

A retrospective analysis was performed in patients diagnosed with intracranial aneurysms from January 2008 to March 2014 who underwent CT angiography with at least 64 sections at 1 of our 4 affiliated hospitals. At each participating center, the institutional review board approved this cohort study. The requirement for informed consent was waived because no diagnostic tests other than routine clinical imaging were used in this study. Additionally, we did not conduct research outside our country of residence.

Patient exclusion criteria were the following: 1) fusiform, traumatic, or mycotic aneurysms; 2) insufficient image quality to evaluate aneurysm geometry and morphology and poorly defined wide-neck aneurysms; 3) inability to identify the location of the ruptured aneurysm on the basis of the pattern of hemorrhage on CT or neurosurgical findings; and 4) an intracranial aneurysm related to arteriovenous malformation.

Definition and Measurement of Morphologic and Geometric Parameters

For each patient with SAH, noncontrast CT and CTA images were evaluated on the workstation that came with the CT scanner for morphologic and geometric variables of aneurysms. Patients were routinely checked at each hospital every day for treatment planning of both ruptured and unruptured aneurysms. CTA was performed with an FOV of 160 mm and a section thickness of 0.5 or 0.625 mm reconstructed at 0.5 or 0.625 mm, resulting in a voxel size of $0.3 \times 0.3 \times 0.5$ (or 0.625) mm. Noncontrast head CT images and neurosurgical findings were reviewed by a neuroradiologist (Z.-B.W., with 25 years of working experience in central nervous system vascular imaging), who was blinded to aneurysm geometry and morphology, to identify the location of the ruptured aneurysm in each patient.

Two neuroradiologists (Z.-Q.H and Z.-H.M, with 5 and 23 years of working experience in central nervous system vascular imaging, respectively) independently obtained measurements, and the average value was used for subsequent statistical analyses.^{11,12} If an aneurysm was detected, the 2 neuroradiologists evaluated several morphologic characteristics: 1) maximum aneurysm height (Fig 1), defined as the maximum distance from the neck center to the dome of the aneurysm; 2) maximal perpendicular height

(H_p), defined as the largest perpendicular distance from the neck plane to the dome of the aneurysm; 3) aneurysm width (W) and neck width (N), defined as the longest diameter of the aneurysm and its neck perpendicular to the H_p ; 4) vessel diameter (D_v), already defined in the literature; and 5) flow angle and parent-daughter angle, as previously defined by Lin et al.^{6,13}

We calculated the following secondary geometric indices: 1) aspect ratio (the ratio of maximum aneurysm height to N); 2) size ratio (the ratio of maximum aneurysm height to the D_v); 3) neck-to-parent-artery ratio (the ratio of N to D_v); and 4) area ratio (the ratio of the area of the aneurysm to the parent artery in the neck plane). Therefore, the area of the aneurysm (A_1) is $\pi \times H_p \times W$, and the area of parent artery within neck (A_2) is $\pi \times D_v \times N$.

All measurements were performed on a workstation with an electronic caliper under $\times 4$ magnification, and maximum-intensity-projection images with 10-mm section thickness and a standardized window setting (window level and window width equal to the Hounsfield unit within the aneurysm) were used. Measurements of morphologic and geometric parameters were performed on a 0.1-mm or 0.1° scale; secondary geometric indices were calculated on a 0.001-point scale. The maximum measurement of W or maximum aneurysm height was defined as the aneurysm size. Aneurysm shape was categorized into “spheric” (defined as an aneurysm ratio of H_p to W or W to H_p of $\geq 80\%$), or “non-spheric”; the aneurysm wall was categorized as smooth (regular pouch without protrusions) or irregular (when blebs, lobes, or protrusions were present). Flow into the aneurysm was considered straight flow when the inflow angle was greater than the main branching angle; otherwise, it was considered as curved flow. If the inflow angle and the main branching angle showed $< 10^\circ$ difference, flow was considered equivalent.

Statistical Analysis

SPSS 17.0 (IBM, Armonk, New York) and Excel 2007 (Microsoft, Redmond, Washington) were used for all statistical analyses. Quantitative data of each geometric parameter were presented in the form of mean \pm SD ($\bar{x} \pm s$), calculated for the ruptured and unruptured groups, and were analyzed with a paired t test. For further analysis, the cutoff value was calculated by the receiver operating characteristic. The criteria of cut-point selection are

Table 1: Geometric parameters of ruptured and unruptured aneurysms ($\bar{x} \pm s$)

Geometric Parameters	Unruptured (n = 63)	Ruptured (n = 63)	P Value
Neck size (mm)	3.1 ± 1.3	3.2 ± 1.2	.783
Aneurysm size (mm)	4.3 ± 2.2	5.3 ± 2.0	.009
Vessel diameter (mm)	2.5 ± 0.6	2.4 ± 0.6	.687
θ_F	121.4° ± 32.7°	130.8° ± 33.6°	.104
θ_P	107.6° ± 26.6°	100.9° ± 27.1°	.159
AR	1.3 ± 0.5	1.7 ± 0.6	<.001
SR	1.7 ± 1.2	2.1 ± 0.9	.029
NPR	1.4 ± 0.7	1.4 ± 0.6	.805
Area ratio	2.0 ± 2.0	2.9 ± 1.9	.011

Note:— θ_F indicates flow angle; θ_P , parent-daughter angle; NPR, neck-to-parent artery ratio.

when the value of (sensitivity + specificity-1) reaches its maximum. Conditional univariable logistic regression analysis was performed to calculate odds ratios of each geometric and morphologic parameter between the 2 groups, and adjusted ORs were taken into the calculation to adjust for aneurysm size, which is an established and strong predictor of aneurysm rupture.^{9,10,14} A P value $\leq .05$ was regarded as statistically significant, and all tests were 2-sided.

RESULTS

General Demographics

Among 2361 patients with 2674 aneurysms, 269 (11.4%) had multiple aneurysms and 84 (3.6%) had symmetric bilateral aneurysms. Of the 84 patients in the clinical trial, 21 were excluded for the following reasons: 1) inability to identify the location of the ruptured aneurysm based on the pattern of hemorrhage or neurosurgical findings ($n = 9$); 2) insufficient CT angiography quality ($n = 3$); 3) the presence of fusiform, mycotic, or dissecting aneurysms ($n = 5$); and 4) aneurysm related to an arteriovenous malformation ($n = 4$). Thus, 63 patients with 126 intracranial aneurysms were enrolled in this cohort. There were 15 (23.8%) men and 48 (76.2%) women, and their mean age was 62.5 ± 9.8 years. The most frequent location for the 126 intracranial aneurysms was at the posterior communicating artery ($n = 68$), followed by the middle cerebral artery ($n = 34$), the internal carotid artery ($n = 20$), the anterior cerebral artery ($n = 2$), and the vertebral artery ($n = 2$).

Aneurysm size, AR, SR, and area ratio in the ruptured group were significantly different from those of the unruptured group ($P < .05$, Table 1), while neck size, vessel diameter, inflow angle, parent-daughter angle, and neck-to-parent artery ratio were not ($P > .05$). For further analysis, the cutoff value was calculated by the receiver operating characteristic (Fig 2). The areas under the curve for aneurysm size, AR, SR, and area ratio were 0.667 (95% CI, 0.571–0.762) sensitivity of 69.8%, specificity of 63.5%; 0.703 (0.612–0.794), sensitivity of 52.4%, specificity of 85.7%; 0.679 (0.585–0.773), sensitivity of 65.1%, specificity of 57.1%; and 0.695 (0.603–0.787), sensitivity of 80.0%, specificity of 48.6%, respectively. The cutoff values of these geometric indices were 4.6, 1.6, 1.7, and 1.5, respectively.

Conditional logistic regression analysis of morphologic and geometric parameters between the 2 groups is given in Table 2. An aneurysm size of ≥ 4.6 mm showed strong association with rupture (OR, 3.625; 95% CI, 1.657–7.929). After adjustment for aneurysm size, an AR of ≥ 1.6 (adjusted OR, 9.521; 95% CI, 2.182–41.535), area

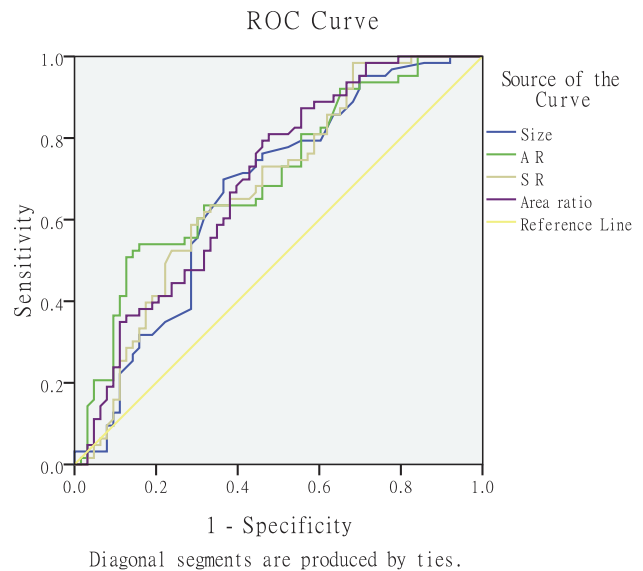


FIG 2. Graph depicting the receiver operating characteristic curves for aneurysm size, AR, SR, and area ratio in the symmetric bilateral aneurysm. The areas under the curve for aneurysm size, AR, SR, and area ratio are the following: 0.667 (95% CI, 0.571–0.762), 0.703 (95% CI, 0.612–0.794), 0.679 (95% CI, 0.585–0.773), and 0.695 (95% CI, 0.603–0.787), respectively. The receiver operating characteristic area for AR (0.703; 95% CI, 0.612–0.794; $P < .001$) tends to be larger than the area under the curve of the other parameters. AR had the highest area under the curve.

ratio of ≥ 1.5 (adjusted OR, 4.089; 95% CI, 1.247–13.406), and irregular wall (adjusted OR, 10.443; 95% CI, 3.394–32.135) were significantly associated with aneurysm rupture, but not SR.

DISCUSSION

Unruptured intracranial aneurysms are common lesions, and aneurysm rupture can be catastrophic.^{2,3,10,12,14} Not all unruptured intracranial aneurysms will rupture, and the management of unruptured intracranial aneurysms remains controversial in neurosurgery. Reliable, simple-to-use predictors of higher rupture risk to aid in treatment decisions for unruptured intracranial aneurysms are not available. In previous studies, the decision-making process was based mainly on size, with the risk of rupture considered significantly increased for aneurysms of ≥ 7 mm).^{10,14,15} However, various authors have shown that a large proportion of ruptured aneurysms are, in fact, < 7 mm.^{16–18} Our study indicates that the mean size of ruptured aneurysms is 5.29 mm (range, 2.0–11.3 mm). More often than not, the ruptured aneurysm is not the largest aneurysm. Factors beyond size may be more important in determining the actual rupture risk.

Irregular Wall and AR of Symmetric Bilateral Aneurysms Predict Rupture

Previous retrospective studies found that aneurysm wall irregularity is associated with increased risk of rupture, but they were not adjusted for aneurysm size.^{19–21} Recently, a large-cohort prospective study found that unruptured aneurysms with a daughter sac (an irregular protrusion of the wall of the aneurysm) are more likely to rupture than aneurysms with a regular shape.¹⁴ Our study shows that after adjustment for aneurysm size, AR and irregular shape are associated with aneurysm rupture. Previous studies on AR indicated conflicting results, finding a significant

Table 2: Conditional logistic regression analysis of geometric and morphologic parameters between unruptured and ruptured aneurysms

	Ruptured (n = 63)		Unruptured (n = 63)		OR (95% CI)	AOR (95% CI)
	No.	%	No.	%		
Aneurysm size ≥4.6 mm	44	69.8	23	36.5	3.625 (1.657–7.929)	–
AR ≥1.6	33	52.4	9	14.3	13.000 (3.086–54.771)	9.521 (2.182–41.535)
SR ≥1.7	41	65.1	27	39.0	2.556 (1.183–5.523)	0.970 (0.320–2.945)
Area ratio ≥1.5	51	80.9	30	47.6	6.250 (2.175–17.958)	4.089 (1.247–13.406)
Aneurysm wall Irregular wall	50	79.4	15	23.8	8.000 (3.157–20.270)	10.443 (3.394–32.135)
Aneurysm shape Spheric	31	49.2	34	53.9	0.833 (0.420–1.653)	1.078 (0.499–2.330)
Flow angles						
Equivalent flow	6	9.5	11	17.5	Reference	Reference
Straight flow	43	68.3	35	55.6	2.175 (0.728–6.497)	1.749 (0.505–6.057)
Curved flow	14	22.2	17	27.0	1.457 (0.405–5.243)	2.054 (0.491–8.589)

Note:—AOR indicates adjusted odds ratios.

difference between the ruptured and unruptured groups, proving that AR is a relevant predictor in estimating the aneurysm rupture risk.^{6,19,22–31} The conflicting results can be explained by the lack of adjustment for patient-specific risk factors for aneurysm rupture and by the use of different imaging techniques and measurement methodology.^{22,27} Regarding AR, only 3 previous studies aimed to minimize the confounding factors by studying patients with multiple intracranial aneurysms. Two studies found that the AR of intracranial aneurysms correlates with aneurysm rupture, but the authors did not adjust for aneurysm size in the multivariable analysis.^{25,31} Our study is similar to a prior one that found that AR is associated with aneurysm rupture after adjusting for aneurysm size and location.²² Additionally, the critical AR for rupture has varied among previous studies, with AR cutoff values ranging from 1.3 to 1.8, and remains controversial.^{6,19,22,23,26} In our study, an AR of ≥1.6 was significantly associated with aneurysm rupture.

Previous studies on flow angle, parent-daughter angle, aneurysm width, and neck width have shown conflicting results, with insignificant or marginally significant *P* values for aneurysm rupture.^{5,13,16,31–33} The conflicting results may be ascribed to limited follow-up data and differences in imaging techniques and measurement methodology. The area ratio takes into account the aneurysm itself (maximal perpendicular height and aneurysm width) and the local vessel (*Dv* and neck width). Our study shows that the area ratio is associated with aneurysm rupture after adjusting for aneurysm size. More than 80% of all ruptured aneurysms had an area ratio of >1.5 (the optimal threshold distinguishing the ruptured from unruptured intracranial aneurysms), whereas 52.38% of all unruptured intracranial aneurysms had an area ratio less than the cutoff value. More important, the area ratio in the ruptured group (2.9 ± 1.9) is larger than that of the unruptured group (2.0 ± 2.0) (*P* = .011).

It has previously been shown that as the intracranial aneurysm enlarges, the blood flow velocity becomes slower within the intracranial aneurysm, reducing the wall shear stress and making the intracranial aneurysm prone to rupture.^{7,30,34–38} From the perspective of hemodynamics, aneurysm area is proportional to the volume of blood contained by the aneurysm per unit of time, and

the area of the parent artery in the neck is proportional to the aneurysm blood flow per unit of time provided by the parent artery via the aneurysm neck. Equal A_2 values but higher A_1 values indicate a greater blood volume contained by the aneurysm per unit of time but slower blood flow velocity and lower mean wall shear stress in the aneurysm, making the risk of aneurysm rupture higher. As for conditions involving the same A_1 values but lower A_2 values, the parent artery provides a reduced volume of blood to the aneurysm via the aneurysm neck, resulting in a slower velocity of blood flow and lower mean wall shear stress in the aneurysm, which also cause a higher rupture risk.

Limitations

One should consider some limitations inherent to this study: This is a retrospective analysis, which could cause biased selection of patients who underwent CT angiography. We used CT angiography data in the research and did not compare results with catheter digital subtraction angiography, which traditionally has been considered the criterion standard for aneurysm detection. However, CT angiography has high sensitivity and specificity for the detection of intracranial aneurysms and good consistency.^{11,12,22,39} Hence, we believe that the chances of misdiagnosis of intracranial aneurysms by CT angiography should be acceptably small. Another limitation of is that the area ratio is a weak predictor with marginally significant odds ratios for aneurysm rupture, even after adjustment for aneurysm size, so a correlation analysis between the area ratio and hemodynamics is needed. Finally, aneurysm size, irregular shape, and area ratio might be a consequence rather than the cause of aneurysm rupture; therefore, a prospective study, involving a geometric model comparison of aneurysms before and after rupture, is necessary.

CONCLUSIONS

We compared the aneurysm characteristics of ruptured and unruptured aneurysms in the same patient, by using CT angiography images according to a standard measurement protocol. AR, irregular shape, and area ratio are independent risk factors for aneurysm rupture. Those aneurysm characteristics alone in the current study can be helpful in distinguishing the ruptured symmetric bilateral intracranial aneurysms from unruptured ones.

ACKNOWLEDGMENT

The authors thank Dr Jian-Jun Zhan (Shantou University Medical College, Shantou, China) for his assistance with the statistical analysis of the data during the preparation of this article.

REFERENCES

1. Vlak MH, Algra A, Brandenburg R, et al. **Prevalence of unruptured intracranial aneurysms, with emphasis on sex, age, comorbidity,**

- country, and time period: a systematic review and meta-analysis. *Lancet Neurol* 2011;10:626–36 CrossRef Medline
2. Li MH, Chen SW, Li YD, et al. Prevalence of unruptured cerebral aneurysms in Chinese adults aged 35 to 75 years: a cross-sectional study. *Ann Intern Med* 2013;159:514–21 CrossRef Medline
 3. Van Gijn J, Kerr RS, Rinkel GJ. Subarachnoid haemorrhage. *Lancet* 2007;369:306–18 CrossRef Medline
 4. Ingall T, Asplund K, Mähönen M, et al. A multinational comparison of subarachnoid hemorrhage epidemiology in the WHO MONICA stroke study. *Stroke* 2000;31:1054–61 CrossRef Medline
 5. Baharoglu MI, Schirmer CM, Hoit DA, et al. Aneurysm inflow-angle as a discriminant for rupture in sidewall cerebral aneurysms: morphometric and computational fluid dynamic analysis. *Stroke* 2010;41:1423–30 CrossRef Medline
 6. Dhar S, Tremmel M, Mocco J, et al. Morphology parameters for intracranial aneurysm rupture risk assessment. *Neurosurgery* 2008;63:185–96; discussion 196–97 CrossRef Medline
 7. Tremmel M, Dhar S, Levy EI, et al. Influence of intracranial aneurysm-to-parent vessel size ratio on hemodynamics and implication for rupture: results from a virtual experimental study. *Neurosurgery* 2009;64: 622–30; discussion 630–31 CrossRef Medline
 8. Jeon JS, Ahn JH, Huh W, et al. A retrospective analysis on the natural history of incidental small paraclinoid unruptured aneurysm. *J Neurol Neurosurg Psychiatry* 2014;85:289–94 CrossRef Medline
 9. Greving JP, Wermer MJ, Brown RD JR, et al. Development of the PHASES score for prediction of risk of rupture of intracranial aneurysms: a pooled analysis of six prospective cohort studies. *Lancet Neurol* 2014;13:59–66 CrossRef Medline
 10. Wiebers DO, Whisnant JP, Huston J III, et al; International Study of Unruptured Intracranial Aneurysms Investigators. Unruptured intracranial aneurysms: natural history, clinical outcome, and risks of surgical and endovascular treatment. *Lancet* 2003;362:103–10 CrossRef Medline
 11. Lubicz B, Levivier M, François O, et al. Sixty-four-row multisection CT angiography for detection and evaluation of ruptured intracranial aneurysms: interobserver and intertechnique reproducibility. *AJNR Am J Neuroradiol* 2007;28:1949–55 CrossRef Medline
 12. Forbes G, Fox AJ, Huston J 3rd, et al. Interobserver variability in angiographic measurement and morphologic characterization of intracranial aneurysms: a report from the International Study of Unruptured Intracranial Aneurysms. *AJNR Am J Neuroradiol* 1996;17:1407–15 Medline
 13. Lin N, Ho A, Gross BA, et al. Differences in simple morphological variables in ruptured and unruptured middle cerebral artery aneurysms. *J Neurosurg* 2012;117:913–19 CrossRef Medline
 14. Morita A, Kirino T, Hashi K, et al; UCAS Japan Investigators. The natural course of unruptured cerebral aneurysms in a Japanese cohort. *N Engl J Med* 2012;366:2474–82 CrossRef Medline
 15. International Study of Unruptured Intracranial Aneurysms Investigators. Unruptured intracranial aneurysms: risk of rupture and risks of surgical intervention. *N Engl J Med* 1998;339:1725–33 CrossRef Medline
 16. Baharoglu MI, Lauric A, Gao BL, et al. Identification of a dichotomy in morphological predictors of rupture status between sidewall-and bifurcation-type intracranial aneurysms. *J Neurosurg* 2012;116: 871–81 CrossRef Medline
 17. Flores BC, Scott WW, Eddleman CS, et al. The A1–A2 diameter ratio may influence formation and rupture potential of anterior communicating artery aneurysms. *Neurosurgery* 2013;73:845–53; discussion 852–53 CrossRef Medline
 18. Rahman M, Ogilvy CS, Zipfel GJ, et al. Unruptured cerebral aneurysms do not shrink when they rupture: multicenter collaborative aneurysm study group. *Neurosurgery* 2011;68:155–60; discussion 160–61 CrossRef Medline
 19. Beck J, Rohde S, el Beltagy M, et al. Difference in configuration of ruptured and unruptured intracranial aneurysms determined by biplanar digital subtraction angiography. *Acta Neurochir (Wien)* 2003;145:861–65; discussion 865 CrossRef Medline
 20. de Rooij NK, Velthuis BK, Algra A, et al. Configuration of the circle of Willis, direction of flow, and shape of the aneurysm as risk factors for rupture of intracranial aneurysms. *J Neurol* 2009;256:45–50 CrossRef Medline
 21. Rohde S, Lahmann K, Beck J, et al. Fourier analysis of intracranial aneurysms: towards an objective and quantitative evaluation of the shape of aneurysms. *Neuroradiology* 2005;47:121–26 Medline
 22. Backes D, Vergouwen MD, Velthuis BK, et al. Difference in aneurysm characteristics between ruptured and unruptured aneurysms in patients with multiple intracranial aneurysms. *Stroke* 2014;45: 1299–303 CrossRef Medline
 23. Amenta PS, Yadla S, Campbell PG, et al. Analysis of nonmodifiable risk factors for intracranial aneurysm rupture in a large, retrospective cohort. *Neurosurgery* 2012;70:693–99; discussion 699–701 CrossRef Medline
 24. Ujiie H, Tamano Y, Sasaki K, et al. Is the aspect ratio a reliable index for predicting the rupture of a saccular aneurysm? *Neurosurgery* 2001;48:495–502; discussion 502–03 CrossRef Medline
 25. Nader-Sepahi A, Casimiro M, Sen J, et al. Is aspect ratio a reliable predictor of intracranial aneurysm rupture? *Neurosurgery* 2004;54: 1343–47; discussion 1347–48 CrossRef Medline
 26. Weir B, Amidei C, Kongable G, et al. The aspect ratio (dome/neck) of ruptured and unruptured aneurysms. *J Neurosurg* 2003;99:447–51 CrossRef Medline
 27. Lauric A, Baharoglu MI, Malek AM. Ruptured status discrimination performance of aspect ratio, height/width, and bottleneck factor is highly dependent on aneurysm sizing methodology. *Neurosurgery* 2012;71:38–45 CrossRef Medline
 28. Ryu CW, Kwon OK, Koh JS, et al. Analysis of aneurysm rupture in relation to the geometric indices: aspect ratio, volume, and volume-to-neck ratio. *Neuroradiology* 2011;53:883–89 CrossRef Medline
 29. Sadatomo T, Yuki K, Migita K, et al. Morphological differences between ruptured and unruptured cases in middle cerebral artery aneurysms. *Neurosurgery* 2008;62:602–09; discussion 602–09 CrossRef Medline
 30. Xiang J, Natarajan SK, Tremmel M, et al. Hemodynamic-morphologic discriminants for intracranial aneurysm rupture. *Stroke* 2011;42:144–52 CrossRef Medline
 31. Hoh BL, Sistrom CL, Firment CS, et al. Bottleneck factor and height-width ratio: association with ruptured aneurysms in patients with multiple cerebral aneurysms. *Neurosurgery* 2007;61:716–22 CrossRef Medline
 32. You SH, Kong DS, Kim JS, et al. Characteristic features of unruptured intracranial aneurysms: predictive risk factors for aneurysm rupture. *J Neurol Neurosurg Psychiatry* 2010;81:479–84 CrossRef Medline
 33. Jiang Y, Lan Q, Wang Q, et al. Correlation between the rupture risk and 3D geometric parameters of saccular intracranial aneurysms. *Cell Biochem Biophys* 2014;70:1417–20 CrossRef Medline
 34. Takao H, Murayama Y, Otsuka S, et al. Hemodynamic differences between unruptured and ruptured intracranial aneurysms during observation. *Stroke* 2012;43:1436–39 CrossRef Medline
 35. Tatehima S, Chien A, Sayre J, et al. The effect of aneurysm geometry on the intra-aneurysmal flow condition. *Neuroradiology* 2010;52: 1135–41 CrossRef Medline
 36. Lauric A, Hippelheuser J, Cohen AD, et al. Wall shear stress association with rupture status in volume matched sidewall aneurysms. *J Neurointerv Surg* 2014;6:466–73 CrossRef Medline
 37. Goubergrits L, Schaller J, Kertzsch U, et al. Statistical wall shear stress maps of ruptured and unruptured middle cerebral artery aneurysms. *J R Soc Interface* 2012;9:677–88 CrossRef Medline
 38. Jou LD, Lee DH, Morsi H, et al. Wall shear stress on ruptured and unruptured intracranial aneurysms at the internal carotid artery. *AJNR Am J Neuroradiol* 2008;29:1761–67 CrossRef Medline
 39. McKinney AM, Palmer CS, Truwit CL, et al. Detection of aneurysms by 64-section multidetector CT angiography in patients acutely suspected of having an intracranial aneurysm and comparison with digital subtraction and 3D rotational angiography. *AJNR Am J Neuroradiol* 2008;29:594–602 CrossRef Medline

MRI Appearance of Intracerebral Iodinated Contrast Agents: Is It Possible to Distinguish Extravasated Contrast Agent from Hemorrhage?

O. Nikoubashman, F. Jablawi, S. Dekeyzer, A.M. Oros-Peusquens, Z. Abbas, J. Lindemeyer, A.E. Othman, N.J. Shah, and M. Wiesmann



ABSTRACT

BACKGROUND AND PURPOSE: Hyperattenuated cerebral areas on postinterventional CT are a common finding after endovascular stroke treatment. There is uncertainty about the extent to which these hyperattenuated areas correspond to hemorrhage or contrast agent that extravasated into infarcted parenchyma during angiography. We evaluated whether it is possible to distinguish contrast extravasation from blood on MR imaging.

MATERIALS AND METHODS: We examined the influence of iodinated contrast agents on T1, T2, and T2* and magnetic susceptibility in a phantom model and an ex vivo animal model. We determined T1, T2, and T2* relaxation times and magnetic susceptibility of iopamidol and iopromide in dilutions of 1:1; 1:2; 1:4; 1:10; and 1:100 with physiologic saline solution. We then examined the appearance of intracerebral iopamidol on MR imaging in an ex vivo animal model. To this end, we injected iopamidol into the brain of a deceased swine.

RESULTS: Iopamidol and iopromide cause a negative susceptibility shift and T1, T2, and T2* shortening. The effects, however, become very small in dilutions of 1:10 and higher. Undiluted iopamidol, injected directly into the brain parenchyma, did not cause visually distinctive signal changes on T1-weighted spin-echo, T2-weighted turbo spin-echo, and T2*-weighted gradient recalled-echo imaging.

CONCLUSIONS: It is unlikely that iodinated contrast agents extravasated into infarcted brain parenchyma cause signal changes that mimic hemorrhage on T1WI, T2WI, and T2*WI. Our results imply that extravasated contrast agents can be distinguished from hemorrhage on MR imaging.

ABBREVIATIONS: GRE = gradient recalled-echo; SE = spin-echo

Hyperattenuated cerebral areas appear on non-contrast-enhanced CT performed shortly after neurointerventional stroke treatment in up to 86% of cases (On-line Fig 1).¹ These postinterventional cerebral hyperattenuations resemble parenchymal hemorrhage but are not space-occupying. There is uncertainty about the true nature of postinterventional cerebral hyperattenuation, specifically the extent to which postinterventional cerebral hyperattenuations correspond to hemorrhage or extravasation of iodinated contrast agent into infarcted parenchyma.¹⁻⁴

In theory, hemorrhage can be distinguished from iodinated contrast agents via MR imaging, given that blood degradation products are paramagnetic and cause specific changes on T2WI and T2*WI, whereas iodine is diamagnetic. However, it has been shown in phantom models that at a field strength of 1.5T, side chains of iodinated contrast agents cause T1 and T2 shortening, which theoretically may mimic the imaging characteristics of intracellular methemoglobin present in early subacute intracerebral hemorrhage.^{5,6} Furthermore, the influence of iodinated contrast agents on susceptibility and T2*WI sequences, which are commonly used in hemorrhage diagnosis, has not been investigated yet, to our knowledge. Hence, we examined the influence of 2 common iodinated contrast agents on magnetic susceptibility and T1, T2, and T2* relaxation in a phantom model and an ex vivo animal model to elucidate whether iodinated contrast agents can be distinguished from blood on MR imaging.

MATERIALS AND METHODS

Phantom Model

We determined relaxation times (T1, T2, and T2*) of undiluted and diluted iopamidol (300 mg/mL, Imeron; Bracco, Milan, Italy)

Received October 9, 2015; accepted after revision January 14, 2016.

From the Departments of Neuroradiology (O.N., S.D., M.W.), Neurosurgery (F.J.), and Neurology (Z.A., N.J.S.), University Hospital Aachen, Aachen, Germany; Institute of Neuroscience and Medicine 4 (O.N., A.M. O.-P., Z.A., J.L., N.J.S.), Forschungszentrum Jülich GmbH, Jülich, Germany; and Department of Radiology (A.E.O.), University Hospital Tübingen, Tübingen, Germany.

Please address correspondence to Omid Nikoubashman, MD, Klinik für Neuro radiologie, Universitätsklinikum Aachen, Pauwelsstr 30, 52074 Aachen, Germany; e-mail: onikoubashman@ukaachen.de

Indicates article with supplemental on-line table.

Indicates article with supplemental on-line photos.

<http://dx.doi.org/10.3174/ajnr.A4755>

and iopromide (Ultravist 300 mg/mL; Bayer HealthCare, Berlin, Germany). Dilutions in physiologic saline solution of 1:2, 1:4, 1:10, and 1:100 were used, with iodine concentrations in postinterventional cerebral hyperattenuations expected to be in the lower range of our tested concentrations. An additional probe containing physiologic saline was measured as a reference (On-line Fig 2). The phantom experiments were conducted on MR imaging scanners with field strengths of 1.5T (Magnetom Symphony; Siemens, Erlangen, Germany) and 3T (Magnetom Trio; Siemens).

At 1.5T, a 2-point method based on a standard multisection multiecho gradient recalled-echo (GRE) MR imaging sequence was used for estimation of the T1 relaxation time.⁷ For mapping of the T2 decay constant, we used a turbo spin-echo sequence with a multiecho acquisition. At 3T, a high-accuracy Look-Locker type T1 mapping sequence (T1 mapping with partial inversion recovery) was used.⁸ T2 mapping was performed by using a multiecho spin-echo sequence; T2* decay was monitored with a multiecho gradient-echo sequence at both field strengths.

To estimate the magnetic susceptibility of the contrast agents, we measured the test vials with concentrations of 1:1, 1:2, 1:4, and 1:10 in a custom-built cylindrical phantom, with the tubes embedded in distilled water and oriented parallel to the magnetic field. The field distribution was estimated on the basis of the phase data of a multiecho gradient-echo acquisition (TR = 60 ms, TE₁ = 3 ms, ΔTE = 4 ms [8 echoes], flip angle = 14°, 1-mm isotropic resolution) on a 3T scanner. The processing of the phase data included threshold-based and manual masking, unwrapping and linear regression in a time domain, and background field correction with in-house software.⁹ The susceptibility distribution inside the tube, χ , is assumed to be constant and can hence be estimated by a single-value minimization of the difference between the measured field and the field generated by dipole convolution:

$$\min_{\chi_{\text{tub}}} \|m_w \cdot [B_{\text{meas}} - B_0 \cdot (\chi_{\text{tube}} \cdot d)]\|_2,^{10}$$

The difference was evaluated in a region, m_w , surrounding the test tube, which was distinctly smaller than the phantom to avoid effects from imperfect background field removal in the outer regions.

For visual assessment of signal changes, 2 neuroradiologists (O.N., S.D.), blinded to the sequences, compared the signal intensity of every tube containing iodinated contrast agent with the signal intensity of saline solution (isointense, hypointense, hyperintense) in randomized order by using the following clinical sequences—a 1.5T scanner: T1WI spin-echo (SE) (TR, 350 ms; TE, 7.8 ms); T2WI TSE (TR, 5350 ms; TE, 120 ms); and T2*WI GRE (TR, 326.2 ms; TE, 13.8 ms); a 3T scanner: T1WI SE (TR, 600 ms; TE, 8.7 ms); T2WI TSE (TR, 4800 ms; TE, 05 ms); and T2*WI GRE (TR, 1100 ms; TE, 19.9 ms). Agreement between observers was evaluated by using a Spearman rank correlation coefficient test.

Ex Vivo Animal Model

We examined the visual aspects of intracerebral iopamidol on MR imaging in an ex vivo animal model. Because the porcine brain is resistant to ischemic stroke, the brain of a recently deceased swine

served as a model for infarcted brain parenchyma. Five milliliters of iopamidol was injected into the brain parenchyma of a recently deceased male Landrace swine (weight, 60 kg) via cranial trepanation. CT and MR imaging were performed immediately before and after injection of iopamidol into the brain parenchyma. Injection of iopamidol took place 60 minutes after cardiac arrest. CT and MR imaging were performed 1 minute and 9 minutes, respectively, after injection of iopamidol. CT scans were obtained on a 16-section CT scanner (Somatom Definition AS; Siemens). CT scans were acquired by using our standard spiral brain sequence (120 kV, 248 mA, H30 kernel) and were evaluated in the axial plane after multiplanar reconstruction (3-mm sections). MR imaging was performed by using a 1.5T MR imaging scanner (Intera; Philips Healthcare, Best, Netherlands). MR imaging comprised axial T1-weighted SE (TR, 350 ms; TE, 7.8 ms), T2-weighted TSE (TR, 5350 ms; TE, 120 ms), and T2*-weighted GRE (TR, 326.2 ms; TE, 13.8 ms) imaging with a section thickness of 3 mm. Two independent neuroradiologists evaluated all sections for visibility of iopamidol by using a tripartite visibility score (no visibility, poor visibility, good visibility). Agreement between observers was evaluated by using a Spearman rank correlation coefficient test.

RESULTS

Phantom Model

Iopamidol and iopromide cause T1, T2, and T2* shortening (On-line Fig 2). Detailed results of our relaxometry measurements are summarized in the On-line Table. Both contrast agents show very similar negative magnetic susceptibility shifts, which are reflected by comparable values of -0.74 ppm for iopamidol and -0.76 ppm for iopromide as estimated by linear regression (On-line Fig 3).

Shortening effects of both contrast agents on T1-weighted SE imaging were visible in all dilutions regardless of field strength (total agreement; Spearman ρ not calculable). However, this effect was subtle in dilutions of 1:4 and higher. Shortening effects of both contrast agents on T2-weighted TSE imaging were visible in dilutions of up to 1:4, while dilutions of 1:10 and higher were not distinguishable from physiologic saline solution, regardless of field strength (total agreement; Spearman $\rho = 1.0$; $P < .001$). T2* shortening was not visible on T2*-weighted GRE imaging regardless of field strength (total agreement; Spearman ρ not calculable).

Ex Vivo Animal Model

Undiluted iopamidol injected directly into the brain parenchyma was clearly visible on CT but did not cause visually distinctive signal changes on T1-weighted SE, T2-weighted TSE, and T2*-weighted GRE imaging (Figure). Concerning this outcome, there was total agreement (100%) between both observers (Spearman ρ not calculable). Small amounts of iopamidol, injected into the lateral ventricles and the subarachnoid space unintentionally, were visible on CT but not on MR imaging.

DISCUSSION

When there are hyperattenuated areas on CT after neurointerventional stroke treatment, one of the most important issues is to determine whether there is underlying hemorrhage, because

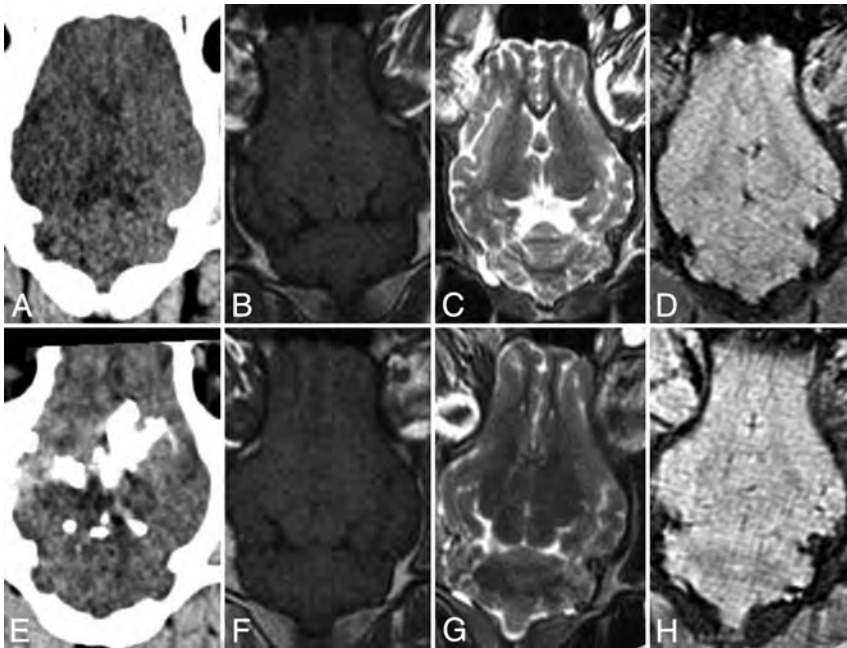


FIGURE. Ex vivo animal model. Porcine brain (Landrace, 60 kg) before (upper row) and after (lower row) direct injection of 5 mL of iopamidol. From left to right: axial CT (A and E) and T1-weighted (B and F), T2-weighted (C and G), and T2*-weighted (D and H) MR imaging. While the injected iodinated contrast agent is clearly visible on CT (E), there are no visually distinctive signal changes on MR imaging (F–H). Compared with the in vitro model, in which pure iopamidol causes visually distinctive signal changes (On-line Fig 2), the lack of signal changes in the ex vivo model could be attributed to rapid dilution of the injected contrast agent and/or the different magnetic environment where the contrast agent is located.

the presence of hemorrhage has crucial implications for further treatment decisions, such as the administration of anticoagulants. Discriminating between hemorrhage and contrast agent with the help of conventional CT is usually based on thresholds and cutoffs, assuming that hemorrhage persists after 24 hours and does not exceed 90 HU.² However, systematic studies, which aimed to validate the value of attenuation cutoffs or the 24-hour cutoff, are lacking to date.² Thus such cutoffs and thresholds may only serve as a rule of thumb, on which clinically relevant decisions should not be based.²

Recent studies dealing with dual-energy CT imply that it is possible to distinguish contrast extravasation from hemorrhage by using this method.^{1,3} However, the limited availability of these scanners remains a relevant hurdle in daily clinical practice. In most institutions, MR imaging may be the technique of choice because it is widely available and hemorrhage causes specific signal changes on MR imaging. However, it has been shown in phantom models that T1 and T2 shortening caused by iodinated contrast agents may theoretically mimic the appearance of intracellular methemoglobin, which is present in early subacute intracerebral hematomas within 3–7 days after hemorrhage.^{5,6} Because many MR imaging examinations are performed within this time period, the differentiation between hemorrhage and extravasated contrast agent may thus be complicated.

Our results confirm that iodinated contrast agents in fact cause visually distinctive T1 and T2 shortening in phantom models (On-line Fig 2).^{5,6} Nevertheless, our data and data from the literature also imply that this effect is negligible when

contrast agents are diluted.⁵ In accordance with the results from the phantom models, even pure iopamidol that was injected directly into the brain parenchyma in an ex vivo animal model did not cause visually distinctive signal changes on T1 SE, T2 TSE, and T2* GRE imaging (Figure). Most interesting, our phantom model has shown that the tested contrast agents at high concentrations produce a negative susceptibility shift that is relatively strong compared with contrast within brain tissue, which typically ranges up to 0.1 ppm. Phase imaging and quantitative susceptibility mapping in patients with stroke might thus reveal a large accumulation of iodinated contrast agent. However, given that iodinated contrast agents are always diluted in large amounts of blood during angiography, signal changes caused by iodinated contrast agents are most likely negligible on MR imaging (On-line Fig 1).

Limitations

Investigating only 2 iodinated contrast agents and performing only 1 animal ex vivo experiment are major limitations

of our study. It is also uncertain whether iodinated contrast agent injected into the brain parenchyma has the same effect on MR imaging as contrast agent accumulated through a damaged blood-brain barrier. Future systematic studies with more adequate stroke models (for example canines) may help to further elucidate in vivo MR imaging characteristics of iodinated contrast agents. Despite the limitations of our study, our experiments may serve as sufficient proof-of-principle, given that results from prior studies and theoretic considerations do not imply that extravasated iodinated contrast agents cause clinically relevant signal changes in MR imaging.

CONCLUSIONS

Our results imply that it is unlikely that iodinated contrast agents, which are extravasated into infarcted brain parenchyma during angiography, cause signal changes that mimic intracellular methemoglobin on T1-weighted, T2-weighted, and T2*-weighted MR imaging. Extravasated contrast agents can be distinguished from hemorrhage on MR imaging with sequences that are common in clinical practice.

Disclosures: Martin Wiesmann—UNRELATED: Consultancy: Stryker Neurovascular, Silk Road Medical; Payment for Lectures (including service on Speakers Bureaus): Bracco, Siemens, Stryker Neurovascular; Payment for Development of Educational Presentations: Abbott, ab medica,* Acandis,* Bayer,* Bracco,* B. Braun,* Codman Neurovascular,* Covidien,* Dahlhausen,* MicroVention,* Penumbra,* phenox,* Philips Healthcare,* Siemens,* Silk Road Medical,* St. Jude,* Stryker Neurovascular*; Travel/Accommodations/Meeting Expenses Unrelated to Activities Listed: Covidien.* *Money paid to the institution.

REFERENCES

1. Tijssen MP, Hofman PA, Stadler AA, et al. **The role of dual energy CT in differentiating between brain haemorrhage and contrast medium after mechanical revascularisation in acute ischaemic stroke.** *Eur Radiol* 2014;24:834–40 CrossRef Medline
2. Nikoubashman O, Reich A, Gindullis M, et al. **Clinical significance of post-interventional cerebral hyperdensities after endovascular mechanical thrombectomy in acute ischaemic stroke.** *Neuroradiology* 2014;56:41–50 CrossRef Medline
3. Renú A, Amaro S, Laredo C, et al. **Relevance of blood-brain barrier disruption after endovascular treatment of ischemic stroke: dual-energy computed tomographic study.** *Stroke* 2015;46:673–79 CrossRef Medline
4. Lummel N, Schulte-Altendorneburg G, Bernau C, et al. **Hyperattenuated intracerebral lesions after mechanical recanalization in acute stroke.** *AJNR Am J Neuroradiol* 2014;35:345–51 CrossRef Medline
5. Hergan K, Doring W, Längle M, et al. **Effects of iodinated contrast agents in MR imaging.** *Eur J Radiol* 1995;21:11–17 CrossRef Medline
6. Ganguly A, Gold GE, Butts Pauly K, et al. **Quantitative evaluation of the relaxivity effects of iodine on GD-DTPA enhanced MR arthrography.** *J Magn Reson Imaging* 2007;25:1219–25 CrossRef Medline
7. Abbas Z, Gras V, Möllenhoff K, et al. **Analysis of proton-density bias corrections based on T1 measurement for robust quantification of water content in the brain at 3 Tesla.** *Magn Reson Med* 2014;72:1735–45 CrossRef Medline
8. Shah NJ, Zaitsev M, Steinhoff S, et al. **A new method for fast multislice T(1) mapping.** *Neuroimage* 2001;14:1175–85 CrossRef Medline
9. Lindemeyer J, Oros-Peusquens AM, Shah NJ. **Multistage Background Field Removal (MUBAFIRE): compensating for B0 distortions at ultra-high field.** *PLoS One* 2015;10:e0138325 CrossRef Medline
10. de Rochefort L, Liu T, Kressler B, et al. **Quantitative susceptibility map reconstruction from MR phase data using Bayesian regularization: validation and application to brain imaging.** *Magn Reson Med* 2010;63:194–206 CrossRef Medline

Prevalence of Intracranial Aneurysms in Patients with Connective Tissue Diseases: A Retrospective Study

S.T. Kim, W. Brinjikji, and D.F. Kallmes



ABSTRACT

BACKGROUND AND PURPOSE: Few studies have examined the prevalence of intracranial aneurysms in connective tissue diseases such as Marfan syndrome, Ehlers-Danlos syndrome, neurofibromatosis type 1, and Loey-Dietz syndrome. We studied the prevalence of intracranial aneurysms and other intracranial neurovascular pathologies such as arteriovenous malformations and intracranial dissections, in these 4 patient populations.

MATERIALS AND METHODS: We retrospectively reviewed all patients who had a clinical diagnosis of Marfan syndrome, Ehlers-Danlos syndrome, neurofibromatosis type 1, or Loey-Dietz syndrome who underwent MRA, CTA, and/or DSA imaging of the intracranial circulation between January 1, 2005, and January 31, 2015. The presence, location, and maximum dimensions of intracranial aneurysms were catalogued. Other neurovascular findings studied included intracranial dissections and arteriovenous fistulas and shunts. Baseline data collected included demographic characteristics (sex, age, smoking history), imaging modality, and cardiovascular comorbidities.

RESULTS: The prevalence of intracranial saccular and fusiform aneurysms was as follows: 14% (8/59) among patients with Marfan syndrome, 12% (12/99) among patients with Ehlers-Danlos syndrome, 11% (5/47) among patients with neurofibromatosis type 1, and 28% (7/25) among patients with Loey-Dietz syndrome. Intracranial dissections were found in 2 patients (3%) with Marfan syndrome and 1 patient (1%) with Ehlers-Danlos syndrome. No intracranial dissections were found in patients with neurofibromatosis type 1 or Loey-Dietz syndrome.

CONCLUSIONS: Patients with connective tissue disorders, including Marfan syndrome, Ehlers-Danlos syndrome, neurofibromatosis type 1, and Loey-Dietz syndrome, have a high prevalence of intracranial aneurysms.

ABBREVIATIONS: EDS = Ehlers-Danlos syndrome; LDS = Loey-Dietz syndrome; NF1 = neurofibromatosis type 1

The association between neurovascular lesions such as intracranial aneurysms and connective tissue diseases has long been a topic of debate. Early studies suggesting an association between Marfan syndrome and intracranial aneurysms were limited to small case series and case reports.¹ However, larger studies have since suggested that there is no association between aneurysms and Marfan syndrome.¹⁻³ Nonetheless, the association is still widely cited in the literature.¹⁻³ In addition to Marfan syndrome, associations between connective tissue diseases, such as neurofibromatosis type 1 (NF1), Ehlers-Danlos syndrome (EDS),

and Loey-Dietz syndrome (LDS), and neurovascular lesions such as intracranial aneurysms have also been suggested. However, relatively few series have been published on the prevalence of aneurysms in these populations.

In this study, we sought to retrospectively characterize neurovascular findings in patients with connective tissue diseases, including Marfan, EDS, NF1, and LDS. Our primary outcome of interest was the prevalence of intracranial aneurysms. Secondary outcomes included the prevalence of intracranial dissections and arteriovenous malformations. We hypothesized that patients with connective tissue diseases would have a higher prevalence of intracranial aneurysms than the general population (ie, >3%).

MATERIALS AND METHODS

Patient Population

Following institutional review board approval, we conducted a retrospective chart review of all patients diagnosed with Marfan syndrome, EDS, NF1, and LDS who underwent MRA, CTA, or

Received October 12, 2015; accepted after revision January 8, 2016.

From the Mayo Medical School (S.T.K.) and Department of Radiology (W.B., D.F.K.), Mayo Clinic, Rochester, Minnesota.

Waleed Brinjikji, MD, Department of Radiology, Mayo Clinic, 200 1st St SW, Rochester, MN 55905; e-mail: brinjikji.waleed@mayo.edu; @wbrinjikji

Indicates article with supplemental on-line table.

<http://dx.doi.org/10.3174/ajnr.A4718>

Table 1: Summary of all data collected for patients with connective tissue diseases who underwent MRA, CTA, or DSA imaging of the head

	Marfan	Ehlers-Danlos	NFI	Loeys-Dietz
No. of patients	59	99	47	25
Mean age (yr)	49.4	41.7	38.3	36.5
No. (%) female	29 (49%)	81 (82%)	23 (49%)	13 (52%)
Cerebral imaging modality				
CTA, No. (%)	16 (27%)	24 (24%)	4 (9%)	9 (36%)
MRA, No. (%)	53 (90%)	85 (86%)	44 (94%)	22 (88%)
DSA, No. (%)	1 (2%)	2 (2%)	9 (19%)	0 (0%)
No. (%) intracranial aneurysms	8 (14%)	12 (12%)	5 (11%)	7 (28%)
No. (%) multiple intracranial aneurysms	2 (3%)	2 (2%)	1 (2%)	1 (4%)
Total No. of aneurysms	12	14	7	8
Location, No. (%):				
ICA	9 (15%)	12 (12%)	3 (6%)	5 (20%)
MCA	0 (0%)	1 (1%)	2 (4%)	0 (0%)
ACA	0 (0%)	0 (0%)	0 (0%)	1 (4%)
AcomA	1 (2%)	1 (1%)	1 (2%)	0 (0%)
PCA	2 (3%)	0 (0%)	0 (0%)	0 (0%)
Basilar	0 (0%)	0 (0%)	0 (0%)	0 (0%)
Vertebral	0 (0%)	0 (0%)	1 (2%)	2 (8%)
Other	0 (0%)	0 (0%)	0 (0%)	0 (0%)
Mean (SD) aneurysm size (mm)	4.4 (7.4)	6.9 (6.5)	11.2 (9.8)	4.8 (4.5)
Other intracranial vascular findings, No. (%)				
AVM	0 (0%)	0 (0%)	0 (0%)	0 (0%)
AVF	1 (2%)	2 (2%)	0 (0%)	0 (0%)
Dissection	2 (3%)	1 (1%)	0 (0%)	0 (0%)
Intracranial hemorrhage, No. (%)	0 (0%)	2 (2%)	2 (4%)	1 (4%)
Comorbidities, No. (%)				
Hypertension	21 (36%)	24 (24%)	15 (32%)	7 (28%)
Hyperlipidemia	24 (41%)	15 (15%)	9 (19%)	5 (20%)
Diabetes mellitus	4 (7%)	3 (3%)	2 (4%)	1 (4%)
Smoking	23 (39%)	32 (32%)	14 (30%)	11 (44%)
Stroke	10 (17%)	7 (7%)	9 (19%)	2 (8%)
Coronary artery disease	8 (14%)	5 (5%)	3 (6%)	2 (8%)

Note:—ACA indicates anterior cerebral artery; AcomA, anterior communicating artery; PCA, posterior cerebral artery.

Table 2: Symptomatic status at presentation of patients with confirmed intracranial aneurysms

	Marfan	Ehlers-Danlos	NFI	Loeys-Dietz
No. with intracranial aneurysms	8	12	5	7
Symptomatic status, No. (%)				
Asymptomatic/incidental	3 (38%)	7 (58%)	2 (40%)	7 (100%)
Headache	3 (38%)	4 (33%)	2 (40%)	0 (0%)
Aneurysm rupture/SAH	0 (0%)	0 (0%)	3 (60%)	0 (0%)
Cranial nerve palsy	4 (50%)	3 (25%)	0 (0%)	0 (0%)

DSA of the intracranial circulation from January 2005 through January 2015. All patients had clinically confirmed Marfan, EDS, NFI, or LDS as determined by medical geneticists at our institution. Patients who had other forms or unconfirmed connective tissue diseases were excluded. All of the above information pertinent to the inclusion and exclusion criteria was obtained through the electronic medical record.

Data Collection

Once the patients were selected, we collected the following data: demographic characteristics (sex, age, smoking history), imaging used (CT angiography, MR angiography, or digital subtraction angiography), and medical history (diabetes, hypertension, stroke, coronary artery disease, dyslipidemia).

The primary outcome of this study was the prevalence of intracranial aneurysms in these disease populations. The presence, location, and maximum dimensions of aneurysms were evaluated

by reviewing CTA, MRA, or DSA images and reports. All images and reports were reviewed by a radiologist with 4 years of experience. In addition, we studied the prevalence of intracranial arteriovenous malformations, arteriovenous fistulas, and intracranial dissections. The symptomatic status of the intracranial aneurysms and dissections was collected in addition to the presence of aneurysm rupture.

Statistical Analysis

Continuous variables are presented as mean \pm SD, and categorical variables, as frequency in percentages. To determine variables independently associated with intracranial aneurysm presence, we performed a multivariate logistic regression analysis adjusting for age, sex, smoking, hypertension, diabetes mellitus, abdominal/thoracic aortic aneurysms, coronary artery disease, and history of stroke. A separate analysis was performed for each connective tissue disease. All statistical analysis was performed by using JMP, Version 12.0.0 (SAS Institute, Cary, North Carolina).

RESULTS

A total of 230 patients fit our inclusion criteria: Fifty-nine patients had Marfan syndrome, 99 patients had EDS, 47 patients had NFI, and 25 patients had LDS. The data presented below are organized in Table 1, along with additional demographic characteristics and imaging findings. The symptom status of each patient with a confirmed intracranial aneurysm is presented in Table 2. A brief description of each connective tissue disease is summarized in Table 3. The presentation and reason for neuroimaging referral for each patient who qualified for our study are summarized in the On-line Table.

Marfan Syndrome

Of the 59 patients who underwent angiographic imaging of the head, 8 individuals (14%) had a total of 12 intracranial aneurysms: 9 saccular aneurysms and 3 fusiform aneurysms. The mean size of the intracranial aneurysms was 5.5 ± 7.4 mm. Among patients with aneurysms, 2 of 8 (33%) were males and 2 patients were younger than 50 years of age. Other intracranial findings were a direct cavernous carotid fistula ($n = 1$) and dissection ($n = 2$). One patient with dissection presented with acute ischemic stroke, and another presented with transient ischemic attacks. There were no cases of subarachnoid hemorrhage. Increasing age was the only variable independently associated with the presence of an intracranial aneurysm (OR, 1.09; 95% CI, 1.01–1.22; $P = .03$). Representative images are provided in Fig 1.

Table 3: Most common features of connective tissue diseases

Clinical Manifestations	Associated Genes	Gene Product
Marfan Marfanoid habitus Aortic root diseases Ectopic lentis Dural ectasia	<i>FBNI</i>	Fibrillin-1
Ehlers-Danlos Joint hypermobility Skin hyperextensibility Abnormal wound healing Mitral valve prolapse	<i>COL5A1</i> <i>COL5A2</i> <i>COL3A1</i>	Type V collagen Type III collagen
NF1 Café-au-lait macules Lisch nodules Neurofibromas Osteoporosis	<i>NFI</i>	Neurofibromin
Loeys-Dietz Aortic aneurysms	<i>TGFBR1</i>	Transforming growth factor β receptor I
Generalized arterial tortuosity	<i>TGFBR2</i>	Transforming growth factor β receptor II
Hypertelorism Bifid/broad uvula or cleft palate	<i>TGFB2</i>	Transforming growth factor β

Ehlers-Danlos Syndrome

Of the 99 patients who underwent angiographic imaging of the head, 12 individuals (12%) had a total of 14 intracranial aneurysms: 9 saccular aneurysms and 5 fusiform aneurysms. The mean size of the intracranial aneurysms was 6.9 ± 6.5 mm. Of the 12 patients with aneurysms and EDS, 1 had type I EDS, 3 had type III EDS, and 7 had type IV EDS. In 1, the type of EDS was unknown. One patient had both a vertebral AVF on the right and a contralateral dissection of the intradural vertebral artery, which presented as acute ischemic stroke. Intracranial hemorrhage occurred in 2 patients, with 1 patient dying from massive hemorrhage secondary to cerebral venous thrombosis and another with repeat incidences of subarachnoid hemorrhages with unknown etiology despite multiple cerebral angiograms. Increasing age was the only variable independently associated with the presence of an intracranial aneurysm (OR, 1.12; 95% CI, 1.02–1.26; $P = .04$). Representative images are provided in Fig 2.

Neurofibromatosis Type 1

Of the 47 patients who underwent angiographic imaging of the head, 5 individuals (11%) had a total of 7 intracranial aneurysms: 6 saccular aneurysms and 1 fusiform aneurysm. The mean size of the intracranial aneurysms was 11.2 ± 9.8 mm. Among patients with aneurysms, 3 of 5 were male (60%), and 3 were younger than 50 years of age. Subarachnoid hemorrhage occurred in 1 patient secondary to intracranial aneurysm rupture and in another secondary to trauma. No patients had intracranial dissections. Hypertension was the only variable independently associated with aneurysm presence (OR, 27.4; 95% CI, 1.69–177.72; $P = .02$). Representative images are provided in Fig 3.

Loeys-Dietz Syndrome

Of the 25 patients who underwent angiographic imaging of the head, 7 (28%) individuals had a total of 8 intracranial aneurysms: 7 saccular aneurysms and 1 fusiform aneurysm. The mean size of the intracranial aneurysms was 4.8 ± 4.5 mm. Among patients with aneurysms, 4 of 7 (57%) were male, and 4 were

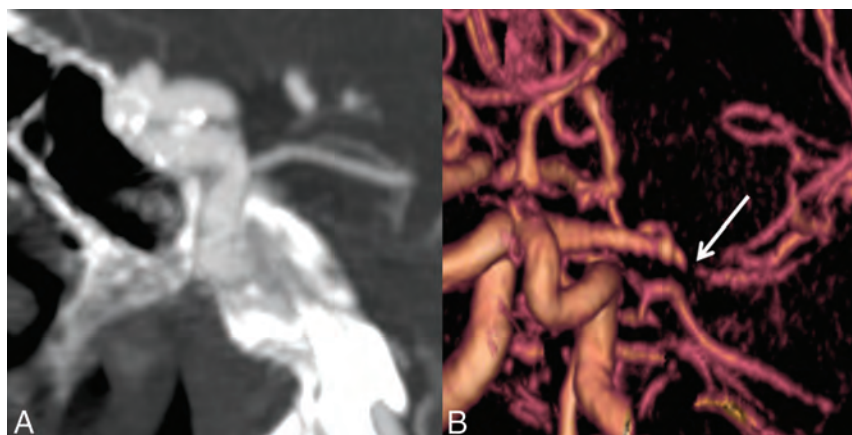


FIG 1. Imaging findings in Marfan syndrome. A, A 25-year-old man with Marfan syndrome with a 4-mm periophthalmic aneurysm of the right ICA. B, 3D reconstruction of a CTA performed for evaluation of acute ischemic stroke and headache in a patient with Marfan syndrome demonstrates smooth tapering of the right MCA, consistent with an acute dissection (arrow).

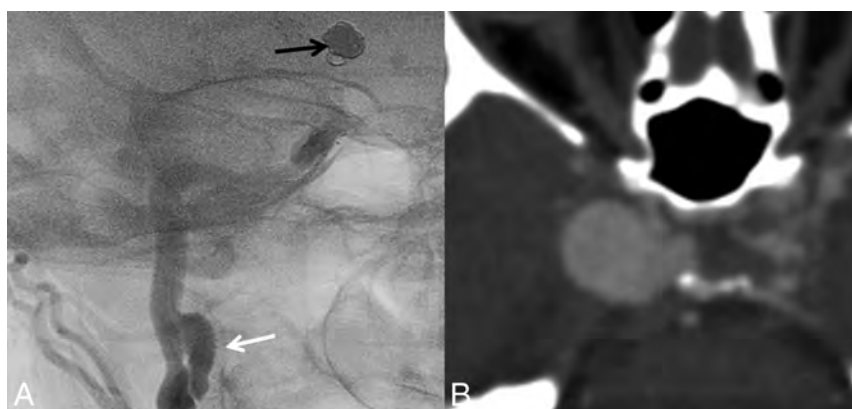


FIG 2. Imaging findings in Ehlers-Danlos syndrome. A, DSA of a cervical carotid dissecting pseudoaneurysm (white arrow) in a patient with Ehlers-Danlos syndrome. Note the coil mass in the supraclinoid ICA from previous coiling of an ICA aneurysm. B, A giant cavernous carotid artery aneurysm in a patient with Ehlers-Danlos syndrome.

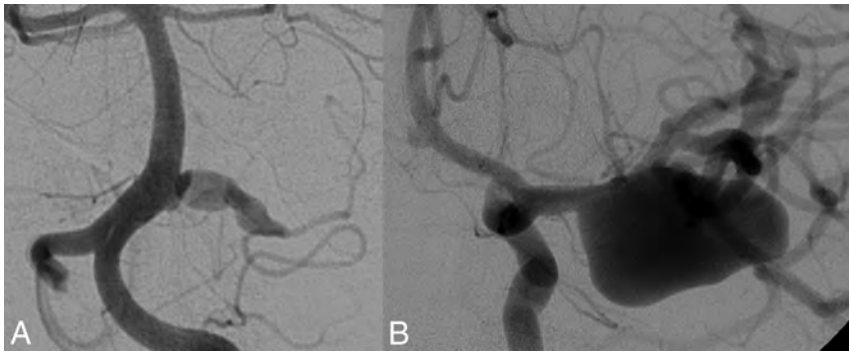


FIG 3. Imaging findings in neurofibromatosis type 1. *A*, Fusiform aneurysm of the right anterior cerebellar artery in a 22-year-old patient with NF1. *B*, The same patient had a giant right MCA aneurysm and a third fusiform aneurysm of an M2 branch.

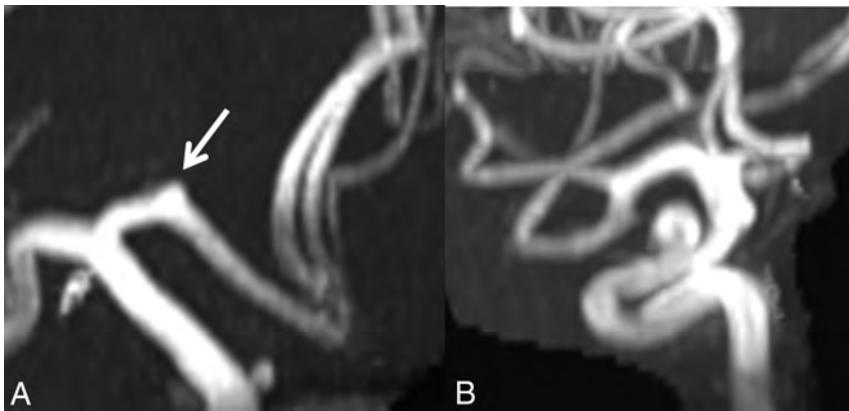


FIG 4. Aneurysms in Loey-Dietz syndrome. *A*, A 3-mm A1 aneurysm (arrow). *B*, A 6-mm supraclinoid ICA aneurysm in a patient with Loey-Dietz syndrome.

younger than 50 years of age. Subarachnoid hemorrhage of unknown etiology in a patient without an intracranial aneurysm occurred in 1 individual. No variables were independently associated with aneurysm presence. Representative images are provided in Fig 4.

DISCUSSION

Our study demonstrates that patients with Marfan syndrome, EDS, NF1, and LDS have a high prevalence of intracranial aneurysms. Compared with the 3.2% of the general population who have intracranial aneurysms, the patients in our study had prevalences ranging from 9% to 28%.⁴ Most of these intracranial aneurysms were found in the anterior circulation, particularly the ICA. On our logistic regression analysis, increasing age was the only variable independently associated with intracranial aneurysm in patients with Marfan syndrome and EDS, and hypertension was the only variable associated with intracranial aneurysm in patients with NF1. The high prevalence of intracranial aneurysms in the population with connective tissue disease has implications for screening these patients, especially because most aneurysms were asymptomatic.

While it is still an ongoing area of debate, relatively large clinical series have called into doubt the association between both Marfan syndrome and EDS and intracranial aneurysms. In a post-mortem series of 25 patients with Marfan syndrome, Conway et al¹ found an aneurysm prevalence of just 4%. In addition, in a

series of 129 patients with Marfan syndrome, van den Berg et al² found no patients who presented with a symptomatic intracranial aneurysm. In a study of 419 patients with EDS or a family history of the disease, Pepin et al⁵ found 6 (1.4%) patients who had intracranial aneurysms. However, the exact prevalence of aneurysms in the Pepin et al series is not known because the number of patients who underwent angiographic imaging was not reported.

To our knowledge, our study represents the largest imaging study to date examining the prevalence of intracranial aneurysms in Marfan syndrome and EDS. Distinct from prior studies, all patients in our series underwent intracranial imaging with CTA, DSA, or MRA, thus allowing a more accurate representation of aneurysm prevalence. More than half of the patients in the Marfan and EDS cohorts were asymptomatic at the time of diagnosis. There is no clear consensus in the literature regarding the prevalence of intracranial aneurysms in patients with NF1. In a large case-control study including 39 patients with NF1 and 526 controls, Maya et al⁶ found a 9% aneurysm prevalence in the NF1 population versus the 0% in controls. However, in a separate study of children

with NF1, Rosser et al⁷ found that only 1 of the 316 patients with NF1 undergoing brain MR imaging had an intracranial aneurysm. However, only 8 of these 316 patients had an MRA performed in addition to the MR imaging.⁷

To date, only 2 previously published studies have examined the prevalence of cerebral aneurysms in a consecutive series of patients with LDS. In the landmark article describing Loey-Dietz syndrome including 90 patients, Loey et al⁸ found that 10% of patients with LDS had intracranial aneurysms. Two patients died from cerebral bleeding. In a study of 25 patients with LDS, Rodrigues et al⁹ found that 7 patients (28%) had intracranial aneurysms; most were in the anterior circulation. These findings are similar to those in our study, which also found that 7 of 25 patients (28%) had intracranial aneurysms. All 7 of the patients with intracranial aneurysms in our LDS cohort were asymptomatic and had incidental findings.

Limitations

Our study has limitations. First, it is retrospective in nature. The multiple imaging modalities (CTA, MRA, and DSA) used to identify intracranial aneurysms can cause differences in the accuracy of aneurysm detection among patients. Although DSA is the most sensitive imaging technique for aneurysm detection, most of our patients underwent only CTA or MRA. In addition, the nongenetic clinical diagnosis used to identify patients with Marfan, EDS, NF1, and LDS can result in misdiagnosis. There is also the possibility

that our study overestimates the prevalence of intracranial aneurysms in all of these patients because our center is a tertiary referral site for patients with complicated forms of these diseases, and it is a high-volume intracranial aneurysm treatment center. If one were to prospectively study a random group of patients with these connective tissue diseases and obtain imaging, the prevalence estimates may be substantially different from those presented here.

CONCLUSIONS

Our study suggests that patients with Marfan syndrome, Ehlers-Danlos syndrome, neurofibromatosis type 1, and Loeys-Dietz syndrome have a high prevalence of intracranial aneurysms. However, it is of key importance to recognize the inevitable yet substantial selection bias of this prevalence study. Nonetheless, these findings further support the need for future prospective studies to understand the risks and benefits of preventative screening in patients with these connective tissue disorders.

Disclosures: David F. Kallmes—UNRELATED: Board Membership: GE Healthcare (Cost-Effectiveness Board)*; Consultancy: ev3/Covidien/Medtronic,* Comments: planning and implementing clinical trials; Grants/Grants Pending: MicroVention,* Sequent Medical,* SurModics,* Codman,* ev3/Covidien/Medtronic,* NeuroSigma*; Travel/Accommodations/Meeting Expenses Unrelated to Activities Listed: ev3/Covidien/Medtronic,* Comments: presentation at an FDA panel meeting. *Money paid to the institution.

REFERENCES

1. Conway JE, Hutchins GM, Tamargo RJ. **Marfan syndrome is not associated with intracranial aneurysms.** *Stroke* 1999;30:1632–36 CrossRef Medline
2. van den Berg JS, Limburg M, Hennekam RC. **Is Marfan syndrome associated with symptomatic intracranial aneurysms?** *Stroke* 1996; 27:10–12 CrossRef Medline
3. Pfohman M, Criddle LM. **Epidemiology of intracranial aneurysm and subarachnoid hemorrhage.** *J Neurosci Nurs* 2001;33:39–41 CrossRef Medline
4. Brown RD Jr, Broderick JP. **Unruptured intracranial aneurysms: epidemiology, natural history, management options, and familial screening.** *Lancet Neurol* 2014;13:393–404 CrossRef Medline
5. Pepin M, Schwarze U, Superti-Furga A, et al. **Clinical and genetic features of Ehlers-Danlos syndrome type IV, the vascular type.** *N Engl J Med* 2000;342:673–80 CrossRef Medline
6. Schievink WI, Riedinger M, Maya MM. **Frequency of incidental intracranial aneurysms in neurofibromatosis type 1.** *Am J Med Genet A* 2005;134A:45–48 CrossRef Medline
7. Rosser TL, Vezina G, Packer RJ. **Cerebrovascular abnormalities in a population of children with neurofibromatosis type 1.** *Neurology* 2005;64:553–55 CrossRef Medline
8. Loeys BL, U. Schwarze, T. Holm, et al. **Aneurysm syndromes caused by mutations in the TGF-beta receptor.** *N Engl J Med* 2006;355: 788–98 CrossRef Medline
9. Rodrigues VJ, Elsayed S, Loeys BL, et al. **Neuroradiologic manifestations of Loeys-Dietz syndrome type 1.** *AJNR Am J Neuroradiol* 2009; 30:1614–19 CrossRef Medline

T1 Signal-Intensity Increase in the Dentate Nucleus after Multiple Exposures to Gadodiamide: Intraindividual Comparison between 2 Commonly Used Sequences

J. Ramalho, M. Ramalho, M. AlObeidy, R.H. Nunes, M. Castillo, and R.C. Semelka



ABSTRACT

BACKGROUND AND PURPOSE: Different T1-weighted sequences have been used for qualitative and quantitative evaluation of T1 signal intensity related to gadolinium deposition in the dentate nucleus in patients who underwent several enhanced MR imaging studies. Our purpose was to perform an intraindividual qualitative and quantitative comparison between T1-weighted spin-echo and 3D magnetization-prepared rapid acquisition of gradient echo sequences in patients who had multiple exposures to gadodiamide.

MATERIALS AND METHODS: Our retrospectively selected population included 18 patients who underwent at least 3 administrations of gadodiamide and had a baseline and a final MR imaging performed with both T1-weighted sequences. Qualitative and quantitative analyses were independently performed. Dentate nucleus/middle cerebellar peduncle signal-intensity ratios and signal changes between the baseline and final examinations were compared by using the Wilcoxon signed rank test. Correlation between quantitative and qualitative evaluations was assessed by using a polyserial correlation test.

RESULTS: The differences between the 2 sequences for both baseline and last examination dentate nucleus/middle cerebellar peduncle ratios were statistically significant ($P = .008$ and $P = .006$, respectively); however, the signal-intensity changes of the ratios with time were not ($P = .64$). The correlation between the qualitative and quantitative analysis was very strong (near-perfect) ($r = 0.9$) for MPRAGE and strong ($r = 0.63$) for spin-echo sequences.

CONCLUSIONS: T1-weighted spin-echo and MPRAGE sequences cannot be used interchangeably for qualitative or quantitative analysis of signal intensity in the dentate nucleus in patients who received gadodiamide. Baseline and final examination ratios should be evaluated across time by using the same sequence. Qualitative analysis performed with MPRAGE correlated better with quantitative analysis and may offer advantages over spin-echo sequences for research purposes.

ABBREVIATIONS: DN = dentate nucleus; eGFR = estimated glomerular filtration rate; GBCA = gadolinium-based contrast agent; MCP = middle cerebellar peduncle; SE = spin-echo

During the past 2 years, several peer-reviewed studies have been published describing an association between progressive high signal intensity on unenhanced T1-weighted images in the globus pallidus and/or dentate nucleus (DN) and the number of administrations of different gadolinium-based contrast agents

(GBCAs), suggesting gadolinium deposition in these structures; this has been confirmed in humans and animals.¹⁻¹¹

One major limitation of retrospective human studies of gadolinium deposition is the variability of the MR imaging protocols used, according to the pathology that is being studied and among different institutions.

Kanda et al⁵ and Adin et al⁸ used qualitative measurements to evaluate signal-intensity changes in patients who underwent multiple GBCA administrations, by using T1-weighted spin-echo (SE),^{5,8} T1 MPRAGE, or T1 FLAIR images.⁸ It is generally assumed that visual analysis correlates well with quantitative analysis, but qualitative assessment of the presence or absence of hyperintensity on T1-weighted MR images is subjective; hence, quantitative signal-intensity measurement is commonly favored.

In most of the published literature, the authors have used T1-weighted SE sequences to quantitatively evaluate the signal intensity and signal changes with time. However, in some studies, dif-

Received November 25, 2015; accepted after revision January 26, 2016.

From the Department of Radiology (J.R., M.R., M.A., R.H.N., M.C., R.C.S.), University of North Carolina at Chapel Hill, Chapel Hill, North Carolina; Department of Neuroradiology (J.R.), Centro Hospitalar de Lisboa Central, Lisbon, Portugal; Department of Radiology (M.R.), Hospital Garcia de Orta, Almada, Portugal; Department of Radiology (M.A.), King Faisal Specialist Hospital and Research Center, Riyadh, Saudi Arabia; and Division of Neuroradiology (R.H.N.), Santa Casa de Misericórdia de São Paulo, São Paulo, Brazil.

Please address correspondence to Joana Ramalho, MD, Neuroradiology Department, Centro Hospitalar de Lisboa Central, Alameda de Santo Antonio dos Capuchos, 1169-050 Lisboa, Portugal; e-mail: Joana-Ramalho@netcabo.pt

<http://dx.doi.org/10.3174/ajnr.A4757>

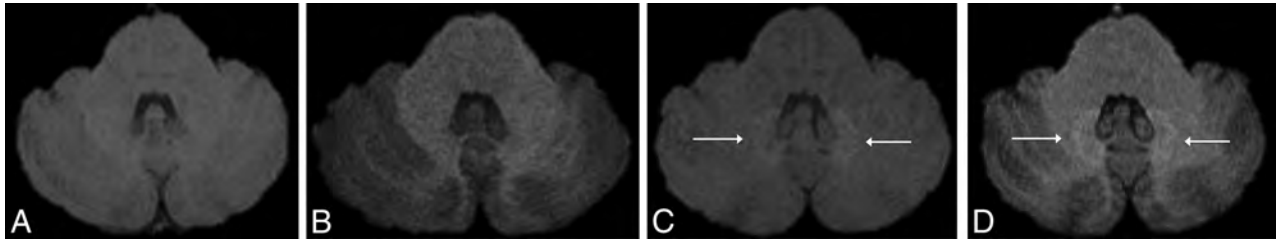


FIG 1. Axial MR images in a 40-year-old male patient with a right frontal low-grade astrocytoma. Unenhanced axial T1-weighted spin-echo (A and C) and 3D MPRAGE MR images (B and D) of the first (A and B) and fifth (2 years later, C and D) gadolinium-enhanced MR imaging examinations at the level of the dentate nuclei of the cerebellum. The images show progressively increased T1 signal of the dentate nuclei (white arrows, C and D). Note that the qualitative analysis was slightly different between the 2 sequences.

Patients' demographic and clinical characteristics

Demographics	
Patients (number)	18
Sex	12 Women
Age (mean \pm SD) (range) (yrs)	52.56 \pm 15.21 (17–76)
eMRIs performed (mean \pm SD) (range)	4.78 \pm 2.51 (2–10)
Interval (MRI _{baseline} – MRI _x) (mean \pm SD) (range)	933 \pm 610.78 (96–1905 days)
Diagnosis (number)	
Meningioma	12
Glioblastoma	2
Low-grade glioma	1
Oligodendroglioma	1
Chordoma	1
Spinal hemangioblastoma	1

Note:—eMRI indicates enhanced MR imaging; yrs, years.

ferent T1-weighted sequences have been interchangeably used, including T1-weighted 3D MPRAGE⁶ and FLASH,¹² to quantitatively evaluate signal-intensity changes in the dentate nucleus. Not surprising, the results among different investigators are somewhat contradictory. The use of different sequences may, in part, explain these differences.¹³ It is unclear whether different T1-weighted sequences may be used interchangeably to qualitatively and quantitatively study gadolinium deposition on the basis of their T1-weighting despite their distinct intrinsic properties. Even though quantitative measurements are undoubtedly recommended for scientific publications, they are difficult to apply in clinical practice. On the other hand, qualitative analysis is applied every day to assess normal brain structures and lesions. Considering the increasing concern regarding GBCA administration, we believe qualitative analysis must be evaluated. Therefore, our aim was to determine whether there are differences between the quantitative analysis performed with T1-weighted SE and T1-weighted MPRAGE sequences and to correlate the qualitative appreciation of the T1 signal intensity of the DN with the quantitative analysis of corresponding sequences.

MATERIALS AND METHODS

Patients

Institutional review board approval was obtained for this single-center (University of North Carolina Hospital at Chapel Hill) retrospective longitudinal observational study with a waiver of informed consent.

From a data base of subjects with multiple GBCA administrations for brain MR imaging studies, we identified 50 consecutive patients who underwent at least 2 brain contrast-enhanced stud-

ies performed with gadodiamide (Omniscan; GE Healthcare, Piscataway, New Jersey) plus an additional last MR imaging for reference. Our center used gadodiamide (Omniscan) for all enhanced MR imaging studies performed before December 2006, irrespective of the patient's renal function. From December 2006 to June 2007, patients with normal renal function received gadodiamide (Omniscan), and after June 2007, the use of gadodiamide (Omniscan) was discontinued. All MR imaging examinations were performed as clinical studies. Because gadodiamide (Omniscan) was the only contrast evaluated, only studies performed before June 2007 were included. Evaluation of medical records permitted exclusion of patients who had undergone contrast agent administration outside our institution or who had undergone MR imaging with a GBCA other than gadodiamide (Omniscan). Patients with abnormal liver or renal function were also excluded. Abnormal liver function was defined by abnormal serum concentrations of aspartate aminotransferase, alanine aminotransferase, total bilirubin, or g-glutamyl transpeptidase. Renal function was evaluated by calculating the estimated glomerular filtration rate (eGFR) and was classified as normal (eGFR > 60 mL/min/m²), moderately abnormal (eGFR between 30 and 60 mL/min/m²), or severely insufficient (eGFR < 30 mL/min/m²).

Among the 50 patients selected, only those who had a first baseline MR imaging and a last MR imaging performed with both T1-weighted SE and 3D MPRAGE sequences were included for analysis (Fig 1). Thus, our final population included 18 patients (12 women, 6 men; mean age, 52.56 \pm 15.21 years). The total number of administered doses of GBCA ranged from 2 to 10 (mean, 4.78 \pm 2.51 doses), and the interval between the first and last examinations ranged from 96 to 1905 days (mean, 933 \pm 610.78 days). A summary of patient data is shown in the Table.

Imaging Protocols

MR imaging was performed by using a 1.5T MR imaging unit (Magnetom Avanto; Siemens, Erlangen, Germany) with a 12-element designed head matrix coil. The MR imaging protocols varied according to the clinical indications but included, in all patients, a fast spin-echo T1-weighted sequence (TR, 623 ms; TE, 13 ms; echo-train length, 1; section thickness, 5 mm; spacing, 1 mm; matrix size, 256 \times 256; and FOV, 165 \times 220) and a T1-weighted 3D MPRAGE sequence (TR, 1740 ms; TE, 3.45 ms; section thickness, 1.0 mm; matrix size, 256 \times 256; FOV, 250 mm) before GBCA injection. A standard dose of 0.1 mmol of gadodiamide per kilogram of body weight was administered intravenously by using

a power injector (Spectris Solaris EP; Medrad, Indianola, Pennsylvania) at a rate of 1.5–2.0 mL/s, followed by a 20-mL saline flush bolus administered at the same rate.

Imaging and Data Analysis

For each patient, the number of gadolinium-enhanced MR imaging examinations performed with gadodiamide was recorded. Both sequences, T1-weighted SE and 3D MPRAGE, in the first (MRI_{baseline}) and last (MRI_x, with x being the number of the contrast-enhanced MR imaging studies) examinations were quantitatively and qualitatively analyzed. Two neuroradiologists, who were blinded to clinical data, independently reviewed all images on a dedicated workstation (Impax, Version 6; Agfa-Gevaert, Mortsel, Belgium). Disagreements were resolved by consensus.

Qualitative Analysis

Signal intensity in the DN on unenhanced T1-weighted images was classified by comparison with the signal intensity of the central normal-appearing white matter of the cerebellum by using a previously described and widely used 4-point grading scale,¹⁴ in which grade 4 indicates prominent hyperintensity; grade 3, faint hyperintensity; grade 2, isointensity; and grade 1, hypointensity. When visible, the DN was defined as an irregularly folded ribbon-like structure located in the medial deep white matter of each cerebellar hemisphere. Variable window and level settings were used when reviewing the MR images.¹⁵

Quantitative Analysis

Oval ROIs were placed on the DN and middle cerebellar peduncle (MCP) on both sides to include as much of each anatomic structure as possible, avoiding lesions, vessels, or artifacts. When the DN was unclear on T1-weighted images, the same section position on T2-weighted images was used to guide ROI placement. Measurements were averaged for both the right and left sides and for both readers. The DN/MCP signal-intensity ratio was calculated by dividing the mean signal intensity of the DN by that of the MCP.

Statistical Analysis

R: A Language and Environment for Statistical Computing (R Core Team; Vienna, Austria)¹⁶ was used for all statistical computing. Statistical significance was defined as a $P < .05$.

Interobserver agreement between the 2 readers' ROI measurements for each structure was evaluated by using the Lin concordance correlation coefficient,¹⁷ grouped by structures for both sides. The strength of the agreement was considered near-perfect when it was >0.99 , substantial when it was 0.95 – 0.99 , moderate when it was 0.90 – 0.95 , and poor when it was <0.90 . Interobserver agreement is illustrated by using Bland-Altman plots (difference plots) (Fig 2).

Interobserver agreement for qualitative data was assessed by using kappa statistics, grouped by structures for both sides, as per the Landis and Koch schema. Conventionally, $\kappa < 0$ is considered poor agreement; 0.01 – 0.20 , slight; 0.21 – 0.40 , fair; 0.41 – 0.60 , moderate; 0.61 – 0.80 , substantial; and 0.81 – 1.00 , near-perfect agreement.

DN/MCP ratios, averaged for both readers for the baseline and

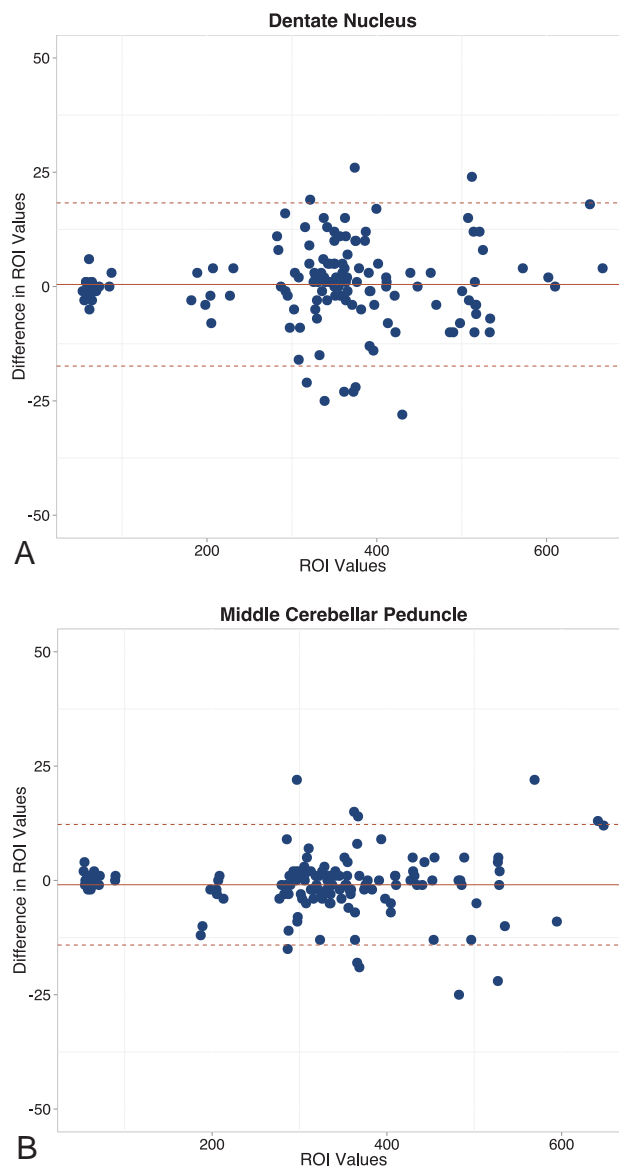


FIG 2. Bland-Altman plots show the differences in average ROI measurements between the 2 readers for the dentate nucleus (A) and middle cerebellar peduncle (B).

final examinations, were calculated for both sequences and compared by using the Wilcoxon signed rank test. This test was also used to evaluate significant differences in change with time in signal-intensity ratios for both sequences.

Correlation between DN/MCP ratios and qualitative signal evaluation of the DN, for both baseline and last examinations, was assessed by using a polyserial correlation test. The strength of correlation was perfect if $r = 1$; very strong, $r \geq 0.70$; strong, $0.40 \leq r < 0.69$; moderate, $0.30 \leq r < 0.39$; weak, $0.20 \leq r < 0.29$; and no or negligible relationship, $0.01 \leq r < 0.19$.

RESULTS

Each reader drew 280 ROIs. The left DN and MCP were not measured in 1 patient due to disease involvement. In this patient, the analysis was performed by using only the right-sided structures.

Interobserver agreement was near-perfect for both evaluated structures: for the DN, it was 0.998 (95% confidence interval,

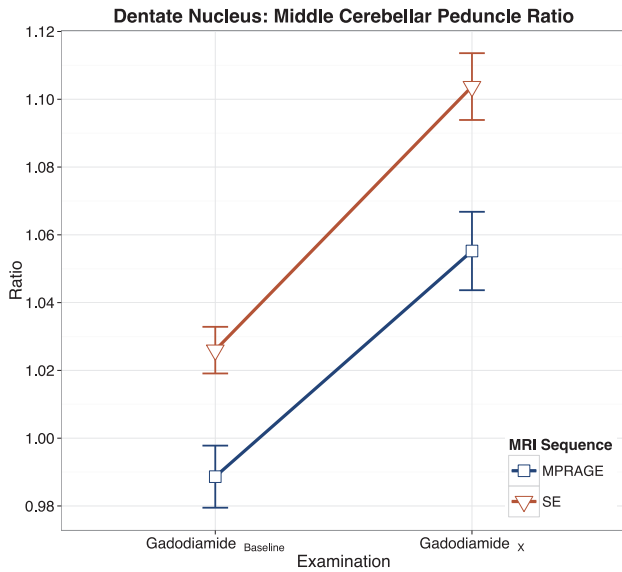


FIG 3. Intraindividual linear graphic representation of the DN/MCP ratios, with error bars, for spin-echo and 3D MPRAGE sequences. Note the higher ratios with SE on both baseline and final examinations.

0.997–0.999), and for the MCP, it was 0.999 (95% confidence interval, 0.998–0.999).

For qualitative analysis, interobserver agreement was also near-perfect, $\kappa = 0.899$. Among the 72 evaluations (4 examinations for each patient: SE MRI_{baseline}, SE MRI_x, MPRAGE MRI_{baseline}, and MPRAGE MRI_x), there were 16 disagreements solved by consensus.

The differences between the 2 sequences for both baseline and last examination DN/MCP ratios were statistically significant ($P = .008$ and $P = .006$, respectively) (Fig 3), but the change in ratio with time was not ($P = .64$).

The correlation between the qualitative and quantitative analysis was very strong (near-perfect) ($r = 0.9$) for the MPRAGE and strong for the SE sequence ($r = 0.63$) (Fig 4).

DISCUSSION

Our results showed that the DN/MCP signal-intensity ratios were significantly different and overall higher with the SE than the MPRAGE sequence. The change with time between the first and last examination for each sequence was not significantly different. The correlation between the qualitative and quantitative evaluations was near-perfect for the MPRAGE sequence and strong for the SE sequence.

Significant differences were found comparing the DN/MCP ratios between the 2 sequences, which we consider an indication that these 2 sequences should not be used interchangeably. Both sequences showed similar signal-intensity progression with time but different signal-intensity ratios at the baseline and last examinations. The performance of both sequences for quantitative evaluations of the T1-weighted signal-intensity changes in the DN was also similar.

Radbruch et al⁶ used both T1-weighted sequences for signal-intensity quantification of the DN. In their study, it was not clear whether the ROI measurements between the first and last examinations were performed by using the same sequence. Our find-

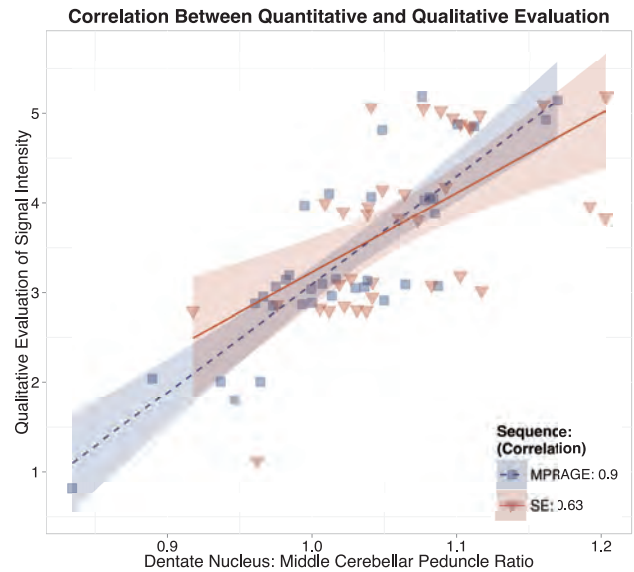


FIG 4. Intraindividual linear graphic representation demonstrating the correlation between qualitative and quantitative (DN/MCP ratio) evaluations of the increased T1 signal intensity within the dentate nucleus for SE and 3D MPRAGE sequences. Note the stronger correlation with MPRAGE (0.9) compared with SE (0.63). Values on the y-axis are represented on an ordinal scale with random vertical offset (jitter) to minimize overlapping.

ings suggest that comparing different sequences between studies may generate inaccurate results. Furthermore, for statistical purposes, the change in signal intensity between the first and last examinations is better than the ratios. Adin et al¹⁸ also appeared to have used SE and MPRAGE interchangeably, and on the basis of our results, we consider that a substantial limitation in their study.

Theoretically, our results are to be expected because SE and MPRAGE sequences are different in nature. SE imaging is a 2D acquisition technique in which short TRs and TEs produce T1-weighted images in which tissue contrast is primarily related to differences in the T1 relaxation time of each tissue.¹⁸ MPRAGE is a T1-weighted 3D sequence acquired with a 3D Fourier transform technique following a magnetization-prepared 180° inversion pulse. The use of an inversion pulse allows greater T1 contrast compared with SE imaging; however, the T1-weighting of different tissues may be considerably different between structures, depending on the selected TI. Signal-to-noise ratios and contrast-to-noise ratios are greater with SE compared with MPRAGE, and the inherently high signal intensity of white matter may account for the lower DN/MCP ratio signal intensity, as seen in our study, because the MCP is a white matter structure.^{18,19} Substantial changes of parameters of the same imaging sequence used can render the comparisons of that sequence inaccurate. However, we believe that because those parameters have been preset, in a way, to avoid tangible changes across systems of the same field strength at our institution, the comparison would be less affected compared with the use of completely different imaging pulse sequences.

Our results suggest that qualitative evaluation is more accurate with MPRAGE than with the SE sequence. The stronger correlation between qualitative and quantitative analysis with MPRAGE may be explained by the greater gray/white matter contrast inher-

ent to this sequence compared with SE. This likely reflects the greater T1-weighted contrast of the MPRAGE sequence achieved by the initial 180° inversion pulse.²⁰

Limitations of our study include the retrospective nature of data acquisition and the small sample size; the strict inclusion criteria limited the sample size of our study. However, we believe that the pair-wise comparison nature of our study compensates for the small sample size. Another possible limitation is the use of the MCP, a white matter structure, as the denominator in the DN ratios because the relative signal intensity of the white matter is higher on the MPRAGE sequence. Because research into the subject of brain deposition is still relatively new, it is still unclear which is the best reference structure for the DN ratio calculation. As previously performed,⁴ we calculated the ratio by using the MCP instead of the base of the pons^{2,3,6} because the latter may exhibit heterogeneous signal intensity related to presumed vascular changes. Additionally, Radbruch et al^{6,21} reported that the ratios of the DN with the pons, cerebellum, and CSF were comparable. Thus, no significant differences for the DN/MCP signal-intensity ratio should be expected.

CONCLUSIONS

T1-weighted SE and MPRAGE sequences should not be used interchangeably for qualitative or quantitative T1 signal-intensity analysis of the DN in patients who undergo several contrast-enhanced MR imaging studies because they are fundamentally different sequences, despite their similar appearance. Both sequences generate similar performance in quantitative analysis on an individual basis. Baseline and final examination ratios should be evaluated by using the same sequence across time, and differences in ratios between the baseline and final examination should be evaluated instead of ratio signal intensity at specific time points. Qualitative analysis is better performed with the MPRAGE sequence, reflecting its intrinsic higher gray–white matter contrast. This sequence seems to be a promising simple screening tool to be used in clinical practice for evaluating patients with multiple administrations of GBCA and may offer advantages over SE sequences for research purposes.

REFERENCES

1. Kanda T, Ishii K, Kawaguchi H, et al. **High signal intensity in the dentate nucleus and globus pallidus on unenhanced T1-weighted MR images: relationship with increasing cumulative dose of a gadolinium-based contrast material.** *Radiology* 2014;270:834–41 CrossRef Medline
2. Errante Y, Cirimele V, Mallio CA, et al. **Progressive increase of T1 signal intensity of the dentate nucleus on unenhanced magnetic resonance images is associated with cumulative doses of intravenously administered gadodiamide in patients with normal renal function, suggesting dechelation.** *Invest Radiol* 2014;49:685–90 CrossRef Medline
3. Quattrocchi CC, Mallio CA, Errante Y, et al. **Gadodiamide and dentate nucleus T1 hyperintensity in patients with meningioma evaluated by multiple follow-up contrast-enhanced magnetic resonance examinations with no systemic interval therapy.** *Invest Radiol* 2015; 50:470–72 CrossRef Medline
4. Ramalho J, Castillo M, AlObaidy M, et al. **High signal intensity in globus pallidus and dentate nucleus on unenhanced T1-weighted MR images: evaluation of two linear gadolinium-based contrast agents.** *Radiology* 2015;276:836–44 CrossRef Medline
5. Kanda T, Osawa M, Oba H, et al. **High signal intensity in dentate nucleus on unenhanced T1-weighted MR images: association with linear versus macrocyclic gadolinium chelate administration.** *Radiology* 2015;275:803–09 CrossRef Medline
6. Radbruch A, Weberling LD, Kieslich PJ, et al. **Gadolinium retention in the dentate nucleus and globus pallidus is dependent on the class of contrast agent.** *Radiology* 2015;275:783–91 CrossRef Medline
7. Stojanov DA, Aracki-Trenkic A, Vojinovic S, et al. **Increasing signal intensity within the dentate nucleus and globus pallidus on unenhanced T1W magnetic resonance images in patients with relapsing-remitting multiple sclerosis: correlation with cumulative dose of a macrocyclic gadolinium-based contrast agent, gadobutrol.** *Eur Radiol* 2016;26:807–15 CrossRef Medline
8. Adin ME, Kleinberg L, Vaidya D, et al. **Hyperintense dentate nuclei on T1-weighted MRI: relation to repeat gadolinium administration.** *AJNR Am J Neuroradiol* 2015;36:1859–65 CrossRef Medline
9. McDonald RJ, McDonald JS, Kallmes DF, et al. **Intracranial gadolinium deposition after contrast-enhanced MR imaging.** *Radiology* 2015;275:772–82 CrossRef Medline
10. Kanda T, Fukusato T, Matsuda M, et al. **Gadolinium-based contrast agent accumulates in the brain even in subjects without severe renal dysfunction: evaluation of autopsy brain specimens with inductively coupled plasma mass spectroscopy.** *Radiology* 2015;276: 228–32 CrossRef Medline
11. Robert P, Lehericy S, Grand S, et al. **T1-Weighted hypersignal in the deep cerebellar nuclei after repeated administrations of gadolinium-based contrast agents in healthy rats: difference between linear and macrocyclic agents.** *Invest Radiol* 2015;50:473–80 CrossRef Medline
12. Weberling LD, Kieslich PJ, Kickingereeder P, et al. **Increased signal intensity in the dentate nucleus on unenhanced T1-weighted images after gadobenate dimeglumine administration.** *Invest Radiol* 2015;50:743–48 CrossRef Medline
13. Kanda T, Oba H, Toyoda K, et al. **Recent advances in understanding gadolinium retention in the brain.** *AJNR Am J Neuroradiol* 2016;37: E1–2 CrossRef Medline
14. Kasahara S, Miki Y, Kanagaki M, et al. **Hyperintense dentate nucleus on unenhanced T1-weighted MR images is associated with a history of brain irradiation.** *Radiology* 2011;258:222–28 CrossRef Medline
15. Roccatagliata L, Vuolo L, Bonzano L, et al. **Multiple sclerosis: hyperintense dentate nucleus on unenhanced T1-weighted MR images is associated with the secondary progressive subtype.** *Radiology* 2009; 251:503–10 CrossRef Medline
16. R Core Team. R: A Language and Environment for Statistical Computing. R Foundation for Statistical Computing (2015). Vienna, Austria. <https://www.R-project.org/>. Accessed August 2015
17. Lin LI. **A concordance correlation coefficient to evaluate reproducibility.** *Biometrics* 1989;45:255–68 CrossRef Medline
18. Wenz F, Hess T, Knopp MV, et al. **3D MPRAGE evaluation of lesions in the posterior cranial fossa.** *Magn Reson Imaging* 1994;12:553–58 CrossRef Medline
19. Reichert M, Morelli JN, Runge VM, et al. **Contrast-enhanced 3-dimensional SPACE versus MP-RAGE for the detection of brain metastases: considerations with a 32-channel head coil.** *Invest Radiol* 2013;48:55–60 CrossRef Medline
20. Fellner F, Holl K, Held P, et al. **A T1-weighted rapid three-dimensional gradient-echo technique (MP-RAGE) in preoperative MRI of intracranial tumours.** *Neuroradiology* 1996;38:199–206 CrossRef Medline
21. Radbruch A, Weberling LD, Kieslich PJ, et al. **High-signal intensity in the dentate nucleus and globus pallidus on unenhanced T1-weighted images: evaluation of the macrocyclic gadolinium-based contrast agent gadobutrol.** *Invest Radiol* 2015;50:805–10 CrossRef Medline

Characteristics of Diffusional Kurtosis in Chronic Ischemia of Adult Moyamoya Disease: Comparing Diffusional Kurtosis and Diffusion Tensor Imaging

K. Kazumata, K.K. Tha, H. Narita, Y.M. Ito, H. Shichinohe, M. Ito, H. Uchino, and T. Abumiya



ABSTRACT

BACKGROUND AND PURPOSE: Detecting microstructural changes due to chronic ischemia potentially enables early identification of patients at risk of cognitive impairment. In this study, diffusional kurtosis imaging and diffusion tensor imaging were used to investigate whether the former provides additional information regarding microstructural changes in the gray and white matter of adult patients with Moyamoya disease.

MATERIALS AND METHODS: MR imaging (diffusional kurtosis imaging and DTI) was performed in 23 adult patients with Moyamoya disease and 23 age-matched controls. Three parameters were extracted from diffusional kurtosis imaging (mean kurtosis, axial kurtosis, and radial kurtosis), and 4, from DTI (fractional anisotropy, radial diffusivity, mean diffusivity, and axial diffusivity). Voxelwise analysis for these parameters was performed in the normal-appearing brain parenchyma. The association of these parameters with neuropsychological performance was also evaluated.

RESULTS: Voxelwise analysis revealed the greatest differences in fractional anisotropy, followed, in order, by radial diffusivity, mean diffusivity, and mean kurtosis. In patients, diffusional kurtosis imaging parameters were decreased in the dorsal deep white matter such as the corona radiata and superior longitudinal fasciculus ($P < .01$), including areas without DTI abnormality. Superior longitudinal fasciculus fiber-crossing areas showed weak correlations between diffusional kurtosis imaging and DTI parameters compared with tissues with a single-fiber direction (eg, the corpus callosum). Diffusional kurtosis imaging parameters were associated with general intelligence and frontal lobe performance.

CONCLUSIONS: Although DTI revealed extensive white matter changes, diffusional kurtosis imaging additionally demonstrated microstructural changes in ischemia-prone deep white matter with abundant fiber crossings. Thus, diffusional kurtosis imaging may be a useful adjunct for detecting subtle chronic ischemic injuries.

ABBREVIATIONS: AD = axial diffusivity; AK = axial kurtosis; CPT = continuous performance task; DKI = diffusional kurtosis imaging; FA = fractional anisotropy; IQ = intelligence quotient; MK = mean kurtosis; MD = mean diffusivity; MMD = Moyamoya disease; RD = radial diffusivity; RK = radial kurtosis; RST = Reading Span Test; SLF = superior longitudinal fasciculus; TMT = Trail-Making Test

Moyamoya disease (MMD) is characterized by compensatory development of enlarged and weak basal perforating arteries (Moyamoya vessels) due to bilateral occlusive changes in the internal carotid system.¹ In addition to cerebral ischemia and intracranial hemorrhage, patients with MMD demonstrate neurocognitive issues, such as executive dysfunction, attention deficits,

and working-memory disturbances.^{2,3} Brain atrophy may explain cognitive impairment in the absence of infarction, but detection of these changes has been hampered by the limited sensitivity of conventional neuroimaging methods. Diffusion tensor imaging is useful for determining white matter integrity and providing parameters sensitive to changes in axons, myelin, and organelle structures.^{4,5} Indeed, DTI analysis has revealed a widespread decline in white matter integrity in the normal-appearing brain with MMD.³ Thus, DTI can detect

Received August 26, 2015; accepted after revision January 7, 2016.

From the Departments of Neurosurgery (K.K., H.S., M.I., H.U., T.A.), Radiobiology and Medical Engineering (K.K.T.), Psychiatry (H.N.), and Biostatistics (Y.M.I.), Hokkaido University Graduate School of Medicine, Sapporo, Japan

The authors have no personal or institutional financial interest in the drugs and imaging modalities described herein.

This study was supported by a grant from the Research Committee on Moyamoya Disease, sponsored by the Ministry of Health, Labor, and Welfare of Japan and the Creation of Innovation Centers for Advanced Interdisciplinary Research Areas Programs, Ministry of Education, Culture, Sports, Science, and Technology, Japan.

Please address correspondence to Ken Kazumata, MD, Department of Neurosurgery, Hokkaido University Graduate School of Medicine, North 15 West 7, Kita, Sapporo 060-8638, Japan; e-mail: kazumata@med.hokudai.ac.jp

Indicates open access to non-subscribers at www.ajnr.org

Indicates article with supplemental on-line appendix and table.

<http://dx.doi.org/10.3174/ajnr.A4728>

Table 1: Characteristics of the study participants

	Control	Moyamoya Disease	P Value
No. of subjects	23	23	—
Age (mean) (range) (yr)	39.0 + 8.1 (25–56)	40.9 + 9.5 (21–58)	.48
Sex (F/M) (No. of subjects)	13:10	17:6	.35
Risk factor (DM, HT, HL) (No. of subjects)	0	5	.049
Symptoms (No. of subjects)			
Asymptomatic	—	13	
TIA	—	10	

Note:—DM indicates diabetes mellitus; HT, hypertension; HL, hyperlipidemia.

early-stage ischemic injury, which potentially predicts future cognitive outcomes. However, DTI is constrained by technical insufficiencies: It is based on the assumption that water molecules diffuse freely and that diffusion can be characterized by a Gaussian distribution.⁵

In addition, the tensor model is based on the observation that in many tissues, water diffusion is anisotropic (ie, the diffusion is more liberal in some directions and more restricted in others). This anisotropic diffusion can be geometrically depicted as an ellipsoid, described by eigenvectors and eigenvalues. This model performs well in regions where fibers are aligned along a single axis. However, it fails in regions with several fiber populations aligned along intersecting axes because it cannot simultaneously map several diffusion maxima.⁶ Furthermore, because hypoxic-ischemic injury induces neurodegeneration and regression of dendrite arborization in gray matter, the diffusion properties of gray matter may also reveal the early stages of ischemic injury.^{7,8} Nevertheless, analyzing isotropic or near-isotropic tissue such as gray matter by DTI may not be valid because its major parameter, fractional anisotropy (FA), reflects structure only if it is spatially oriented.⁶ A more recent method called diffusional kurtosis imaging (DKI) quantifies the deviation of water molecule diffusion from the Gaussian distribution without assuming any specific diffusion model.^{6,9} Its parameters are thought to represent the complexity of tissue microstructure.⁶ Previous studies have suggested that DKI is sufficiently sensitive to detect age-related alterations in white matter microstructure.^{10,11} Furthermore, measurements of diffusion anisotropy by DKI can reveal sex-related and pathologic changes in gray matter.^{12,13} Thus, using DKI to evaluate the diffusion properties of gray matter and white matter in patients with MMD may be useful for detecting subtle microstructural changes due to ischemia.

Diffusional kurtosis has been investigated to explore tissue reversibility in acute cerebral infarction.^{14–16} However, there is a paucity of information regarding the microstructural properties measured by DKI in chronic ischemia in living humans. To expand on our prior DTI study, we investigated whether adults with MMD and no overt cerebral infarctions have altered diffusional kurtosis in the entire cerebrum. An exploratory voxel-based whole-brain analysis was performed to map regional DKI parameters and to compare DKI and DTI parameters. We also explored correlations of diffusion parameters with measures of neurocognitive impairment in an ROI analysis.

MATERIALS AND METHODS

Participants

This prospective study was approved by the Research Ethics Committee of Hokkaido University Hospital, and written informed consent was obtained from all participants. Participants in the present study are the same as those of our previous study analyzing the relationship between DTI parameters and neuropsychological test scores.³ The selection

period was 25 months (April 2012 through April 2014). Twenty-three patients (6 men and 17 women; 21–58 years of age; mean age, 40.9 ± 9.5 years) were enrolled. The control group also consisted of 23 subjects (10 men and 13 women; 25–56 years of age; mean age, 39.0 ± 8.1 years). A brief summary of patient characteristics is provided in Table 1.

Neuropsychological Assessment

Neuropsychological examinations consisted of the Wechsler Adult Intelligent Scale-III, Wisconsin Card Sorting Test, Trail-Making Test (TMT; parts A and B), continuous performance task (CPT), Stroop test, and Reading Span Test (RST). The details of neuropsychological examinations and the results are provided in the On-line Appendix.³

MR Image Acquisition

MR imaging was performed with a 3T scanner (Achieva TX; Philips Healthcare, Best, the Netherlands). 3D magnetization-prepared rapid acquisition of gradient echo T1-weighted imaging and axial single-shot spin-echo echo-planar DKI were acquired to evaluate subtle gray and white matter alterations, respectively. The scan parameters for DKI were as follows: TR = 5051 ms, TE = 85 ms, flip angle = 90°, FOV = 224 × 224 mm², matrix size = 128 × 128, b-values = 0, 1000, and 2000 s/mm², number of diffusion gradient directions = 32, section thickness = 3 mm, intersection gap = 0 mm, number of sections = 43, and NEX = 1. The 3D-MPRAGE imaging was performed with TR = 6.8 ms, TE = 3.1 ms, flip angle = 8°, and TI = 1100 ms.

Image Processing

Registration between the echo-planar images with no diffusion weighting ($b=0$ s/mm²) and the corresponding DKI data and correction for eddy current distortion were performed at the MR imaging operator console. The DKI data were processed by using Matlab R2012b (MathWorks, Natick, Massachusetts) and Diffusional Kurtosis Estimator (Version 2.5.1; <http://nitrc.org/projects/dke>).¹⁷ Seven DKI and DTI parameters were extracted from the Diffusional Kurtosis Estimator: mean kurtosis (MK), radial kurtosis (RK), axial kurtosis (AK), FA, mean diffusivity (MD), radial diffusivity (RD), and axial diffusivity (AD). The DTI parameters (FA, MD, RD, and AD) were calculated from a portion of the DKI data by using a monoexponential model that assumes a Gaussian probability diffusion function by using data from b-values of 0 and 1000 s/mm².¹⁷

Following calculation of DKI and DTI parameters, the $b=0$ echo-planar images were warped to the standardized T2 template

of SPM8 (<http://www.fil.ion.ucl.ac.uk/spm/software/spm12>). This transformation matrix was applied to the DKI/DTI parameter map of each patient. The warped DKI/DTI maps were averaged and smoothed with a 6-mm full width at half maximum Gaussian kernel to form customized DKI/DTI templates. Native DKI/DTI maps of all patients and control subjects were then warped to the customized, respective DKI/DTI templates. Individual maps were then smoothed with a 6-mm full width at half maximum Gaussian kernel. The warped and smoothed DKI/DTI maps were used for group comparisons between the controls and patients with MMD. To investigate the pathology underlying DKI parameters and the influence of fiber crossings on DTI parameters, we investigated the correlations of DKI and DTI parameters in white matter tracts consisting of either a single fiber direction or crossing fibers (ie, multiple directions).¹⁸ The ROIs were placed on the genu of the corpus callosum (ie, a structure with a single fiber direction) and deep white matter tracts corresponding to the bilateral superior longitudinal fasciculus (SLF) (multiple fiber directions) by using the JHU white matter atlas available in FSL (<http://fsl.fmrib.ox.ac.uk/fsl/fslwiki/>).¹⁹

Data Analysis

Whole-brain diffusion parameters were compared voxel by voxel between the controls and patients with MMD by using SPM8, which implemented the general linear model. We used the 2-sample *t* test model, and age was considered a covariate. An explicit mask generated by averaging the normalized CSF space of all participants was applied. To explore group differences across both gray matter and white matter, we set statistical significance at $P < .01$ without correction for family-wise error and clusters of 50 voxels or more. The number of voxels demonstrating a significant difference between the controls and patients with MMD was extracted. The Pearson product-moment correlation coefficient was calculated to investigate the correlation between the DKI and DTI parameters by using DKI/DTI values extracted from the ROI analysis.

We also investigated whether the significant changes in DKI/DTI parameters were associated with neuropsychological examination scores. A threshold *T* value of 2.42, corresponding to $P < .01$ without correction for family-wise error, was applied to the *T* contrast map of DKI/DTI parameters obtained by comparing controls and patients, and binary mask images containing voxels above the threshold value were generated. The DKI/DTI parameter values included in the masks were extracted from DKI/DTI of the patients with MMD. The Pearson product-moment correlation coefficients were used for analyses involving the Wechsler Adult Intelligent Scale-III, TMT (parts A and B and the difference in score between TMT-A and TMT-B [B-A]). Patients were further subgrouped into 2, according to their performance scores, error numbers, and reaction time on the Wisconsin Card Sorting Test, Stroop test, CPT, and RST; and the DKI/DTI parameters were compared between these 2 subgroups by using *t* tests (Online Appendix). For all correlations and comparisons, a *P* value $< .05$ was considered statistically significant to explore the possible relationship between neuropsychological scores and diffusion parameters.

RESULTS

Spatial Distribution of DTI/DKI Differences on Voxel-Based Analysis

Areas with decreased MK included the right frontal white matter, bilateral thalami, portions of the occipital white matter, corona radiata, corpus callosum, and portions of frontal and parietal white matter corresponding to the posterior segment of the superior longitudinal fasciculus (Fig 1). The decrease in FA was most extensive within the white matter (161,625 voxels), with its decrease amounting to 12,833 voxels (7.9%) (Fig 2). Significant MK, RK, and AK decreases were observed in 6180 voxels (3.8%), 3828 voxels (2.4%), and 3043 voxels (1.9%), respectively. In contrast, 9028 voxels (5.6%) showed a significant increase in MD; 10,062 (6.2%), in RD; and 548 (0.3%), in AD compared with controls. Figure 1 shows DKI/DTI overlap maps, with MK/RK/AK/FA decreases and MD/RD increases. Areas with FA decrease were more extensive than those with MK decrease; however, the posterior segment of the SLF showed a decrease in only MK/RK. The increase in MD/RD was remarkable in the corona radiata; however, the posterior segment of the SLF showed a decrease in MK/RK without an increase in MD/RD. Decreased AK was observed without changes in AD for the bilateral thalami, corona radiata, and portions of the temporo-occipital white matter. There was no cortical gray matter with altered DKI/DTI parameters in patients.

Correlation of DTI and DKI Parameters

Correlations between DKI and DTI parameters were examined in both the genu of the corpus callosum and the bilateral SLF (Table 2). In the corpus callosum of both controls and patients with MMD, MK correlated positively with FA ($r > 0.78$, $P < .01$), while inverse correlations with MK were found for MD/RD/AD ($r < -0.82$, $P < .001$). In the corpus callosum, RK correlated inversely with RD ($r < -0.84$, $P < .001$), and AK inversely correlated with AD of the corpus callosum ($r < -0.64$, $P < .001$). A significant correlation between MK and FA was observed in the left SLF of controls, but this was to a lesser degree compared with that in the corpus callosum. No correlation was found between MK and FA in the right SLF of controls. In both controls and patients, correlations between MK and MD/RD/AD were found in the right and left SLFs, albeit to a lesser degree than corpus callosum correlations. The results of correlation between DKI and DTI parameter values are summarized in Table 2.

Association of DKI/DTI Parameters with Neuropsychological Performance Tests

The DKI parameter (AK) showed significant correlations with motor intelligence quotient (IQ), full-scale IQ, perceptual organization, and processing speed evaluated on the Wechsler Adult Intelligent Scale-III (Fig 3A, $r > 0.42$, $P < .05$). Both DKI (MK) and DTI (FA, MD, and RD) parameters showed significant correlations with the TMT part B (Fig 3B, $r > 0.44$, $P < .05$). The Stroop test performance showed moderate positive correlations with MK, RK, and FA and negative correlations with MD, RD, and AD ($P < .05$). RST was associated with MK and AK ($P < .05$). The correlations between diffusion parameters and neuropsychological scores (Wisconsin Card Sorting Test, Stroop Test, CPT, and RST) are shown in Table 3.

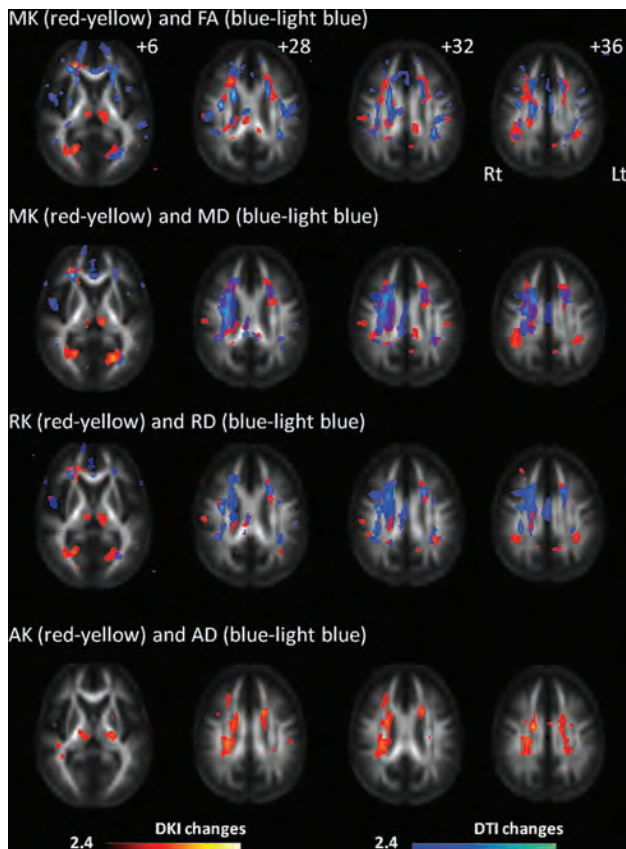


FIG 1. Changes in diffusional kurtosis imaging and diffusion tensor imaging parameters in Moyamoya disease shown in maps of 3 diffusional kurtosis parameters (mean kurtosis, radial kurtosis, and axial kurtosis) and 4 diffusion tensor parameters (fractional anisotropy, mean diffusivity, radial diffusivity, and axial diffusivity). Areas with significant changes in a combination of DKI/DTI parameters are as follows: decreased MK (red-yellow)/decreased FA (blue-light blue), decreased MK (red-yellow)/increased MD (blue-light blue), decreased RK (red-yellow)/increased RD (blue-light blue), and decreased AK (red-yellow)/increased AD (blue-light blue). Values from statistical parametric mapping analysis are projected onto axial sections of the average brain space of FA ($z = 12, 28, 32, 36$ mm). MK decrease is observed in the thalamus, a portion of the genu and body of the corpus callosum, corona radiata, frontoparietal subcortical white matter, and superior longitudinal fasciculus. RK decrease is observed in part of the frontoparietal subcortical white matter, thalamus, corona radiata, and occipital white matter. AK decrease is observed in the thalamus, temporo-occipital white matter, part of the SLF, and corona radiata. The radiologic convention is adopted, with the left side of the brain on the right side of axial panels. The color scale represents T values, with colored regions exceeding the significance threshold of $P < .01$ ($T = 2.42$) with a minimum cluster size of 50 voxels. Rt indicates right; Lt, left.

DISCUSSION

We explored the added benefit of diffusional kurtosis measurements in the assessment of ischemic burden due to chronic ischemia in adult MMD. This study confirmed our prior finding that chronic ischemia in MMD preferentially affects the microstructure of normal-appearing white matter.³ Detecting microstructural changes due to chronic ischemia potentially enables early identification of patients at risk of cognitive impairment.^{3,20} However, detecting microstructural changes has been hampered by the limited sensitivity of DTI in fiber-crossing areas.⁷ In this study, DKI demonstrated microstructural changes, predominantly in the dorsal part of the deep white matter, where conventional MR imaging frequently demonstrates ischemic lesions.²¹ The significant changes in DKI parameters were associated with neuropsychological scores reflecting general intelligence, executive function, attention, and working memory. Thus, DKI is considered a useful adjunct to conventional DTI, particularly for its ability to detect nascent microstructural changes in areas with abundant fiber crossings.

In this study, we demonstrated that DTI showed widespread regions with alterations in FA, MD, and RD. The finding is consistent with previous studies, in which DTI showed more extensive white matter changes compared with DKI parameters. Other studies have demonstrated superior sensitivity of DKI to detect white matter changes compared with DTI.^{11,22,23} DKI showed significant decreases in frontoparietal subcortical structures and deep white matter. A decrease in DKI parameters, a shift of diffusional kurtosis toward free water diffusion, has commonly been interpreted as a reduction in tissue complexity.²⁴ Considering the location of the DKI alterations, a reduction in complexity is thought to reflect microstructural changes in myelin and/or axonal attenuation. In the corona radiata, DTI (MD/RD) demonstrated more significant changes compared with DKI (MK/RK). Deep white matter tracts are vulnerable to chronic ischemia because they are located in the terminal field of the blood supply. Myelin degeneration or increased periventricular extracellular fluid may increase RD, while tissue complexity in a radial direction may be maintained, in some part, by glial proliferation.²⁵ In a previous study, a trend toward decreased AD was found via analysis of tract-specific spatial statistics,³ whereas the voxel-based analysis of the present study did not show definitive AD changes in white matter. AD decreases in axonal fragmentation; however, axonal degeneration or reduced axonal attenuation can increase AD. In contrast with AD, AK showed significant changes in the

Table 2: Correlation between DKI and DTI parameters^a

	Corpus Callosum				Rt. SLF				Lt. SLF			
	CNT		MMD		CNT		MMD		CNT		MMD	
	<i>r</i>	<i>P</i>	<i>r</i>	<i>P</i>	<i>r</i>	<i>P</i>	<i>r</i>	<i>P</i>	<i>r</i>	<i>P</i>	<i>r</i>	<i>P</i>
MK vs FA	0.78	.000	0.80	.000	0.08	.715	0.60	.002	0.42	.047	0.47	.022
MK vs MD	-0.90	.000	-0.86	.000	-0.60	.002	-0.68	.000	-0.41	.049	-0.49	.017
MK vs RD	-0.90	.000	-0.87	.000	-0.54	.008	-0.73	.000	-0.49	.018	-0.55	.006
MK vs AD	-0.87	.000	-0.82	.000	-0.50	.014	-0.46	.028	-0.19	.386	-0.35	.101
RK and RD	-0.88	.000	-0.84	.000	-0.72	.000	-0.56	.005	-0.47	.025	-0.38	.072
AK and AD	-0.75	.000	-0.64	.000	-0.44	.036	-0.61	.001	-0.47	.025	-0.68	.000

Note:—Rt. indicates right; Lt., left; CNT, controls; *r*, Pearson product-moment correlation coefficient.

^aAll *P* values, except .715, .386, .101, and .072, indicate significant correlation between DKI and DTI parameters.

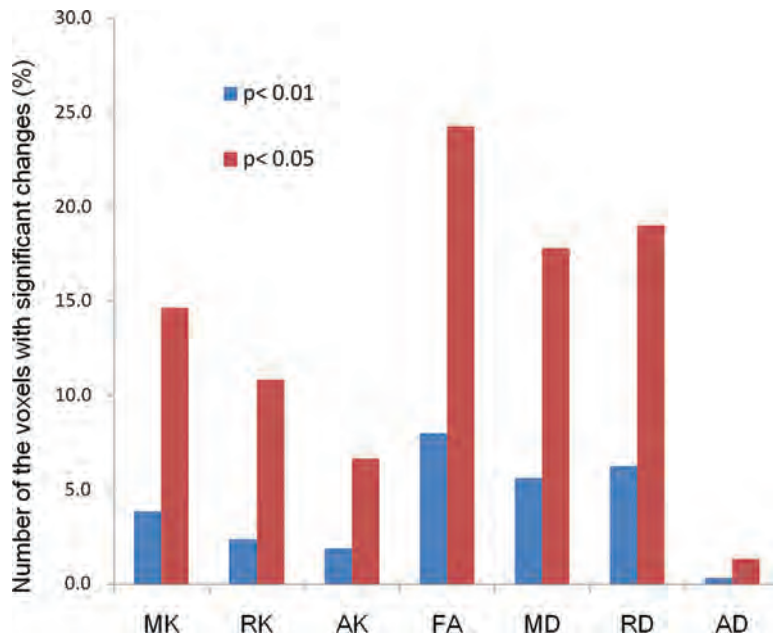


FIG 2. The bar graph indicates the number of the voxels with significant changes relative to the total number of white matter voxels in statistical parametric mapping comparing controls and patients with Moyamoya disease. Bar heights indicate decreases in MK/RK/AK/FA and increases in MD/RD/AD for 2 levels of threshold applied in group comparisons (blue, $P < .01$; red, $P < .05$, respectively).

corona radiata in the voxel-based analysis. Thus, alterations in AD would be marginal at best in patients, while tissue complexity parallel to the principal diffusion direction could be decreased in the corona radiata of patients. Weak correlations between FA and MK in the SLF of controls could be attributed to the crossing/kissing of white matter fibers. The SLF contains abundant crossing fibers projecting from the corona radiata and corpus callosum.¹⁸ Several fiber populations aligned along intersecting axes in 1 voxel would diminish anisotropy.²⁶

The DKI parameters in patients showed moderate positive correlations with impaired general intelligence and frontal lobe dysfunction. These results are consistent with previous reports showing a relationship between cognitive performance and white matter fiber tracts integrating parietofrontal cortical areas.²⁷⁻²⁹ In MMD, performance IQ is preferentially affected compared with verbal IQ.¹ In the present study, AK was significantly correlated with neuropsychological performance on tests evaluating executive function and working memory (motor IQ, perceptual organization, and processing speed), while no correlation was found with verbal IQ. In an experimental animal model of chronic white matter ischemia, damage to myelin preceded axonal damage, suggesting that the change in myelin is the primary pathologic event.³⁰ Our observation of a stronger correlation between AK, rather than AD, and general intellectual ability measured by the Wechsler Adult Intelligent Scale-III may imply that a reduction in axonal density and/or axonal degeneration, a more advanced stage of chronic ischemic injury, is better described by AK than AD. Previous investigations by using DTI and probabilistic tractography have shown correlations between neuropsychological examinations and the FA of subcortical white matter. Consistent with previous studies, we observed correlations between DTI parameters and the scores of neuropsychological tests evaluating

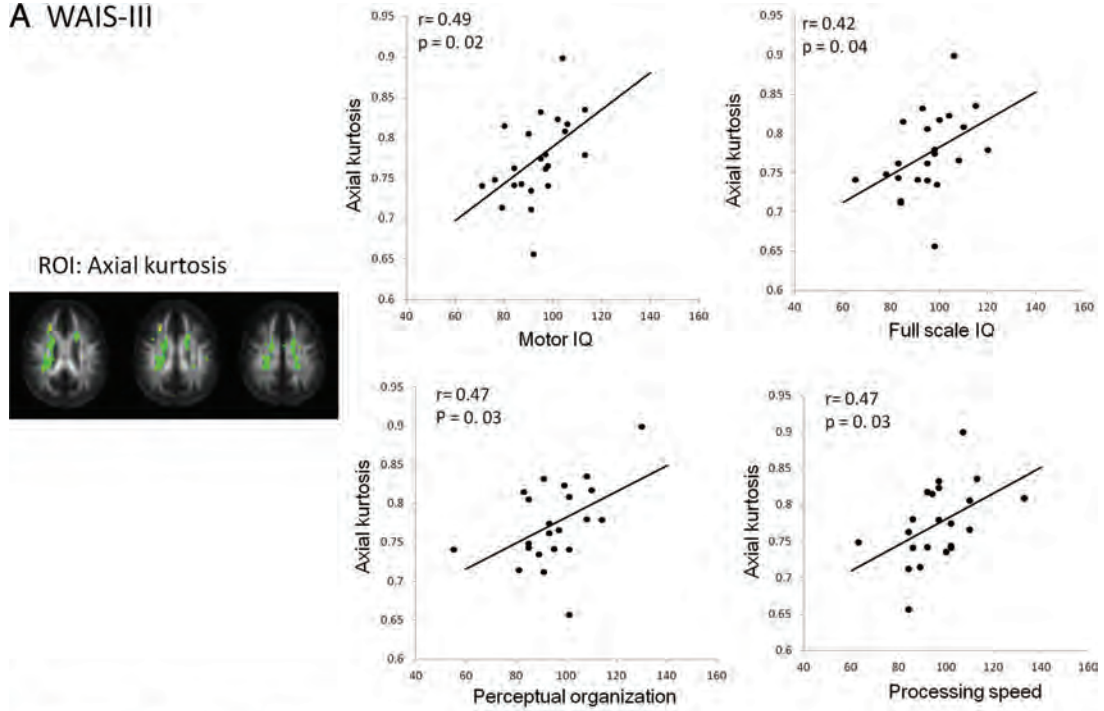
frontal lobe function in the present study. A significant correlation of FA/MD/RD with scores on the Trail-Making Test suggests that demyelination alone could affect part of the frontal lobe functions.

Transient ischemic attack followed by hyperventilation is a characteristic symptom of childhood MMD, and syncope attacks are occasionally observed in both children and adults with MMD.¹ The spatial characteristics of nascent brain injury are important for understanding frontal-dominant neurocognitive dysfunction in adult MMD. Pyramidal neocortical neurons (layers 3, 5, and 6) in the prefrontal cortex are known to be highly vulnerable to hypoxic-ischemic insults.^{31,32} These hypoxic-ischemic insults can damage the brain and potentially induce neuronal death or regression of dendritic structure.⁸ We speculate that microstructural alteration precedes gross volumetric reductions in gray matter. Previous study has revealed gray matter atrophy in the posterior cingulate cortex, suggesting that more widespread gray matter changes might be observed in diffusion parameters, particularly in the frontal lobe.³ DKI could reveal early microstructural changes less constrained by partial volume effects.³³ Nevertheless, despite discrete white matter damage, no substantial changes in diffusion parameters were found in the cortical gray matter in MMD. Pathologic tissue changes such as glial proliferation may underlie the lack of significant changes in the diffusion parameters of the cortices. A new diffusion MR imaging technique, including neurite orientation dispersion and density imaging, may detect subtle microstructural changes in the cortex and is potentially sensitive to initial ischemic changes before the overt volumetric reductions.^{34,35}

The present study revealed microstructural change in the thalamus, a finding that has never been emphasized with regard to cognitive function in MMD. The mediodorsal thalamus connects to the prefrontal cortex. This is potentially important because innervation of the thalamoprefrontal circuit could modulate prefrontal neural circuits, which are associated with cognitive as well as affective performance.³⁶

There are several limitations to this study. The statistical power to detect group differences in DKI parameters is significantly influenced by the number of subjects in a study.³⁷ Therefore, the spatial characteristics of the DKI/DTI alterations found in this study may not represent the topography of ischemic burden in adult MMD.³⁷ We extracted DKI/DTI values from the contrast T maps generated from group comparisons between controls and patients to explore the relationship between abnormal diffusion parameters in patients and neuropsychological test performance. Although we found an association with neuropsychological test scores, voxel-based correlation analysis would per-

A WAIS-III



B Trail making test (B)

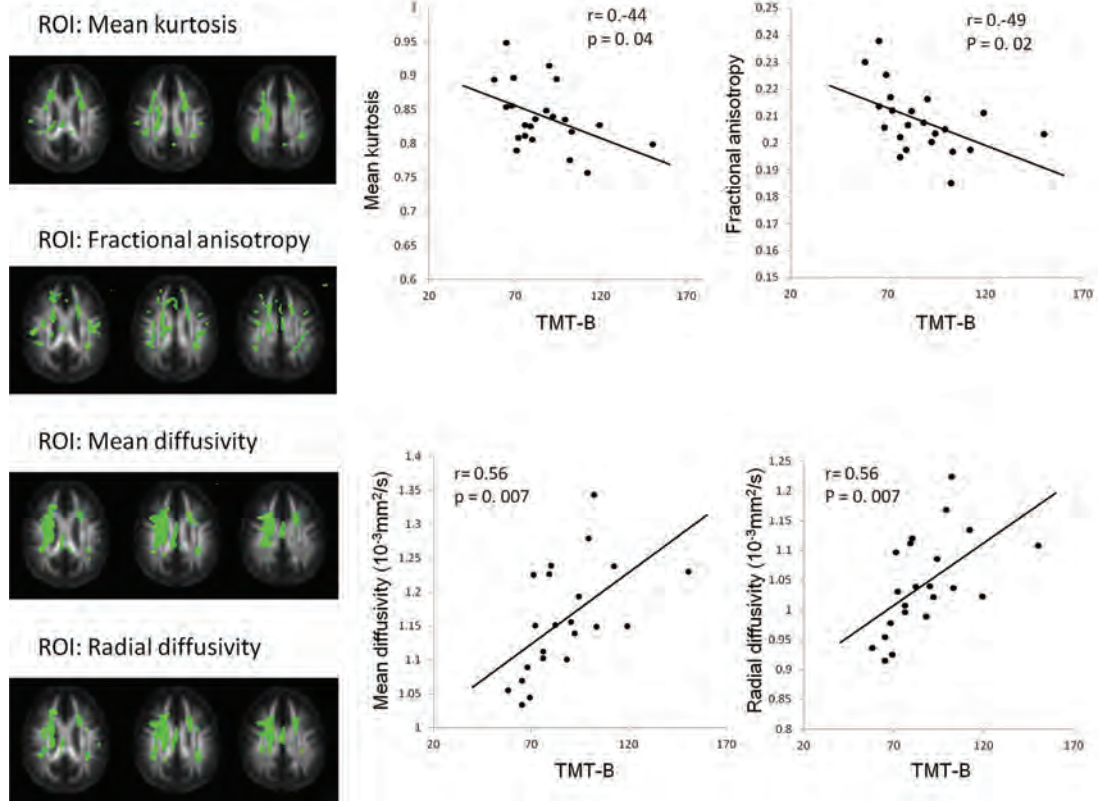


FIG 3. Scatterplots indicating a significant correlation between neuropsychological test performance and diffusion parameters. Pearson moment-product correlation coefficient r and P values are demonstrated in each scatterplot. ROIs (green) for each parameter (AK, MK, FA, MD, and RD) are demonstrated with FA template images generated from 23 controls and 23 patients. A, Performance scores evaluated on the Wechsler Adult Intelligent Scale-III are significantly associated with axial kurtosis. Axial kurtosis is positively correlated with full-scale IQ ($r = 0.42$, $P = .04$) and subscores such as motor IQ ($r = 0.49$, $P = .02$), perceptual organization ($r = 0.47$, $P = .03$), and processing speed ($r = 0.47$, $P = .03$). B, Trail-Making Test, part B is inversely correlated with DKI/DTI parameters (MK; $r = -0.44$, $P = .04$; and FA; $r = -0.49$, $P = .02$) and positively correlated with DTI parameters (MD; $r = 0.56$, $P = .007$; and RD; $r = 0.56$, $P = .007$).

Table 3: Correlations of diffusion parameters with neuropsychological examinations^a

	WCST	Stroop	CPT	RST
MK	—	.004 ^b	—	.048 ^b
RK	—	.007 ^b	—	—
AK	—	.045 ^c	—	.036 ^c
FA	—	.024 ^b	—	—
MD	—	.012 ^b	—	—
RD	—	.014 ^b	—	—
AD	—	.031 ^c	—	—

Note:—WCST indicates Wisconsin Card Sorting Test, Stroop; Stroop test.

^aData are *P* values. Correlations of diffusional kurtosis imaging and diffusion tensor imaging parameters with neuropsychological examinations were evaluated in patients with MMD. Three diffusional kurtosis parameters (MK, RK, and AK) and 4 diffusion tensor parameters (FA, MD, RD, and AD) were analyzed. Diffusion parameters and locations that demonstrated significant relationships with clinical variables follow.

^bTwo-tailed *t* test.

^cOne-tailed *t* test.

mit an objective evaluation of the neural substrates associated with cognitive impairment. Finally, we used a combination of *b*-values of 0 and 1000 s/mm² for DTI. DTI parameters are reported as dependent on *b*-values. For DKI, the *b*-values of 0, 1000, and 2000 s/mm² used in the present study would be feasible for practical clinical applications. Nevertheless, a different combination of *b*-values and methods for parameter estimation could alter the relationship between DKI and DTI with regard to sensitivity and specificity, which requires further investigation.²¹

CONCLUSIONS

The results of the present study suggest an additional value of DKI as an adjunct to DTI. DKI parameters can become useful neuroimaging markers to track ischemic burden in adult MMD.

Disclosures: Ken Kazumata—*RELATED: Grant:* This study was supported by a grant from the Research Committee on Moyamoya Disease, sponsored by the Ministry of Health, Labor, and Welfare of Japan.* Khin K. Tha—*RELATED: Grant:* This work was supported (in part) by the Creation of Innovation Centers for Advanced Interdisciplinary Research Areas Program, Ministry of Education, Culture, Sports, Science, and Technology, Japan.* Masaki Ito—*RELATED: Grant:* Research Committee on Moyamoya Disease, sponsored by the Ministry of Health, Labor, and Welfare of Japan*; *UNRELATED: Grants/Grants Pending:* Masaki Ito was funded by a fellowship (grant) ¥2,000,000 J (approximately US \$18,000) for 1 year from SENSHIN Medical Research Foundation donated by the Mitsubishi Corporation, Japan. Funding began April 1, 2015. Takeo Abumiya—*RELATED: Grant:* grant from the Research Committee on Moyamoya Disease, sponsored by the Ministry of Health, Labor, and Welfare of Japan.* *Money paid to the institution.

REFERENCES

1. Kuroda S, Houkin K. **Moyamoya disease: current concepts and future perspectives.** *Lancet Neurol* 2008;7:1056–66 [CrossRef Medline](#)
2. Karzmark P, Zeifert PD, Bell-Stephens TE, et al. **Neurocognitive impairment in adults with Moyamoya disease without stroke.** *Neurosurgery* 2012;70:634–38 [CrossRef Medline](#)
3. Kazumata K, Tha KK, Narita H, et al. **Chronic ischemia alters brain microstructural integrity and cognitive performance in adult Moyamoya disease.** *Stroke* 2015;46:354–60 [CrossRef Medline](#)
4. Tha KK, Terae S, Nakagawa S, et al. **Impaired integrity of the brain parenchyma in non-geriatric patients with major depressive disorder revealed by diffusion tensor imaging.** *Psychiatry Res* 2013;212:208–15 [CrossRef Medline](#)
5. Bassler PJ, Mattiello J, LeBihan D. **MR diffusion tensor spectroscopy and imaging.** *Biophys J* 1994;66:259–67 [Medline](#)
6. Jensen JH, Helpert JA, Ramani A, et al. **Diffusional kurtosis imaging: the quantification of non-gaussian water diffusion by means of magnetic resonance imaging.** *Magnetic Reson Med* 2005;53:1432–40 [Medline](#)
7. Back SA. **Cerebral white and gray matter injury in newborns: new insights into pathophysiology and management.** *Clin Perinatal* 2014;41:1–24 [CrossRef Medline](#)
8. Zhang S, Boyd J, Delaney K, et al. **Rapid reversible changes in dendritic spine structure in vivo gated by the degree of ischemia.** *J Neurosci* 2005;25:5333–38 [Medline](#)
9. Fieremans E, Jensen JH, Helpert JA. **White matter characterization with diffusional kurtosis imaging.** *Neuroimage* 2011;58:177–88 [CrossRef Medline](#)
10. Li X, Gao J, Hou X, et al. **Diffusion kurtosis imaging with tract-based spatial statistics reveals white matter alterations in preschool children.** *Conf Proc IEEE Eng Med Biol Soc* 2012;2012:2298–301 [CrossRef Medline](#)
11. Coutu JP, Chen JJ, Rosas HD, et al. **Non-Gaussian water diffusion in aging white matter.** *Neurobiol Aging* 2014;35:1412–21 [CrossRef Medline](#)
12. Gong NJ, Wong CS, Chan CC, et al. **Aging in deep gray matter and white matter revealed by diffusional kurtosis imaging.** *Neurobiol Aging* 2014;35:2203–16 [CrossRef Medline](#)
13. Caverzasi E, Henry RG, Vitali P, et al. **Application of quantitative DTI metrics in sporadic CJD.** *Neuroimage Clin* 2014;4:426–35 [CrossRef Medline](#)
14. Weber RA, Hui ES, Jensen JH, et al. **Diffusional kurtosis and diffusion tensor imaging reveal different time-sensitive stroke-induced microstructural changes.** *Stroke* 2015;46:545–50 [CrossRef Medline](#)
15. Grinberg F, Farrher E, Ciobanu L, et al. **Non-Gaussian diffusion imaging for enhanced contrast of brain tissue affected by ischemic stroke.** *PLoS One* 2014;9:e89225 [CrossRef Medline](#)
16. Umesh Rudrapatna S, Wieloch T, Beirup K, et al. **Can diffusion kurtosis imaging improve the sensitivity and specificity of detecting microstructural alterations in brain tissue chronically after experimental stroke? Comparisons with diffusion tensor imaging and histology.** *Neuroimage* 2014;97:363–73 [CrossRef Medline](#)
17. Tabesh A, Jensen JH, Ardekani BA, et al. **Estimation of tensors and tensor-derived measures in diffusional kurtosis imaging.** *Magn Reson Med* 2011;65:823–36 [CrossRef Medline](#)
18. Reijmer YD, Leemans A, Heringa SM, et al; Vascular Cognitive Impairment Study group. **Improved sensitivity to cerebral white matter abnormalities in Alzheimer's disease with spherical deconvolution based tractography.** *PLoS One* 2012;7:e44074 [CrossRef Medline](#)
19. Wakana S, Jiang H, Nagae-Poetscher LM, et al. **Fiber tract-based atlas of human white matter anatomy.** *Radiology* 2004;230:77–87 [Medline](#)
20. Cheng HL, Lin CJ, Soong BW, et al. **Impairments in cognitive function and brain connectivity in severe asymptomatic carotid stenosis.** *Stroke* 2012;43:2567–73 [Medline](#)
21. Schmidt R, Seiler S, Loitfelder M. **Longitudinal change of small-vesSEL disease-related brain abnormalities.** *J Cereb Blood Flow Metab* 2015 Apr 22. [Epub ahead of print] [CrossRef Medline](#)
22. Kamagata K, Tomiyama H, Hatano T, et al. **A preliminary diffusional kurtosis imaging study of Parkinson disease: comparison with conventional diffusion tensor imaging.** *Neuroradiology* 2014;56:251–58 [CrossRef Medline](#)
23. Fieremans E, Benitez A, Jensen JH, et al. **Novel white matter tract integrity metrics sensitive to Alzheimer disease progression.** *AJNR Am J Neuroradiol* 2013;34:2105–12 [CrossRef Medline](#)
24. Steven AJ, Zhuo J, Melhem ER. **Diffusion kurtosis imaging: an emerging technique for evaluating the microstructural environment of the brain.** *AJR Am J Roentgenol* 2014;202:W26–33 [CrossRef Medline](#)
25. Cechetti F, Pagnussat AS, Worm PV, et al. **Chronic brain hypoperfusion causes early glial activation and neuronal death, and subsequent long-term memory impairment.** *Brain Res Bull* 2012;87:109–16 [CrossRef Medline](#)

26. Jbabdi S, Behrens TE, Smith SM. **Crossing fibres in tract-based spatial statistics.** *Neuroimage* 2010;49:249–56 CrossRef Medline
27. Gläscher J, Rudrauf D, Colom R, et al. **Distributed neural system for general intelligence revealed by lesion mapping.** *Proc Natl Acad Sci U S A* 2010;107:4705–09 CrossRef Medline
28. Deary IJ, Weiss A, Batty GD. **Intelligence and personality as predictors of illness and death: how researchers in differential psychology and chronic disease epidemiology are collaborating to understand and address health inequalities.** *Psychol Sci Public Interest* 2010;11:53–79 CrossRef Medline
29. Barbey AK, Colom R, Solomon J, et al. **An integrative architecture for general intelligence and executive function revealed by lesion mapping.** *Brain* 2012;135:1154–64 CrossRef Medline
30. Kurumatani T, Kudo T, Ikura Y, et al. **White matter changes in the gerbil brain under chronic cerebral hypoperfusion.** *Stroke* 1998;29:1058–62 Medline
31. Lin CS, Polsky K, Nadler JV, et al. **Selective neocortical and thalamic cell death in the gerbil after transient ischemia.** *Neuroscience* 1990;35:289–99 Medline
32. Fukuda A, Muramatsu K, Okabe A, et al. **NMDA receptor-mediated differential laminar susceptibility to the intracellular Ca²⁺ accumulation induced by oxygen-glucose deprivation in rat neocortical slices.** *J Neurophysiol* 1998;79:430–38 Medline
33. Yang AW, Jensen JH, Hu CC, et al. **Effect of cerebral spinal fluid suppression for diffusional kurtosis imaging.** *J Magn Reson Imaging* 2013;37:365–71 CrossRef Medline
34. Jelescu IO, Veraart J, Adisetiyo V, et al. **One diffusion acquisition and different white matter models: how does microstructure change in human early development based on WMTI and NODDI?** *Neuroimage* 2015;107:242–56 CrossRef Medline
35. Zhang H, Schneider T, Wheeler-Kingshott CA, et al. **NODDI: practical in vivo neurite orientation dispersion and density imaging of the human brain.** *Neuroimage* 2012;61:1000–16 CrossRef Medline
36. Ferguson BR, Gao WJ. **Development of thalamocortical connections between the mediodorsal thalamus and the prefrontal cortex and its implication in cognition.** *Front Hum Neurosci* 2014;8:1027 Medline
37. Szczepankiewicz F, Lätt J, Wirestam R, et al. **Variability in diffusion kurtosis imaging: impact on study design, statistical power and interpretation.** *Neuroimage* 2013;76:145–54 CrossRef Medline

Improved Leakage Correction for Single-Echo Dynamic Susceptibility Contrast Perfusion MRI Estimates of Relative Cerebral Blood Volume in High-Grade Gliomas by Accounting for Bidirectional Contrast Agent Exchange

K. Leu, J.L. Boxerman, T.F. Cloughesy, A. Lai, P.L. Nghiemphu, L.M. Liao, W.B. Pope, and B.M. Ellingson



ABSTRACT

BACKGROUND AND PURPOSE: Contrast agent extravasation through a disrupted blood-brain barrier potentiates inaccurate DSC MR imaging estimation of relative CBV. We explored whether incorporation of an interstitial washout rate in a leakage-correction model for single-echo, gradient-echo DSC MR imaging improves relative CBV estimates in high-grade gliomas.

MATERIALS AND METHODS: We modified the traditional model-based postprocessing leakage-correction algorithm, assuming unidirectional contrast agent extravasation (Boxerman-Weisskoff model) to account for bidirectional contrast agent exchange between intra- and extravascular spaces (bidirectional model). For both models, we compared the goodness of fit with the parent leakage-contaminated relaxation rate curves by using the Akaike Information Criterion and the difference between modeled interstitial relaxation rate curves and dynamic contrast-enhanced MR imaging by using Euclidean distance in 21 patients with glioblastoma multiforme.

RESULTS: The bidirectional model had improved Akaike Information Criterion versus the bidirectional model in >50% of enhancing tumor voxels in all 21 glioblastoma multiformes ($77\% \pm 9\%$; $P < .0001$) and had reduced the Euclidean distance in >50% of enhancing tumor voxels for 17/21 glioblastoma multiformes ($62\% \pm 17\%$; $P = .0041$). The bidirectional model and dynamic contrast-enhanced-derived k_{ep} demonstrated a strong correlation ($r = 0.74 \pm 0.13$). On average, enhancing tumor relative CBV for the Boxerman-Weisskoff model exceeded that for the bidirectional model by $16.6\% \pm 14.0\%$.

CONCLUSIONS: Inclusion of the bidirectional exchange in leakage-correction models for single-echo DSC MR imaging improves the model fit to leakage-contaminated DSC MR imaging data and significantly improves the estimation of relative CBV in high-grade gliomas.

ABBREVIATIONS: AIC = Akaike Information Criterion; bidir model = bidirectional model; BW model = Boxerman-Weisskoff model; ΔR_2^* = transverse relaxation rate; DCE = dynamic contrast-enhanced; GBM = glioblastoma multiforme; k_{ep} = transfer constant from the extracellular extravascular space back to the blood plasma; K^{trans} = contrast transfer coefficient; rCBV = relative cerebral blood volume

The most common DSC MR imaging metric in neuro-oncology is relative CBV (rCBV),¹ which has been used for grading gliomas,^{2,3} predicting low-grade to high-grade transformation,^{4,5}

distinguishing recurrent tumor from pseudoprogression,^{6,7} differentiating tumor regression from pseudoresponse,⁸ and assessing overall treatment response.^{9,10} Relative CBV is typically calculated by integrating the dynamic first-pass change in the transverse relaxation rate (ΔR_2^*) resulting from bolus injection of a gadolinium-based contrast agent, which transiently causes a dose-dependent change in the magnetic susceptibility of blood.¹¹ This technique mimics the classic indicator-dilution theory,¹² which assumes intravascular compartmentalization of injected contrast agent “tracer.” However, common gadolinium-based contrast agents extravasate in lesions with blood-brain barrier disruption,¹³ including malignant gliomas. The exchange of con-

Received September 5, 2015; accepted after revision January 28, 2016.

From the UCLA Brain Tumor Imaging Laboratory (K.L., B.M.E.), Center for Computer Vision and Imaging Biomarkers; Department of Bioengineering (K.L., B.M.E.), Henry Samueli School of Engineering and Applied Science; and UCLA Neuro-Oncology Program (T.F.C., A.L., P.L.N., B.M.E.), University of California, Los Angeles, Los Angeles, California; Departments of Radiological Sciences (K.L., W.B.P., B.M.E.), Biomedical Physics (B.M.E.), Neurology (A.L., P.L.N.), and Neurosurgery (L.M.L.), David Geffen School of Medicine, University of California, Los Angeles, Los Angeles, California; and Department of Diagnostic Imaging (J.L.B.), Rhode Island Hospital and Alpert Medical School of Brown University, Providence, Rhode Island.

This work was supported by the American Cancer Society Research Scholar Grant RSG-15-003-01-CCE (B.M.E.); National Institutes of Health/National Cancer Institute R21CA167354 (B.M.E.); UCLA Jonsson Comprehensive Cancer Center Seed Grant (B.M.E.); National Brain Tumor Society Research Grant (B.M.E.); Siemens Healthcare Research Grant (B.M.E.); Art of the Brain (T.F.C.); Ziering Family Foundation in memory of Sigi Ziering (T.F.C.); Singleton Family Foundation (T.F.C.); Clarence Klein Fund for Neuro-Oncology (T.F.C.); National Institutes of Health National Institute of General Medical Sciences training grant, GM08042 (K.L.); and the University of California, Los Angeles Medical Scientist Training Program (K.L.).

Please address correspondence to Benjamin M. Ellingson, PhD, UCLA Brain Tumor Imaging Laboratory, Departments of Radiological Sciences and Psychiatry, David Geffen School of Medicine, University of California, Los Angeles, 924 Westwood Blvd, Suite 615, Los Angeles, CA 90024; e-mail: bellingson@mednet.ucla.edu; @ben_ellingson

Indicates open access to non-subscribers at www.ajnr.org

<http://dx.doi.org/10.3174/ajnr.A4759>

trast agent between the intravascular and the extravascular extracellular space, which is the objective measurement in dynamic contrast-enhanced (DCE) MR imaging,^{14–16} contaminates the desired DSC MR imaging signal, depending on pulse sequence parameters and underlying tumor biology.¹⁷

A popular model-based DSC MR imaging leakage-correction method proposed by Weisskoff and Boxerman^{2,18,19} linearly fits measured $\Delta R_2^*(t)$ to 2 constant functions derived from the average relaxation rate in nonenhancing tissue, one of which is permeability-weighted. Deviation from the reference function is used to derive corrected rCBV for each voxel. A limiting assumption of this approach is that contrast agent reflux from the interstitial space back to blood plasma is negligible within the time frame of DSC MR imaging signal acquisition (~2 minutes). However, standard models quantifying contrast agent exchange between blood plasma and the interstitium (ie, DCE MR imaging¹⁴) use 2-compartment pharmacokinetics to account for bidirectional transport of contrast agent. We hypothesized that incorporating bidirectional contrast agent transport into the original DSC MR imaging signal model improves rCBV estimates in brain tumors. To test this hypothesis, we compared model-based DSC MR imaging leakage-correction methods with and without consideration of bidirectional transport by using simulations and clinical application to high-grade gliomas.

MATERIALS AND METHODS

Patients

We studied 24 sequential patients with histologically proved glioblastoma multiforme (GBM) treated with maximal surgical resection followed by radiation therapy and concurrent temozolomide and both DSC MR imaging and DCE MR imaging performed at initial tumor progression. Of these, 2 patients illustrated no bolus of contrast during the DSC acquisition and 1 DSC dataset was corrupted by significant motion. Thus, 21 patients (15 men; mean age, 54 years; range, 30–73 years) were included in the final cohort. Progression was defined prospectively by the treating neuro-oncologists if subsequent scans showed >2 sequential months of increasing contrast enhancement and worsening mass effect or evidence of neurologic decline. Specifically, progression was defined as $\geq 25\%$ increase in the sum of enhancing lesion volumes, new enhancing lesions of >1 cm in maximum dimension, an unequivocal qualitative increase in nonenhancing tumor, or an unequivocal new area of non-contrast-enhancing tumor. Additionally, progression must have occurred >3 months following completion of radiation therapy. All participants gave informed written consent to have both DSC MR imaging and DCE MR imaging data collected. All procedures complied with the principles of the Declaration of Helsinki and were approved by the institutional review board at University of California, Los Angeles.

DSC MR Imaging and DCE MR Imaging

We retrospectively reviewed DSC MR imaging and DCE MR imaging scans (3T, Magnetom Trio or Magnetom Skyra; Siemens, Erlangen, Germany), acquired in the same scan session in all 21 patients. T1 maps were generated from 5 precontrast T1-weighted images (flip angles = 5°, 10°, 15°, 20°, 30°) before DCE MR imaging (3D spoiled gradient-echo sequence, 16 sections, 130 time

points, 5-second time resolution, TE/TR = 1.87/5 ms, 25° flip angle, 3-mm section thickness, 256 × 192 matrix, 24-cm FOV). The DCE MR imaging was acquired for ~10 minutes, which was the waiting time between preload and DSC contrast injections for this study. Contrast agent bolus (0.1 mmol/kg) (gadopentetate dimeglumine, Magnevist; Bayer HealthCare Pharmaceuticals, Wayne, New Jersey) was injected after 10–13 baseline images, serving as a preload¹³ for DSC MR imaging (gradient-echo EPI, TE/TR = 32/1840 ms, 35° flip angle, 120 time points, bolus injection after 20–25 baseline images, 9–20 sections, 5-mm section thickness, 128 × 128 matrix size, 24-cm FOV). The same amount of contrast agent was used for the DSC MR imaging studies. Conventional postcontrast T1-weighted imaging was subsequently performed. Patients were excluded if DCE MR imaging or DSC MR imaging was corrupted by motion or technical error.

Image Registration and ROI Selection

All conventional and DCE MR images for each subject were registered to baseline DSC MR images by using a 12-*df* affine transformation with a mutual information cost function (FSL; <http://www.fmrib.ox.ac.uk/fsl>). If required, manual alignment was subsequently performed (tkregister2, Freesurfer; <http://surfer.nmr.mgh.harvard.edu/>). Contrast-enhancing tumor ROIs were defined in 3D by using custom scripts (Analysis of Functional Neuro Images [AFNI]; <http://afni.nimh.nih.gov/afni>), excluding hemorrhage, large vessels, and central necrosis, followed by manual editing to exclude nonlesion voxels.²⁰ Tumor sizes ranged from 2.8 to 106.6 mL, with an average enhancing volume of 40.1 ± 28.4 mL. Spheric ROIs of 1.6 mL were also selected in normal-appearing, contralateral white matter for rCBV normalization.

Computation of DSC MR Imaging rCBV

All simulations and calculations were performed in Matlab (MathWorks, Natick, Massachusetts) by using custom scripts. Uncorrected rCBV was calculated from trapezoidal integration of the original DSC MR imaging relaxation rate–time curve, $\Delta \hat{R}_2^*(t)$. The whole-brain average relaxation rate for nonenhancing voxels (Equations 3 and 4, all equations are in the Appendix) was used for both the original Boxerman-Weisskoff model¹⁹ (BW model) and the new bidirectional exchange model (bidir model). Linear least-squares optimization was used to determine the free parameters for both the bidir-model (via Equation 7) and the BW model (Equation 5, with $k_{ep} = 0$) algorithms, and the corrected rCBV was computed from Equation 8. The average run-time per patient in Matlab was 19.5 ± 6.7 seconds for the bidir model and 18.3 ± 6.2 seconds for the BW model (3.2-GHz Intel Core i5, 32 GB RAM). Tumor rCBV for each method was subsequently normalized to median rCBV within the normal-appearing white matter ROI.

Simulation of DSC MR Imaging rCBV

The whole-brain average relaxation rate, $\Delta \hat{R}_2^*(t)$, was chosen from a sample patient and corresponds to the curve with $K_1 = 1$, $K_2 = 0$, and $k_{ep} = 0$. $K_2 = 0.05$ (adding T1-dominant leakage) with $k_{ep} = 0$ was set to simulate the BW model. A nonzero k_{ep} (0.002 or 0.005) was used to simulate the bidir model of $\Delta \hat{R}_2^*(t)$. For $k_{ep} = 0.1$, the simulation is reflective of the correction of relaxation rate curves at “arterylike” voxels.

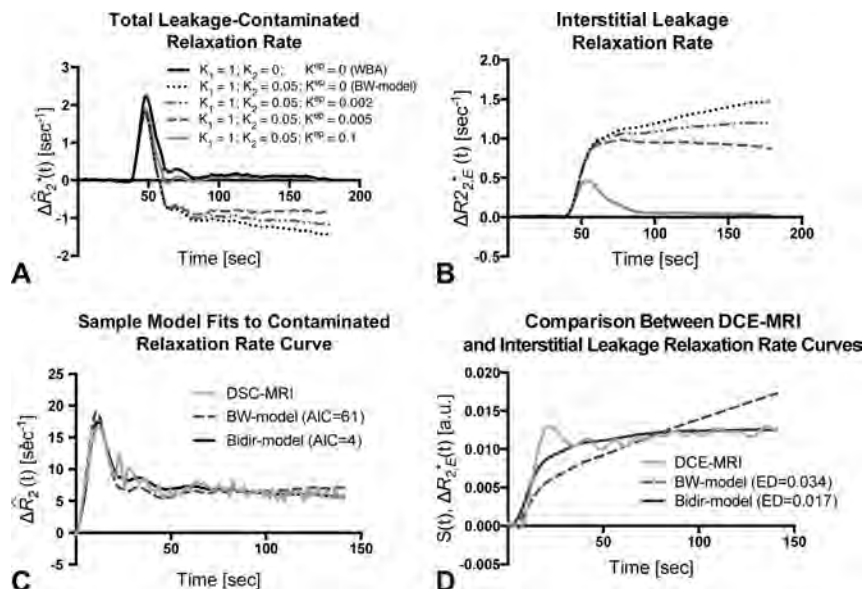


FIG 1. Sample simulated model results for all patients with GBM. *A*, Total leakage-contaminated relaxation rate and the component from interstitial leakage (*B*) for T1-dominant leakage-associated relaxation enhancement. Whole-brain average relaxation rate (WBA) is simulated with $K_2 = 0$ and $k_{ep} = 0$. $K_{ep} = 0$ with nonzero K_2 simulates the BW model. Inclusion of a washout term (nonzero k_{ep}) in the bidir model yields less rise in $\Delta R_{2,E}^*(t)$ and closer approximation of the tail of $\Delta \hat{R}_2^*(t)$ to WBA. *C*, The bidir model fit to the sample leakage-contaminated relaxation rate curve has substantially improved AIC compared with the BW model for T2*-dominant leakage-associated relaxation enhancement in a patient with GBM. *D*, The standardized interstitial leakage relaxation rate from the bidir model better tracks standardized DCE MR imaging signal than the BW model for the tumor voxel used in *C*, with substantially improved Euclidean distance.

Goodness of Fit Analysis

For each enhancing tumor voxel for all patients, we computed the Akaike Information Criterion (AIC) between the leakage-contaminated relaxation rate $\Delta \hat{R}_2^*(t)$ (Equation 1) and its model fit (Equation 5) for the BW model and bidir-model:

$$9) \quad AIC = n \times \ln(RSS/n) + 2(p + 1),$$

where n is the number of fitted time points (injection to the end of the DSC MR imaging acquisition), RSS is the sum of the squared residuals, and p is the number of free parameters (2 for the BW model, 3 for the bidir-model).²¹ Differences in the BW model and bidir model AIC were calculated for all voxels with $k_{ep} > 0$.

We also computed the Euclidean distance (square root of the sum of the squared differences) between the interstitial leakage relaxation rate curves, $\Delta R_{2,E}^*(t)$, generated by the BW model and bidir model corrections and the DCE MR imaging signal, in which the DCE MR imaging signal was upsampled from a 5-second resolution to a 1.8-second resolution to match that of the DSC MR imaging data via linear interpolation by using the Matlab function “resample.” Because interstitial leakage relaxation rate curves and DCE MR imaging signals have units of 1/s and mM, respectively, both were standardized to an area under the curve equal to unity and were vectorized for computation of the Euclidean distance. Higher AIC and Euclidean distance imply worse fits. Two-sample t tests were used to compare whether the AIC and Euclidean distance measurements were significantly different between the 2 leakage-correction methods.

Postprocessing of DCE MR Imaging

DCE MR imaging biomarkers, k_{ep} and contrast transfer coefficient (K^{trans}), were derived via a fit to the model of Tofts and Kermode.¹⁴ As described, the temporal resolution of the DCE MR imaging data was upsampled to match the DSC MR imaging data. For the DCE MR imaging analysis, the “whole-brain average” served as the arterial input function for the DCE model fit. This was done to mirror the DSC bidir model analysis, in which the “whole-brain average” effectively serves as the arterial input function. Voxels with highly fluctuating time courses in either the DSC or DCE images were eliminated from the analysis.

Correlation between DSC- and DCE-Derived Imaging Biomarkers

DSC MR imaging biomarkers, k_{ep} and $rCBV$, were derived as described in the Appendix. Voxelwise Pearson correlation coefficients between the DSC- and DCE-derived parameters were performed in Matlab within contrast-enhancing tumor only, for each patient independently. In this study, we report means and SDs of the correlation coefficients from all 21 patients.

RESULTS

Simulation of the Bidir Model

Figure 1 compares the simulated total leakage contaminated relaxation rate, $\Delta \hat{R}_2^*(t)$, (Fig 1A) and the component from interstitial leakage, $\Delta R_{2,E}^*(t)$, (Fig 1B) for various conditions according to the Tofts and Kermode model,¹⁴ assuming T1-dominant leakage-associated relaxation enhancement. For the BW model, $\Delta R_{2,E}^*(t)$ rises with time in the absence of washout. For nonzero k_{ep} , there is less rise in $\Delta R_{2,E}^*(t)$ and closer approximation of the tail of $\Delta \hat{R}_2^*(t)$ to $\Delta \bar{R}_2^*(t)$, reflecting tumors with different contrast agent pharmacokinetics. For $k_{ep} = 0.1$, the tail of $\Delta R_{2,E}^*(t)$ approaches zero, but because the first-pass of $\Delta \hat{R}_2^*(t)$ differs from that of $\Delta \bar{R}_2^*(t)$, correction of relaxation rate curves at “arterylike” voxels by using K_1 and K_2 is still required to achieve accurate $rCBV$ estimates.

Figure 1C plots sample $\Delta \hat{R}_2^*(t)$, with T2*-dominant leakage-associated relaxation enhancement for a representative patient, with superimposed BW model and bidir model fit relaxation rate curves. In this example, the BW model overestimates the first-pass curve, underestimates the second and third passes, and overestimates the tail. The bidir model better approximates $\Delta \hat{R}_2^*(t)$ over all time points, visually, and has substantially improved the AIC, quantitating an improved fit to the total leakage-contaminated relaxation rate curve.

Figure 1D plots standardized DCE MR imaging signal for the tumor voxel used in Fig 1C, with superimposed standardized interstitial leakage relaxation rate curves, $\Delta R_{2,E}^*(t)$, from the BW model and bidir model. The standardized interstitial leakage re-

laxation rate continually rises with time for the BW model, whereas it better tracks standardized DCE MR imaging for the bidir model, with a substantially improved Euclidean distance.

Goodness of Fit Analysis

Figure 2 plots the percentage of voxels in which the bidir model outperformed the BW model for AIC and Euclidean distance metrics in whole brain and tumor for the 21 patients with GBM. The bidir model had better AIC performance than the BW model in >50% of whole-brain (mean, $71\% \pm 6\%$, $P < .0001$) and tumor (mean, $77\% \pm 9\%$, $P < .0001$) voxels in all patients, and better Euclidean distance performance in >50% of whole-brain voxels (mean, $80\% \pm 9\%$, $P < .0001$) for all patients and in tumor voxels (mean, $62\% \pm 17\%$, $P = .0041$) for 17 of the 21 patients. All were statistically significant for a 1-sample *t* test with null hypothesis of 50%.

Correlation between DSC- and DCE-Derived Imaging Biomarkers

We then performed a voxelwise correlation between the DSC-derived imaging biomarkers from the bidirectional leakage-correction algorithm (k_{ep} and rCBV) with the DCE-derived imaging

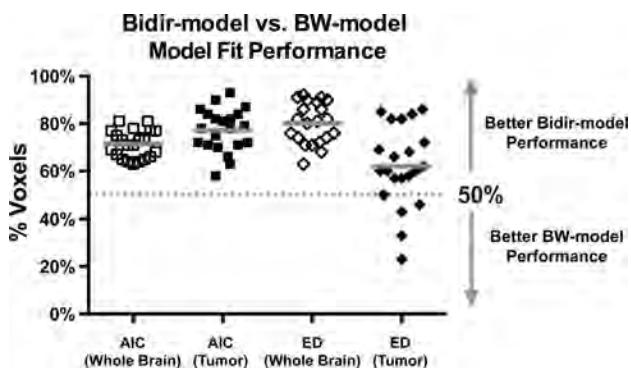


FIG 2. Percentage of voxels (with mean and SD) in which the bidir model outperformed the BW model on Akaike Information Criterion and Euclidean distance (ED) metrics within whole brain and tumor for all 21 patients with GBM. The gray line represents the group mean percentage of voxels.

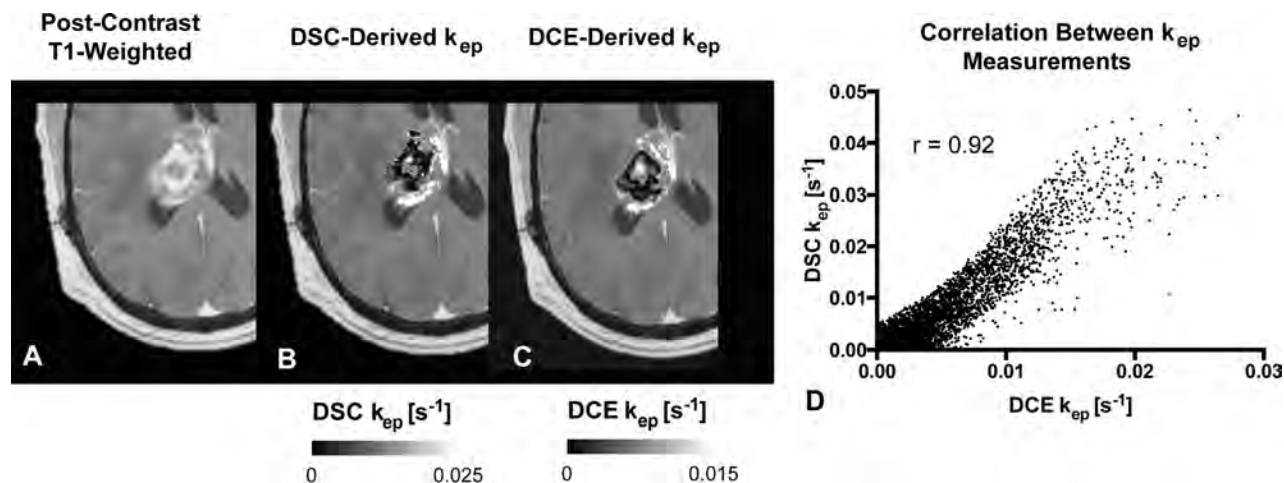


FIG 3. Comparison between DSC- and DCE-derived k_{ep} measurements within tumor. A, Example of anatomic MR imaging of a patient with recurrent glioblastoma. B, DSC-derived k_{ep} measurements within the tumor. C, Corresponding DCE-derived k_{ep} measurements. D, Scatterplot between B and C demonstrates high correlation ($r = 0.92$) for this tumor. Note that areas of low k_{ep} are similar in both DSC- and DCE-derived maps.

biomarkers (k_{ep} and K^{trans}). The Pearson correlation coefficient between the 2 k_{ep} measurements was 0.74 ± 0.13 across the 21 patients, with a weak correlation between the Pearson correlation coefficient and tumor size ($r = 0.11$). Figure 3 demonstrates an example of the correlation between DSC- and DCE-derived k_{ep} . A correlation test was performed between the bidirectional model-derived rCBV and DCE-derived K^{trans} , with a moderate correlation of 0.49 ± 0.22 . A moderate correlation was also found between rCBV and plasma volume fraction (vp) at 0.54 ± 0.12 . Finally, the correlation between the same rCBV and k_{ep} was $r = 0.29 \pm 0.26$. The average K^{trans} value was 0.0015 ± 0.0018 seconds⁻¹ (0.09 ± 0.11 minutes⁻¹), DCE K_{ep} was 0.0050 ± 0.0023 seconds⁻¹ (0.30 ± 0.14 minutes⁻¹), DSC k_{ep} was 0.0057 ± 0.0042 seconds⁻¹ (0.34 ± 0.25 minutes⁻¹), vp was 0.01 ± 0.01 , and rCBV was 1.98 ± 1.24 .

Difference in rCBV between the Bidir Model and BW Model

Figure 4 compares rCBV maps processed without leakage correction and with the BW model or bidir model, in 2 different patients with GBM, one with T1-dominant leakage ($K_2 > 0$) on average in contrast-enhancing tumor voxels and the other with T2*-dominant leakage ($K_2 < 0$). For all patients, average uncorrected rCBV was 1.98 ± 1.24 , the average BW model-corrected rCBV was 1.59 ± 0.89 , and the average bidir model-corrected rCBV was 1.35 ± 0.80 . The average difference between BW model-corrected and the bidir model-corrected rCBV was $16.6\% \pm 14.0\%$. A closer inspection of the T2*-dominant-versus-T1-dominant voxels (as defined by a negative or positive K_2 , respectively) revealed that the difference between the 2 correction methods in T2*-dominant voxels was $37.7\% \pm 42.6\%$, while the same metric for T1-dominant voxels was $5.8\% \pm 3.4\%$.

DISCUSSION

By incorporating the Tofts and Kermode model into the single-echo DSC MR imaging relaxation rate equation, we developed an improved postprocessing leakage-correction method accounting for bidirectional contrast agent transport between the intravascular and interstitial spaces that commonly occurs in angiogenic

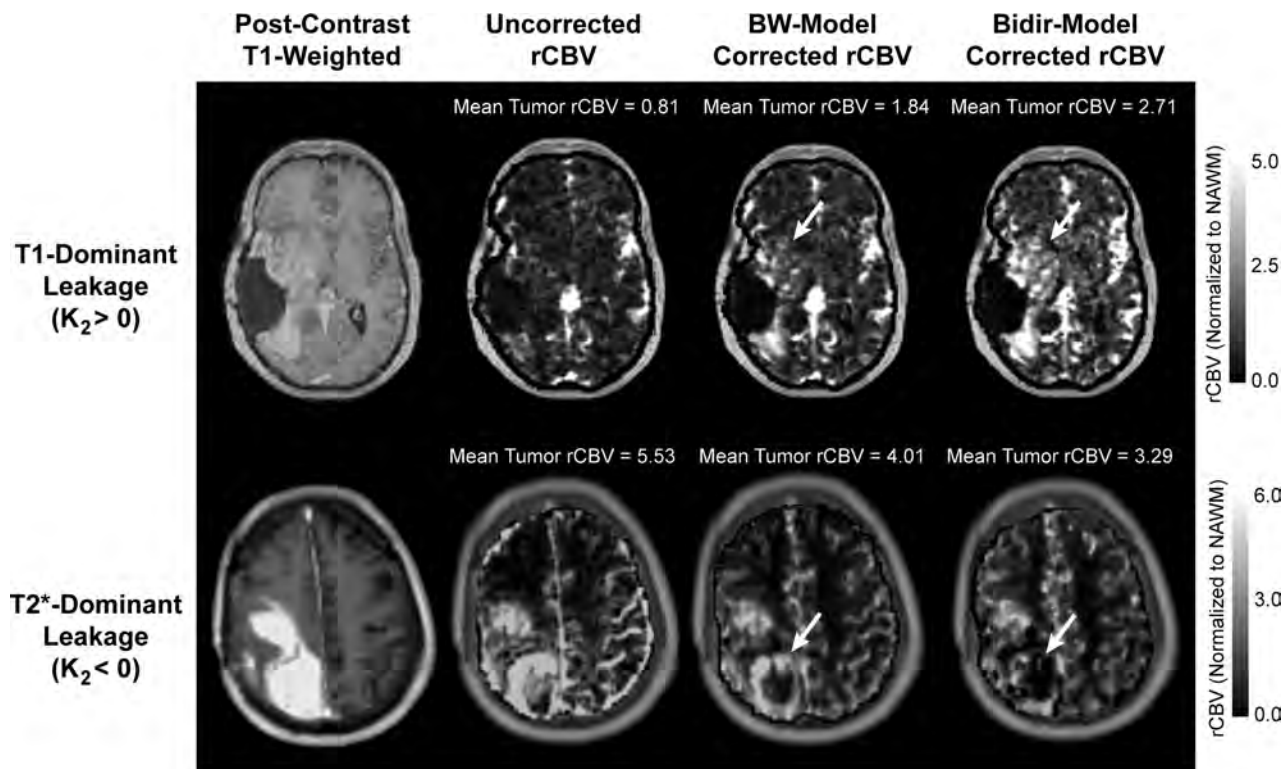


FIG 4. Comparison of uncorrected, BW model–corrected, and bidir model–corrected rCBV in a GBM with T1-dominant leakage on average in contrast-enhancing voxels (*first row*) and a GBM with T2*-dominant leakage (*second row*). For T1-dominant leakage, mean tumor rCBV is underestimated by using the BW model compared with the bidir model, with the converse true for T2*-dominant leakage. Arrows depict regions of the tumor with large changes in estimated rCBV between leakage-correction models.

high-grade gliomas. Our results demonstrate the importance of considering the interstitial washout term, even when modeling the relaxation rate changes during short image acquisitions. For instance, in the simulation, we observed differences between the bidir model and the BW model fits to relaxation rate data in high-grade gliomas in the first-pass curve (as early as 10–20 seconds after injection). Furthermore, inclusion of a washout term in the bidir model alleviates the error in relaxation rate estimates for arteries and normal brain introduced by conventional models constrained to increasing contrast agent concentration with time in all tissues.

Our results suggest that the conventional BW model undercorrects rCBV, with insufficiently increased and decreased rCBV compared with uncorrected rCBV in T1-dominant and T2*-dominant leakage scenarios, respectively. Furthermore, because the low flip angle DSC MR imaging protocol was largely T2*-dominant and the largest discrepancies between the bidir model and BW model estimates of rCBV existed for T2* dominant voxels, our results suggest that the bidir model may be particularly advantageous over the BW model for correcting the residual T2* effects frequently encountered in dual-echo gradient-echo acquisitions. This algorithm can be performed without a substantial increase in postprocessing computation time over the unidirectional model; therefore, the bidirectional model can simply replace the previous model in routine clinical work and for evaluating tumor grade, distinguishing pseudoprogression from true progression, and evaluating treatment response.

Several postprocessing leakage-correction techniques have

previously been proposed.^{22,23} The method by Boxerman-Weisskoff,^{2,18,19} which linearly fits measured $\Delta\hat{R}_2^*(t)$ to 2 constant functions derived from the average relaxation rate in nonenhancing tissue, can be applied quickly to conventional single-echo (spin-echo or gradient-echo) acquisitions and contrast agent injection schemes. Improved correlation of rCBV with glioma grade compared with uncorrected rCBV¹⁹ provides anecdotal evidence of the benefit of the BW model, which has also been shown to improve correlation of gadolinium-based rCBV measures over those obtained by using the intravascular magnetic iron oxide nanoparticles agent as a criterion standard.²⁴

Bjornerud et al²⁵ proposed a method that reduces the sensitivity of rCBV correction to mean transit time that could be combined with the bidir model scheme. Most interesting, Schmiedeskamp et al²³ used a multiecho, gradient-echo, spin-echo acquisition scheme to correct for T1 and T2* leakage by using a backflow term; however, results were highly dependent on literature values for $r_{2,E}^*$ and $r_{2,P}^*$, the T2* relaxation effects of gadolinium in the extravascular space and plasma, respectively, which can vary quite substantially depending on the literature source. Additionally, Quarles et al¹⁷ suggested that these values could vary from tumor to tumor, depending on physiologic factors such as interstitial, vascular, and cell volume fractions and vessel and cell size. An advantage of the bidir model correction method is the lack of assumptions for $r_{2,E}^*$ and $r_{2,P}^*$. All of these leakage-correction algorithms aim to isolate the relaxation rate due to the residual intravascular contrast agent by eliminating the T1- and T2*-related contributions to the relaxation rate from the extravasated contrast agent. They do not “add

back” T2* relaxation that would have been realized had the extravasated contrast agent not left the plasma space, so “corrected rCBV” may still differ from that computed for a tumor with no vascular permeability, all other parameters (including true blood volume) being equal.

One potential limitation to this study is its retrospective design, which may have yielded a selection bias in the sample. Specifically, all patients were chosen because they failed standard therapy. Another potential limitation is the lack of correlation with a criterion standard, such as histology, or with CBV estimates by using intravascular agents such as iron oxide contrast agents. Moreover, AIC is a unitless quantity, which can compare relative goodness of fit between models but does not have a direct test to determine whether one model is significantly better than the other. Finally, the current study only included patients with glioblastoma; therefore, we were unable to recommend a threshold between low-grade and high-grade gliomas by using the new leakage-correction algorithm.

CONCLUSIONS

The bidir model more accurately corrects for the T1 or T2* enhancement arising from contrast agent extravasation due to blood-brain barrier disruption in high-grade gliomas by incorporating interstitial washout rates into the DSC MR imaging relaxation rate model. To this end, the bidir model may potentially improve patient diagnosis and evaluation of treatment response by more accurately estimating rCBV in DSC MR imaging.

APPENDIX

Following Equation A6 of Boxerman et al,¹⁹ the leakage-contaminated DSC MR imaging relaxation rate–time curve, $\Delta\hat{R}_2^*(t)$, equals the intravascular contrast-driven transverse relaxation rate change, $\Delta R_2^*(t)$ plus $\Delta R_{2,E}^*(t)$, a tissue-leakage term describing the simultaneous T1 and T2* relaxation effects resulting from gadolinium extravasation:

$$1) \quad \Delta\hat{R}_2^*(t) = \Delta R_2^*(t) + \Delta R_{2,E}^*(t) = \Delta R_2^*(t) + \left[r_{2,E}^* - \frac{TR}{TE} \times \left(\frac{E_1}{1 - E_1} \right) \times r_1 \right] C_E(t),$$

where $E_1 = e^{-TR/T_{1o}}$, T_{1o} is the precontrast tissue T_1 , r_1 is the T_1 relaxivity of gadolinium, $C_E(t)$ is the concentration of gadolinium in the extravascular extracellular space, and $r_{2,E}^*$ represents the T2* relaxation effects of gadolinium extravasation, as described by Quarles et al¹⁷ and Schmiedeskamp et al.²³ From the original Tofts and Kermode model describing bidirectional contrast agent flux between the intravascular and extravascular compartments,¹⁴ we can estimate the concentration in the extravascular space as:

$$2) \quad C_E(t) = k^{\text{trans}} \otimes [C_p(t) \times e^{-k_{\text{ep}}t}],$$

where k^{trans} and k_{ep} are the transfer coefficients for intra- to extravascular and extra- to intravascular contrast flux, respectively, and $C_p(t)$ is the plasma contrast concentration. $C_p(t)$ and $\Delta R_2^*(t)$ can be defined as scaled versions of the whole-brain average relaxation rate in nonenhancing voxels, $\Delta\bar{R}_2^*(t)$ ¹⁹:

$$3) \quad C_p(t) = k \times \Delta\bar{R}_2^*(t)$$

$$4) \quad \Delta R_2^*(t) = K_1 \times \Delta\bar{R}_2^*(t).$$

Combining Equations 1-4 yields the following:

$$5) \quad \Delta\hat{R}_2^*(t) = K_1 \times \Delta\bar{R}_2^*(t) - K_2 \int_0^t \Delta\hat{R}_2^*(\tau) \times e^{-k_{\text{ep}}(t-\tau)} d\tau,$$

where

$$6) \quad K_2 = \left[r_{2,E}^* - \frac{TR}{TE} \times \left(\frac{E_1}{1 - E_1} \right) \times r_1 \right] \times k^{\text{trans}} \times k.$$

K_1 , K_2 , and k_{ep} (units of second⁻¹) are the free parameters of Equation 5. In general, K_1 depends on CBV, vessel size, and other physiologic factors, while K_2 is related to vascular permeability. Substituting $k_{\text{ep}} = 0$, which occurs with no backflow of extravasated contrast agent, yields the original Boxerman-Weisskoff leakage-correction algorithm, where K_1 and K_2 are solved by linear least-squares fit to $\Delta\hat{R}_2^*(t)$.¹⁹ For the bidir model correction method, a linear least-squares fit to K_1 , K_2 , and k_{ep} can be used with the methodology of Murase,²⁶ as described by the following equation:

$$7) \quad \Delta\hat{R}_2^*(t) = (K_2 + k_{\text{ep}} \times K_1) \int_0^{t_k} \Delta\bar{R}_2^*(\tau) d\tau - k_{\text{ep}} \times \int_0^{t_k} \Delta\hat{R}_2^*(\tau) d\tau + K_1 \times \Delta\bar{R}_2^*(t).$$

Integrating the corrected relaxation rate–time curve yields the following expression for leakage-corrected rCBV:

$$8) \quad rCBV_{\text{corr}} = rCBV + K_2 \int_0^T \int_0^t \Delta\bar{R}_2^*(\tau) \times e^{-k_{\text{ep}}(t-\tau)} d\tau dt.$$

Disclosures: Timothy F. Cloughesy—UNRELATED: Consultancy: F. Hoffmann-La Roche; Genentech; Celgene, Tocagen, AbbVie, Novocure, StemCycle, Novartis, Nektar, Newgen, Notable Labs, Upshire-Smith, VBL. Albert Lai—UNRELATED: Consultancy: Genentech, F. Hoffmann-La Roche, Novocure. Linda Liao—UNRELATED: Grants/Grants Pending: Northwest Biotherapeutics.* Comments: research grant. Whitney B. Pope—UNRELATED: Consultancy: Guerbet. *Money paid to the institution.

REFERENCES

1. Cha S, Knopp EA, Johnson G, et al. **Intracranial mass lesions: dynamic contrast-enhanced susceptibility-weighted echo-planar perfusion MR imaging.** *Radiology* 2002;223:11–29 CrossRef Medline
2. Aronen HJ, Gazit IE, Louis DN, et al. **Cerebral blood volume maps of gliomas: comparison with tumor grade and histologic findings.** *Radiology* 1994;191:41–51 CrossRef Medline
3. Law M, Yang S, Wang H, et al. **Glioma grading: sensitivity, specificity, and predictive values of perfusion MR imaging and proton MR spectroscopic imaging compared with conventional MR imaging.** *AJNR Am J Neuroradiol* 2003;24:1989–98 Medline
4. Law M, Oh S, Babb JS, et al. **Low-grade gliomas: dynamic susceptibility-weighted contrast-enhanced perfusion MR imaging—prediction of patient clinical response.** *Radiology* 2006;238:658–67 CrossRef Medline
5. Danchaivijitr N, Waldman AD, Tozer DJ, et al. **Low-grade gliomas: do changes in rCBV measurements at longitudinal perfusion-weighted MR imaging predict malignant transformation?** *Radiology* 2008;247:170–78 CrossRef Medline

6. Boxerman JL, Ellingson BM, Jeyapalan S, et al. **Longitudinal DSC-MRI for distinguishing tumor recurrence from pseudoprogression in patients with a high-grade glioma.** *Am J Clin Oncol* 2014 Nov 26. [Epub ahead of print] Medline
7. Gahramanov S, Varallyay C, Tyson RM, et al. **Diagnosis of pseudo-progression using MRI perfusion in patients with glioblastoma multiforme may predict improved survival.** *CNS Oncol* 2014;3:389–400 CrossRef Medline
8. Schmainda KM, Zhang Z, Prah M, et al. **Dynamic susceptibility contrast MRI measures of relative cerebral blood volume as a prognostic marker for overall survival in recurrent glioblastoma: results from the ACRIN 6677/RTOG 0625 multicenter trial.** *Neuro Oncol* 2015;17:1148–56 CrossRef Medline
9. Leu K, Enzmann DR, Woodworth DC, et al. **Hypervascular tumor volume estimated by comparison to a large-scale cerebral blood volume radiographic atlas predicts survival in recurrent glioblastoma treated with bevacizumab.** *Cancer Imaging* 2014;14:31 CrossRef Medline
10. LaViolette PS, Cohen AD, Prah MA, et al. **Vascular change measured with independent component analysis of dynamic susceptibility contrast MRI predicts bevacizumab response in high-grade glioma.** *Neuro Oncol* 2013;15:442–50 CrossRef Medline
11. Villringer A, Rosen BR, Belliveau JW, et al. **Dynamic imaging with lanthanide chelates in normal brain: contrast due to magnetic susceptibility effects.** *Magn Reson Med* 1988;6:164–74 CrossRef Medline
12. Meier P, Zierler KL. **On the theory of the indicator-dilution method for measurement of blood flow and volume.** *J Appl Physiol* 1954;6:731–44 Medline
13. Paulson ES, Schmainda KM. **Comparison of dynamic susceptibility-weighted contrast-enhanced MR methods: recommendations for measuring relative cerebral blood volume in brain tumors.** *Radiology* 2008;249:601–13 CrossRef Medline
14. Tofts PS, Kermode AG. **Measurement of the blood-brain barrier permeability and leakage space using dynamic MR imaging, 1: fundamental concepts.** *Magn Reson Med* 1991;17:357–67 CrossRef Medline
15. Roberts HC, Roberts TP, Brasch RC, et al. **Quantitative measurement of microvascular permeability in human brain tumors achieved using dynamic contrast-enhanced MR imaging: correlation with histologic grade.** *AJNR Am J Neuroradiol* 2000;21:891–99 Medline
16. Ludemann L, Wurm R, Zimmer C. **Pharmacokinetic modeling of Gd-DTPA extravasation in brain tumors.** *Invest Radiol* 2002;37:562–70 Medline
17. Quarles CC, Gochberg DF, Gore JC, et al. **A theoretical framework to model DSC-MRI data acquired in the presence of contrast agent extravasation.** *Phys Med Biol* 2009;54:5749–66 Medline
18. Donahue KM, Krouwer HG, Rand SD, et al. **Utility of simultaneously acquired gradient-echo and spin-echo cerebral blood volume and morphology maps in brain tumor patients.** *Magn Reson Med* 2000;43:845–53 Medline
19. Boxerman JL, Schmainda KM, Weisskoff RM. **Relative cerebral blood volume maps corrected for contrast agent extravasation significantly correlate with glioma tumor grade, whereas uncorrected maps do not.** *AJNR Am J Neuroradiol* 2006;27:859–67 Medline
20. Ellingson BM, Cloughesy TF, Lai A, et al. **Quantitative volumetric analysis of conventional MRI response in recurrent glioblastoma treated with bevacizumab.** *Neuro Oncol* 2011;13:401–09 CrossRef Medline
21. Burnham KP, Anderson DR. *Model Selection and Inference: A Practical Information-Theoretic Approach.* New York: Springer-Verlag; 1998
22. Quarles CC, Ward BD, Schmainda KM. **Improving the reliability of obtaining tumor hemodynamic parameters in the presence of contrast agent extravasation.** *Magn Reson Med* 2005;53:1307–16 Medline
23. Schmiedeskamp H, Andre JB, Straka M, et al. **Simultaneous perfusion and permeability measurements using combined spin- and gradient-echo MRI.** *J Cereb Blood Flow Metab* 2013;33:732–43 CrossRef Medline
24. Boxerman JL, Prah DE, Paulson ES, et al. **The role of preload and leakage correction in gadolinium-based cerebral blood volume estimation determined by comparison with MION as a criterion standard.** *AJNR Am J Neuroradiol* 2012;33:1081–87 CrossRef Medline
25. Bjornerud A, Sorensen AG, Mouridsen K, et al. **T1- and T2*-dominant extravasation correction in DSC-MRI, part I: theoretical considerations and implications for assessment of tumor hemodynamic properties.** *J Cereb Blood Flow Metab* 2011;31:2041–53 CrossRef Medline
26. Murase K. **Efficient method for calculating kinetic parameters using T1-weighted dynamic contrast-enhanced magnetic resonance imaging.** *Magn Reson Med* 2004;51:858–62 Medline

Lesion Heterogeneity on High-Field Susceptibility MRI Is Associated with Multiple Sclerosis Severity

 D.M. Harrison,  X. Li,  H. Liu,  C.K. Jones,  B. Caffo,  P.A. Calabresi, and  P. van Zijl



ABSTRACT

BACKGROUND AND PURPOSE: Susceptibility MR imaging contrast variations reflect alterations in brain iron and myelin content, making this imaging tool relevant to studies of multiple sclerosis lesion heterogeneity. In this study, we aimed to characterize the relationship of high-field, susceptibility contrasts in multiple sclerosis lesions to clinical outcomes.

MATERIALS AND METHODS: Twenty-four subjects with multiple sclerosis underwent 7T MR imaging of the brain, disability examinations, and a fatigue inventory. The inverse of T2* relaxation time (R2*), frequency, and relative susceptibility (from quantitative susceptibility mapping) were analyzed in 306 white matter lesions.

RESULTS: Most lesions were hypointense on R2* (88% without a rim, 5% with). Lesions that were hyperintense on quantitative susceptibility mapping were more frequent in relapsing-remitting than in progressive multiple sclerosis (54% versus 35%, $P = .018$). Hyperintense lesion rims on quantitative susceptibility maps were more common in progressive multiple sclerosis and patients with higher levels of disability and fatigue. Mean lesion R2* was inversely related to disability and fatigue and significantly reduced in progressive multiple sclerosis. Relative susceptibility was lower in lesions in progressive multiple sclerosis (median, -0.018 ppm; range, -0.070 to 0.022) than in relapsing-remitting MS (median, -0.010 ppm; range, -0.062 to 0.052 ; $P = .003$).

CONCLUSIONS: A progressive clinical phenotype and greater disability and fatigue were associated with lower R2* and relative susceptibility values (suggestive of low iron due to oligodendrocyte loss) and rimmed lesions (suggestive of chronic inflammation) in this multiple sclerosis cohort. Lesion heterogeneity on susceptibility MR imaging may help explain disability in multiple sclerosis and provide a window into the processes of demyelination, oligodendrocyte loss, and chronic lesion inflammation.

ABBREVIATIONS: EDSS = Expanded Disability Status Scale; MFIS = Modified Fatigue Impact Scale; MSFC = Multiple Sclerosis Functional Composite; PPMS = primary-progressive multiple sclerosis; QSM = quantitative susceptibility mapping; R2* = inverse of T2* relaxation time; RRMS = relapsing-remitting multiple sclerosis; SPMS = secondary-progressive multiple sclerosis

Quantification of white matter lesions on MR imaging is an effective tool for clinical care and clinical trials in multiple sclerosis. However, correlations between white matter lesions and disability remain modest, and most patients with progressive

forms of MS continue to accumulate disability despite little change in T2 lesion burden.¹ Dissociation between what is seen on MR imaging and in the clinic may, in part, be due to the lack of pathologic specificity of lesions on conventional imaging. MS lesions are quite heterogeneous, with at least 4 pathologic subtypes

Received October 22, 2015; accepted after revision January 4, 2016.

From the Department of Neurology (D.M.H.), University of Maryland School of Medicine, Baltimore, Maryland; Departments of Neurology (D.M.H., P.A.C.), Radiology and Radiological Science (X.L., C.K.J., P.v.Z.), and Biostatistics (B.C.), Johns Hopkins University School of Medicine, Baltimore, Maryland; F.M. Kirby Research Center for Functional Brain Imaging (X.L., H.L., C.K.J., P.v.Z.), Kennedy Krieger Institute, Baltimore, Maryland; and Department of Radiology (H.L.), Guangdong Academy of Medical Sciences, Guangdong General Hospital, Guangzhou, China.

Dr Harrison conceptualized and designed the study, participated in recruitment, participated in image analysis, and was primarily responsible for data analysis and manuscript preparation. Dr Li developed the methods for image analysis and performed postacquisition image processing, in addition to editing the manuscript. Dr Liu participated in image analysis and manuscript editing. Dr Jones assisted with development of methods for image acquisition and analysis and participated in manuscript editing. Dr Caffo was involved in biostatistical analyses and participated in manuscript editing. Dr Calabresi participated in study design and recruitment

and manuscript editing. Dr van Zijl participated in study design, development of image-acquisition methods, development of image-analysis methods, and manuscript editing.

This study was supported, in part, by National Institutes of Health Supplemental Grants 5P41RR15241-09S1 and 5P41EB015909 (P. van Zijl) and Bayer Schering Pharma (P.A. Calabresi). Time for data analysis was supported by the National Institutes of Health Mentored Grant K23NS072366 (D.M. Harrison).

Please address correspondence to Daniel M. Harrison, MD, Department of Neurology, University of Maryland School of Medicine, 110 South Poca St, Third Floor, Baltimore, MD 21201; e-mail: dharrison@som.umaryland.edu

 Indicates open access to non-subscribers at www.ajnr.org

 Indicates article with supplemental on-line table.

 Indicates article with supplemental on-line photos.

<http://dx.doi.org/10.3174/ajnr.A4726>

described² and different stages of lesion evolution having been observed (ie, acute inflammation, chronically inactive, and chronic-active inflammation).³

Integrating susceptibility-weighted imaging into lesion analysis in MS may provide an *in vivo* means to evaluate lesion heterogeneity and improve specificity. Postacquisition processing of susceptibility MR imaging provides quantitative maps of the inverse of T2* relaxation time (R2*) and phase images that reveal underlying tissue heterogeneity in exquisite detail,⁴ especially at higher magnetic fields.⁵ The magnetic susceptibility of brain tissue, measured by R2* relaxation and phase contrast, is primarily driven by tissue concentrations of myelin and iron,⁶ making susceptibility-weighted MR imaging quite relevant in MS. Initial studies by using this technique on high-field MR imaging in MS have attempted to quantify lesion iron content with R2* and have revealed lesion patterns on phase imaging that may be indicative of acute inflammation, chronic demyelination, and iron loss or deposition.⁷⁻¹⁰ However, the nature of R2* and phase make interpretation of the meaning of contrast alterations difficult. Because both iron and myelin have a similar effect on the R2* value, differentiation of their respective impacts is not possible.^{11,12} Because phase is a nonlocal measure, phase contrast can be influenced by the magnetic susceptibility of adjacent tissues, the orientation of the head in the magnetic field, and the shape of a lesion, resulting in unreliable quantification of phase shifts and artifacts such as false rims around lesions.¹³

Quantitative susceptibility mapping (QSM) is a recently developed analysis technique capable of providing accurate measures of inherent tissue magnetic susceptibility without the influence of adjacent tissues, head orientation, or lesion geometry.¹³⁻¹⁶ QSM may also help differentiate the effects of myelin and iron when combined with R2*.^{11,12} We have recently reported on MS lesion contrast patterns seen on R2*, phase, and QSM by 7T MR imaging.¹⁷ In this article, we take this investigation further, to determine whether quantitative and qualitative lesion heterogeneity on multiparametric, high-field susceptibility MR imaging is related to clinical heterogeneity in patients with MS.

MATERIALS AND METHODS

Approvals, Consents, and Participants

Protocols were approved by the institutional review boards at Johns Hopkins University School of Medicine and the Kennedy Krieger Institute. Volunteers with diagnoses of relapsing-remitting (RRMS), secondary-progressive (SPMS), and primary-progressive (PPMS) MS, as assigned by their treating physicians, were prospectively recruited from the Johns Hopkins Multiple Sclerosis Center. Written, informed consent was obtained from all participants.

MR Imaging Protocol and Image Analysis

Our protocol for MR imaging acquisition and lesion analysis was previously reported in detail¹⁷ and is thus only briefly discussed here. Whole-brain MR imaging was performed on a 7T Achieva scanner (Philips Healthcare, Best, the Netherlands) with the following sequences: 3D gradient-echo and magnetization-prepared FLAIR. All images were acquired with 1.0-mm isotropic resolution.

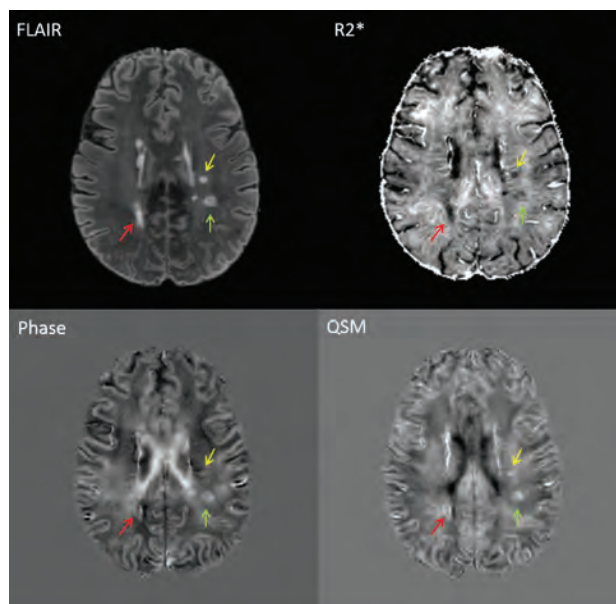


FIG 1. Examples of lesions seen on FLAIR, R2*, phase, and QSM. Each colored arrow indicates the same lesion seen on each of the 4 image contrasts. Lesions were initially identified on FLAIR images. Quantitative gray-scale values (ranging from black to white) for the above images are as follows: R2* = 0–283.78 Hz, phase = –48.69 to 40.00 Hz, QSM = –0.58 to 0.40 ppm.

3D gradient-echo data were processed to generate R2*, frequency, and susceptibility maps. Our methods for performing this task have been discussed in detail in previous publications.^{17,18} The effective relaxation rate (R2*) was estimated by fitting a monoexponential curve to the squared magnitude signal decay for all TEs by using the power method.^{11,19} Laplacian-based phase unwrapping²⁰ and the V-SHARP method were used to generate the local frequency shift map.²¹ Dipole inversion was calculated to obtain QSM images by using the LSQR method.²⁰ Relative susceptibility (from QSM) was calculated relative to the mean susceptibility of the central CSF region in the lateral ventricles.

Magnetization-prepared FLAIR images were coregistered to the TE 12-ms 3D–gradient recalled-echo magnitude image. A random sample of hyperintense (on magnetization-prepared FLAIR) MS lesions was chosen from each scan. Only supratentorial lesions with distinct borders and ovoid-like shapes were chosen to allow more uniform analysis. Each lesion was manually segmented on magnetization-prepared FLAIR. For each lesion, R2*, phase, and QSM images (Fig 1) were reviewed and lesions were labeled as hypointense, isointense, or hyperintense relative to local white matter. If a lesion was found to have a rim, the intensity of the rim was described as hypointense or hyperintense relative to the lesion core and adjacent white matter. Mean values for R2*, frequency (from phase), and relative susceptibility (from QSM) in each lesion mask were calculated as a mean of all voxels within that mask, as previously described.¹⁷

Disability Measures

Expanded Disability Status Scale (EDSS) examinations were performed, and subjects were labeled as highly disabled versus less disabled by separating EDSS scores into tertiles and assigning the

highly disabled category to the upper tertile (EDSS \geq 5.0). The Multiple Sclerosis Functional Composite (MSFC) was administered, and the National Multiple Sclerosis Society Clinical Outcomes Assessment Task Force dataset was used for normalization.^{22,23} The Modified Fatigue Impact Scale (MFIS) was administered, and clinically significant fatigue was defined as MFIS \geq 40.^{24,25}

Statistical Analysis

Statistical analysis was performed in STATA 10.1 IC (StataCorp, College Station, Texas). Group differences were evaluated by χ^2

Table 1: Demographic and clinical characteristics of study sample

Demographics/Characteristics	
No. of subjects	24
No. of lesions	306
Lesions per subject analyzed (median) (range)	12 (2–29)
Age (mean) (SD) (yr)	44.3 (10.0)
Sex (No.) (%)	
Female	12 (50%)
Male	12 (50%)
Disease duration (mean) (SD) (yr)	11.2 (7.6)
Clinical phenotype (No.) (%)	
Relapsing-remitting	21 (88%)
Secondary-progressive	2 (8%)
Primary-progressive	1 (4%)
On MS treatment (No.) (%)	19 (79%)
EDSS score (median) (range)	3.0 (1.5–6.5)
MFIS score (mean) (SD)	37.7 (19.3)
9-HPT, dominant hand (mean) (SD)	23.0 (6.6) seconds
9-HPT, nondominant hand (mean) (SD)	27.7 (17.9) seconds
Timed 25-ft walk (mean) (SD)	5.3 (2.4) seconds
PASAT-3 score (mean) (SD)	46.3 (9.8)
MSFC z score (mean) (SD)	-0.27 (1.54)

Note:—9-HPT indicates Nine Hole Peg Test; PASAT-3, Paced Auditory Serial Addition Test, 3-second delay.

(proportions) or Wilcoxon rank sum (quantitative values) tests. The relationship between quantitative MR imaging values and clinical outcomes was tested by linear mixed-effects regression.²⁶ In addition to accounting for the fixed effects of covariates (age and sex), the random-effects portion of the regression model accounts for intrasubject correlations and intersubject variability in the number of lesions contributing to the model. Because R2*, frequency, and relative susceptibility are reported on different quantitative scales, each value was converted to a z score by using the overall mean and SD. This allowed direct comparisons on a universal scale and for combining parameters through summed z scores. Given the exploratory nature of this study, actual (as opposed to adjusted) *P* values are reported throughout, allowing readers to directly assess the statistical validity of the results.

RESULTS

We reviewed scans from 24 participants with MS (21 RRMS, 2 SPMS, 1 PPMS; Table 1). Most participants were on disease-modifying therapy (79%) at the time of their scan, and the population was moderately disabled (median EDSS score, 3.0; range, 1.5–6.5).

A total of 306 lesions were selected. Figure 2 provides examples of the commonly identified lesion patterns on R2*, phase, and QSM. The count and proportion of lesion patterns are listed in the On-line Table. Most lesions were hypointense with no rim (88%) or had a hyperintense rim (5%) on R2* maps. The most common patterns on phase were the following: isointense with no rim (thus invisible, 129 lesions [42%]) and hyperintense with no rim (90 lesions [29%]). Forty-eight (16%) lesions were noted to have a rim on phase. The most common patterns on QSM were hyperintense with no rim (158 lesions [52%]) and isointense with no rim (thus invisible, 110 [36%]). Twenty-five (9%) lesions were noted to have a rim on QSM.

No significant differences in the R2* appearance of lesions were noted for RRMS versus progressive phenotypes (SPMS/PPMS). However, lesions with a hyperintense rim on phase were over-represented in subjects with SPMS/PPMS (26% versus 11%, *P* = .006). Similarly, lesions with any rim on QSM occurred more frequently in subjects with SPMS/PPMS compared with RRMS (23% versus 6%, *P* < .001). This difference was most influenced by a higher proportion of lesions with an isointense core and a hyperintense rim in those with SPMS/PPMS compared with RRMS (16% versus 4%, *P* = .001). Conversely, hyperintense QSM lesions without any rim occurred more frequently in subjects with RRMS compared with SPMS/PPMS (54% versus 35%, *P* = .018).

In subjects with more severe disability (EDSS \geq 5.0), lesions were more likely to be hypointense with no rim on

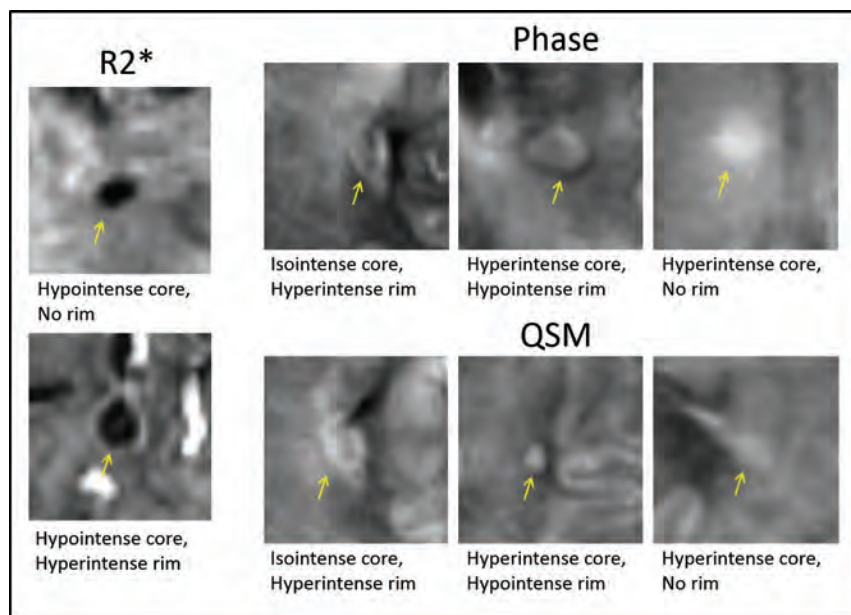


FIG 2. Examples of common lesion patterns on R2*, phase, and QSM. Yellow arrows indicate lesions identified and shown here as samples of common lesion patterns found on each image contrast. Lesions were identified by the intensity of their core and outer rim when visually compared with surrounding white matter. Only a small portion of lesions were invisible on R2* (6%), whereas a larger proportion were invisible on phase (42%) and QSM (36%).

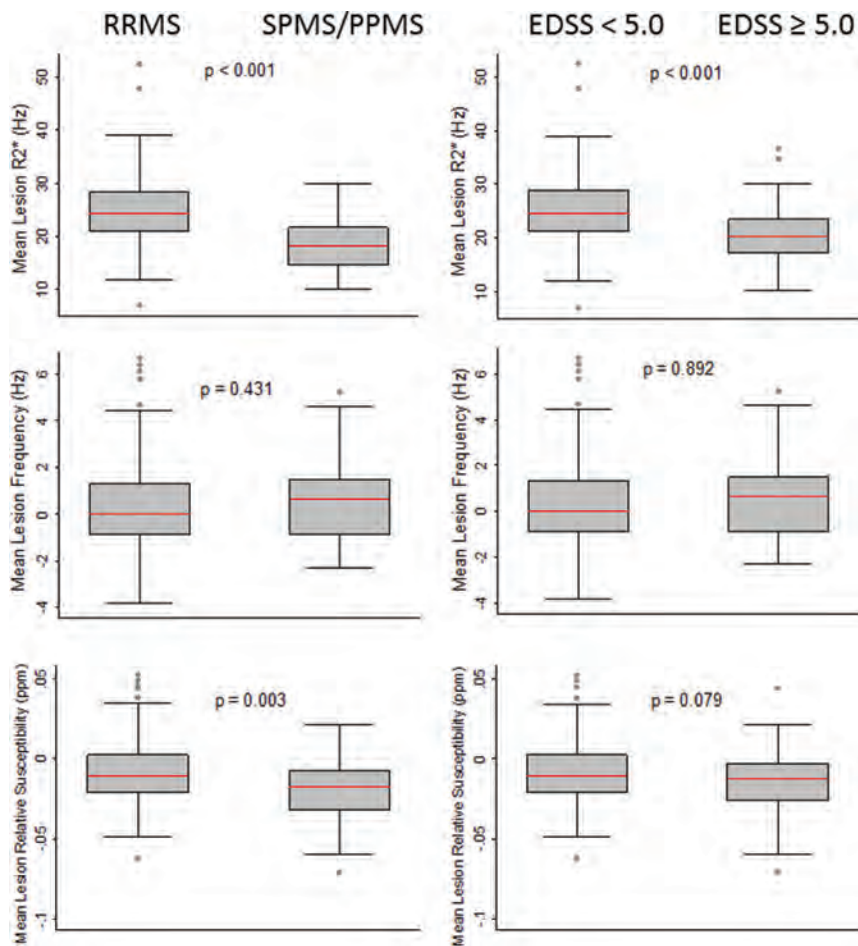


FIG 3. Quantitative comparison of lesion susceptibility values by disease subtype and level of disability. Box-and-whisker plots showing a quantitative comparison of mean lesion $R2^*$, frequency (from phase), and relative susceptibility (from QSM) between subjects with RRMS and SPMS/PPMS (left column) and those with lower-versus-higher levels of disability based on the EDSS score (right column). Lesion $R2^*$ values were significantly lower in SPMS/PPMS and $EDSS \geq 5.0$, and mean lesion relative susceptibility was lower in SPMS/PPMS. Lesion values were taken as the mean of all voxels within each lesion. Red lines indicate the median value for all lesions in each group. P values represent the results of Wilcoxon rank sum testing.

$R2^*$ (95% versus 85%, $P = .015$). Lesions with an isointense core and hyperintense rim on phase and QSM were also noted more commonly in more severely disabled subjects and in those with clinically significant fatigue compared with those with lower disability ($EDSS < 5.0$) or without fatigue.

Mean lesion $R2^*$ was significantly lower in patients with SPMS/PPMS or $EDSS \geq 5.0$ (Fig 3). Mean relative susceptibility (from QSM) in lesions was significantly lower in subjects with SPMS/PPMS (median, -0.018 ppm; range, -0.070 to 0.022) compared with RRMS (median, -0.010 ppm; range, -0.062 to 0.052 ; $P = .003$).

In a multivariate linear mixed-model regression, mean lesion $R2^*$ had a significant inverse relationship with the EDSS score (Fig 4). No significant relationships were found between EDSS and mean lesion frequency or relative susceptibility. However, mean lesion $R2^*$ and relative susceptibility values combined (summed z scores) had a significant inverse relationship with EDSS (Fig 4). The magnitude of the regression coefficient for the relationship between EDSS and $R2^* +$ relative susceptibility was

greater than that for the $R2^*$ value alone: -0.307 (-0.536 , -0.079) versus -0.232 (-0.366 , -0.097), respectively.

Mean lesion $R2^*$ values were positively related to the MSFC score ($P = .012$, On-line Fig 1), and the combined index of $R2^* +$ relative susceptibility was positively related to the MSFC score ($P = .010$).

Mean lesion $R2^*$ values were inversely related to the MFIS score ($P = .039$, On-line Fig 2). No significant relationships were found between MFIS scores and mean lesion frequency, relative susceptibility, or the combination of either with $R2^*$.

DISCUSSION

Our results indicate that multiparametric susceptibility MR imaging reveals heterogeneity of white matter lesions in MS and this lesion heterogeneity is related to the clinical heterogeneity seen in patients. Although previous work has shown heterogeneity in MS lesions on phase contrast, we found changes on $R2^*$ and QSM to be most clinically relevant.^{8,9} Subjects with RRMS were more likely to have hyperintense lesions with no rim on QSM, whereas lesions with isointense cores and hyperintense rims on phase and QSM were more likely in subjects with SPMS/PPMS, greater disability, or fatigue. Progressive phenotypes of MS and greater disability and fatigue were also associated with lower $R2^*$ and relative susceptibility values in lesions. These results suggest that multiparametric susceptibility MR imaging provides clinically relevant characterization of MS lesions.

The possible pathologic basis of the observed lesion patterns and quantification of magnetic susceptibility is informed by prior histopathologic and imaging correlative studies. Most of the magnetic susceptibility signal in the human brain is determined by tissue concentrations of myelin and iron, along with a contribution from the anisotropic properties of tissue architecture.^{11,12,18,27}

Histopathologic myelin content is positively correlated with $R2^*$ and inversely correlated with relative susceptibility (due to diamagnetic properties).^{11,12} Thus, demyelination results in a reduced $R2^*$ value and an elevation of relative susceptibility. Iron, on the other hand, has a paramagnetic effect on relaxation and susceptibility, causing both the $R2^*$ value and relative susceptibility to increase with iron deposition.^{11,12} The effect of changes in myelin and iron content on phase is more difficult to interpret, likely due to sensitivity to tissue architecture and nonlocal phase effects.^{7,8,28}

Given the parallel effects of myelin and iron on $R2^*$ and the

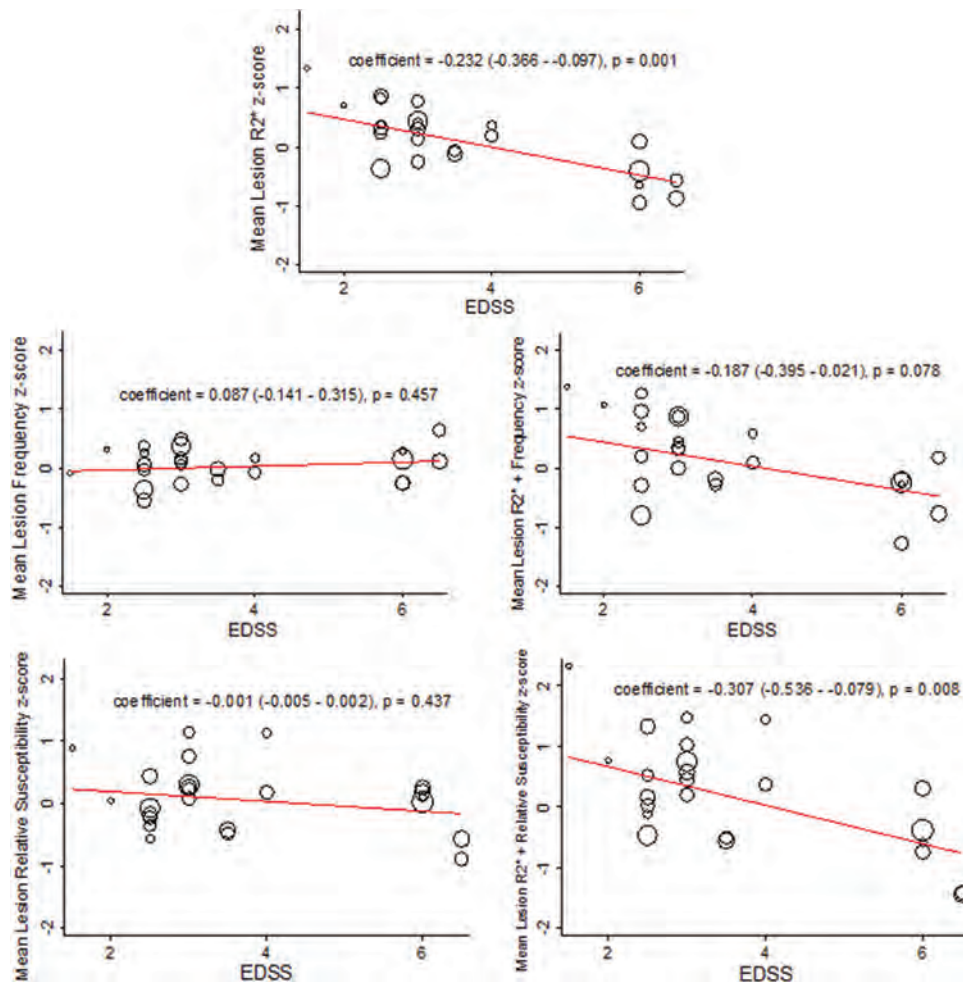


FIG 4. Relationship between EDSS and quantitative R2*, frequency, and relative susceptibility values. Shown are the results of linear mixed-model regression (adjusted for age and sex) for prediction of the quantitative MR imaging value by the Expanded Disability Status Scale score as represented by a fitted-values plot. A significant inverse relationship was found between R2* and EDSS and for a combined index of R2* + relative susceptibility and EDSS. The *open circles* represent fitted values based on the fixed and random effects from the model, with each *circle* thus representing 1 subject and the size of the *circle* weighted for the number of lesions that particular subject contributed to the model. The regression coefficient for the fixed-effects portion of the model is shown in each panel, along with the *P* value for the significance of that coefficient. To place all quantitative values in an equivalent space, we converted all values to z score units (based on mean and SD from all lesions).

Table 2: Hypothesized alterations in myelin and iron content in MS lesions associated with commonly observed R2*/QSM lesion contrast patterns

R2* Intensity	QSM Intensity	Alteration in Myelin Content	Alteration in Iron Content
Hypo	Hyper	↓	↔
Hypo	Iso	↓	↓
Iso	Hyper	↓	↑

Note:—Hypo indicates hypointensity; Hyper, hyperintensity; Iso, isointensity; ↑, increase; ↓, decrease; ↔, little-to-no change.

opposing effects of myelin and iron on QSM, analyzing both in tandem may help separate the influence of myelin and iron on magnetic susceptibility (Table 2).^{11,12,17} The overwhelming majority of lesions in this study were hypointense on R2*, which would indicate either a loss of myelin, a reduction in iron, or both. Pathology-imaging correlation studies have confirmed that most lesions with low R2* have nearly absent myelin staining and low iron content.⁷ A lesion with low R2* being hyperintense on QSM would indicate that most of the signal change is due to myelin loss without a meaningful change in iron content. On the other hand,

a lesion hypointense on R2* and isointense on QSM may indicate a lesion with reductions in both iron and myelin content. Most of the iron found in normal white matter is bound to ferritin within oligodendrocytes and oligodendrocyte progenitor cells,^{7,29} in which iron is necessary for enzymatic functions, including those involved with myelin lipid biosynthesis.³⁰ A smaller amount of iron can be found within myelin sheaths and microglia.⁷ Loss of iron from MS lesions is thus most likely to indicate a significant reduction in oligodendrocytes, which has been confirmed pathologically.⁷

Knowledge of the underlying pathologic causes of R2* and QSM signal changes may allow stratification of the lesion patterns observed in this study along a similar classification scheme as proposed by Lucchinetti et al.² Lesions that were hypointense on R2* and hyperintense on QSM likely correspond to type I and II white matter lesions, in which there is demyelination, some remyelination, and little change in oligodendrocytes. We found this lesion type more prominently in RRMS. Type III and IV lesions have demyelination, no remyelination, and a loss of oligodendro-

cytes through apoptotic mechanisms, all likely making these lesion subtypes of greater clinical consequence. A higher proportion of lesions of these subtypes would be expected to manifest lower mean R2* and less increased relative susceptibility values, indicating more severe demyelination and iron loss. We found this lesion pattern associated with progressive MS and more disability and fatigue.

Lucchinetti et al² also described a rim of active destruction of oligodendrocytes and demyelination occurring in a ring of periplaque white matter in type IV lesions, a lesion subtype only seen in PPMS in their study. It is possible that type IV lesions were being observed in their study, with lesion rims resulting in signal alterations through the release of intracellular iron stores as oligodendrocytes are destroyed and/or a rim of severe demyelination. This possibility would be consistent with our finding of a higher proportion of visible lesion rims on phase and QSM in patients with a progressive phenotype, higher levels of disability, and greater fatigue.

The presence of lesions with and without observable rims may also be indicative of the stage of evolution of a lesion. Histopathology allows temporal staging of lesions as acute inflammatory, chronic inflammatory/slowly expanding, and chronic-inactive.³ The infiltration of inflammatory cells into acutely inflamed MS lesions leads to a temporary increase in iron content due to enzymatic activity in microglia and macrophages⁷ and release of intracellular stores from injured oligodendrocytes and myelin sheaths.³¹ Acutely increased iron at the same time as active demyelination would result in a counterbalancing effect on R2* and an additive effect to increase magnetic susceptibility. An early increase in frequency (from phase) and relative susceptibility (from QSM) has been previously described in longitudinal lesion studies, with subsequent decrease as free iron is scavenged and remyelination occurs.^{27,32} This would explain our finding of a higher proportion of hyperintense lesions on QSM and higher R2* and relative susceptibility values in patients with RRMS (in whom lesions are more likely to be in an early stage of development) compared with those with progressive disease.

On the other hand, lesions with an isointense core and a hyperintense rim may represent slowly expanding, chronically inflamed lesions. Activated microglia at the rim of a lesion is a pathologic hallmark of lesions that are gradually expanding due to chronic inflammation. Slowly expanding lesions with activated microglia are seen more commonly in patients with progressive MS³ and have been proposed as a mechanism for progressive disability accumulation.³³ In chronic-active lesions, CD68 staining (microglia, macrophages) colocalizes with iron and ferritin at the outer rim of lesions, consistent with iron-rich, M1-polarized, nonphagocytic macrophages.^{7,34} Iron uptake at the lesion rim enhances M1 polarization, resulting in proinflammatory tumor necrosis factor α and inducible nitric oxide synthase release and inhibition of the phagocytic M2 macrophage phenotype, which is necessary for tissue repair.³⁴ Lesions of this type also have shown reductions in oligodendrocytes and no oligodendrocyte progenitor (NG2) cells, further inhibiting tissue repair.³⁵ The expected myelin and iron properties of chronic-active lesions are consistent with those in lesions that are R2* hypointense and isointense with a hyperintense rim on QSM, which were found in a higher pro-

portion in subjects with progressive disease and greater disability and fatigue in this study.

Although lesion rims were found in higher proportion on phase images compared with QSM, lesion rims seen on these 2 contrasts may not have the same pathologic meaning. Lesion modeling data have shown that the geometry of a lesion can lead to false classification of solid lesions as shell-shaped on phase, which is not the case for QSM.¹³ Furthermore, due to magnetic dipole effects, phase rims can appear as hyper- or hypointense, depending on orientation, in addition to being influenced by adjacent structures such as veins and crossing fiber tracts.¹³ Although previous publications have suggested that the presence of rims on phase may represent blood-brain barrier breakdown in acute lesions,⁹ subsequent data have shown that this change is more likely due to a transition from anisotropic to isotropic tissue architecture, along with some false rims.^{13,27} Our analysis of phase images furthers the argument of the benefits of QSM over phase. In addition to the potential presence of false lesion rims, we found a higher proportion of lesions that were invisible on phase, and lesion frequency was not related to disability measures.

This study has limitations. The lack of contrast administration or longitudinal follow-up tempers our conclusions as to the relationship between R2* and QSM findings and inflammatory states and lesion evolution. Furthermore, although our conclusions as to the pathologic meaning of susceptibility signal alterations in lesions are supported by prior histopathologic-imaging studies, without postmortem data in this cohort, such conclusions can only be speculative. In addition, although the total number of lesions evaluated here were quite high, only 24 subjects were assessed, which limits conclusions on relapsing-versus-progressive MS. Further stratification of subjects with progressive disease into primary- and secondary-progressive may also have yielded further pathologic insight, but it was not possible due to the small sample size. The restriction of lesion analysis to individual ovoid lesions can also potentially be criticized. Before conclusions can be drawn on the utility of susceptibility imaging in MS, future work should investigate the meaning of susceptibility alterations in larger areas of lesion formation, normal-appearing white matter, cortical gray matter, and other structures. The results reported here should thus be considered preliminary, with further work necessary to confirm or refute these conclusions. Our planned future work will include administration of contrast agents, follow-up scanning, and recruitment of a larger cohort.

CONCLUSIONS

Despite limitations, we believe that our findings have profound implications for MS research. Our results imply that combined analysis of R2* and QSM imaging may provide an in vivo probe into tissue myelin and iron content and thus into the impact of white matter inflammation on axonal tracts and oligodendrocytes. We have also shown that R2* and QSM analysis can provide qualitative and quantitative measures of the lesion heterogeneity, which explain the varying clinical manifestations of MS. Use of such tools is necessary to gain a greater understanding of the mechanisms of disability progression in MS and may hold promise as imaging outcome measures for trials of remyelinating and neuroprotective medications.

ACKNOWLEDGMENTS

We thank Janelle Aquino, Michaela Seigo, Stephanie Syc, and Anna Whetstone and the dedicated Kirby Center staff.

Disclosures: Daniel M. Harrison—RELATED: Grant: National Institutes of Health*; Support for Travel to Meetings for the Study or Other Purposes: National Institutes of Health*; UNRELATED: Consultancy: Mallinckrodt Pharmaceuticals, Genzyme, EMD Serono, MedImmune; Grants/Grants Pending: Bayer,* EMD Serono,* National Multiple Sclerosis Society*; OTHER: Dr Harrison has received research support from Bayer Neurosciences and EMD Serono and has received consulting fees from Mallinckrodt Pharmaceuticals, Genzyme, EMD Serono, and MedImmune. Craig K. Jones—RELATED: Grant: Philips Healthcare,* Comments: I was previously paid, in part, from a grant from Philips Healthcare to Kennedy Krieger Institute. Brian Caffo—RELATED: Grant: National Institutes of Health.* Peter A. Calabresi—RELATED: Grant: Bayer*; UNRELATED: Consultancy: Vertex, Vaccinex, Merck, Prothena; Grants/Grants Pending: Novartis,* MedImmune,* Biogen Idec*; Payment for Lectures (including service on Speakers Bureaus): Multiple Sclerosis Association of America, Vindico Communications; OTHER: Dr Calabresi has received research funding from Biogen Idec, Vertex, Novartis, MedImmune, and Bayer and honoraria for consulting from Vaccinex, Vertex, Abbott Laboratories, Merck, and Prothena. Peter van Zijl—RELATED: Grant: Philips Healthcare*; UNRELATED: Grants/Grants Pending: Philips Healthcare*; Payment for Lectures (including service on Speakers Bureaus): Philips Healthcare*; Patents (planned, pending, or issued): Philips Healthcare,* Comments: They licensed some of my patents; Royalties: Philips Healthcare,* Comments: from patent licensing; Travel/Accommodations/Meeting Expenses Unrelated to Activities Listed: Philips Healthcare.* *Money paid to the institution.

REFERENCES

1. Barkhof F. MRI in multiple sclerosis: correlation with expanded disability status scale (EDSS). *Mult Scler* 1999;5:283–86 CrossRef Medline
2. Lucchinetti C, Brück W, Parisi J, et al. Heterogeneity of multiple sclerosis lesions: implications for the pathogenesis of demyelination. *Ann Neurol* 2000;47:707–17 Medline
3. Kutzelnigg A, Lucchinetti CF, Stadelmann C, et al. Cortical demyelination and diffuse white matter injury in multiple sclerosis. *Brain* 2005;128(pt 11):2705–12 CrossRef Medline
4. Rauscher A, Sedlacik J, Barth M, et al. Magnetic susceptibility-weighted MR phase imaging of the human brain. *AJNR Am J Neuroradiol* 2005;26:736–42 Medline
5. Deistung A, Rauscher A, Sedlacik J, et al. Susceptibility weighted imaging at ultra high magnetic field strengths: theoretical considerations and experimental results. *Magn Reson Med* 2008;60:1155–68 CrossRef Medline
6. Langkammer C, Krebs N, Goessler W, et al. Susceptibility induced gray-white matter MRI contrast in the human brain. *Neuroimage* 2012;59:1413–19 CrossRef Medline
7. Bagnato F, Hametner S, Yao B, et al. Tracking iron in multiple sclerosis: a combined imaging and histopathological study at 7 Tesla. *Brain* 2011;134(pt 12):3602–15 CrossRef Medline
8. Yao B, Bagnato F, Matsuura E, et al. Chronic multiple sclerosis lesions: characterization with high-field-strength MR imaging. *Radiology* 2012;262:206–15 CrossRef Medline
9. Absinta M, Sati P, Gaitán MI, et al. Seven-Tesla phase imaging of acute multiple sclerosis lesions: a new window into the inflammatory process. *Ann Neurol* 2013;74:669–78 CrossRef Medline
10. Hammond KE, Metcalf M, Carvajal L, et al. Quantitative in vivo magnetic resonance imaging of multiple sclerosis at 7 Tesla with sensitivity to iron. *Ann Neurol* 2008;64:707–13 CrossRef Medline
11. Deistung A, Schäfer A, Schweser F, et al. Toward in vivo histology: a comparison of quantitative susceptibility mapping (QSM) with magnitude-, phase-, and R2*-imaging at ultra-high magnetic field strength. *Neuroimage* 2013;65:299–314 CrossRef Medline
12. Stuber C, Morawski M, Schäfer A, et al. Myelin and iron concentration in the human brain: a quantitative study of MRI contrast. *Neuroimage* 2014;93(pt 1):95–106 CrossRef Medline
13. Eskreis-Winkler S, Deh K, Gupta A, et al. Multiple sclerosis lesion geometry in quantitative susceptibility mapping (QSM) and phase imaging. *J Magn Reson Imaging* 2015;42:224–29 CrossRef Medline
14. Liu C, Li W, Tong KA, et al. Susceptibility-weighted imaging and quantitative susceptibility mapping in the brain. *J Magn Reson Imaging* 2015;42:23–41 CrossRef Medline
15. Wang Y, Liu T. Quantitative susceptibility mapping (QSM): decoding MRI data for a tissue magnetic biomarker. *Magn Reson Med* 2015;73:82–101 CrossRef Medline
16. Wharton S, Bowtell R. Whole-brain susceptibility mapping at high field: a comparison of multiple- and single-orientation methods. *Neuroimage* 2010;53:515–25 CrossRef Medline
17. Li X, Harrison DM, Liu H, et al. Magnetic susceptibility contrast variations in multiple sclerosis lesions. *J Magn Reson Imaging* 2016;43:463–73 CrossRef Medline
18. Li X, Vikram DS, Lim IA, et al. Mapping magnetic susceptibility anisotropies of white matter in vivo in the human brain at 7 T. *Neuroimage* 2012;62:314–30 CrossRef Medline
19. Miller AJ, Joseph PM. The use of power images to perform quantitative analysis on low SNR MR images. *Magn Reson Imaging* 1993;11:1051–56 CrossRef Medline
20. Li W, Wu B, Liu C. Quantitative susceptibility mapping of human brain reflects spatial variation in tissue composition. *Neuroimage* 2011;55:1645–56 CrossRef Medline
21. Li W, Avram AV, Wu B, et al. Integrated Laplacian-based phase unwrapping and background phase removal for quantitative susceptibility mapping. *NMR Biomed* 2014;27:219–27 CrossRef Medline
22. Fischer JS, Rudick RA, Cutter GR, et al. The Multiple Sclerosis Functional Composite Measure (MSFC): an integrated approach to MS clinical outcome assessment—National MS Society Clinical Outcomes Assessment Task Force. *Mult Scler* 1999;5:244–50 CrossRef Medline
23. Rudick R, Antel J, Confavreux C, et al. Recommendations from the National Multiple Sclerosis Society Clinical Outcomes Assessment Task Force. *Ann Neurol* 1997;42:379–82 CrossRef Medline
24. Flachenecker P, Kümpfel T, Kallmann B, et al. Fatigue in multiple sclerosis: a comparison of different rating scales and correlation to clinical parameters. *Mult Scler* 2002;8:523–26 CrossRef Medline
25. Achiron A, Givon U, Magalashvili D, et al. Effect of Alfacalcidol on multiple sclerosis-related fatigue: a randomized, double-blind placebo-controlled study. *Mult Scler* 2015;21:767–75 CrossRef Medline
26. Laird NM, Ware JH. Random-effects models for longitudinal data. *Biometrics* 1982;38:963–74 CrossRef Medline
27. Wiggermann V, Hernandez Torres E, Vavasour IM, et al. Magnetic resonance frequency shifts during acute MS lesion formation. *Neurology* 2013;81:211–18 CrossRef Medline
28. Yablonskiy DA, Luo J, Sukstanskii AL, et al. Biophysical mechanisms of MRI signal frequency contrast in multiple sclerosis. *Proc Natl Acad Sci U S A* 2012;109:14212–17 CrossRef Medline
29. Hulet SW, Heyliger SO, Powers S, et al. Oligodendrocyte progenitor cells internalize ferritin via clathrin-dependent receptor mediated endocytosis. *J Neurosci Res* 2000;61:52–60 Medline
30. Connor JR, Menzies SL. Relationship of iron to oligodendrocytes and myelination. *Glia* 1996;17:83–93 Medline
31. Hametner S, Wimmer I, Haider L, et al. Iron and neurodegeneration in the multiple sclerosis brain. *Ann Neurol* 2013;74:848–61 CrossRef Medline
32. Chen W, Gauthier SA, Gupta A, et al. Quantitative susceptibility mapping of multiple sclerosis lesions at various ages. *Radiology* 2014;271:183–92 CrossRef Medline
33. Prineas JW, Kwon EE, Cho ES, et al. Immunopathology of secondary-progressive multiple sclerosis. *Ann Neurol* 2001;50:646–57 CrossRef Medline
34. Mehta V, Pei W, Yang G, et al. Iron is a sensitive biomarker for inflammation in multiple sclerosis lesions. *PLoS One* 2013;8:e57573 CrossRef Medline
35. Chang A, Nishiyama A, Peterson J, et al. NG2-positive oligodendrocyte progenitor cells in adult human brain and multiple sclerosis lesions. *J Neurosci* 2000;20:6404–12 Medline

Cortical Perfusion Alteration in Normal-Appearing Gray Matter Is Most Sensitive to Disease Progression in Relapsing-Remitting Multiple Sclerosis

 S.-P. Hojjat,  M. Kincal,  R. Vitorino,  C.G. Cantrell,  A. Feinstein,  L. Zhang,  L. Lee,  P. O'Connor,  T.J. Carroll, and  R.I. Aviv



ABSTRACT

BACKGROUND AND PURPOSE: The role of gray matter in multiple sclerosis is increasingly evident; however, conventional images demonstrate limitations in cortical lesion identification. Perfusion imaging appears sensitive to changes in tissue type and disease severity in MS. We sought to use bookend perfusion to quantify parameters in healthy controls and normal-appearing and lesional tissue at different relapsing-remitting MS stages.

MATERIALS AND METHODS: Thirty-nine patients with relapsing-remitting MS and 19 age-matched healthy controls were prospectively recruited. The Minimal Assessment of Cognitive Function in MS battery was used to assess cognitive performance. Perfusion parameters, including cerebral blood flow and volume and mean transit time, were compared for healthy controls and normal-appearing and lesional tissue for all study groups. Dispersion of perfusion measures for white matter lesions and cortical lesions was assessed.

RESULTS: Twenty of the 39 patients with relapsing-remitting MS were cognitively impaired. Significant differences were displayed between all relapsing-remitting MS subgroups and healthy controls in all comparisons except for normal-appearing gray matter CBV between healthy controls and unimpaired patients with relapsing-remitting MS and for all normal-appearing white matter perfusion parameters between healthy controls and unimpaired patients with relapsing-remitting MS. White matter lesion but not cortical lesion perfusion was significantly reduced in cognitively impaired patients with relapsing-remitting MS versus unimpaired patients with relapsing-remitting MS. Perfusion reduction with disease progression was greater in normal-appearing gray matter and normal-appearing white matter compared with cortical lesions and white matter lesions. Smaller dispersion was observed for cortical lesions compared with white matter lesions for each perfusion parameter.

CONCLUSIONS Quantitative GM and WM analysis demonstrated significant but disproportionate white matter lesion, cortical lesion, normal-appearing white matter, and normal-appearing gray matter changes present between healthy controls and patients with relapsing-remitting MS with and without cognitive impairment, necessitating absolute rather than relative lesion perfusion measurement.

ABBREVIATIONS: CL = cortical lesion; NAGM = normal-appearing gray matter; NAWM = normal-appearing white matter; RRMS = relapsing-remitting MS; RRMS-I = impaired patients with relapsing-remitting MS; RRMS-NI = nonimpaired patients with relapsing-remitting MS; WML = white matter lesion

Multiple sclerosis is a chronic inflammatory demyelinating disease of the central nervous system,¹ characterized by initial increased blood-brain barrier permeability and perivascular lymphocyte migration.² Cognitive impairment is present in 40%–65% of patients with MS and correlates with cortical lesion vol-

ume.^{3,4} Clinical-pathologic correlation by using high-field ex vivo MR imaging has demonstrated limitations in prospective cortical lesion identification by using proteolipid protein staining as a reference standard,⁵ prompting the testing of surrogate techniques for in vivo assessment of cortical lesions.

Recently, studies demonstrated the potential for perfusion MR imaging to identify cortical abnormalities, even in the absence of structural differences, suggesting that perfusion is sensitive to changes not visible on routine structural imaging.^{2,6–10} Perfusion changes appear sensitive to tissue type and disease activity and severity and are most commonly described in the context of white matter lesions. Reduced CBF, normal or reduced CBV, and in-

Received November 3, 2015; accepted after revision January 12, 2016.

From the Departments of Psychiatry (A.F.), Neurology (L.L.), and Medical Imaging (S.-P.H., M.K., R.V., R.I.A., L.Z.), Sunnybrook Health Sciences Centre, Toronto, Ontario, Canada; Departments of Medicine (P.O., L.L.), Psychiatry (A.F.), and Medical Imaging (S.-P.H., R.I.A.), University of Toronto, Toronto, Ontario, Canada; and Departments of Biomedical Engineering (C.G.C., T.J.C.) and Radiology (T.J.C.), Northwestern University, Chicago, Illinois.

This study was supported by the Canadian Institute of Health Research operating grant 130366, the National Institutes of Health grant EB017928, the American Heart Association grants 20380798 and 14PRE20380810, and a Biogen fellowship funding award.

Please address correspondence to Seyed-Parsa Hojjat, PhD, Sunnybrook Health Sciences Centre, 2075 Bayview Ave, Room AB-204, Toronto, ON, M4N 3M5 Canada; e-mail: Parsa.Hojjat@sunnybrook.ca

 Indicates open access to non-subscribers at www.ajnr.org

 Indicates article with supplemental on-line tables.

<http://dx.doi.org/10.3174/ajnr.A4737>

creased or unchanged MTT have been previously demonstrated in white matter lesions (WMLs) compared with normal-appearing white matter (NAWM) in relapsing-remitting MS (RRMS).⁷ While a few studies have assessed cortical perfusion,^{9,10} scant data describe perfusion changes in cortical lesions.² By virtue of the semiquantitative dynamic susceptibility contrast MR imaging perfusion technique, Peruzzo et al² reported that cortical lesion perfusion changes as a percentage difference between cortical lesions and normal-appearing gray matter (NAGM), effectively normalizing perfusion results by NAGM. While this approach addresses potential issues of interscan variability, it assumes stability of NAGM perfusion, ignoring changes that occur with disease progression that would significantly alter the cortical lesion/NAGM ratio and result in erroneous measurements.⁶

DSC-MR imaging remains the most widely used method for MR imaging perfusion assessment and may be used to derive quantitative rather than semiquantitative perfusion measurements by calibrating T1 signal change before and after the DSC sequence. This bookend perfusion MR imaging technique¹¹ generates reliable, reproducible, and validated quantitative perfusion measurements,¹² precluding the need for normalization against a reference tissue type. The objective of this study was to use bookend perfusion MR imaging to quantify absolute perfusion changes within cortical lesions (CLs), WMLs, NAWM, and NAGM at different RRMS disease stages. We hypothesized that absolute lesion and NAGM/NAWM perfusion predictably changes with increased disease severity and progression.

MATERIALS AND METHODS

Patients

Subjects with RRMS were prospectively recruited for this ethics board-approved study from tertiary referral MS clinics at Sunnybrook and St. Michael's hospitals during 1 year. MS diagnosis was established by using the revised McDonald criteria by a senior MS neurologist (20 years' experience). Participant clinical histories, including age, sex, education level, disease duration, medication, and relapses, were recorded. Exclusion criteria were drug/alcohol abuse, relapse or corticosteroid use within the past 3 months, premorbid psychiatric history, head injury (including loss of consciousness), and concurrent morbidity (cerebrovascular disease and MR imaging/gadolinium contraindications including impaired renal function). All participants were specifically recruited for this study as controls, age- and sex-matched to patients with RRMS. Written consent included a discussion of the small potential risks associated with gadolinium injection and was obtained from all participants after confirming gadolinium and MR imaging eligibility with glomerular filtration rate determination and a standardized MR imaging contraindication questionnaire. Thirty-nine patients and 19 age-matched healthy participants were recruited.

Neuropsychological Assessment

All participants with RRMS were assessed for cognitive impairment by using the Minimal Assessment of Cognitive Function in MS with the purpose of dichotomizing patients with RRMS into those who were cognitively intact and those who were impaired. The Minimal Assessment of Cognitive Function in MS was recommended by an expert panel for clinical monitoring and research and was performed

within 1 week of MR imaging. This 90-minute cognitive battery covers 5 cognitive domains by performing 7 tests: learning and memory (California Verbal Learning Test-II, Brief Visuospatial Test-revised); processing speed and working memory (Paced Auditory Serial Addition and Symbol Digit Modalities Test); executive function (Delis-Kaplan Executive Function System); verbal fluency (Controlled Oral Work Association Test); and visuospatial perception/spatial processing (Judgment of Line Orientation Test). Anxiety and depression were also assessed through administration of the Hospital Anxiety and Depression Scale. Age- and sex-adjusted normative data were used to convert raw test scores to z scores. Z scores less than -1.5 for a single test defined impairment, and patients impaired on ≥ 2 tests were considered impaired.

Image Acquisition

MR imaging was performed on a 3T MR imaging system (Achieva; Philips Healthcare, Best, the Netherlands) with an 8-channel phased array coil. The acquisitions included volumetric T1 (TR/TE/flip angle, 9.5/2.3 ms/12°; number of averages, 1; FOV, 24 cm; section thickness, 1.2 mm; matrix size, 256 × 219); proton density/T2 (TR/TE/flip angle, 2500/10.7 ms/90°; FOV, 23 cm; section thickness, 3 mm; matrix, 256 × 263); phase-sensitive inversion recovery (TR/TE, 3374/15 ms; FOV, 23 cm; section thickness, 3 mm; matrix, 400 × 255; in-plane voxel size, 0.43 × 0.43); and field-echo echo-planar imaging DSC (TR/TE/flip angle, 1633/30 ms/60°; FOV, 22 cm; section thickness, 4 mm; matrix, 96 × 93; in-plane voxel size, 2.3 × 2.4 mm; no gap; signal bandwidth, 1260 Hz/pixel; sections, 24). A 25-mL bolus of saline at a rate of 5 mL/s was applied after administering 10 mL of gadobutrol (Gadovist; Bayer Schering Pharma, Berlin, Germany) (1 mmol/mL) with a power injector at 5 mL/s. Sixty images were acquired at 1.6-second intervals with the injection occurring at the fifth volume. A segmented inversion recovery Look-Locker EPI sequence was performed immediately before and after the DSC sequence (TR/TE/flip angle, 29/14 ms/20°; TI, 15.8 ms; FOV, 22 cm; matrix, 128 × 126; 15 lines in *k*-space per acquisition; section thickness, 4 mm; 60 time points; scan time, 73 seconds). After the last imaging time, a 3000-ms delay was placed to ease longitudinal magnetization recovery.

Image Processing

Statistical Parametric Mapping (SPM8; <http://www.fil.ion.ucl.ac.uk/spm/software/spm12>) was used for coregistering structural T1- and proton density/T2-weighted images. Segmentation of intracranial tissue was automatically performed, by a validated technique using the structural T1 images, into GM, WM, and CSF.¹³ Cortical lesions, WM lesions, and T1 holes were manually traced by a clinician (10 years of experience) on phase-sensitive inversion recovery and T2 and T1 images, respectively, by using Analyze 8.0 (Mayo Clinic, Rochester, Minnesota). The fractional brain volume was calculated for the segmented tissues.

A series of registrations, including linear registration (FMRIB Linear Image Registration Tool, FLIRT; <http://www.fmrib.ox.ac.uk/>) followed by multiresolution nonlinear registration with 4 subsampling levels by using nonlinear intensity modulation (FMRIB Nonlinear Registration Tool; FNIRT; <http://fsl.fmrib.ox.ac.uk/fsl/fslwiki/FNIRT>), were performed to register structural T1- and proton density/T2-weighted images with the segmented

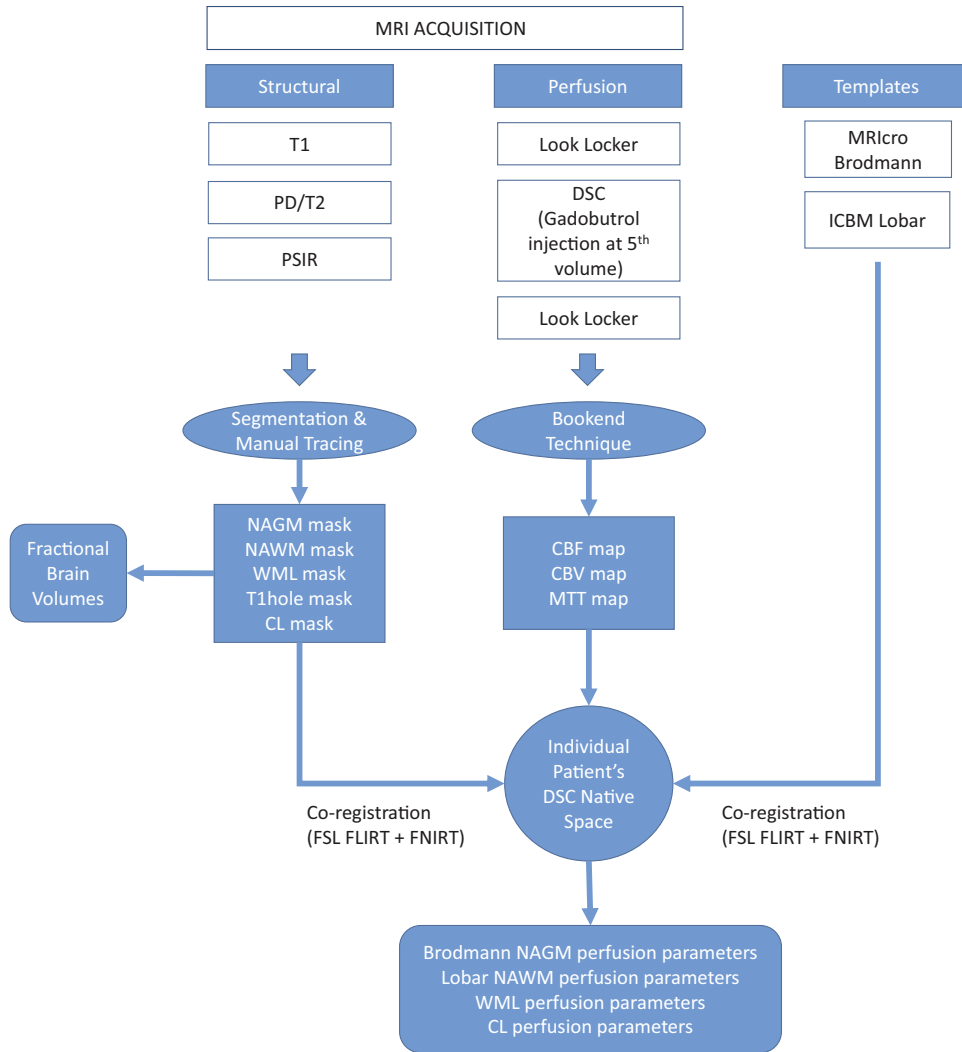


FIG 1. Block diagram representation of the image acquisition and processing pipeline. PSIR indicates phase-sensitive inversion recovery; PD, proton density.

ROIs to the corresponding precontrast EPI sequence. To better guide the alignment, we iteratively smoothed images by using a full width half maximum Gaussian kernel. The kernel sizes used at each resolution level were 6, 4, 2, 2 mm and 4, 2, 0, 0 mm for the moving images and perfusion images, respectively. Last, the MRicro Brodmann template (Neuropsychology Laboratory, Columbia, South Carolina) and the ICBM lobar templates (Laboratory of Neuroimaging, Keck School of Medicine, University of Southern California, Los Angeles, California) were registered, by using the same registration regimen, to the transformed T1 images in EPI space. The templates were used to calculate the average GM and WM perfusion parameters for each participant.

An automated island labeling technique based on the 8 connected components criteria was applied to WML and CL segmentation masks to separately label individual lesions (Matlab; MathWorks, Natick, Massachusetts) for every patient (Figs 1 and 2).

Bookend Perfusion

The bookend technique was used to calculate quantitative perfusion parameters, including cerebral blood volume, flow, and

mean transit time.^{11,14,15} Briefly, the bookend technique calibrates relative values to quantitative values on the basis of parenchymal T1 changes (in milliseconds) in response to the contrast agent injections (precontrast versus postcontrast) used as part of a DSC perfusion scan. Bookend perfusion scanning explicitly accounts for the intravascular-to-extravascular water exchange rates that can bias the quantitative values through careful modeling with a 2-compartment model included as a water correction factor. The T1 changes in normal-appearing white matter (WM T1) relative to the blood pool change measure during the distribution phase of the agent, qCBV in WM, independent of an arterial input function (Equation 1):

$$1) \quad qCBV = WCF \times \frac{k_h}{\rho} \times \frac{\left[\frac{1}{T1_{precontrast}} - \frac{1}{T1_{postcontrast}} \right]_{WM}}{\left[\frac{1}{T1_{precontrast}} - \frac{1}{T1_{postcontrast}} \right]_{blood\ pool}} \times \left(100 \frac{g}{mL} \right),$$

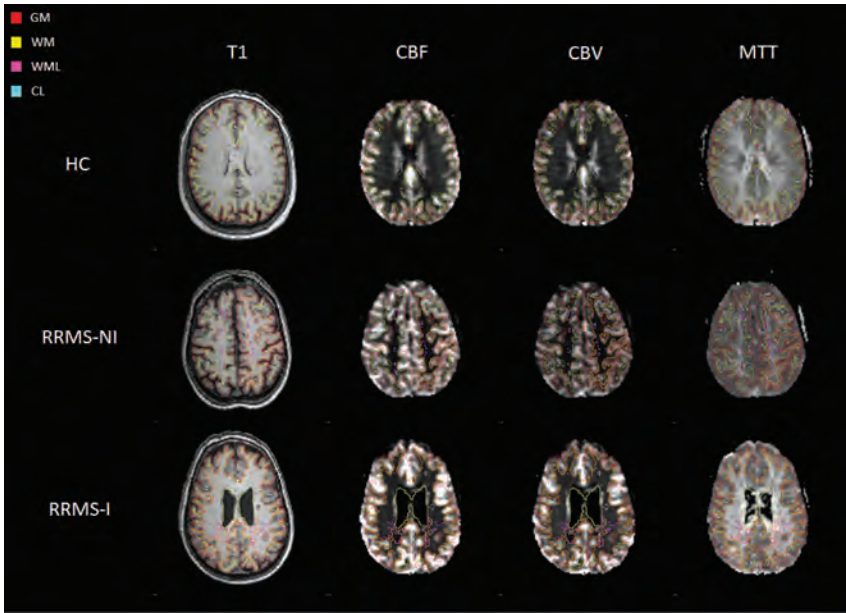


FIG 2. Representative section of T1 and perfusion images in perfusion space for the different study groups with overlays of the investigated ROIs.

where ρ represents average brain attenuation of 1.04 mL/g, and $K_h = 0.74$ is a constant used to correct for hematocrit between capillaries and arteries.¹⁶ WCF represents the water correction factor as defined in Equation 2 for WM in 1.5T field strength:

$$2) \quad WCF(\Delta R_1) = 8.2 \times 10^{-3} \Delta R_1^2 + 0.25 \Delta R_1 + 0.51,$$

where ΔR_1 is the change in T1 of the blood because of gadolinium injection.

rCBF is computed by deconvolving tissue concentration–time curves and the arterial input function (AIF) by using singular value decomposition of the reformulation of Equation 3:

$$3) \quad C(t) = rCBF \times [AIF \otimes R(t)],$$

where $R(t)$ is the residue function¹⁷ and $C(t)$ is tissue concentration at time t . $rCBV$ is then obtained by calculating the ratio of the area under the curve of the tissue–concentration–time curve and the AIF. CBF values are then derived by using Equation 4^{11,14,15}:

$$4) \quad qCBF = rCBF \times qCBV/rCBV.$$

Average perfusion values (CBF/CBV/MTT) were then calculated for every CL and WML by using the respective perfusion image. An empiric volume threshold of 3 voxels was chosen to eliminate small islands resulting from the automated lesion labeling algorithm and to account for the partial volume effect.²

Statistical Analysis

Univariate general linear and logistic regressions were performed to compare demographic, clinical, and volume data among 3 groups on all continuous outcomes and categorical variables, respectively. $P < .017$ (ie, $.05/3$) was considered significant to account for multiple comparisons.

The Lilliefors test confirmed the absence of normality of distribution of perfusion data. Median and interquartile range were calculated for the segmented tissues. The Wilcoxon rank

sum test (Matlab) was used to compare NAGM and NAWM tissues across cognitively unimpaired and impaired patients with RRMS and the healthy GM and WM of controls, with corrected $P < .017$ identified as significantly different. Independent assessments were also performed by using the Wilcoxon rank sum test to compare lesion perfusion across disease groups and with the corresponding normal-appearing tissue within each patient group, with $P < .05$ as significantly different.

A dispersion metric for each lesion type was calculated after removal of outliers defined as $1.5 \times$ away from the first and third quartiles to quantify the degree of heterogeneity, calculated as the number of SDs encompassing the distribution of the corresponding perfusion parameter (Equation 5):

$$5) \quad \text{Dispersion } (L) = \left[\frac{\max(L) - \min(L)}{\sigma} \right],$$

where L corresponds to the lesion vector of interest and σ represents the SD of L .

RESULTS

Of 39 patients with RRMS enrolled in the study, 20 (51.3%) met the criteria for cognitive impairment. The participant demographic and fractional brain volumes are listed in Table 1. WML, CL, NAWM, and NAGM perfusion values for each patient group and healthy controls are summarized in Table 2. Significant CBF and CBV reduction was observed in NAGM and NAWM in patients with impairment with relapsing-remitting MS (RRMS-I) compared with other groups. No MTT differences were observed between RRMS groups for NAWM, though NAGM was modestly prolonged in RRMS-I compared with patients without impairment with relapsing-remitting MS (RRMS-NI). NAGM CBF and CBV were significantly reduced and MTT was prolonged compared with healthy control GM for all comparisons except between healthy controls and RRMS-NI for CBV. NAWM CBF and CBV were significantly lower and MTT was prolonged between healthy controls and RRMS-I but not RRMS-NI. WMLs demonstrated significant CBF and CBV reduction compared with NAWM in patients with RRMS-NI (33% and 31%) and those with RRMS-I (26% and 23%), respectively. WMLs also demonstrated mild but significant MTT prolongation compared with NAWM in patients with RRMS-NI and RRMS-I. WML CBF and CBV in RRMS-I were significantly lower compared with RRMS-NI (Table 2). No absolute CL perfusion difference was present between RRMS-I and RRMS-NI, though both CBF and CBV were modestly elevated and MTT was prolonged in RRMS-I. CLs showed significant CBF and CBV reduction compared with NAGM for RRMS-NI (48% and 44%) and RRMS-I (27% and

19%), respectively. Significant MTT prolongation was present in CLs compared with NAGM for RRMS-I (15%).

Scatterplots of the average CBF and CBV for CL and WML are illustrated in Figs 3 and 4, respectively. Four classifiers are highlighted in each figure, including standard lesions (neither CBF nor CBV outliers), CBF outliers, CBV outliers, and CBV × CBF outliers. As expected, standard CLs and WMLs present similar CBF and CBV compared with the whole CL and WML analysis, respectively, for both RRMS groups (On-line Table 1). However, CBF outliers and CBV outliers showed higher median values. MTT outliers (not shown) demonstrated reduced WML perfusion for each group. No MTT outliers were present within RRMS-I. On-line Table 2 illustrates the dispersion of the perfusion values for each lesion for both RRMS groups, demonstrating smaller dispersion values for CLs compared with WMLs for each perfusion parameter.

DISCUSSION

Progressive NAGM and NAWM CBF and CBV reduction was demonstrated with cognitive impairment. Significant differences were seen between both RRMS subgroups and healthy controls in all comparisons except for NAGM CBV between healthy controls and RRMS-NI and for all NAWM perfusion parameters between healthy controls and RRMS-NI. CL perfusion was not significantly different between RRMS subgroups. However, the CL/NAGM ratio was fallaciously lower in RRMS-I compared with RRMS-NI due to a greater NAGM than CL perfusion reduction, minimizing the difference between CL and NAGM perfusion. Similarly, despite significant WML/NAWM perfusion reduction between RRMS-NI and RRMS-I, the WML/NAWM ratios were also reduced with cognitive impairment. These findings underscore the limitations of using either NAWM or NAGM regions to normalize cortical lesion or white matter lesion perfusion values and emphasize the need for absolute perfusion measurement.²

Consistently larger reductions were measured within the NAWM and NAGM with cognitive impairment compared with WMLs and CLs, respectively. This finding highlights the importance of considering these apparently normal regions in addition to conventional structural and lesional parameters during the assessment of cognitive impairment in patients with MS.^{1,18,19} Our results are supported by previous studies demonstrating NAGM and NAWM perfusion abnormalities with MS disease progression and in cognitively impaired patients with RRMS.^{6,9,20} They also highlight the increasingly recognized role of perfusion as a surrogate of cognitive impairment.⁶ We demonstrate greater sensitivity of NAGM to cognitive impairment than NAWM with differences demonstrated between healthy control GM/WM and RRMS-NI only for NAGM. Indeed, a recent study

Table 1: Participant demographic data, neurocognitive scores, and fractional brain volume^a

	HC (n = 19)	RRMS-NI (n = 19)	RRMS-I (n = 20)
Demographics			
Age (yr)	49.0 ± 7.1	46.4 ± 7.2	48.1 ± 4.7
Female sex (No.) (%)	14 (73.68)	15 (78.95)	12 (60)
Education (yr)	16.9 ± 2.9 ^b	16.1 ± 1.3	14.6 ± 1.9 ^b
Disease duration (yr)	0.0 ± 0.0	11.8 ± 5.4	11.6 ± 4.9
HADS-A (log) (median) (IQR)	3 (1–6) ^{b,c}	6 (5–7) ^c	8 (7–10) ^b
HADS-D (log) (median) (IQR)	2 (1–3) ^b	3 (1,5) ^d	8 (6–10) ^{b,d}
EDSS median (IQR)	NA	1.5 (1–2) ^d	2.5 (2–3) ^d
Percentage fractional brain volume			
BPF	79 ± 9 ^b	75 ± 6	72 ± 8 ^b
fC	45.15 ± 5.12	43.43 ± 3.91	41.87 ± 5.50
fWM	31.66 ± 4.07 ^b	29.61 ± 2.83	28.35 ± 3.5 ^b
fCL	0.00 ± 0.00 ^b	0.01 ± 0.01	0.01 ± 0.02 ^b
fBG	1.35 ± 0.19	1.31 ± 0.18	1.25 ± 0.22
fTh	0.68 ± 0.12 ^b	0.64 ± 0.14	0.55 ± 0.14 ^b
fWML	0.00 ± 0.00 ^b	0.67 ± 0.74	0.92 ± 0.90 ^b
fTI hole	0.00 ± 0.00 ^b	0.23 ± 0.22	0.410 ± 0.506 ^b
fCSF	21.16 ± 8.78 ^b	24.10 ± 6.24	26.64 ± 7.32 ^b

Note:—HADS indicates Hospital Anxiety [A] and Depression [D] Scale; EDSS, Extended Disability Status Scale; BPF, brain parenchymal fraction; fC, fractional cortical volume; fWM, fractional white matter volume; fCL, fractional cortical lesions volume; fBG, fractional basal ganglia volume; fTh, fractional thalamus volume; fWML, fractional white matter lesions volume; fTI hole, fractional TI hole volume; fCSF, fractional CSF volume; HC, healthy controls; NA, not applicable; IQR, interquartile range.

^a All values are means unless otherwise specified. Significant *P* value < .017.

^b HC vs RRMS-I.

^c HC vs RRMS-NI.

^d RRMS-NI vs RRMS-I.

Table 2: Comparison of perfusion parameters between study groups^a

	HC (n = 19)		RRMS-NI (n = 19)				RRMS-I (n = 20)			
	WM	GM	WML	NAWM	CL	NAGM	WML	NAWM	CL	NAGM
CBF (mL/100 g per min)	21.8 ^b (19.7–28.4)	44.0 ^f (37.9–49.5)	14.4 ^{d,e} (9.9–20.2)	21.5 ^{d,e} (16.0–29.5)	21.4 ^c (15.7–32.3)	41.1 ^{c,d,f} (29.8–55.7)	12.5 ^{d,e} (8.1–18.5)	17.0 ^{b,d,e} (13.2–25.2)	23.1 ^c (15.4–34.3)	31.7 ^{c,d,f} (24.6–44.5)
CBV (mL/100 g)	1.5 ^b (1.2–1.9)	2.8 ^f (2.1–3.2)	1.1 ^{d,e} (0.8–1.6)	1.6 ^{d,e} (1.2–2.1)	1.4 ^c (1.1–2.0)	2.5 ^{c,d} (1.9–3.4)	1.0 ^{d,e} (0.7–1.4)	1.3 ^{b,d,e} (1.0–1.7)	1.7 ^c (1.2–2.4)	2.1 ^{c,d,f} (1.7–2.7)
MTT (min)	4.3 ^b (3.9–5.0)	3.8 ^f (3.4–4.3)	4.8 ^e (4.1–5.9)	4.6 ^e (4.1–5.2)	4.3 (3.5–4.9)	3.9 ^{d,f} (3.3–4.4)	5.0 ^e (4.2–6.0)	4.8 ^{b,e} (4.3–5.2)	4.6 ^c (3.9–5.4)	4.0 ^{c,d,f} (3.5–4.6)

Note:—HC indicates healthy controls.

^a Normal-appearing GM and WM tissues are compared across patients with RRMS who were cognitively unimpaired and impaired and with healthy controls with corrected *P* < .017 (ie, .05/3) identified as significantly different. Lesion perfusion was also independently compared across disease groups and with the corresponding normal-appearing tissue within each patient group with *P* < .05 identified as significantly different. The values represent medians; the interquartile range for values are giving in parentheses.

^b HC WM vs NAWM.

^c CL vs NAGM.

^d RRMS-NI vs RRMS-I.

^e WML vs NAWM.

^f HC GM vs NAGM.

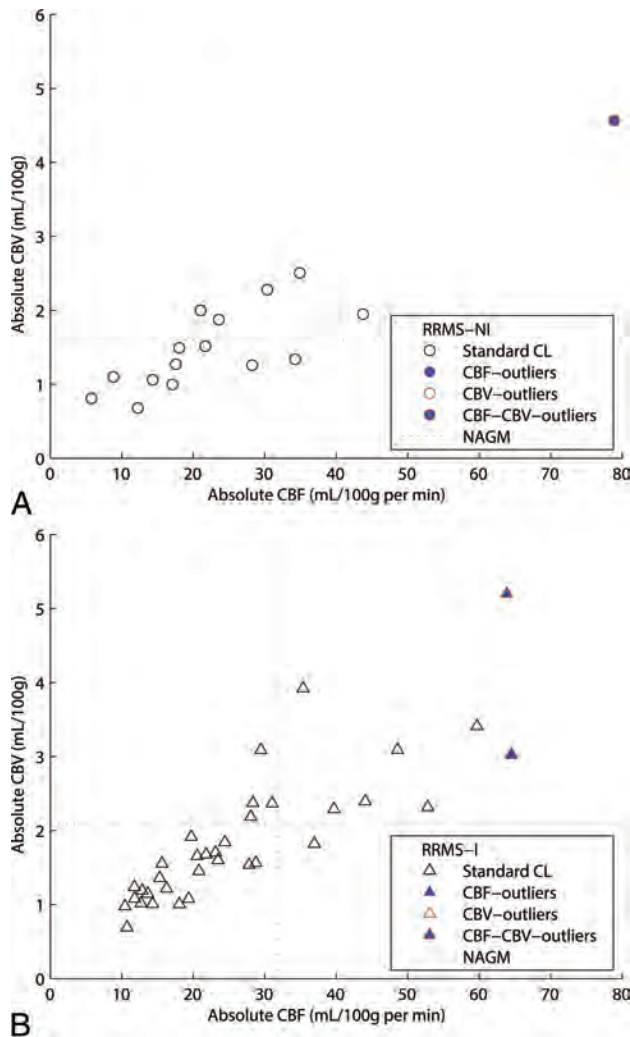


FIG 3. Distribution of the absolute perfusion cortical lesion results in the construction of 4 different populations: Standard CL (neither CBF nor CBV outliers), CBF outliers, CBV outliers, and CBV-CBF outliers (CBV outliers that are also CBF outliers). Absolute values of cerebral blood flow and cerebral blood volume are reported on the x-axis and y-axis, respectively. Each RRMS-NI lesion (A) is represented by a *circle*, and RRMS-I lesion (B) is represented by a *triangle*.

using pseudocontinuous arterial spin-labeled/labeling perfusion found significant GM perfusion differences between healthy controls and patients with very early RRMS, independent of structural differences.⁹

The absence of CL CBF or CBV differences compared with WMLs between the RRMS subgroups is supported by histopathologic studies showing that unlike WMLs, there is little inflammatory infiltration, activation, or evidence for plasma protein extravasation in CLs.²¹⁻²³ This also explains the greater difficulty in prospective clinical identification of CLs on imaging such as double inversion recovery or FLAIR, because the more tightly packed cortical structures prevent fulminant inflammation and edema formation, which characterizes and assists in the visualization of WMLs.²⁴⁻²⁷ In support of this assertion, CLs were associated with less dispersion and fewer perfusion outliers than WMLs. The greater outliers in WMLs imply increased lesion perfusion heterogeneity and confirm different pathophysiologic mechanisms for CL and WML formation.^{3,28-31}

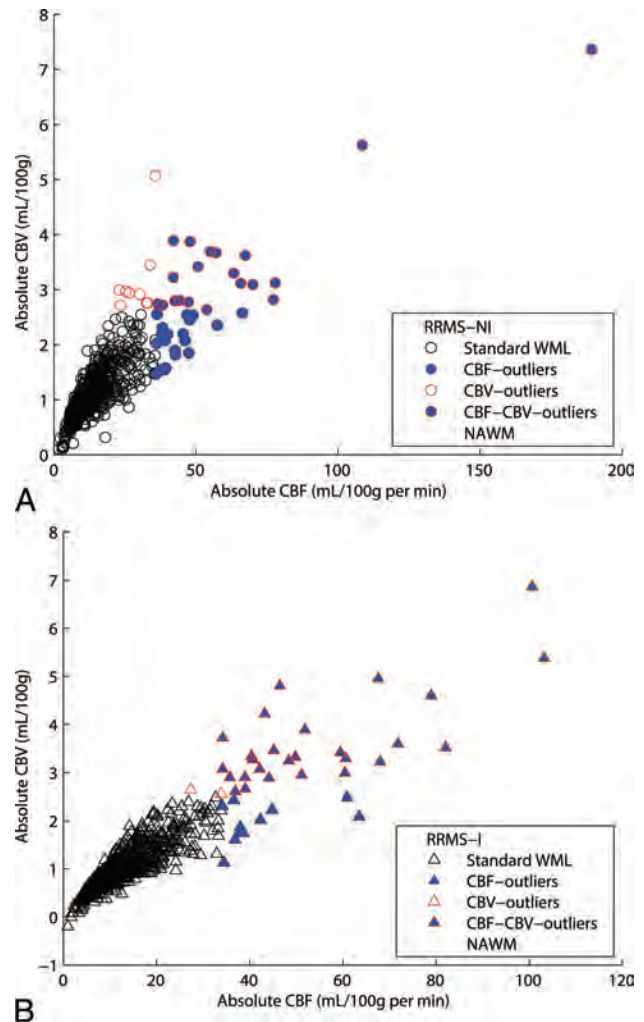


FIG 4. Distribution of the absolute perfusion white matter lesion results in the construction of 4 different populations by using the interquartile range method: Standard WML (neither CBF nor CBV outliers), CBF outliers, CBV outliers, and CBV-CBF outliers (CBV outliers that are also CBF outliers). Absolute values of cerebral blood flow and cerebral blood volume are reported on the x-axis and y-axis, respectively. Each RRMS-NI lesion (A) is represented by a *circle*, and RRMS-I lesion (B) is represented by a *triangle*.

CLs were identified by using phase-sensitive inversion recovery. Existing clinical and high-field-strength research imaging sequences detect a fraction of histopathologically identified lesions.^{30,31} Therefore, we cannot entirely exclude the presence of CLs within the so-called NAGM ROI. It could be argued that these lesions may account for the strength of NAGM differences presented. However, considering the voxelwise analytic approach, the total number of voxels constituting CLs is expected to be fractional compared with the total number of true NAGM voxels; therefore, we believe this contribution to be trivial. Only imaging-pathologic correlation studies could truly resolve this question. Another limitation of this work is the relatively low resolution of perfusion images in comparison with structural T1- and T2-weighted images, resulting in partial volume effects during structural-to-perfusion image registration, whereby CL and WML ROIs may be eliminated or altered in size. To address this issue, we applied volume thresholding of the registered segmentations;

however, complete elimination of these artifacts is not possible. Future studies could use differences in perfusion characteristics between CLs and WMLs to prospectively identify and segment lesions on the native perfusion images.

GM abnormalities in MS could occur due to 2 underlying pathogenic mechanisms (primary GM damage and GM damage secondary to WM damage), which cumulatively contribute to degeneration of axons and GM demyelination.²⁸ Primary GM abnormality may result from meningeal inflammation caused by soluble cytotoxic/myelinotoxic factors as demonstrated by Magliozzi et al,³² who depicted a spatial relation between ectopic meningeal B-cell follicles and a superficial-to-deep gradient of cortical pathology. GM neuroaxonal degeneration secondary to WM damage has been associated with a state of “virtual hypoxia” due to high adenosine triphosphate production caused by abnormal distribution of sodium channels in active white matter lesions, which are protein-positive for amyloid precursor.^{33,34} Excitotoxicity and axonal damage due to glutamate imbalance, discriminatory reaction to acetylcholinesterase inhibitor rivastigmine, and variation in firing patterns among different sodium channels have, furthermore, been thought to be involved in GM damage secondary to WM abnormality.³⁵⁻³⁷ Perfusion abnormalities in the absence of structural anomalies have been previously observed in patients with RRMS without and with cognitive impairment.^{9,38} In a preceding study using the same patient cohort, we further demonstrated cortical perfusion reduction to be independent of white matter volume.³⁸ These observations collectively suggest a primary vascular or mitochondrial disturbance as the most probable mechanism of GM abnormality in our patient cohort.

There remains a need for tools and techniques to assess the integrity of the cortex and to detect cortical lesions. Techniques that enable CL detection with high sensitivity and specificity could aid in better quantifying the relationship between CL and clinical outcomes such as physical/cognitive impairment and treatment effect. While only imaging-pathologic correlation studies could truly validate CL detection, the magnitude of 30%–50% perfusion differences between NAGM and CLs is very encouraging and provides ample signal for discrimination, unlike attempts in structural MR imaging. Future work includes the use of image-processing techniques such as texture analysis to enable better detection of CLs by exploiting the large NAGM/CL perfusion differences seen.^{39,40}

CONCLUSIONS

Significant WML, CL, NAWM, and NAGM changes are present between healthy controls and cognitively impaired patients with RRMS. The greatest changes are present within NAGM and NAWM, necessitating absolute rather than relative lesion perfusion measurement.

Disclosures: Charles G. Cantrell—RELATED: Grant: American Heart Association (14PRE20380810).* Anthony Feinstein—RELATED: Grant: MS Society of Canada*; UNRELATED: Payment for Lectures (including service on Speakers Bureaus): Merck Serono, Teva Neurosciences, Biogen, Novartis, Comments: Speaker's honoraria. Liesly Lee—UNRELATED: Consultancy: Novartis Canada, Biogen Canada, Genzyme, Serono, Canada, Teva Neurosciences, Comments: have served and given lectures for named companies associated with therapeutics in multiple sclerosis; Grants/Grants Pending: Site Principal Investigator for clinical trials with the following companies:

Biogen Canada, Genzyme, Serono Canada, Teva Neurosciences, Novartis Canada; Payment for Development of Educational Presentations: Biogen Canada, Serono Canada, Novartis Canada, Comments: chairing educational venues in multiple sclerosis. *Money paid to the institution.

REFERENCES

1. Kutzelnigg A, Lucchinetti CF, Stadelmann C, et al. **Cortical demyelination and diffuse white matter injury in multiple sclerosis.** *Brain* 2005;128:2705–12 CrossRef Medline
2. Peruzzo D, Castellaro M, Calabrese M, et al. **Heterogeneity of cortical lesions in multiple sclerosis: an MRI perfusion study.** *J Cereb Blood Flow Metab* 2013;33:457–63 CrossRef Medline
3. Calabrese M, Agosta F, Rinaldi F, et al. **Cortical lesions and atrophy associated with cognitive impairment in relapsing-remitting multiple sclerosis.** *Arch Neurol* 2009;66:1144–50 Medline
4. Calabrese M, Poretto V, Favaretto A, et al. **Cortical lesion load associates with progression of disability in multiple sclerosis.** *Brain* 2012;135:2952–61 CrossRef Medline
5. Yao B, Hametner S, van Gelderen P, et al. **7 Tesla magnetic resonance imaging to detect cortical pathology in multiple sclerosis.** *PLoS One* 2014;9:e108863 CrossRef Medline
6. Aviv RI, Francis PL, Tenenbein R, et al. **Decreased frontal lobe gray matter perfusion in cognitively impaired patients with secondary-progressive multiple sclerosis detected by the bookend technique.** *AJNR Am J Neuroradiol* 2012;33:1779–85 CrossRef Medline
7. Adhya S, Johnson G, Herbert J, et al. **Pattern of hemodynamic impairment in multiple sclerosis: dynamic susceptibility contrast perfusion MR imaging at 3.0 T.** *Neuroimage* 2006;33:1029–35 CrossRef Medline
8. Law M, Saindane AM, Ge Y, et al. **Microvascular abnormality in relapsing-remitting multiple sclerosis: perfusion MR imaging findings in normal-appearing white matter.** *Radiology* 2004;231:645–52 CrossRef Medline
9. Debernard L, Melzer TR, Van Stockum S, et al. **Reduced grey matter perfusion without volume loss in early relapsing-remitting multiple sclerosis.** *J Neurol Neurosurg Psychiatry* 2014;85:544–51 CrossRef Medline
10. Francis PL, Jakubovic R, O'Connor P, et al. **Robust perfusion deficits in cognitively impaired patients with secondary-progressive multiple sclerosis.** *AJNR Am J Neuroradiol* 2013;34:62–67 CrossRef Medline
11. Carroll TJ, Horowitz S, Shin W, et al. **Quantification of cerebral perfusion using the “bookend technique”: an evaluation in CNS tumors.** *Magn Reson Imaging* 2008;26:1352–59 CrossRef Medline
12. Shin W, Horowitz S, Ragin A, et al. **Quantitative cerebral perfusion using dynamic susceptibility contrast MRI: evaluation of reproducibility and age- and gender-dependence with fully automatic image postprocessing algorithm.** *Magn Reson Med* 2007;58:1232–41 CrossRef Medline
13. Ashburner J, Friston KJ. **Unified segmentation.** *Neuroimage* 2005;26:839–51 CrossRef Medline
14. Shah MK, Shin W, Parikh VS, et al. **Quantitative cerebral MR perfusion imaging: preliminary results in stroke.** *J Magn Reson Imaging* 2010;32:796–802 CrossRef Medline
15. Srouf JM, Shin W, Shah S, et al. **SCALE-PWI: a pulse sequence for absolute quantitative cerebral perfusion imaging.** *J Cereb Blood Flow Metab* 2011;31:1272–82 CrossRef Medline
16. Rempp KA, Brix G, Wenz F, et al. **Quantification of regional cerebral blood flow and volume with dynamic susceptibility contrast-enhanced MR imaging.** *Radiology* 1994;193:637–41 CrossRef Medline
17. Sakaie KE, Shin W, Curtin KR, et al. **Method for improving the accuracy of quantitative cerebral perfusion imaging.** *J Magn Reson Imaging* 2005;21:512–19 CrossRef Medline
18. Dineen RA, Vilisaar J, Hlinka J, et al. **Disconnection as a mechanism for cognitive dysfunction in multiple sclerosis.** *Brain* 2009;132:239–49 Medline
19. Roosendaal SD, Geurts JJ, Vrenken H, et al. **Regional DTI differences**

- in multiple sclerosis patients. *Neuroimage* 2009;44:1397–403 CrossRef Medline
20. Rocca MA, Amato MP, De Stefano N, et al; MAGNIMS Study Group. **Clinical and imaging assessment of cognitive dysfunction in multiple sclerosis.** *Lancet Neurol* 2015;14:302–17 CrossRef Medline
 21. Sánchez MP, Nieto A, Barroso J, et al. **Brain atrophy as a marker of cognitive impairment in mildly disabling relapsing-remitting multiple sclerosis.** *Eur J Neurol* 2008;15:1091–99 CrossRef Medline
 22. van Horssen J, Brink BP, de Vries HE, et al. **The blood-brain barrier in cortical multiple sclerosis lesions.** *J Neuropathol Exp Neurol* 2007;66:321–28 CrossRef Medline
 23. Brink BP, Veerhuis R, Breij EC, et al. **The pathology of multiple sclerosis is location-dependent: no significant complement activation is detected in purely cortical lesions.** *J Neuropathol Exp Neurol* 2005;64:147–55 CrossRef Medline
 24. Rao SM, Leo GJ, Bernardin L, et al. **Cognitive dysfunction in multiple sclerosis. I. Frequency, patterns, and prediction.** *Neurology* 1991;41:685–91 CrossRef Medline
 25. Rovaris M, Youstry T, Calori G, et al. **Sensitivity and reproducibility of fast-FLAIR, FSE, and TGSE sequences for the MRI assessment of brain lesion load in multiple sclerosis: a preliminary study.** *J Neuroimaging* 1997;7:98–102 CrossRef Medline
 26. Bakshi R, Ariyaratana S, Benedict RH, et al. **Fluid-attenuated inversion recovery magnetic resonance imaging detects cortical and juxtacortical multiple sclerosis lesions.** *Arch Neurol* 2001;58:742–48 CrossRef Medline
 27. Benedict RH, Zivadinov R. **Predicting neuropsychological abnormalities in multiple sclerosis.** *J Neurol Sci* 2006;245:67–72 CrossRef Medline
 28. Geurts JJ, Barkhof F. **Grey matter pathology in multiple sclerosis.** *Lancet Neurol* 2008;7:841–51 CrossRef Medline
 29. Giorgio A, Stromillo ML, Rossi F, et al. **Cortical lesions in radiologically isolated syndrome.** *Neurology* 2011;77:1896–99 CrossRef Medline
 30. Klaver R, De Vries HE, Schenk GJ, et al. **Grey matter damage in multiple sclerosis: a pathology perspective.** *Prion* 2013;7:66–75 CrossRef Medline
 31. Stadelmann C, Wegner C, Brück W. **Inflammation, demyelination, and degeneration: recent insights from ms pathology.** *Biochim Biophys Acta* 2011;1812:275–82 CrossRef Medline
 32. Magliozzi R, Howell O, Vora A, et al. **Meningeal B-cell follicles in secondary progressive multiple sclerosis associate with early onset of disease and severe cortical pathology.** *Brain* 2007;130:1089–104 Medline
 33. Craner MJ, Newcombe J, Black JA, et al. **Molecular changes in neurons in multiple sclerosis: altered axonal expression of Nav1.2 and Nav1.6 sodium channels and NA⁺/CA2⁺ exchanger.** *Proc Natl Acad Sci U S A* 2004;101:8168–73 CrossRef Medline
 34. Stys PK. **Axonal degeneration in multiple sclerosis: is it time for neuroprotective strategies?** *Ann Neurol* 2004;55:601–03 CrossRef Medline
 35. Waxman SG. **The neuron as a dynamic electrogenic machine: modulation of sodium-channel expression as a basis for functional plasticity in neurons.** *Philos Trans R Soc Lond B Biol Sci* 2000;355:199–213 CrossRef Medline
 36. Geurts JJ, Wolswijk G, Bö L, et al. **Altered expression patterns of group I and II metabotropic glutamate receptors in multiple sclerosis.** *Brain* 2003;126:1755–66 CrossRef Medline
 37. Parry AM, Scott RB, Palace J, et al. **Potentially adaptive functional changes in cognitive processing for patients with multiple sclerosis and their acute modulation by rivastigmine.** *Brain* 2003;126:2750–60 CrossRef Medline
 38. Hojjat S, Cantrell C, Carroll T, et al. **Bookend perfusion reduction in the absence of structural differences in cognitively impaired versus unimpaired RRMS patients.** *Mult Scler* 2016 Feb 4. [Epub ahead of print] Medline
 39. Haijek M; Benoit-Cattin H; European Cooperation in the Field of Scientific and Technical Research (organizace), et al. *Texture Analysis for Magnetic Resonance Imaging.* Prague: Med4publishing; 2006
 40. Harrison LC, Raunio M, Holli KK, et al. **MRI texture analysis in multiple sclerosis: toward a clinical analysis protocol.** *Acad Radiol* 2010;17:696–707 CrossRef Medline

A Diffusion Tensor Imaging Study on White Matter Abnormalities in Patients with Type 2 Diabetes Using Tract-Based Spatial Statistics

Y. Xiong, Y. Sui, Z. Xu, Q. Zhang, M.M. Karaman, K. Cai, T.M. Anderson, W. Zhu, J. Wang, and X.J. Zhou



ABSTRACT

BACKGROUND AND PURPOSE: Patients with type 2 diabetes mellitus have considerably higher risk of developing cognitive impairment and dementia. WM changes in these patients have been reported. Our aim was to demonstrate that gradual and continuous WM change and the associated cognitive decline in patients with type 2 diabetes mellitus can be captured by DTI parameters, which can be used to complement neuropsychological test scores in identifying patients with type 2 diabetes mellitus with and without mild cognitive impairment.

MATERIALS AND METHODS: Forty-two patients with type 2 diabetes mellitus, divided into a group with mild cognitive impairment ($n = 20$) and a group with normal cognition ($n = 22$), were enrolled with age-, sex-, and education-matched healthy controls ($n = 26$). 3T DTI followed by Tract-Based Spatial Statistics analysis was used to investigate the differences in fractional anisotropy, mean diffusivity, axial diffusivity (λ_1), and radial diffusivity (λ_{23}) among the groups. A receiver operating characteristic analysis assessed the performance of DTI parameters for separating the 2 groups with type 2 diabetes mellitus.

RESULTS: The whole-brain Tract-Based Spatial Statistics analysis revealed that 7.3% and 24.9% of the WM exhibited decreased fractional anisotropy and increased mean diffusivity ($P < .05$), respectively, between the diabetes mellitus with mild cognitive impairment and the diabetes mellitus with normal cognition groups, while considerably larger WM regions showed fractional anisotropy (36.6%) and mean diffusivity (58.8%) changes between the diabetes mellitus with mild cognitive impairment and the healthy control groups. These changes were caused primarily by an elevated radial diffusivity observed in the patients with diabetes mellitus with mild cognitive impairment. Radial diffusivity also exhibited subtle but statistically significant changes between the diabetes mellitus with normal cognition and the healthy control groups. Analyses on individual fiber tracts showed pronounced fractional anisotropy reduction and mean diffusivity elevation in regions related to cognitive functions. The receiver operating characteristic analysis on the right cingulum (hippocampus) showed that fractional anisotropy produced a larger area under the curve (0.832) than mean diffusivity (0.753) for separating mild cognitive impairment from normal cognition among patients with type 2 diabetes mellitus. When fractional anisotropy was combined with mean diffusivity, the area under the curve was further improved to 0.857.

CONCLUSIONS: DTI parameters can show a substantial difference between patients with type 2 diabetes mellitus with and without mild cognitive impairment, suggesting their potential use as an imaging marker for detecting cognitive decline in patients with type 2 diabetes mellitus. More important, DTI parameters may capture gradual and continuous WM changes that can be associated with early stages of cognitive decline in patients with type 2 diabetes mellitus before they can be diagnosed clinically by using conventional neuropsychological tests.

ABBREVIATIONS: DM-MCI = diabetes mellitus with mild cognitive impairment; DM-NC = diabetes mellitus with normal cognition; FA = fractional anisotropy; HC = healthy control; MCI = mild cognitive impairment; MD = mean diffusivity; TBSS = Tract-Based Spatial Statistics; T2DM = type 2 diabetes mellitus; ROC = receiver operating characteristic

Type 2 diabetes mellitus (T2DM) is a prevalent disease that affects >360 million people worldwide and is projected to rise to 552 million cases by 2030.¹ This metabolic disease can affect a number of

organs, including the brain, eye, kidney, heart, vasculature, and peripheral nerves due to long-term sustained hyperglycemia. Brain damage caused by diabetes has attracted increased attention during

Received July 14, 2015; accepted after revision January 7, 2016.

From the Departments of Radiology (Y.X., W.Z.) and Neurology (Q.Z.), Tongji Hospital, and Department of Pathophysiology (Z.X., J.W.), Tongji Medical College, Huazhong University of Science and Technology, Wuhan, China; and Center for Magnetic Resonance Research (Y.X., Y.S., M.M.K., K.C., X.J.Z.) and Departments of Radiology (K.C., T.M.A., X.J.Z.), Bioengineering (Y.S., X.J.Z.), and Neurosurgery (X.J.Z.), University of Illinois Hospital and Health Sciences System, Chicago, Illinois.

This work was supported, in part, by the National Natural Science Foundation of China (grant Nos. 81171308 and 81471230), the National Program of the Ministry of Science and Technology of China during the "12th Five-Year Plan" (grant No. 2011BAI08B10), and the US National Institutes of Health (grant No. 1S10RR028898).

Paper previously presented in part at: Annual Meeting of the International Society for Magnetic Resonance in Medicine, May 30–June 5, 2015; Toronto, Ontario, Canada.

Please address correspondence to X. Joe Zhou, PhD, Advanced Imaging Center, Ste 103, 2242 W Harrison St, Chicago, IL 60612; e-mail: xjzhou@uic.edu; Jianzhi Wang, PhD, Department of Pathophysiology, Tongji Medical College, Huazhong University of Science and Technology, 13 Hangkong Rd, 430030, Wuhan, P.R. China; e-mail: wangjz@mail.hust.edu.cn

Indicates open access to non-subscribers at www.ajnr.org

Indicates article with supplemental on-line table.

Indicates article with supplemental on-line photos.

<http://dx.doi.org/10.3174/ajnr.A4740>

recent years. Longitudinal population-based studies have revealed that the relative risk of dementia is 1.2–2.8 times higher in individuals with diabetes relative to those without.^{2,3}

Although neuropsychological tests such as the Mini-Mental State Examination and the Montreal Cognitive Assessment remain the prevailing methods for evaluating patients with T2DM with and without cognitive decline, a number of neuroimaging studies have emerged to investigate the compromised brain functions of patients with T2DM by measuring changes in perfusion,⁴ metabolism,⁵ spontaneous brain activity at resting state,⁶ and functional connectivity.⁷ The observed functional changes have been associated with sustained hyperglycemia and the resulting alterations in cerebral vasculature, neurotrophic factors, and neurotransmitters.⁸ To study the underlying brain structural changes associated with the functional and metabolic abnormalities, Zhang et al⁹ compared the gray matter volume of patients with T2DM with and without mild cognitive impairment (MCI) and concluded that middle temporal gyrus atrophy was associated with an increased risk of MCI in patients with T2DM. Cerebral atrophy and WM hyperintensities were also reported in patients with T2DM¹⁰ and were linked to compromised cognition.¹¹ Additionally, recent studies focusing on type 1 diabetes mellitus revealed WM changes in the superior parietal lobule¹² and more pronounced WM hyperintensities in patients with slower information processing.¹³ The observed changes in WM are of particular interest, given its important role as a conduit to transmit neuronal signals to the functional units in the gray matter.

DTI is a powerful neuroimaging method to study WM structural changes in many neurologic disorders, including MCI and Alzheimer disease.¹⁴ In a study by Hsu et al,¹⁵ decreased fractional anisotropy (FA) was found in the frontal lobe of patients with T2DM with both global and voxel-based analyses. Decreased FA in the cingulum bundle and uncinate fasciculus,¹⁶ and increased mean diffusivity (MD) in the bilateral hemisphere tracts,¹⁷ were also reported. Recently, Zhang et al¹⁸ observed that patients with T2DM with various degrees of cognitive impairment exhibited widespread WM disruptions, which correlated well with executive dysfunction.

Although the risk of developing cognitive impairment is considerably elevated among patients with T2DM, not all patients with T2DM develop cognitive impairment based on neuropsychological tests. This raises an interesting and important question of whether the observed WM change occurs only in patients with T2DM with cognitive impairment or in all patients with T2DM. We hypothesize that the WM change in patients with T2DM, in accordance with cognitive decline, is a gradual and continuous process that may not be adequately reflected by neuropsychological test scores but can be captured by DTI. The present study, therefore, aimed to test this hypothesis by subdividing the patients with T2DM into 2 groups, those exhibiting MCI and those without, and investigating their DTI parameter changes against a third group of age-, sex-, and education-matched healthy subjects. Additionally, the study also intended to demonstrate that DTI parameters can be used quantitatively to complement neuropsychological test scores in characterizing patients with T2DM with and without MCI.

MATERIALS AND METHODS

Subjects

With approval by the institutional review board, we used a prospective cross-sectional study design with a recruitment of 70 right-handed adult subjects who provided written informed consent. Among the subjects, 44 were patients with T2DM (between 51 and 72 years of age; 27 women) recruited from the endocrinology clinic of Tongji Hospital of China between May 2013 and May 2014. Detailed information about hypoglycemic agent application, family history, and clinical symptoms and complications was collected. Clinical examinations and laboratory tests, including blood biochemistry; lipids and cholesterol levels; plasma glucose and glycosylated hemoglobin A1c levels; and body mass index, were performed.

Diagnosis of T2DM was based on established criteria (ie, diabetes symptoms and a fasting plasma glucose level of >7.0 mmol/L or a random plasma glucose level of >11.1 mmol/L or a 2-hour glucose level of >11.1 mmol/L after an oral glucose tolerance test), according to the American Diabetes Association recommendations.¹⁹ A battery of neuropsychological tests was performed on the 44 patients with confirmed T2DM to assess their cognitive functions as detailed in the next subsection. On the basis of the results of the neuropsychological tests, the patients with T2DM were divided into 2 groups with and without cognitive impairment. Twenty-six subjects with euglycemia (between 50 and 73 years of age; 17 women; fasting glucose level of <7.0 mmol/L, glycosylated hemoglobin A1c percentage of $<6.0\%$) with normal cognition (Montreal Cognitive Assessment score of ≥ 28 and Mini-Mental State Examination score of ≥ 27) were also enrolled to serve as age-, sex-, and education-matched healthy controls (denoted as the healthy control [HC] group hereafter).

For all 3 groups, we used the following exclusion criteria: 1) organic lesions in the brain, such as brain tumors, cerebral infarction, hemorrhage, or vascular malformation; 2) a history of stroke, epilepsy, head trauma, or brain surgery; 3) systemic organic disease or a history of tumors; 4) moderate and severe hypertension (systolic pressure of ≥ 160 mm Hg or diastolic pressure of ≥ 100 mm Hg), or hyperlipidemia; 5) any contraindication to MR imaging examination, such as the presence of metallic implants, fixed metal dentures, pacemaker, or claustrophobia; or 6) other types of diabetes. In addition to the above criteria, 2 patients were excluded from data analysis because of excessive motion during the MR imaging ($n = 1$) or scanner malfunction ($n = 1$), resulting in 42 patients with T2DM and 26 healthy controls (no exclusions) whose imaging data were used in the final analysis.

Cognitive Assessment

All patients underwent comprehensive physical, neurologic, and neuropsychological assessments, which included the Mini-Mental State Examination, Montreal Cognitive Assessment, Hachinski Ischemic Score, Activities of Daily Living Test, and Auditory Verbal Learning Test, performed by 2 neurologists (Z.X. and Q.Z.), to subdivide the patients with T2DM into 2 groups with and without MCI. The inclusion criteria for the MCI group were the following: 1) memory decline; 2) both Montreal Cognitive Assessment and Mini-Mental State Examination scores of ≤ 27 ;

and 3) absence of any other physical or mental disorders that can lead to cognitive impairment, resulting in 20 patients with T2DM in the MCI group (the DM-MCI group). The remaining 22 patients formed the group with normal cognition (the DM-NC group). The Hachinski Ischemic Score and Activities of Daily Living tests were used to exclude vascular dementia and evaluate the daily life abilities. Consistency in age, sex, and education level among the DM-MCI, DM-NC, and HC groups was determined with a 1-way ANOVA and a χ^2 test.

Image Acquisition

MR images were acquired on a 3T MR imaging scanner (Discovery MR750; GE Healthcare, Milwaukee, Wisconsin) by using a commercial 32-channel head coil. The subjects were padded with flexible foam to limit head motion. Using axial T2 FLAIR (TR/TE/TI = 8400/160/2100 ms, section thickness = 5 mm, section spacing = 1.5 mm, matrix size = 256×256 , FOV = 24.0×24.0 cm², and NEX = 1) and a sagittal T1-weighted 3D brain volume imaging sequence (TR/TE/TI = 8.2/3.2/450 ms, flip angle = 12°, section thickness = 1 mm, matrix size = $256 \times 256 \times 160$, FOV = 25.6×25.6 cm², and NEX = 1), we obtained high-resolution anatomic images to exclude possible lesions specified in the exclusion criteria. Following anatomic imaging, DTI data were obtained in the axial plane by using a single-shot diffusion-weighted echo-planar imaging sequence with the following parameters: TR/TE = 8500/66.3 ms, FOV = 25.6×25.6 cm², matrix size = 128×128 , section thickness = 2 mm, number of sections = 70, number of diffusion gradient directions = 64, b-value = 1000 s/mm², number of images at a b-value of 0 s/mm² = 5, acceleration factor = 2, and scan time = 9 minutes 55 seconds.

fMRI of the Brain Software Library and Tract-Based Spatial Statistics

The diffusion tensor images were processed by using the fMRI of the Brain Software Library (<http://www.fmrib.ox.ac.uk/fsl>), or FSL.²⁰ Voxelwise statistical analysis of the images was performed by using Tract-Based Spatial Statistics (TBSS; <http://fsl.fmrib.ox.ac.uk/fsl/fslwiki/TBSS>)²¹ with the following steps: First, brain was extracted by using the Brain Extraction Tool (<http://fsl.fmrib.ox.ac.uk/fsl/fslwiki/BET>). An FSL “eddy” tool (<http://fsl.fmrib.ox.ac.uk/fsl/fslwiki/eddy>) was applied as a preventive measure to reduce inconsistent image distortion. After generating the FA maps by using the FMRIB Diffusion Toolbox (<http://fsl.fmrib.ox.ac.uk/fsl/fslwiki/FDT>), we aligned the images from all subjects to an FA standard template through a nonlinear coregistration. The aligned FA maps were then averaged to produce a group mean image, which was used to generate an FA skeleton highlighting the tracts common to the entire group. For each subject, an FA threshold of 0.2 was used before projecting the aligned FA map onto this skeleton. The resulting skeletonized FA maps were then fed into a voxelwise group-level analysis.²² In addition to FA, diffusivity maps based on MD, axial diffusivity (λ_1 , the principal eigenvalue), and radial diffusivity (λ_{23} , the average of the 2 remaining eigenvalues) were generated by using the same steps outlined above. Using an FSL permutation test (FSL Randomise tool with 500 permutations; <http://fsl.fmrib.ox.ac.uk/fsl/fslwiki/Randomise>), we tested FA, MD, λ_1 , and λ_{23} for differences be-

tween the means of the DM-MCI, DM-NC, and HC groups. A significance level of $P < .05$ was used for each of the 4 DTI parameters (FA, MD, λ_1 , and λ_{23}) to declare differences among the patient groups.

ROI-Based Quantitative Analysis

The Johns Hopkins University WM tractography atlas²³ in FSL was used as a standard for WM parcellation. The entire WM was parceled into 48 ROIs by using the 1-mm Johns Hopkins University-ICBM labels (<http://fsl.fmrib.ox.ac.uk/fsl/fslwiki/Atlases>). Specific fiber tracts reported to be relevant to MCI in previous studies²⁴⁻²⁶ were selected in the telencephalon as well as 4 regions in the cerebellum and the brain stem (Fig 1). FA and MD were calculated by averaging the pixel values in each ROI and were reported as mean \pm SD. Using SPSS 17.0 software (IBM, Armonk, New York), we performed a receiver operating characteristic (ROC) analysis to determine the area under the ROC curve for assessing the performance of separating the DM-MCI and DM-NC groups when FA and MD of the right cingulum (hippocampus) were used individually or in combination via a logistic regression algorithm.

The ROC analysis for the combination of FA and MD was performed by using a binomial (bivariate) logistic regression with patient condition (DM-MCI or DM-NC) as the dichotomous criterion variable and FA and MD as the dichotomous predictor variables. This method estimated the probability (P_0) of being in the DM-MCI group by using the following logistic function:

$$P_0 = \exp(a_0 + a_1FA + a_2MD) / [1 + \exp(a_0 + a_1FA + a_2MD)],$$

where a_0 is a constant and a_1 and a_2 are the regression coefficients for FA and MD, respectively. The regression coefficients were determined by using a maximum likelihood method.²⁷

RESULTS

Clinical Data

The clinical and neuropsychological characteristics of the 3 subject groups are summarized in the On-line Table. No significant difference was observed among the 3 groups in age ($P = .130$), sex ($P = .854$), years of education ($P = .216$), and body mass index ($P = .291$). The DM-MCI group exhibited a higher level of glycosylated hemoglobin A1c ($P = .008$) and a trend toward a significant increase in disease duration ($P = .066$) compared with the DM-NC group.

Whole-Brain DTI Comparisons among Groups

The whole-brain TBSS analysis revealed that 7.3% (10,102/137,832 voxels) and 24.9% (34,353/137,832 voxels) of the parcellated regions exhibited decreased FA and increased MD, respectively, in the DM-MCI group compared with the DM-NC group (Fig 2). Analysis of the individual eigenvalues illustrated that the reduced FA and increased MD in the DM-MCI group were caused primarily by an elevated radial diffusivity (λ_{23}), rather than changes in axial diffusivity (λ_1) (Fig 2). Compared with the results in Fig 2, more extensive changes in FA (36.6%; 50,384/137,832 voxels) and MD (58.8%; 81,104/137,832 voxels) of the WM regions across the entire brain were observed between the DM-MCI and the HC

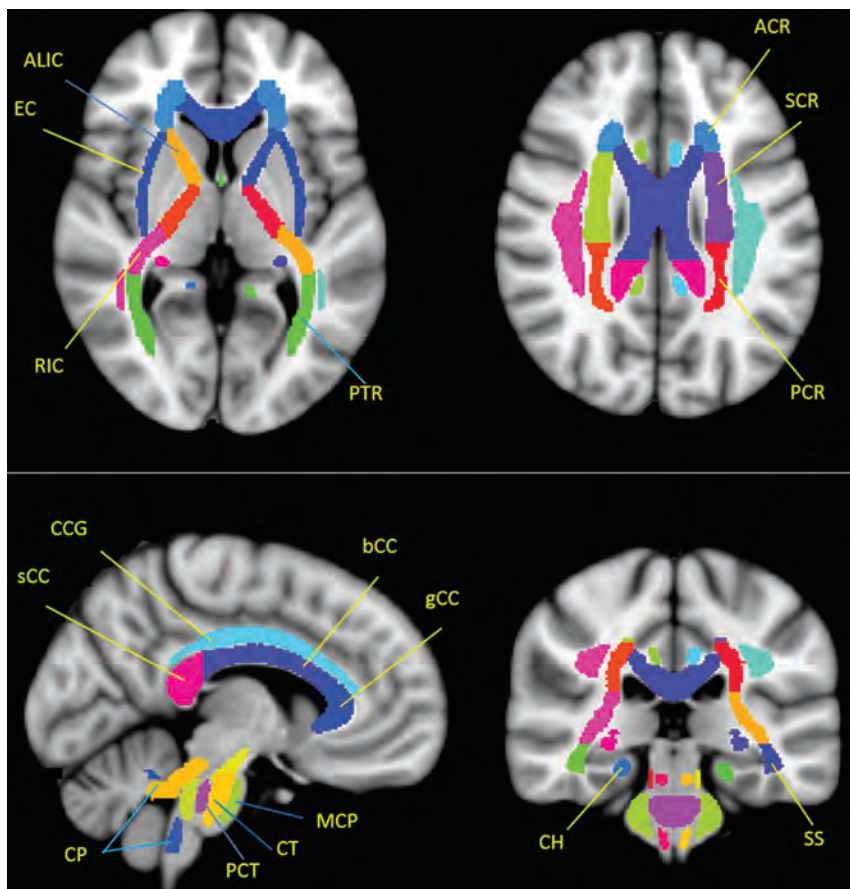


FIG 1. Selected ROIs in the individual fiber analysis according to a Johns Hopkins University–ICBM labels 1-mm template. “.R and .L” in the text indicate right and left side, respectively. In the telencephalon, ALIC indicates anterior limb of internal capsule; ACR, anterior corona radiata; g/b/s CC, corpus callosum (genu/body/splenium); CCG, cingulum (cingulate gyrus); CH, cingulum (hippocampus); EC, external capsule; PCR, posterior corona radiata; PTR, posterior thalamic radiation (including optic radiation); RIC, retrolenticular part of internal capsule; SCR, superior corona radiata; SS, sagittal striatum (including the inferior longitudinal fasciculus and inferior fronto-occipital fasciculus). In the cerebellum and brain stem, CP, indicates cerebellar peduncle; CT, corticospinal tract; MCP, middle cerebellar peduncle; and PCT, pontine crossing tract (a part of MCP).

groups (Fig 3). In addition, λ_1 also showed noticeable changes in Fig 3. These observations indicate that DTI parameters of the DM-NC group differed from those of the HC group; this difference suggests that gradual WM changes have already occurred in the patients with DM-NC, even when neuropsychological tests did not indicate MCI. These findings support our hypothesis. Additional evidence to reinforce our hypothesis can be found in Fig 4, where a direct comparison between the DM-NC and the HC groups reveals moderate changes in radial diffusivity (λ_{23}) in several regions, including the bilateral external capsule and the temporal WM areas, as well as the right frontal WM areas and corona radiata.

Differences in FA and MD of Specific Fiber Tracts among the Groups

Tables 1 and 2 summarize the FA and MD differences ($P < .05$ with false discovery rate correction), respectively, in the selected fibers across the 3 groups. Among the 15 fiber tracts analyzed by using the Johns Hopkins University atlas,²³ significantly decreased FA and increased MD were observed in the

left external capsule between the DM-MCI and DM-NC groups. Additionally, we also observed FA differences in the left anterior limb of the internal capsule, right and left anterior corona radiata, left posterior thalamic radiation, and right and left cingulum (hippocampus), and MD differences in the left retrolenticular part of internal capsule, left superior corona radiata, and right sagittal striatum. These differences, which suggest that FA and MD may serve as alternative surrogates to the conventional neuropsychological test scores, are illustrated in Fig 5A (for FA), -B (for MD). More important, when the DM-NC and the HC groups were compared, significant differences in FA were found in the right corticospinal tract and right cerebral peduncle, and differences in MD were found in the right retrolenticular part of internal capsule and right external capsule. Again, these observations support our hypothesis. Overall, the atlas-based analyses on individual fiber tracts suggested that pronounced FA reduction and/or MD elevation occurred mainly in the internal/external capsule, corona radiata, and cingulum (in the vicinity of the hippocampus) regions.

ROC Analysis

The feasibility of using FA and MD to separate the DM-MCI and DM-NC groups, as indicated by Fig 5, is further demonstrated in an ROC analysis. Figure 6A shows the ROC curves in the right cingulum (hippocampus), using DTI parameters for distinguishing DM-MCI (positive) and DM-NC (negative). FA (area under the ROC curve = 0.832; 95% CI, 0.705–0.958) had a higher area under the ROC curve than MD (0.753; 95% CI, 0.608–0.899). When we combined FA and MD by using a logistic regression model, the area under the ROC curve was further improved to 0.857 (95% CI, 0.735–0.979). Figure 6B shows a scatterplot with all data of patients with T2DM. The best cutoff values of FA and MD, determined by using a Youden index, are indicated by the vertical and the horizontal dashed lines, respectively. The black dashed line corresponds to the cutoff probability of the best sensitivity (0.864) and specificity (0.800) when combining FA and MD.

DISCUSSION

The results of this study (Figs 2–4 and Tables 1 and 2) provided evidence to support our hypothesis that the WM change in patients with T2DM is a gradual and continuous process that may not be adequately reflected by neuropsychological test scores but can be captured in DTI parameters. The observations were made

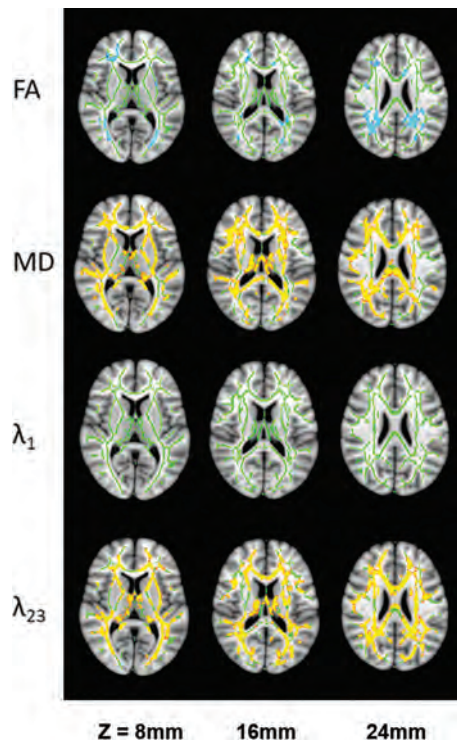


FIG 2. Differences in FA, MD, axial diffusivity (λ_1), and radial diffusivity (λ_{23}) between the DM-MCI and the DM-NC groups in 3 representative sections (see On-line Fig 1 for a complete set of images with whole-brain coverage). All results were obtained from an FSL TBSS analysis. A Montreal Neurological Institute-152 T1 1-mm brain standard space was used as a background image (gray-scale). Green indicates the FA skeleton with a threshold of 0.2 highlighting the fibers used in the comparison; blue–light-blue (thickened for better visibility), regions with decreased FA, MD, λ_1 , or λ_{23} ; and red–yellow (thickened for better visibility), regions with increased FA, MD, λ_1 , or λ_{23} .

possible by dividing the patients with T2DM into 2 groups according to their cognitive functions and examining changes in DTI metrics in each group against healthy controls. Using a prevalent DTI analysis tool, FSL, we observed not only decreased FA and increased MD in the brains of the patients with T2DM with clinically confirmed MCI compared with those without (Figs 2 and 5), but also subtle yet important changes in radial diffusivity (λ_{23}) between the DM-NC and the HC groups (Fig 4). These results have not been reported previously, to our knowledge. We also observed widespread FA and MD changes between the DM-MCI and the HC groups (Fig 3), which reinforced the findings in a recent study.¹⁸

The widespread WM differences in Fig 2 indicate that the observed changes in DTI metrics are strongly coupled with cognitive decline. Using individual eigenvalues, we were able to determine that the FA and MD changes were associated with elevated radial diffusivity, instead of decreased axial diffusivity. Previous studies have related elevated radial diffusivity to a compromised myelin sheath and reduced axial diffusivity to axonal damage.^{28,29} Thus, the WM changes in Fig 2 are likely caused by changes in the myelin sheath or increased interstitial space between the myelin-covered axons in patients with DM-MCI. The exact mechanism explaining why long-term sustained hyperglycemia would compromise the myelin sheath remains unclear. Small-vessel alterations asso-

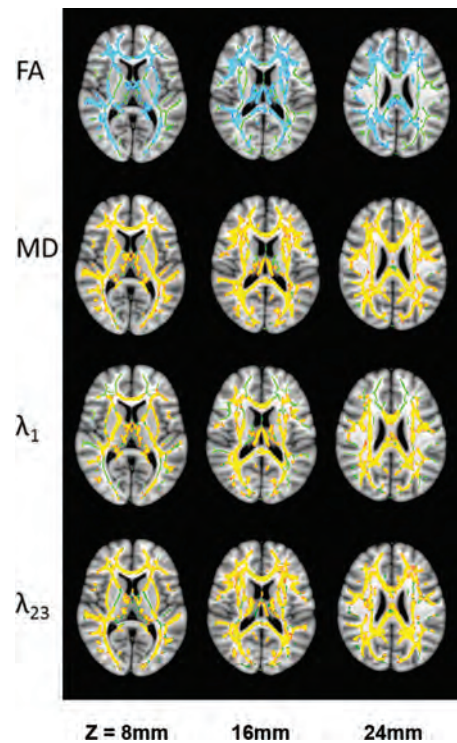


FIG 3. Group differences in FA, MD, axial diffusivity (λ_1), and radial diffusivity (λ_{23}) between the DM-MCI and the HC groups in 3 representative sections (see On-line Fig 2 for a complete set of images with whole-brain coverage). All other details are the same as in the legend for Fig 2.

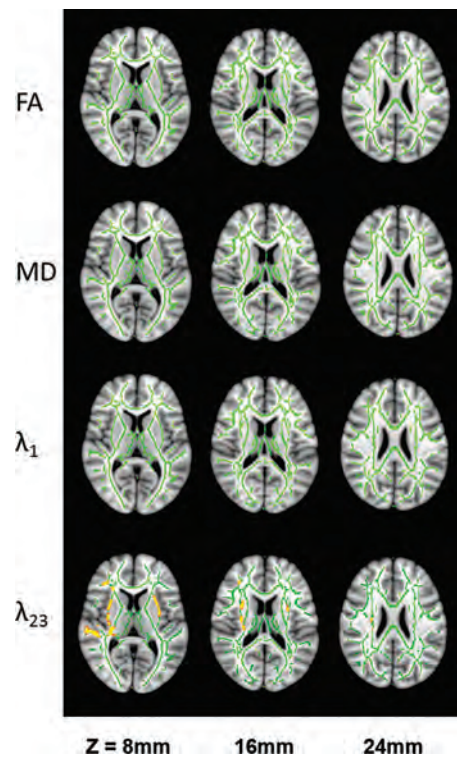


FIG 4. Group differences in FA, MD, axial diffusivity (λ_1), and radial diffusivity (λ_{23}) between the DM-NC and the HC groups in 3 representative sections (see On-line Fig 3 for a complete set of images with whole-brain coverage). All other details are the same as in the legend for Fig 2.

Table 1: FA values in specific fiber tracts with significant differences among groups ($P < .05$)

JHU WM Atlas	FA (DM-MCI)	FA (DM-NC)	FA (HC)	P Value
ALIC.L	0.595 ± 0.025	0.610 ± 0.021		.044
ACR.R	0.472 ± 0.024	0.487 ± 0.019		.035
ACR.L	0.471 ± 0.029	0.488 ± 0.018		.022
PTR.L	0.620 ± 0.038	0.641 ± 0.027		.045
EC.L	0.478 ± 0.020	0.490 ± 0.017		.043
CH.R	0.585 ± 0.040	0.616 ± 0.024		.004
CH.L	0.579 ± 0.027	0.599 ± 0.026		.019
CT.R		0.548 ± 0.030	0.569 ± 0.017	.003
CP.R		0.590 ± 0.021	0.608 ± 0.019	.002

Note:—R indicates right; L, left; ALIC, anterior limb of internal capsule; ACR, anterior corona radiata; CH, cingulum (hippocampus); EC, external capsule; PTR, posterior thalamic radiation (including the optic radiation); CP, cerebellar peduncle; CT, corticospinal tract; JHU, Johns Hopkins University.

Table 2: MD values ($\times 10^{-3}$ mm²/s) in specific fiber tracts with significant differences among groups ($P < .05$)

JHU WM Atlas	MD (DM-MCI)	MD (DM-NC)	MD (HC)	P Value
RIC.L	0.780 ± 0.026	0.760 ± 0.029		.031
SCR.L	0.732 ± 0.029	0.712 ± 0.026		.021
SS.R	0.839 ± 0.037	0.815 ± 0.030		.024
EC.L	0.758 ± 0.029	0.739 ± 0.026		.030
RIC.R		0.773 ± 0.030	0.755 ± 0.021	.021
EC.R		0.784 ± 0.044	0.756 ± 0.027	.009

Note:—R indicates right; L, left; RIC, the retrolenticular part of internal capsule; SCR, superior corona radiata; SS, sagittal striatum (including the inferior longitudinal fasciculus and inferior fronto-occipital fasciculus); EC, external capsule; JHU, Johns Hopkins University.

ciated with hypoperfusion and inflammatory factors can be possible causes.³⁰

Although both Figs 2 and 3 compare the DM-MCI group against subjects without clinically confirmed cognitive impairment, the results are considerably different. In addition to changes in radial diffusivity, Fig 3 also shows extensive changes in axial diffusivity (λ_1), suggesting axonal damage in patients with DM-MCI compared with HC. A number of studies have shown that T2DM and Alzheimer disease share several pathogeneses, including insulin deficit, glucose-mediated toxicity, and amyloid- β peptide accumulation.^{8,31} One of the important pathologic bases of Alzheimer disease is neurofibrillary tangles,³² caused by the phosphorylated τ protein. As a terminal axonal lesion, neurofibrillary tangles and subsequent synapse loss can lead to progressive loss of memory and compromised cognition. The similar mechanism may explain the observed λ_1 elevation in Fig 3. More important, the increase in radial diffusivity in the patients with DM-NC shown in Fig 4 can be a significant finding because it suggests minor-to-moderate damage to the myelin sheath in the early phase of cognitive decline (eg, amnesia) in patients with T2DM before they can be clinically diagnosed by using neuropsychological test scores.

Our investigation of regional WM alterations was focused on the telencephalon because of its pivotal role in cognition and dementia. Not surprising, DTI parameter changes were observed in the cingulum near the hippocampus, which is related to learning and memory,²⁴ as well as in the anterior limb and the retrolenticular area of the internal capsule. Furthermore, the FA or MD differences between the DM-NC and HC groups in the corticospinal tract and external capsule (Tables 1 and 2) provide more

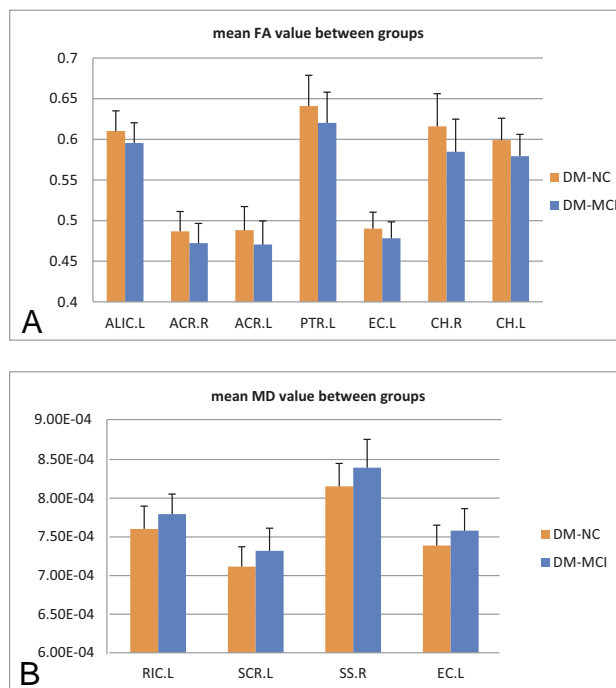


FIG 5. Differences in FA (A) and MD (B) values for specific fiber tracts in an atlas-based ROI analysis between the DM-MCI (blue) and the DM-NC (orange) groups. All fibers in the figure show a statistically significant difference ($P < .05$). The bar height indicates the mean, and the line on top of the bar represents the SD. L indicates left; R, right; ALIC, anterior limb of internal capsule; ACR, anterior corona radiata; CH, cingulum (hippocampus); EC, external capsule; PTR, posterior thalamic radiation (including the optic radiation); RIC, retrolenticular part of internal capsule; SCR, superior corona radiata; SS, sagittal striatum (including the inferior longitudinal fasciculus and inferior fronto-occipital fasciculus).

specific evidence to support our hypothesis that early changes during the course of cognitive decline can be detected by DTI before the patients become symptomatic.

The present study has also demonstrated that FA and MD can become potential imaging markers (Fig 6) that are sensitive to cognitive declines in patients with T2DM. These markers can be used individually or combined to complement the existing neuropsychological tests. Zhang et al¹⁸ recently reported that FA changes in the external capsule were correlated with executive dysfunction. Reijmer et al¹⁷ observed that increased MD was associated with slowing information processing and worsened memory performance. These studies, together with our results, all indicate that FA and MD can quantitatively characterize the cognitive decline process, which would eventually lead to clinical symptoms to be reflected in the neuropsychological scores.

Our study has several limitations. First, despite the attempt to exclude other causes of WM changes, it is still possible that an underlying process independent of diabetes mellitus is associated with the cognitive decline. Patients without diabetes with similar cognition need to be studied to control for the possibility that the cognitive decline rather than diabetes mellitus is associated with changes in DTI measures. Nonetheless, the present study suggests that DTI metrics have the potential to predict cognitive impairment in patients with T2DM (Fig 6). Second, although we excluded subjects with severe and moderate hypertension or hyper-

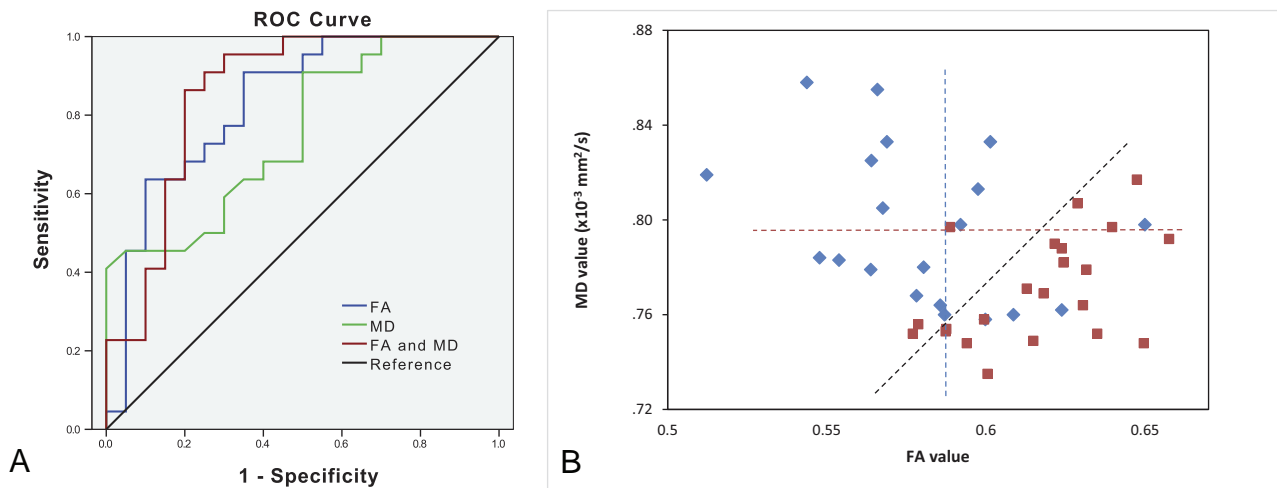


FIG 6. A, ROC curves for FA (blue), MD (green), and a combination of FA and MD (red) of the right cingulum (hippocampus) for separating DM-MCI and DM-NC patients. B, Scatterplots of FA versus MD for all patients with DM-NC (red) and DM-MCI (blue). The dashed lines indicate the cutoff values for FA (blue), MD (red), and the combination of FA and MD (black). The black dashed line corresponds to a sensitivity of 0.864 and a specificity of 0.800.

lipidemia, a small number of subjects with mild hypertension or hyperlipidemia were included to increase the statistical power. We observed very similar results in separate analyses with and without the inclusion of subjects with mild hypertension (or hyperlipidemia), indicating that the effect caused by mild hypertension or hyperlipidemia was not substantial. Third, because rigorous clinical diagnosis of MCI remains a challenge, dividing the patients with T2DM into the DM-MCI and DM-NC groups can be subject to inaccuracy. Last, given the slow development of MCI, a longitudinal study would be needed to test whether DTI measures can predict the development of cognitive impairment in patients with T2DM.

CONCLUSIONS

Our study has demonstrated that DTI parameters can show a significant difference between patients with T2DM with and without MCI, suggesting their potential role as an imaging marker for detecting cognitive decline in patients with T2DM. More important, our study also indicates that the DTI parameters may capture gradual and continuous WM changes that can be associated with early stages of cognitive decline in patients with T2DM before they can be diagnosed clinically by using the conventional neuropsychological test scores.

ACKNOWLEDGMENTS

The authors are grateful to Dr Keith R. Thulborn for helpful discussions and to Dr Winnie Mar for proofreading the manuscript.

Disclosures: Yi Sui—UNRELATED: Consultancy: GE Healthcare. Xiaohong Joe Zhou—RELATED: Grant: National Institutes of Health*; UNRELATED: Consultancy: Horizon Medical Physics Services; Grants/Grants Pending: AbbVie Pharmaceuticals*; Royalties: Elsevier Publishing; Stock/Stock Options: Apple, Google. *Money paid to the institution.

REFERENCES

- Whiting DR, Guariguata L, Weil C, et al. **IDF Diabetes Atlas: global estimates of the prevalence of diabetes for 2011 and 2030.** *Diabetes Res Clin Pract* 2011;94:311–21 CrossRef Medline
- McCrimmon RJ, Ryan CM, Frier BM. **Diabetes and cognitive dysfunction.** *Lancet* 2012;379:2291–99 CrossRef Medline
- Biessels GJ, Staekenborg S, Brunner E, et al. **Risk of dementia in diabetes mellitus: a systematic review.** *Lancet Neurol* 2006;5:64–74 CrossRef Medline
- Rusinek H, Ha J, Yau PL, et al. **Cerebral perfusion in insulin resistance and type 2 diabetes.** *J Cereb Blood Flow Metab* 2015;35:95–102 CrossRef Medline
- Sahin I, Alkan A, Keskin L, et al. **Evaluation of in vivo cerebral metabolism on proton magnetic resonance spectroscopy in patients with impaired glucose tolerance and type 2 diabetes mellitus.** *J Diabetes Complications* 2008;22:254–60 CrossRef Medline
- Cui Y, Jiao Y, Chen YC, et al. **Altered spontaneous brain activity in type 2 diabetes: a resting-state functional MRI study.** *Diabetes* 2014;63:749–60 CrossRef Medline
- Musen G, Jacobson AM, Bolo NR, et al. **Resting-state brain functional connectivity is altered in type 2 diabetes.** *Diabetes* 2012;61:2375–79 CrossRef Medline
- Umegaki H. **Type 2 diabetes as a risk factor for cognitive impairment: current insights.** *Clin Interv Aging* 2014;9:1011–19 CrossRef Medline
- Zhang Y, Zhang X, Zhang J, et al. **Gray matter volume abnormalities in type 2 diabetes mellitus with and without mild cognitive impairment.** *Neurosci Lett* 2014;562:1–6 CrossRef Medline
- de Bresser J, Tiehuis AM, van den Berg E, et al; Utrecht Diabetic Encephalopathy Study Group. **Progression of cerebral atrophy and white matter hyperintensities in patients with type 2 diabetes.** *Diabetes Care* 2010;33:1309–14 CrossRef Medline
- Moran C, Phan TG, Chen J, et al. **Brain atrophy in type 2 diabetes: regional distribution and influence on cognition.** *Diabetes Care* 2013;36:4036–42 CrossRef Medline
- Antenor-Dorsey JA, Meyer E, Rutlin J, et al. **White matter microstructural integrity in youth with type 1 diabetes.** *Diabetes* 2013;62:581–89 CrossRef Medline
- Nunley KA, Ryan CM, Orchard TJ, et al. **White matter hyperintensities in middle-aged adults with childhood-onset type 1 diabetes.** *Neurology* 2015;84:2062–69 CrossRef Medline
- Stahl R, Dietrich O, Teipel SJ, et al. **White matter damage in Alzheimer disease and mild cognitive impairment: assessment with diffusion-tensor MR imaging and parallel imaging techniques.** *Radiology* 2007;243:483–92 CrossRef Medline
- Hsu JL, Chen YL, Leu JG, et al. **Microstructural white matter abnormality in type 2 diabetes mellitus.** *Diabetes Care* 2011;34:1000–06 CrossRef Medline

- malities in type 2 diabetes mellitus: a diffusion tensor imaging study. *Neuroimage* 2012;59:1098–105 CrossRef Medline
16. Hoogenboom WS, Marder TJ, Flores VL, et al. **Cerebral white matter integrity and resting-state functional connectivity in middle-aged patients with type 2 diabetes.** *Diabetes* 2014;63:728–38 CrossRef Medline
 17. Reijmer YD, Brundel M, de Bresser J, et al; Utrecht Vascular Cognitive Impairment Study Group. **Microstructural white matter abnormalities and cognitive functioning in type 2 diabetes: a diffusion tensor imaging study.** *Diabetes Care* 2013;36:137–44 CrossRef Medline
 18. Zhang J, Wang Y, Wang J, et al. **White matter integrity disruptions associated with cognitive impairments in type 2 diabetic patients.** *Diabetes* 2014;63:3596–605 CrossRef Medline
 19. American Diabetes Association. **Diagnosis and classification of diabetes mellitus.** *Diabetes Care* 2013;36(suppl 1):S67–74 CrossRef Medline
 20. Jenkinson M, Beckmann CF, Behrens TE, et al. **FSL.** *Neuroimage* 2012;62:782–90 CrossRef Medline
 21. Smith SM, Jenkinson M, Johansen-Berg H, et al. **Tract-based spatial statistics: voxelwise analysis of multi-subject diffusion data.** *Neuroimage* 2006;31:1487–505 CrossRef Medline
 22. Smith SM, Johansen-Berg H, Jenkinson M, et al. **Acquisition and voxelwise analysis of multi-subject diffusion data with tract-based spatial statistics.** *Nat Protoc* 2007;2:499–503 CrossRef Medline
 23. Mori S, Oishi K, Jiang H, et al. **Stereotaxic white matter atlas based on diffusion tensor imaging in an ICBM template.** *Neuroimage* 2008;40:570–82 CrossRef Medline
 24. Seib DR, Martin-Villalba A. **Neurogenesis in the normal ageing hippocampus: a mini-review.** *Gerontology* 2015;61:327–35 CrossRef Medline
 25. Chua TC, Wen W, Slavin MJ, et al. **Diffusion tensor imaging in mild cognitive impairment and Alzheimer's disease: a review.** *Curr Opin Neurol* 2008;21:83–92 CrossRef Medline
 26. Liu Y, Spulber G, Lehtimäki KK, et al. **Diffusion tensor imaging and tract-based spatial statistics in Alzheimer's disease and mild cognitive impairment.** *Neurobiol Aging* 2011;32:1558–71 CrossRef Medline
 27. Menard SW. *Applied Logistic Regression Analysis.* Thousand Oaks, California: Sage; 2002:1–120
 28. Neil JJ. **Diffusion imaging concepts for clinicians.** *J Magn Reson Imaging* 2008;27:1–7 CrossRef Medline
 29. Song SK, Sun SW, Ramsbottom MJ, et al. **Dysmyelination revealed through MRI as increased radial (but unchanged axial) diffusion of water.** *Neuroimage* 2002;17:1429–36 CrossRef Medline
 30. Peterson JW, Bö L, Mörk S, et al. **Transected neurites, apoptotic neurons, and reduced inflammation in cortical multiple sclerosis lesions.** *Ann Neurol* 2001;50:389–400 CrossRef Medline
 31. Biessels GJ, Deary IJ, Ryan CM. **Cognition and diabetes: a lifespan perspective.** *Lancet Neurol* 2008;7:184–90 CrossRef Medline
 32. Butterfield DA, Di Domenico F, Barone E. **Elevated risk of type 2 diabetes for development of Alzheimer disease: a key role for oxidative stress in brain.** *Biochim Biophys Acta* 2014;1842:1693–706 CrossRef Medline

Electrophysiologic Validation of Diffusion Tensor Imaging Tractography during Deep Brain Stimulation Surgery

V.A. Coenen, C. Jenkner, C.R. Honey, and B. Mädler



ABSTRACT

BACKGROUND AND PURPOSE: Diffusion tensor imaging fiber tractography–assisted planning of deep brain stimulation is an emerging technology. We investigated its accuracy by using electrophysiology under clinical conditions. We hypothesized that a level of concordance between electrophysiology and DTI fiber tractography can be reached, comparable with published modeling approaches for deep brain stimulation surgery.

MATERIALS AND METHODS: Eleven patients underwent subthalamic nucleus deep brain stimulation. DTI scans and high-resolution T1- and T2-weighted MR imaging was performed at 3T. Corticospinal tracts were traced. We studied electrode positions and current amplitudes that elicited corticospinal tract effects during the operation to determine relative corticospinal tract distance. Postoperatively, 3D deep brain stimulation electrode contact locations and stimulation patterns were applied for the same corticospinal tract distance estimation.

RESULTS: Intraoperative electrophysiologic ($n = 40$) clinical effects in 11 patients were detected. The mean intraoperative electrophysiologic corticospinal tract distance was 3.0 ± 0.6 mm; the mean image-derived corticospinal tract distance (DTI fiber tractography) was 3.0 ± 1.3 mm. The 95% limits of agreement were ± 2.4 mm. Postoperative electrophysiology ($n = 44$) corticospinal tract activation effects were encountered in 9 patients; 39 were further evaluated. Mean electrophysiologic corticospinal tract distance was 3.7 ± 0.7 mm; for DTI fiber tractography, it was 3.2 ± 1.9 mm. The 95% limits of agreement were ± 2.5 mm.

CONCLUSIONS: DTI fiber tractography depicted the medial corticospinal tract border with proved concordance. Although the overall range of measurements was relatively small and variance was high, we believe that further use of DTI fiber tractography to assist deep brain stimulation procedures is advisable if inherent limitations are respected. These results confirm our previously published electric field simulation studies.

ABBREVIATIONS: CST = corticospinal tract; DBS = deep brain stimulation; EPio = intraoperative electrophysiology; EPpo = postoperative electrophysiology; FT = fiber tractography; STN = subthalamic nucleus

DTI fiber tractography (FT) to assist deep brain stimulation (DBS) emerges as an interesting technology in different indications for the treatment of chronic medically refractory

disorders.^{1,2} Several groups are now aware of the clinical benefits that arise from the application of this direct targeting technology. The true anatomic structures that translate into adverse effects of stimulation are often not understood. Very likely, DBS modulates fibers that can be visualized with DTI FT. This noninvasive imaging technology might directly show the structures on which DBS exerts its effects and might prove to be a promising technology in direct and individualized targeting for DBS. DTI FT–assisted DBS has already led to a better understanding of the treatment of tremor, Parkinson disease, pain, and depression.^{1–9} In the latter, it has led to the description of a completely new target region (the superolateral branch of the medial forebrain bundle).^{6,9,10}

Before the application of DBS, DTI FT had become part of the standard armamentarium for microneurosurgical resections of eloquently located brain lesions.^{11,12} However, despite a study that showed the superiority of DTI-based neurosurgery for clinical

Received August 24, 2015; accepted after revision January 22, 2016.

From the Department of Stereotactic and Functional Neurosurgery (V.A.C., B.M.) and the Clinical Trial Unit (C.J.), Freiburg University Medical Center, Freiburg, Germany; Surgical Center for Movement Disorders/Division of Neurosurgery (C.R.H.) and Department of Physics and Astronomy (B.M.), University of British Columbia, Vancouver, British Columbia, Canada; and Philips Healthcare (B.M.), Hamburg, Germany.

Paper previously presented in part at: Congress of the European Society of Stereotactic and Functional Neurosurgery, September 17–20, 2014; Maastricht, the Netherlands.

Please address correspondence to Volker A. Coenen, MD, Department of Stereotactic and Functional Neurosurgery, Albert-Ludwigs-University, Freiburg, Breisacher Str 64, D-79106 Freiburg (i.Br.), Germany; e-mail: volker.coenen@uniklinik-freiburg.de

Indicates open access to non-subscribers at www.ajnr.org

<http://dx.doi.org/10.3174/ajnr.A4753>

outcome during resection in eloquent regions,¹³ there have also been reports of the inferiority of DTI FT to depict the true extension of the corticospinal tract (CST) during brain tumor surgery.¹⁴ Hahn et al¹⁵ and Nimsky et al¹⁶⁻¹⁸ have extensively investigated the application error of DTI FT and found it to be roughly 5 mm in the cortical region. In our own previous report,⁵ we have tried to assess the application error of DWI-based depiction of the deep-seated CST during deep brain stimulation surgery under anatomically “undistorted” conditions.

Intuitively, DBS surgery warrants an even higher accuracy than neuronavigated microneurosurgical approaches, but nevertheless visually controlled, because among other factors, the effective positioning of an electrode or probe predominantly relies on a geometrically accurate depiction of the target region with an imaging technology. For the DWI technology, the accuracy was determined to be 3 mm in the z-direction (vertical).⁵ On the basis of our own experience in DTI-assisted DBS, we concluded that it is possible to use DTI FT to visualize target structures for functional stereotactic and neurosurgical procedures.^{4,6,8,19} However, as of today, a clear determination of the validity of a DTI-based depiction of fiber tracts during stereotactic and functional procedures and its rigorous evaluation with sound electrophysiologic methods is lacking in the literature.

We present a study that tries to give more insight into these problems. Applying 2 methods, intraoperative electrophysiologic determination of the CST border (EPio) based on a current spread model²⁰ and postoperative electrophysiologic evaluation (EPpo) based on readily implanted DBS electrode positions, a finite element model and a voltage-driven approach,^{19,21} we aimed to determine an electrophysiologic validation of the DTI FT-based depiction of the CST during subthalamic nucleus (STN) DBS surgery. Taking all possible methodologic inaccuracies into account, we hypothesized that a level of concordance of 2–3 mm between electrophysiology and DTI FT can be reached, which justifies further use of our previously published modeling approaches for DBS surgery.¹⁹

MATERIALS AND METHODS

Ethics

This study received approval from the University of British Columbia clinical research ethics board (reference No. H06–04023). Patients gave written informed consent for participation in this study. The study followed the tenets of the Declaration of Helsinki.

Patient Cohort

Eleven patients underwent bilateral STN DBS surgery for advanced Parkinson disease (9 men; mean age, 55 ± 9.6 years) according to standardized selection guidelines. All patients had a preoperative levodopa challenge test evaluated with Part III of the Unified Parkinson's Disease Rating Scale with an improvement of >40%.

Imaging Studies

Preoperative MR imaging was conducted 1–3 months before the operation on a whole-body 3T MR imaging scanner (Intera; Philips Healthcare, Best, the Netherlands), equipped with a high-

performance dual-mode gradient coil (maximum amplitude, 80 mT/m; maximum slew rate, 200 T/m/s) by using a 6-element phased array head coil.

The examination was preceded by a quick T1-weighted survey and a parallel imaging reference scan. Anatomic data were obtained with a 3D MPRAGE sequence (3D T1 turbo field echo): axial FOV = 212 mm and 132 mm coverage in the superoinferior direction with an isotropic acquisition voxel size of 1 mm³, TE = 6 ms, TR = 10 ms, turbo-factor = 169, linear profile order, inversion preparation with an adiabatic hyperbolic secant pulse, TI = 950 ms, shot interval = 3000 ms, sensitivity-encoding = 1.7. For visualization of the area of the subthalamic nucleus, we used a multisection T2-weighted fast spin-echo sequence with similar FOVs and voxel dimensions. The coverage in superoinferior directions was reduced to 116 mm to focus on the area of the mid-brain and its nuclei. Further parameters were the following: turbo factor = 15, TE = 80 ms, linear profile order, TR = 3000 ms, sensitivity encoding = 2.0. The concept of reduced refocusing angles (120°) was used to reduce the specific absorption rate and therefore scan time. The examination was concluded with a DTI scan for subsequent application of fiber tracking. Scan parameters for DTI were as follows: single-shot spin-echo EPI with second-order shim, TE = 60 ms, TR = 10,500 ms, $b=800$ s/mm², FOV = 212 mm, matrix = 106 × 106 leading to an in-plane voxel size of 2 × 2 mm². We acquired 70 sections with 2-mm thickness and no intersection gap to cover the entire brain. Diffusion encoding was performed in 15 noncollinear directions on an icosahedral geodesic grid to sample all spheric directions isotropically, followed by the non-diffusion-weighted reference scan (B0 image). All scans were performed in an axial orientation.

Fiber Tracking of the CST

Fiber tracking of the CST was performed in a deterministic approach as described before.²² In brief, the fractional anisotropy level was kept at 0.2. Minimal fiber length was set to 45 mm. Seed density was held at 5.0. Maximal directional change of fibers was chosen between 35° and 50°. The complete precentral gyrus served as the seed region for the fiber tracking. Identification of the precentral gyrus was based on the criterion of Yousry et al.²³

STN DBS Surgery and Postoperative Programming

The detailed implantation procedure has been previously described.⁶ In brief, stereotactic implantation of DBS electrodes was performed with a stereotactic frame (Universal Compact Head Frame; Integra Radionics, Burlington, Massachusetts) with the patient under local anesthesia. A combined micro-/macroelectrode (FHC MME; Medtronic, Minneapolis, Minnesota) was inserted into the brain by using a microTargeting Drive (Medtronic). Microelectrode recordings followed by macrostimulation studies were performed. All patients had DBS electrodes placed bilaterally and received an implantable impulse generator (Kinetra neurostimulator; Medtronic) under general anesthesia during the same procedure. Postoperatively, all patients underwent a helical 3D CT approximately 6 weeks after the operation to corroborate the final STN DBS electrode location.

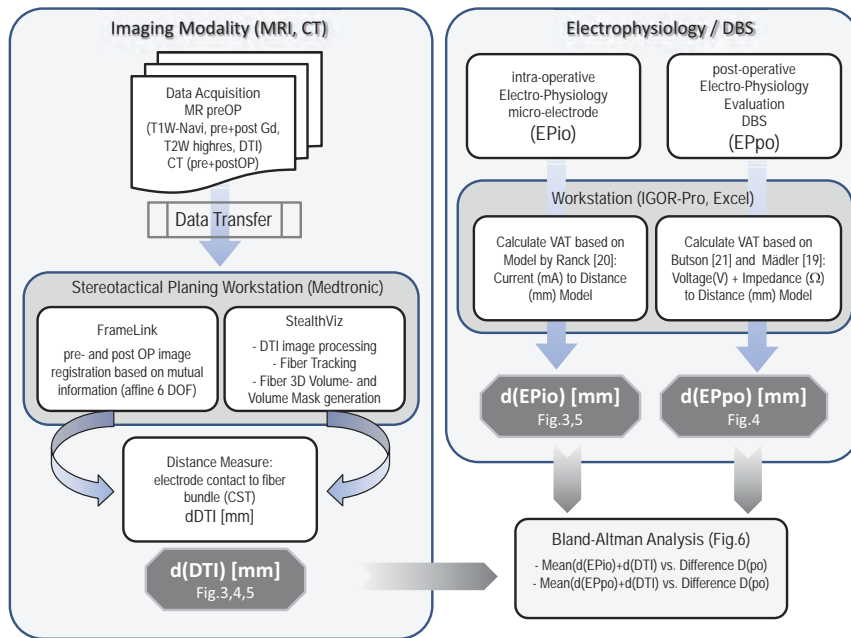


FIG 1. Flow chart of the procedures. Post OP indicates postoperative; preOP, preoperative; DOF, deformation; EPio, intraoperative electrophysiology; EPpo, postoperative electrophysiology; Navi, Navigation (Sequence); pre, before; post, after; VAT, volume of activated tissue; highres, high-resolution.

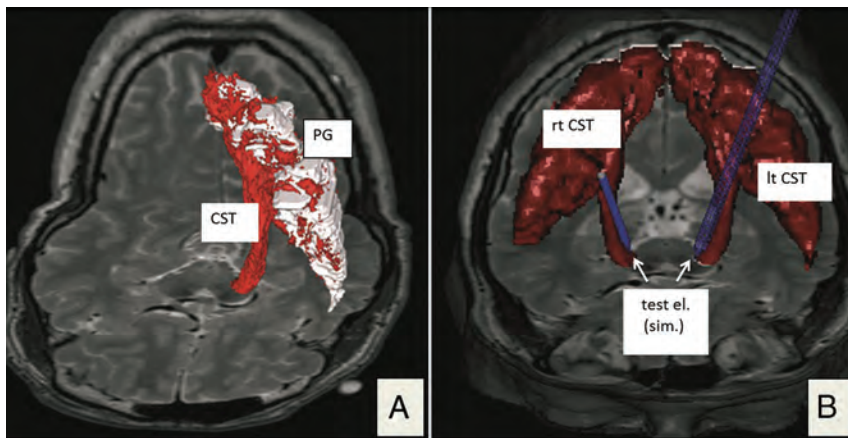


FIG 2. 3D renditions of the corticospinal tract. *A*, Depiction of a left CST (red) in the fiber-tracking software (StealthViz DTI; Medtronic) but already depicted as a DICOM hull structure. *B*, Bilateral visualization of the transferred DICOM structure in the planning software (FrameLink 5.0; Medtronic Surgical Navigation). Blue probe simulations indicate intraoperatively tested electrode positions (test el.). PG indicates precentral gyrus; test el. (sim.), simulated test electrode position.

First Experiment: EPio and Detection of the Medial CST Border

Experimental settings are explained in Fig 1. After mapping the STN location, we performed macrostimulation to confirm a contralateral clinical benefit (reduction of rigidity, reduced bradykinesia) at a low threshold (≤ 1 mA, 100 μ s, 130 Hz) and a high threshold for adverse events (> 3 mA). Constant current stimulation was applied. The adverse events were typically of a capsular nature (indicating the medial border of the internal capsule). These effects were contralateral facial contractions, contraction of the arm and hand, capsular dysarthria, or conjugate eye-movement disorders. These effects and the respective electrode position were noted for later simulation and evaluation (Fig 2) of the elec-

trophysiologic distance compared with the DTI FT detection of the CST, respectively.⁵ According to Ranck,²⁰ a power law distance-to-current relationship of the volume of activated tissue could be shown for various myelinated fibers when stimulated with a monopolar electrode setting. From the empiric data (Fig 1 in Ranck²⁰), we were able to derive a generalized power law relationship (linear relationship on double logarithmic scaling) between the applied current and the diameter of the volume of activated tissue for clinically relevant settings (applied current in the milliampere regimen) and hence a predictor of the dimensions for the relevant electromagnetic field used for stimulation. The minimal distance in millimeters at which stimulation settings cause neurologic adverse events for this intraoperative setting is called d(EPio) (Fig 1, right column).²⁰

Second Experiment: EPpo and Detection of the Medial Internal Capsule/CST Border Based on DBS Electrodes

The preoperative 3T MR imaging studies and postoperative 3D CT data were integrated in the StealthViz DTI software application (Medtronic Navigation, Louisville, Colorado) on a stand-alone Linux workstation (Intel, Santa Clara, California), by using the automatic fusion mode of the software. The fusion quality was inspected visually and was scrutinized appropriately for further analysis in every case. Evaluation of a relevant effective electrode contact with a capsular adverse event was performed from fused CT data (Fig 3) and was expressed relative to the midcommissural point coordinates (Fig 4). After identifying each effective electrode contact from CT, we determined its location

with respect to the STN (as determined by the high-resolution T2-weighted MR imaging) (Fig 3) and its shortest distance to the CST (as displayed with fiber tracking) (Fig 3A). Clinical effects and capsular adverse events were tested with increments of 0.5 V in a voltage-constant stimulation mode. Therapeutic impedances were measured during capsular responses (see above) to allow an estimation of electric field sizes¹⁹ and thus the electrophysiologic distance to the CST, according to the work of Butson et al.²¹

As elaborately described in Mädlar et al,¹⁹ we adopted a simple model to estimate the volume of activated tissue based on a monopolar stimulation design of the DBS electrode, by fitting a 2D polynomial to the empiric data obtained by Butson

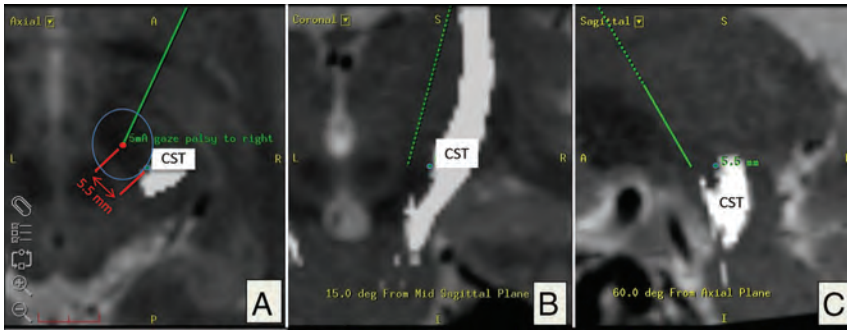


FIG 3. Evaluation based on intraoperative electrophysiology: corticospinal tract depiction in axial, coronal, and sagittal (A–C) planes. A, Red dot indicates post hoc simulation of the intraoperative position of the test electrode in the planning software (Framelink 5.0; Medtronic Surgical Navigation) according to microTargeting Drive settings. In this example, 5 mA of intraoperative stimulation resulted in “gaze palsy” as capsular effect. The shortest spatial distance to the medial CST border of 5.5 mm is indicated with a blue circle. Both coordinates (electrode tip, medial border of CST) were recorded and later plotted (Fig 4). Note that the CST is located posterior and lateral relative to the position of the electrode (A).

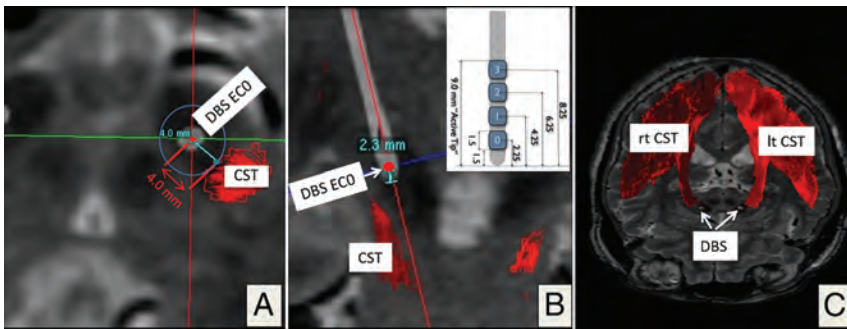


FIG 4. Postoperative electrophysiological evaluation by using CT depiction of the DBS electrode artifacts. The 3D helical postoperative CT is superimposed on the planning data. Reconstruction along the main DBS electrode (white) axis, quasi-axial (A) and coronal (B). The minimal spatial distance to the medial border of the CST is 4.0 mm. B, The DBS electrode (inset; geometry; DBS lead model 3389; Medtronic) is seen as a white structure in the STN region. In this example, electrode contact 0 (ECO, deepest contact, 2.3 mm from the electrode tip) elicited capsular effects during postoperative clinical testing. C, 3D rendering of the right (rt) and left (lt) CSTs with DBS electrode artifacts from helical CT.

et al.²¹ Input parameters are the stimulation voltage at the DBS contact and the measured impedance for this electrode placement in the patient. The resulting parameter is the diameter of the volume of activated tissue, which can be geometrically placed around the actual electrode contact. $d(EPpo)$ is the radius of the volume of activated tissue in millimeters under stimulation settings (voltage and impedance) when the electromagnetic field touches the CST and causes the described neurologic adverse events (Fig 1).

Statistics and Methods for Comparison of Experimental Results

A Bland-Altman (or Tukey mean) difference plot is a common modus operandi to analyze the agreement between 2 different measurement methods,²⁴ in our case distance measurements performed with DTI FT and intraoperative electrophysiology as well as DTI FT compared with postoperative electrophysiology. Because there are multiple measurements per patients, an adjustment proposed by Bland and Altman (2007)²⁵ was used for the calculation of the SD. A 95% concordance level is the average difference $\pm 1.96 \times SD$ of the difference and is a measure showing

whether 2 separate measurement acquisitions are congruent. Correlation analysis by using Spearman correlation coefficients are applied to give further insight.

RESULTS

Clinical

The preoperative Parkinson medication was reduced postoperatively by 45% from baseline in combination with the initiation of stimulation, indicating successful STN DBS surgery. No worsening of the patients occurred in the immediate postoperative period. Clinically relevant effective electrode contacts were within the limits given in the literature for the sensorimotor STN.

First Experiment (EPio)

Intraoperatively, we elicited 40 CST adverse events in 11 patients (with multiple measurements per patient at different electrode positions): conjugate forced eye deviation ($n = 15$); face contraction ($n = 10$); throat contraction, partly with dysarthria ($n = 8$); dysarthria ($n = 4$); unilateral forced eye opening ($n = 1$); foot contraction ($n = 1$); and hand contraction ($n = 1$) between 2 and 5 mA (3 ± 1.3 mA). In the post hoc analysis, these adverse events were analyzed on the basis of the simulated electrode position and the DTI-based rendition of the CST

(Fig 2). The electrophysiological distance to the internal capsule was 2.9 ± 0.6 mm, as calculated by Ranck (1975)²⁰; the mean image-derived distance (DTI FT) was 3.0 ± 1.3 mm. The mean average difference (bias) between the 2 measurements was 0.0 ± 1.2 . This led to limits of agreement of ± 2.44 mm. The Spearman correlation between the measurements was 0.34 (Fig 5).

Second Experiment (EPpo)

Forty-four internal capsule effects were encountered during postoperative programming (multiple measurements per patient): dysarthria ($n = 19$), facial contraction ($n = 15$), hand contraction ($n = 3$), forced eye deviation ($n = 5$), and throat contraction ($n = 2$). Therapeutic impedances were measured during initial programming. Due to limitations of the finite-element electric field estimation model (limitations in voltage and impedances),^{19,21} 39 adverse events in 9 patients could be further evaluated. The electrophysiological distance to the CST was 3.7 ± 0.6 mm. The imaging-derived distance based on DTI FT between the effective electrode contact and the medial bor-

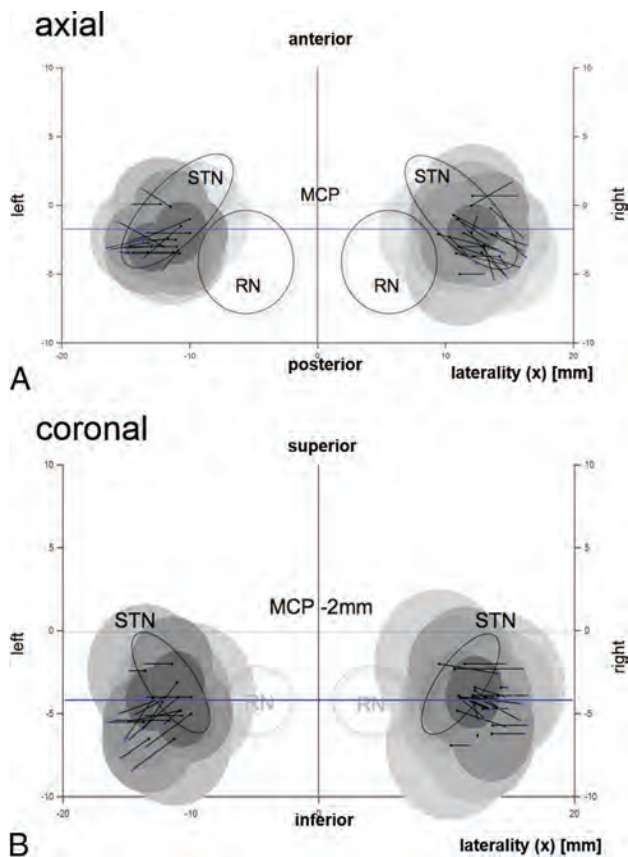


FIG 5. Graphic depiction of the EPio experiment results. Atlas templates in axial (A, 6.2 mm below the midcommissural point [MCP]) and coronal sections (B, 2 mm behind the MCP) (idealized according to Schaltenbrand and Wahren⁴⁶). Intraoperative electrode positions are represented by black dots. Black lines represent the shortest distance in space to the CST as depicted with the DTI technology. Blue dots show the individual CST penetration in space. Shaded circles indicate estimated volumes of activated tissue around a test electrode, specific to the current that was applied to elicit an electrophysiologic CST response according to Ranck (1975), (Fig 1).²⁰ CST (blue dots) corresponds nicely with electric field borders, indicating that medial CST definition with DTI reliably predicts the CST border as measured with electrophysiology. RN indicates red nucleus. (Of note in A, the CST is always located posterior and lateral to the STN region.)

der of the CST was 3.3 ± 1.6 mm. The mean average difference (bias) between the 2 measurements was 0.4 ± 1.3 . This led to limits of agreement of ± 2.5 mm. The Spearman correlation between the measurements was 0.44.

DISCUSSION

The application of the DTI FT–based delineation of the CST in its most proximal, thus cortical, parts during microsurgical resection has long been debated. The localization error determined was 5 mm and led to the application of “sheath regions” surrounding fiber tracts at risk, which artificially maximized the extension of the cross-sectional diameter of the CST.^{17,18,26–28} With this approach, functional integrity could be spared in the vicinity of the CST. Examples in the literature showed that purely relying on fiber-tract delineation without safety margins led to a detrimental patient outcome.¹⁴ With a root square mean error of distortion of 3–5 mm for neuronavigation (depending on the use of CT or MR imaging, respectively), the accuracy demands for the DTI FT–

based depiction of the CST and other fiber structures are obviously lower for neuronavigated interventions than for functional stereotactic procedures. The success of functional stereotactic procedures is, among other factors, mainly based on accurate imaging. The localization accuracy of stereotactic frames ranges between 1.5 and 2 mm.^{29,30} However the vector error can be as high as 3.15 mm. Thus, a new imaging technique should probably not be far outside this accuracy range. However, with the DTI FT–assisted DBS approach, structures that were merely not known or simply not directly visible (dentatorubrothalamic tract, medial forebrain bundle) became readily targetable regions that otherwise would have to be explored and found by literally hunting through the brain on multiple paths with additional bleeding risks.

We have described the use of a comparable imaging technology, DWI, in a rather similar setting of STN DBS surgery.⁵ Other groups have tried to approach the accuracy level of DTI in clinical DBS procedures and have come to the conclusion that the use of DBS surgery with this technology cannot be advised.³¹ While this conclusion might be true, in our opinion, these authors based their results on imaging data, software use, and a study setup that was not geared to looking at the specific questions asked.³² Therefore, a specific approach designed to look at this problem, albeit still in a clinical setting, appeared appropriate.

Other groups used approaches rather similar to ours to look at the electrophysiologic effects of stimulation of the internal capsule.^{33,34} Duerden et al³⁴ used an approach in which they retrospectively mapped capsular effects (muscle contractions of different body parts) to MR imaging anatomy (albeit not DTI). The aim of this study was to draw conclusions on the capsular topography in the posterior limb and to generate a probabilistic electrophysiologic data base. With their curved electrode used for lesioning, the authors could directly map fibers of the internal capsule with good spatial accuracy. Their electrophysiologic map represents the typical topographic representation of muscle groups (face toward the knee of the internal capsule, leg toward the posterior aspect).³⁴ Chaturvedi et al³³ published an interesting study, again with a different angle on capsular anatomy. In a single patient undergoing STN DBS, they used electromyographic recordings to show activations of distinct muscle groups. They used detailed simulation models based on the DTI-based tissue anisotropy and inhomogeneity. In their computation, cable models of axonal pathways were shaped. They debated the use of a simple voltage-distance approach. According to their data, it is likely that a DBS electrophysiologic model that does not take the interactions between (anisotropic) tissue and electric field into account will likely overestimate the actual current spread.³⁴

In our study, the results of the Bland-Altman plots (Fig 6) give hints of a good concordance of the 2 measurements (DTI and electrophysiology). However, in our measurements, the range of distances was small and thus the relative error seems high. This is predominantly because there was no dramatic displacement of an electrode during measurements and naturally the CST can only be maximally 1–5 mm away from any stimulation point (the STN is a target region close to the CST). The Spearman correlations of 0.34 (EPio) and 0.44 (EPpo) only showed a trend toward correlation between electrophysiology and imaging.

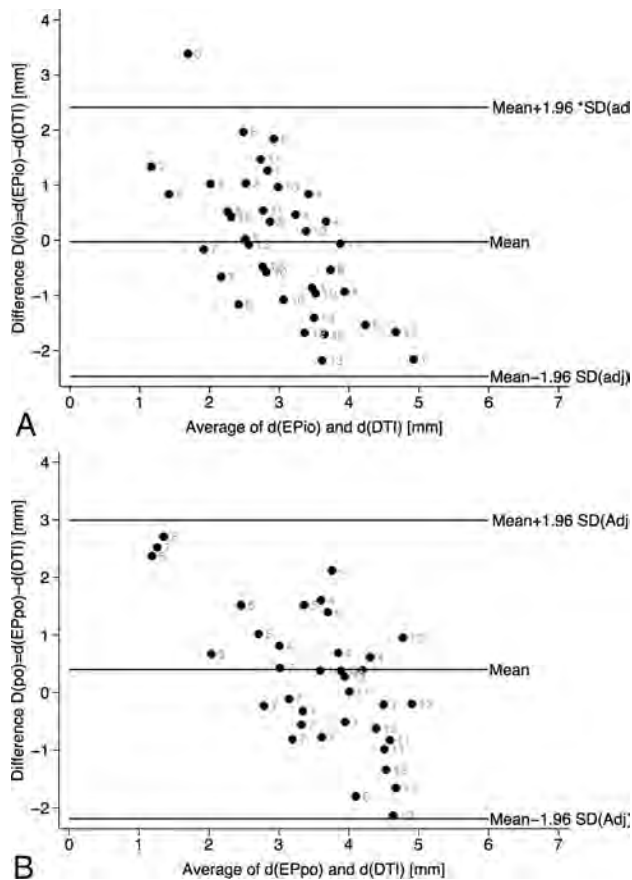


FIG 6. A, Bland-Altman plot, intraoperative measurements. Gray labels indicate individual patients. B, Bland-Altman plot, postoperative measurements. Gray labels indicate individual patients.

However, when cautiously interpreting our results, we can state the following: With the use our approach, a concordance of 2.44–2.5 mm, respectively, was found between DTI FT and electrophysiologic macrostimulation. It is important to carefully discuss these concordance levels in light of the methods applied and the interpretations they allow.

If one assumes that electrophysiology resembles a kind of criterion standard in depicting neuronal structures in the living human brain, a concordance level might allow an extrapolation toward the application accuracy of DTI FT. The concordance levels are not the same as the accuracy of the method but might help reflect on it.

The resolution of MR imaging itself is in the range of 2 mm. However, in light of previous studies, which came to the conclusion that the neuronavigation localization error (root square mean error of distortion) of DTI is 5 mm, our extrapolated localization error (2.5 mm) is much better and actually almost within the error of a frame-based stereotactic system itself (which can be up to 2 mm; the vector error can be up to 3.15 mm). Moreover, our own clinical experience with the DTI FT–assisted approach is such that the actual error ranges are lower than the 2.4–2.5 mm found here. However, our analysis would likely warrant a larger sample to allow a mere “shrinkage” of the limits of agreement to clearly prove our assumptions true. If these error ranges are taken together, we would cautiously suggest that the concordance levels detected here are acceptable in the context of DTI FT–assisted

DBS. The evaluation itself shows that the 2 methods (electrophysiology and DTI) are congruent for the distance measurements for which they were applied.

We and other groups have already applied this technology to directly target fiber tracts with improved clinical benefit for the patients,^{1–4,6,8,9,35,36} to scrutinize the adverse events of DBS^{1,6,19,35} or to develop new target regions for DBS surgery.^{9,10} All these applications almost render the present study outdated. However, this study might help to establish solid ground for any of these efforts with respect to electrophysiologic validation of the DTI technology in the functional and stereotactic neurosurgical setting.

Limitations

Limitations of DTI-based fiber tracking are related to the design of the DTI sequence itself, its various methods of data acquisition, limited signal-to-noise ratio, partial volume effects, and the intrinsically large size of intraplanar voxels during in vivo DTI applications. Furthermore, there are limitations of the described fiber assignment by continuous tractography algorithm. There might be ambiguities in following the correct connection pathways in areas of crossing, kissing, or branching fibers. These ambiguities are clearly a limitation of the single diffusion tensor model, combined with a relatively low spatial resolution (approximately 2-mm isotropic voxel dimension).^{37–39} Nevertheless, these results from deterministic fiber tracking appear to be justified if anatomic descriptions of displayed fiber tracts such as the CST can be followed. However, the results of the DTI FT application can be rather diverse.²² This diversity, among other factors, depends on the software used.

Deterministic versus Probabilistic Algorithms. We were dealing with patients with Parkinson disease. This, in itself, limits the scanning time for more sophisticated approaches such as DTI for probabilistic approaches. To our knowledge, no software is validated (and certified) with probabilistic tracking in the context of surgical treatment.

The accuracy of fusion is very difficult to interpret. It is especially difficult to determine, for EPpo, the accuracy of the localization of the DBS electrode. Visually performed accuracy checks appear to show good agreement when landmarks in different imaging modalities (CSF spaces, vessels, bony landmarks) are used to compare the validity of the fusion. In the clinical context, this is everyday practice, for example, if preoperative nonstereotactic MR imaging is fused to a stereotactic CT scan. In this respect, this is a valid approach. The fusion accuracy of MR imaging and postoperative CT has previously been determined to be 0.5 mm for the localization of DBS electrodes from postoperative CT.^{40,41} This accuracy, however, is only part of the overall accuracy of this part of our evaluation method (EPpo). The fusion software applied here to fuse CT and MR imaging (T1, T2, DTI sequences) uses an affine algorithm with 6 *df*. To our knowledge, certified surgical planning systems are not yet equipped with algorithms that compensate for local deformations (typically for DTI) with elastic registration (eg, in the region of the anterior pons or in the frontal lobe, close to the corpus callosum). However, we do not think that these deformations play a major role for visualization of the CST or other fiber structures in the midbrain. We have used the post-

operative determination of electrode positions with CT multiple times in previous work.^{1,4,6-8,10,42,43}

Accuracy of Simulation of the Intraoperative Test Electrode Position. The accuracy of the determination of the position of the macrotip of the test electrode (EPio) will be dependent on the accuracy of the stereotactic frame^{29,30} and thus will be 1.5–2 mm. Due to air entering the CSF spaces, brain shift might occur during the operation, theoretically leading to a wrong positioning of the test or DBS electrodes.⁴⁴ We and other groups have found that brain shift only plays a minor role in displacements of DBS electrodes and can be prevented by sealing the CSF space.⁴⁵ Intraoperative lateral fluoroscopy, which is regularly performed during the operation, did not show any deviation of the microelectrodes during the operation. However, a second plane (anteroposterior) was not acquired. The postoperative DBS-electrode position serves as a surrogate marker for the intraoperative position because a DBS electrode is placed on a predefined microelectrode track after testing.⁴¹ No deviations with respect to the implanted trajectory were seen on postoperative inspection. We thus assume that the intraoperative positioning of test electrodes was accurate. Furthermore, intraoperative microrecordings and test stimulations showed typical results, indicating that the targeted tissue was stimulated at typical and planned electrode positions.

Clinical Detection of Capsular Effects as Opposed to Electrophysiological Measurements. One could argue that it would be more accurate to detect capsular adverse events with surface or needle electromyography. However, at the design stage of this study, we did not apply to our ethics committee for use of this method. In the clinical context, we believe, however, that a detection of the medial border of the CST, as performed every day during STN surgery, is accurate enough to draw conclusions.

Simulation of the Electric Field. We are implicitly using 2 simplified versions of electric field simulations: Both simulations look at the electric fields as rather spherelike structures. In our first modeling approach (EPio), empirical data from the literature was used. We were able to extract an empirical distance/current amplitude (mm/mA) relation from their analysis and applied it to our intraoperative electrophysiological distance measurements.²⁰ In the second modeling approach (EPpo), we used a voltage- and impedance-driven model that was developed on the electrode geometry also used here.^{19,21} These models assume that the current density field surrounding the active contact of a DBS electrode unfolds in tissues that have an equal distribution of impedances throughout their volume. We know that this is not true and that the electric field is not likely to be optimally represented with a spherelike simulation because it will look more deformed and deflected in reality.²¹ However, if one concludes that the current density field expands uniformly on all sides until it is deflected by a larger fiber tract, the assumption of a spherelike electric field is reasonable.¹⁹ Most interesting, both approaches (the current-driven one and the voltage- and impedance-driven approach) come to almost the same results when looking at concordance to DTI FT.

CONCLUSIONS

DTI FT depicted the medial CST border in concordance with electrophysiology under 2 different conditions and modeling approaches (EPio and EPpo). Under both conditions, electrophysiological measurements are clearly related to the DTI FT. It is not possible to directly draw conclusions on the application accuracy of DTI FT itself from our data. One of the reasons is the inherent limitation of the electrophysiologic methods to detect the medial CST border (thickness of fibers; do we really stimulate most medial fibers in the CST?). Our data show that electrophysiology and DTI FT are concordant with ± 2.44 and ± 2.5 mm (95% limits of agreement) around the mean difference of the 2 measurements, respectively. Given that related to the clinical approach, only measurements in a range of 1–5 mm were possible, the actual value of the levels of agreement have to be critically judged. Although one can assume that there is some concordance, are the clinical concordance levels acceptable? Assuming that electrophysiology serves as a criterion standard, true mean distance values of 1–5 mm are plausible. The placement error of a stereotactic frame can range up to 2 mm in the single directions (x, y, z), and a mean vector error can be as high as 3.15 mm.²⁹

Assuming that there is a certain clinical dependence between the limits of agreement and the accuracy of the DTI FT method, a maximum error of ± 2.5 mm would be acceptable, especially in light of a 5-mm error in previous surgical DTI studies.^{15,17,28} Multiple factors add up to a combined application accuracy, and the present study was not designed to look at the accuracy but at concordance of 2 methods to determine the unknown value that expresses the distance between an electrode and the CST. Our own clinical experience with DTI FT–assisted targeting is that such an error, in reality, is smaller than our 2.5 mm; thus, in interpreting the data here, we are likely dealing with inherent limitations of the method applied, which we tried to discuss above. In any case, our results are within the framework of our own previously published and postulated simulation studies for DBS fiber tracts and electric fields.¹⁹

Scientific groups, including ours, successfully use the DTI FT technology to assist functional neurosurgical procedures.^{2-4,7,8,36,42,43} With all caution, our results would allow the further use of DTI FT to assist DBS procedures and to explore the effects and adverse events of DBS and lesion surgery.^{1,6,19,35,36} The future will show whether the development leads to a broader application of these direct DTI FT planning strategies based on individual “functional” anatomy. Clinical studies that investigate this technology are underway and are the focus of our ongoing research (www.clinicaltrials.gov; Deep brain Stimulation for Tremor Tractography Versus Traditional, NCT02491554; One Pass thalamic and subthalamic stimulation, NCT02288468).

Disclosures: Volker A. Coenen—UNRELATED: Consultancy: Dr Coenen has been a consultant for Medtronic (neuromodulation); Grants/Grants Pending: German Research Foundation,* BrainLinks–BrainTools (cluster of excellence),* Wilhelm-Tönnis Foundation; Payment for Lectures (including service on Speakers Bureaus): Dr Coenen has occasionally received travel fees and honoraria from Medtronic, Boston Scientific; OTHER RELATIONSHIPS: Dr Coenen has ongoing Investigator Initiated Trials with Boston Scientific and Medtronic; OTHER: V.A.C. acted as a clinical consultant in the evaluation of StealthViz DTI (Medtronic Navigation) in this defined project between the University of British Columbia and Medtronic Navigation. V.A.C. has

received limited funding as Principal Investigator for Investigator Initiated Trials from Medtronic and Boston Scientific. V.A.C. was supported with a stipend from the Wilhelm Tönis Foundation from the German Society of Neurological Surgeons. Christopher R. Honey—UNRELATED: *Grants/Grants Pending*: Medtronic*; *Payment for Lectures (including service on Speakers Bureaus)*: Medtronic*; *OTHER*: C.R.H. acted as a clinical consultant in the evaluation of StealthViz DTI (Medtronic Navigation) in this defined project between the University of British Columbia and Medtronic Navigation. Burkhard Mädler—UNRELATED: *Employment*: I am currently employed by Philips Healthcare, who did not provide any financial support for this study. Data collection and analysis were already completed before I became an employee of Philips. Only the period of manuscript drafting coincides with my employment status. *Money paid to the institution.

REFERENCES

- Coenen VA, Schlaepfer TE, Allert N, et al. **Diffusion tensor imaging and neuromodulation: DTI as key technology for deep brain stimulation.** *Int Rev Neurobiol* 2012;107:207–34 CrossRef Medline
- Henderson JM. **“Connectomic surgery”: diffusion tensor imaging (DTI) tractography as a targeting modality for surgical modulation of neural networks.** *Front Integr Neurosci* 2012;6:15 CrossRef Medline
- Barkhoudarian G, Klochov T, Sedrak M, et al. **A role of diffusion tensor imaging in movement disorder surgery.** *Acta Neurochir (Wien)* 2010;152:2089–95 CrossRef Medline
- Coenen VA, Allert N, Mädler B. **A role of diffusion tensor imaging fiber tracking in deep brain stimulation surgery: DBS of the dentato-rubro-thalamic tract (drt) for the treatment of therapy-refractory tremor.** *Acta Neurochir (Wien)* 2011;153:1579–85; discussion 1585 CrossRef Medline
- Coenen VA, Fromm C, Kronenburger M, et al. **Electrophysiological proof of diffusion-weighted imaging-derived depiction of the deep-seated pyramidal tract in human.** *Zentralbl Neurochi* 2006;67:117–22 CrossRef Medline
- Coenen VA, Honey CR, Hurwitz T, et al. **Medial forebrain bundle stimulation as a pathophysiological mechanism for hypomania in subthalamic nucleus deep brain stimulation for Parkinson’s disease.** *Neurosurgery* 2009;64:1106–14; discussion 1114–15 CrossRef Medline
- Coenen VA, Kieslbach K, Mader I, et al. **Diffusion tensor magnetic resonance imaging (DTI) tractography-guided deep brain stimulation in neuropathic pain.** *Acta Neurochir (Wien)* 2015;157:739–41 CrossRef Medline
- Coenen VA, Mädler B, Schiffbauer H, et al. **Individual fiber anatomy of the subthalamic region revealed with diffusion tensor imaging: a concept to identify the deep brain stimulation target for tremor suppression.** *Neurosurgery* 2011;68:1069–75; discussion 1075–76 CrossRef Medline
- Coenen VA, Schlaepfer TE, Maedler B, et al. **Cross-species affective functions of the medial forebrain bundle—implications for the treatment of affective pain and depression in humans.** *Neurosci Biobehav Rev* 2011;35:1971–81 CrossRef Medline
- Schlaepfer TE, Bewernick BH, Kayser S, et al. **Rapid effects of deep brain stimulation for treatment-resistant major depression.** *Biol Psychiatry* 2013;73:1204–12 CrossRef Medline
- Coenen VA, Krings T, Mayfrank L, et al. **Three-dimensional visualization of the pyramidal tract in a neuronavigation system during brain tumor surgery: first experiences and technical note.** *Neurosurgery* 2001;49:86–92; discussion 92–83 Medline
- Coenen VA, Krings T, Weidemann J, et al. **Sequential visualization of brain and fiber tract deformation during intracranial surgery with three-dimensional ultrasound: an approach to evaluate the effect of brain shift.** *Neurosurgery* 2005;56:133–41; discussion 133–41 Medline
- Wu JS, Zhou LF, Tang WJ, et al. **Clinical evaluation and follow-up outcome of diffusion tensor imaging-based functional neuronavigation: a prospective, controlled study in patients with gliomas involving pyramidal tracts.** *Neurosurgery* 2007;61:935–48; discussion 948–49 CrossRef Medline
- Kinoshita M, Yamada K, Hashimoto N, et al. **Fiber-tracking does not accurately estimate size of fiber bundle in pathological condition: initial neurosurgical experience using neuronavigation and subcortical white matter stimulation.** *Neuroimage* 2005;25:424–29 CrossRef Medline
- Hahn HK, Klein J, Nimsky C, et al. **Uncertainty in diffusion tensor based fibre tracking.** *Acta Neurochir Suppl* 2006;98:33–41 CrossRef Medline
- Nimsky C, Ganslandt O, Buchfelder M, et al. **Intraoperative visualization for resection of gliomas: the role of functional neuronavigation and intraoperative 1.5 T MRI.** *Neurol Res* 2006;28:482–87 CrossRef Medline
- Nimsky C, Ganslandt O, Fahlbusch R. **Implementation of fiber tract navigation.** *Neurosurgery* 2006;58:ONS-292–303; discussion ONS-303–04 Medline
- Nimsky C, Ganslandt O, Hastreiter P, et al. **Preoperative and intraoperative diffusion tensor imaging-based fiber tracking in glioma surgery.** *Neurosurgery* 2007;61:178–85; discussion 186 Medline
- Mädler B, Coenen VA. **Explaining clinical effects of deep brain stimulation through simplified target-specific modeling of the volume of activated tissue.** *AJNR Am J Neuroradiol* 2012;33:1072–80 CrossRef Medline
- Ranck JB Jr. **Which elements are excited in electrical stimulation of mammalian central nervous system: a review.** *Brain Res* 1975;98:417–40 CrossRef Medline
- Butson CR, Maks CB, McIntyre CC. **Sources and effects of electrode impedance during deep brain stimulation.** *Clin Neurophysiol* 2006;117:447–54 CrossRef Medline
- Burgel U, Madler B, Honey CR, et al. **Fiber tracking with distinct software tools results in a clear diversity in anatomical fiber tract portrayal.** *Cent Eur Neurosurg* 2009;70:27–35 CrossRef Medline
- Yousry TA, Schmid UD, Alkadhi H, et al. **Localization of the motor hand area to a knob on the precentral gyrus: a new landmark.** *Brain* 1997;120(pt 1):141–57 CrossRef Medline
- Bland JM, Altman DG. **Statistical methods for assessing agreement between two methods of clinical measurement.** *Lancet* 1986;1:307–10 Medline
- Bland JM, Altman DG. **Agreement between methods of measurement with multiple observations per individual.** *J Biopharm Stat* 2007;17:571–82 CrossRef Medline
- Nimsky C, Ganslandt O, Merhof D, et al. **Intraoperative visualization of the pyramidal tract by diffusion-tensor-imaging-based fiber tracking.** *Neuroimage* 2006;30:1219–29 CrossRef Medline
- Nimsky C, Ganslandt O, von Keller B, et al. **Intraoperative high-field MRI: anatomical and functional imaging.** *Acta Neurochir Suppl* 2006;98:87–95 CrossRef Medline
- Nimsky C, Ganslandt O, Fahlbusch R. **Implementation of fiber tract navigation.** *Neurosurgery* 2007;61:306–17; discussion 317–18 CrossRef Medline
- Holloway KL, Gaede SE, Starr PA, et al. **Frameless stereotaxy using bone fiducial markers for deep brain stimulation.** *J Neurosurg* 2005;103:404–13 CrossRef Medline
- Bjartmarz H, Rehnrona S. **Comparison of accuracy and precision between frame-based and frameless stereotactic navigation for deep brain stimulation electrode implantation.** *Stereotact Funct Neurosurg* 2007;85:235–42 CrossRef Medline
- Said N, Elias WJ, Raghavan P, et al. **Correlation of diffusion tensor tractography and intraoperative macrostimulation during deep brain stimulation for Parkinson disease.** *J Neurosurg* 2014;121:929–35 CrossRef Medline
- Coenen VA, McIntyre CC. **Letter to the Editor: Correlation of diffusion tensor imaging and intraoperative macrostimulation.** *J Neurosurg* 2015;123:291–92 CrossRef Medline
- Chaturvedi A, Butson CR, Lempka SF, et al. **Patient-specific models of deep brain stimulation: influence of field model complexity on neural activation predictions.** *Brain Stimul* 2010;3:65–67 CrossRef Medline
- Duerden EG, Finnis KW, Peters TM, et al. **Three-dimensional somatotopic organization and probabilistic mapping of motor responses from the human internal capsule.** *J Neurosurg* 2011;114:1706–14 CrossRef Medline

35. Sajonz B, Mädler B, Herberhold S, et al. **A case of tremor reduction and almost complete ageusia under bilateral thalamic (VIM) deep brain stimulation in essential tremor—a therapeutic dilemma.** *Acta Neurochir (Wien)* 2011;153:2361–63 CrossRef Medline
36. Sweet JA, Walter BL, Gunalan K, et al. **Fiber tractography of the axonal pathways linking the basal ganglia and cerebellum in Parkinson disease: implications for targeting in deep brain stimulation.** *J Neurosurg* 2014;120:988–96 CrossRef Medline
37. Kreher BW, Mader I, Kiselev VG. **Gibbs tracking: a novel approach for the reconstruction of neuronal pathways.** *Magn Reson Med* 2008;60:953–63 CrossRef Medline
38. Mori S, Kaufmann WE, Davatzikos C, et al. **Imaging cortical association tracts in the human brain using diffusion-tensor-based axonal tracking.** *Magn Reson Med* 2002;47:215–23 CrossRef Medline
39. Wakana S, Jiang H, Nagae-Poetscher LM, et al. **Fiber tract-based atlas of human white matter anatomy.** *Radiology* 2004;230:77–87 CrossRef Medline
40. Pinsker MO, Herzog J, Falk D, et al. **Accuracy and distortion of deep brain stimulation electrodes on postoperative MRI and CT.** *Zentralbl Neurochir* 2008;69:144–47 CrossRef Medline
41. Shin M, Lefaucheur JP, Penholate MF, et al. **Subthalamic nucleus stimulation in Parkinson's disease: postoperative CT-MRI fusion images confirm accuracy of electrode placement using intraoperative multi-unit recording.** *Neurophysiol Clin* 2007;37:457–66 Medline
42. Coenen VA, Allert N, Paus S, et al. **Modulation of the cerebello-thalamo-cortical network in thalamic deep brain stimulation for tremor: a diffusion tensor imaging study.** *Neurosurgery* 2014;75:657–69; discussion 669–70 CrossRef Medline
43. Sajonz BE, Mädler B, Herberhold S, et al. **Stimulation induced hypo-geusia in thalamic deep brain stimulation for tremor: an underestimated yet common side effect.** *J Neurol Neurosurg Psychiatry* 2015 Apr 21. [Epub ahead of print] CrossRef Medline
44. Coenen VA, Abdel-Rahman A, McMaster J, et al. **Minimizing brain shift during functional neurosurgical procedures: a simple burr hole technique that can decrease CSF loss and intracranial air.** *Cent Eur Neurosurg* 2011;72:181–85 CrossRef Medline
45. Elias WJ, Fu KM, Frysinger RC. **Cortical and subcortical brain shift during stereotactic procedures.** *J Neurosurg* 2007;107:983–88 CrossRef Medline
46. Schaltenbrand W, Wahren. *Atlas of Stereotaxy of the Human Brain*, Stuttgart: Georg Thieme-Verlag; 1977

Neurovascular Manifestations of Hereditary Hemorrhagic Telangiectasia: A Consecutive Series of 376 Patients during 15 Years

W. Brinjikji, V.N. Iyer, V. Yamaki, G. Lanzino, H.J. Cloft, K.R. Thielen, K.L. Swanson, and C.P. Wood

ABSTRACT

BACKGROUND AND PURPOSE: Hereditary hemorrhagic telangiectasia is associated with a wide range of neurovascular abnormalities. The aim of this study was to characterize the spectrum of cerebrovascular lesions, including brain arteriovenous malformations, in patients with hereditary hemorrhagic telangiectasia and to study associations between brain arteriovenous malformations and demographic variables, genetic mutations, and the presence of AVMs in other organs.

MATERIALS AND METHODS: Consecutive patients with definite hereditary hemorrhagic telangiectasia who underwent brain MR imaging/MRA, CTA, or DSA at our institution from 2001 to 2015 were included. All studies were re-evaluated by 2 senior neuroradiologists for the presence, characteristics, location, and number of brain arteriovenous malformations, intracranial aneurysms, and nonshunting lesions. Brain arteriovenous malformations were categorized as high-flow pial fistulas, nidus-type brain AVMs, and capillary vascular malformations and were assigned a Spetzler-Martin score. We examined the association between baseline clinical and genetic mutational status and the presence/multiplicity of brain arteriovenous malformations.

RESULTS: Three hundred seventy-six patients with definite hereditary hemorrhagic telangiectasia were included. One hundred ten brain arteriovenous malformations were noted in 48 patients (12.8%), with multiple brain arteriovenous malformations in 26 patients. These included 51 nidal brain arteriovenous malformations (46.4%), 58 capillary vascular malformations (52.7%), and 1 pial arteriovenous fistula (0.9%). Five patients (10.4%) with single nidal brain arteriovenous malformation presented with hemorrhage. Of brain arteriovenous malformations, 88.9% (88/99) had a Spetzler-Martin score of ≤ 2 . Patients with brain arteriovenous malformations were more likely to be female (75.0% versus 57.6%, $P = .01$) and have a family history of hereditary hemorrhagic telangiectasia (95.8% versus 84.8%, $P = .04$). The prevalence of brain arteriovenous malformation was 19.7% in endoglin (*ENG*) mutations and 12.5% in activin receptor-like kinase (*IACVRL1*) mutations.

CONCLUSIONS: Our study of 376 patients with hereditary hemorrhagic telangiectasia demonstrated a high prevalence of brain arteriovenous malformations. Nidal brain arteriovenous malformations and capillary vascular malformations occurred in roughly equal numbers.

ABBREVIATIONS: BAVM = brain arteriovenous malformation; DVA = developmental venous anomaly; HHT = hereditary hemorrhagic telangiectasia

Hereditary hemorrhagic telangiectasia (HHT), also known as Rendu-Osler-Weber disease, is an autosomal dominant disorder affecting vascular beds in multiple organ systems. Pathognomonic vascular lesions in HHT include arteriovenous malformations and telangiectasias of the skin, mucous membranes, and visceral organs, including the lung, liver, gastrointestinal tract, brain, and spinal cord.¹ HHT is diagnosed clinically by using the

Curacao criteria,² which include spontaneous and recurrent epistaxis, mucocutaneous telangiectasias (lips, oral cavity, face and fingers), visceral AVMs (brain, liver, gastrointestinal, lung, and so forth), and a diagnosis of HHT in a first-degree relative by using the same criteria. Patients who meet ≥ 3 of the 4 criteria are labeled as having “definite HHT,” while those with 2 of the 4 criteria are labeled as having “possible” or “suspected” HHT.³

Patients with HHT can present with myriad CNS complications, including vascular malformations of the brain and spinal cord. There has been much interest in studying the prevalence, characteristics, and natural history of brain AVMs (BAVMs) and other vascular anomalies in patients with HHT due to their associated morbidity. While several studies have examined the prevalence of vascular malformations and anomalies in patients with HHT, few have sought to provide a detailed characterization of the anatomic, angiographic, and clinical correlates of these le-

Received October 30, 2015; accepted after revision January 28, 2016.

From the Departments of Radiology (W.B., H.J.C., K.R.T., C.P.W.), Pulmonary and Critical Care Medicine (V.N.I., V.Y.), and Neurosurgery (G.L.), Mayo Clinic, Rochester, Minnesota; and Department of Pulmonary and Critical Care Medicine (K.L.S.), Mayo Clinic, Scottsdale, Arizona.

Please address correspondence to Waleed Brinjikji, MD, Mayo Clinic, Department of Radiology, 200 1st St SW, Rochester, MN 55905; e-mail: brinjikji.waleed@mayo.edu; @wbrinjikji

<http://dx.doi.org/10.3174/ajnr.A4762>

Table 1: Patient population and prevalence of vascular lesions

	Patients with Definite HHT No (%)
No. of patients	376
Mean age (SD) (yr)	53.0 (43.4)
Sex	
Male	151 (40.1)
Female	225 (59.8)
Imaging	
CTA/MRA	140 (37.2)
DSA	46 (12.2)
MRI	365 (97.1)
Curacao criteria	
Epistaxis	334 (88.8)
Mucocutaneous telangiectasia	327 (87.0)
Visceral AVMs	321 (85.4)
Family history	324 (86.2)
Mutation analysis	
<i>ENG</i>	61 (49.6)
<i>ACVRL1</i>	48 (39.0)
<i>SMAD4</i>	14 (11.4)
Chest CT	311 (82.7)
Pulmonary AVMs	176 (56.6)
Abd/pelv CT	344 (91.5)
Hepatic vascular malformations	185 (53.8)
Other GI vascular malformations	8 (2.3)
Neuroimaging findings	
Cerebral AVM	48 (12.8)
DVA	45 (12.0)
Cavernoma/focal hemosiderin deposition	13 (3.5)
Capillary telangiectasia	9 (2.4)
Cerebral aneurysm	8 (2.1)

Note:—Abd indicates abdominal; pelv, pelvic; GI, gastrointestinal.

sions. The aims of the present study were the following: 1) to determine the prevalence of cerebral vascular lesions, including BAVMs and nonshunting vascular lesions such as developmental venous anomalies (DVAs), intracranial aneurysms, and cavernous malformations in the HHT population; 2) to subclassify BAVMs by using previously described criteria⁴; and 3) to determine whether there are any associations between the presence of BAVMs and demographic variables, vascular lesions in other organs, and genetic mutation status.

MATERIALS AND METHODS

Patient Population

The study was approved by our institutional review board. We included all patients with definite HHT with available neuroimaging studies (cerebral angiography, CT angiography, MR imaging, and/or MR angiography) seen at our institution from January 2001 to May 2015. Patients were initially identified by querying our electronic medical record for the terms HHT, hereditary hemorrhagic telangiectasia, Osler-Weber-Rendu, or Rendu-Osler-Weber. We also searched for any patients with an International Classification of Diseases-9 code for HHT (448.0) in their electronic medical record. Then, all the shortlisted patient records were individually reviewed to determine which Curacao criteria were met. Only those meeting ≥ 3 Curacao criteria and with available neuroimaging studies were included in the final cohort. Patients meeting ≤ 2 Curacao criteria (ie, patients with suspected HHT) were excluded.

Demographic and Clinical Data

The following baseline demographic data were collected for each patient: age, sex, HHT mutation status (if available), and family history.

Table 2: Characteristics of AVMs

	No. (%)
Patients with AVMs	48 (100.0)
No. of AVMs	110 (100.0)
Patients with nidus-type	28 (58.3)
Patients with capillary vascular malformations	31 (64.6)
Patients with pial AVF	1 (2.1)
No. with multiple AVMs	26 (54.2)
No. of AVMs in patients	
1	22 (45.8)
2	14 (29.2)
3	5 (10.4)
>3	7 (14.6)
Location	
Frontal	48 (43.6)
Parietal	15 (13.6)
Occipital	12 (10.9)
Temporal	14 (12.7)
Cerebellar	17 (15.4)
Brain stem	2 (1.8)
Basal ganglia/thalamic	2 (1.8)
Spetzler Martin size	
<3 cm	97 (97.0)
3–6 cm	2 (2.0)
>6 cm	1 (1.0)
Eloquent location	
Yes	51 (51.0)
No	49 (49.0)
Deep venous drainage	
Yes	16 (16.1)
No	83 (83.9)
Spetzler Martin score	
1	43 (43.4)
2	45 (45.5)
3	10 (10.1)
4	0 (0.0)
5	1 (1.0)
Presenting with hemorrhage	5 (10.4)

HHT mutations were classified as *ENG* mutations (as seen in HHT1), *ACVRL1* mutations (as seen in HHT2) and *SMAD4* mutations. Information on the presence of HHT-associated complications, including epistaxis; liver, gastrointestinal, or pulmonary AVMs; and mucocutaneous telangiectasia was collected as well.

Imaging Evaluation

All neuroimaging was evaluated by 2 senior neuroradiologists with 15 and 20 years of experience and a senior radiology resident. Images were re-evaluated for the presence of BAVMs, DVA, intracranial aneurysms, cavernous malformations, and capillary telangiectasias. In case of disagreement, a consensus was reached with the help of a third neuroradiologist. BAVMs were classified according to the criteria put forth by Krings et al⁴ as high-flow “single-hole” pial fistulas, nidus-type BAVMs, and capillary vascular malformations. A pial AVF was defined by the presence of shunting in association with an abnormally dilated pial artery and the absence of an intervening nidus. Nidus-type BAVMs were defined by the presence of an abnormal network of dilated vessels (ie, a nidus) present between the feeding artery and draining vein. Capillary vascular malformations were defined by the presence of a blush of abnormal vessels seen either during the capillary phase of cerebral angiography with a single draining vein or by an area of fluffy, stainlike enhancement on contrast-enhanced CT or MR imaging, with a nondilated feeding artery and

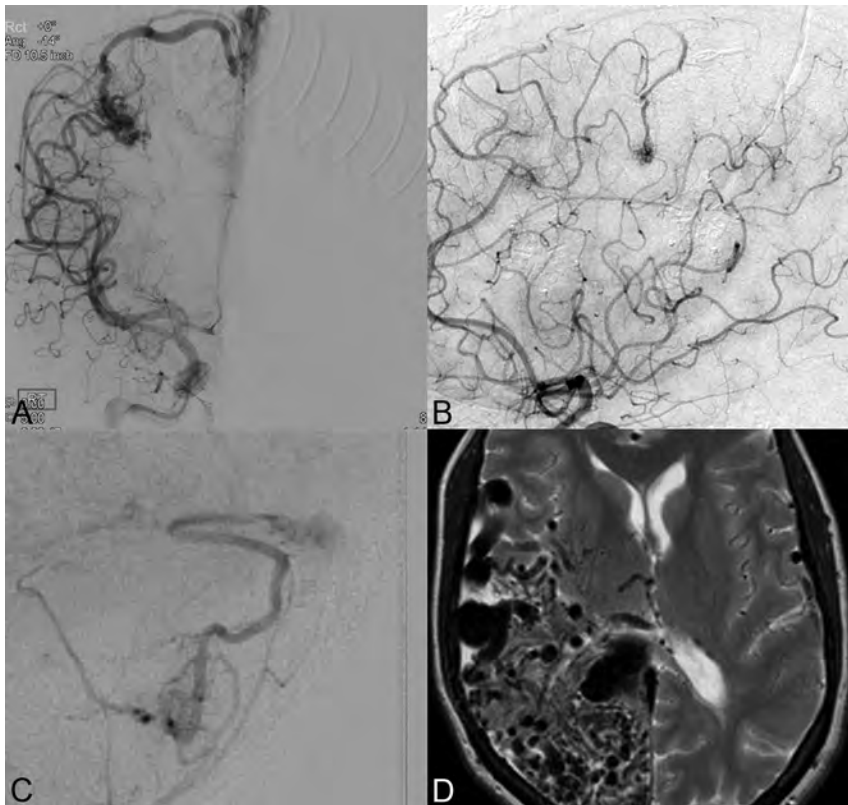


FIG 1. Characteristics of nidus AVMs. *A* and *B*, Superficially located nidus AVMs in the frontal lobes of 2 patients with definite HHT. The lesions lack features such as venous stenoses or intranidal aneurysms and drain into superficial veins. *C*, A cerebellar nidus AVM in a patient with definite HHT, which drains into a superficial cerebellar vein and into the transverse sinus. *D*, Diffuse AVM involving a large portion of the right cerebral hemisphere. The AVM has multiple large venous ectasias and drains into the deep and superficial venous systems.

draining vein. Capillary vascular malformations did not show flow voids on MR imaging. The Spetzler-Martin score was calculated for each BAVM, and the presence of hemorrhage at the time of diagnosis was also recorded. In assessing the Spetzler-Martin score and eloquent location was defined as the sensorimotor, language or visual cortex, hypothalamus, thalamus, brainstem, cerebellar nuclei or regions directly adjacent to these structures. The locations of DVAs, aneurysms, cavernous malformations, and capillary telangiectasias were recorded as well.

Statistical Analysis

Continuous variables were compared by using the Student *t* test, and categorical variables, with the χ^2 test. All analyses were performed by using JMP 12.0 (SAS Institute, Cary, North Carolina). We determined prevalence of BAVMs, DVAs, intracranial aneurysms, and cavernomas in the HHT population. We also tested for differences in age, sex, and HHT gene mutation, and the presence of other vascular abnormalities between patients with HHT and BAVMs and those without. Additional tests were performed to determine variables associated with BAVM multiplicity.

RESULTS

Patient Population

Three hundred seventy-six patients with definite HHT were included in this study. The mean patient age was 53.0 ± 43.4 years, and most were women ($n = 225, 59.8\%$). Manifestations of HHT

included epistaxis in 334 (88.8%) patients, mucocutaneous telangiectasias in 327 (87.0%), visceral AVMs in 321 (85.4%), and a positive family history of HHT in 324 (86.2%) patients. One hundred thirty-three patients had genetic testing, of whom 123 (27.1%) had positive findings on a genetic test. Of the 123 with positive findings on a genetic test, 61 (49.6%) had endoglin (*ENG*) mutations, 48 (39.0%) had activin receptor-like kinase 1 (*ACVRL1*) mutations, and 14 (11.4%) had SMAD family member 4 (*SMAD4*) mutations. Of the 10 with negative findings on a genetic test, all 10 met at least 3 Curacao criteria, suggesting a diagnosis of definite HHT. Of the 311 patients with chest CTs, 176 (56.6%) had pulmonary AVMs. Of the 344 patients with abdomen and pelvis CTs, 185 patients (53.8%) had evidence of hepatic vascular malformations. These data are summarized in Table 1.

Prevalence and Characteristics of Brain AVMs

One hundred ten BAVMs were found in 48 patients (12.8%), including 26 patients with multiple BAVMs. These included 51 nidus BAVMs (46.4%), 58 capillary vascular malformations (52.7%), and 1 pial arteriovenous fistula (0.9%). Hemorrhage was the presenting manifestation in 5 patients (10.4%), each with a single nidus BAVM; all lesions were successfully treated on the first presentation. The 2 most common locations of BAVMs were the frontal lobes ($n = 48, 43.6\%$) and the cerebellum ($n = 17, 15.4\%$). Size measurements were available for 100 lesions, exact cortical location was available for 100 lesions, and venous drainage data were available for 99 lesions. Complete Spetzler-Martin scores were calculated for 99 BAVMs, of which most ($n = 88, 88.9\%$) had scores of ≤ 2 . Of the characterizable BAVMs, 97 (97.0%) had a nidus size of < 3 cm, 51 (51.0%) were in an eloquent location, and 16 (16.1%) had deep venous drainage. These data are summarized in Table 2.

Of the 51 nidus BAVMs, 40 (78.4%) were supratentorial and 11 (21.6%) were infratentorial. A nidus size of > 3 cm was seen in 2 nidus BAVMs (4.8%), and 10 (25.0%) had deep venous drainage. Twenty-six nidus BAVMs (63.4%) were in an eloquent location; 80.0% (32 nidus BAVMs) had a Spetzler-Martin score of ≤ 2 . Representative examples of nidus-type BAVMs are shown in Fig 1.

Of the 58 capillary vascular malformations, 50 (86.2%) were supratentorial and 8 (13.8%) were infratentorial. All measured < 1 cm in maximal diameter. Twenty-four (41.4%) were in an eloquent location, 6 (10.3%) had a deep venous drainage, and 56 (96.5%) had a Spetzler-Martin score of ≤ 2 . Representative examples of capillary vascular malformations are provided in Fig 2. These data are summarized in Table 3.

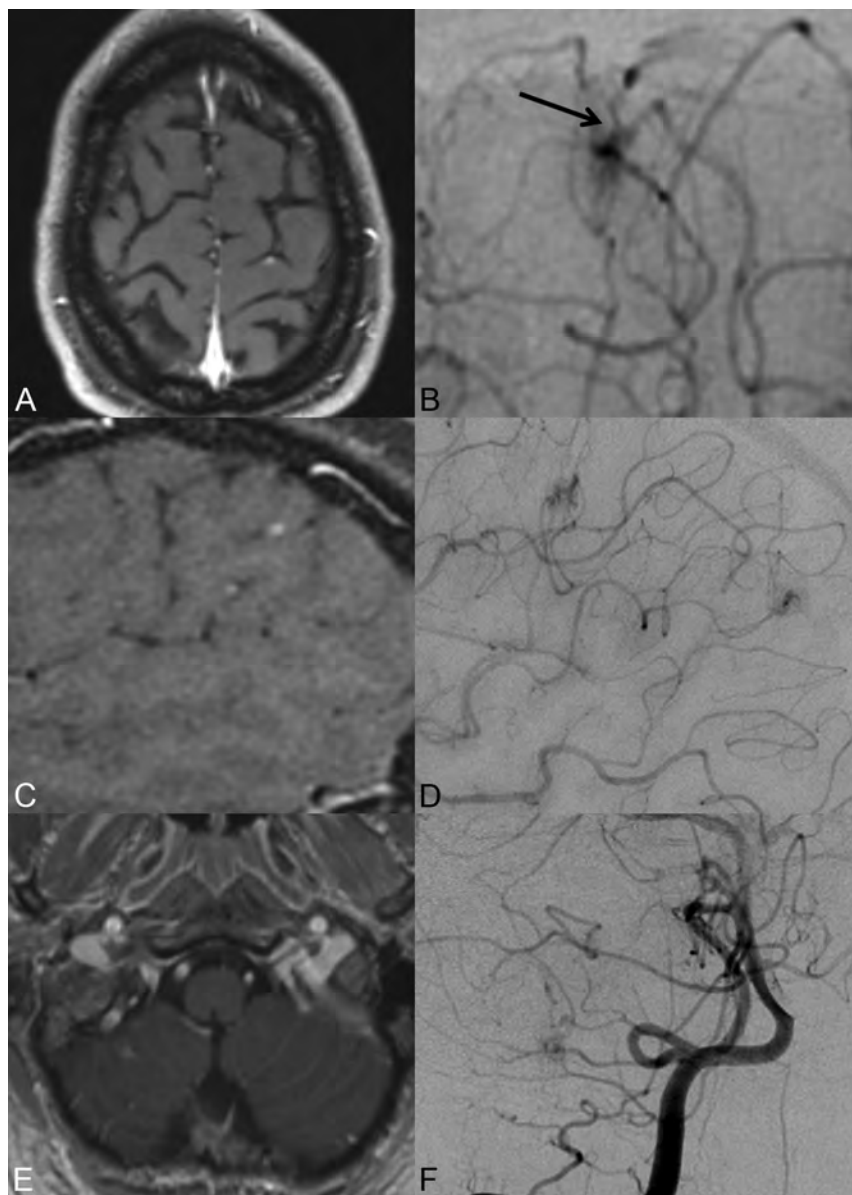


FIG 2. A, T1 contrast-enhanced MR image demonstrates a punctate focus of enhancement. The corresponding angiographic view (B) shows a capillary vascular malformation with a small draining vein. C, T1 contrast-enhanced MR image shows a punctate focus of enhancement in the parietal lobe in a patient with definite HHT. D, Cerebral angiography in this patient shows 2 capillary vascular malformations in the parietal lobe, one of which was occult on MR imaging. E, T1 contrast-enhanced MR imaging demonstrates a small focus of enhancement in the right cerebellar hemisphere. F, A corresponding cerebral angiogram demonstrates a capillary vascular malformation with a single feeding artery and draining vein.

Prevalence and Characteristics of Nonshunting Cerebral Vascular Lesions

Fifty-two DVAs were noted in 45 patients (12.0%), with 4 patients having >1 DVA. The most common locations were in the frontal lobes (19, 36.5%) and the cerebellum (17, 32.7%). All DVAs were asymptomatic.

Twenty-eight cavernomas were noted in 13 patients (3.5%), with 5 patients having multiple cavernomas. The most common locations for cavernomas were the frontal lobes ($n = 12$, 42.9%) and occipital lobes ($n = 7$, 25.0%). Only 1 cavernoma was symptomatic and was surgically removed.

Thirteen capillary telangiectasias were noted in 9 patients

(2.4%). Two patients had >1 capillary telangiectasia. The most common location for capillary telangiectasia was the brain stem ($n = 6$, 46.2%). These data are summarized in Table 4. Representative examples of nonshunting vascular lesions are provided in Fig 3.

Eight patients (2.1%) had 16 cerebral aneurysms. Three patients (37.5%) had multiple aneurysms. Five aneurysms (31.3) were associated with AVMs, and 1 aneurysm (6.3%) bled. The mean aneurysm size was 3.8 ± 2.0 mm. Aneurysms were most commonly located in the territory of the internal carotid artery (50.0%). These data are summarized in Table 5. Representative examples of aneurysms are provided in Fig 4.

Clinical and Genetic Variables Associated with BAVMs

Patients with BAVMs were more likely to be women (75.0% versus 57.6%, $P = .01$) and have a positive family history for HHT (95.8% versus 84.8%, $P = .04$). Genetic mutational status was available for 18 patients with BAVMs and 105 without BAVMs. *ENG* mutations were present in 66.6% of the patients with BAVMs (12/18) and in 46.7% (49/105) of those without them. The overall prevalence of BAVMs in patients with *ENG* mutations was 19.7% versus 12.5% in patients with *ACVRL1* mutations and 0% in those with *SMAD4* mutations. There was no difference in the mean age of patients with and without BAVMs ($P = .38$) and no difference in the proportion of patients with pulmonary AVMs ($P = .46$) or gastrointestinal AVMs ($P = .27$). These data are summarized in Table 6.

Clinical Characteristics of Patients with Single-versus-Multiple BAVMs

As mentioned previously, multiple BAVMs were found in 26 patients, and 22 had a single BAVM.

Among patients with multiple BAVMs, 7 had gene testing, of whom 6 (85.7%) had *ENG* mutations. Among patients with single BAVMs, 11 had gene testing, of whom 6 (54.5%) were positive for *ENG* mutations. Overall, multiple BAVMs were present in 9.8% (6/61) of patients with *ENG* mutations compared with 2.1% (1/48) of patients with *ACVRL1* and 0% of those with *SMAD4* mutations. No variables were associated with AVM multiplicity.

DISCUSSION

Our study of 376 consecutive patients with a diagnosis of definite HHT found the prevalence of BAVMs to be 12.8%, with a rela-

Table 3: Characteristics of AVMs by AVM Type

	Nidal AVM (n = 51) (46.4)	CVM (n = 58) (52.7)	Pial AVF (n = 1) (0.0)
Location			
Frontal	21 (37.9)	26 (44.8)	1 (100.0)
Parietal	4 (7.8)	11 (19.0)	0 (0.0)
Occipital	7 (13.7)	5 (8.6)	0 (0.0)
Temporal	8 (15.7)	6 (10.3)	0 (0.0)
Cerebellar	10 (19.6)	7 (12.1)	0 (0.0)
Brain stem	1 (2.0)	1 (1.7)	0 (0.0)
Basal ganglia/thalamic	0 (0.0)	2 (3.5)	0 (0.0)
Spetzler Martin size			
<3 cm	39 (95.1)	58 (100.0)	0 (0.0)
3–6 cm	1 (2.4)	0 (0.0)	1 (100.0)
>6 cm	1 (2.4)	0 (0.0)	0 (0.0)
Eloquent location			
Yes	26 (63.4)	24 (41.4)	1 (100.0)
No	15 (36.6)	34 (58.6)	0 (0.0)
Deep venous drainage			
Yes	10 (25.0)	6 (10.3)	0 (0.0)
No	30 (75.0)	52 (89.7)	1 (100.0)
Spetzler Martin score			
1	13 (32.5)	30 (51.7)	0 (0.0)
2	19 (47.5)	26 (44.8)	0 (0.0)
3	7 (17.5)	2 (3.5)	0 (0.0)
4	0 (0.0)	0 (0.0)	1 (100.0)
5	1 (2.5)	0 (0.0)	0 (0.0)

Note:—CVM indicates capillary vascular malformation.

Table 4: Nonshunting vascular lesions

	Capillary		
	Telangiectasia	Cavernoma	DVA
No. of patients	9	13	45
No. of lesions	13	28	52
No. with multiple lesions	2 (22.2)	5 (48.5)	4 (8.9)
No. of lesions in patients			
1	7 (77.7)	8 (61.5)	41 (91.1)
2	1 (11.1)	1 (7.7)	2 (4.4)
3	0 (0.0)	0 (0.0)	1 (2.2)
>3	1 (11.1)	4 (30.8)	1 (2.2)
Location			
Frontal	2 (15.4)	12 (42.9)	19 (36.5)
Parietal	0 (0.0)	2 (7.1)	6 (11.5)
Occipital	0 (0.0)	7 (25.0)	3 (5.8)
Temporal	2 (15.4)	2 (7.1)	3 (5.8)
Cerebellar	1 (7.7)	3 (10.7)	17 (32.7)
Brain stem	6 (46.2)	1 (3.6)	3 (5.8)
Basal ganglia/thalamic	2 (15.4)	1 (3.6)	1 (1.9)

tively even split between capillary vascular malformations and nidus-type BAVMs. More than 80% of BAVMs were supratentorial. Only 3% had a nidus size of >3 cm, and < 20% had deep venous drainage. Approximately 10% of patients with BAVMs presented with rupture. Variables associated with the presence of a BAVM included female sex and a positive family history of HHT. Similar to prior studies, we demonstrated a higher prevalence of both single and multiple BAVMs among patients with *ENG* mutations. These findings are important because they provide further insight into the prevalence, risk factors, and characteristics of cerebral AVMs in the HHT population.

Large prospective screening studies have demonstrated BAVM prevalence rates between 10% and 20%, depending on the HHT population being screened.^{5–10} These are similar to rates in

our study in which we found a 12.8% BAVM prevalence. In general, most studies have demonstrated a similar prevalence of BAVMs in male and female patients, unlike our study, which demonstrated a preponderance of women in the HHT group.^{7–9,11–13} In general, the prevalence of cerebral AVMs has been shown to be higher in patients with *ENG* mutations compared with those with *ACVRL1* mutations.^{8,10} Lesion multiplicity is thought to be a hallmark of HHT. According to 1 recently published study, 44% of patients with HHT with cerebral vascular malformations had at least 2 different brain malformations.⁴ In our series, >50% of patients with BAVMs had multiple AVMs. On the basis of the high prevalence of cerebral AVMs in the HHT population, most experts agree that screening MR imaging is warranted for both adults and children.¹⁴

While several studies have examined the prevalence of AVMs in the HHT population, few studies have sought to characterize these lesions. In a study of 75 patients with 125 BAVMs, Krings et al⁴ found that nearly two-thirds of BAVMs were capillary vascular malformations. Similar to findings in our study, they found that these lesions were primarily supratentorial with a superficial location and were <1 cm. A report from the Bicêtre Hospital found that approximately 20% of AVMs were capillary vascular malformations, with a similar distribution in size and location compared with those in our study.¹⁵ Differences in the prevalence of capillary vascular malformations between studies are likely due to a combination of differences in imaging techniques (ie, they are more easily detected angiographically than on MR imaging) and indications for imaging, because these lesions are often detected incidentally and are not associated with hemorrhage, seizure, or headache.⁴

Capillary vascular malformations are distinct from capillary telangiectasia because they consist of a feeding artery, dilated capillary bed, and, generally, a single draining vein. Meanwhile, capillary telangiectasias consist of numerous thin-walled ectatic capillaries interspersed between normal brain parenchyma and lack an identifiable feeding artery, though they can sometimes have a draining vein. Capillary telangiectasias are typically angiographically occult and are located in the pons, while capillary vascular malformations are best appreciated angiographically and have a supratentorial location.

In our series, nidus-type AVMs represented the most common type of BAVM. More than 95% of these lesions had a small nidus, and approximately 50% were in an eloquent location. A vast majority were superficially located and had superficial venous drainage. These findings are similar to those in a number of studies that have demonstrated that >90% of nidus AVMs have a Spetzler-Martin score of ≤2 and are typically located in a superficial, supratentorial location with pial-based feeding arteries.^{4,15–17} These lesions tend to measure 1–2 cm and tend to lack features such as arterial stenoses, associated aneurysms, multiple draining veins, venous ectasia, and venous reflux.⁴ Unlike capillary vascular malformations however, nidus-type BAVMs do not have a completely benign natural history because these lesions can rupture, as seen in our study.

Most interesting, we found a relatively high prevalence of DVAs (12.0%), capillary telangiectasias (2.4%), and cavernomas (3.5%). In the general population, the prevalence of DVAs is

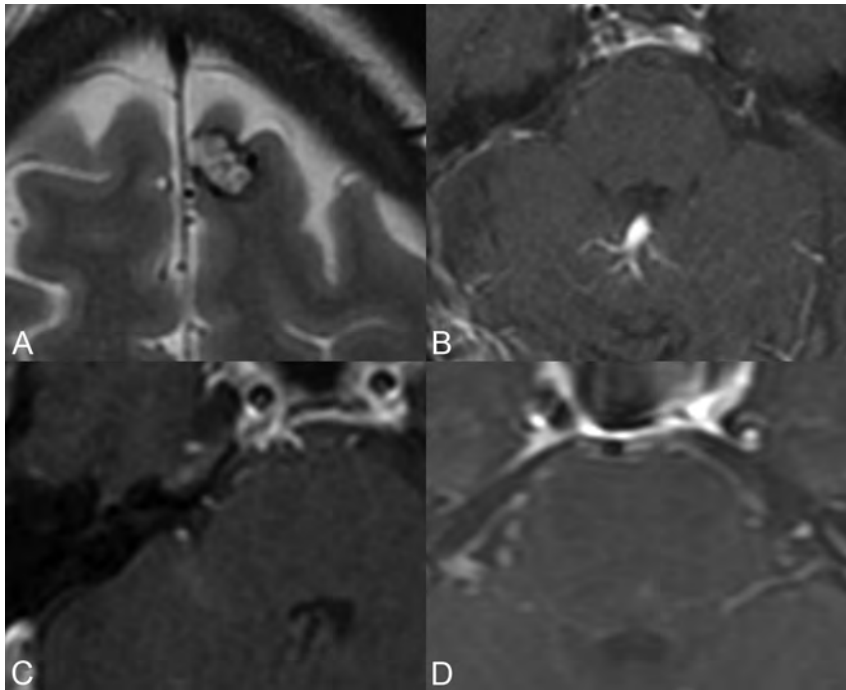


FIG 3. A, T2-weighted MR image demonstrates a typical cavernoma. B, T1 contrast-enhanced MR image demonstrates a large developmental venous anomaly in the cerebellar vermis, with a typical caput medusae appearance. C and D, T1 contrast-enhanced MRIs demonstrate the typical appearance of capillary telangiectasias.

Table 5: Characteristics of saccular aneurysms

	No (%)
Total patients	8 (100.0)
Multiple	3 (37.5)
Total No. of aneurysms	16
Location	
Internal carotid artery	8 (50.0)
Anterior cerebral artery	1 (6.3)
Middle cerebral artery	3 (18.8)
Basilar tip	1 (6.3)
Anterior communicating artery	3 (18.8)
Mean size (mm) (SD)	3.8 (2.0)
AVM-associated	5 (31.3)
SAH	1 (6.3)

about 2%, while capillary telangiectasias and cavernomas are present in about 0.5% of patients. Most DVAs, capillary telangiectasias, and cavernomas are found incidentally. All 3 of these lesions typically have a benign natural history in both the HHT and general populations. While prior studies have suggested that patients with HHT have higher rates of telangiectasias and DVAs, an association between HHT and cavernomas has not been demonstrated, to our knowledge. One possible explanation for the higher rates of these lesions in patients with HHT compared with the general population is that capillary telangiectasias, cavernomas, and DVAs have all been linked to elevations in vascular endothelial growth factor (*VEGF*) expression.¹⁸⁻²⁰ Some authors have reported an association between cerebral AVMs and vascular anomalies such as DVAs and capillary telangiectasias; however, this is thought to be rare. The high prevalence of DVAs and BAVMs in the HHT population could potentially be problematic in the setting of a BAVM draining into a DVA. However, such a finding is rare and has been reported in only a few case reports.²¹

The rate of cerebral aneurysms in our study was 2%, which is similar to the rate reported in the general population.²² Approximately one-third of aneurysms in our series were associated with BAVMs. One recently published study demonstrated a higher rate of visceral arterial aneurysms in the HHT population, attributing this to alterations in the transforming growth factor- β signaling pathway.²³ While some studies indicate that alterations in the transforming growth factor- β signaling pathway play a role in the pathogenesis of intracranial aneurysms, no study to date has demonstrated a higher prevalence of intracranial aneurysms in the HHT population when compared to the general population.²⁴

Limitations

Our study has limitations. First, because this was not a prospective screening study, there are substantial limitations in the ascertainment of cases. Patients who present with symptoms such as headache, seizure, or focal neurologic symptoms may be more likely to have a neurovascular lesion than those who present for asymptomatic screening.

While it is possible that we overestimated the prevalence of neurovascular lesions in the HHT population due to this limitation, the prevalence of cerebral AVMs in our study was similar to that reported in the literature. Another limitation is that we did not have information regarding genotypes for most patients. While both patients with HHT1 and HHT2 present with higher rates of BAVMs than the general population, most studies have demonstrated a higher rate of BAVMs in the HHT1 population. Another limitation is that not all patients with BAVMs underwent 4-vessel cerebral angiography. Cerebral angiography is significantly more sensitive than contrast-enhanced MR imaging and MRA in detecting smaller arteriovenous malformations and is a better way to characterize these lesions. However, lesions that are occult on MR imaging are probably more likely to be capillary vascular malformations, which are known to have a benign natural history.

CONCLUSIONS

Our study of 376 patients with suspected or definite HHT demonstrated a high prevalence of cerebral AVMs (BAVMs) and nonshunting vascular lesions, including DVAs, capillary telangiectasias, and cavernomas. Hemorrhage was the presenting feature in 10% of patients with BAVMs. More than 50% of patients with BAVMs had multiple cerebral AVMs, with the most common lesions being capillary vascular malformation-type BAVMs, followed by nidus-type BAVMs. Future research is needed to determine the predictors of BAVM formation and multiplicity in the HHT population and to better determine

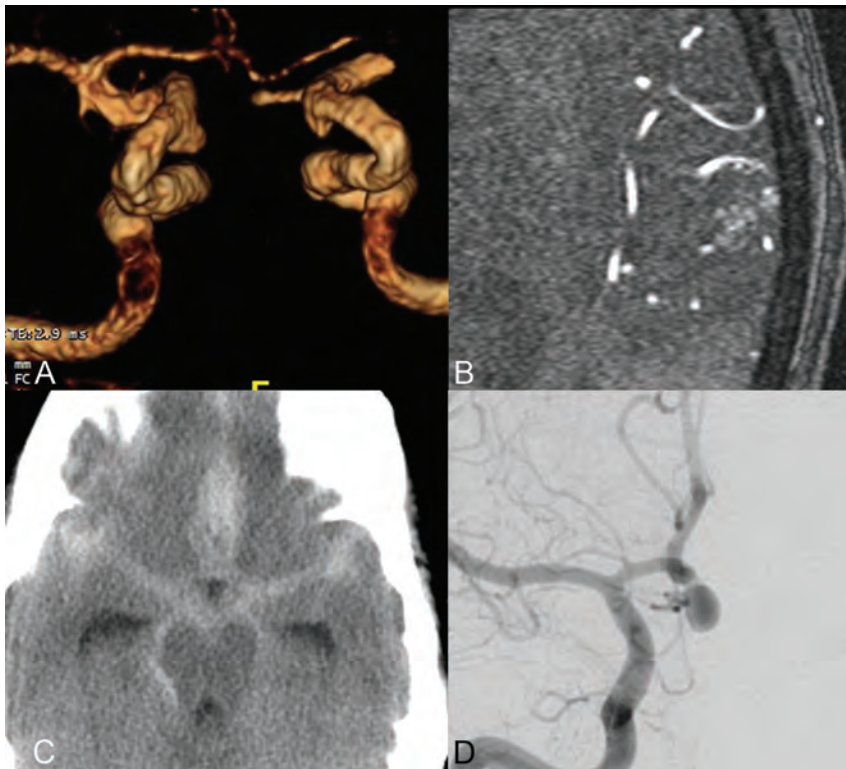


FIG 4. A, 3D reconstruction of an MRA demonstrates bilateral carotid siphon aneurysms and a dysplastic right MCA. B, This patient has a 1.5-cm nidal AVM in the left MCA territory. C, Noncontrast head CT shows diffuse subarachnoid hemorrhage in a patient with HHT with an 8-mm ruptured anterior communicating artery aneurysm (D).

Table 6: Risk factors for AVMs and AVM multiplicity

	Yes AVM	No AVM	P	Multiple AVM	Single AVM	P
No.	48	328		26	22	
Mean age (yr)	50.2 (18.2)	53.5 (46.0)	.38	49.5 (19.1)	51.0 (17.5)	.77
Sex						
Male	12 (25.0)	139 (42.4)	.01	6 (23.1)	6 (27.3)	.74
Female	36 (75.0)	189 (57.6)		20 (76.9)	16 (72.7)	
Curacao criteria						
Epistaxis	39 (81.3)	295 (89.9)	.07	22 (84.6)	17 (77.3)	.52
Mucocutaneous telangiectasia	43 (89.6)	284 (86.6)	.56	22 (84.6)	21 (95.5)	.22
Family history	46 (95.8)	278 (84.8)	.04	26 (100.0)	20 (90.9)	.12
Pulmonary AVMs	26 (61.9)	150 (55.8)	.46	14 (63.6)	12 (60.0)	.81
Abdominal vascular malformations	20 (45.5)	191 (54.3)	.27	8 (36.4)	12 (57.1)	.23

the natural history and optimum treatment options for these lesions.

Disclosures: Giuseppe Lanzino—UNRELATED: Consultancy: Covidien/ev3.**Money paid to the institution.

REFERENCES

- McDonald J, Bayrak-Toydemir P, Pyeritz RE. Hereditary hemorrhagic telangiectasia: an overview of diagnosis, management, and pathogenesis. *Genet Med* 2011;13:607–16 CrossRef Medline
- Shovlin CL, Guttmacher AE, Buscarini E, et al. Diagnostic criteria for hereditary hemorrhagic telangiectasia (Rendu-Osler-Weber syndrome). *Am J Med Genet* 2000;91:66–67 Medline
- McDonald J, Wooderchak-Donahue W, VanSant Webb C, et al. Hereditary hemorrhagic telangiectasia: genetics and molecular diagnostics in a new era. *Front Genet* 2015;6:1 Medline
- Krings T, Kim H, Power S, et al; Brain Vascular Malformation Consortium HHT Investigator Group. Neurovascular manifestations in hereditary hemorrhagic telangiectasia: imaging features and genotype-phenotype correlations. *AJNR Am J Neuroradiol* 2015;36:673–80 CrossRef Medline
- Salaria M, Taylor J, Bogwitz M, et al. Hereditary haemorrhagic telangiectasia, an Australian cohort: clinical and investigative features. *Intern Med J* 2014;44:639–44 CrossRef Medline
- Latino GA, Al-Saleh S, Carpenter S, et al. The diagnostic yield of rescreening for arteriovenous malformations in children with hereditary hemorrhagic telangiectasia. *J Pediatr* 2014;165:197–99 CrossRef Medline
- Saleh M, Carter MT, Latino GA, et al. Brain arteriovenous malformations in patients with hereditary hemorrhagic telangiectasia: clinical presentation and anatomical distribution. *Pediatr Neurol* 2013;49:445–50 CrossRef Medline
- Ni Bhuachalla CF, O'Connor TM, Murphy M, et al. Experience of the Irish National Centre for hereditary hemorrhagic telangiectasia 2003–2008. *Respir Med* 2010;104:1218–24 CrossRef Medline
- Al-Saleh S, Mei-Zahav M, Faughnan ME, et al. Screening for pulmonary and cerebral arteriovenous malformations in children with hereditary haemorrhagic telangiectasia. *Eur Respir J* 2009;34:875–81 CrossRef Medline
- Mahadevan J, Ozanne A, Yoshida Y, et al. Hereditary haemorrhagic telangiectasia cerebrospinal localization in adults and children: review of 39 cases. *Interv Neuro-radiol* 2004;10:27–35 Medline
- Woodall MN, McGettigan M, Figueroa R, et al. Cerebral vascular malformations in hereditary hemorrhagic telangiectasia. *J Neurosurg* 2014;120:87–92 CrossRef Medline
- Kjeldsen AD, Moller TR, Brusgaard K et al. Clinical symptoms according to genotype amongst patients with hereditary hemorrhagic telangiectasia. *J Intern Med* 2005;258:349–55 Medline CrossRef
- Letteboer TG, Mager JJ, Snijder RJ, et al. Genotype-phenotype relationship in hereditary haemorrhagic telangiectasia. *J Med Genet* 2006;43:371–77 Medline
- Faughnan ME, Palda VA, Garcia-Tsao G, et al; HT Foundation International - Guidelines Working Group. International guidelines for the diagnosis and management of hereditary haemorrhagic telangiectasia. *J Med Genet* 2011;48:73–87 CrossRef Medline
- Krings T, Ozanne A, Chng SM, et al. Neurovascular phenotypes in hereditary haemorrhagic telangiectasia patients according to age: review of 50 consecutive patients aged 1 day–60 years. *Neuroradiology* 2005;47:711–20 CrossRef Medline
- Krings T, Ozanne A, Chng SM, et al. Hereditary hemorrhagic telangiectasia: neurovascular phenotypes and endovascular treatment. *Clin Neuroradiol* 2006;16:76–90 CrossRef
- Brinjikji W, Iyer VN, Sorenson T, et al. Cerebrovascular manifestations of hereditary hemorrhagic telangiectasia. *Stroke* 2015;46:3329–37 CrossRef Medline
- Zhu Y, Wu Q, Fass M, et al. In vitro characterization of the angiogenic phenotype and genotype of the endothelia derived from spo-

- radic cerebral cavernous malformations.** *Neurosurgery* 2011;69:722–31; discussion 731–32 CrossRef Medline
19. Abe T, Morishige M, Ooba H, et al. **The association between high VEGF levels and multiple probable punctuate cavernous malformations.** *Acta Neurochir (Wien)* 2009;151:855–59 CrossRef Medline
20. Hao Q, Su H, Marchuk DA, et al. **Increased tissue perfusion promotes capillary dysplasia in the ALK1-deficient mouse brain following VEGF stimulation.** *Am J Physiol Heart Circ Physiol* 2008;295:H2250–56 CrossRef Medline
21. Fok KF, Holmin S, Alvarez H, et al. **Spontaneous intracerebral hemorrhage caused by an unusual association of developmental venous anomaly and arteriovenous malformation.** *Interv Neuroradiol* 2006;12:113–21 Medline
22. Vlak MH, Algra A, Brandenburg R, et al. **Prevalence of unruptured intracranial aneurysms, with emphasis on sex, age, comorbidity, country, and time period: a systematic review and meta-analysis.** *Lancet Neurol* 2011;10:626–36 CrossRef Medline
23. Moulinet T, Mohamed S, Deibener-Kaminsky J, et al. **High prevalence of arterial aneurysms in hereditary hemorrhagic telangiectasia.** *Int J Cardiol* 2014;176:1414–16 CrossRef Medline
24. Bakir-Gungor B, Sezerman OU. **The identification of pathway markers in intracranial aneurysm using genome-wide association data from two different populations.** *PLoS One* 2013;8:e57022 CrossRef Medline

Reduced Myelin Water in the White Matter Tracts of Patients with Niemann-Pick Disease Type C

J. Davies-Thompson, I. Vavasour, M. Scheel, A. Rauscher, and J.J.S. Barton



ABSTRACT

SUMMARY: Previous studies using diffusion tensor imaging to examine white matter in Niemann-Pick disease type C have produced mixed results. However, diffusion tensor imaging does not directly measure myelin and may be affected by other structural changes. We used myelin water imaging to more directly examine demyelination in 2 patients with Niemann-Pick disease type C. The results suggest that this technique may be useful for identifying regional changes in myelination in this condition.

ABBREVIATIONS: NPC = Niemann-Pick disease type C; MWF = myelin water fraction; P01 = Patient 1; P02 = Patient 2

Niemann-Pick disease type C (NPC) is a progressive lysosomal storage disease caused by a mutation in the *NPC1* or *NPC2* gene leading to intracellular accumulation of cholesterol systemically and glycosphingolipids in the nervous system. Previous studies have shown reduced gray matter in a variety of cerebral regions, including the thalamus and hippocampus,¹ while others have correlated reductions in cerebellum gray matter with clinical severity scores.² Measures of white matter may also be useful, though studies using diffusion tensor imaging have provided mixed results, with some noting widespread changes in white matter tracts,¹ while others found localized reductions to specific structures.^{3,4} Nevertheless, callosal fractional anisotropy values and callosal volume correlated with clinical severity scores,⁴ suggesting that indices of the integrity of white matter tracts could also be an objective gauge of disease status. Such findings are consistent with reduced myelination being a noticeable neuropathologic finding in NPC.⁵

However, inferences about the status of myelin from measures of fractional anisotropy on diffusion tensor imaging can be prob-

lematic because fractional anisotropy can also be altered by a reduction in the number of axons or changes in axonal structure caused by swelling or abnormal branching. This is particularly relevant because animal NPC models have shown abnormal branching and swelling of axons.⁶ Hence, a more direct in vivo measure of myelin may be clinically desirable. Here, we evaluated the use of myelin water imaging,⁷ a technique that measures the amount of water present within the myelin of white matter tracts and has been used previously to measure abnormalities in multiple sclerosis,⁸ to examine the distribution and extent of demyelination in 2 patients with NPC.

MATERIALS AND METHODS

Subjects

Patient 1 (P01) is a man who presented at 29 years of age. He developed a mild hand-action tremor at 16 years of age and slurring of speech at 17 years of age. In his early twenties, he developed progressive imbalance and incoordination of his hands. His examination showed a score of 29/30 on the Mini-Mental State Examination. He had slurred dysarthria, intention tremor, and limb dysmetria as well as truncal and gait ataxia. MR imaging showed mild cortical atrophy. Genetic testing showed 2 mutations in the *NPC1* gene: allele 1 c.C3019G (p.P1007A) and allele 2 c.C2780T (p.A927V). He started *N*-butyl-deoxynojirimycin (Miglstat) in September 2008 (29 years of age) and was scanned at 33 and 34 years of age.

Patient 2 (P02) is a woman who presented at 26 years of age. A psychological assessment showed problems with visuomotor sequencing, complex verbal reasoning, and written expression. Otherwise, she had only noted some mild balance problems. She scored 29/30 on the Mini-Mental State Examination. She had mildly impaired tandem gait. MR imaging showed patchy confluent hyperintense white matter changes, most prominent in the

Received November 10, 2015; accepted January 5, 2016.

From the Crossmodal Perception and Plasticity Laboratory (J.D.-T.), Center of Mind/Brain Sciences, University of Trento, Trento, Italy; Human Vision and Eye Movement Laboratory (J.D.-T., J.J.S.B.), Departments of Medicine (Neurology), Ophthalmology, and Visual Sciences, Department of Radiology (I.V.), and Department of Pediatrics, and UBC MRI Research Centre (A.R.), University of British Columbia, Vancouver, British Columbia, Canada; and Department of Radiology (M.S.), Charité University Clinics, Berlin, Germany.

J. Davies-Thompson and I. Vavasour contributed equally to this article.

Please address correspondence to Jodie Davies-Thompson, MD, Centre for Mind/Brain Sciences, University of Trento, Via delle Regole 101, 38060 Mattarello (TN), Italy; e-mail: Jodie.DaviesThompson@unitn.it

Indicates open access to non-subscribers at www.ajnr.org

<http://dx.doi.org/10.3174/ajnr.A4719>

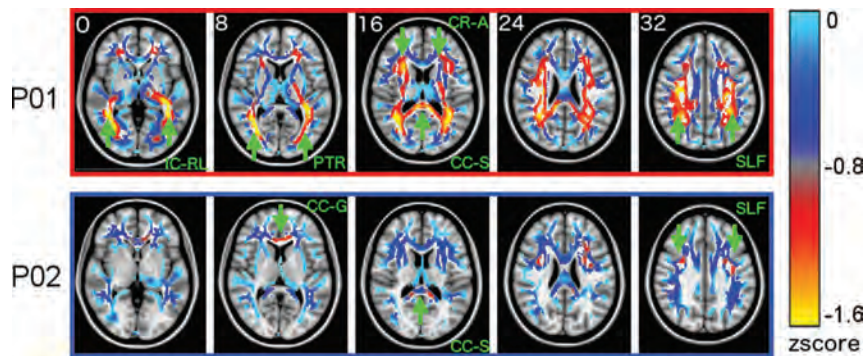


FIG 1. Whole-brain myelin water z score maps in the 2 patients. Statistical z score maps show the difference between patients and their respective control subjects, where negative z scores indicate reduced myelin water. For clarity, maps were spatially smoothed with a Gaussian 6-mm filter and are shown on a diluted fractional anisotropy skeleton. Statistical maps (minimum thresholded at $z = -1.6$ for clarity) are overlaid on the average Montreal Neurological Institute brain. *Green arrows* highlight areas where the myelin is substantially reduced in the patients compared with their controls. IC-RL indicates retrolenticular portion of internal capsule; PTR, posterior thalamic radiation including the optic radiation; CR-A, anterior corona radiata; SLF, superior longitudinal fasciculus; CC-G, genu of corpus callosum; CC-S, splenium of the corpus callosum.

posterior periventricular regions. Genetic testing showed 2 mutations associated with Niemann-Pick disease type C: exon 18 c.2621A>T (p.Asp874Val) and exon 23 c.3508C>G (p.His1170Asp). She began treatment with Miglustat in April 2011 (27 years of age) and was scanned at 28 and 29 years of age.

Fifteen healthy control subjects took part in this study. Eight men (mean age, 31.9 years) acted as control subjects for P01, while 7 women (mean age, 30.3 years) acted as control subjects for P02.

Imaging Parameters

A T1-weighted high-resolution structural scan (3D-T1-turbo field echo with sensitivity encoding: TR, 10 ms; turbo field echo, 3000 ms; TE, 6 ms; TI, 845.88 ms; 170 sections; FOV, 240 mm; voxel size, 1×1 mm; section thickness, 1 mm) was collected as well as a multiecho axial gradient and spin-echo scan⁷ for T2 measurement (TR, 1000 ms; TE, 10, 20, 30...320 ms; 20 sections acquired at 5-mm thickness reconstructed at 2.5-mm section thickness; in-plane voxel size, 1×1 mm; sensitivity encoding, 2232×192 matrix).

Myelin Water Fraction Analysis

The signal decay curve obtained by the T2 relaxation sequence was modeled by multiple exponential components, and the T2 distribution was estimated by using non-negative least squares with the extended phase graph algorithm.⁷ The myelin water fraction (MWF) in each image voxel was computed as the ratio of the area under the T2 distribution with times of 10–40 ms to the total area under the distribution. The MWF images were then registered to the T1-weighted anatomic scan.

To compare the patients' myelin water fraction maps with those of the healthy population, we matched a normative 3D atlas representing the mean and SD for myelin water fraction from each group of age-matched healthy controls. The healthy myelin water fraction maps were calculated, nonlinearly aligned to Montreal Neurological Institute standard space, and averaged. MWF maps for patients were also nonlinearly aligned to Montreal Neurological Institute space. For each voxel, a z score was calcu-

lated comparing the patient MWF values with the corresponding control group distribution.

The Juelich histologic white matter atlas in FSL (<http://neuro.debian.net/pkgs/fsl-juelich-histological-atlas.html>) was used to create tracts of interest. Average MWF values from each fiber tract were then extracted and averaged across the hemisphere. MWF values from the patients were compared with those from aged-matched controls by using Crawford t-tests.⁹

RESULTS

Paired sample tests of the tract-of-interest analysis showed that the results were stable across the 2 visits for P01 [$t(60) = -1.62, P = .11$] and P02 [$t(60) = 1.44, P = .15$]; therefore, because our analysis of the results across visits showed high

reproducibility and stability of data, we averaged data across the 2 visits.

Figure 1 shows the average MWF z score maps for both patients, indicating the location of regions with reduced myelin compared with those of the controls. The patient with the less clinically severe condition (P02) showed focal, patchy reductions in MWF, while the patient with the more clinically severe condition (P01) showed extensive, widespread reductions across entire fiber tracts.

A global analysis for each of the 3 classes revealed that P01 had a reduction in MWF for projection [$t(7) = -2.46, P < .05, \eta = -2.61$], association [$t(7) = -2.49, P < .05, \eta = -2.64$], and commissural fibers [$t(7) = -2.41, P < .05, \eta = -2.56$]. For P02, MWF values were not reduced in this global analysis, for association [$t(6) = -0.18, P = .43, \eta = -0.2$], projection [$t(6) = -1.09, P = .16, \eta = -1.17$], or commissural fibers [$t(6) = -1.33, P = .12, \eta = -1.42$]. Regional analysis of different tracts (Fig 2) revealed significant MWF reductions for P01 in 4 projection tracts, 4 association tracts, and 1 commissural tract. In P02, the less affected patient, only 2 commissural tracts showed significantly reduced MWF.

A paired-samples *t* test, collapsed across all fibers, showed significantly lower MWF for the patient with the more clinically severe condition, P01, compared with P02 [$t(16) = -4.488, P < .001$].

DISCUSSION

We conducted a detailed examination of the distribution of reduced myelination in the cerebral cortex of 2 patients with NPC. In the clinically worse patient, there was reduced MWF in a large number of association fibers. We also observed large reductions of MWF in the corpus callosum of both patients, paralleling prior reports of reduced callosal fractional anisotropy⁴ and cortical thickness of the corpus callosum¹⁰ in this disorder. However, reductions in the MWF of projection tracts were only observed in the more clinically affected patient.

The physiologic basis for regional variation in NPC remains unclear¹; nevertheless, this is a well-documented phenomenon in animal and human models.^{11,12} For example, in humans, some

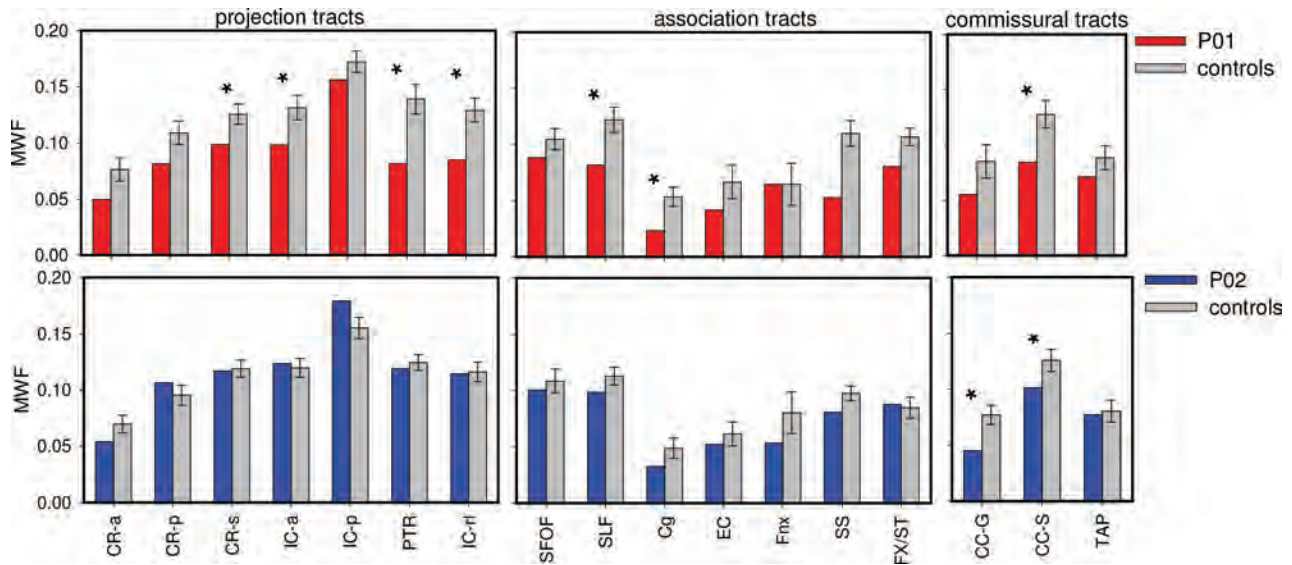


FIG 2. Tract analysis for patients (red and blue bars) and their age-matched control subjects (gray bars). CR-a indicates anterior corona radiata, CR-p, posterior corona radiata; CR-s, superior corona radiata; IC-a, anterior limb of internal capsule; IC-p, posterior limb of internal capsule; PTR, posterior thalamic radiation including optic radiation; IC-rl, retrolenticular portion of internal capsule; SFOF, superior fronto-occipital fasciculus; SLF, superior longitudinal fasciculus; Cg, cingulum including the hippocampus; EC, external capsule; Fnx, column and body of fornix; SS, sagittal stratum including inferior longitudinal fasciculus and inferior fronto-occipital fasciculus; Fx/ST, fornix and stria terminalis; CC-g, genu of the corpus callosum; CC-s, splenium of corpus callosum; TAP, tapetum. Asterisks indicate $P < .05$ as determined by Crawford t-tests.⁹ Error bars show 1 standard error of the mean.

studies show regions with selectively reduced fractional anisotropy, such as in the corpus callosum⁴ and the superior cerebellar peduncle,³ while others have shown widespread variations in the reduction of fractional anisotropy.¹

Our results also contain 3 important observations relevant to the possible use of MWF to monitor disease status. First, the data for MWF were consistent during a year, indicating that they are reproducible and reliable. Second, the contrast between our patients indicates that MWF may correlate with clinical severity. However, further studies are required to show whether the measure is sensitive to changes in clinical severity with time, which could be either deterioration through natural progression or improvement with therapy. Third, our whole-brain analysis showed reduced MWF in some but not all areas of a fiber tract, suggesting that the effects of this disorder are focal and patchy in milder stages of the disease. This effect of severity may explain discrepancies in prior studies, with some showing focal and others diffuse effects.

Because other neuronal abnormalities are present in NPC, combined use of both MWF and diffusion tensor imaging in future assessment of this disease may help elucidate the contributing pathologic factors affecting white matter tracts in NPC.

Disclosures: Jodie Davies-Thompson—UNRELATED: Grants/Grants Pending: Canadian Institutes of Health Research.* Irene Vavasour—UNRELATED: Travel/Accommodations/Meeting Expenses Unrelated to Activities Listed: Hoffman-La Roche, Comments: reimbursement for conference expenses (International Society of Magnetic Resonance in Medicine, 2014). Jason J.S. Barton—RELATED: serves on the Scientific Advisory Board for Vycor Medical Corporation and is funded by the Canadian Institutes of Health Research operating grants MOP-102567, MOP-106511, and MOP-130566. *Money paid to the institution.

REFERENCES

1. Walterfang M, Fahey M, Desmond P, et al. White and gray matter alterations in adults with Niemann-Pick disease type C: a cross-sectional study. *Neurology* 2010;75:49–56 CrossRef Medline
2. Walterfang M, Abel LA, Desmond P, et al. Cerebellar volume correlates with saccadic gain and ataxia in adult Niemann-Pick type C. *Mol Genet Metabol* 2013;108:85–89 CrossRef Medline
3. Scheel M, Abegg M, Lanyon LJ, et al. Eye movement and diffusion tensor imaging analysis of treatment effects in a Niemann-Pick type C patient. *Mol Genet Metabol* 2010;99:291–95 CrossRef Medline
4. Lee R, Apkarian K, Jung ES, et al. Corpus callosum diffusion tensor imaging and volume measures are associated with disease severity in pediatric Niemann-Pick disease type C1. *Pediatr Neurol* 2014;51:669–674.e5 CrossRef Medline
5. Elleder M, Jirásek A, Smid F, et al. Niemann-Pick disease type C: study on the nature of the cerebral storage process. *Acta Neuropathol* 1985;66:325–36 CrossRef Medline
6. Zervas M, Somers KL, Thrall MA, et al. Critical role for glycosphingolipids in Niemann-Pick disease type C. *Curr Biol* 2001;11:1283–87 CrossRef Medline
7. Prasloski T, Rauscher A, MacKay AL, et al. Rapid whole cerebrum myelin water imaging using a 3D GRASE sequence. *Neuroimage* 2012;63:533–39 CrossRef Medline
8. Vavasour IM, Whittall KP, MacKay AL, et al. A comparison between magnetization transfer ratios and myelin water percentages in normals and multiple sclerosis patients. *Magn Reson Med* 1998;40:763–68 CrossRef Medline
9. Crawford JR, Garthwaite PH. Methods of testing for a deficit in single-case studies: evaluation of statistical power by Monte Carlo simulation. *Cogn Neuropsychol* 2006;23:877–904 CrossRef Medline
10. Walterfang M, Fahey M, Abel L, et al. Size and shape of the corpus callosum in adult Niemann-Pick type C reflects state and trait illness variables. *AJNR Am J Neuroradiol* 2011;32:1340–46 CrossRef Medline
11. Walkley SU, Suzuki K. Consequences of NPC1 and NPC2 loss of function in mammalian neurons. *Biochim Biophys Acta* 2004;1685:48–62 CrossRef Medline
12. March PA, Thrall MA, Brown DE, et al. GABAergic neuroaxonal dystrophy and other cytopathological alterations in feline Niemann-Pick disease type C. *Acta Neuropathol* 1997;94:164–72 CrossRef Medline

Fate of Coiled Aneurysms with Minor Recanalization at 6 Months: Rate of Progression to Further Recanalization and Related Risk Factors

J.P. Jeon, Y.D. Cho, J.K. Rhim, D.H. Yoo, W.-S. Cho, H.-S. Kang, J.E. Kim, and M.H. Han



ABSTRACT

BACKGROUND AND PURPOSE: Minor recanalization in coiled aneurysms may remain stable with time or may progress to major recanalization. Our aim was to monitor the aneurysms displaying minor recanalization in imaging studies at 6 months, gauging major recanalization rates and related risk factors through extended follow-up.

MATERIALS AND METHODS: Sixty-five aneurysms (in 65 patients) showing minor recanalization in follow-up imaging at 6 months were reviewed retrospectively. Medical records and radiologic data accruing during extended monitoring (mean, 24.8 ± 8.2 months) were assessed. Univariate and multivariate analyses were conducted to identify risk factors for progression from minor-to-major recanalization.

RESULTS: Progression to major recanalization was observed in 24 (36.9%) of the initially qualifying aneurysms during a follow-up of 112.5 aneurysm-years, for an annual rate of 17.84% per aneurysm-year. Progression was determined chronologically as follows: 14 (58.3%) at 6 months, 8 (33.3%) at 18 months, and 2 (8.4%) at 30 months. Stent deployment significantly decreased the occurrence of major recanalization (OR = 0.22, $P = .03$), whereas antiplatelet therapy (OR = 0.82, $P = .75$), posterior location (OR = 0.24, $P = .20$), and second coiling for recanalized aneurysms (OR = 0.96, $P = .96$) were unrelated.

CONCLUSIONS: Our analysis determined a 36.9% rate of major recanalization during a follow-up of 112.5 aneurysm-years in coiled aneurysms showing minor recanalization at 6 months. Stent deployment alone conferred a protective effect, preventing further recanalization without additional treatment. Given the fair probability of late major recanalization, aneurysms showing minor recanalization at 6 months should be monitored diligently, particularly in the absence of stent placement.

ABBREVIATIONS: DM = diabetes mellitus; HTN = hypertension; UIA = unruptured intracranial aneurysm; WSS = wall shear stress

Physicians are sometimes at a loss in predicting the potential outcomes of coiled aneurysms if minor recanalization is found during follow-up intervals. This is precisely why recanalization rates and related risk factors (based on initial angiographic results) have been addressed in most prior studies. Unfortunately, end points have thus far been measured as all recanalizations (major and minor),¹ major recanalization only,² or retreatment rates,³ leaving a void with respect to the clinical course of aneurysms showing minor recanalization. In general, minor recanalization is not an indication for additional treatment, though progression to

major recanalization may eventually call for further intervention. Lejeune et al⁴ described a series of 21 coiled aneurysms subjected to additional surgical treatment for major recanalization (Raymond class 3). Lin et al⁵ also reported that residual necks of 1–2 mm may expand to 4–25 mm during a mean of 9 years. Accordingly, further study of the progression from minor-to-major recanalization is needed to devise proper treatment and management. For this study, we investigated treatment outcomes in aneurysms showing minor recanalization 6 months after coiling, assessing the clinical course, rate of progression to major recanalization, and related risk factors.

MATERIALS AND METHODS

A retrospective analysis was conducted, reviewing 1035 aneurysms in 898 patients who had undergone coil embolization between January 2008 and December 2010 at Seoul National University Hospital. Nonsaccular aneurysms ($n = 70$) with fusiform shapes or resulting from dissection, trauma, or infection were excluded. In accord with institutional protocol, follow-up radio-

Received November 5, 2015; accepted after revision January 28, 2016.

From the Department of Neurosurgery (J.P.J.), Hallym University College of Medicine, Chuncheon, Korea; and Departments of Radiology (Y.D.C., J.K.R., D.H.Y., M.H.H.) and Neurosurgery (W.S.C., H.-S.K., J.E.K.), Seoul National University College of Medicine, Seoul, Korea.

Please address correspondence to Young Dae Cho, MD, Department of Radiology, Seoul National University Hospital, Seoul National University College of Medicine, 28 Yongon-dong, Jongno-gu, Seoul, Korea, 110-744; e-mail: aronnn@empal.com

Indicates article with supplemental on-line table.

<http://dx.doi.org/10.3174/ajnr.A4763>

logic examinations via 3D time-of-flight MR angiography, including source images, were conducted at 6, 12, 18, 24, and 36 months after coil embolization. Conventional angiography was advised if posttreatment MRA was not feasible or if major recanalization of an aneurysm was suspected by noninvasive diagnostics. As stipulated by the Raymond classification, recanalization at 6 months was defined as contrast filling the aneurysm neck (minor recanalization) or dome (major recanalization) at follow-up imaging.² The primary study end point was major recanalization during extended follow-up in coiled aneurysms showing only minor recanalization at 6 months. To categorize extended anatomic outcomes, we applied the Raymond scale as follows: progressive aneurysmal occlusion (no contrast filling within aneurysm), stable stationary state (contrast filling the neck of the aneurysm only, no change relative to the 6-month status), or major recanalization (saccular contrast filling, further recanalization relative to the 6-month status).

Medical records were reviewed for multiple parameters, including sex, age, clinical presentation (unruptured intracranial aneurysm [UIA] or subarachnoid hemorrhage), aneurysmal status (initial or recanalized aneurysm), hypertension (HTN), diabetes mellitus (DM), smoking, and history of antiplatelet therapy. Angiographic variables assessed included the size of the aneurysm and its neck, location (anterior-versus-posterior circulation),⁶ type of aneurysm (sidewall-versus-bifurcation), depth-to-neck ratio, packing density, stent deployment, and type of coil (hydrogel-modified coils [HydroSoft coils; MicroVention, Tustin, California] and polyglycolic acid/lactide copolymer-coated coils [Matrix coils; Stryker, Kalamazoo, Michigan]). According to the length of the bioactive coil used (relative to the total length of the coil inserted), aneurysms were grouped as bare ($\leq 50\%$) or bioactive ($> 50\%$) coils.⁷ This study was approved by the institutional review boards.

Endovascular Procedure and Angiographic Follow-Up

Most of the endovascular procedures were conducted with the patient under general anesthesia, by using an Integris V (Philips Healthcare, Best, the Netherlands) scanner in each instance. Dual-agent antiplatelet therapy (loading doses of clopidogrel and aspirin [ie, 300 mg each] given 1 day before the procedure, with an additional morning dose of clopidogrel [75 mg] and aspirin [100 mg] on the day of the procedure) was administered if stent protection was anticipated in patients with unruptured aneurysms.⁸ In poor responders to clopidogrel, signaled by VerifyNow P2Y12 assay (Accumetrics, San Diego, California), cilostazol was added. We prescribed single-agent (clopidogrel) therapy if stent placement was not planned, adding aspirin in poor responders. In patients presenting with SAH, antiplatelet medications were withheld. A bolus of heparin (3000 IU), given on placement of the femoral arterial sheath, was thereafter sustained by hourly doses (1000 IU); activated clotting time was monitored each hour. After the procedure, continuance of the dual antiplatelet therapy was advised for at least 3 months postoperatively, followed by single-agent maintenance for at least 1 year in patients with stent deployment. In the absence of a stent, antiplatelet therapy was selectively used for patients with prior antiplatelet medication histories, coil protrusion, and procedural thromboembolism.

Patients were grouped according to immediate angiographic status after coil embolization, by using the Raymond scale, as either successful occlusion (complete occlusion or residual neck) or residual sac. Immediate angiographic results and follow-up diagnoses were interpreted by 2 experienced neurointerventionists (Y.D.C., 8 years' experience; H.-S.K., 13 years' experience). In cases of discrepancy between the reviewers, a consensus was reached by the third interventional neuroradiologist (M.H.H., > 25 years experience).

Statistics

Continuous data were presented as the mean \pm SD. A χ^2 or Fisher exact test and an unpaired *t* test were used to assess categorical and continuous variables, respectively. Univariate analysis was applied to evaluate factors pertaining to recanalization after coiling. Risk factors for progression from minor-to-major recanalization were determined by using a logistic regression model to analyze variables with *P* values $< .20$. The average annual major recanalization transformation rate was calculated as the major recanalization count divided by total aneurysm-years of follow-up. We used standard software (SPSS, Version 19; IBM, Armonk, New York) for all the above, setting statistical significance at *P* $< .05$.

RESULTS

Characteristics of Coiled Aneurysms with Minor Recanalization at 6-Month Follow-Up

A total of 965 saccular aneurysms were treated by coil embolization between January 2008 and December 2010. After we excluded 66 aneurysms that lacked 6-month postembolization follow-up, including 16 patients in a vegetative state and 10 deaths, 899 aneurysms were initially eligible for the study. Another 34 aneurysms followed for 6 months only were also excluded. Of the remaining 865 aneurysms, 742 were completely occluded at the 6-month point and 58 demonstrated major recanalization. Ultimately, 65 aneurysms in 65 patients (48 women, 73.8%; mean age, 57.9 ± 11.0 years) qualified for study during a mean extended follow-up of 24.8 ± 8.2 months, each showing minor recanalization 6 months after coiling. Most lesions involved the anterior (56/65, 86.2%) rather than posterior (9/65, 13.8%) circulation. In the anterior circulation, the distribution was as follows: internal carotid artery, 16; anterior cerebral artery, including the anterior communicating artery, 21; middle cerebral artery, 9; and posterior communicating artery, 10. Sidewall and bifurcation aneurysms occurred in 15 (23.1%) and 50 (76.9%) patients, respectively. As an initial angiographic outcome, 54 coiled aneurysms (83.1%) were successfully occluded. The mean size of aneurysms was estimated at 6.3 ± 3.2 mm, with 45 (69.2%) being ≤ 7 mm. Sixteen (24.6%) patients presented with SAH. The depth-to-neck ratio was > 1 in 38 aneurysms (58.5%). HydroSoft and Matrix coils were used for 26 and 6 subjects, respectively. The bioactive coil group (length of bioactive coil used [relative-to-total length of the coil inserted] $> 50\%$) included 20 coils (30.8%), and all were HydroSoft. Stents were present in 19 patients (29.2%): Enterprise (Codman & Shurtleff, Raynham, Massachusetts) in 17 and Neuroform (Stryker Neurovascular) in 2. A single stent was used in 18 patients, while double stents were used in 1 patient.

Table 1: Demographic and angiographic characteristics of coiled aneurysms showing minor recanalization in follow-up images at 6 months (N = 65)

Variables	Stationary (n = 41)	Major Recanalization (n = 24)	P Value ^a
Clinical			
Female	30 (73.2%)	18 (75.0%)	.87
Age (yr)	58.1 ± 12.0	57.6 ± 9.2	.86
HTN	27 (65.9%)	12 (50.0%)	.21
DM	3 (7.3%)	0 (0%)	.29
Hyperlipidemia	4 (9.8%)	2 (8.3%)	1.00
Smoking	4 (9.8%)	5 (20.8%)	.21
Aneurysmal			
Location			
Anterior	33 (80.5%)	23 (95.8%)	
Posterior	8 (19.5%)	1 (4.2%)	.08
Presentation			
UIA	33 (80.5%)	16 (66.7%)	
SAH	8 (19.5%)	8 (33.3%)	.21
Status			
Initial	28 (68.3%)	20 (83.3%)	
Recanalized (2nd coiling)	13 (31.7%)	4 (16.7%)	.18
Bifurcation aneurysm	31 (75.6%)	19 (79.2%)	.74
Maximum size (mm)	6.3 ± 2.7	6.2 ± 4.1	.93
D/N ratio (>1)	22 (53.7%)	16 (66.7%)	.30
Neck size (mm)	4.7 ± 2.1	4.0 ± 1.6	.22
Procedural			
Stent	16 (39.0%)	3 (12.5%)	.02
Balloon	4 (9.8%)	4 (16.7%)	.41
Bioactive coil (>50%)	13 (31.7%)	7 (29.2%)	.83
Initial occlusion			.47
Successful occlusion	33 (80.5%)	21 (87.5%)	
Residual sac	8 (19.5%)	3 (12.5%)	
Antiplatelet maintenance	25 (61.0%)	10 (41.7%)	.13

Note:—D/N indicates depth-to-neck.

^aP < .05 is significant.

Table 2: Logistic regression model assessing the risk of progression to major recanalization in coiled aneurysms showing minor recanalization at 6 months (N = 65)

Variables	Odds Ratio	95% Confidence		P Value ^a
		Interval		
Antiplatelet maintenance	0.82	0.25–2.68		.75
Posterior location	0.24	0.03–2.15		.20
Recanalized aneurysm	0.96	0.22–4.30		.96
Stent	0.22	0.06–0.87		.03

^aP < .05 is significant.

Rates of HTN, smoking, and antiplatelet therapy were 60.0% (39/65), 13.8% (9/65), and 53.8% (35/65), respectively. Characteristics of aneurysms that qualified for the study are detailed in the On-line Table.

Morphologic Changes to Major Recanalization in Coiled Aneurysms with Minor Recanalization at 6 Months

Overall, 24 (36.9%) coiled aneurysms with minor recanalization at 6 months progressed to major recanalization during 112.5 aneurysm-years of follow-up, whereas none had become occluded. No instances of bleeding occurred during the follow-up. The chronology of change from minor-to-major recanalization was as follows: 14 (58.3%) at 6 months, 8 (33.3%) at 18 months, and 2 (8.4%) at 30 months. Acquired major recurrences had the following characteristics: women, 75.0% (18/24); age, 57.6 ± 9.2 years; anterior location, 95.8% (23/24); SAH presentation, 33.3% (8/24); bifurcation type, 79.2% (19/24); aneurysm size, 6.2 ± 4.1 mm; neck size, 4.0 ± 1.6 mm, HydroSoft coils of >50%, 29.2% (7/24); depth-to-neck ratio of >1, 66.7% (16/24); stent deploy-

ment, 12.5% (3/24); second coiling for recanalized aneurysms, 16.7% (4/24); and antiplatelet therapy, 41.7% (10/24). Univariate analysis indicated an association between the presence of a stent and morphologic change to major recanalization (P = .02). Other variables, such as SAH presentation (P = .21), bifurcation type (P = .74), second coiling for recanalized aneurysms (P = .18), antiplatelet therapy (P = .13), use of a balloon (P = .41), residual sac as an immediate postembolization finding (P = .47), and depth-to-neck ratio >1 (P = .30), were unrelated to a change in recanalization status (Table 1). Binary logistic regression analyses underscored the protective effect of stent placement on transformation to major recanalization (OR = 0.22; 95% CI, 0.06–0.87; P = .03), whereas other variables, including antiplatelet therapy (OR = 0.82; 95% CI, 0.25–2.68; P = .75), posterior location (OR = 0.24; 95% CI, 0.03–2.15; P = .20), and second coiling for recanalized aneurysms (OR = 0.96; 95% CI, 0.22–4.30; P = .96), had no bearing on observed transformation to major recanalization (Table 2).

The overall annual rate of major recanalization in coiled aneurysms with minor recanalization at 6-month follow-up was 17.84% per aneurysm-year. The rate of change from minor-to-major recanalization was 7.79% per year in instances of stent deployment, as opposed to 16.67% without stent placement. With the Kaplan-Meier method, estimated cumulative survival at 30 months in the absence of major recanalization with and without stent deployment was 81.3% versus 47.4% (P = .07).

DISCUSSION

Minor recanalization in aneurysms may remain stable with time or may progress to major recanalization. To our knowledge, accurate information on the likelihood of transforming from minor-to-major recanalization has been lacking. In our analyses, 36.9% of coiled aneurysms displaying minor recanalization at 6 months progressed to major recanalization during a follow-up of 112.5 aneurysm-years, for an overall annual rate of 17.84% per aneurysm-year.

Previous studies have reported variable rates (10.7%–33.6%) of overall recanalization in coiled aneurysms, with major recanalization ranging from 3.9% to 20.7%.^{1,2} The propensity for recanalization in aneurysms is known to be a factor of presentation (SAH versus UIA), aneurysm size, and initial therapeutic results.³ Ruptured (versus nonruptured) aneurysms are more likely to recanalize.^{2,9} Spontaneous clot lysis at rupture points or thrombus within the sac may contribute to a higher coil compaction in patients presenting with SAH,⁹ which is the aim of interventionists. Sluzewski et al¹⁰ reported that coiled aneurysms with volumes of

<600 mm³ did not undergo recanalization at packing densities of >24%. Morales et al¹¹ also showed that intra-aneurysmal hemodynamics, such as blood flow velocity and wall shear stress (WSS), may be reduced by increasing packing attenuation to near 30%. In our institution, we have tried to obtain high packing density and achieve anatomically complete occlusion regardless of presentation. In particular, complete occlusion is mandatory in ruptured aneurysms. As a result of the effort, the mean coil packing density was 32.1% ± 9.2%, and the difference noted in subset packing densities was not significant according to presentation (UIA, 30.8 ± 7.2%; SAH, 34.9 ± 12.1%; *P* = .15), except in 17 re-embolized aneurysms (where estimating packing attenuation was not feasible).

Migration of a coil into the thrombus may also lead to major recanalization with time.¹² However, saccular thrombus is more easily detected in larger-sized aneurysms than in smaller ones. The aneurysm size did not differ significantly according to the presentation (SAH, 6.0 ± 2.6 mm; UIA, 6.4 ± 3.4 mm; *P* = .66) in our cohort. Thus, we speculate that the relatively small-sized aneurysms and the higher packing densities of this cohort may be responsible for the lack of a significant correlation between SAH presentation and the rate of progression to major recanalization.

In a study by Cognard et al,⁹ a clinical correlation between aneurysm size and recanalization rate (2–3 mm, 8.7%; 4–5 mm, 9.0%; 6–8 mm, 22.0%) was found. The aneurysm size of >10 mm has been considered a risk factor for future recanalization.^{13–15} Niimi et al¹³ also reported that 82% (9/11) of recanalization events occurred in larger aneurysms (≥10 mm). Hetts et al¹⁴ investigated outcomes of coiling with and without stent replacement (Neuroform stent) in unruptured aneurysms in the Matrix and Platinum Science Trial. In their study, aneurysm size of ≥10 mm was associated with target aneurysm recurrence, which was defined as aneurysm rupture after treatment, retreatment, or death from an unknown cause. McDougall et al¹⁵ also assessed target aneurysm recurrence at 12 ± 3 months according to coil types (Matrix² versus bare metal). Target aneurysm recurrence was associated with incomplete occlusion, ruptured state, and larger aneurysm of ≥10 mm. Mean aneurysm size in this investigation was 6.3 ± 3.2 mm. The size did not differ significantly between the stable stationary group and the major recanalization group (stably stationary, 6.3 ± 2.7 mm, versus major recanalization, 6.2 ± 4.1 mm; *P* = .93). Five cases (7.7%) with minor recanalization at 6 months after coiling were large aneurysms of >10 mm. Two (40.0%) of 5 large aneurysms and 22 (36.7%) of 60 small aneurysms (<10 mm) showed major recanalization, respectively (*P* = 1.00). Therefore, we speculate that our results could be more appropriate for clinical evaluation of small-sized aneurysms with minor recanalization at 6-month follow-up imaging.

The initial therapeutic result is another reputed risk factor for future recanalization. Ries et al³ showed that signs of a residual aneurysm immediately after endovascular treatment significantly increased the risk of recanalization, compared with completely occluded lesions (OR = 3.96, *P* = .006). However, projected recanalization rates of completely occluded coiled aneurysms and aneurysms with neck remnants after coiling were similar. In this study, initial angiographic results were stratified as successful oc-

clusion (complete occlusion or residual neck) or residual sac. The higher rate of recanalization found in aneurysms showing minor recanalization 6 months after initial successful occlusion (versus residual sac) was not statistically significant (38.9% versus 27.3%, *P* = .47). Recently, Ogilvy et al¹⁶ devised a reliable recanalization stratification scale for projecting recanalization based on aneurysm-specific variables, initial occlusion status, and treatment-related factors. Aneurysm-specific variables, such as a size of >10 mm, ruptured state/presence of thrombus, and residual aneurysm (Raymond score of 3), are each awarded 2 points. As treatment-related factors, use of coils only, stent assistance, and flow diverter use earned 0, -1, and -2 points, respectively. If sums of individual scores were ≥5, the probability of retreatment was high (recanalization of >73.2%). Nevertheless, these results may not fully reflect the impact of risk factors, such as larger size, SAH presentation, and incomplete occlusion, on the progression from minor-to-major recanalization. Timing and duration of follow-up must be considered. Major recanalization largely emerged during the 12 months after embolization. In particular, 46.9% of all recanalizations (40% of which were major) were detected within the first 6 months of follow-up.² For our purposes, only aneurysms showing minor recanalization 6 months after coiling were studied. Subjects were also monitored diligently during a mean extended follow-up of 24.8 ± 8.2 months.

Raymond et al² previously examined recanalization risk factors relative to the length of follow-up (<17 months versus 17–37 months versus >37 months). In patients followed for <17 months, the initial therapeutic result was the sole variable associated with recanalization; whereas in patients followed for 17–37 months, aneurysm and neck sizes and initial therapeutic results constituted risk factors. In patients followed for >37 months, aneurysm and neck sizes and SAH presentation were associated with recanalization. These results imply that recanalization developing longer term is dependent on inherent risk factors, with incomplete therapeutic occlusion primarily responsible in the short term. Hence, we thought that differing characteristics of subjects in our cohort, such as minor recanalization at 6 months, the relatively longer extended follow-up, and the stipulated study end point (minor to major recanalization), might explain the lack of significant correlation evident between risk factors established elsewhere and progression to major recanalization.

The association between aneurysm location and recanalization remains controversial. Raymond et al² showed that recanalization rates at various sites (basilar bifurcation, 39.4%; MCA bifurcation, 32.1%; posterior communicating artery, 37.2%) did not differ substantially. On the other hand, Kwon et al¹ determined higher recanalization rates in coiled aneurysms of the posterior circulation and MCA due to technical difficulties. However, on the basis of study end point differences (all recanalization, major and minor) and selection bias (due to stent placement), the previous studies^{1,2} failed to accurately depict the clinical correlation between aneurysm location and minor-to-major progressive recanalization. In our subjects, the rate of transformation to major recanalization was more pronounced in the anterior circulation (overall: 23/56, 41.1%; ICA: 5/16, 31.3%; anterior cerebral artery: 10/21, 47.6%; MCA: 2/9, 22.2%; posterior communicating artery: 6/10, 60%) than in the posterior circulation (1/9, 11.1%).

Rates of stent deployment differed by location, approaching statistical significance (anterior circulation: 14/56, 25.0% [ICA, 5; anterior cerebral artery, 5; MCA, 4; posterior communicating artery, 0]; posterior circulation: 5/9, 55.6%; $P = .08$). These differing rates of stent deployment may explain the relatively higher proportion of major recanalization events in the anterior circulation.

Hemodynamic forces are thought to figure prominently in aneurysms that recanalize. Luo et al¹⁷ have indicated that high WSS and flow velocity, both observed near remnant necks, likely prompt recanalization in coiled aneurysms if occlusion is subtotal. In patients with treated aneurysms that were stable, WSS and blood flow velocity near neck remnants after embolization were lower in 83.3% (5/6). Irie et al¹⁸ similarly confirmed that areas at neck remnants, subject to higher WSS and flow velocity, corresponded with recanalization in coiled aneurysms showing subtotal occlusion. Higher postembolization WSS at aneurysm necks may predispose to recanalization in totally occluded aneurysms as well,¹⁹ as indicated by higher maximum WSS and spatially averaged WSS in recanalized aneurysms at systole (relative to pretreatment status) and a relative decrease in WSS by 70%–80% in nonrecanalized counterparts. Indeed, elevated WSS due to repetitive flow impingement may encourage recanalization of aneurysms.

Ortega et al²⁰ have documented that blood flow near remnant necks increases maximum WSS by approximately 50 Pa at systole in basilar tip aneurysms. In clinical practice, stents have been used in anticipation of diverting flow and promoting endothelialization at aneurysm necks, while also achieving higher coil-packing densities.^{21,22} Recanalization rates in the range of 6.6%–13% have been reported after stent-assisted coil embolization.^{23,24} Cho et al²⁵ have also shown that stent implantation reduced recanalization rates 6 months after coiling (stented, 1.9%; nonstented, 10.2%) and at final follow-up (stented, 8.3%; nonstented, 18.5%). With respect to recanalized aneurysms, stent placement likewise reduced the major recanalization rate 6 months after retreatment (OR = 0.16; $P = .01$).²⁶ Still, the ability to prevent further recanalization (from minor to major) through stent deployment has yet to be clearly demonstrated. Our study indicates that stent placement does help prevent progression from minor-to-major recanalization (OR = 0.22; $P = .03$), and this benefit is conferred long term, past the 6-month follow-up point.

Although some physicians find a 6-month determination of clinical course adequate in coiled aneurysms with minor recanalization, the durability of coiled aneurysms is a major concern due to relatively high recanalization rates (10.7%–33.6%).^{1,2} Given that 46.9% of recanalization events take place in the first 6 months after embolization,² follow-up imaging is generally initiated within 6 months. However, the fate of aneurysms showing minor recanalization in the first follow-up images is often difficult to predict. Although treatment outcomes, including recanalization rates and related risk factors, have been well-described, potential transformation from minor-to-major recanalization may be a separate issue in terms of providing appropriate information and planning further follow-up. For this study, we have focused on the fate of aneurysms showing minor recanalization at 6-month follow-up, investigating a sizeable sampling (65 qualifying lesions) through strict patient monitoring. Consequently, the outcomes

are likely valid. Nevertheless, there are concerns of possible selection bias, based on retrospective design and extent of stent deployment. Although, TOF MRA can be helpful in estimating the degree of recanalization, stent artifacts obscuring minor recanalization could occur.^{27–30} Moreover, the mean aneurysm size in our subjects was estimated at 6.3 ± 3.2 mm. In Korea, coiled aneurysms ≤ 10 mm account for 89.3% of lesions in a national cohort of unruptured aneurysms.¹ As such, the fate of larger aneurysms (>10 mm) in this setting may differ.

CONCLUSIONS

In this study, a 36.9% rate of progression to major recanalization was determined in coiled aneurysms showing minor recanalization at 6 months. The cohort was followed for 112.5 aneurysm-years, yielding an annual transformation rate of 17.84% per aneurysm-year. The presence of a stent was the only variable analyzed that conferred a protective effect, preventing progression to major recanalization. The finding of minor recanalization at 6 months, especially in the absence of stent placement, is cause for continued monitoring of coiled aneurysms, due to a fair risk of late major recanalization.

ACKNOWLEDGMENTS

We thank Sung-Eun Kim for her help with the data collection and statistical support.

Disclosures: Moon Hee Han—UNRELATED: Consultancy: MicroVention.* *Money paid to the institution.

REFERENCES

1. Kwon SC, Kwon OK; Korean Unruptured Cerebral Aneurysm Coiling (KUCAC) Investigators. **Endovascular coil embolization of unruptured intracranial aneurysms: a Korean multicenter study.** *Acta Neurochir (Wien)* 2014;156:847–54 CrossRef Medline
2. Raymond J, Guilbert F, Weill A, et al. **Long-term angiographic recurrences after selective endovascular treatment of aneurysms with detachable coils.** *Stroke* 2003;34:1398–403 CrossRef Medline
3. Ries T, Siemonsen S, Thomalla G, et al. **Long-term follow-up of cerebral aneurysms after endovascular therapy—prediction and outcome of retreatment.** *AJNR Am J Neuroradiol* 2007;28:1755–61 CrossRef Medline
4. Lejeune JP, Thines L, Taschner C, et al. **Neurosurgical treatment for aneurysm remnants or recurrences after coil occlusion.** *Neurosurgery* 2008;63:684–91; discussion 691–92 CrossRef Medline
5. Lin T, Fox AJ, Drake CG. **Regrowth of aneurysm sacs from residual neck following aneurysm clipping.** *J Neurosurg* 1989;70:556–60 CrossRef Medline
6. Cho YD, Jeon JP, Rhim JK, et al. **Progressive thrombosis of small saccular aneurysms filled with contrast immediately after coil embolization: analysis of related factors and long-term follow-up.** *Neuroradiology* 2015;57:615–23 CrossRef Medline
7. White PM, Lewis SC, Nahser H, et al; HELPS Trial Collaboration. **HydroCoil Endovascular Aneurysm Occlusion and Packing Study (HELPS trial): procedural safety and operator-assessed efficacy results.** *AJNR Am J Neuroradiol* 2008;29:217–23 CrossRef Medline
8. Cho YD, Lee WJ, Kim KM, et al. **Stent-assisted coil embolization of posterior communicating artery aneurysms.** *AJNR Am J Neuroradiol* 2013;34:2171–76 CrossRef Medline
9. Cognard C, Weill A, Spelle L, et al. **Long-term angiographic follow-up of 169 intracranial berry aneurysms occluded with detachable coils.** *Radiology* 1999;212:348–56 CrossRef Medline

10. Sluzewski M, van Rooij WJ, Slob MJ, et al. **Relation between aneurysm volume, packing, and compaction in 145 cerebral aneurysms treated with coils.** *Radiology* 2004;231:653–58 CrossRef Medline
11. Morales HG, Kim M, Vivas EE, et al. **How do coil configuration and packing density influence intra-aneurysmal hemodynamics? AJNR Am J Neuroradiol** 2011;32:1935–41 CrossRef Medline
12. van Rooij WJ, Sprengers ME, Sluzewski M, et al. **Intracranial aneurysms that repeatedly reopen over time after coiling: imaging characteristics and treatment outcome.** *Neuroradiology* 2007;49:343–49 CrossRef Medline
13. Niimi Y, Song J, Madrid M, et al. **Endosaccular treatment of intracranial aneurysms using Matrix coils: early experience and mid-term follow-up.** *Stroke* 2006;37:1028–32 CrossRef Medline
14. Hetts SW, Turk A, English JD, et al; Matrix and Platinum Science Trial Investigators. **Stent-assisted coiling versus coiling alone in unruptured intracranial aneurysms in the Matrix and Platinum Science trial: safety, efficacy, and mid-term outcomes.** *AJNR Am J Neuroradiol* 2014;35:698–705 CrossRef Medline
15. McDougall CG, Johnston SC, Gholkar A, et al; MAPS Investigators. **Bioactive versus bare platinum coils in the treatment of intracranial aneurysms: the MAPS (Matrix and Platinum Science) trial.** *AJNR Am J Neuroradiol* 2014;35:935–42 CrossRef Medline
16. Ogilvy CS, Chua MH, Fusco MR, et al. **Validation of a system to predict recanalization after endovascular treatment of intracranial aneurysms.** *Neurosurgery* 2015;77:168–73; discussion 173–74 CrossRef Medline
17. Luo B, Yang X, Wang S, et al. **High shear stress and flow velocity in partially occluded aneurysms prone to recanalization.** *Stroke* 2011;42:745–53 CrossRef Medline
18. Irie K, Anzai H, Kojima M, et al. **Computational fluid dynamic analysis following recurrence of cerebral aneurysm after coil embolization.** *Asian J Neurosurg* 2012;7:109–15 CrossRef Medline
19. Li C, Wang S, Chen J, et al. **Influence of hemodynamics on recanalization of totally occluded intracranial aneurysms: a patient-specific computational fluid dynamic simulation study.** *J Neurosurg* 2012;117:276–83 CrossRef Medline
20. Ortega J, Hartman J, Rodriguez J, et al. **Post-treatment hemodynamics of a basilar aneurysm and bifurcation.** *Ann Biomed Eng* 2008;36:1531–46 CrossRef Medline
21. Lawson MF, Newman WC, Chi YY, et al. **Stent-associated flow remodeling causes further occlusion of incompletely coiled aneurysms.** *Neurosurgery* 2011;69:598–603; discussion 603–04 CrossRef Medline
22. Chalouhi N, Jabbour P, Singhal S, et al. **Stent-assisted coiling of intracranial aneurysms: predictors of complications, recanalization, and outcome in 508 cases.** *Stroke* 2013;44:1348–53 CrossRef Medline
23. Hwang SK, Hwang G, Bang JS, et al. **Endovascular Enterprise stent-assisted coil embolization for wide-necked unruptured intracranial aneurysms.** *J Clin Neurosci* 2013;20:1276–79 CrossRef Medline
24. Luo CB, Teng MM, Chang FC, et al. **Stent-assisted coil embolization of intracranial aneurysms: a single center experience.** *J Chin Med Assoc* 2012;75:322–28 CrossRef Medline
25. Cho WS, Hong HS, Kang HS, et al. **Stability of cerebral aneurysms after stent-assisted coil embolization: a propensity score-matched analysis.** *Neurosurgery* 2015;77: 208–16; discussion 216–17 CrossRef Medline
26. Cho YD, Lee JY, Seo JH, et al. **Does stent implantation improve the result of repeat embolization in recanalized aneurysms? Neurosurgery** 2012;71(2 suppl operative):ons253–59; discussion ons259 CrossRef Medline
27. Jeon JP, Cho YD, Rhim JK, et al. **Effect of stenting on progressive occlusion of small unruptured saccular intracranial aneurysms with residual sac immediately after coil embolization: a propensity score analysis.** *J Neurointerv Surg* 2015 Oct 27. [Epub ahead of print] CrossRef Medline
28. Cho YD, Kim KM, Lee WJ, et al. **Time-of-flight magnetic resonance angiography for follow-up of coil embolization with Enterprise stent for intracranial aneurysm: usefulness of source images.** *Korean J Radiol* 2014;15:161–68 CrossRef Medline
29. Choi JW, Roh HG, Moon WJ, et al. **Optimization of MR parameters of 3D TOF-MRA for various intracranial stents at 3.0T MRI.** *Neurointervention* 2011;6:71–77 CrossRef Medline
30. van Amerongen MJ, Boogaarts HD, de Vries J, et al. **MRA versus DSA for follow-up of coiled intracranial aneurysms: a meta-analysis.** *AJNR Am J Neuroradiol* 2014;35:1655–61 CrossRef Medline

Prediction of Carotid Intraplaque Hemorrhage Using Adventitial Calcification and Plaque Thickness on CTA

L.B. Eisenmenger, B.W. Aldred, S.-E. Kim, G.J. Stoddard, A. de Havenon, G.S. Treiman, D.L. Parker, and J.S. McNally



ABSTRACT

BACKGROUND AND PURPOSE: Carotid intraplaque hemorrhage is associated with stroke, plaque thickness, stenosis, ulceration, and adventitial inflammation. Conflicting data exist on whether calcification is a marker of plaque instability, and no data exist on adventitial calcification. Our goal was to determine whether adventitial calcification and soft plaque (a rim sign) help predict carotid intraplaque hemorrhage.

MATERIALS AND METHODS: This was a retrospective cohort study of 96 patients who underwent carotid MRA and CTA within 1 month, from 2009 to 2016. We excluded occlusions ($n = 4$) and near occlusions ($n = 0$), leaving 188 carotid arteries. Intraplaque hemorrhage was detected by using MPRAGE. Calcification, adventitial pattern, stenosis, maximum plaque thickness (total, soft, and hard), ulceration, and intraluminal thrombus on CTA were recorded. Atherosclerosis risk factors and medications were recorded. We used mixed-effects multivariable Poisson regression, accounting for 2 vessels per patient. For the final model, backward elimination was used with a threshold of $P < .10$. Receiver operating characteristic analysis determined intraplaque hemorrhage by using the area under the curve.

RESULTS: Our final model included the rim sign (prevalence ratio = 11.9, $P < .001$) and maximum soft-plaque thickness (prevalence ratio = 1.2, $P = .06$). This model had excellent intraplaque hemorrhage prediction (area under the curve = 0.94), outperforming the rim sign, maximum soft-plaque thickness, NASCET stenosis, and ulceration (area under the curve = 0.88, 0.86, 0.77, and 0.63, respectively; $P < .001$). Addition of the rim sign performed better than each marker alone, including maximum soft-plaque thickness (area under the curve = 0.94 versus 0.86, $P < .001$), NASCET stenosis (area under the curve = 0.90 versus 0.77, $P < .001$), and ulceration (area under the curve = 0.90 versus 0.63, $P < .001$).

CONCLUSIONS: The CTA rim sign of adventitial calcification with internal soft plaque is highly predictive of carotid intraplaque hemorrhage.

ABBREVIATIONS: AUC = area under the curve; IPH = intraplaque hemorrhage; ROC = receiver operating characteristic

Carotid atherosclerotic plaque contributes to 10%–15% of ischemic strokes in the United States.¹ MR imaging–detected carotid intraplaque hemorrhage (IPH) is an accepted marker of plaque instability and stroke risk independent of stenosis, with an annual stroke rate as high as 45% in patients with >50% stenosis

and IPH.^{2–5} Carotid IPH can be detected with heavily T1-weighted sequences, including the MPRAGE sequence, which can discriminate between IPH and lipid/necrotic core.⁶ MPRAGE is superior in detecting IPH compared with conventional MR imaging sequences, with higher sensitivity, specificity, and interrater reliability compared with 3D TOF or FSE T1WI sequences.⁷

Lumen markers have been linked to IPH, including stenosis, plaque thickness, and ulceration. These markers can be detected

Received November 20, 2015; accepted after revision January 28, 2016.

From the Department of Radiology (L.B.E., B.W.A., S.-E.K., G.S.T., D.L.P., J.S.M.), Utah Center for Advanced Imaging Research; Department of Orthopedics (G.J.S.), Design and Biostatistics Center; Department of Neurology (A.d.H.); and Department of Surgery (G.S.T.), University of Utah, Salt Lake City, Utah; and Department of Surgery (G.S.T.), VA Salt Lake City Health Care System, Salt Lake City, Utah.

This work was supported by the Radiological Society of North America Research Scholar Grant; the University Intramural Seed Grant; the Study Design and Biostatistics Center, with funding, in part, from the National Center for Research Resources and the National Center for Advancing Translational Sciences; National Institutes of Health, grant 8UL1TR000105 (formerly UL1RR025764); and the Radio Frequency Coil and Electronics laboratory.

Paper previously presented at: Annual Meeting of the Radiological Society of North America, November 20 to December 4, 2015; Chicago, Illinois.

Please address correspondence to J. Scott McNally, MD, PhD, University of Utah, Department of Radiology, 30 North 1900 East #1A071, Salt Lake City, UT 84132-2140; e-mail: scott.mcnally@hsc.utah.edu

 Indicates article with supplemental on-line photo.

<http://dx.doi.org/10.3174/ajnr.A4765>

by CTA. IPH is known to increase in prevalence with increasing lumen stenosis.⁸ Additional studies have suggested that CTA-detected ulceration can be used as a surrogate marker for IPH.⁹ Plaque thickness has also recently been associated with high plaque signal on 3D TOF imaging, attributed to IPH.^{10,11} Recently, we found that these markers in combination (plaque thickness, millimeter stenosis, and ulceration) allow optimal discrimination of IPH in a model including the clinical factors of age and male sex.¹² Together these factors may provide clues to the pathogenesis of IPH.

Most recently, studies have linked IPH with adventitial inflammation and microvessel permeability detectable by using dynamic contrast-enhanced MR imaging.^{8,13} Adventitial inflammation and oxidative stress have also been linked to endothelial bone-morphogenic proteins,¹⁴ suggesting that adventitial calcification may also represent a marker of adventitial inflammation¹⁵; however, this has not yet been investigated in the setting of IPH. Vascular calcification is often seen with carotid plaque, though conflicting data exist in relation to plaque vulnerability. One study of 30 patients found that fibrous cap inflammation more often occurs in noncalcified than in calcified plaques, suggesting that calcification indicates plaque stability.¹⁶ An additional study of patients with symptomatic plaques (recent TIA, stroke, or amaurosis fugax) versus asymptomatic patients with critical stenosis found that the percentage of plaque calcification area was 2-fold greater in asymptomatic-versus-symptomatic plaques, and there was an inverse relationship between calcification and macrophage infiltration.¹⁷ A different study investigating 611 carotid plaques by CT and MR imaging found that larger calcification volume was associated with higher IPH prevalence and a lower lipid core prevalence, suggesting that calcification may not be a stabilizing factor.¹⁸ However, these studies evaluated total calcification volume or its binary presence or absence, and adventitial calcification coupled with soft plaque has not yet been addressed, to our knowledge.

Because IPH is becoming more clinically relevant in identifying cryptogenic stroke sources¹⁹ and IPH indicates a medically refractory population with high future stroke risk,⁴ prediction models are greatly needed in patients undergoing alternate imaging such as CTA. Of clinical relevance, a CTA-IPH prediction model would be especially useful in patients with contraindications to MR imaging (eg, with pacemakers) or as a cost-saving measure to prevent unneeded MR imaging in patients with very high or very low likelihood of IPH. Current prediction models discussed above based on plaque thickness, stenosis, and ulceration leave room for improvement. Because adventitial inflammation is highly associated with IPH and chronic inflammation is associated with calcification, this study was undertaken to determine whether adventitial calcification with internal soft plaque (a rim sign) could aid in carotid IPH prediction. Our hypothesis was that the rim sign may help predict carotid IPH compared with standard markers, including soft-plaque thickness, stenosis, or ulceration alone.

MATERIALS AND METHODS

Clinical Study Design

Institutional review board approval was obtained for this retrospective cohort study from 2009 to 2016 in patients who under-

went both CTA and MRA work-up of carotid disease at the University Medical Center and VA Medical Center in Salt Lake City, Utah. Due to the retrospective nature, informed consent was not required by the institutional review board. The only inclusion criteria were MRA and CTA performed within 1 month in the same patient within the study timeframe. Ninety-six patients qualified for the study, with 192 carotid arteries. Exclusions included carotid occlusions ($n = 4$) and near occlusions ($n = 0$) because lumen markers are difficult or impossible to determine in these cases. No vessels underwent carotid surgery or stent placement between scans. One hundred eighty-eight carotid arteries were left in the final analysis. Although a few scans exhibited mild motion artifacts primarily from swallowing, no carotid images were sufficiently limited to be excluded from interpretation.

MR Imaging Protocol

Images were obtained on 1.5 and 3T MR imaging scanners (Trio, Verio, and Prisma; Siemens, Erlangen, Germany) with standard or custom carotid coils.²⁰ Our standard clinical MRA protocol includes axial TOF, axial MPRAGE, coronal precontrast, post-contrast arterial, and venous phase T1-weighted images. Coronal postcontrast MRA neck images extended from the aortic arch through the circle of Willis.

IPH Determination by MPRAGE

Our prior research has shown that MPRAGE images have high intra- and interobserver agreement at both field strengths, with or without specialized coils, and that the MPRAGE-positive area highly correlates with the IPH area on histology.⁶ MPRAGE parameters included the following: 3D, TR/TE/TI = 6.39/2.37/370 ms, flip angle = 15°, FOV = 130 × 130 × 48 mm³, matrix = 256 × 256 × 48, voxel = 0.5 × 0.5 × 1.0 mm³, fat saturation, acquisition time ~ 5 minutes. Images were obtained from 20 mm below to 20 mm above the carotid bifurcation at a 1.0-mm section thickness.²¹ To produce 3D images, we used a secondary phase-encoding gradient in the section-select direction, and measurements for all section-selection phase encodings were performed with rapid acquisition in each segment. Carotid IPH was determined by MPRAGE-positive plaque with at least 1 voxel demonstrating at least 2-fold higher signal intensity relative to adjacent sternocleidomastoid muscle as previously described.⁶

CTA Protocol

CTA was performed with a 64-section scanner (Definition or Definition AS; Siemens), with dose modulation and 100–120 kVp (peak). Images were obtained from the aortic arch through the skull vertex at a thickness of 0.625 mm. Intravenous access was through an antecubital vein by using an 18- or 20-ga angiocatheter. A total of 100 mL of iopamidol (Isovue 370; Bracco, Princeton, New Jersey) was injected at 4 mL/s. Bolus monitoring used an ROI in the ascending aorta and a trigger at 100 HU. Injections were performed with a 10-second delay. Multiplanar reformats were created, and images were reviewed on a PACS workstation on CTA settings (window 96, level 150 HU) and were modified as required to depict CTA lumen markers and calcification.

Imaging Reviewers

All carotid imaging markers were determined by consensus of 2 reviewers blinded to stroke status and clinical covariates. In cases of disagreement, consensus was obtained with a third reviewer. CTA lumen and calcification markers were determined separately, and reviewers were blinded to MR imaging IPH status. All reviewers had experience with neurovascular imaging interpretation and included a radiology resident in training (L.B.E.), neuroradiology fellow (B.W.A.), and board-certified neuroradiology attending physician (J.S.M.). κ analysis was performed to determine the rim sign interrater reliability (0.85) and intrarater reliability (0.86). CTA calcification examples are shown in Figs 1 and 2.

CTA Markers

CTA markers included the time between MR imaging and CTA, presence of calcification, adventitial calcification pattern, per-

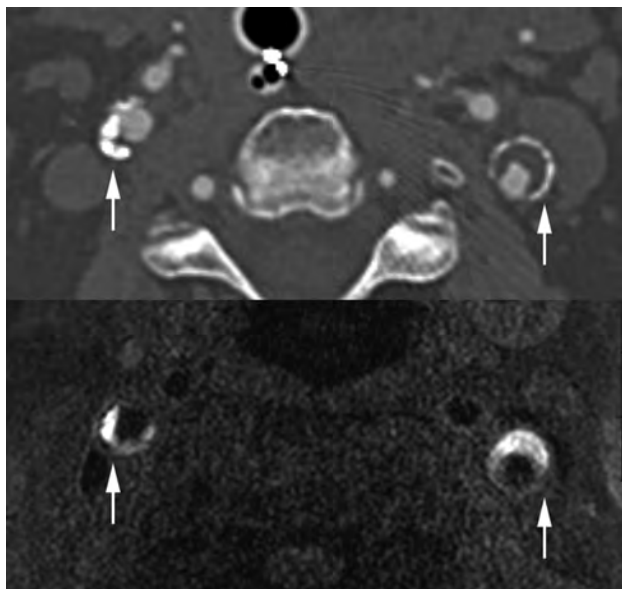


FIG 1. Positive rim sign and carotid IPH. Top: Carotid CTA with positive rim signs (arrows) in both carotid plaques. Bottom: MPRAGE with bilateral carotid IPH (arrows) in the same patient. IPH was defined by MPRAGE-positive plaque, using a signal threshold of 2-fold signal intensity over the adjacent sternocleidomastoid muscle.

centage diameter stenosis, millimeter stenosis, maximum total plaque thickness, maximum soft-plaque thickness, maximum hard-plaque thickness, ulceration, and intraluminal thrombus. All measurements were obtained by using the submillimeter tool on a PACS workstation.

Time between CTA and MR Imaging

The time between scans was recorded in days and was used as a potential confounder for the association between CTA markers and MR imaging–detected IPH.

CTA Calcification Markers

Carotid arteries with thin adventitial calcification of <2 mm were subdivided into 2 groups: A positive rim sign was defined as adventitial calcification (<2 -mm thick) with internal soft plaque (≥ 2 -mm thickness), and a negative rim sign was defined as adventitial calcification (<2 -mm thick) with minimal if any internal soft plaque (<2 -mm thickness). “Bulky calcification” was defined as calcification measuring ≥ 2 -mm thick without associated thin adventitial calcification measuring <2 -mm thick.

CTA Lumen Markers

Percentage diameter stenosis was determined by using NASCET criteria on contrast CTA. Briefly, the diameter (b) at the level of maximal stenosis and diameter (a) of the ICA distal to the stenosis were used to calculate percentage diameter stenosis by using the formula $[(a - b) / a] \times 100\%$. Carotid stenosis was measured at the narrowest segment of the carotid plaque (b) on axial images, perpendicular to the long axis of the vessel on multiplanar reformats by using a submillimeter measurement tool on a PACS workstation. The distal ICA diameter (a) was measured beyond the bulb where the walls are parallel and no longer tapering per NASCET criteria.²²⁻²⁴ We performed the multivariable regression analysis by using both the NASCET measurement of percentage diameter stenosis $[(a - b) / a] \times 100\%$ and the previously described millimeter stenosis (b) measurement.²⁵ Near occlusions were excluded from percentage stenosis calculation and were identified by the following CTA criteria: visible bulb stenosis, distal ICA diameter of ≤ 3 mm, and distal ICA/distal external carotid artery ratio of ≤ 1.25 originally adapted from standard conven-

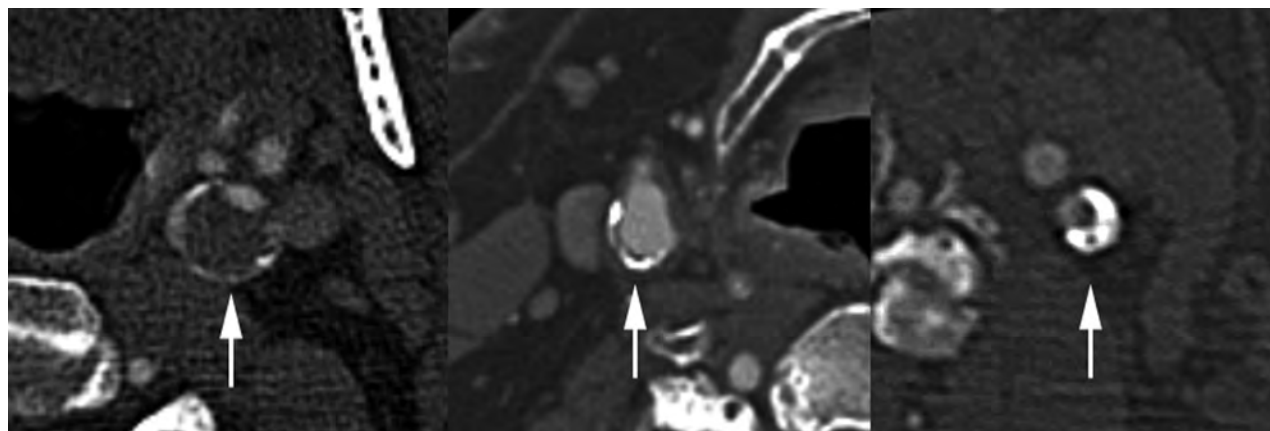


FIG 2. CTA calcification. Left: Positive rim sign (arrow), adventitial calcification measuring <2 mm in thickness with adjacent soft plaque measuring ≥ 2 mm in thickness. Middle: Adventitial calcification without a rim sign (arrow), adventitial calcification measuring <2 mm in thickness with <2 mm adjacent soft plaque. Right: Bulky calcification (arrow), calcified plaque of ≥ 2 mm.

tional angiography.^{24,25} The presence of ulceration was determined on CTA images by using a size threshold of 2 mm reported in prior studies.⁹ Intraluminal thrombus was defined by an intraluminal filling defect on CTA as previously described.²⁶ Maximum plaque thickness was measured in the transverse plane on CTA. These CTA lumen markers are shown in the On-line Fig 1. In addition, maximum soft-plaque and hard-plaque thicknesses were measured on CTA, as previously described.²⁷

Clinical Demographics

Clinical demographics were determined by retrospective chart review. Carotid atherosclerosis risk factors of age, male sex, diabetes, hypertension, hyperlipidemia, body mass index, and smoking status were identified. These were determined by retrospective chart review, with standard clinical definitions. For hypertension, the diagnosis was made when the average of ≥ 2 diastolic blood pressure measurements on at least 2 subsequent visits was ≥ 90 mm Hg or when the average of multiple systolic blood pressure readings on ≥ 2 subsequent visits was ≥ 140 mm Hg. For hyperlipidemia, the diagnosis was made when low-density lipoprotein was >100 mg/dL. Cardiovascular medications were recorded, including antiplatelets, anticoagulants, statins, and antihypertensives.

Statistical Analysis

Intrater (test-retest) reliability for the presence of the rim sign was assessed for 1 reviewer (J.S.M.), and interrater reliability for the presence of the rim sign was assessed for 2 reviewers (J.S.M. and L.B.E.), both with a κ coefficient. Statistical modeling was performed by using generalized estimating equations to account for data clustering, with up to 2 carotid arteries per patient. Carotid arteries were treated as separate units or units of analysis grouped within each subject because IPH may be associated with local markers of carotid plaque vulnerability (plaque calcification pattern, thickness, stenosis, and other lumen markers). At the patient level, systemic clinical factors affecting both carotid arteries (age, male sex, and other cardiovascular risk factors and medications) were considered in the model as potential confounding variables. Given that >1 marker for IPH was being studied, potential confounding was investigated on the outcome variable or groups positive and negative for IPH, so only 1 data table was required, with P values from univariable generalized estimating equation Poisson regression models. The Poisson regression approach directly estimates the risk ratio, or prevalence ratio in our case, which is more intuitive to interpret than an odds ratio from a logistic regression approach.²⁸ Next, all potential confounding variables with $P < .10$ from a univariable model were placed in an initial multivariable generalized estimating equation Poisson regression model for IPH and then were eliminated in a backward fashion until all remaining variables met the threshold $P < .10$. Liberal significance criteria, $P < .10$, were used to protect against residual confounding.²⁹

For hypothesis testing of which markers are predictive of IPH, we used the traditional $P < .05$. In binary outcome models, 5 outcome events for every predictor variable are sufficient to avoid overfitting.³⁰ With 44 carotid IPH events and 144 non-IPH events, $44/5 = 8.8$, or up to 8 predictor variables could be included

Table 1: Clinical characteristics

Characteristic	Patients (N = 96)
Age (mean) (SD) (yr)	65.7 (13.4)
Male sex (No.) (%)	75 (78.1)
BMI (mean) (SD) (kg/m ²)	28.0 (4.9)
Smoking (No.) (%)	
Current smoker	28 (29.2)
Prior smoker	24 (25.0)
Hypertension (No.) (%)	75 (78.1)
Hyperlipidemia (No.) (%)	61 (64.2)
Diabetes (No.) (%)	38 (39.6)
Antihypertension (No.) (%)	60 (62.5)
Statins (No.) (%)	50 (52.1)
Antiplatelets (No.) (%)	50 (52.1)
Anticoagulation (No.) (%)	9 (9.4)
Days between CTA and MRA (mean) (SD)	5.9 (8.6)

Note:—BMI indicates body mass index.

in the model without overfitting, exceeding the number of variables remaining in the final model. To assess the discriminatory potential of each marker or combination of markers, we reported clustered data area under the receiver operating characteristic (ROC) curve (AUC), with bootstrapped 95% confidence intervals.³¹ Similarly, AUCs were compared by using the clustered method of Pepe et al.³¹ To guard against overfitting and optimism of the AUCs, in which an AUC could be higher in the present sample of patients than it would in future patients, we performed a bootstrap validation for each clustered data AUC calculation on the fixed list of predictors in the model.³² Given that in all cases the optimism was $<1\%$, so that the original AUCs and bootstrapped validated AUCs were identical to the precision reported, there was no need to report both. All statistical analyses were performed with STATA 13.1 statistical software (StataCorp, College Station, Texas).

RESULTS

Clinical Characteristics

Ninety-six patients were recruited for the study. Patients were predominantly older men (mean age, 65.7 ± 13.4 years; 78.1% male) with carotid atherosclerosis risk factors (54.2% were current or prior smokers, 78.1% had hypertension, 64.2% had hyperlipidemia, 39.6% had diabetes), and many were on medical therapy for carotid disease (62.5% on antihypertensives, 52.1% on statins, 52.1% on antiplatelets) (Table 1).

Imaging and Clinical Characteristics by Vessel

We evaluated imaging and clinical characteristics by vessel in groups positive and negative for IPH in Table 2. Each patient contributed 2 carotid arteries, with the exception of 4 carotid occlusions, leaving 188 carotid arteries for the final sample. Carotid stenosis was worse in the group positive for IPH versus the negative one (NASCET stenosis of 53.5% versus 24.9% and millimeter stenosis of 2.27 versus 3.60 mm, $P < .001$). Maximum plaque thickness was also higher in the group positive for IPH versus the negative one (5.93 versus 3.42 mm, $P < .001$), as was maximum soft-plaque thickness (5.26 versus 2.99 mm, $P < .001$) and maximum hard-plaque thickness (2.97 versus 1.91 mm, $P = .002$). There was higher prevalence of plaque ulceration (56.8% versus 29.9%, $P = .005$) and intraluminal thrombus, though this was rare and not significantly different between the 2 groups

Table 2: Carotid plaque CTA markers associated with IPH^a

Imaging and Clinical Characteristics by Vessel	IPH (-) (n = 144)	IPH (+) (n = 44)	P Value
Carotid NASCET percentage stenosis (mean) (SD)	24.9 (29.5)	53.5 (24.5)	<.001
Mild (0%–49.9%) (No.) (%)	112 (77.8)	16 (36.4)	
Moderate (50%–69.9%) (No.) (%)	16 (11.1)	14 (31.8)	
Severe (70%–99.9%) (No.) (%)	16 (11.1)	14 (31.8)	
Carotid mm stenosis (mean) (SD)	3.60 (1.47)	2.27 (1.21)	<.001
Carotid maximum total plaque thickness (mean) (SD) (mm)	3.42 (1.83)	5.93 (1.48)	<.001
Carotid maximum soft-plaque thickness (mean) (SD) (mm)	2.99 (1.60)	5.26 (1.50)	<.001
Carotid maximum hard-plaque thickness (mean) (SD) (mm)	1.91 (1.72)	2.97 (1.18)	.002
Carotid plaque ulceration (No.) (%)	43 (29.9)	25 (56.8)	.005
Carotid intraluminal thrombus (No.) (%)	11 (7.6)	6 (13.6)	.185
Carotid calcification present (No.) (%)	103 (71.5)	43 (97.7)	.015
Bulky calcification (≥2 mm) (No.) (%) ^b	66 (45.8)	36 (81.8)	.001
Thin adventitial calcification (<2 mm)			
Rim sign + (No.) (%)	17 (11.8)	39 (88.6)	<.001
Rim sign - (No.) (%)	60 (41.7)	4 (9.1)	<.001
Days between MRA and CTA (No.) (SD)	5.6 (8.2)	6.9 (9.3)	.453
Male sex (No.) (%)	103 (71.5)	43 (97.7)	.017
Age (mean) (SD) (yr)	63.4 (14.1)	73.5 (7.2)	<.001
BMI (mean) (SD) (kg/m ²)	28.0 (5.2)	28.1 (4.2)	.955
Smoking (No.) (%)			
Current smoker	49 (34.0)	4 (9.1)	.019
Prior smoker	34 (23.6)	13 (29.6)	.534
Hypertension (No.) (%)	110 (76.4)	37 (84.1)	.382
Hyperlipidemia (No.) (%)	88 (61.1)	33 (78.6)	.092
Diabetes (No.) (%)	50 (34.7)	24 (54.6)	.057
Antihypertension (No.) (%)	85 (59.0)	33 (75.0)	.143
Statin (No.) (%)	68 (47.2)	29 (65.9)	.080
Antiplatelets (No.) (%)	69 (47.9)	27 (61.4)	.206
Anticoagulation (No.) (%)	13 (9.0)	5 (11.4)	.713

Note:—IPH (-) indicates no MPRAGE positive plaque, and IPH absence; IPH (+), MPRAGE positive plaque, and IPH presence. Bulky calcification indicates calcified plaque of ≥2 mm. Two types of adventitial calcification were recorded, both with <2-mm adventitial calcification: Rim sign -, <2-mm soft plaque; Rim sign +, ≥2mm soft plaque.

^a From the 96 patients, 188 carotid arteries were analyzed after excluding occlusions (*n* = 4) and near occlusions (*n* = 0). Means/SDs were calculated using ordinary formulas. We based significance tests and *P* values on univariable generalized estimating equation Poisson regression, taking into account the correlation of up to 2 carotid arteries per person. Factors with *P* < .10 were included in the initial multivariable Poisson regression analysis.

Table 3: Final model of CTA markers associated with IPH^a

Carotid IPH Prediction	PR	P Value	95% CI
Carotid plaque rim sign (present versus absent)	11.9	<.001	4.4–32.0
Maximum soft-plaque thickness (per 1-mm increase)	1.2	.06	0.99–1.40

Note:—PR indicates prevalence ratio.

^a After multivariable Poisson regression with sequential backward elimination of factors that did not meet the threshold of *P* < .10, the final carotid IPH model depended on the positive rim sign and maximum soft-plaque thickness.

(13.6% versus 7.6%, *P* = .185). Some factors were potential confounders between groups positive and negative for IPH (*P* < .10), requiring multivariable regression.

Multivariable Generalized Estimating Equation Poisson Regression Analysis

Multivariable regression analysis was performed with the outcome of carotid IPH and the primary predictor, the rim sign. Potential confounders were eliminated in a backward fashion with a threshold of *P* > .10. At this threshold, CTA predictors of IPH included the rim sign (prevalence ratio = 11.9; 95% CI, 4.4–32.0; *P* < .001) and maximum soft-plaque thickness (prevalence ratio = 1.2; 95% CI, 0.99–1.40; *P* = .06) (Table 3).

IPH ROC Comparison Analysis

ROC comparison analysis for IPH is shown in Fig 3. The final IPH prediction model was excellent in determining carotid IPH (AUC = 0.94; 95% CI, 0.90–0.97). The final model performed significantly better than the rim sign alone (AUC = 0.94 versus 0.88, *P* < .001), maximum soft-plaque thickness alone (AUC = 0.94 versus 0.86, *P* < .001), NASCET stenosis alone (AUC = 0.94 versus 0.77, *P* < .001), and ulceration alone (AUC = 0.94 versus 0.63, *P* < .001) (Fig 3A). In addition, IPH prediction with-versus-without the rim sign was significantly better in models using maximum soft-plaque thickness (AUC = 0.94 versus 0.86, *P* < .001), NASCET stenosis (0.90 versus 0.77, *P* < .001), or ulceration (0.90 versus 0.63, *P* < .001).

DISCUSSION

Carotid MR imaging optimally detects carotid stroke sources and future stroke risk by characterizing IPH.^{2–5} Major barriers to progress are that the pathophysiology of carotid IPH is unknown and there are no known treatments or preventative measures available. Another barrier is that many patients undergo other imaging, including CTA, during work-up, and IPH status is unknown without additional MR imaging with its associated costs and contraindications (eg, pacemaker). Our study shows that of the CTA markers predicting IPH, adventitial calcification with internal soft plaque, a rim sign, performs best. Identifying IPH by using CTA markers would greatly benefit clinicians. IPH status can identify stroke sources that would otherwise be ignored and diagnosed as cryptogenic if stenosis is

<50%.¹⁹ In addition, IPH is known to be refractory to standard medical management with an up to 45% annual stroke risk in patients with >50% stenosis.⁴ Identification of carotid IPH is becoming more and more clinically relevant, indicating the need for early optimal medical therapy, close follow-up intervals for stenosis progression or new ischemic stroke symptoms, and identification of patients with treatment failure necessitating surgery or stent placement.

The underlying mechanism behind this association of IPH and the rim sign is uncertain. A potential link between IPH and adventitial pathology may lie with adventitial neovessel proliferation and inflammation.⁸ Adventitial inflammation and oxidative stress have been linked to endothelial bone-morphogenic pro-

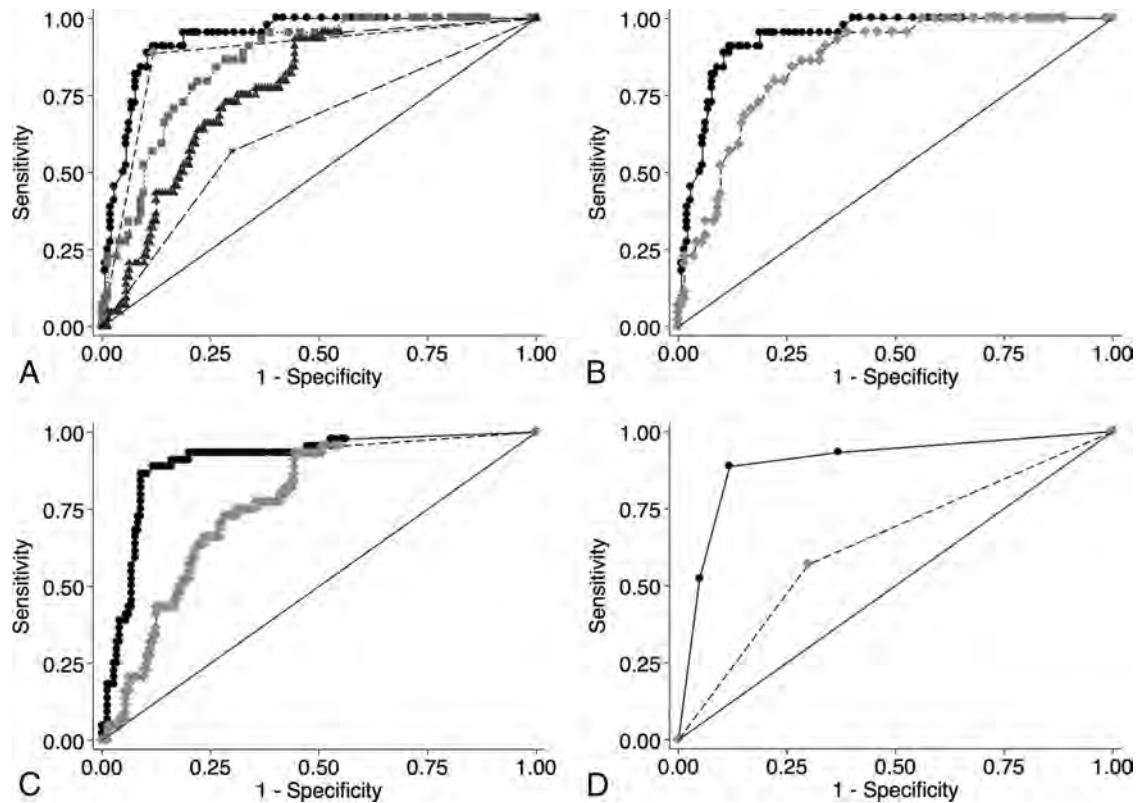


FIG 3. A, ROC comparison analysis demonstrates the superiority of the final model (rim sign and maximum soft-plaque thickness) in predicting carotid IPH. 1) Rim sign + maximum soft-plaque thickness (*black circles*). The *solid line* indicates AUC = 0.94 (95% CI, 0.90–0.97). 2) Rim sign (*light gray diamonds*). The *dashed line* indicates AUC = 0.88, (95% CI, 0.83–0.94). 3) Maximum soft-plaque thickness (*light gray squares*). The *dotted line* indicates AUC = 0.86 (95% CI, 0.80–0.91). 4) NASCET stenosis (*dark gray triangles*). The *dashed-dotted line* indicates AUC = 0.77 (95% CI, 0.70–0.84). 5) Ulceration (*x*). The *large dashed line* indicates AUC = 0.63, (95% CI, 0.55–0.72). B, ROC comparison of the rim sign in addition to maximum soft-plaque thickness in predicting IPH. 1) Rim sign + maximum soft-plaque thickness (*black circles*). The *solid line* indicates AUC = 0.94 (95% CI, 0.90–0.97). 2) Maximum soft-plaque thickness (*light gray diamonds*). The *dotted line* indicates AUC = 0.86, (95% CI, 0.80–0.91) ($P < .001$). C, ROC comparison of the rim sign in addition to NASCET stenosis in predicting IPH. 1) Rim sign + NASCET stenosis (*black circles*). The *solid line* indicates AUC = 0.90 (95% CI, 0.85–0.96). 2) NASCET stenosis (*light gray diamonds*). The *dotted line* indicates AUC = 0.77 (95% CI, 0.70–0.84) ($P < .001$). D, ROC comparison of the rim sign in addition to ulceration in predicting IPH. 1) Rim-sign + ulceration (*black circles*). The *solid line* indicates AUC = 0.90 (95% CI, 0.84–0.96). 2) Ulceration (*light gray diamonds*). The *dotted line* indicates AUC = 0.63 (95% CI, 0.55–0.72) ($P < .001$).

tein-4 production by endothelial cells.¹⁴ IPH has also been shown to be stimulated by the angiotensin pathway in animal models,³³ and blockade of the angiotensin system inhibits vascular calcification by suppressing bone-morphogenic protein-2.³⁴ Bone-morphogenic protein-4 and bone-morphogenic protein-2 are known to stimulate pathways leading to vascular calcification, with interactions among endothelial cells, macrophages, and pericytic myofibroblasts forming a vascular osteogenic triad.¹⁴ The rim sign of adventitial calcification may therefore be a marker of adventitial neovessel dysfunction and hemorrhage propensity.

Our study also shows not only that IPH prevalence is high with a rim sign but that it further increases with increasing soft-plaque thickness. This finding corresponds with prior research demonstrating a high ROC AUC by using soft-plaque thickness to predict high plaque signal on 3D TOF, though this was only assessed in severe stenosis groups.^{10,11} Further research has demonstrated that soft-plaque thickness on CTA is highly predictive of carotid IPH on T1WI sequences.²⁷ One limitation of these prior studies was that TOF and other T1-weighted images have poor sensitivity and specificity compared with the MPRAGE sequence.⁷ Most important, our study confirms this high association of IPH with

soft-plaque thickness. This association is not surprising because IPH is known to stimulate plaque growth with time.³⁵ Larger plaques may be inherently more unstable and prone to hemorrhage, potentially due to a larger lipid-rich core and/or a higher number or more permeable plaque neovessels.

Most interesting, some factors did not remain in our final model for carotid IPH. One of these factors, stenosis (NASCET percentage or millimeter), was associated with IPH on univariable analysis but did not significantly contribute to IPH after multivariable regression. While initial reports found that stenosis was associated with IPH,⁸ we have recently shown that stenosis alone is a poor discriminator of IPH compared with multivariable models combining plaque markers and clinical markers.¹² In addition, prior research indicates that plaque ulceration may be used as a surrogate marker for IPH.⁹ However, our current study shows that ulceration was a poor predictor of IPH, performing worse than NASCET stenosis. The relatively poor prediction of IPH by using ulceration is in line with predictions by other groups.²⁷ Our data add to previous studies on soft-plaque thickness by finding additional IPH discrimination by using the rim sign, with significantly higher ROC curves.

Because there was varied time between MR imaging and CTA in this retrospective study, we elected to exclude patients with >1 month between scans. In data not shown, we found that the association between the CTA rim sign and IPH remained high even in patients with CTA and MRA scans separated by months to years. This outcome suggests that carotid IPH may continue for long periods, an observation supported by multiple prior studies showing MR imaging IPH signal persisting for months to years.³⁵⁻³⁸

A limitation of our study is related to the narrow population undergoing stroke work-up, limiting generalizability to the population as a whole. Still, this is the population often undergoing CTA to determine stroke etiology based on stenosis, and our results may help determine IPH status and further refine stroke risk in this important group.³⁻⁵ Finally, while this study is limited due to its retrospective nature and inability to determine causation, these data add further support to the ability of CTA to suggest the presence or absence of IPH with a high level of discrimination. Future prospective studies could test whether adventitial calcification and plaque thickness precede IPH or vice versa.

CONCLUSIONS

Carotid IPH can be highly predicted by CTA markers, including the rim sign of adventitial calcification and internal soft plaque. Because CTA is often used in patients undergoing stroke work-up, a rim sign combined with soft-plaque thickness may identify carotid stroke sources that would otherwise be ignored using lumen stenosis or ulceration. The rim sign could also be used to identify patients with a high likelihood of having IPH, to enrich recruitment for future studies aimed at preventing stroke in this high-risk population.

Disclosures: J. Scott McNally—RELATED: Grant: Radiological Society of North America Research Scholar Grant (RSCH1414). * University of Utah Intramural Seed Grant (51900178). * Money paid to the institution.

REFERENCES

- Go AS, Mozaffarian D, Roger VL, et al; American Heart Association Statistics Committee and Stroke Statistics Subcommittee. **Heart Disease and Stroke Statistics: 2013 update—a report from the American Heart Association.** *Circulation* 2013;127:e6–e245 CrossRef Medline
- Treiman GS, McNally JS, Kim SE, et al. **Correlation of carotid intraplaque hemorrhage and stroke using 1.5 T and 3 T MRI.** *Magn Reson Insights* 2015;8(suppl 1):1–8 CrossRef Medline
- Saam T, Hetterich H, Hoffmann V, et al. **Meta-analysis and systematic review of the predictive value of carotid plaque hemorrhage on cerebrovascular events by magnetic resonance imaging.** *J Am Coll Cardiol* 2013;62:1081–91 CrossRef Medline
- Hosseini AA, Kandiyil N, Macsweeney ST, et al. **Carotid plaque hemorrhage on magnetic resonance imaging strongly predicts recurrent ischemia and stroke.** *Ann Neurol* 2013;73:774–84 CrossRef Medline
- Gupta A, Baradaran H, Schweitzer AD, et al. **Carotid plaque MRI and stroke risk: a systematic review and meta-analysis.** *Stroke* 2013;44:3071–77 CrossRef Medline
- McNally JS, Yoon HC, Kim SE, et al. **Carotid MRI detection of intraplaque hemorrhage at 3T and 1.5T.** *J Neuroimaging* 2015;25:390–96 CrossRef Medline
- Ota H, Yarnykh VL, Ferguson MS, et al. **Carotid intraplaque hemorrhage imaging at 3.0-T MR imaging: comparison of the diagnostic performance of three T1-weighted sequences.** *Radiology* 2010;254:551–63 CrossRef Medline
- Sun J, Song Y, Chen H, et al. **Adventitial perfusion and intraplaque hemorrhage: a dynamic contrast-enhanced MRI study in the carotid artery.** *Stroke* 2013;44:1031–36 CrossRef Medline
- U-King-Im JM, Fox AJ, Aviv RI, et al. **Characterization of carotid plaque hemorrhage: a CT angiography and MR intraplaque hemorrhage study.** *Stroke* 2010;41:1623–29 CrossRef Medline
- Gupta A, Baradaran H, Mtui EE, et al. **Detection of symptomatic carotid plaque using source data from MR and CT angiography: a correlative study.** *Cerebrovasc Dis* 2015;39:151–61 CrossRef Medline
- Gupta A, Mtui EE, Baradaran H, et al. **CT angiographic features of symptom-producing plaque in moderate-grade carotid artery stenosis.** *AJNR Am J Neuroradiol* 2015;36:349–54 CrossRef Medline
- McLaughlin A, Hinckley PJ, Treiman SM, et al. **Optimal prediction of carotid intraplaque hemorrhage using clinical and lumen imaging markers.** *AJNR Am J Neuroradiol* 2015;36:2360–66 CrossRef Medline
- Mendes J, Parker DL, McNally S, et al. **Three-dimensional dynamic contrast enhanced imaging of the carotid artery with direct arterial input function measurement.** *Magnetic Reson Med* 2014;72:816–22 CrossRef Medline
- Sorescu GP, Sykes M, Weiss D, et al. **Bone morphogenic protein 4 produced in endothelial cells by oscillatory shear stress stimulates an inflammatory response.** *J Biol Chem* 2003;278:31128–35 CrossRef Medline
- Towler DA, Shao JS, Cheng SL, et al. **Osteogenic regulation of vascular calcification.** *Ann N Y Acad Sci* 2006;1068:327–33 CrossRef Medline
- Wahlgren CM, Zheng W, Shaalan W, et al. **Human carotid plaque calcification and vulnerability: relationship between degree of plaque calcification, fibrous cap inflammatory gene expression and symptomatology.** *Cerebrovasc Dis* 2009;27:193–200 CrossRef Medline
- Shaalan WE, Cheng H, Gewertz B, et al. **Degree of carotid plaque calcification in relation to symptomatic outcome and plaque inflammation.** *J Vasc Surg* 2004;40:262–69 CrossRef Medline
- van den Bouwhuijsen QJ, Bos D, Ikram MA, et al. **Coexistence of calcification, intraplaque hemorrhage and lipid core within the asymptomatic atherosclerotic carotid plaque: the Rotterdam Study.** *Cerebrovasc Dis* 2015;39:319–24 CrossRef Medline
- Freilinger TM, Schindler A, Schmidt C, et al. **Prevalence of nonstenosing, complicated atherosclerotic plaques in cryptogenic stroke.** *JACC Cardiovasc Imaging* 2012;5:397–405 CrossRef Medline
- Hadley JR, Roberts JA, Goodrich KC, et al. **Relative RF coil performance in carotid imaging.** *Magn Reson Imaging* 2005;23:629–39 CrossRef Medline
- Zhu DC, Ferguson MS, DeMarco JK. **An optimized 3D inversion recovery prepared fast spoiled gradient recalled sequence for carotid plaque hemorrhage imaging at 3.0 T.** *Magn Reson Imaging* 2008;26:1360–66 CrossRef Medline
- North American Symptomatic Carotid Endarterectomy Trial: methods, patient characteristics, and progress.** *Stroke* 1991;22:711–20 CrossRef Medline
- Fox AJ. **How to measure carotid stenosis.** *Radiology* 1993;186:316–18 CrossRef Medline
- Fox AJ, Eliasziw M, Rothwell PM, et al. **Identification, prognosis, and management of patients with carotid artery near occlusion.** *AJNR Am J Neuroradiol* 2005;26:2086–94 Medline
- Bartlett ES, Walters TD, Symons SP, et al. **Quantification of carotid stenosis on CT angiography.** *AJNR Am J Neuroradiol* 2006;27:13–19 Medline
- Menon BK, Singh J, Al-Khataami A, et al; Calgary CTA Study Group. **The donut sign on CT angiography: an indicator of reversible intraluminal carotid thrombus?** *Neuroradiology* 2010;52:1055–56 CrossRef Medline
- Trelles M, Eberhardt KM, Buchholz M, et al. **CTA for screening of complicated atherosclerotic carotid plaque—American Heart Association type VI lesions as defined by MRI.** *AJNR Am J Neuroradiol* 2013;34:2331–37 CrossRef Medline
- Zou GY, Donner A. **Extension of the modified Poisson regression**

- model to prospective studies with correlated binary data.** *Stat Methods Med Res* 2013;22:661–70 CrossRef Medline
29. Maldonado G, Greenland S. **Simulation study of confounder-selection strategies.** *Am J Epidemiol* 1993;138:923–36 Medline
30. Vittinghoff E, McCulloch CE. **Relaxing the rule of ten events per variable in logistic and Cox regression.** *Am J Epidemiol* 2007;165:710–18 CrossRef Medline
31. Pepe M, Longton G, Janes H. **Estimation and comparison of receiver operating characteristic curves.** *Stata J* 2009;9:1 Medline
32. Harrell FE Jr, Lee KL, Mark DB. **Multivariable prognostic models: issues in developing models, evaluating assumptions and adequacy, and measuring and reducing errors.** *Stat Med* 1996;15:361–87 Medline
33. Cheng C, Tempel D, van Haperen R, et al. **Atherosclerotic lesion size and vulnerability are determined by patterns of fluid shear stress.** *Circulation* 2006;113:2744–53 CrossRef Medline
34. Li M, Wu P, Shao J, et al. **Losartan inhibits vascular calcification by suppressing the BMP2 and Runx2 expression in rats in vivo.** *Cardiovasc Toxicol* 2016;16:172–81 CrossRef Medline
35. Takaya N, Yuan C, Chu B, et al. **Presence of intraplaque hemorrhage stimulates progression of carotid atherosclerotic plaques: a high-resolution magnetic resonance imaging study.** *Circulation* 2005;111:2768–75 CrossRef Medline
36. Sun J, Underhill HR, Hippe DS, et al. **Sustained acceleration in carotid atherosclerotic plaque progression with intraplaque hemorrhage: a long-term time course study.** *JACC Cardiovasc Imaging* 2012;5:798–804 CrossRef Medline
37. Underhill HR, Yuan C, Yarnykh VL, et al. **Arterial remodeling in [corrected] subclinical carotid artery disease.** *JACC Cardiovasc Imaging* 2009;2:1381–89 CrossRef Medline
38. Yamada N, Higashi M, Otsubo R, et al. **Association between signal hyperintensity on T1-weighted MR imaging of carotid plaques and ipsilateral ischemic events.** *AJNR Am J Neuroradiol* 2007;28:287–92 Medline

Do Radiologists Report the TNM Staging in Radiology Reports for Head and Neck Cancers? A National Survey Study

 B. Ko,  U. Parvathaneni,  P.A. Hudgins, and  Y. Anzai

ABSTRACT

BACKGROUND AND PURPOSE: CT and MR imaging are widely used for the staging of head and neck cancer. Currently, there are no data regarding whether the primary tumor, nodes, metastasis (TNM) staging is routinely incorporated into radiology reports. We conducted a national survey to determine whether radiologists routinely address staging, in particular regarding T (primary tumor) and N (nodal).

MATERIALS AND METHODS: The survey was sent to 782 members of the American Society of Head and Neck Radiology. The survey asked whether they assign TN staging in reports. If they do assign TN staging, what are the reasons for doing so, and if not, what are the barriers or reasons for not including it in the radiology report? The method of measuring the size of the primary tumor and pathologic lymph nodes was also queried.

RESULTS: A total of 229 responses were returned (29.3% response rate). Approximately half (49%; 95% confidence interval, 43.55–54.5%) of the responders thought that incorporating TN staging is important. However, only 24.5% (95% confidence interval, 19.8%–29.2%) stated that they routinely assigned TN staging in their radiology reports. The most common barriers were being afraid of being inaccurate (59%) and being unable to remember the staging classifications (58.2%); 76.9% indicated that they measure a primary tumor in 3D.

CONCLUSIONS: Staging head and neck cancer based on imaging presents unique challenges. Nearly half of the responding radiologists think it is important to incorporate TN staging in radiology reports, though only a quarter of them routinely do so in practice.

ABBREVIATIONS: H&N = head and neck; TNM = (primary) tumor, nodes, metastasis

CT and MR imaging are widely used for the staging of a newly diagnosed head and neck (H&N) squamous cell carcinoma.^{1–4} Treatment decisions depend on various factors, including the stage of disease, pathologic type, comorbidities, certain risk factors such as human papillomavirus status, and the patient's preference regarding treatment. Consistent, accurate, and precise characterization of H&N cancer on the imaging report is thus an integral component of staging of H&N squamous cell carcinoma.

The primary tumor, nodes, metastasis (TNM) classification of the American Joint Committee on Cancer/Union for International Cancer Control is a widely accepted staging system. The tumor stage impacts treatment decisions, predicts prognosis, and helps determine the patient's eligibility for various clinical trials.

An explicit statement of the American Joint Committee on Cancer TNM classification in radiology reports has not been the standard practice to date.^{3,5} The value of incorporating staging information into radiology reports on treatment decisions or, ultimately, outcomes has not been previously studied or reported, to our knowledge.

Currently, there are no data regarding how often TNM staging information is routinely incorporated into radiology reports for patients with H&N squamous cell carcinoma. We conducted a national survey to determine whether radiologists routinely report the stage of the primary tumor and metastatic nodes in their final imaging interpretation in patients with H&N cancer. In addition, we explored the perceived barriers and values of incorporating TN staging among radiologists. Because cross-sectional imaging was emphasized, and not PET/CT, questions regarding distant metastases were not included.

The aim of this pilot study, therefore, was to assess the current practice of assigning a TN stage in the radiology report. This information may improve understanding in current practice and permit an open discussion among radiologists, oncologists, surgeons, administrators, and payers regarding how standardized

Received September 10, 2015; accepted after revision January 18, 2016.

From the Departments of Radiation Oncology (B.K., U.P.) and Radiology (Y.A.), University of Washington, Seattle, Washington; Department of Radiology and Imaging Sciences (P.A.H.), Emory University, Atlanta, Georgia; and Department of Radiology and Imaging Sciences (Y.A.), University of Utah Health Care, Salt Lake City, Utah.

Please address correspondence to Yoshimi Anzai, MD, MPH, Department of Radiology and Imaging Sciences, University of Utah, 30 North 1900 East, 1A071, Salt Lake City, UT 84132; e-mail: Yoshimi.Anzai@hsc.utah.edu; @yoshimianzai

<http://dx.doi.org/10.3174/ajnr.A4742>

Survey Questions

Question 1. Nature of practice:

- a) Academic, b) private, c) both

Question 2. Years of Experience

- a) <2 years, b) 2-5 years, c) 5-8 years, d) >8 years

Question 3. Do you sub-specialize in Head and Neck Radiology?

- a) Yes, b) No

Question 4. Do you routinely issue a radiology report using TN(M) staging?

- a) Yes, b) No

Question 5. In your opinion, what are the barriers that might prevent radiologists from using the TN(M) staging system during reporting? (Check all that apply)

- a) Afraid of inaccuracy
b) Time-consuming
c) Unable to remember the staging classification
d) No reimbursement
e) Not required
f) Other: (Space included for comments)

Question 6. If you are currently incorporating the TN(M) staging system, what are the reasons for this practice? (Check all that apply)

- a) Believe in added values required from surgery or oncology colleagues
b) Educational value
c) Help the treatment decision
d) Not applicable
e) Other: (Space included for comments)

Question 7. How do you measure the size of primary H&N tumor?

- a) One dimension in the axial plane,
b) Bi-dimension in the axial plane,
c) Three dimensions including the cranio-caudal dimension

Question 8. How do you measure cervical lymph nodes?

- a) Short axial dimension,
b) Longest axial dimension
c) Bi-dimension
d) Three dimensions including the cranio-caudal dimension

Question 9. How important do you think it is to incorporate TN(M) staging into a radiology report?

- a) Very important, b) Somewhat important, c) Neutral,
d) Not very important, e) Not important

FIG 1. Survey questions.

radiology reports could potentially add value to the care of the patient with H&N cancer.⁶

MATERIALS AND METHODS

Procedure

The study was approved by University of Washington institutional review board. An electronic survey (Fig 1) was sent to 782 active members of the American Society of Head and Neck Radiology via their e-mail address in April 2014. Nonresponders were contacted with a reminder after 1 week. Data were collected anonymously by using Catalyst software (<http://www.amd.com/en-us/innovations/software-technologies/catalyst>) to protect responders' privacy. Participants were not required to answer all questions and could choose to omit certain responses according to their level of comfort.

The survey asked the following questions: 1) the nature of practice (academic versus private); 2) years of experience; 3) whether the radiologist subspecialized in H&N radiology, determined by self-identification; 4) their practice of routine assignment of TN staging in CT/MR reports; 5) the reasons for not explicitly reporting the stage in reports; or 6) the reasons for assigning the stage in reports; and 7) the importance of incorporating TN or TNM staging in a radiology report.

In addition, we asked the method of measuring the primary tumor and cervical lymph node size because these measures impact the assignment of T and N staging. The different methods of measuring can have varying prognosis and treatment modalities.^{4,7,8}

Figure 1 shows the copy of survey.

Instrument

Questions were formulated with multiple-choice answers by using the Catalyst software. Seven questions were limited to only 1 choice, whereas 2 questions provided the possibility of choosing multiple answers. The 2 questions, 5) What are the reasons you do not explicitly report the stage in reports, and 6) What are the reasons you do assign the stage in reports, also included an additional "Other" answer with a comment box available for any responses not listed as an answer choice.

Statistical Analysis

Response statistics were given in the Catalyst software. Data were analyzed by using standard descriptive statistics. Further frequency tabulation and descriptive statistics were calculated

by using Excel, Version 14.4.4 (Microsoft, Redmond, Washington). Confidence interval calculation was performed by using The Survey System (<http://www.surveysystem.com/sscalc.htm>).

RESULTS

Participant Demographics

A total of 229 responses were received within 2 weeks (29.3% response rate). More than 62.8% (95% CI, 57.5%–68.0%) of the responders were in an academic practice, 23.8% (95% CI, 19.2%–28.4%) of responders were in private practice, and 13.5% (95% CI, 9.8%–17.2%) reported being in combined private and academic practice; 63.3% had >8 years of experience, 12.7% of the responders had 5–8 years of experience, 17.0% had 2–5 years of experience, and 7.0% of responders had <2

Table 1: Survey responder demographics

Variable	No. of Responses	Frequency
Nature of Practice	229	
Academic	144	62.8%
Private	54	23.8%
Both	31	13.5%
Years of Experience	229	
<2 years	16	7.0%
2–5 years	39	17.0%
5–8 years	29	12.7%
>8 years	145	63.3%
Subspecialty	229	
Head and neck radiology	165	72.1%
Other subspecialization of radiology	64	27.9%

Table 2: Perceived barriers to incorporating staging in radiology reports^a

Answer	No. of Responses (n = 227)	Frequency
Afraid of inaccuracy	134	59.0%
Unable to remember staging classification	132	58.2%
Time-consuming	106	46.7%
Not required	81	35.7%
Other	74	32.6%
No reimbursement	41	18.1%

^a The sum of responses exceeds the total number of responses ($n = 227$) because participants were able to choose multiple answers for this particular question.

years of experience. Subspecialization in H&N radiology was reported by 72.1% of respondents (Table 1).

Reasons for Not Incorporating TN Staging in Routine Radiology Reports

Of the total participants, 24.5% stated that they routinely assigned TN staging in radiology reports. Furthermore, 30.3% (95% CI, 24%–36.5%) of those who subspecialize in H&N radiology routinely perform TN staging. The 2 most frequent responses to potential reasons for not stating the TN stage in reports or barriers to such staging were fear of inaccuracies and being unable to remember the staging classification (Table 2). These responses may be due to the periodic changes of TNM classification⁹ because the system is reviewed every 7–10 years and there are changes in the staging system at various subsites. Approximately one-third thought that reporting staging was not required, and 18% did not give the stage due to lack of reimbursement.

Of the 32.6% who replied “other,” the answers were broadly categorized as follows: 40.5% responded that insufficient clinical data were provided to accurately report TN staging and that staging without considering clinical data was not advised. For example, vocal cord mobility is an important factor for staging laryngeal cancer and cannot always be accurately determined solely on imaging.¹⁰ 16.2% stated that referring physicians prefer to do it themselves to prevent conflicting readings and that referring physicians prefer not to have radiology TNM staging in the report. 13.5% responded that their imaging interpretation including all necessary staging information, just not in the final TN staging. Staging being done with referring physicians at a Tumor Board setting was reported in 10.8%. Not interpreting PET scans that are essential for staging was reported in 8.1%. Finally, 5.4% reported

Table 3: Reasons for assigning TN staging in radiology reports^a

Answer	No. of Responses (n = 115)	Frequency
Believe in added value required from surgery or oncology colleagues	60	52.2%
Help the treatment decision	50	43.5%
Not applicable	40	34.8%
Educational value	38	33.0%
Other	17	14.8%

^a The sum of responses exceeds the total number of responses ($n = 115$) because participants were able to choose multiple answers for this particular question.

that the referring clinician may not fully understand the complexity of staging based solely on imaging.

Reasons for Incorporating TN Staging in Routine Radiology Reports

Responders who routinely assign TN staging indicated that the reasons for such practice are the following; 1) They believe it adds value to the report, 2) it helps determine treatment decisions, and 3) it is of educational value (Table 3). “Not applicable” was available for those who did not routinely assign TN staging. The number of people who answered this question ($n = 115$) exceeded the number responding that they routinely assign TN staging. We speculate that some selected the reasons for incorporating TN staging on the basis of their expertise, despite not routinely assigning TN staging in their reports. Other responses included the following: 1) to speak same language as head and neck surgery colleagues, 2) marketing, 3) faster presentation at the Tumor Board, and 5) the pathology department follows the College of American Pathologists protocol to assign pTNM staging, as such radiologists should assign rTNM staging.

Measurements of Primary Tumor

The survey also asked how radiologists measure the size of a primary H&N tumor, which is an important determinant of TN staging. Measuring a primary tumor in 3D was reported in 76.9% (95% CI, 72.2%–81.5%), 17.3% (95% CI, 13.2%–21.4%) of the responders measure a primary tumor in 2D, and 5.8% (95% CI, 3.3%–8.1%) of participants measure a primary tumor in 1D (ie, in the axial plane; Figs 2 and 3).

Measurements of Cervical Lymph Node Size

Measurements of cervical lymph node size were quite variable. The survey showed 37.3% (95% CI, 32.6%–42.6%) of respondents measured lymph nodes in the longest axial dimension, 17.3% (95% CI, 13.2%–21.4%) reported that they measure along the short axial dimension, 28.4% (95% CI, 23.5%–33.3%) of responders measure cervical lymph nodes in 2 and 16.9% (95% CI, 12.8%–21%) responders measured in 3D, including the craniocaudal dimension.

Perceived Importance of Incorporating TN Staging into Routine Practice

Approximately half (48.9%) of the responders answered that assigning TN staging was important, and 34.9% were neutral in their views. Only 16.2% thought it was not important (Table 4). However, among the respondents who indicated that TN staging was important, 53.6% were not incorporating the stage into their routine dictations.

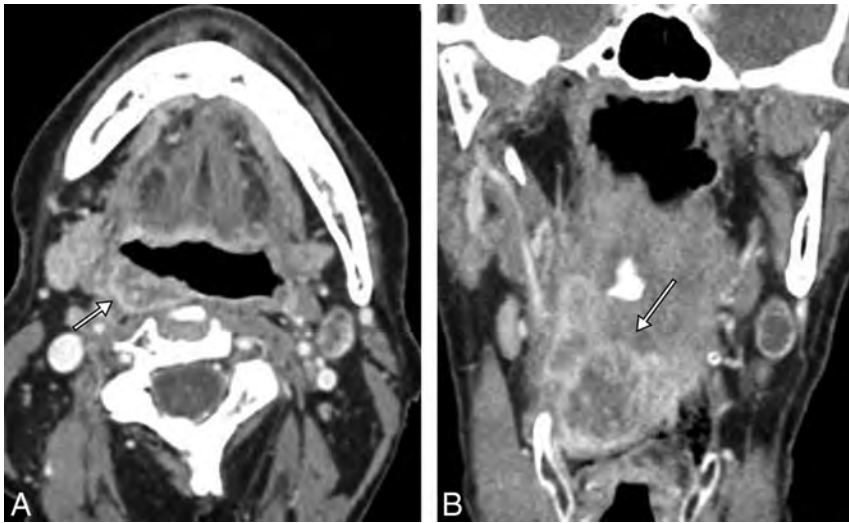


FIG 2. Contrast-enhanced axial (A) and coronal (B) CT images of a patient with posterior pharyngeal wall cancer. The transaxial dimension is 2.5 cm (*short arrow*), though the craniocaudal dimension exceeds 4 cm (*long arrow*). Therefore, based on size alone, the stage is T3. Addition of concurrent chemotherapy to radiation therapy would be appropriate in a T3, but not a T2 lesion. Additional factors that would upstage this tumor, as described in American Joint Committee on Cancer, 7th edition (<https://cancerstaging.org/Pages/default.aspx>) are extension to the larynx, involvement of extrinsic tongue muscles, medial pterygoid muscle involvement, or hard palate or mandible invasion. These are all imaging-based characteristics.

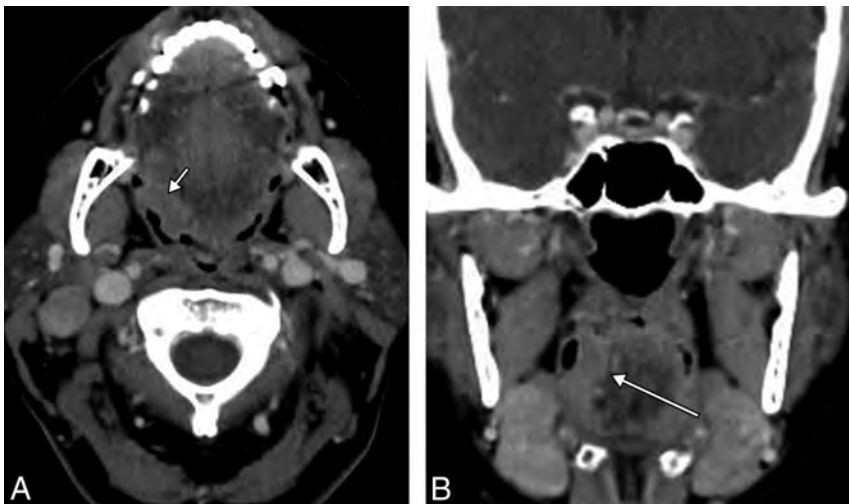


FIG 3. Contrast-enhanced axial (A) and coronal (B) CT images of a patient with squamous cell carcinoma of the right base of the tongue. Although the transaxial dimension is 1.8 cm (*short arrow*), the craniocaudal dimension is 3.5 cm, technically at least a T2 lesion, if only the size is considered. These measurements can only be accurately acquired on imaging. Note that the largest craniocaudal dimension (*long arrow*) is submucosal, and on the basis of physical examination alone, this tumor could be grossly understaged.

DISCUSSION

We conducted this survey to understand the current practice among radiologists primarily in the United States regarding the use of the TNM staging, and more specifically the TN characteristics, in their routine reports. Our goal is to open a discussion among radiologists, referring physicians, administrators, and payers on how radiology reports could provide relevant staging information in an unambiguous fashion.¹¹

To our knowledge, this is the first reported national survey regarding imaging-based staging for practicing neuroradiologists and H&N radiologists. We found that approximately half of the

responding radiologists viewed it as important to incorporate TN staging in reports, though only 24.5% of radiologists routinely assign a stage in these reports.

One of the more common factors preventing radiologists from using TN staging appeared to be a lack of sufficient clinical data available to the radiologist. TN staging based solely on imaging findings is thus perceived to be inaccurate. Some radiologists thought that with incomplete history and clinical data, it was outside their scope of practice to routinely report formal TN staging. They also replied that applying TN staging on the basis of imaging alone can lead to incomplete data and may potentially carry medical-legal ramifications. For practices with robust electronic medical records allowing readily available clinical information, this concern may not be a major barrier. One subsite where staging might be limited by not knowing the clinical examination results is staging of laryngeal cancer,¹⁰ where vocal cord mobility would change the T stage. Another subsite where lack of clinical information may limit accurate imaging-based staging is oral cavity cancer, where mucosal extent is clearly assessed by the physical examination. Cross-sectional imaging does not demonstrate the extent of the superficial mucosal portion of the oral cavity lesion. If this information is not available in the electronic medical records, the interpretation could include all other imaging findings needed for staging.

Some responders thought that radiologists must provide surgeons and treating physicians with the relevant staging information, but it is treating physicians' responsibility to merge the clinical and radiology information to stage the patient. No studies to date have addressed how often radiology reports include all relevant staging information

for treating physicians to determine accurate staging. A structured reporting system incorporating the American Joint Committee on Cancer staging system may help provide complete information necessary for staging each head and neck subsite. To mitigate the perceived limitations related to lack of clinical information, the radiology report could state, "Stage based on imaging alone is T2 N1," for example. Another method of reporting could be similar to the pathology report, by using a lowercase *r*, for example *r*T2 N1, similar to *c*T2 N1, which represents staging based on clinical examination.

In addition, an important goal of cross-sectional imaging such

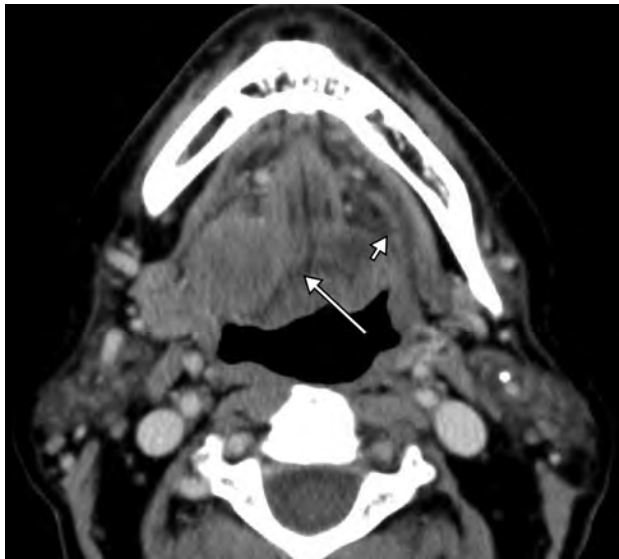


FIG 4. Axial contrast-enhanced CT at the floor of mouth level. Clinically, this tumor was staged as T2 right oral cavity squamous cell carcinoma because there was mucosal ulceration and a >2-cm palpable mass. However, there is invasion of the lateral and posterior genioglossus muscle (*long arrow*). Note a normal hyoglossus muscle on the left (*short arrow*); tumor has completely replaced right hyoglossus muscle. This is upstaged to T4a on the basis of CT findings, changing the prognosis and treatment.

Table 4: Perceived importance of incorporating TN staging in radiology reports

Answer	No. of Responses (n = 229)	Frequency
Very important	44	19.2%
Somewhat important	68	29.7%
Neutral	80	34.9%
Not very important	18	7.9%
Not important	19	8.3%

as CT or MR imaging is to address the deeper extension of tumor (Fig 4), not to measure the superficial mucosal extent of a tumor. A superficial tongue lesion with no deep invasion may not be visible on CT or MR imaging and therefore would be potentially understaged on the basis of imaging alone. Contrary to other body sites, such as lung cancer in which staging is based solely on imaging findings, the staging of H&N cancer sometimes requires knowledge of the clinical findings. In these settings, the dictation can be as thorough as possible so that Tumor Board members can assign a stage. These examples support the above-mentioned concerns of radiologists, and such limitations should be acknowledged. A multidisciplinary Tumor Board setting is an ideal situation to discuss the clinical and imaging findings and assign a single TN stage, so that proper treatment can be planned.

This survey revealed that 76.9% of the responders measure a primary H&N tumor in 3D. It is critically important because the staging depends on the largest dimension of a tumor, which is not necessarily the largest transaxial dimension (Fig 2). For example, a 1.8-cm tonsil cancer in the transaxial dimension may extend more than 2 cm in the craniocaudal dimension, which should be staged at least T2 based on size, and not T1 (Fig 3). Even though response evaluation criteria in solid tumors require only 1D measurement to address the therapeutic effect of investigational drugs

in clinical trials, 3D measurement of H&N cancer more accurately reflects real tumor burden in an individual patient.^{12,13}

The measurement of cervical lymph nodes was more variable than that for primary tumors among the survey responders. It has been reported that the short axial diameter of lymph nodes is the most accurate indicator of metastatic versus normal or reactive nodes.^{8,14} The largest diameter of the lymph node also affects the nodal staging, which is not necessarily the largest transaxial diameter of the lymph nodes. With the advancement of CT technology and isometric voxel size, coronal or sagittal reformatted images are routinely obtained in most current practices.¹⁵ Thus, measuring the largest dimension of a lymph node is essential for accurate nodal staging.

TN staging in radiology reports is critical in providing essential information for treatment planning and prognosis of various cancers.^{16,17} It allows precise preoperative extent of tumor, which enhances levels of objectivity of clinical staging based on physical examination.¹⁸ The Quality and Productivity: Proposed Case Study performed by the National Institute for Health and Care Excellence in the United Kingdom demonstrated that TNM classification not explicitly stated but rather implied in free text format led to delays in treatment or incorrect decisions regarding treatment.¹⁹ This study showed that structured radiology reports that include explicit TNM staging for cervical, endometrial, ovarian, prostate, and rectal cancer improved prognostic accuracy and reduced cost on the basis of reduced time seeking clarification, with approximate saving of £2900 (US \$4,150) per 100,000 population (www.evidence.nhs.uk/qualityandproductivity).¹⁹

One of the limitations of the current study is that it was sent to only members of the American Society of Head and Neck Radiology. These results may not apply to a broader and less specialized group of radiologists. The argument can be made that all oncologic studies should be interpreted and reported by subspecialists because treatment regimens vary, on the basis almost entirely of the stage. The importance of providing accurate staging, especially in the H&N, cannot be overemphasized. A future study might include the assessment of the clinical practice of incorporating FDG-PET for staging H&N cancer^{20,21} and reporting of TNM staging of H&N cancer on FDG-PET.

CONCLUSIONS

Staging H&N cancer based on imaging presents unique challenges, but also opportunities. Although some H&N cancers may not be accurately staged with imaging, staging for most H&N cancer is determined by the size and local extent, best noted on cross-sectional imaging, often in conjunction with PET. Future study is needed to determine whether assigning an imaging-based stage could improve treatment decisions for patients with H&N cancer or impact referring physicians' and patients' satisfaction.

REFERENCES

1. Curtin HD, Ishwaran H, Mancuso AA, et al. **Comparison of CT and MR imaging in staging of neck metastases.** *Radiology* 1998;207:123–30 [CrossRef Medline](#)
2. Hudgins PA, Kingdom TT, Weissler MC, et al. **Selective neck dissection: CT and MR imaging findings.** *AJNR Am J Neuroradiol* 2005;26:1174–77 [Medline](#)

3. Yousem DM, Gad K, Tufano RP. **Resectability issues with head and neck cancer.** *AJNR Am J Neuroradiol* 2006;27:2024–36 Medline
4. Mukherji SK, Mancuso AA, Mendenhall W, et al. **Can pretreatment CT predict local control of T2 glottic carcinomas treated with radiation therapy alone?** *AJNR Am J Neuroradiol* 1995;16:655–62 Medline
5. Patel SG, Shah JP. **TNM staging of cancers of the head and neck: striving for uniformity among diversity.** *CA Cancer J Clin* 2005;55:242–58; quiz 261–62, 64 Medline
6. Knechtges PM, Carlos RC. **The evolving role of radiologists within the health care system.** *J Am Coll Radiol* 2007;4:626–35 CrossRef Medline
7. Mancuso AA, Harnsberger HR, Muraki AS, et al. **Computed tomography of cervical and retropharyngeal lymph nodes: normal anatomy, variants of normal, and applications in staging head and neck cancer, Part II: pathology.** *Radiology* 1983;148:715–23 CrossRef Medline
8. van den Brekel MW, Castelijns JA, Snow GB. **The size of lymph nodes in the neck on sonograms as a radiologic criterion for metastasis: how reliable is it?** *AJNR Am J Neuroradiol* 1998;19:695–700 Medline
9. Takes RP, Rinaldo A, Silver CE, et al. **Future of the TNM classification and staging system in head and neck cancer.** *Head Neck* 2010;32:1693–711 CrossRef Medline
10. Gilbert K, Dalley RW, Maronian N, et al. **Staging of laryngeal cancer using 64-channel multidetector row CT: comparison of standard neck CT with dedicated breath-manuever laryngeal CT.** *AJNR Am J Neuroradiol* 2010;31:251–56 CrossRef Medline
11. Glastonbury CM, Bhosale PR, Choyke PL, et al. **Do radiologists have stage fright? Tumor staging and how we can add value to the care of patients with cancer.** *Radiology* 2016;278:11–12 CrossRef Medline
12. Street E, Hadjiiski L, Sahiner B, et al. **Automated volume analysis of head and neck lesions on CT scans using 3D level set segmentation.** *Med Phys* 2007;34:4399–408 CrossRef Medline
13. Hadjiiski L, Mukherji SK, Gujar SK, et al. **Treatment response assessment of head and neck cancers on CT using computerized volume analysis.** *AJNR Am J Neuroradiol* 2010;31:1744–51 CrossRef Medline
14. van den Brekel MW, Stel HV, Castelijns JA, et al. **Cervical lymph node metastasis: assessment of radiologic criteria.** *Radiology* 1990;177:379–84 CrossRef Medline
15. Kato H, Kanematsu M, Watanabe H, et al. **Metastatic retropharyngeal lymph nodes: comparison of CT and MR imaging for diagnostic accuracy.** *Eur J Radiol* 2014;83:1157–62 CrossRef Medline
16. UyBico SJ, Wu CC, Suh RD, et al. **Lung cancer staging essentials: the new TNM staging system and potential imaging pitfalls.** *Radiographics* 2010;30:1163–81 CrossRef Medline
17. Lee SC, Jain PA, Jethwa SC, et al. **Radiologist's role in breast cancer staging: providing key information for clinicians.** *Radiographics* 2014;34:330–42 CrossRef Medline
18. Schwartz LH, Panicek DM, Berk AR, et al. **Improving communication of diagnostic radiology findings through structured reporting.** *Radiology* 2011;260:174–81 CrossRef Medline
19. Addenbrooke's Hospital, Cambridge University Hospitals NHS Foundation Trust. **Template reports for radiology cancer staging: improving information to guide treatment decisions.** 2014. www.evidence.nhs.uk/qualityandproductivity. Accessed January 4, 2016
20. Roh JL, Park JP, Kim JS, et al. **18F fluorodeoxyglucose PET/CT in head and neck squamous cell carcinoma with negative neck palpation findings: a prospective study.** *Radiology* 2014;271:153–61 CrossRef Medline
21. Mukherji SK, Bradford CR. **Controversies: is there a role for positron-emission tomographic CT in the initial staging of head and neck squamous cell carcinoma?** *AJNR Am J Neuroradiol* 2006;27:243–45 Medline

Reduced Field-of-View Diffusion Tensor Imaging of the Optic Nerve in Retinitis Pigmentosa at 3T

Y. Zhang, X. Guo, M. Wang, L. Wang, Q. Tian, D. Zheng, and D. Shi



ABSTRACT

BACKGROUND AND PURPOSE: Diffusion tensor imaging may reflect pathology of the optic nerve; however, the ability of DTI to evaluate alterations of the optic nerve in retinitis pigmentosa has not yet been assessed, to our knowledge. The aim of this study was to investigate the diagnostic potential of reduced FOV–DTI in optic neuropathy of retinitis pigmentosa at 3T.

MATERIALS AND METHODS: Thirty-eight patients and thirty-five healthy controls were enrolled in this study. Measures of visual field and visual acuity of both eyes in all subjects were performed. A reduced FOV–DTI sequence was used to derive fractional anisotropy, apparent diffusion coefficient, principal eigenvalue, and orthogonal eigenvalue of the individual optic nerves. Mean fractional anisotropy, ADC, and eigenvalue maps were obtained for quantitative analysis. Further analyses were performed to determine the correlation of fractional anisotropy, ADC, principal eigenvalue, and orthogonal eigenvalue with optic nerves in patients with mean deviation of the visual field and visual acuity, respectively.

RESULTS: The optic nerves of patients with retinitis pigmentosa compared with control subjects showed significantly higher ADC, principal eigenvalue, and orthogonal eigenvalue and significantly lower fractional anisotropy ($P < .01$). For patients with retinitis pigmentosa, the mean deviation of the visual field of the optic nerve was significantly correlated with mean fractional anisotropy ($r = 0.364$, $P = .001$) and orthogonal eigenvalue ($r = -0.254$, $P = .029$), but it was not correlated with mean ADC ($P = .154$) and principal eigenvalue ($P = .337$). Moreover, no correlation between any DTI parameter and visual acuity in patients with retinitis pigmentosa was observed ($P > .05$).

CONCLUSIONS: Reduced FOV–DTI measurement of the optic nerve may serve as a biomarker of axonal and myelin damage in optic neuropathy for patients with retinitis pigmentosa.

ABBREVIATIONS: FA = fractional anisotropy; λ_{\perp} = orthogonal eigenvalue; $\lambda_{//}$ = principal eigenvalue; MDVF = mean deviation of the visual field; ON = optic nerve; rFOV = reduced FOV; RP = retinitis pigmentosa; VA = visual acuity; VF = visual field

Retinitis pigmentosa (RP) is a common refractory visual disease and accounts for a large proportion of hereditary visual impairment. It is characterized by the progressive death of rod and cone photoreceptors, which leads to corresponding visual field (VF) defects.¹ As a heterogeneous group of inherited retinal degenerative diseases,² RP displays extreme genetic heterogeneity. More than 80 disease genes have been identified so far, 58 of which

correspond to nonsyndromic RP.³ Clinical features of RP include night blindness, progressive loss of peripheral VFs, reduced or nondetectable electroretinogram amplitudes, and characteristic pigmentary degenerative changes of the retina.

Several studies observed that the retinal nerve fiber layer, formed by expansion of optic nerve (ON) fibers, is significantly thinner in patients with RP by using optical coherence tomography,^{4,5} which reflects the changes of the ON in RP. Furthermore, the occurrence of optic neuropathy in RP was confirmed by a postmortem study that showed that total axon counts of the ON were significantly decreased in patients with end-stage RP compared with healthy controls.⁶ However, in vivo diagnosis of optic neuropathy in patients with RP remains challenging because conventional MR imaging and ophthalmologic examinations often fail to detect ON disease.

Recently, DTI has emerged as a noninvasive imaging method with great potential to investigate the morphology and function of the ON in vivo.^{7,8} However, there has been no study of DTI in

Received September 7, 2015; accepted after revision February 6, 2016.

From the Departments of Radiology (Y.Z., M.W., L.W., Q.T., D.S.) and Ophthalmology (X.G.), Zhengzhou University People's Hospital, Henan Provincial People's Hospital, Zhengzhou, China; and GE Healthcare (D.Z.), Beijing, China.

This study was supported by the National Natural Science Foundation of China Grant (No. 81271534).

Please address correspondence to Dapeng Shi, MD, Zhengzhou University People's Hospital, Henan Provincial People's Hospital, Department of Radiology, #7 Wei Wu Rd, Zhengzhou, Henan 450003, China; e-mail: cjr.shidapeng@vip.163.com

Indicates open access to non-subscribers at www.ajnr.org

<http://dx.doi.org/10.3174/ajnr.A4767>

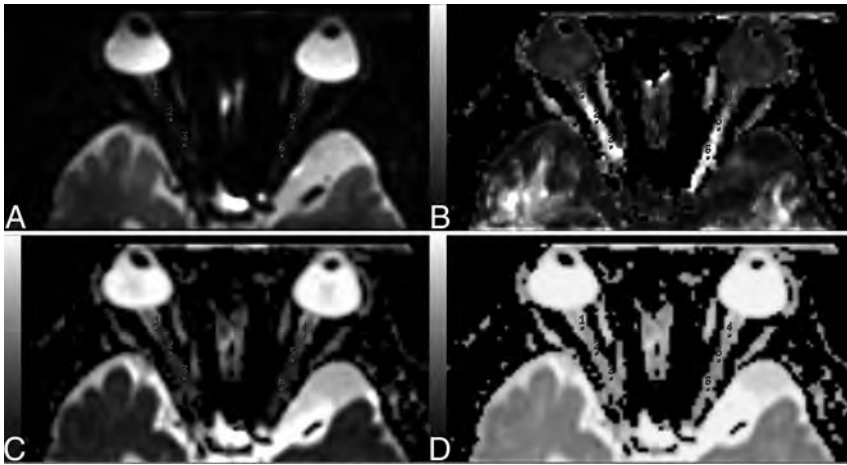


FIG 1. Non-diffusion-weighted (B_0) image and FA, ADC, and eigenvector maps of DTI. Three ROIs are placed over each intraorbital nerve on the $b=0$ image (A). ROIs on the $b=0$ -averaged image (A) are then transferred onto the FA (B), ADC (C), and eigenvector (D) maps.

optic neuropathy of RP to date, especially reduced FOV-DTI (rFOV-DTI) at 3T, which has the potential advantages of improved signal-to-noise ratio and reduced susceptibility-related artifacts over conventional DTI.^{9,10} This study set out to investigate the potential clinical utility of rFOV-DTI in diagnosing optic neuropathy in RP at 3T. Specifically, we hypothesized that quantitative rFOV-DTI might reveal the injury to the ON of RP, which may be related to visual functions, including both VF and visual acuity (VA).

MATERIALS AND METHODS

Subjects

Thirty-eight patients (24 males, 14 females; mean age, 37 years; range, 6–62 years) with RP were recruited for this study from August 2014 to September 2015 from Zhengzhou University People's Hospital. No patient had any potentially contributory history of trauma, poisoning, or metabolic or autoimmune diseases. Each patient underwent a complete ophthalmologic examination. Diagnosis of RP was made according to the following criteria: 1) a history of night blindness, with gradual loss of VA during the day; 2) progressive VF defects, from peripheral to central, leading to typical tunnel vision; 3) typical fundus changes: optic disc pallor, attenuated retinal arterioles, and peripheral intraretinal pigment deposits in a bone-spicule configuration; and 4) abnormal findings on electroretinography: moderately reduced or almost non-detectable amplitudes of a- and b-waves and prolonged time intervals from stimuli to peak rod or cone isolated responses.^{4,5,11,12} Patients who had other ocular diseases, such as age-related macular degeneration, ischemic optic neuropathy, glaucoma, diabetic retinopathy, and optic neuritis were excluded.^{1,7,8}

Thirty-five healthy volunteers (22 males, 13 females; mean age, 36 years; range, 9–60 years) were enrolled as a control group. All healthy volunteers completed formal ophthalmologic evaluation, including VA and VF. No healthy volunteers had any ophthalmologic or neurologic disorders. The bilateral corrected VA of healthy subjects was ≥ 0.8 .

This study was approved by the local ethics committee, and all subjects provided informed consent in writing in accordance with the Declaration of Helsinki.

MR Imaging Protocol

A 3T whole-body scanner (Discovery MR 750; GE Healthcare, Milwaukee, Wisconsin) equipped with an 8-channel head coil was used, and subjects were instructed to close their eyes and remain still during the MR imaging study. Routine MR imaging of the brain and orbits was performed to exclude intracranial and intraorbital diseases. A 1-mm isotropic-resolution anatomic 3D T1-weighted acquisition based on a magnetization-prepared rapid acquisition of gradient echo sequence was acquired. For the rFOV-DTI acquisition, a diffusion-weighted spin-echo single-shot echo-planar imaging with a 2D excitation pulse was used. Thirty noncollinear diffusion directions with $b=600$ s/mm²

and a B_0 image were acquired with the following parameters: TR = 1800 ms, TE = 90 ms, FOV = 16×8 cm², matrix = 96×48 , section thickness = 2 mm with a 0-mm section gap, NEX = 6. The DTI scanning plane was oriented approximately parallel to the ON with the scanned volume from the infraorbital rim to the supraorbital rim. The acquisition time of rFOV-DTI was 5 minutes 37 seconds.

MR Imaging Postprocessing

Postprocessing of rFOV-DTI was performed by using FuncTool software (GE Healthcare) on an ADW4.5 workstation (GE Healthcare). Fractional anisotropy (FA), ADC, and eigenvector maps were calculated on a pixel-by-pixel basis. Each ON was manually segmented by 2 experienced neuroradiologists blinded to the clinical conditions of the patient, on the basis of the section of the B_0 images where the intraorbital nerve could be clearly seen. To further reduce measurement errors, we manually drew 3 ROIs (each with an area of 2 mm²) at the level of intraorbital ON on the B_0 image. ROIs were then transferred to the corrected FA, ADC, and eigenvector maps (Fig 1). For each ON, mean FA, ADC, principal eigenvalue ($\lambda_{\parallel} = \lambda_1$), and orthogonal eigenvalue [$\lambda_{\perp} = (\lambda_2 + \lambda_3)/2$]¹³ were calculated. The routine orbital MR images of patients with RP were reviewed by 2 experienced neuroradiologists.

Ophthalmologic Examination

The Humphrey Visual Field Analyzer (Carl Zeiss Meditec, Dublin, California) was used to assess the VF, and analysis was performed while pupils were in natural state. Subjects were instructed to keep their eyes open and focus their vision on the central target to the best of their ability. The threshold testing program 30–2 was selected to detect central 30° VF with sighting mark III and background 31.5asb. Results with fixation losses of <20%, false-negatives of <33%, and false-positives of <15% were considered reliable.¹² The test was performed twice, and the more reliable result was used for analysis, to reduce learning effects. The data were only included in the study if reliable data were obtained in repeat tests. The mean deviation of the visual field (MDVF) was obtained for quantitative analysis. The best corrected VA was measured

with the international standard VA chart and was converted to a logarithm of minimum angle of resolution.

Statistical Analysis

Statistical analyses were performed by using SPSS 17.0 (IBM, Armonk, New York). For DTI measurement, differences between patients and controls and differences between right and left eyes were both evaluated by using an independent-samples *t* test and paired *t* test, respectively. Spearman rank correlations were calculated between DTI parameters (FA, ADC, $\lambda//$, and $\lambda\perp$) and visual function (MDVF and VA) in patients with RP. *P* values < .05 were considered statistically significant.

RESULTS

Epidemiologic and pathologic information of all 38 patients and 35 controls are shown in Table 1. The results of orbital MR imaging are shown in Fig 2, and no morphologic and signal-intensity abnormality of the ONs in patients with RP was observed. All DTI measurements from patients and controls are summarized in Table 2. We made the following observations:

1) Mean FA from the right ONs in the patient group was lower than that from homolateral nerves in the control group ($P < .001$), and the mean FA from the left ONs in the patient group was

lower than that from the homolateral nerves in the control group ($P < .001$).

2) Mean ADC from the right ONs in the patient group was higher than that from the homolateral nerves in the control group ($P < .001$), and mean ADC from the left ONs in the patient group was higher than that from the homolateral nerves in the control group ($P < .001$).

3) Mean $\lambda//$ from the right ONs in the patient group was higher than that from the homolateral nerves in the control group ($P = 0.003$), and mean $\lambda//$ from the left ONs in the patient group was higher than that from the homolateral nerves in the control group ($P = .001$).

4) Mean $\lambda\perp$ from the right ONs in the patient group was higher than that from the homolateral nerves in the control group ($P < .001$), and mean $\lambda\perp$ from the left ONs in the patient group was higher than that from the homolateral nerves in the control group ($P < .001$).

5) All DTI parameters (FA, ADC, $\lambda//$, $\lambda\perp$) between the right and left nerves in patients showed no significant differences ($P > .05$).

DTI measurements of both right and left nerves of the patients were compared with those of the controls (Fig 3). Significant correlations between MDVF and mean FA ($r = 0.364$, $P = .001$) and between MDVF and $\lambda\perp$ ($r = -0.254$, $P = .029$) (Fig 4) were observed for patients with RP, but no correlation between MDVF and mean ADC ($P = .154$) or between MDVF and $\lambda//$ ($P = .337$) was seen. Moreover, none of DTI parameters for ONs in RP were correlated with VA ($P > .05$).

Table 1: Epidemiologic and pathologic information of patients with RP and controls

	Patients (n = 38)	Controls (n = 35)	P Value
Sex (male/female)	24:14	22:13	.979
Age (yr) ^a	37 ± 15 (6~62)	36 ± 14 (9~60)	.921
Eyes (N _R /N _L)	76 (38:38)	70 (35:35)	/
MDVF (dB) ^b			
R	-30.26 ± 8.94 (-37.00~-4.68)	-0.69 ± 0.98 (-2.00~1.23)	.000 ^c
L	-29.41 ± 9.73 (-35.68~-3.85)	-0.54 ± 1.15 (-2.71~1.45)	.000 ^c
VA (LogMAR) ^b			
R	0.52 ± 0.70 (0~2)	-0.067 ± 0.08 (-0.2~0.1)	.000 ^c
L	0.52 ± 0.68 (0~2)	-0.065 ± 0.072 (-0.2~0.1)	.000 ^c

Note:—LogMAR indicates logarithm of minimal angle of resolution; N_R, number of right eyes; N_L, number of left eyes; R, right eye; L, left eye; /, not available.

^a Values are mean ± SD (range).

^b Values from patient group are median ± interquartile range (range), and values from control group are mean ± SD (range).

^c Significant difference is noted between patients and controls.

DISCUSSION

In this study, the use of rFOV-DTI for in vivo characterization of ONs in patients with RP has been investigated for the first time. Routine orbital MR imaging showed no morphologic and signal ab-

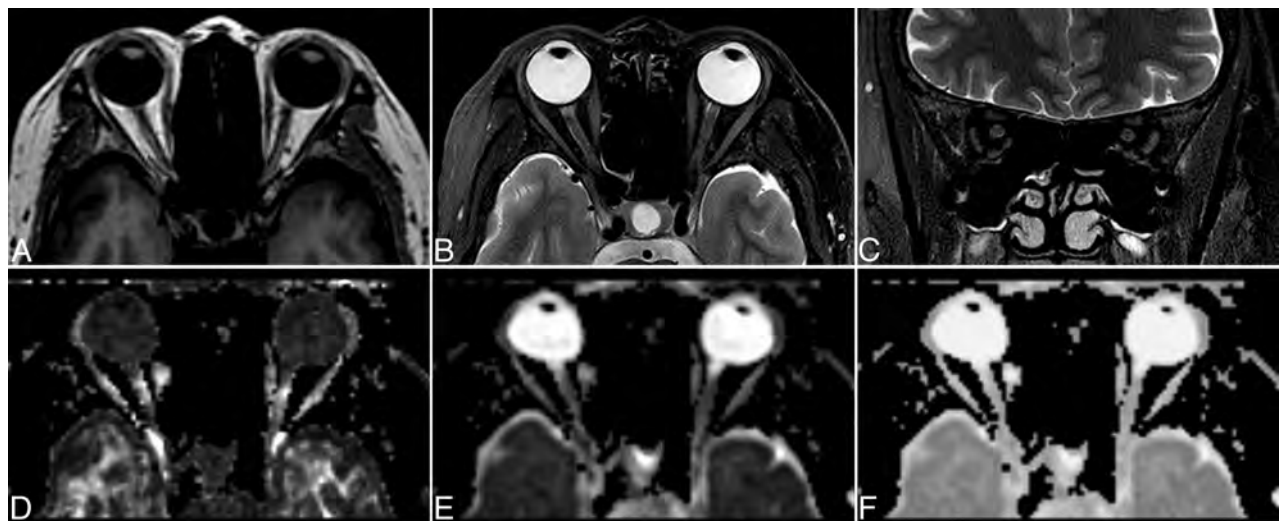


FIG 2. Routine orbital MR imaging of patients with RP together with DTI maps. Axial T1WI (A), axial fat-saturated T2WI (B), coronal fat-saturated T2WI (C), and the corresponding FA (D), ADC (E), and eigenvector maps (F) of DTI in a 48-year-old patient with RP.

Table 2: DTI parameter data^a of patients with RP and controls

	Patients (n = 38)	Controls (n = 35)	t Value	P Value
FA				
R	0.442 ± 0.077	0.572 ± 0.046	-8.840	.000 ^b
L	0.447 ± 0.067	0.581 ± 0.044	-10.083	.000 ^b
ADC (×10 ⁻³ mm ² s ⁻¹)				
R	1.367 ± 0.250	1.099 ± 0.166	5.417	.000 ^b
L	1.343 ± 0.218	1.068 ± 0.122	6.667	.000 ^b
λ// (×10 ⁻³ mm ² s ⁻¹)				
R	5.548 ± 0.288	5.361 ± 0.231	3.030	.003 ^b
L	5.521 ± 0.250	5.333 ± 0.191	3.609	.001 ^b
λ⊥ (×10 ⁻³ mm ² s ⁻¹)				
R	4.526 ± 0.249	4.218 ± 0.146	6.511	.000 ^b
L	4.503 ± 0.213	4.187 ± 0.106	8.041	.000 ^b

Note:—R indicates right eye; L, left eye.

^a Values are mean ± SD.

^b Significant difference between patient nerves and control nerves as determined by using an independent-samples t test.

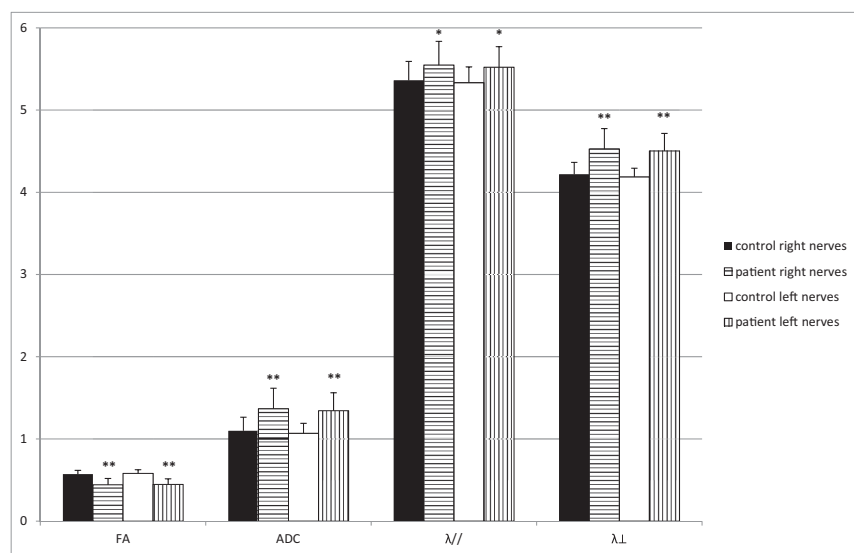


FIG 3. The DTI measures of both right and left ONs of patients are compared with corresponding normal ONs of controls. Bar graphs of mean FA, ADC, principal eigenvalue, and orthogonal eigenvalue averaged across the right and left optic nerves are shown in 38 patients with RP compared with the homolateral optic nerves of 35 controls. The *error bars* denote the SDs across subjects. The units of the ADC, λ//, and λ⊥ measures are in ×10⁻³ mm² per second⁻¹. The *asterisk* indicates a significant difference compared with the homolateral nerves of controls (**P* < .01; ***P* < .001).

normality, whereas DTI measurements showed that mean ADC, λ//, and λ⊥ for ONs in patients with RP were higher than those of controls, and mean FA was lower than that of controls. Hence, rFOV-DTI measurements convey potentially useful information in the diagnosis of optic neuropathy in RP. Furthermore, FA and λ⊥ respectively decreased and increased with the reduced VF.

In vivo DTI of the ON is challenging in practice due to its small dimension, which increases the vulnerability to motion and magnetic susceptibility artifacts. The effect of the hyperintense signal from surrounding orbital fat and CSF is also pronounced.^{7,8,14,15} In our study, rFOV-DTI was achieved with 90° 2D echo-planar radiofrequency excitation followed by a refocusing 180° pulse at 3T. This technique allows multisection imaging, and contiguous sections using this method can be obtained with no section gap as needed in zonal oblique multisection EPI.¹⁶ Also, the SNR does not depend on the number of sections because neighboring sections are not significantly excited by the 2D excitation pulse. Consequently, rFOV 2D excitation, compared with

conventional excitation, is more advantageous in alleviating several problematic issues.^{9,10,16,17} When we compared the measurements of healthy subjects with those obtained by using conventional DTI as reported in past studies, the mean FA and ADC were in agreement (0.587 ± 0.023, 0.928 ± 0.111 × 10⁻³ mm²s⁻¹),^{7,18} whereas discrepancy existed in the mean λ// and λ⊥ (0.874 ± 0.262 × 10⁻³ mm²s⁻¹, 2.088 ± 0.136 × 10⁻³ mm²s⁻¹).^{7,19} As expected, λ// and λ⊥ are subject to larger variance subsequent to different scan protocols and hardware compared with ADC and FA.^{7-9,18,19}

FA measures the level of diffusion anisotropy and has been most widely used to assess the integrity of white matter tracts.⁷ Gradual loss of retinal ganglion cells in patients with RP takes place with the progressive death of photoreceptor cells, governed by the trans-synaptic neuronal degeneration mechanism,²⁰⁻²² and may lead to axonal degeneration, axonal disruption or loss, and demyelination in the ONs of patients with RP. In chronic ON damage in RP, as the integrity of axon and myelin is compromised, ON tissue is no longer tightly packed and the widened interstitial space leads to decreased levels of diffusion anisotropy. This outcome explains the reduced FA for the ON in patients with RP compared with controls. These results were similar to those reported in glaucoma.^{8,23}

VF loss in patients with RP has been attributed to the death of photoreceptors.⁴ With the death of photoreceptor

cells and following loss of retinal ganglion cells, optic neuropathy of RP advances. VF defects may reflect ON damage in RP. The significant correlation of the VF defect with FA reduction in patients with RP suggests that the reduced anisotropy is of functional relevance and may reflect axonal disruption or loss and demyelination. A previous study by Khong et al²⁴ showed that ADC was not as sensitive as FA for the assessment of neural tissue degeneration. This finding may explain ADC values for ONs in RP being higher than those in controls and not correlating with VF in our study. Another study²³ in glaucoma also suggested that FA is more sensitive than ADC in assessing ON damage.

The λ// and λ⊥, as the biomarkers for the integrity of axons and myelin respectively, are commonly used to gather pathologic information of ON disease.^{13,25,26} In this study, both λ// and λ⊥ values for ONs in patients with RP were observed to be higher than those of controls; this finding likely indicates that axon and myelin injury might be linked. Because optic neuropathy in RP is

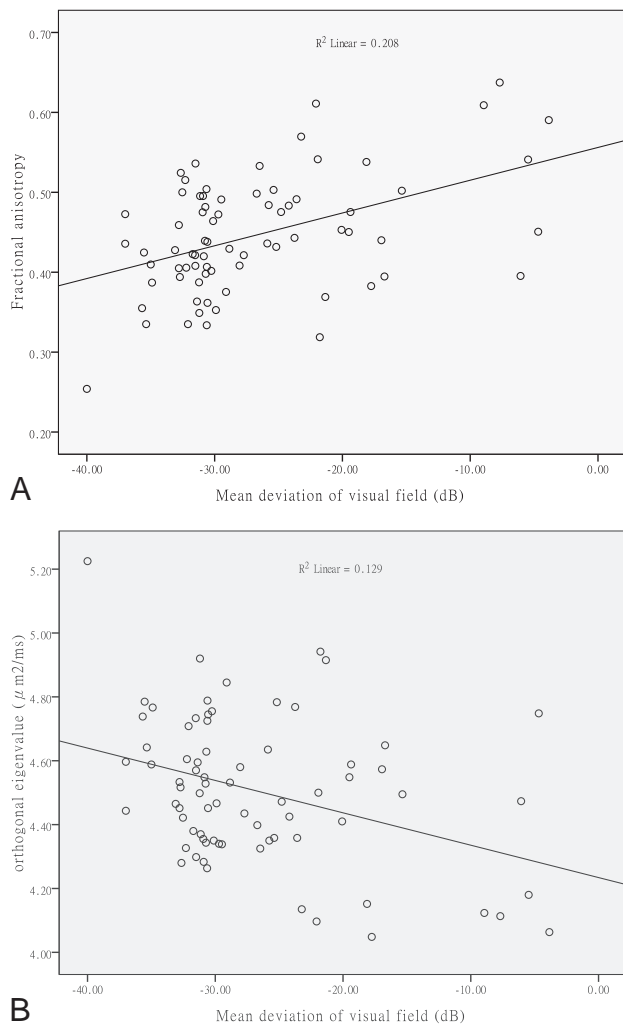


FIG 4. Correlation of DTI data with visual function. Plot of FA and orthogonal eigenvalue versus mean deviation of the visual field, respectively, averaged across the pixels inside the ROIs along the optic nerves of 38 patients with RP (76 affected eyes).

the result of gradual loss of retinal ganglion cells, axonal degeneration in the ON rather than demyelination might be the leading consequence of ON damage in patients with RP. However, our study showed that there was a significant correlation of λ_{\perp} with VF, but no correlation of $\lambda_{//}$ with VF in patients with RP. In general, in patients with RP, there is a delay between pathologic changes and clinically evident symptoms.¹¹ Consequently, patients with RP diagnosed by typical symptoms in our study were likely manifesting a chronic stage of ON damage. A previous study²⁷ revealed that $\lambda_{//}$ becomes less informative as pathologic conditions of the human central nervous system progress from acute to chronic. Hence, changes of $\lambda_{//}$ in patients compared with controls were detected, but no correlation of $\lambda_{//}$ with visual function was seen, which was similar to the observation in our previous study in glaucoma.⁸

A previous study by Ohno et al¹ using DTI showed correlation of FA in the optic radiation with VA but not with VF; in this study, results from rFOV-DTI showed correlation between FA for ONs and VF, but no statistically significant correlation was observed for any other parameters. This might be attributed to the patho-

logic difference between the ON and optic radiation in patients with RP, and further studies are needed to better understand the trans-synaptic degeneration mechanism in RP.

There are several limitations to this study. First, there is a lack of correlation analysis between DTI measurements and the disease time course of RP, which could be an important factor in the damage of ONs. Only the age of onset of symptoms in RP was obtained, which is an imprecise measure of disease severity and gives little or no indication of the time point when photoreceptor degeneration actually began.¹¹ Second, suppression of CSF was not performed, and the hyperintense signal may obscure signal changes of the ON and lead to potential underestimation of diffusion anisotropy measures such as FA.²⁸ However, the consistency of measurements such as FA with those obtained by using acquisitions with both fat and CSF suppression¹⁹ supports the validity of the results. Third, the relatively long scan time (5 minutes 37 seconds) may still limit the clinical use of this technique, given the susceptibility to motion.

CONCLUSIONS

The present study demonstrated that rFOV-DTI measurements of the ON may reflect pathologic conditions in patients with RP and may serve as a biomarker of axonal and myelin damage in the optic neuropathy of RP. The use of rFOV-DTI in optic neuropathy of RP may allow early assessment of the status of the ON in this patient group. The alterations of ON reflected in rFOV-DTI measurements would also be valuable for assessing treatment trials in patients with RP.

ACKNOWLEDGMENTS

We are grateful to the staff at the Center of Translation Medicine, Zhengzhou University People's Hospital (Henan Provincial People's Hospital), for their assistance in this project.

Disclosures: Yanqiu Zhang, Ling Wang, Qin Tian, Dapeng Shi—RELATED: Grant: National Natural Science Foundation of China Grant (No. 81271534).**Money paid to the institution.

REFERENCES

- Ohno N, Murai H, Suzuki Y, et al. **Alteration of the optic radiations using diffusion tensor MRI in patients with retinitis pigmentosa.** *Br J Ophthalmol* 2015;99:1051–54 CrossRef Medline
- Delyfer MN, Lèveillard T, Mohand-Saïd S, et al. **Inherited retinal degenerations: therapeutic prospects.** *Biol Cell* 2004;96:261–69 CrossRef Medline
- RetNet. The Retinal Information Network. <https://sph.uth.edu/Retnet/>. Accessed October 30, 2015
- Walia S, Fishman GA, Edward DP, et al. **Retinal nerve fiber layer defects in RP patients.** *Invest Ophthalmol Vis Sci* 2007;48:4748–52 CrossRef Medline
- Walia S, Fishman GA. **Retinal nerve fiber layer analysis in RP patients using Fourier-domain OCT.** *Invest Ophthalmol Vis Sci* 2008; 49:3525–28 CrossRef Medline
- Eng JG, Agrawal RN, Tozer KR, et al. **Morphometric analysis of optic nerves and retina from an end-stage retinitis pigmentosa patient with an implanted active epiretinal array.** *Invest Ophthalmol Vis Sci* 2011;52:4610–16 CrossRef Medline
- Wang MY, Qi PH, Shi DP. **Diffusion tensor imaging of the optic nerve in subacute anterior ischemic optic neuropathy at 3T.** *AJNR Am J Neuroradiol* 2011;32:1188–94 CrossRef Medline
- Wang MY, Wu K, Xu JM, et al. **Quantitative 3-T diffusion tensor imaging in detecting optic nerve degeneration in patients with**

- glaucoma: association with retinal nerve fiber layer thickness and clinical severity.** *Neuroradiology* 2013;55:493–98 CrossRef Medline
9. Wheeler-Kingshott CA, Trip SA, Symms MR, et al. **In vivo diffusion tensor imaging of the human optic nerve: pilot study in normal controls.** *Magn Reson Med* 2006;56:446–51 CrossRef Medline
 10. Tang L, Wen Y, Zhou Z, et al. **Reduced field-of-view DTI segmentation of cervical spine tissue.** *Magn Reson Imaging* 2013;31:1507–14 CrossRef Medline
 11. Hartong DT, Berson EL, Dryja TP. **Retinitis pigmentosa.** *Lancet* 2006;368:1795–809 CrossRef Medline
 12. Murakami Y, Yoshida N, Ikeda Y, et al. **Relationship between aqueous flare and visual function in retinitis pigmentosa.** *Am J Ophthalmol* 2015;159:958–63.e1 CrossRef Medline
 13. Xu J, Sun SW, Naismith RT, et al. **Assessing optic nerve pathology with diffusion MRI: from mouse to human.** *NMR Biomed* 2008;21:928–40 CrossRef Medline
 14. Wheeler-Kingshott CA, Parker GJ, Symms MR, et al. **ADC mapping of the human optic nerve: increased resolution, coverage, and reliability with CSF-suppressed ZOOM-EPI.** *Magn Reson Med* 2002;47:24–31 CrossRef Medline
 15. Trip SA, Wheeler-Kingshott C, Jones SJ, et al. **Optic nerve diffusion tensor imaging in optic neuritis.** *Neuroimage* 2006;30:498–505 CrossRef Medline
 16. Saritas EU, Cunningham CH, Lee JH, et al. **DWI of the spinal cord with reduced FOV single-shot EPI.** *Magn Reson Med* 2008;60:468–73 CrossRef Medline
 17. Attenberger UI, Rathmann N, Sertdemir M, et al. **Small field-of-view single-shot EPI-DWI of the prostate: evaluation of spatially-tailored two-dimensional radiofrequency excitation pulses.** *Z Med Phys* 2015 Aug 20. [Epub ahead of print] CrossRef Medline
 18. Hickman SJ, Wheeler-Kingshott CA, Jones SJ, et al. **Optic nerve diffusion measurement from diffusion-weighted imaging in optic neuritis.** *AJNR Am J Neuroradiol* 2005;26:951–56 Medline
 19. Techavipoo U, Okai AF, Lackey, et al. **Toward a practical protocol for human optic nerve DTI with EPI geometric distortion correction.** *J Magn Reson Imaging* 2009;30:699–707 CrossRef Medline
 20. Gartner S, Henkind P. **Pathology of retinitis pigmentosa.** *Ophthalmology* 1982;89:1425–32 CrossRef Medline
 21. Stone JL, Barlow WE, Humayun MS, et al. **Morphometric analysis of macular photoreceptors and ganglion cells in retinas with retinitis pigmentosa.** *Arch Ophthalmol* 1992;110:1634–39 CrossRef Medline
 22. Humayun MS, Prince M, de Juan E Jr. **Morphometric analysis of the extramacular retina from postmortem eyes with retinitis pigmentosa.** *Invest Ophthalmol Vis Sci* 1999;40:143–48 Medline
 23. Garaci FG, Bolacchi F, Cerulli A, et al. **Optic nerve and optic radiation neurodegeneration in patients with glaucoma: in vivo analysis with 3-T diffusion-tensor MR imaging.** *Radiology* 2009;252:496–501 CrossRef Medline
 24. Khong PL, Zhou LJ, Ooi GC, et al. **The evaluation of Wallerian degeneration in chronic paediatric middle cerebral artery infarction using diffusion tensor MR imaging.** *Cerebrovasc Dis* 2004;18:240–47 CrossRef Medline
 25. Song SK, Sun SW, Ju WK, et al. **Diffusion tensor imaging detects and differentiates axon and myelin degeneration in mouse optic nerve after retinal ischemia.** *Neuroimage* 2003;20:1714–22 CrossRef Medline
 26. Michielse S, Coupland N, Camicioli R, et al. **Selective effects of aging on brain white matter microstructure: a diffusion tensor imaging tractography study.** *Neuroimage* 2010;52:1190–201 CrossRef Medline
 27. Naismith RT, Xu J, Tutlam NT, et al. **Disability in optic neuritis correlates with diffusion tensor-derived directional diffusivities.** *Neurology* 2009;72:589–94 CrossRef Medline
 28. Bhagat YA, Beaulieu C. **Diffusion anisotropy in subcortical white matter and cortical gray matter: changes with aging and the role of CSF-suppression.** *J Magn Reson Imaging* 2004;20:216–27 CrossRef Medline

A New Ultrasound Marker for Bedside Monitoring of Preterm Brain Growth

J.A. Roelants, I.V. Koning, M.M.A. Raets, S.P. Willemsen, M.H. Lequin, R.P.M. Steegers-Theunissen, I.K.M. Reiss, M.J. Vermeulen, P. Govaert, and J. Dudink

ABSTRACT

BACKGROUND AND PURPOSE: Preterm neonates are at risk for neurodevelopmental impairment, but reliable, bedside-available markers to monitor preterm brain growth during hospital stay are still lacking. The aim of this study was to assess the feasibility of corpus callosum–fastigium length as a new cranial sonography marker for monitoring of preterm brain growth.

MATERIALS AND METHODS: In this longitudinal prospective cohort study, cranial ultrasound was planned on the day of birth, days 1, 2, 3, and 7 of life; and then weekly until discharge in preterm infants born before 29 weeks of gestational age. Reproducibility and associations between clinical variables and corpus callosum–fastigium growth trajectories were studied.

RESULTS: A series of 1–8 cranial ultrasounds was performed in 140 infants (median gestational age at birth, 27⁺² weeks (interquartile range, 26⁺¹ to 28⁺¹; 57.9% male infants). Corpus callosum–fastigium measurements showed good-to-excellent agreement for inter- and intraobserver reproducibility (intraclass correlation coefficient >0.89). Growth charts for preterm infants between 24 and 32 weeks of gestation were developed. Male sex and birth weight SD score were positively associated with corpus callosum–fastigium growth rate.

CONCLUSIONS: Corpus callosum–fastigium length measurement is a new reproducible marker applicable for bedside monitoring of preterm brain growth during neonatal intensive care stay.

ABBREVIATIONS: BW = birth weight; CC = corpus callosum; CCF = corpus callosum–fastigium; CUS = cranial ultrasound; GA = gestational age; HELLP = hemolysis, elevated liver enzymes, low platelet count; NICU = neonatal intensive care unit

Brain growth is an important predictor of neurodevelopmental outcome in preterm infants.^{1–4} In neonatal intensive care units (NICUs), brain growth is usually monitored by manual measurement of head circumference. However, head circumference measurement has a low interrater agreement and does not correspond well with actual brain development.^{5,6} Therefore, there is a need for a new reliable bedside marker for monitoring preterm brain growth in clinical practice.

Brain structures measured by cranial ultrasound (CUS) could provide clinically applicable markers for brain growth. A few sonographic markers of brain growth have been used in the past, mainly measuring the corpus callosum (CC) or cerebellum, thereby reflecting growth of a small part of the brain only.^{7–11} In addition to currently available markers of preterm brain development, we propose that the length between the genu of the CC and the fastigium (roof of the fourth ventricle) could serve as a new marker for brain growth.

The aim of this study was to evaluate the usefulness of corpus callosum–fastigium (CCF) length and CC length, an existing marker, as markers for monitoring brain growth in preterm infants during the NICU stay. We assessed the reproducibility of CC and CCF length measurements, developed growth charts for preterm infants between 24 and 32 weeks of gestation, and evaluated prenatal and postnatal characteristics possibly associated with CC and CCF growth trajectories. We hypothesized that both measurements are highly reproducible. Furthermore, we hypothesized that CCF and CC growth trajectories are associated with prenatal and postnatal determinants of neurodevelopmental outcome in preterm infants.

Received October 15, 2015; accepted after revision January 5, 2016.

From the Division of Neonatology (J.A.R., M.M.A.R., I.K.M.R., M.J.V., P.G., J.D.), Department of Radiology (J.D.), and Intensive Care Unit (J.D.), Erasmus MC–Sophia Children's Hospital, Rotterdam, the Netherlands; Departments of Obstetrics and Gynecology (J.A.R., I.V.K., S.P.W., R.P.M.S.-T.) and Biostatistics (S.P.W.), Erasmus MC, University Medical Center, Rotterdam, the Netherlands; and Department of Radiology (M.H.L.), University Medical Center Utrecht, Utrecht, the Netherlands.

The authors report no conflict of interest.

Paper previously presented in part at: First Congress of the Joint European Neonatal Societies, September 16–20, 2015; Budapest, Hungary.

Please address correspondence to Jeroen Dudink, MD, PhD, Department of Pediatrics, Division of Neonatology, Erasmus MC–Sophia Children's Hospital, Wytemaweg 80, 3015 CN, Rotterdam, the Netherlands; e-mail: j.dudink@erasmusmc.nl

<http://dx.doi.org/10.3174/ajnr.A4731>

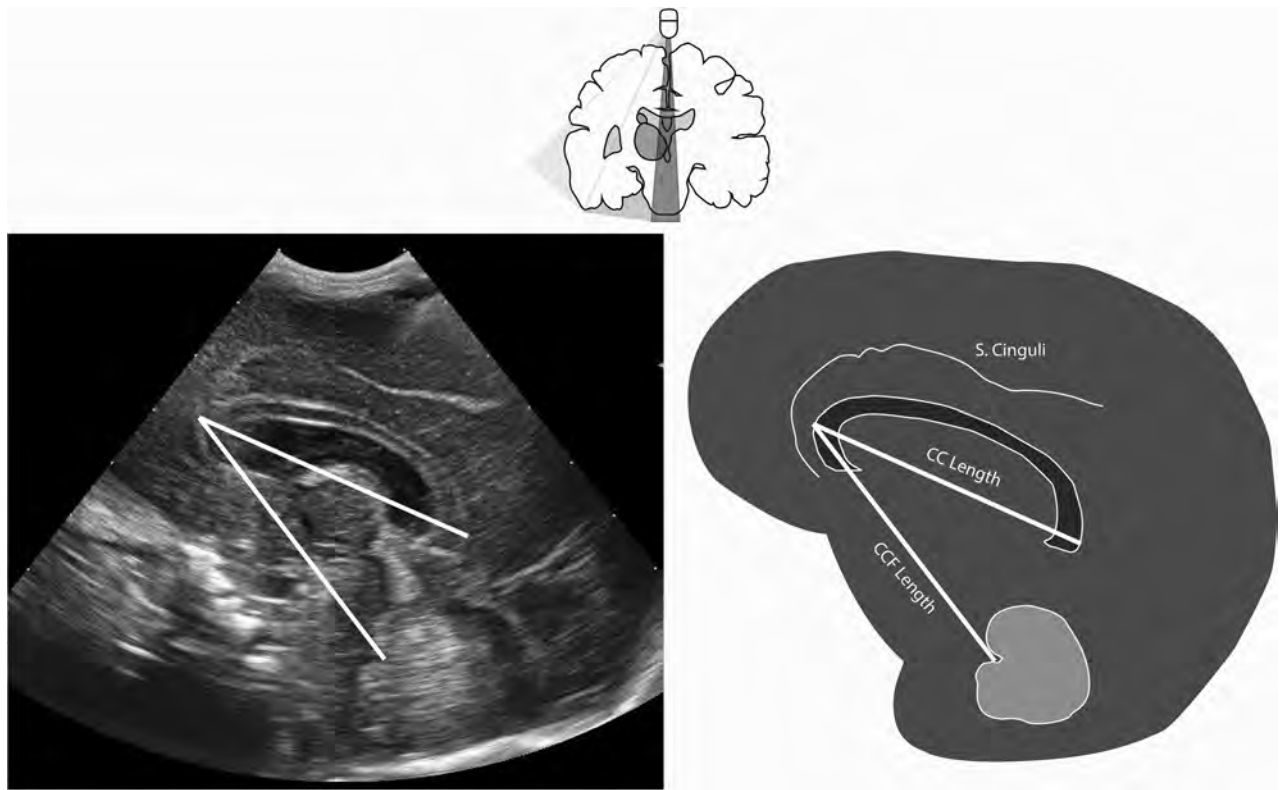


FIG 1. In the upper part, we show the coronal view of the brain and the position of the sonography probe for assessment of the corresponding correct sagittal plane below. Measurements of the corpus callosum–fastigium and corpus callosum length are displayed in the sagittal sonography view (*left*) and schematically (*right*). S. Cinguli indicates sulcus cinguli.

MATERIALS AND METHODS

This prospective observational cohort study was performed at the level III NICU of the Sophia Children’s Hospital, Erasmus MC, Rotterdam, the Netherlands. The local medical ethics review board approved this study. Written parental consent was obtained before participation. Between 2010 and 2012, all newly admitted singleton, preterm infants born before 29 weeks’ gestational age (GA) were eligible for enrollment. We applied the following exclusion criteria: 1) unknown GA at birth; 2) major congenital abnormalities, and 3) extensive brain injury (including intraventricular hemorrhage grade III, posthemorrhagic ventricular dilation, and venous infarction). The latter complications are expected to influence the validity of the measurements due to possible midline shift and expected altered brain growth. GA at birth was dated by using the first day of the last menstrual period and was confirmed by first trimester crown rump length measurement on sonography. Postnatal age was expressed by postmenstrual age, calculated as GA at birth + weeks and days of postnatal age. Pregnancy and neonatal characteristics were collected prospectively. Maternal characteristics were collected retrospectively from medical records. Pregnancy complications, including intrauterine growth retardation and pre-eclampsia and hemolysis, elevated liver enzymes, low platelet count (HELLP) syndrome were obtained from obstetric records and were defined on the basis of clinical definitions according to national guidelines.¹²

Cranial Sonography and Measurements

CUS was performed according to the standard local protocol on the day of birth; on days 1, 2, 3, and 7 of life; and then weekly until

discharge. The protocol was only disregarded on clinical grounds (eg, hemodynamic instability). One researcher (M.M.A.R.) performed all CUS by using a MyLab 70 scanner (Esaote, Genoa, Italy), with a convex neonatal probe (7.5 MHz). Measurements were performed off-line by using the Mylab software (Esaote). Measurements of CC and CCF length were performed on a standard sagittal plane. In this plane, a complete corpus callosum (genu to the splenium) and distinct vermis of the cerebellum, including the fastigium, had to be visualized. CCF length was measured from the genu of the corpus callosum (outer border) to the fastigium. CC length was measured from outer to outer border (genu to the splenium, Fig 1). All measurements were performed by 1 investigator (M.M.A.R.). To establish the reliability, a second investigator (J.A.R.), blinded to the previous results, measured 30 randomly selected scans of varying quality and of neonates with different GAs.

Statistical Methods

Data were analyzed by using SPSS (Release 21 for Windows; IBM, Armonk, New York) and R statistical and computing software (<http://www.r-project.org/>). *P* values < .05 were statistically significant. Median value and interquartile range and means and SDs were used as appropriate.

Intraobserver and interobserver agreements for CC and CCF lengths were evaluated by using the intraclass correlation coefficient and Bland-Altman plots.¹³ The intraclass correlation coefficient was analyzed by using a 2-way mixed model. Cutoff values were in accordance with Landis and Koch.¹⁴ Growth charts were developed for CCF and CC growth as a function of postmenstrual

Table 1: Baseline characteristics^a

	N = 140	Missing ^b
Maternal characteristics		
Age (yr) (mean) (SD)	30 (5.6)	0
Ethnicity ^c		0
Dutch	74 (52.9%)	
Other Western	9 (6.4%)	
Non-Western	57 (40.7%)	
Maternal smoking during pregnancy	26 (18.6%)	17
IVF/ICSI	9 (6.4%)	0
IUGR	42 (30%)	4
PE/HELLP syndrome	37 (26.4%)	0
Chorioamnionitis	37 (26.4%)	0
PPROM	32 (22.9%)	0
Neonatal characteristics		
GA at birth (wk ⁺ days ^s)	27 ⁺² (26 ⁺¹ –28 ⁺¹)	0
Male sex	81 (57.9%)	0
BW (g)	955 (780–1125)	0
Use of antenatal steroids	127 (90.7%)	2
Apgar score at fifth minute	8 (7–9)	0
CRIB score	3 (1–6)	1
Death	17 (12.1%)	0
Days on mechanical ventilation	5 (1–14)	3
Days to regain birth weight	9 (7–12)	14
Sepsis	67 (47.9%)	0
IVH grade I or II	32 (22.9%)	0
Severe BPD	15 (10.7%)	33

Note:—IVF/ICSI indicates in vitro fertilization with or without intracytoplasmic sperm injection; IUGR, intrauterine growth retardation; PE, pre-eclampsia; PPRM, prolonged premature rupture of membranes; CRIB, clinical risk index for babies; IVH, intraventricular hemorrhage; BPD, bronchopulmonary disease.

^aBaseline data of maternal and neonatal characteristics are presented as median (interquartile range) or No. (%) unless otherwise specified.

^bMissing data were mainly due to early transfer to a secondary hospital.

^cEthnicity was reported to provide insight in the generalizability of the study population.

age (weeks) and weight (grams). To model the relation between the measured CCF and CC lengths and a predefined list of covariates, we estimated linear mixed models by using lme (in the R nlme package; <http://www.inside-r.org/r-doc/nlme/lme>).¹⁵ To account for the within-subject correlation, we used a random intercept and random coefficient of GA and a power variance function to model the residual covariance. The predefined covariates were GA at birth, birth weight (BW) SD score, sex, intrauterine growth retardation (defined as estimated fetal weight below 10th percentile), pre-eclampsia/HELLP, chorioamnionitis, death, sepsis, and days on mechanical ventilation. In all models, both GA and GA² (square of GA) were used as covariates. The additional predictors were added to this basic model separately (termed “univariable models” below) and all at once (the multivariable model).

RESULTS

Of 336 neonates admitted to our NICU during the study period, 152 were eligible for inclusion. Twelve neonates were excluded because they met the exclusion criterion of extensive brain injury, resulting in a sample size of 140 neonates. Baseline maternal and neonatal characteristics are listed in Table 1. The median gestational age at birth was 27⁺² weeks (interquartile range, 26⁺¹–28⁺¹); the median birth weight was 955 g (interquartile range, 780–1125 g). The number of sonography scans per neonate ranged from 1 to 8.

Reproducibility

The mean interobserver difference was -0.3207 ± 1.4527 mm for CCF ($P = .244$) and 0.4600 ± 1.8463 mm for CC length ($P = .183$).

The ICCs for interobserver and intraobserver analysis showed excellent agreement for both CCF and CC length (respectively, intraobserver: 0.958; 95% CI, 0.912–0.980; interobserver: 0.885; 95% CI, 0.770–0.944; and intraobserver: 0.922; 95% CI, 0.844–0.962; and interobserver: 0.893; 95% CI, 0.783–0.948). Figure 2 shows Bland-Altman plots of interobserver and intraobserver agreement for both measurements.

CC and CCF Length

The mean CCF length was 40.9 ± 2.97 mm, with a range from 34.0 to 54.3 mm. The mean CC length was 36.3 ± 3.33 mm, with a range from 26.6 to 48.8 mm. Growth charts of CCF and CC lengths by postmenstrual age and by weight are shown in Fig 3.

Linear Mixed Models

Results of univariable analyses are shown in Table 2 for CC and CCF growth. The multivariable analysis confirmed a positive association between the BW SD score and the CCF growth rate and a negative association between female sex and the CCF growth rate. For the CC growth rate, a positive association was found with the BW SD score by using multivariable analysis.

DISCUSSION

In this report, we demonstrated that CCF length, measured by using CUS, is a reproducible and feasible marker that could serve as a new bedside tool to monitor preterm infant brain growth during the NICU stay. We provided growth charts of CCF and CC length for preterm infants from 24 to 32 weeks' postmenstrual age. We found that a higher BW SD score results in an increased CCF and CC growth rate during the hospital stay, while female infants have a slower CCF growth compared with male infants.

Previous sonography studies have evaluated only a limited number of brain structures as potential markers for brain growth or predictors for neurodevelopmental outcome in preterm infants.^{7–10} One explanation for this is that the brain has few easily recognizable and consistent landmarks for reliable measurements on CUS. The CC, a flat bundle of white matter that connects the left and right hemispheres, is one of the brain structures that is easily visualized and recognizable on CUS.¹⁶ Prematurity is known to affect CC development, by the early transition from intrauterine to extrauterine life and by postnatal stress and injury,¹⁷ leading to both structural and functional impairment.^{18,19} Associations have been found between the length and thickness of the CC and brain volumes and neurodevelopmental outcome.^{11,20,21} Further studies should elucidate whether CC length can be considered a proxy of telencephalon development, creating an impression of white matter development and brain maturation.

The advantages of using CCF length in the monitoring of brain growth rely on anatomic and practical issues. CCF length may be considered a marker of diencephalon and mesencephalon development and vermis growth. The diencephalon includes the thalamus, a neural relay center crucial for adequate cogni-

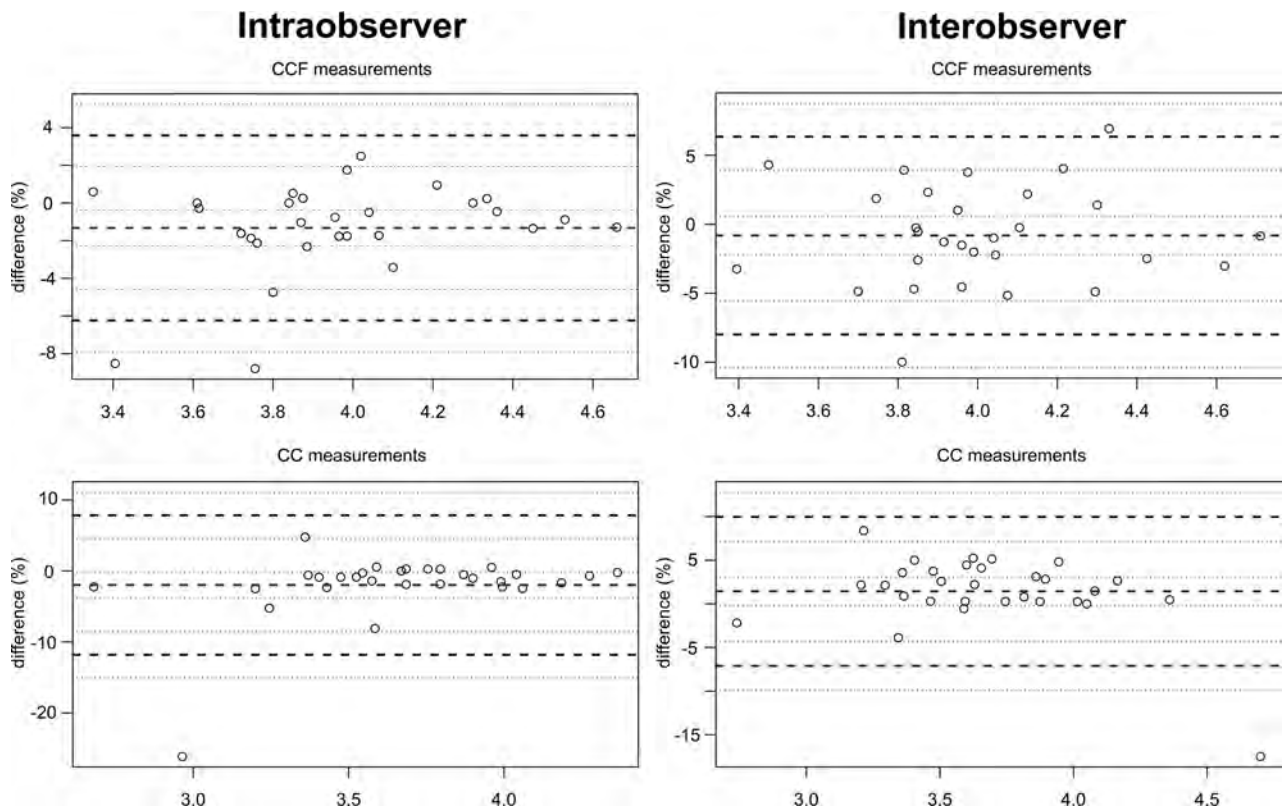


FIG 2. Reproducibility of corpus callosum–fastigium and corpus callosum lengths by using Bland-Altman plots. The middle dashed lines depict the average measurement bias in percentage differences. The bold dashed horizontal lines represent the 95% limits of agreement for these percentage differences.

tive function.²² Altered development of the thalamus, and thus of the diencephalon, may lead to adverse neurodevelopmental outcome. Several studies showed impaired thalamus volume and extreme vulnerability of the thalamus to be neonatal risk factors after preterm birth.^{23,24} Whether thalamic injury or growth impairment directly influences CCF length needs to be further studied.

One of the other advantages of CCF length measurement is the use of CUS instead of MR imaging or head circumference measurements. In Table 3, the pros and cons of every method are depicted. Although volumetric MR imaging is increasingly used for growth assessment of the preterm brain, its use for serial assessment is still very limited.² Head circumference measurement has a low interrater agreement and limited association with long-term outcome and does not measure actual brain growth, but growth of the skull and the subarachnoid spaces, which are frequently enlarged in preterm infants.^{5,6,25} Measurement of CCF length is not considered a burden compared with head circumference measurement because it can be performed on routine CUS, which is often recommended weekly in preterm infants.²⁶ Both CCF length and CC length can already be measured prenatally because the CC and the fastigium are visible on sonography at around 18 weeks of gestation; this feature allows the use of the same marker prenatally and postnatally for monitoring of brain growth.²⁷

In accordance with previous studies, we showed satisfactory reproducibility for CC length.⁷ CCF reproducibility was excellent too; this finding suggests that both measurements are feasible for

longitudinal evaluation of brain growth. Increasing lengths with increasing ages and weights, as shown in the growth charts, support the use of these markers in clinical practice.

We observed a nonlinear growth pattern for CC and CCF length. Previous studies found an intrauterine constant growth rate of 0.20–0.22 mm/day of the CC.^{28,29} Also in preterm infants, a constant-though-slower growth rate was observed.⁷ In contrast to previous studies, we performed longitudinal measurements (1–8 scans per infant), allowing a more reliable estimation of CC growth. Other brain structures, such as the vermis of the cerebellum, show a nonlinear growth pattern as well.⁸ Because we are the first to evaluate the use of CCF length, no literature is available for comparison, to our knowledge. We did expect a nonlinear growth pattern based on current literature.

In Fig 3, parts of the weight charts are gray because we advise not using these parts as a reference curve. We chose to analyze and present the complete original data of infants with a postmenstrual age between 24 and 32 weeks and not to select ideal reference cases. The drawback is seen in the upper part of the weight charts; the curves appear to go down above 1400 g and, despite the very small numbers, the confidence interval narrows. This finding, of course, does not reflect an incline of brain size, but rather selection and censoring. These data are not “first measurements” (reflecting intrauterine accomplished growth) but are follow-up data of patients with prolonged NICU admission, representing the most complex cases (eg, with severe chronic lung disease) not stable enough to be discharged early. In conclusion, the last part of this curve depicts valid data that you would expect in a NICU

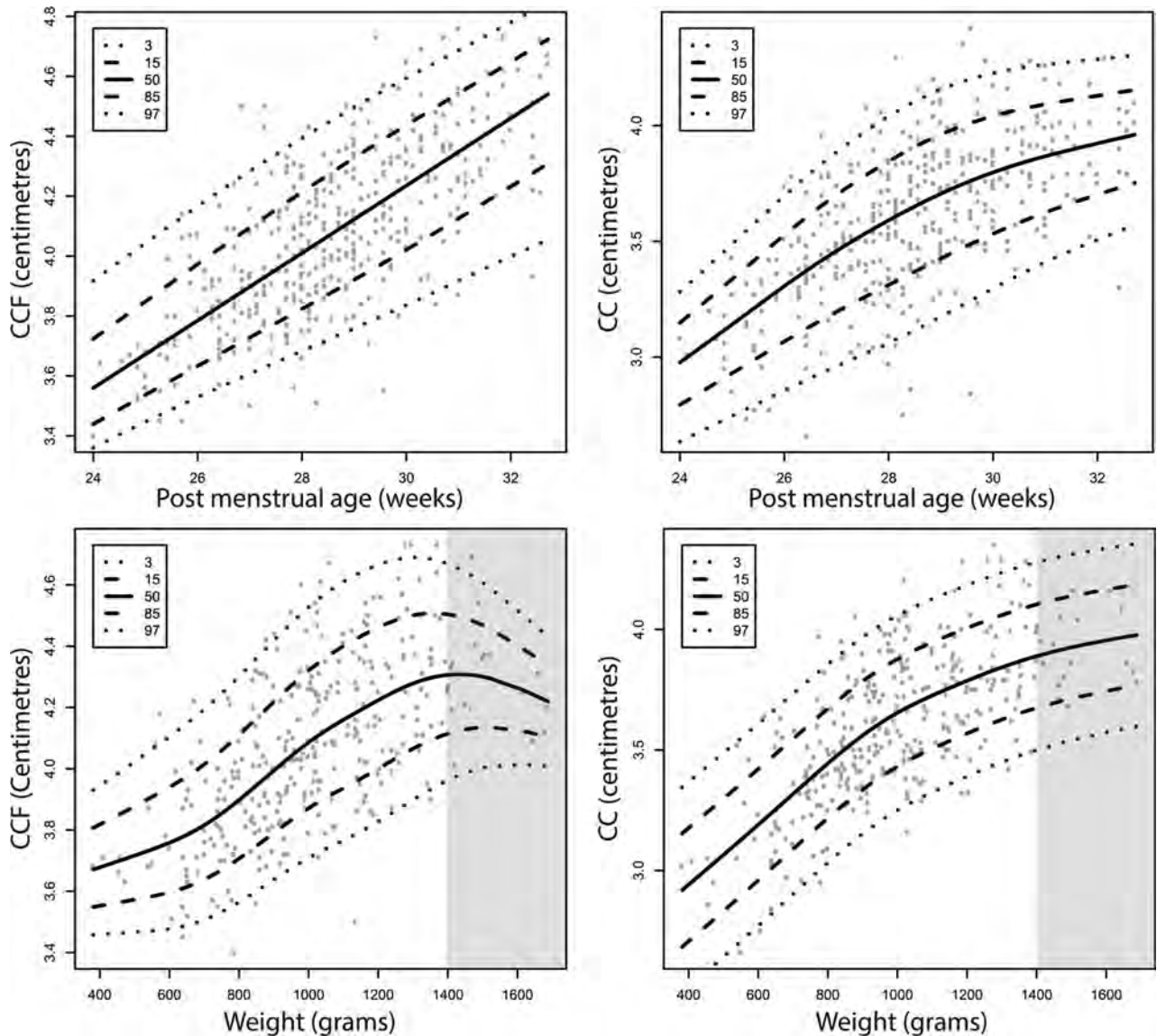


FIG 3. Growth charts of corpus callosum–fastigium (*left*) and corpus callosum (*right*) length for preterm neonates as a function of postmenstrual age (in days) and weight (in grams). On the y-axis, CCF (*left*) and CC (*right*) lengths are presented in centimeters. The gray areas indicate the parts of the weight charts that should not be used as reference curves.

Table 2: Linear mixed models^a

	CCF Growth						CC Growth					
	Univariable			Multivariable			Univariable			Multivariable		
	β	SE	P	β	SE	P	β	SE	P	β	SE	P
GA at birth	0.029	0.012	.022 ^b	0.011	0.017	.518	0.024	0.017	.146	0.004	0.021	.857
BW SDS	0.053	0.009	<.0001 ^b	0.050	0.014	<.001 ^b	0.094	0.011	<.001 ^b	0.075	0.017	<.001 ^b
Sex (female)	-0.109	0.030	<.001 ^b	-0.070	0.029	.018 ^b	-0.066	0.043	.124	-0.003	0.035	.938
IUGR (no)	0.094	0.033	.005 ^b	-0.034	0.045	.451	0.267	0.041	<.001 ^b	0.046	0.054	.390
PE/HELLP (yes)	-0.064	0.035	.068	0.000	0.038	.992	-0.200	0.045	<.001 ^b	-0.052	0.046	.260
Chorioamnionitis (yes)	0.030	0.035	.397	0.031	0.035	.370	0.136	0.047	.004 ^b	0.069	0.042	.106
Death (yes)	-0.103	0.048	.033 ^b	-0.061	0.046	.186	-0.200	0.064	.002 ^b	-0.105	0.054	.057
Sepsis (yes)	-0.034	0.031	.272	-0.021	0.029	.477	-0.050	0.042	.239	-0.043	0.035	.218
Days on mechanical ventilation	-0.001	0.002	.432	0.002	0.002	.340	-0.003	0.002	.160	0.002	0.002	.397

Note:—SDS indicates SD score; SE, standard error; IUGR, intrauterine growth retardation; PE, pre-eclampsia.

^a The effect estimates of maternal and neonatal characteristics on CCF and CC growth in both univariable and multivariable linear mixed models are shown. The effect estimates (β), standard errors, and P values are given.

^b Significant.

Table 3: Pros and cons of different methods for assessment of brain growth

	HC	CUS	MRI
Patient friendly	++	++	—
Bedside available	++	++	—
Serial measurement possible	++	++	—
Fast measurement	++	+	—
Reproducible	±	+	++
Reflecting actual brain growth	—	+	++
Low costs	++	+	—
Dimension	1D	2D	3D

Note:—++ indicates very good; +, acceptable; —, bad agreement with the corresponding item; ±, mediocre; HC, head circumference.

population, but we consider these not representative of normal growth in preterm infants.

The decreased growth rate of the CCF length in female infants is in accordance with previous studies, which identified sex differences in brain structures and neurodevelopmental outcome.^{30,31} The positive association between BW SD score and CCF and CC growth rate is also in accordance with current literature.³²

One investigator who was trained in visualizing a standard sagittal plane performed all the scans. This likely improved the quality of the scans and may have enhanced the reproducibility. We realize, therefore, that the clinical applicability is probably overestimated in our cohort. Reliable measurements and a correct sagittal plane by using CUS depend on the experience of the observer but are easy to learn. Recently developed software to identify the sagittal plane automatically may further increase the reproducibility and clinical applicability.³³

This study has some limitations. First, in the Netherlands, preterm neonates are transferred to a secondary hospital relatively early, accounting for very little data in our cohort of infants born at 29 weeks' gestation and limited data of infants after 30 weeks' gestation. Although white matter injury is already visible on scans after a few days, brain atrophy is often only noticeable after weeks to months.³⁴ Our short follow-up time could explain why we did not find an association between expected clinical variables, such as sepsis and days on mechanical ventilation, and CCF or CC growth rate. Second, including all scans between 24 and 32 weeks' postmenstrual age may have influenced the reliability of the growth charts; that preterm infants lose weight after birth and start to grow days later is a common finding. Brain growth may be limited before regaining birth weight (usually after 10 days). This limitation may have increased variation in CC and CCF lengths. Extremely preterm and clinically unstable infants have longer NICU stays and are likely to undergo more CUS. This feature might have biased our growth charts. On the other hand, our data reflect clinical practice in a neonatal intensive care setting.

In future studies, it would be interesting to compare fetal and preterm CCF growth. Currently, we are scanning fetuses in the second and third trimesters of pregnancy to develop reference curves for fetal brain growth, which could also serve as an ideal growth curve for preterm neonates. We were not yet able to assess the association between feeding regimens and growth during the NICU stay and CCF growth trajectories. This is of interest because it may have clinical implications for nutritional practices. Moreover, CCF length can possibly be used as an outcome measure in nutritional and other intervention studies. It would be of main

interest to assess whether CCF length, possibly combined with other available markers of brain growth such as CC length, could serve as a predictor of neurodevelopmental outcome. The clinical applicability may extend beyond the NICU stay into the outpatient follow-up period because the anterior fontanelle can be used as an acoustic window until approximately 6 months in most infants.

CONCLUSIONS

There is a lack of bedside markers for brain growth in preterm infants during the NICU stay. We propose a feasible, new sonography measurement called "corpus callosum–fastigium length" with high reproducibility for monitoring brain growth in preterm infants during the hospital stay. This marker may help clinicians determine whether preterm infants show adequate postnatal brain growth and may eventually be used as an outcome measure in nutritional and other intervention studies. Further research is warranted to assess whether this marker could also serve as an early predictor for short-term and long-term neurodevelopmental outcome.

REFERENCES

1. Young JM, Powell TL, Morgan BR, et al. **Deep grey matter growth predicts neurodevelopmental outcomes in very preterm children.** *Neuroimage* 2015;111:360–68 CrossRef Medline
2. Lee W, Al-Dossary H, Raybaud C, et al. **Longitudinal cerebellar growth following very preterm birth.** *J Magn Reson Imaging* 2015 Nov 23. [Epub ahead of print] CrossRef Medline
3. Stiles J, Jernigan TL. **The basics of brain development.** *Neuropsychol Rev* 2010;20:327–48 CrossRef Medline
4. Park HW, Yoon HK, Han SB, et al. **Brain MRI measurements at a term-equivalent age and their relationship to neurodevelopmental outcomes.** *AJNR Am J Neuroradiol* 2014;35:599–603 CrossRef Medline
5. Kan E, Roberts G, Anderson PJ, et al; Victorian Infant Collaborative Study Group. **The association of growth impairment with neurodevelopmental outcome at eight years of age in very preterm children.** *Early Hum Dev* 2008;84:409–16 CrossRef Medline
6. Sutter K, Engstrom JL, Johnson TS, et al. **Reliability of head circumference measurements in preterm infants.** *Pediatr Nurs* 1997;23:485–90 Medline
7. Anderson NG, Laurent I, Cook N, et al. **Growth rate of corpus callosum in very premature infants.** *AJNR Am J Neuroradiol* 2005;26:2685–90 Medline
8. Imamoglu EY, Gursoy T, Ovali F, et al. **Nomograms of cerebellar vermis height and transverse cerebellar diameter in appropriate-for-gestational-age neonates.** *Early Hum Dev* 2013;89:919–23 CrossRef Medline
9. Hagmann CF, Robertson NJ, Acolet D, et al. **Cerebral measurements made using cranial ultrasound in term Ugandan newborns.** *Early Hum Dev* 2011;87:341–47 CrossRef Medline
10. Maunu J, Parkkola R, Rikalainen H, et al; PIPARI Group. **Brain and ventricles in very low birth weight infants at term: a comparison among head circumference, ultrasound, and magnetic resonance imaging.** *Pediatrics* 2009;123:617–26 CrossRef Medline
11. Rademaker KJ, Lam JN, Van Haastert IC, et al. **Larger corpus callosum size with better motor performance in prematurely born children.** *Semin Perinatol* 2004;28:279–87 CrossRef Medline
12. NVOG (Dutch Society of Obstetrics and Gynaecology). www.nvog.nl. Accessed September 7, 2015
13. Bland JM, Altman DG. **Statistical methods for assessing agreement between two methods of clinical measurement.** *Lancet* 1986;1:307–10 Medline

14. Landis JR, Koch GG. **The measurement of observer agreement for categorical data.** *Biometrics* 1977;33:159–74 CrossRef Medline
15. Pinheiro JC, Bates DM. *Mixed Effect Models in S and S-Plus.* New York: Springer-Verlag; 2000
16. Aboitiz F, Scheibel AB, Fisher RS, et al. **Fiber composition of the human corpus callosum.** *Brain Res* 1992;598:143–53 CrossRef Medline
17. Shim SY, Jeong HJ, Son DW, et al. **Altered microstructure of white matter except the corpus callosum is independent of prematurity.** *Neonatology* 2012;102:309–15 CrossRef Medline
18. Grunewaldt KH, Fjortoft T, Bjuland KJ, et al. **Follow-up at age 10 years in ELBW children: functional outcome, brain morphology and results from motor assessments in infancy.** *Early Hum Dev* 2014;90:571–78 CrossRef Medline
19. Shim SY, Jeong HJ, Son DW, et al. **Serial diffusion tensor images during infancy and their relationship to neuromotor outcomes in preterm infants.** *Neonatology* 2014;106:348–54 CrossRef Medline
20. Andronikou S, Ackermann C, Laughton B, et al. **Corpus callosum thickness on mid-sagittal MRI as a marker of brain volume: a pilot study in children with HIV-related brain disease and controls.** *Pediatr Radiol* 2015;45:1016–25 CrossRef Medline
21. Liu F, Cao S, Liu J, et al. **Ultrasound measurement of the corpus callosum and neural development of premature infants.** *Neural Regen Res* 2013;8:2432–40 Medline
22. Eaton-Rosen Z, Melbourne A, Orasanu E, et al. **Longitudinal measurement of the developing thalamus in the preterm brain using multi-modal MRI.** *Med Image Comput Comput Assist Interv* 2014; 17(pt 2):276–83 Medline
23. Keunen K, Kersbergen KJ, Groenendaal F, et al. **Brain tissue volumes in preterm infants: prematurity, perinatal risk factors and neurodevelopmental outcome: a systematic review.** *J Matern Fetal Neonatal Med* 2012;25(suppl 1):89–100 CrossRef Medline
24. Rose J, Vassar R, Cahill-Rowley K, et al. **Neonatal physiological correlates of near-term brain development on MRI and DTI in very-low-birth-weight preterm infants.** *Neuroimage Clin* 2014;5:169–77 CrossRef Medline
25. Armstrong DL, Bagnall C, Harding JE, et al. **Measurement of the subarachnoid space by ultrasound in preterm infants.** *Arch Dis Child Fetal Neonatal Ed* 2002;86:F124–26 CrossRef Medline
26. Govaert P, De Vries LS. *An Atlas of Neonatal Brain Sonography.* 2nd ed. London: Mac Keith; 2010
27. Tepper R, Kidron D, Hershkovitz R. **Sonographic measurements of the fetal fastigium between 20 and 40 weeks' gestation.** *J Ultrasound Med* 2009;28:1657–61 Medline
28. Achiron R, Achiron A. **Development of the human fetal corpus callosum: a high-resolution, cross-sectional sonographic study.** *Ultrasound Obstet Gynecol* 2001;18:343–47 CrossRef Medline
29. Malinge G, Zakut H. **The corpus callosum: normal fetal development as shown by transvaginal sonography.** *AJR Am J Roentgenol* 1993;161:1041–43 CrossRef Medline
30. Constable RT, Ment LR, Vohr BR, et al. **Prematurely born children demonstrate white matter microstructural differences at 12 years of age, relative to term control subjects: an investigation of group and gender effects.** *Pediatrics* 2008;121:306–16 CrossRef Medline
31. Skiöld B, Alexandrou G, Padilla N, et al. **Sex differences in outcome and associations with neonatal brain morphology in extremely preterm children.** *J Pediatr* 2014;164:1012–18 CrossRef Medline
32. Franz AR, Pohlandt F, Bode H, et al. **Intrauterine, early neonatal, and postdischarge growth and neurodevelopmental outcome at 5.4 years in extremely preterm infants after intensive neonatal nutritional support.** *Pediatrics* 2009;123:e101–09 CrossRef Medline
33. Yaqub M, Rueda S, Kopuri A, et al. **Plane localization in 3D fetal neurosonography for longitudinal analysis of the developing brain.** *IEEE J Biomed Health Inform* 2015 May 20. [Epub ahead of print] Medline
34. Dudink J, Mercuri E, Al-Nakib L, et al. **Evolution of unilateral perinatal arterial ischemic stroke on conventional and diffusion-weighted MR imaging.** *AJNR Am J Neuroradiol* 2009;30:998–1004 CrossRef Medline

MR Imaging of the Pituitary Gland and Postsphenoid Ossification in Fetal Specimens

 T.M. Mehemed,  Y. Fushimi,  T. Okada,  M. Kanagaki,  A. Yamamoto,  T. Okada,  T. Takakuwa,  S. Yamada, and  K. Togashi



ABSTRACT

BACKGROUND AND PURPOSE: A thorough knowledge of fetal growth and development is key to understanding both the normal and abnormal fetal MR imaging findings. We investigated the size and signal intensity of the normal pituitary gland and the intrasphenoidal ossification around the Rathke pouch in formalin-fixed fetuses on MR imaging.

MATERIALS AND METHODS: Thirty-two fetuses with undamaged brains were included in this study (mean age, 19.93 weeks; age range, 12–31 weeks). Visual inspection of the pituitary and ossification around the Rathke pouch in the sphenoid bone or the postsphenoid ossification was conducted. The extent of pituitary and postsphenoid ossification, pituitary/pons signal ratio, and postsphenoidal ossification/sphenoid bone signal ratio was compared according to gestational age.

RESULTS: The pituitary gland was identified as a hyperintense intrasellar structure in all cases, and postsphenoid ossification was identified as an intrasphenoidal hyperintense area in 27 of the 32 cases (84%). The mean pituitary/pons signal ratio was 1.13 ± 0.18 and correlated weakly with gestational age ($R^2 = 0.243$), while the mean postsphenoid ossification/sphenoid bone signal ratio was 2.14 ± 0.56 and did not show any increase with gestational age ($R^2 = 0.05$). No apparent change in the size of pituitary hyperintensity was seen with gestational age ($R^2 = 0.001$). Postsphenoid ossification showed an increase in size with gestational age ($R^2 = 0.307$).

CONCLUSIONS: The fetal pituitary gland was hyperintense on T1-weighted images and the pituitary/pons ratio and extent of postsphenoid ossification correlated weakly with gestational age.

ABBREVIATION: SP = sphenoid bone

The pituitary gland of fetuses and neonates is hyperintense on T1-weighted images, with no distinct signal differences between the anterior and posterior lobes, thus differing it from the adult pituitary gland.¹ The pituitary gland plays an essential role in the maintenance of homeostasis, metabolism, reproduction, growth, and lactation and comprises 2 different parts in terms of function and embryologic origin: the adenohypophysis and the

neurohypophysis. During embryologic development, the adenohypophysis is formed by the Rathke pouch, which is derived from oral ectoderm from the roof of the stomodeum. Conversely, the neurohypophysis is derived from neural ectoderm. The ventral diencephalon extends downward, forming the infundibular process, which later differentiates into the neurohypophysis.^{2–5}

The Rathke pouch is supposed to elongate, forming the adenohypophyseal stalk and connecting to the stomodeum through a cleft surrounded by the ossification centers of the medial hypophyseal cartilages. Several disagreements remain regarding the development of the pituitary gland, such as whether remnant pituitary tissue exists at the pharynx in adulthood^{6,7} or at the cranio-pharyngeal canal.⁸ The postsphenoid contains 2 medial and 2 lateral ossification centers, and the medial centers usually fuse to form a single ossification center,⁹ but normal variations in timing are speculated to exist in terms of complete fusion of the ossification centers.^{10–12} The adenohypophyseal stalk would normally be obliterated later and fully separated from the stomodeum by the development and ossification of the postsphenoid skull base cartilages. Defects in this fusion will lead to nonobliteration of the

Received October 24, 2015; accepted after revision January 20, 2016.

From the Department of Diagnostic Imaging and Nuclear Medicine (T.M.M., Y.F., Tomohisa Okada, M.K., A.Y., Tsutomu Okada, K.T.), Human Health Science (T.T., S.Y.), and Congenital Anomaly Research Center (S.Y.), Kyoto University Graduate School of Medicine, Kyoto, Japan.

This work was supported by Japan Society for the Promotion of Science KAKENHI grant Nos. 25461815, 15K08134, 15H01121, 26220004, 24119002; and R&D of Molecular Imaging Equipment for Malignant Tumor Therapy Support, supported by the New Energy and Industrial Technology Development Organization, Japan.

Please address correspondence to Yasutaka Fushimi, MD, PhD, Department of Diagnostic Imaging and Nuclear Medicine, Kyoto University Graduate School of Medicine, Kawaharacho, Sakyo-ku, Kyoto, 606-8507, Japan; e-mail: yfushimi@kuhp.kyoto-u.ac.jp

 Indicates open access to non-subscribers at www.ajnr.org

<http://dx.doi.org/10.3174/ajnr.A4808>

adenohypophyseal stalk connecting the Rathke pouch to the stomodaeum, creating a patent canal connecting the sella turcica and pharynx, known as the craniopharyngeal canal.¹³⁻¹⁵ A patent craniopharyngeal canal with a small diameter can be observed in healthy patients.⁸ We will refer to the ossification around the Rathke pouch as “postsphenoid ossification” for simplicity in this study.^{6,16}

Fetal MR imaging offers a useful tool for assessing congenital anomalies in fetuses.¹⁷ Recent advances in MR imaging, such as the development of much faster imaging sequences, have increased the use of fetal MR imaging applications as complementary studies to ultrasonography, particularly for congenital anomalies of the fetal brain. Fetal MR imaging before 18 weeks' gestation is limited by the small size of the fetus and the higher frequency of fetal motion, in addition, some congenital anomalies may not have formed yet. Fetal MR imaging has been reported to be most beneficial in the assessment of central nervous system anomalies for which interventions can be performed, such as neural tube defects.¹⁸⁻²⁰ Congenital hypopituitarism due to either a pituitary developmental abnormality with or without additional hypothalamic and forebrain structural deformities is associated with genetic abnormalities in transcription factors and signaling molecules; therefore, visualization of the fetal pituitary is important for management of hypopituitarism.²¹ Interpreting images from fetal pituitary MR imaging can be challenging due to the limited training opportunities.^{19,22} Fetal MR imaging also involves challenges such as positioning the pregnant mother in the scanner and the lack of suitable coils for pregnant women. Knowledge of normal findings for fetal pituitary, sellar, and parasellar structures is particularly important in the diagnosis of craniopharyngeal canal anomalies, but fetal MR imaging for early-stage pregnancy is currently challenging.

A thorough knowledge of fetal growth and development is key to understanding both normal and abnormal fetal MR imaging findings. The purpose of this study was to investigate the size and signal intensity of the normal pituitary gland and postsphenoid ossification for formalin-fixed fetuses on MR imaging.

MATERIALS AND METHODS

Kyoto Collection

This study was approved by the local institutional review board and written informed consent was waived. About 44,000 aborted fetuses are collected and stored at the Congenital Anomaly Research Center of Kyoto University; in most cases, pregnancy was terminated for socioeconomic reasons, under the Maternity Protection Law of Japan.²³ Seventy-six induced aborted fetuses (mean age, 21.32 weeks; age range, 12–40 weeks) were randomly chosen for this study, from which the 32 fetuses (mean age, 19.93 weeks; age range, 12–31 weeks) with undamaged brains were included in the final analysis. None of the cases included in this study showed any apparent intracranial cephaloceles or tumors.

MR Imaging Parameters

All scans were conducted with a 1.5T MR imaging system (Excelart Vantage, powered by Atlas; Toshiba Medical Systems, Tokyo, Japan) with knee or head coils. After obtaining localizers, a 3D gradient-echo sequence was used for T1-weighted images

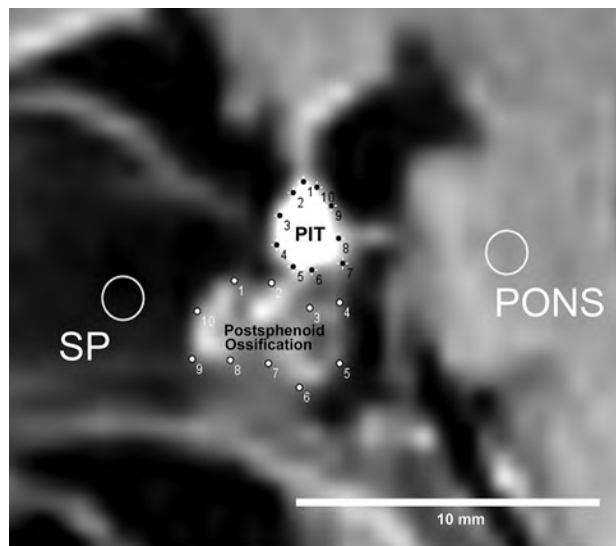


FIG 1. Method of ROI analysis. First, 10 points are manually placed on the contour of both the pituitary (PIT) and postsphenoid ossification, and a round ROI (diameter, 5 pixels) is drawn on both the pons and sphenoid bone. With the convex hull function of ImageJ software, these 10 points are automatically connected to provide an ROI defining the contours of both the pituitary gland and postsphenoid ossification.

with the following parameters: TR, 30 ms; TE, 7 ms; flip angle, 50°; FOV, 180 × 135 mm; matrix, 256 × 192; 120 sections with a thickness of 0.70 mm, resulting in isotropic resolution of 0.70 mm; number of averages, 2; bandwidth, 122; total scan time, 25 minutes 21 seconds.

Visual Assessment

The fetal intrasellar pituitary gland was visually evaluated to compare signal intensities of the pituitary and pons and to determine whether the anterior and posterior lobes of the pituitary could be recognized and differentiated.

Postsphenoid ossification was visually evaluated to determine whether it could be recognized. If recognized, the shape of postsphenoid ossification was classified as condensed hyperintensity, diffusely spreading hyperintensity, or rim-shaped hyperintensity.

Visual inspections were performed separately by 2 neuroradiologists (Y.F., with 17 years of experience, T.M.M., with 5 years of experience). They reached a consensus in any case with a discrepancy.

ROI Analysis

ROIs were defined by 2 neuroradiologists (Y.F., 17 years of experience, T.M.M., 5 years of experience). ROIs were placed for the pituitary, pons, postsphenoid ossification, and sphenoid bone (SP) on sagittal T1WI. We used the convex hull function of ImageJ software (National Institutes of Health, Bethesda, Maryland) for pituitary gland and postsphenoid ossification, by manually choosing 10 points on the contour of the pituitary gland and postsphenoid ossification. A fixed, round ROI (diameter, 5 pixels) was used for the SP and pons (Fig 1). The ROI of the SP was placed so as not to include hyperintensity, which corresponds to ossification in the presphenoid. The area and mean signal intensity of each ROI were calculated. The pituitary/pons ratio and postsphenoid ossification/SP signal intensity ratios were calculated. The

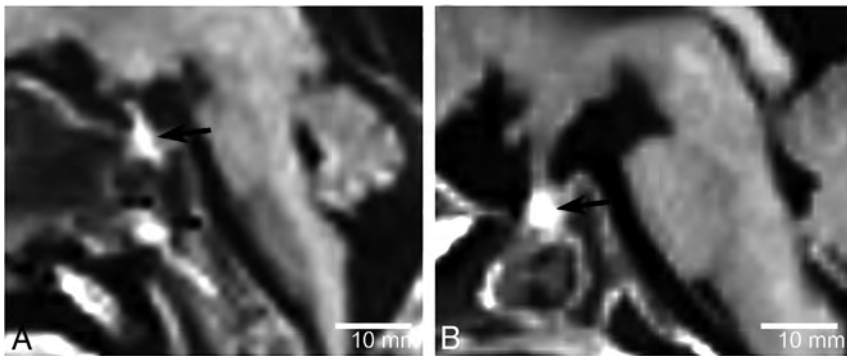


FIG 2. Sagittal T1WI of a 12-week-old fetus (A) and a 31-week-old fetus (B). The fetal pituitary gland shows homogeneous hyperintensity on T1WI (arrows). No clear distinction between the anterior and posterior lobes of the pituitary gland is visualized.

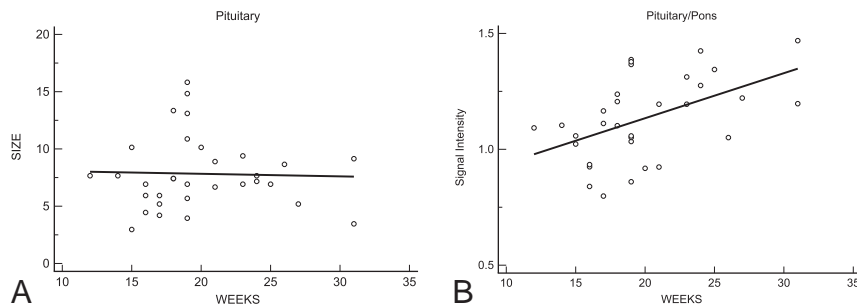


FIG 3. Area of the pituitary hyperintensity as a function of gestational age in weeks (A). No apparent change in the hyperintense area is seen with increasing gestational age in weeks ($R^2 = 0.001$). The pituitary/pons signal ratios as a function of gestational age in weeks are shown (B). The pituitary/pons signal ratio shows a weak increase with gestational age ($R^2 = 0.243$).

averages of each ROI by 2 observers were adopted for further analysis.

Statistical Analysis

Interobserver agreement (κ coefficient values) between the 2 observers was calculated for both signal intensity ratios and area. Linear regression analysis was conducted to reveal any changes in the pituitary/pons or postsphenoid ossification/SP signal ratios and pituitary or postsphenoid ossification area with gestational age. R^2 values were calculated.

RESULTS

Damage to the brain associated with the abortion procedure and formalin-fixation process was found in 44 cases, which were then excluded from analysis. The 32 cases with undamaged brains were included in the final analysis. No CNS abnormalities were apparent in these fetal brains.

Pituitary Gland

All fetuses showed a characteristic appearance of a homogeneous hyperintense pituitary gland compared with the pons, and no cases showed any distinction between the anterior and posterior lobes of the pituitary gland on visual inspection (Fig 2). No change in size of the pituitary hyperintensity was apparent with gestational age ($R^2 = 0.001$, Fig 3A).

The mean pituitary/pons signal ratio was 1.13 ± 0.18 , and a slight increase with gestational age was identified ($R^2 = 0.243$;

Fig 3B). Interobserver agreement was substantial ($\kappa = 0.67$) for the pituitary/pons signal ratio.

Postsphenoid Ossification

Postsphenoid ossification was identified as an intrasphenoidal hyperintensity on T1WI in 27 of the 32 cases (84%). The shape of the postsphenoid ossification was recognized as condensed hyperintensity in 15 cases (55%), diffusely spread hyperintensity in 4 (15%), and rim-shaped hyperintensity in 8 (30%) (Fig 4).

Postsphenoid ossification showed an increase in size with increasing gestational age ($R^2 = 0.307$, Fig 5A).

The mean postsphenoid ossification/SP signal ratio was 2.14 ± 0.56 and did not show any increase with gestational age ($R^2 = 0.05$, Fig 5B). Interobserver agreement was moderate ($\kappa = 0.59$) for postsphenoid ossification/SP signal ratio.

DISCUSSION

The pituitary gland showed a homogeneous hyperintense signal on MR imaging in all fetuses, and no distinction between adenohypophysis and neurohypophysis was evident in this study. Although previous reports have shown pituitary hyperintensity in neonates and fetus older than 21 weeks,^{1,20} hyperintensity of the pituitary gland was also demonstrated in fetal specimens younger than 21 weeks of gestation in this study. Histologic changes within the anterior pituitary lobe with increasing amounts of endoplasmic reticulum, high-level synthesis of pituitary protein, and the higher fraction of bound water molecules due to hormonal secretion are thought to cause hyperintensity of the anterior lobe on T1WI.²⁰ Such hormonal hyperactivity was also observed in women during pregnancy and postpartum as anterior pituitary hyperintensity.^{24,25} A weak correlation between the pituitary/pons signal ratio and gestational weeks was shown in this study; these findings were contradictory to those in previous studies targeting prematurely born neonates.^{1,26} The population of fetuses in this study was approximately 11–12 gestational weeks, younger than the ages in previous reports; this difference may be the cause of the discrepancy in the relationship between the pituitary signal and gestational weeks. The pituitary gland did not show any increase in size with gestational age in our study population, probably because an increase in pituitary size may not be evident during a period of weeks or the pituitary may remain nonfunctional, with the fetus relying solely on maternal hormones.²³

Postsphenoid ossification was visualized as a hyperintense intrasphenoidal structure just inferior to the sellar floor. Postsphenoid ossification showed different shapes and increasing size with gestational age and would be expected to progress to mature bone tissue. Postsphenoid ossification showed a hyperintense intras-

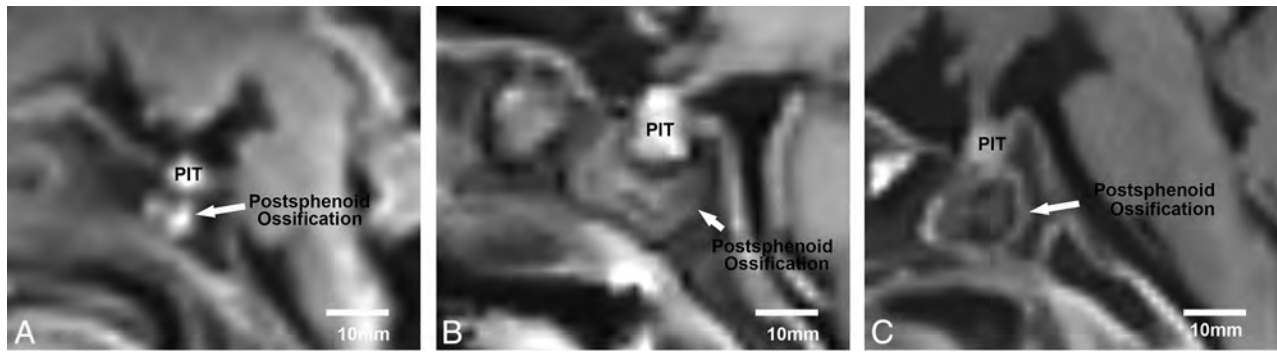


FIG 4. Postsphenoid ossification was identified as an intrasphenoidal hyperintense area on T1WI in 27 of the 32 cases (84%). Representative images are shown of different shapes of postsphenoid ossification hyperintensity on sagittal T1WI: a 19-week-old fetus showing condensed hyperintensity (A), a 19-week-old fetus showing diffusely spreading hyperintensity (B), and a 31-week-old fetus showing rim-shaped hyperintensity (C). The most common shape of postsphenoid ossification hyperintensity was condensed hyperintensity, appearing in 15 of 27 cases (55%).

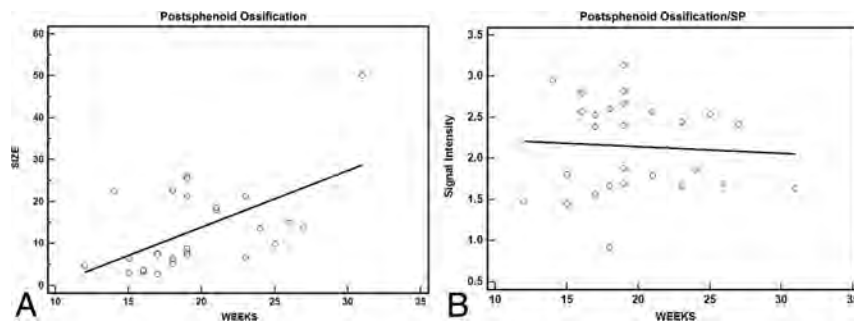


FIG 5. Postsphenoid ossification hyperintensity area as a function of gestational age in weeks (A). A positive correlation is seen between the postsphenoid ossification hyperintensity area and gestational age in weeks ($R^2 = 0.307$). The postsphenoid ossification/SP signal ratio as a function of gestational age in weeks (B). The postsphenoid ossification/SP signal ratio does not show any increase with gestational age ($R^2 = 0.05$).

phenoidal signal on T1WI in 84% of fetuses in this study along the route of the adenohypophyseal stalk of the postsphenoid. The medial ossification centers of the postsphenoid, which later form the sella turcica, usually unite to form a single ossification center, but such unity may not happen as soon as the individual centers form, which may, in turn, cause the variable timing in the disappearance of the craniopharyngeal canal, not restricted to a specific gestational age.^{10,14,16,27}

Imaging findings for postsphenoid ossification have been discussed in the literature only as hyperattenuation on CT and low intensity on T2-weighted images,¹⁶ and the characteristic appearance of postsphenoid ossification on T1WI as shown in this study has not been previously reported, to our knowledge, due to a lack of fetal MR imaging data on intrasphenoidal lesions. Calcification usually appears as a low signal on both T1WI and T2WI, but calcium salts interact with water protons in the process of ossification, in turn slowing the precession to near the Larmor frequency and potentially leading to short T1 relaxation times.^{28,29} Knowledge of the origins of such intrasphenoidal hyperintensities and the various shapes (condensed, diffusely spreading, and rim-shaped) (Fig 4) may be beneficial for neuroradiologists in understanding the developmental process and avoiding a misdiagnosis of intrasphenoidal tumor. Variations in the appearance of postsphenoid ossification may be attributable to the different physical shapes at different steps of the ossification process and the

amount of water protons surrounding the calcium salts, but further study is required.

Several limitations to this study must be considered when interpreting these results. All fetuses included in our study were aborted fetuses that had been fixed in formaldehyde. Formaldehyde fixation has been reported to modify T1 and T2 relaxation times of tissues through alteration of tissue microstructures. Such effects mean that our results might differ from those of in vivo fetal MR imaging, but several MR imaging studies have covered formalin-fixed fetal specimens,^{16,30} and we have demonstrated the similar appearance of fetal pituitary

hyperintensity reported from in vivo studies.^{1,31} Further in vivo fetal MR imaging studies may be expected for validation of our results. Another limitation was the small number of cases included in this study, and a larger number of cases might have more precisely clarified the relationship between gestational age and the size of the pituitary gland or postsphenoid ossification. Because negative correlations between pituitary hyperintensity and postnatal time were revealed in 88 neonates¹ and 121 infants,²⁶ more cases may be required for better evaluation of correlations in this study. In the future, more detailed volumetric analysis of the fetal pituitary gland and postsphenoid ossification with a larger in vivo study population and radiologic-histologic correlations will further enhance the relevance of the present results.

CONCLUSIONS

This study demonstrated that the fetal pituitary gland was hyperintense on T1WI, and both the pituitary/pons ratio and the size of postsphenoid ossification correlated weakly with gestational age.

Disclosures: Yasutaka Fushimi—RELATED: Grant: This work was supported by Japan Society for the Promotion of Science KAKENHI grant Nos. 25461815, 15K08134, 15H01121, 26220004, 24119002; and R&D of Molecular Imaging Equipment for Malignant Tumor Therapy Support, supported by New Energy and Industrial Technology Development Organization, Japan.* Tsumotomu Okada—RELATED: Grant: Japan Soci-

REFERENCES

1. Kitamura E, Miki Y, Kawai M, et al. **T1 signal intensity and height of the anterior pituitary in neonates: correlation with postnatal time.** *AJNR Am J Neuroradiol* 2008;29:1257–60 CrossRef Medline
2. Dubois PM, Elamraoui A. **Embryology of the pituitary gland.** *Trends Endocrinol Metab* 1995;6:1–7 CrossRef Medline
3. Dorton AM. **The pituitary gland: embryology, physiology, and pathophysiology.** *Neonatal Netw* 2000;19:9–17 Medline
4. Bancalari RE, Gregory LC, McCabe MJ, et al. **Pituitary gland development: an update.** *Endocr Dev* 2012;23:1–15 CrossRef Medline
5. Ikeda H, Suzuki J, Sasano N, et al. **The development and morphogenesis of the human pituitary gland.** *Anat Embryol (Berl)* 1988;178:327–36 CrossRef Medline
6. Hori A, Schmidt D, Rickels E. **Pharyngeal pituitary: development, malformation, and tumorigenesis.** *Acta Neuropathol* 1999;98:262–72 CrossRef Medline
7. Pugnale N, Waridel F, Bouzourène H, et al. **Pharyngeal pituitary non-functioning adenoma with normal intra-sellar gland: massive tumor shrinkage on octreotide therapy.** *Eur J Endocrinol* 2003;148:357–64 CrossRef Medline
8. Abele TA, Salzman KL, Harnsberger HR, et al. **Craniopharyngeal canal and its spectrum of pathology.** *AJNR Am J Neuroradiol* 2014;35:772–77 CrossRef Medline
9. Madeline LA, Elster AD. **Suture closure in the human chondrocranium: CT assessment.** *Radiology* 1995;196:747–56 CrossRef Medline
10. Kjaer I. **Radiographic determination of prenatal basicranial ossification.** *J Craniofac Genet Dev Biol* 1990;10:113–23 Medline
11. Ricciardelli EJ. **Embryology and anatomy of the cranial base.** *Clin Plast Surg* 1995;22:361–72 Medline
12. Zhang Q, Wang H, Udagawa J, et al. **Morphological and morphometric study on sphenoid and basioccipital ossification in normal human fetuses.** *Congenit Anom (Kyoto)* 2011;51:138–48 CrossRef Medline
13. Arey LB. **The craniopharyngeal canal reviewed and reinterpreted.** *Anat Rec* 1950;106:1–16 CrossRef Medline
14. Cho KH, Chang H, Yamamoto M, et al. **Rathke's pouch remnant and its regression process in the prenatal period.** *Childs Nerv Syst* 2013;29:761–69 CrossRef Medline
15. Kjaer I, Russell BG. **The craniopharyngeal canal indicating the presence of pharyngeal adenopituitary tissue.** *Eur J Radiol* 1995;20:212–14 CrossRef Medline
16. Nemzek WR, Brodie HA, Hecht ST, et al. **MR, CT, and plain film imaging of the developing skull base in fetal specimens.** *AJNR Am J Neuroradiol* 2000;21:1699–706 Medline
17. Glenn OA, Barkovich J. **Magnetic resonance imaging of the fetal brain and spine: an increasingly important tool in prenatal diagnosis: part 2.** *AJNR Am J Neuroradiol* 2006;27:1807–14 Medline
18. Garel C. **Imaging the fetus: when does MRI really help?** *Pediatr Radiol* 2008;38(suppl 3):S467–70 Medline
19. Levine D. **Timing of MRI in pregnancy, repeat exams, access, and physician qualifications.** *Semin Perinatol* 2013;37:340–44 CrossRef Medline
20. Schmook MT, Brugger PC, Weber M, et al. **Forebrain development in fetal MRI: evaluation of anatomical landmarks before gestational week 27.** *Neuroradiology* 2010;52:495–504 CrossRef Medline
21. Mehta A, Hindmarsh PC, Mehta H, et al. **Congenital hypopituitarism: clinical, molecular and neuroradiological correlates.** *Clin Endocrinol (Oxf)* 2009;71:376–82 CrossRef Medline
22. Al-Mukhtar A, Kasprian G, Schmook MT, et al. **Diagnostic pitfalls in fetal brain MRI.** *Semin Perinatol* 2009;33:251–58 CrossRef Medline
23. Shiota K. **Development and intrauterine fate of normal and abnormal human conceptuses.** *Congenit Anom* 1991;31:67–80 CrossRef
24. Elster AD, Sanders TG, Vines FS, et al. **Size and shape of the pituitary gland during pregnancy and post partum: measurement with MR imaging.** *Radiology* 1991;181:531–35 CrossRef Medline
25. Miki Y, Asato R, Okumura R, et al. **Anterior pituitary gland in pregnancy: hyperintensity at MR.** *Radiology* 1993;187:229–31 CrossRef Medline
26. Argyropoulou MI, Xydis V, Kiortsis DN, et al. **Pituitary gland signal in pre-term infants during the first year of life: an MRI study.** *Neuroradiology* 2004;46:1031–35 CrossRef Medline
27. Sasaki H, Kodama G. **Developmental studies on the postsphenoid of the human sphenoid bone.** In: Bosma JF, ed. *Symposium on the Development of the Basicranium*. Bethesda: National Institutes of Health; 1976:177–91
28. Elster AD, Burdette JH. *Questions & Answers in Magnetic Resonance Imaging*. St. Louis; Mosby; 2001
29. Wehrli FW. **Magnetic resonance of calcified tissues.** *J Magn Reson* 2013;229:35–48 CrossRef Medline
30. Kinoshita Y, Okudera T, Tsuru E, et al. **Volumetric analysis of the germinal matrix and lateral ventricles performed using MR images of postmortem fetuses.** *AJNR Am J Neuroradiol* 2001;22:382–88 Medline
31. Caruso RD, Rosenbaum AE, Sherry RG, et al. **Pituitary gland: variable signal intensities on MRI—a pictorial essay.** *Clin Imaging* 1998;22:327–32 CrossRef Medline

Quiet T1-Weighted Pointwise Encoding Time Reduction with Radial Acquisition for Assessing Myelination in the Pediatric Brain

 N. Aida,  T. Niwa,  Y. Fujii,  K. Nozawa,  M. Enokizono,  K. Murata, and  T. Obata



ABSTRACT

BACKGROUND AND PURPOSE: T1-weighted pointwise encoding time reduction with radial acquisition (PETRA) sequences require limited gradient activity and allow quiet scanning. We aimed to assess the usefulness of PETRA in pediatric brain imaging.

MATERIALS AND METHODS: We included consecutive pediatric patients who underwent both MPRAGE and PETRA. The contrast-to-noise and contrast ratios between WM and GM were compared in the cerebellar WM, internal capsule, and corpus callosum. The degree of myelination was rated by using 4-point scales at each of these locations plus the subcortical WM in the anterior frontal, anterior temporal, and posterior occipital lobes. Two radiologists made all assessments, and the intra- and interrater agreement was calculated by using intraclass correlation coefficients. Acoustic noise on MPRAGE and PETRA was measured.

RESULTS: We included 56 patients 5 days to 14 years of age (mean age, 36.6 months) who underwent both MPRAGE and PETRA. The contrast-to-noise and contrast ratios for PETRA were significantly higher than those for MPRAGE ($P < .05$), excluding the signal ratio for cerebellar WM. Excellent intra- and interrater agreement were obtained for myelination at all locations except the cerebellar WM. The acoustic noise on PETRA (58.2 dB[A]) was much lower than that on MPRAGE (87.4 dB[A]).

CONCLUSIONS: PETRA generally showed better objective imaging quality without a difference in subjective image-quality evaluation and produced much less acoustic noise compared with MPRAGE. We conclude that PETRA can substitute for MPRAGE in pediatric brain imaging.

ABBREVIATIONS: CC = corpus callosum; ICC = intraclass correlation coefficient; PETRA = pointwise encoding time reduction with radial acquisition

MR imaging is widely used for brain assessment in both adults and children, enabling the noninvasive and detailed evaluation of morphologic and functional abnormalities.^{1,2} However, MR imaging has some drawbacks. Of note, an average scanning time of 20–30 minutes is usually required for a routine brain examination, during which the patient is subjected to loud acoustic noise. Consequently, the application of MR imaging is limited in infants and small children, who often need sedation to undergo MR imaging.^{3–5} Even under sedation, the acoustic noise from MR

imaging can make children restless or cause them to awaken, resulting in severe motion artifacts or incomplete examinations.

With the increased use of MR imaging in children, it is important to reduce the loudness of MR imaging scanners to ensure that scans are completed with minimal distress to the child and minimal artifacts on the acquired images. Because the acoustic noise of MR imaging is produced by the vibration of gradient coils during the scan, noise reduction can be achieved by decreasing the noise from these coils. One such method involves sealing gradient coils in a vacuum chamber.⁶ More recently, several methods have been introduced to reduce acoustic noise that do not involve altering the scanner hardware. These techniques include the use of acoustically optimized pulse shapes of the gradient coils to cancel single frequencies extended by a second frequency,⁷ ultrashort TE sequences such as zero TE,⁸ sweep imaging with Fourier transformation,⁹ and pointwise encoding time reduction with radial acquisition (PETRA).¹⁰ Of these, PETRA requires limited gradient activity, which creates a particularly quiet MR imaging scan.¹⁰ Considering that quiet sequences should be useful for reducing patient stress during the scan, this technique might particularly

Received October 30, 2015; accepted after revision January 20, 2016.

From the Department of Radiology (N.A., T.N., Y.F., K.N., M.E.), Kanagawa Children's Medical Center, Yokohama, Japan; Department of Radiology (T.N.), Tokai University School of Medicine, Isehara, Japan; Siemens Healthcare K.K. (K.M.), Ohsaki, Tokyo, Japan; and Research Center for Charged Particle Therapy (T.O.), National Institute of Radiological Sciences, Chiba, Japan.

Please address correspondence to Tetsu Niwa, MD, PhD, Department of Radiology, Tokai University School of Medicine, 143 Shimokasuya, Isehara, 259-1193, Japan; e-mail: niwat@tokai-u.jp

 Indicates article with supplemental on-line table.

<http://dx.doi.org/10.3174/ajnr.A4747>

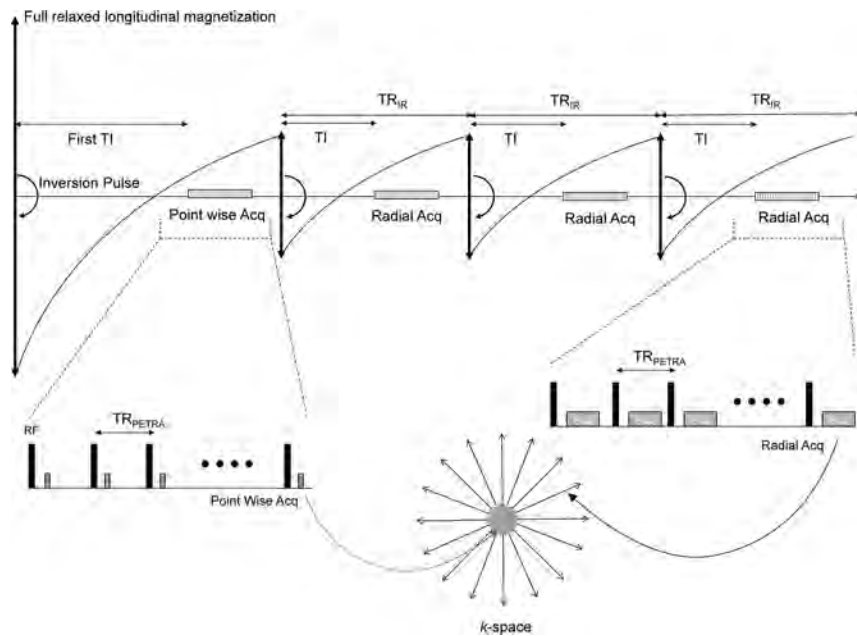


FIG 1. Pulse sequence diagram for the inversion pulse of the PETRA sequence. The center part of the k -space is acquired with pointwise encoding after the first inversion pulse, and the outer edge of the volumetric k -space is acquired with radial projections after the second and later inversion pulses. Acq indicates acquisition.

benefit children. PETRA sequencing uses an inversion recovery pulse to yield T1WI, which is a basic MR imaging sequence that can be used to assess myelination in children.

In this study, we therefore aimed to compare the measurements of pediatric brain myelination obtained by using a quiet T1-weighted PETRA sequence with those captured by MPRAGE to assess the suitability of PETRA for pediatric brain imaging.

MATERIALS AND METHODS

Patients

We performed T1-weighted PETRA in addition to routine MR imaging in all pediatric patients undergoing brain MR imaging with sedation from May to October 2013. To avoid unnecessary delays and to keep scanning times short, we did not perform PETRA for emergency cases and we excluded older children who did not require sedation. We added T1-weighted PETRA after routine MR imaging examinations without additional sedation for consecutive patients, excluding cases with severe motion artifacts. Our institutional review board (Kanagawa Children's Medical Center) approved this prospective study, and written consent was obtained from the parents.

MR Imaging

All MR imaging examinations were performed on a 3T clinical scanner (Magnetom Verio; Siemens, Erlangen, Germany) by using a 32-channel head coil. The routine MR imaging brain sequence included axial and coronal T2-weighted fast spin-echo, axial MPRAGE, and axial DWI. In addition, T1-weighted PETRA was performed.

PETRA uses an ultrashort TE sequence that acquires k -space data in a combination of the central and outer part of the k -space during different processes.¹⁰⁻¹² Particularly, the central part of the k -space is acquired with pointwise encoding after the first inversion pulse, whereas the outer edge of volumetric k -space is

acquired by using radial projections after the second and later inversion pulses (Fig 1). PETRA keeps gradients invariable for almost an entire repetition, and the gradients change only slightly at the end of each repetition. As a result, PETRA achieves minimal vibration of the gradient coils, generating only residual acoustic noise because of radiofrequency switching.

In this study, we adjusted PETRA sequences for clinical use with children. First, PETRA was set to have the shortest possible acquisition time while maintaining sufficient spatial resolution. Second, the first TI on PETRA was individualized to obtain an appropriate contrast for the pediatric brain. The first TI might greatly affect the contrast of the PETRA image because the central part of the k -space is acquired with a first inversion pulse in the PETRA sequence (Fig 1) and the T1 value of the brain is known to be longer in infants and small children than in older children and adults.^{13,14} Therefore, the first TI was set

to a longer value than that used in adult scans. We measured the T1 value of each child before PETRA sequencing by using double flip angle FLASH sequences with the following parameters: TR/TE = 10/1.37 ms; double flip angle = 3°, 19°; FOV = 230 mm; matrix = 95 × 128; thickness = 4 mm; number of sections = 19; acquisition time = 26 seconds.

A T1 map was subsequently generated by the MR imaging scanner software. We placed an ROI that corresponded to the contour of the brain parenchyma at the level of the basal ganglia on the T1 map, and the T1 value of the brain parenchyma was measured, excluding values of ≥ 3000 ms to remove the CSF space. Then, the first TI on PETRA was set as the measured T1 value multiplied by 0.7, and we set the upper and lower limits of the first TI at 1000 and 1800 ms, respectively; if the measured T1 value exceeded these limits, the first TI was set at 1000 or 1800 ms, respectively. This method was determined by a pilot study and a study with adult volunteers (N.A., unpublished data, April 2013). The imaging parameters for PETRA and MPRAGE are shown in Table 1. The actual MPRAGE parameters varied depending on the child's head size.

Image Analysis

PETRA images were reformatted in the axial plane in the same section angulation and thickness as those for MPRAGE. Images were assessed qualitatively and quantitatively.

Quantitative Analysis

Quantitative analysis was performed by assessing the imaging contrast and calculating the contrast-to-noise and signal ratios between WM and GM on MPRAGE and PETRA. The signal intensity and SD at the WM and adjacent GM were measured by a neuroradiologist (M.E., with 8 years of experience in neuroradiology) by ROI placement. This analysis was conducted by selecting a population with relatively advanced myelination (ie, children older than 7 months of

Table 1: Parameters of MPRAGE and PETRA

Parameters	MPRAGE			PETRA
	Small FOV	Middle FOV	Large FOV	
FOV (mm)	150	200	240	285
Orientation	Axial	Axial	Axial	Sagittal
First TI (ms)	NA	NA	NA	1000–1800
TI (ms)	800	800	800	700
TR (ms)	1570	1570	1570	3.75
TE (ms)	2.14	2.79	2.77	0.07
Echo space (ms)	5.2	5.2	5.2	3.75
Flip angle (degrees)	9	9	9	6
Section thickness (ms)	1.0	1.0	1.0	0.8
Section oversampling (%)	100	36.4	25.0	0
Matrix	154 × 192	168 × 192	224 × 256	352 × 352
Radial spokes	NA	NA	NA	35,000
GRAPPA	2	2	2	NA
Resolution (mm)	0.98 × 0.78 × 1.00	1.04 × 1.04 × 1.00	0.94 × 0.94 × 1.00	0.81 × 0.81 × 0.81
Scan time (min/sec)	3:27	3:05	3:05	4:20

Note:—NA indicates not available; GRAPPA, generalized autocalibrating partially parallel acquisition.

Table 2: White–gray matter contrast for MPRAGE and PETRA

Assessed Location	Contrast-to-Noise Ratio			Contrast Ratio		
	MPRAGE	PETRA	P Value	MPRAGE	PETRA	P Value
Cerebellar white matter	4.02 ± 0.78	6.48 ± 1.75	<.001	1.27 ± 0.06	1.26 ± 0.01	.82
Anterior part of the posterior limb of the internal capsule	2.25 ± 0.68	3.69 ± 0.87	<.001	1.11 ± 0.04	1.17 ± 0.05	<.001
Corpus callosum						
Genu	6.74 ± 2.36	8.41 ± 3.90	.004	1.46 ± 0.12	1.59 ± 0.20	<.001
Splenium	6.01 ± 1.87	8.17 ± 3.07	<.001	1.42 ± 0.10	1.45 ± 0.12	<.001

age). ROIs were placed at the following anatomic structures: the cerebellar WM and the adjacent cortex, the anterior part of the posterior limb of the internal capsule and thalami, the genu and splenium of the corpus callosum (CC), and the adjacent cerebral cortex. The contrast-to-noise and contrast ratios were calculated by using the following formulas, where SI is the signal intensity and SD is the standard deviation:

Contrast-to-Noise Ratio

$$= (\text{Mean SI}_{\text{WM}} - \text{Mean SI}_{\text{GM}}) / [(\text{SD}_{\text{WM}}^2 + \text{SD}_{\text{GM}}^2)]^{1/2}$$

Contrast Ratio = Mean SI_{WM}/Mean SI_{GM}.

The ROI measurement was performed on both the right and left sides, except for the corpus callosum, and the calculated values were averaged.

Qualitative Assessment

Qualitative assessments were provided by experienced radiologists (K.N. and Y.F., who had 20 and 10 years of experience in pediatric neuroradiology, respectively). The radiologists independently rated the degree of myelination on MPRAGE and PETRA in a random order by using a clinical PACS viewer. The following 2 sections were used for this assessment: section 1, at the level of the inferior (temporal) horn of the lateral ventricle; and section 2, at the level of the foramina of Monro. In turn, the following anatomic locations were evaluated at each section: the subcortical WM in the anterior temporal lobe and the cerebellar WM at section 1; and the anterior part of the posterior limb of the internal capsule, genu, and splenium of the CC, and the subcortical WM in the anterior frontal and posterior occipital lobe at section 2. Be-

cause myelination appears as a relative hypersignal on T1WI, the degree of the myelination was assessed by the signal intensity at each anatomic location in comparison with the adjacent GM. The following 4-point scale was used for this assessment: 0, hyposignal; 1, isosignal; 2, slight hypersignal; and 3, prominent hypersignal.

Acoustic Noise

In addition to the patient study, we also measured acoustic noise by MPRAGE and PETRA during the scan of a phantom by using a 32-channel head coil. The acoustic noise level of each sequence was recorded by using a microphone (NL-32; Rion, Tokyo, Japan), which was placed horizontally at a distance of 2.5 m from the front panel of the MR imaging scanner. The measurements took 10 seconds to complete, and they were repeated 16 times. The measured noise values were averaged for each sequence. For comparison, the ambient sound level was measured 8 times for 10 seconds each.

Statistical Analysis

Statistical analyses were performed by using the MedCalc software package for Windows, Version 15.4 (MedCalc Software, Mariakerke, Belgium), and we considered *P* values < .05 to indicate a statistically significant difference. The contrast-to-noise and signal ratios for MPRAGE and PETRA were compared by using paired sample *t* tests. Inter- and intrarater agreement for the myelination scores between MPRAGE and PETRA was evaluated by calculating the intraclass correlation coefficient (ICC). ICCs were interpreted by using the criteria reported by Landis and Koch¹⁵: an ICC of 0.01–0.20 indicated slight agreement; an ICC of 0.21–0.40, fair agreement; an ICC of 0.41–0.60, moderate agreement; an ICC of 0.61–0.80, substantial agreement; and an ICC of 0.81–1.0, near-perfect agreement.

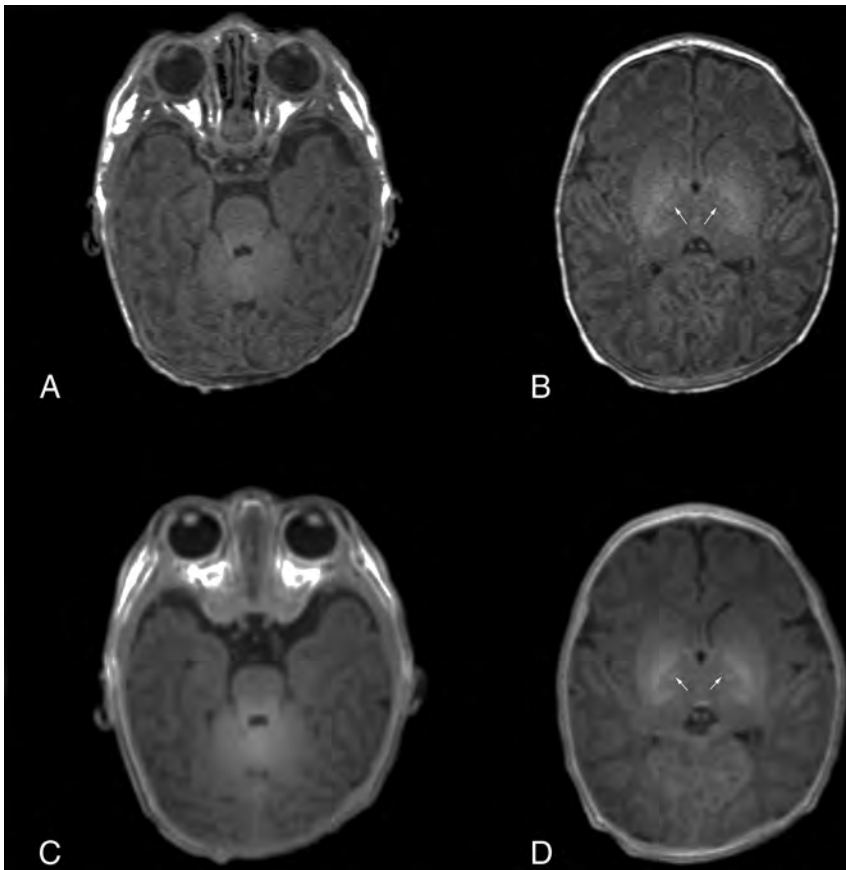


FIG 2. Images of a 9-day-old neonate. MPRAGE (A and B) and PETRA (C and D) images show slight hypersignals in the cerebellar WM and the anterior part of the posterior limb of the internal capsule (arrows), indicating myelination.

RESULTS

Patients

We added T1-weighted PETRA after routine MR imaging examinations for 76 consecutive patients, of whom 20 were excluded because of severe motion artifacts. Thus, 56 patients (age range, 5 days to 14 years; mean age, 36.6 months; median age, 25 months) were enrolled in this study.

MR imaging was performed for the following reasons: developmental delay ($n = 25$), autism ($n = 4$), epilepsy ($n = 4$), rigidity of the limbs ($n = 3$), small head size ($n = 2$), large head size ($n = 1$), eye-movement disorder ($n = 2$), mental retardation ($n = 1$), headache ($n = 1$), follow-up examination of congenital cytomegalovirus infection ($n = 2$), screening for patients with neurofibromatosis type 1 ($n = 2$) and café-au-lait spots on the skin ($n = 1$), agenesis of the CC detected on fetal ultrasonography ($n = 1$), phenylketonuria ($n = 1$), hypoxic ischemic injury ($n = 1$), cardiopulmonary resuscitation ($n = 1$), follow-up examination of mitochondrial encephalomyopathy, lactic acidosis and strokelike episodes syndrome ($n = 1$), encephalopathy ($n = 1$), folate receptor α deficiency ($n = 1$), and diabetes insipidus ($n = 1$).

Image Analysis

The results of the MRIs were as follows: no abnormality ($n = 29$), WM volume loss ($n = 6$), hypogenesis ($n = 3$) and agenesis ($n = 1$) of the CC, parenchymal atrophy ($n = 3$), small cerebellum ($n = 3$), small cerebellum and brain stem ($n = 2$), cerebellar dysplasia

and heterotopia ($n = 1$), patchy T2 prolongation in the WM due to congenital cytomegalovirus infection ($n = 2$), multiple foci of T2 prolongation in patients with neurofibromatosis type 1 ($n = 2$), medial temporal sclerosis ($n = 1$), small foci of hypoxic change at the watershed area ($n = 1$), subacute infarction of the territory of the left middle cerebral artery ($n = 1$), and ventricular dilation ($n = 1$). The measured T1 value of the brain parenchyma ranged from 1273 to 2618 ms (mean, 1816 ± 288 ms). Thus, for the designated interval of 1000–1800 ms, we set the first TI at a mean of 1283 ± 213 ms for PETRA.

Quantitative Analysis

The WM–GM contrast was measured in 49 patients older than 7 months of age. The ROI measurements could not be performed at the CC in 4 patients (1 case of CC agenesis and 3 cases of CC hypogenesis). The results of the WM–GM contrast for MPRAGE and PETRA are summarized in Table 2. Contrast-to-noise ratios were significantly higher for PETRA than for MPRAGE at all the assessed locations. Contrast ratios were significantly higher for PETRA than for MPRAGE in the anterior part of the posterior limb of the internal capsule and in the genu and splenium of the CC. Contrast ratios were not significantly different between MPRAGE and PETRA in the cerebellar WM.

Qualitative Analysis

The assessed myelination scores for each reader are summarized in the On-line Table. Myelination at the CC was not assessed in 1 case with CC agenesis and another case with CC hypoplasia. In 1 case with a hypoplastic CC splenium, only the genu was assessed. Myelination of the CC was assessed in 1 case with slight CC hypoplasia.

The mean differences in the PETRA to MPRAGE scores for reader 1 were -0.07 – 0.09 ; the corresponding values for reader 2 were -0.16 – 0.09 (On-line Table). Interrater correlation for the degree of myelination was substantial or nearly perfect between MPRAGE and PETRA at almost all assessed locations (ICC range, 0.80–1.00; Figs 2–4). The ICC was <0.01 for the intrarater correlation of the cerebellar WM rated by reader 2, in which all the cases on PETRA were scored 3, and 51 (91.1%) cases were scored 3 on MPRAGE (the remaining cases were scored 2). Interrater correlation was almost perfect (ICC range, 0.87–0.99) at most assessed locations. The ICC was also <0.01 for the interrater correlation for the cerebellar WM on PETRA, where all the cases on PETRA were scored 3 by reader 2 and 52 (92.9%) cases were scored 3 by reader 1 (with the remainder scored 2).

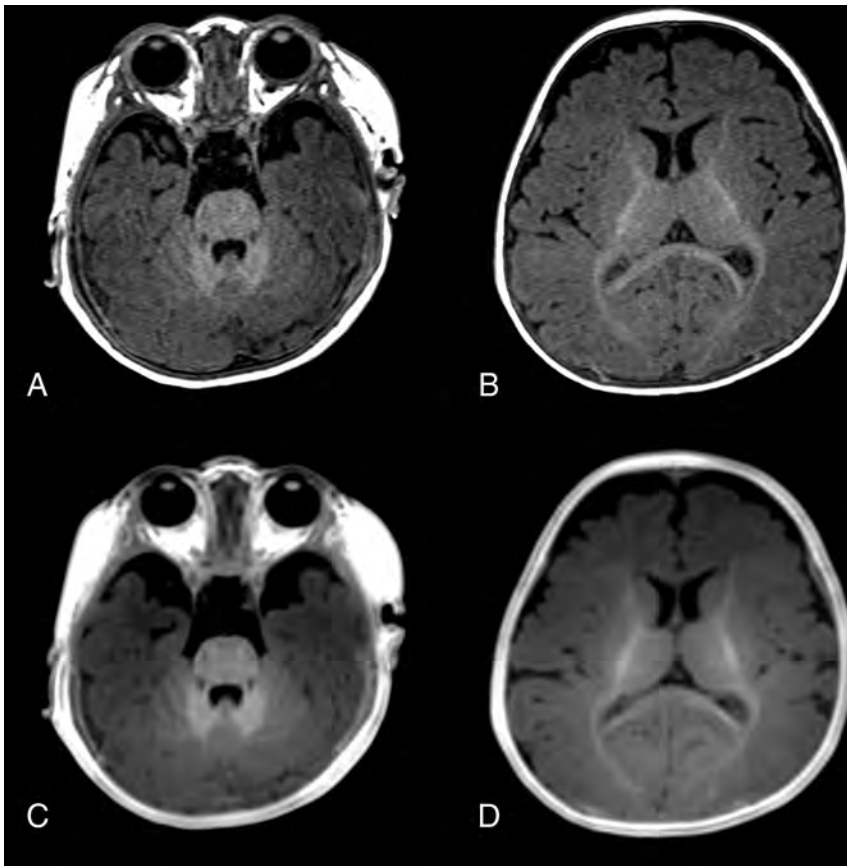


FIG 3. Images of a 5-month-old girl. MPRAGE (A and B) and PETRA (C and D) images both show prominent hypersignals in the cerebellar WM, slight hypersignal in the anterior part of the posterior limb of the internal capsule and the splenium of the corpus callosum, and isosignal in the cerebral cortex at the genu of the corpus callosum and in the subcortical WM of the occipital lobe, indicating myelination.

Acoustic Noise

The mean acoustic noise levels of MPRAGE and PETRA were 87.4 and 58.2 dB(A), respectively, set against an ambient sound level of 53.4 dB(A). Notably, the acoustic noise level of PETRA was only 4.8 dB(A) higher than that of ambient sound.

DISCUSSION

We found that PETRA had a generally better WM–GM contrast than MPRAGE. In addition, there were relatively small differences in subjective image quality between MPRAGE and PETRA. Intra-rater agreement for MPRAGE and PETRA was substantial or nearly perfect for most of the assessed locations. Although the ICC for the cerebellar WM score on PETRA was very low for reader 2, this result may have been because reader 2 rated all the scores as 3 for cerebellar WM myelination. Actually, small differences were noted in the intrarater and interrater agreement for the cerebellar WM scores. Thus, although further investigation is clearly warranted, these results suggest that there may be no differences in the assessment of myelination between MPRAGE and PETRA.

The assessment of brain myelination as an indicator of brain maturation is one of the main uses of T1WI in pediatrics.¹⁶ Newer 3T MR imaging scanners yield lower contrast on spin-echo T1WI than 1.5T scanners because of T1 prolongation.¹⁷ Therefore, gradient-echo sequences such as MPRAGE provide better contrast

than conventional spin-echo T1WI.¹⁸ In addition, volumetric acquisition by using a 3D gradient-echo sequence provides greater anatomic detail for pathologic assessment than conventional 2D spin-echo T1WI. Indeed, the use of a 3D gradient-echo sequence may play a role as important as T1WI on a 3T MR imaging.¹⁹ In a previous study of the production of contrast-enhanced images by using PETRA,¹¹ equal or better imaging quality was obtained by PETRA compared with MPRAGE for brain tumors. Our results suggest that PETRA also offers quality comparable with that of MPRAGE for noncontrast T1WI of the pediatric brain.

PETRA sequences need to be specified for the pediatric brain. Therefore, we set the first TI on PETRA depending on the individual T1 values, which were measured before PETRA scanning. In fast gradient-echo sequences, longitudinal relaxation of the proton is fully recovered at the first echo, whereas it is partially recovered at subsequent pulses, eventually achieving steady-state. Therefore, several echoes are usually not obtained at first, which is called a “dummy pulse.”²⁰ With PETRA, however, data are collected from the beginning of the echoes after the first TI to obtain a better signal-to-noise ratio. PETRA acquires data by a pointwise

method at the center of *k*-space from the first inversion recovery and from radial projection at the outer edge of the *k*-space after subsequent inversion pulses. Thus, setting the first TI might greatly affect the resulting imaging contrast, so we set the first TI according to individual T1 values. A longer first TI might lead to a better contrast on PETRA, but it means prolongation of the acquisition time. Therefore, we set the first TI to the shortest possible value, preserving the imaging quality for clinical use. The actual setting of the first TI was determined by a preliminary volunteer study. Although further assessment will be needed to determine the appropriate first TI, our results may be appropriate for PETRA T1WI. On the other hand, this process is complex and time-consuming. Therefore, we propose that the first TI be set at 1800 ms for infants 4 months or younger and 1300 ms for infants and children older than 4 months of age for clinical use, according to the measured T1 value.

Currently, PETRA has some limitations when setting the sequence. In the current implementation, patients were only scanned with PETRA in the sagittal plane, so section orientation differed between MPRAGE and PETRA. Notably, the parameter setting and spatial resolution differed between PETRA and MPRAGE. In addition, a small FOV cannot be applied for PETRA, and although we set PETRA at a resolution similar to that

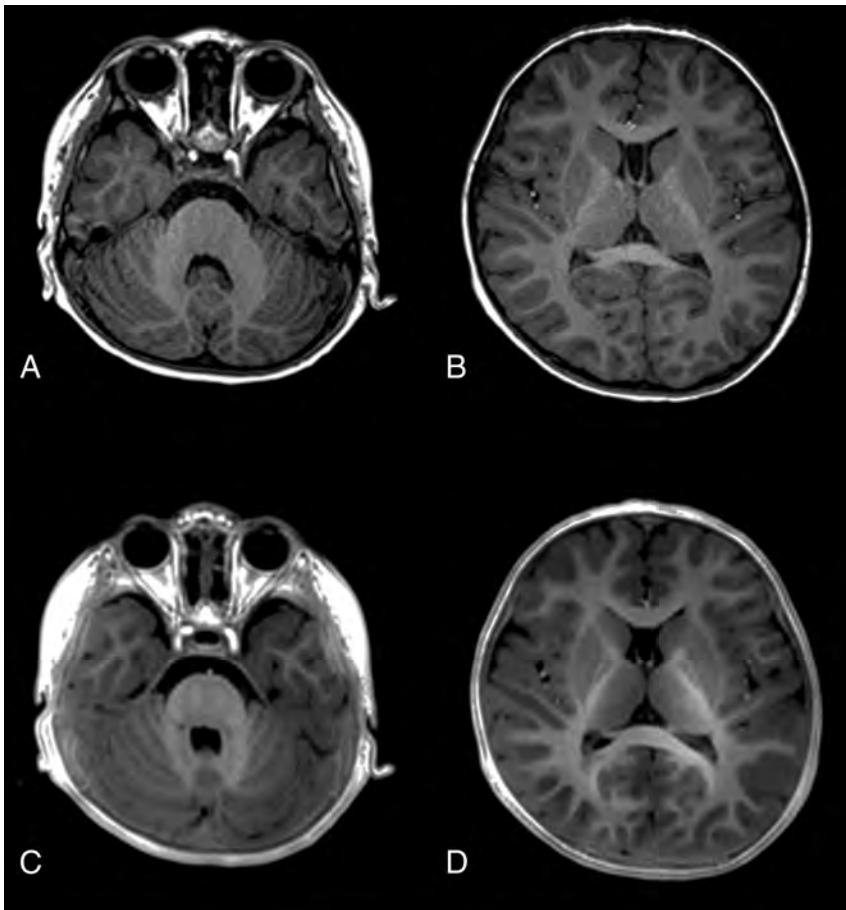


FIG 4. Images of a 27-month-old boy. MPRAGE (A and B) and PETRA (C and D) images both show prominent hypersignals at all assessed locations, including the cerebellar WM, anterior part of the posterior limb of the internal capsule, genu and splenium of the corpus callosum, and the subcortical WM at the temporal, frontal, and occipital lobes, indicating myelination.

of MPRAGE, the acquisition time was about 1 minute longer than that of MPRAGE. This might affect the imaging contrast results for PETRA compared with MPRAGE in this study.

Generally, radial acquisition needs a large number of total spokes. However, we used reduced radial spokes on PETRA for clinical use with children to acquire MR data in a relatively short time. However, this use resulted in undersampling for a radial k -space acquisition. To improve imaging quality when working with undersampled data, we used 2 techniques before the radial spokes were gridded to the Cartesian grid on PETRA, namely, adaptation of the attenuation matrix to the attenuation present in the Cartesian center of the k -space and application of a certain plateau level at the periphery.^{10,21,22} On the other hand, these processes lead to image blurring, which might affect the imaging analysis in this study.

We found that acoustic noise on PETRA was much less than on MPRAGE; this difference was attributed to the unique gradient-pulse sequence of PETRA. PETRA yielded only a slight increase in acoustic noise over background noise, achieving an almost silent sequence. Ida et al¹¹ previously measured the acoustic noise of MPRAGE and PETRA by using a clinical 3T MR imaging scanner, which resulted in noise levels of 78.1 dB(A) and 51.4 dB(A), respectively. These results are consistent with our results, indicating negligible acoustic noise when using PETRA, which

should translate to clinical benefit when performing MR imaging examinations in children. Although we measured only a short period for acoustic noise on PETRA, we think that our measurements contained representative noise levels.

The limitations of this study are as follows: First, the sample size was relatively small and comprised a heterogeneous population. The assessed myelination process was, therefore, not based on a normal population. In addition, we only assessed the individual differences between MPRAGE and PETRA, and future studies will be needed to investigate the detectability of intracranial lesions on PETRA, such as ischemic, metabolic, hemorrhagic, and hamartomatous, and some neurodegenerative diseases; those were generally well-visualized on T1WI. We did not assess the utility of PETRA for potential pathologic conditions, but we believe that PETRA could visualize good imaging contrast for neuropathology. On the other hand, detailed morphologic evaluation on PETRA may need more radial spokes for k -space data acquisition to avoid image blurring. Although a relatively wide age range was included in this study, we only included patients who needed sedating agents. Consequently, it was a large population of relatively small children. Thus, this can introduce a selection bias. Sec-

ond, the qualitative analysis was performed in patients older than 7 months of age because in infants and small children, it was difficult to put the ROI in areas where the myelination showed less progression. Therefore, we only assessed myelination qualitatively for children 7 months of age and younger. In addition, image noise was not assessed because of the differences in the reconstruction methods used for MPRAGE and PETRA.

CONCLUSIONS

Compared with MPRAGE, the use of PETRA generally achieved better objective imaging quality without a difference in subjective image quality. In addition, PETRA produced near-silent scanning conditions. Therefore, PETRA can substitute for MPRAGE when scanning pediatric patients.

ACKNOWLEDGMENTS

The authors would like to thank Dr David M. Grodzki, Magnetic Resonance, Siemens AG, Erlangen, Germany, and Mr Yasutake Muramoto, Department of Radiology, Kanagawa Children's Medical Center, for their technical advice.

Disclosures: Noriko Aida—UNRELATED: Grants/Grants Pending: The Japan Society for the Promotion of Science Grants-in-Aid for Scientific Research grant No. 26461843. Katsutoshi Murata—UNRELATED: Employment: Siemens Healthcare K.K.

REFERENCES

1. Tochchio S, Kline-Fath B, Kanal E, et al. **MRI evaluation and safety in the developing brain.** *Semin Perinatol* 2015;39:73–104 CrossRef Medline
2. Leach JL, Holland SK. **Functional MRI in children: clinical and research applications.** *Pediatr Radiol* 2010;40:31–49 CrossRef Medline
3. Arlachov Y, Ganatra RH. **Sedation/anaesthesia in paediatric radiology.** *Br J Radiol* 2012;85:e1018–31 CrossRef Medline
4. Slovis TL. **Sedation and anesthesia issues in pediatric imaging.** *Pediatr Radiol* 2011;41(suppl 2):514–16 CrossRef Medline
5. Starkey E, Sammons HM. **Sedation for radiological imaging.** *Arch Dis Child Educ Pract Ed* 2011;96:101–06 CrossRef Medline
6. Katsunuma A, Takamori H, Sakakura Y, et al. **Quiet MRI with novel acoustic noise reduction.** *MAGMA* 2002;13:139–44 CrossRef Medline
7. Segbers M, Rizzo Sierra CV, Duifhuis H, et al. **Shaping and timing gradient pulses to reduce MRI acoustic noise.** *Magn Reson Med* 2010;64:546–53 CrossRef Medline
8. Weiger M, Pruessmann KP, Hennel F. **MRI with zero echo time: hard versus sweep pulse excitation.** *Magn Reson Med* 2011;66:379–89 CrossRef Medline
9. Idiyatullin D, Corum C, Park JY, et al. **Fast and quiet MRI using a swept radiofrequency.** *J Magn Reson* 2006;181:342–49 CrossRef Medline
10. Grodzki DM, Jakob PM, Heismann B. **Ultrashort echo time imaging using pointwise encoding time reduction with radial acquisition (PETRA).** *Magn Reson Med* 2012;67:510–18 CrossRef Medline
11. Ida M, Wakayama T, Nielsen ML, et al. **Quiet T1-weighted imaging using PETRA: initial clinical evaluation in intracranial tumor patients.** *J Magn Reson Imaging* 2015;41:447–53 CrossRef Medline
12. Dournes G, Grodzki D, Macey J, et al. **Quiet submillimeter MR imaging of the lung is feasible with a PETRA sequence at 1.5 T.** *Radiology* 2015;276:258–65 CrossRef Medline
13. Williams LA, Gelman N, Picot PA, et al. **Neonatal brain: regional variability of in vivo MR imaging relaxation rates at 3.0 T—initial experience.** *Radiology* 2005;235:595–603 CrossRef Medline
14. Gelman N, Ewing JR, Gorell JM, et al. **Interregional variation of longitudinal relaxation rates in human brain at 3.0 T: relation to estimated iron and water contents.** *Magn Reson Med* 2001;45:71–79 Medline
15. Landis JR, Koch GG. **The measurement of observer agreement for categorical data.** *Biometrics* 1977;33:159–74 CrossRef Medline
16. Counsell SJ, Maalouf EF, Fletcher AM, et al. **MR imaging assessment of myelination in the very preterm brain.** *AJNR Am J Neuroradiol* 2002;23:872–81 Medline
17. Tachibana Y, Niwa T, Kwee TC, et al. **Effective performance of T(1)-weighted FLAIR imaging with BLADE in pediatric brains.** *Magn Reson Med Sci* 2012;11:17–26 CrossRef Medline
18. Sarikaya B, McKinney AM, Spilseth B, et al. **Comparison of spin-echo T1- and T2-weighted and gradient-echo T1-weighted images at 3T in evaluating very preterm neonates at term-equivalent age.** *AJNR Am J Neuroradiol* 2013;34:1098–103 CrossRef Medline
19. Tortora D, Panara V, Mattei PA, et al. **Comparing 3T T1-weighted sequences in identifying hyperintense punctate lesions in preterm neonates.** *AJNR Am J Neuroradiol* 2015;36:581–86 CrossRef Medline
20. Busse RF, Riederer SJ. **Steady-state preparation for spoiled gradient echo imaging.** *Magn Reson Med* 2001;45:653–61 CrossRef Medline
21. Pipe JG, Menon P. **Sampling density compensation in MRI: rationale and an iterative numerical solution.** *Magn Reson Med* 1999;41:179–86 Medline
22. Pipe JG. **Reconstructing MR images from undersampled data: data-weighting considerations.** *Magn Reson Med* 2000;43:867–75 Medline

Cranial Ultrasonography in Infantile Encephalitic Beriberi: A Useful First-Line Imaging Tool for Screening and Diagnosis in Suspected Cases

 N.A. Wani,  U.A. Qureshi,  K. Ahmad, and  N.A. Choh

ABSTRACT

BACKGROUND AND PURPOSE: Brain imaging is central to the diagnosis of infantile encephalitic beriberi. Because cranial sonography findings have not been described in infantile encephalitic beriberi, our aim was to investigate its role in the diagnosis of this condition.

MATERIALS AND METHODS: We performed a retrospective review of head sonography of infants (admitted between November 1, 2014, and March 31, 2015) who presented with encephalopathy. Cranial ultrasonography scans were studied for the alteration of echogenicity of the basal ganglia.

RESULTS: Of the 145 consecutive infants who presented with encephalopathy, 58 had thiamine-responsive encephalopathy (infantile encephalitic beriberi) and 87 had encephalopathy due to other causes. Forty-eight of 145 infants with encephalopathy showed hyperechoic basal ganglia. A hyperechoic appearance of the basal ganglia on cranial ultrasonography was found to have a sensitivity of 71% (41/58) and a specificity of 92% (80/87) in diagnosing infantile encephalitic beriberi. The sensitivity of cranial sonography increased with age. It was a maximum of 93% (14/15) in the 5 months and older age group. Specificity was a maximum of 100% (18/18) in infants older than 5 months of age. Sensitivity was maximum in Wernicke encephalopathy at 90% (18/20) and least in the acidotic form at 43% (10/23). Follow-up showed gradual normalization of the hyperechoic appearance of the basal ganglia during 8 weeks in 26/41 (63%), with mild atrophy of the basal ganglia in 6/41 (15%).

CONCLUSIONS: Hyperechogenicity of the basal ganglia on cranial ultrasonography is a sensitive finding for the diagnosis of infantile encephalitic beriberi in infants who present with Wernicke encephalopathy.

ABBREVIATIONS: cUS = cranial ultrasonography; IEBB = infantile encephalitic beriberi

Thiamine deficiency disease is called beriberi and may have neurologic (dry beriberi) or cardiovascular (wet beriberi) manifestations. Thiamine deficiency is found in alcoholics and rice-eating populations consuming polished rice.¹ Wernicke encephalopathy, characterized by ataxia, confusional state, and ocular motor abnormalities, is an acute neurologic manifestation of beriberi that can be seen in adults and children. Neurologic manifestations of thiamine deficiency in infants are nonspecific and include encephalopathy, vomiting, nystagmus, ptosis, moaning, and convulsions—infantile encephalitic beriberi (IEBB). Infants may develop beriberi, including its encephalitic form, if they are

exclusively breastfeeding from thiamine-deficient mothers. Rapid diagnosis of infantile encephalitic beriberi is essential to prevent mortality and neurologic sequelae. Imaging can facilitate early diagnosis of IEBB.¹⁻⁴

The infant brain can be imaged with CT, MR imaging, and cranial ultrasonography (cUS). Use of CT for imaging the infant brain is associated with the radiation-related risks due to use of ionizing radiation and iodinated contrast agents. Apart from these risks, limited spatial resolution of CT for imaging of the infant brain is an additional disadvantage.⁵⁻⁸ Neuroimaging with MR imaging is considered optimal for the diagnosis of IEBB.^{3,4} However, MR imaging requires transfer of sick infants from the intensive care unit to the imaging center and frequently requires sedation before imaging.⁶⁻⁹ In addition, MR imaging may not be available to all in developing countries. Cranial ultrasonography is free from radiation hazards, less expensive than MR imaging, and often widely available, even in the developing countries. cUS is portable and can be performed rapidly at the bedside.^{5,9,10} cUS can be repeated easily if and when deemed necessary without

Received November 14, 2015; accepted after revision January 20, 2016.

From the Departments of Pediatric Radiology (N.A.W.) and Pediatrics (U.A.Q., K.A.), Government Medical College, Srinagar, Jammu and Kashmir, India; and Department of Radiology (N.A.C.), SheriKashmir Institute of Medical Sciences, Srinagar, Jammu and Kashmir, India.

Please address correspondence to Nisar A. Wani, MD, Department of Pediatric Radiology, Govt GB Pant Children Hospital Sonwar, Srinagar Pin-190016, Jammu and Kashmir, India; e-mail: ahmad77chinar@gmail.com

<http://dx.doi.org/10.3174/ajnr.A4756>

compromising patient safety. MR imaging findings have been documented in IEBB, but there is no previous study describing cranial sonography findings in IEBB, to our knowledge. The present study aimed to evaluate the role of cUS in the diagnosis of IEBB.

MATERIALS AND METHODS

A retrospective review of cranial ultrasonography of all infants who were admitted between November 1, 2014, and March 31, 2015 with encephalopathy at our institution was performed. The study was approved by the institutional review board. A waiver of informed consent was granted for this retrospective analysis.

Encephalopathy had been diagnosed by the presence of 2 of the following symptoms: altered state of consciousness, seizures, and altered personality or cognition. All of these children had been investigated for the cause of encephalopathy. Laboratory investigations included complete blood count, serum biochemistry and electrolyte levels, blood sugar levels, and blood gases. CSF examination had been done at the discretion of the treating physician. Blood ammonia levels, tandem mass spectrometry, and urine gas chromatography–mass spectrometry had been performed to rule out inborn errors of metabolism.

Thiamine had been given at admission as a 100-mg intravenous infusion in all the infants with encephalopathy.

Infants were divided into 2 groups: 1) those who had encephalopathy due to thiamine deficiency, labeled IEBB; and 2) those who had a diagnosis other than IEBB.

The diagnosis of thiamine deficiency had been made by a dramatic response to thiamine (in all) and low blood thiamine levels (in 7). Detailed epidemiologic, dietary, clinical, laboratory, and treatment data of these children had been obtained.

Cranial ultrasonography had been performed with the Acuson X300 scanner (Siemens Medical Solutions, Malvern, Pennsylvania) by using the anterior fontanelle as the window, by a pediatric radiologist (N.A.W.) or sonologist with 3–5 years' experience performing head sonography in infants. A multifrequency (3–7.5 MHz) phased array (sectoral) transducer with a small footprint had been used for scanning the brain parenchyma in the coronal and sagittal planes. All infants had the first cUS at initial presentation. Repeat scans were performed 2–3 weeks after the initial presentation and serially thereafter at intervals of 2–4 weeks.

Archived cUS studies were independently interpreted in retrospect by 2 radiologists with 5 and 8 years' experience in interpreting head sonography. The radiologists who interpreted the cUS studies were blinded to the clinical diagnosis and reviewed sonograms for normal anatomy and focal or diffuse altered echogenicity of brain parenchyma, with particular focus on deep gray matter structures. The basal ganglia were labeled as hyperechoic when their echogenicity was comparable with that of the choroid plexus or slightly less; and they were labeled mildly hyperechoic when the echogenicity was more than that of gray matter and comparable with that of periventricular white matter. The presence of ventricular dilation and any space-occupying lesion was sought on cUS. Initial findings were serially assessed in the follow-up studies.

Statistical Analysis

The accuracy of cUS was assessed by calculating sensitivity and specificity. Comparison of proportions and percentages was performed by applying χ^2 and Fisher exact tests. All significant variables on univariate analysis were subjected to multivariate analysis. Agreement between 2 radiologists was calculated with linear weighted κ by using VassarStats: Website for Statistical Computation (<http://www.vassarstats.net/>). Ninety-five percent confidence intervals were calculated. Statistical software, SPSS 20 (IBM, Armonk, New York), was used for all other data analysis. *P* values < .05 were considered significant.

RESULTS

One hundred forty-five consecutive infants with encephalopathy were included in the study. Fifty-eight of 145 (40%) had IEBB, and 87/145 (60%) had encephalopathy due to causes other than IEBB.

Forty-one infants (41/58) with IEBB had positive findings on cUS. There were 13 male and 28 female infants in the age range of 35 days to 9 months (mean age, 3.5 months). Consanguinity was present in 4, and sibling death due to similar illness, in 2. All the infants were exclusively breastfed by mothers, 29/41 (71%) of whom resided in rural areas. Complementary diet (solid food introduced after 6 months) was not started in 12 infants despite being at least 6 months of age. Maternal staple diet consisted of polished rice consumed after washing it multiple times. As a part of cultural practice, 28/41 (68%) lactating mothers consumed a diet that was restricted to soup derived from boiling meat with rice. We noticed 3 patterns: 1- to 2-month-old infants (16/41) presented with lactic acidosis. Infants older than 5 months of age (11/41) presented with Wernicke encephalopathy. The intermediate group (14/41) had mixed features of acidosis and Wernicke encephalopathy.

Clinical and laboratory features of infants in the IEBB group with positive findings and negative findings on cUS are compared in the Table. There was no statistically significant difference in individual clinical features between the 2 subgroups.

Forty-one of 58 (71%) infants with IEBB had symmetric hyperechoic basal ganglia on cUS, and 17/58 (29%) had normal findings on cUS. Seven of 87 (8%) infants with encephalopathy due to other reasons had symmetric hyperechoic basal ganglia, and 80/87 (92%) had normal findings on cUS or findings other than hyperechoic basal ganglia (Fig 1).

Forty-eight of 145 infants with encephalopathy showed hyperechoic basal ganglia. Forty-one of 48 (85%) with hyperechoic basal ganglia had IEBB, and 17/97 (17.5%) with nonhyperechoic basal ganglia had IEBB. A hyperechoic appearance of the basal ganglia on cUS was found to have a sensitivity of 71% (41/58; 95% CI, 57.99%–80.82%) and a specificity of 92% (80/87; 95% CI, 84.31%–96.05%) in diagnosing IEBB. The sensitivity of head ultrasonography increased with age. It was 55% (16/29; 95% CI, 37.55%–71.59%), 78% (11/14; 95% CI, 52.41%–92.43%), and 93% (14/15; 95% CI, 70.18%–98.81%) in the age groups of 1–2 months, 3–4 months, and 5 months and older, respectively. The specificity of head ultrasonography was 91% (40/44; 95% CI, 78.8%–96.4%) in the age group of 1–2 months, 88% (22/25; 95% CI, 70.9%–95.8%) in the age group of 3–4 months, and 100%

Clinical features of infants with IEBB with hyperechoic basal ganglia ($n = 41$) and normal basal ganglia ($n = 17$) on HUS, with univariate analysis showing the relationship between different variables and the presence of hyperechoic basal ganglia on HUS

	Hyperechoic BG (No.) (%)	Normal BG (No.) (%)	P Value
Age			
1–2 mo	16 (39%)	13 (76%)	.019
3–4 mo	11 (27%)	3 (18%)	
≥ 5 mo	14 (34%)	1 (6%)	
Sex			
Male	13 (32%)	7 (41%)	.551
Female	28 (68%)	10 (59%)	
Clinical symptom complex			
WE	18 (44%)	2 (12%)	.001
Mixed	13 (32%)	2 (12%)	
Acidosis	10 (24%)	13 (76%)	
Clinical features			
Systemic			
Fever	11 (27%)	3 (18%)	.523
Vomiting/reflux	21 (51%)	12 (70%)	.247
Diarrhea	5 (12%)	3 (18%)	.681
Decreased feeding	16 (39%)	5 (29%)	.560
Constipation	1 (2%)	0 (0%)	>.999
CNS			
Altered sensorium	41 (100%)	17 (100%)	
Irritability	22 (43)	12 (70%)	.260
Lethargy	8 (19%)	2 (12%)	.707
Moaning	29 (71%)	14 (82%)	.514
Vacant stare	16 (39%)	3 (18%)	.137
Ptosis	18 (44%)	2 (12%)	.032
Divergent squint	13 (32%)	2 (12%)	.188
Gross motor delay	2 (5%)	0 (0%)	>.999
Motor regression	1 (2%)	0 (0%)	>.999
Seizures	15 (36%)	3 (18%)	.217
Tonic posturing	10 (24%)	3 (18%)	.736
Hypotonia	2 (5%)	0 (0%)	>.999
CVS			
Shock	19 (46%)	14 (82%)	.019
Tachycardia	18 (44%)	15 (88%)	.003
Metabolic			
Acidotic breathing	10 (24%)	13 (76%)	<.001

Note:—HUS indicates head ultrasonography; CVS, cardiovascular system; BG, basal ganglia; WE, Wernicke encephalopathy.

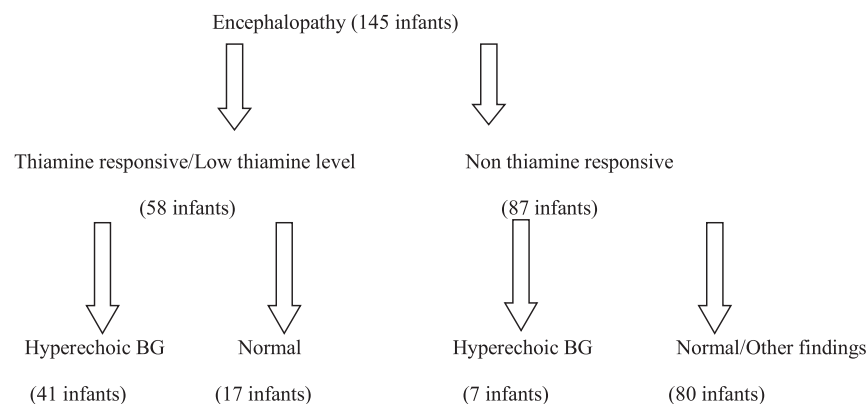


FIG 1. Breakdown of infants with encephalopathy. “Hyperechoic BG” indicates cUS finding of increased echogenicity of the bilateral basal ganglia. “Normal” indicates cUS showing normal brain parenchyma and basal ganglia echogenicity. “Other findings” indicates cUS abnormalities other than hyperechoic basal ganglia-like hydrocephalus or a mass lesion.

(18/18; 95% CI, 78.47%–100%) in infants older than 5 months of age. The sensitivity also varied with clinical presentation. The sensitivity was maximum in Wernicke encephalopathy, 90% (18/20; 95% CI, 69.9%–97.2%), and least in acidotic forms, 43% (10/23; 95% CI, 25.63%–63.19%). The specificity was similar, 92% (80/87; 95% CI, 84.31%–96.05%) in Wernicke encephalopathy, mixed and acidotic forms.

Univariate analysis (Table) showed that in IEBB, infants in the upper age groups, presenting with Wernicke encephalopathy and without shock, had a statistically significant presence of hyperechoic basal ganglia. Sex, standard base excess, and seizures were not significantly associated with this condition.

Multivariate logistic regression analysis showed that clinical presentation was an independent risk factor for positive findings of hyperechoic basal ganglia on cranial sonography (Wernicke encephalopathy: OR = 9.810; 95% CI, 1.085–88.687; mixed: OR = 7.560; 95% CI, 1.113–51.335). Shock was not an independent factor in depicting the positive findings on sonography (OR = 0.778; 95% CI, 0.110–5.643).

cUS Imaging

The basal ganglia showed a bilaterally symmetric hyperechoic appearance in 41 infants with IEBB in the initial scan at presentation. Hyperechoic putamina (Figs 2A and 3A, -B) were seen in 41/41 (100%) infants. The caudate nuclei appeared hyperechoic (Figs 3A, -B and 4A, -B) in 31/41 (76%); an isolated hyperechoic appearance of the bilateral putamen was seen in 10/41 (24%). Slight hyperechogenicity of the bilateral median thalami (Fig 5) was seen in 3/41 (7%). None of the scans showed any midline shift or mass lesion/hemorrhage. Seven infants with encephalopathy other than IEBB had hyperechoic basal ganglia on head ultrasonography. Bilateral putamina were hyperechoic in 7/7 (100%); caudate nuclei, in 5/7 (71%); and thalami, in 4/7 (57%).

Mild increased echogenicity of the basal ganglia was noted in infants 1–2 months of age, comprising 16/41 (39%) cases with positive findings of IEBB on cUS. Children older than 2 months of age, comprising 25/41 (61%) cases positive for IEBB, showed a distinctly hyperechoic appearance of the basal ganglia. Twelve of 16 (75%) infants younger than 2 months of age showed hyperechoic putamina and caudate nuclei, and 4/16 (25%) had hyperechoic putamina only. Nineteen of 25 (76%) infants older than 2 months of age showed hyperechoic putamina and caudate nuclei, and 6/25 (24%) had hyperechoic putamina only. There was no correlation between the age of the children and the relative involvement of the putamen and caudate nucleus ($\chi^2 = 0.09$, $P = .764$).

Follow-up scans showed regression of basal ganglia hyperechogenicity (Fig 2B) after thiamine administration, with almost normal appearance of basal ganglia in 2–4 weeks in 18/41; in 4–8 weeks, an additional 8/23 children showed resolution of basal ganglia hyperechogenicity, totaling 26/41 (63%) infants. Twenty-two of 26 infants with resolu-

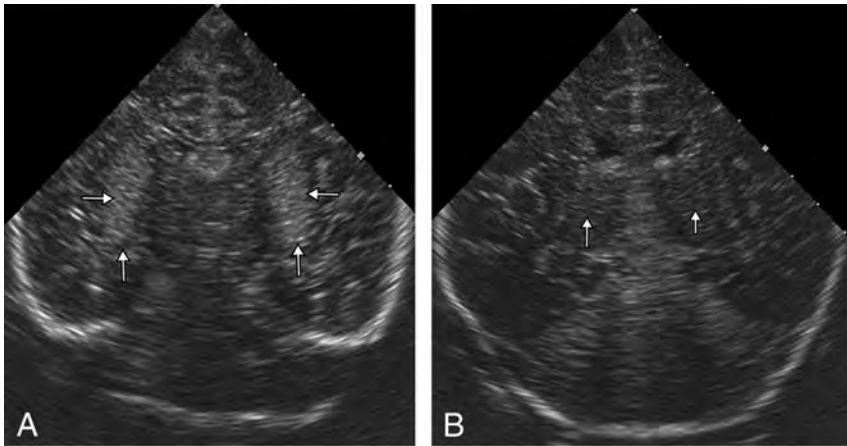


FIG 2. A 3-month-old girl with encephalopathy, reflux, and ptosis due to IEBB. *A*, Coronal plane cUS shows a bilaterally symmetric hyperechoic putamen (arrows). *B*, Follow-up cUS (after thiamine supplementation) in the coronal plane 6 weeks later shows very minimal hyperechogenicity in the putamen (arrows). Hyperechogenicity has regressed compared with the initial cUS (*A*).

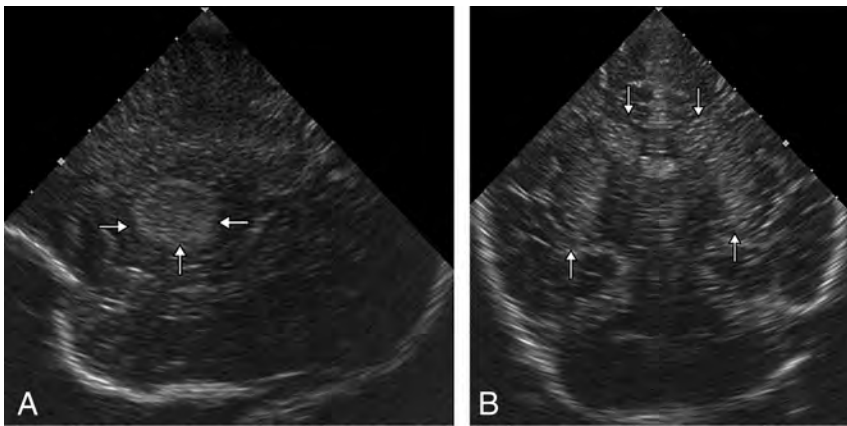


FIG 3. A 3-month-old girl with encephalopathy, reflux, and ptosis due to IEBB. *A*, Sagittal plane cUS shows a hyperechoic putamen (arrows). *B*, Coronal plane cUS shows a bilaterally symmetric hyperechoic caudate nucleus (downward arrows) and putamen (upward arrows).

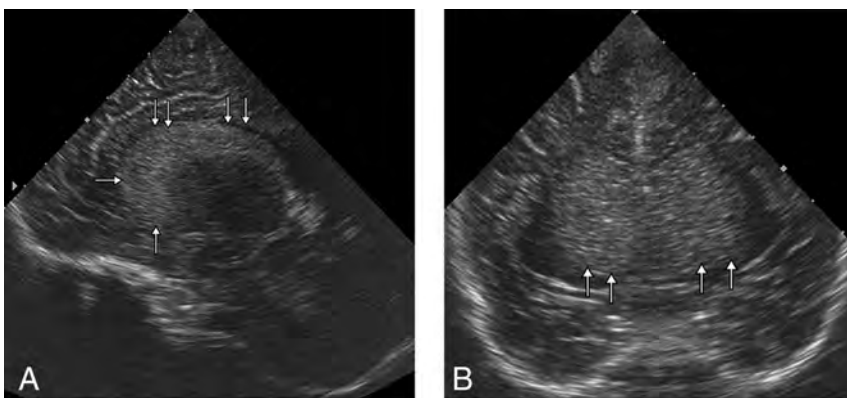


FIG 4. A 4-month-old boy with encephalopathy, moaning, and seizures diagnosed as IEBB. *A*, Sagittal plane cUS shows a curvilinear hyperechoic structure representing the caudate nucleus (arrows). *B*, Coronal plane cUS shows a bilateral symmetric hyperechoic caudate head (arrows).

tion of basal ganglia hyperechogenicity achieved developmental milestones at an appropriate age, and 4/26 showed motor delay at follow-up. Fifteen of 41 (37%) infants did not have normalization of basal ganglia echogenicity at follow-up; 4/15 were followed for

lesions and are never seen in the absence of putaminal signal changes in IEBB.^{2,4}

Ultrasonography can be used for imaging of the brain in infants, without risk of radiation exposure, and is readily available.

<4 weeks. Ten children (10/15) with persistent basal ganglia hyperechogenicity showed delayed developmental milestones. Mild ventricular dilation of the lateral ventricles was seen in 6/41 (15%). Three children (3/6) showed ventricular dilation at 2–4 weeks, and 3 (3/6) showed ventriculomegaly after 4 weeks.

The symptomatic response to thiamine in IEBB was dramatic with moaning and tachycardia subsiding within 4 hours, and vacant stare and ptosis, in 6 hours. Lethargy persisted for 24 hours. In patients with developmental delay, milestones and tone were slow to recover during 4–14 weeks. Normal breastfeeding was achieved in a mean of 6 hours. The mean duration of the hospital stay was 3.25 days. At discharge, patients were put on 6 weeks of daily thiamine, with dietary advice to the mothers.

DISCUSSION

Early and rapid diagnosis of IEBB is essential so that thiamine is administered in time to prevent permanent brain damage and neurologic morbidity in the child.^{11,12} Thiamine levels can be determined in body fluids, but the procedure is time-consuming and may not be available to all. MR imaging of the brain is considered optimal for a rapid imaging-based diagnosis of IEBB.^{3,4,13}

Several studies and case reports have documented abnormal findings on brain MR imaging in infants with IEBB.^{3,4,13} MR imaging in IEBB shows signal-intensity changes in the basal ganglia and cerebral cortex universally, besides changes in the medial thalami, periaqueductal gray matter, and mammillary bodies. Extra-basal ganglia changes (in the brain stem and mammillary bodies) are reported to be less frequent in the IEBB seen in the developing countries where symmetric T2WI hyperintense signal intensity involving the putamina alone or along with the caudate nuclei may be considered suggestive of the diagnosis in the presence of relevant clinical features. Altered-signal-intensity lesions in the thalami and cerebral cortex are seen in a small proportion of children with IEBB.^{2,4} These lesions are always seen in the presence of basal ganglia

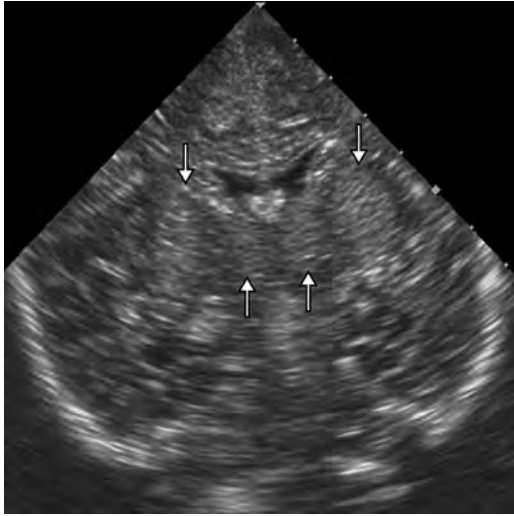


FIG 5. A 3-month-old boy with encephalopathy, ptosis, moaning, and reflux due to IEBB. Coronal plane cUS shows bilaterally symmetric hyperechoic putamen (*downward arrows*) and mildly hyperechoic thalami (*upward arrows*).

Cranial ultrasonography has been described as useful in conditions like hypoxic-ischemic injury and inborn errors of metabolism. However, there is no previous study describing cUS findings in IEBB, to our knowledge. This prompted us to undertake the present study.

Our study showed a hyperechoic appearance of the basal ganglia (putamen and caudate nucleus) on cUS in 71% of infants with IEBB. Putaminal hyperechogenicity was seen in all, and caudate hyperechogenicity was seen in 76% of the infants with abnormal findings on cUS. Putaminal and caudate changes on brain MR imaging are reported to be universally present in IEBB according to both Western and Indian literature.^{2,4,13} Studies from the thiamine-deficient Indian population report changes in the thalami, cerebral cortex, mammillary bodies, and brain stem in a smaller percentage of infants, always in the presence of basal ganglia lesions. We could not delineate cortical or brain stem changes in any infant, though a mild hyperechoic appearance of the thalami was seen in 7%.

We have shown, in a sizeable cohort of infants with IEBB, that cUS detects main brain parenchymal changes that support the clinical diagnosis. Although some aspects of brain parenchymal changes are only or better seen with MR imaging, most salient features of basal ganglia involvement in IEBB were easily detected with cUS. The sensitivity and specificity of cUS were high for the diagnosis of IEBB in infants older than 5 months of age with features of Wernicke encephalopathy.

Hyperechoic basal ganglia on cUS in an infant with encephalopathy, metabolic acidosis, gastroesophageal reflux, and ptosis from the lower socioeconomic strata of developing countries suggest a diagnosis of IEBB. In the absence of blood thiamine levels and the availability of MR imaging, cUS may be useful in the triage of such infants. Infants older than 5 months of age with hyperechoic basal ganglia on cUS should always receive parenteral thiamine. cUS can rule out hydrocephalus, space-occupying lesion-like hemorrhage/abscess, or extra-axial collection as the cause and should be part of routine evaluation in such infants.¹⁴⁻¹⁸ The dif-

ferential diagnosis of hyperechoic deep gray matter structures on cUS includes severe hypoxic-ischemic injury, inborn errors of metabolism, and encephalitis/congenital infection.^{5,10,19-22} Clinical features, serologic/biochemical investigations, and CSF analysis can help in making the proper diagnosis.^{2,23}

The basal ganglia are metabolically very active in children having high concentrations of mitochondria and increased glucose use. Thiamine deficiency resulting in deficient adenosine triphosphate production consequent to defective thiamine-dependent oxidative glucose metabolism preferentially manifests with changes in the basal ganglia in children.^{4,11-13} Vasogenic and cytotoxic edema has been proposed as the underlying cause of basal ganglia changes in IEBB. An edematous appearance of the basal ganglia on cUS manifests with increased echogenicity. Basal ganglia changes in IEBB have been documented as reversible with early thiamine supplementation, and failure to administer thiamine may result in permanent brain damage.^{4,11,13}

We were able to recognize basal ganglia lesions on cUS at presentation and continued with thiamine supplementation with favorable immediate clinical outcome in all. Basal ganglia hyperechogenicity was demonstrated to decrease slowly with thiamine, reverting to a normal appearance in 6–8 weeks in 63% (26/41). In 37% (15/41) of children, the basal ganglia showed persistent hyperechogenicity, and 15% (6/41) showed some atrophy of the basal ganglia with ventriculomegaly in the follow-up.

Limitations

The low sensitivity of hyperechoic basal ganglia on cUS in infants younger than 2 months of age (55%) and in infants who present with clinical acidosis (43%) prevents its use as a screening tool for the diagnosis of IEBB in these patients. The suboptimal and inadequate visualization of changes in the thalami, brain stem, and mammillary bodies may limit the usefulness of cUS in cases in which changes are seen predominantly in these structures. An inadequate acoustic window through a closed anterior fontanelle makes cUS difficult in infants with craniosynostosis. Closure of the anterior fontanelle with time also limits the duration of long-term follow-up with cUS.

CONCLUSIONS

cUS is a preferable initial imaging technique for the infant brain because it is cheap and readily available, even in developing countries; is safe from radiation risk; and does not need transfer of infants and sedation before examination. Access across the anterior fontanelle is optimal in the age group afflicted with IEBB. Hyperechogenicity of the basal ganglia on cUS is a sensitive finding (90%) for the diagnosis of IEBB in infants who present with Wernicke encephalopathy. Sensitivity is, however, low in those presenting with clinical acidosis (43%). In the appropriate clinical settings, symmetric hyperechoic basal ganglia on cUS in an infant are also highly specific for the diagnosis of IEBB.

REFERENCES

1. Soukaloun D, Kounnavong S, Pengdy B, et al. **Dietary and socioeconomic factors associated with beriberi in breastfed Lao infants.** *Ann Trop Paediatr* 2003;23:181–86 Medline
2. Rao SN, Mani S, Madap K, et al. **High prevalence of infantile enceph-**
AJNR Am J Neuroradiol 37:1535–40 Aug 2016 www.ajnr.org **1539**

- alitic beriberi with overlapping features of Leigh's disease. *J Trop Pediatr* 2008;54:328–32 CrossRef Medline
3. Zuccoli G, Siddiqui N, Bailey A, et al. **Neuroimaging findings in pediatric Wernicke encephalopathy: a review.** *Neuroradiology* 2010; 52:523–29 CrossRef Medline
 4. Wani NA, Qureshi UA, Jehangir M, et al. **Infantile encephalitic beriberi: magnetic resonance imaging findings.** *Pediatr Radiol* 2016; 46:96–103 CrossRef Medline
 5. Leijser LM, de Vries LS, Rutherford MA, et al. **Cranial ultrasound in metabolic disorders presenting in the neonatal period: characteristic features and comparison with MR imaging.** *AJNR Am J Neuroradiol* 2007;28:1223–31 CrossRef Medline
 6. Lowe LH, Bailey Z. **State-of-the-art cranial sonography, part 1: modern techniques and image interpretation.** *AJR Am J Roentgenol* 2011;196:1028–33 CrossRef Medline
 7. Wezel-Meijler Gv, de Vries LS. **Cranial ultrasound: optimizing utility in the NICU.** *Curr Pediatr Rev* 2014;10:16–27 CrossRef Medline
 8. Hagmann CF, Robertson NJ, Acolet D, et al. **Cranial ultrasound findings in well newborn Ugandan infants.** *Arch Dis Child Fetal Neonatal Ed* 2010;9:F338–44 CrossRef Medline
 9. Epelman M, Daneman A, Chauvin N, et al. **Head ultrasound and MR imaging in the evaluation of neonatal encephalopathy: competitive or complementary imaging studies?** *Magn Reson Imaging Clin N Am* 2012;20:93–115 CrossRef Medline
 10. Yamagata T, Yano S, Okabe I, et al. **Ultrasonography and magnetic resonance imaging in Leigh disease.** *Pediatr Neurol* 1990;6:326–29 CrossRef Medline
 11. Mimouni-Bloch A, Goldberg-Stern H, Strausberg R, et al. **Thiamine deficiency in infancy: long-term follow-up.** *Pediatr Neurol* 2014;51: 311–16 CrossRef Medline
 12. Crook MA, Sriram K. **Thiamine deficiency: the importance of recognition and prompt management.** *Nutrition* 2014;30:953–54 CrossRef Medline
 13. Kornreich L, Bron-Harlev E, Hoffmann C, et al. **Thiamine deficiency in infants: MR findings in the brain.** *AJNR Am J Neuroradiol* 2005; 26:1668–74 Medline
 14. Yikilmaz A, Taylor GA. **Sonographic findings in bacterial meningitis in neonates and young infants.** *Pediatr Radiol* 2008;38:129–37 CrossRef Medline
 15. van Leyen K, Klötzsch C, Harrer JU. **Brain tumor imaging with transcranial sonography: state of the art and review of the literature.** *Ultraschall Med* 2011;32:572–81 CrossRef Medline
 16. Fischer AQ. **The use of ultrasound in evaluating neurologic diseases of childhood.** *Neurol Clin* 1990;8:759–74 Medline
 17. Babcock DS. **Sonography of the brain in infants: role in evaluating neurologic abnormalities.** *AJR Am J Roentgenol* 1995;165:417–23 CrossRef Medline
 18. Simanovsky N, Taylor GA. **Sonography of brain tumors in infants and young children.** *Pediatr Radiol* 2001;31:392–98 CrossRef Medline
 19. Fariello G, Dionisi-Vici C, Orazi C, et al. **Cranial ultrasonography in maple syrup urine disease.** *AJNR Am J Neuroradiol* 1996;17:311–15 Medline
 20. Forstner R, Hoffmann GF, Gassner I, et al. **Glutaric aciduria type I: ultrasonographic demonstration of early signs.** *Pediatr Radiol* 1999; 29:138–43 CrossRef Medline
 21. de Vries LS, Gunardi H, Barth PG, et al. **The spectrum of cranial ultrasound and magnetic resonance imaging abnormalities in congenital cytomegalovirus infection.** *Neuropediatrics* 2004;35:113–19 CrossRef Medline
 22. de Vries LS, Verboon-Macielek MA, Cowan FM, et al. **The role of cranial ultrasound and magnetic resonance imaging in the diagnosis of infections of the central nervous system.** *Early Hum Dev* 2006; 82:819–25 CrossRef Medline
 23. Qureshi UA, Wani NA, Ahmad K, et al. **Infantile Wernicke's encephalopathy.** *Arch Dis Child* 2015;100:648 CrossRef Medline

Spectrum of Clinical and Associated MR Imaging Findings in Children with Olfactory Anomalies

T.N. Booth and N.K. Rollins

ABSTRACT

BACKGROUND AND PURPOSE: The olfactory apparatus, consisting of the bulb and tract, is readily identifiable on MR imaging. Anomalous development of the olfactory apparatus may be the harbinger of anomalies of the secondary olfactory cortex and associated structures. We report a large single-site series of associated MR imaging findings in patients with olfactory anomalies.

MATERIALS AND METHODS: A retrospective search of radiologic reports (2010 through 2014) was performed by using the keyword “olfactory”; MR imaging studies were reviewed for olfactory anomalies and intracranial and skull base malformations. Medical records were reviewed for clinical symptoms, neuroendocrine dysfunction, syndromic associations, and genetics.

RESULTS: We identified 41 patients with olfactory anomalies (range, 0.03–18 years of age; M/F ratio, 19:22); olfactory anomalies were bilateral in 31 of 41 patients (76%) and absent olfactory bulbs and olfactory tracts were found in 56 of 82 (68%). Developmental delay was found in 24 (59%), and seizures, in 14 (34%). Pituitary dysfunction was present in 14 (34%), 8 had panhypopituitarism, and 2 had isolated hypogonadotropic hypogonadism. CNS anomalies, seen in 95% of patients, included hippocampal dysplasia in 26, cortical malformations in 15, malformed corpus callosum in 10, and optic pathway hypoplasia in 12. Infratentorial anomalies were seen in 15 (37%) patients and included an abnormal brain stem in 9 and an abnormal cerebellum in 3. Four patients had an abnormal membranous labyrinth. Genetic testing was performed in 23 (56%) and findings were abnormal in 11 (48%).

CONCLUSIONS: Olfactory anomalies should prompt careful screening of the brain, skull base, and the pituitary gland for additional anomalies. Genetic testing should be considered.

ABBREVIATIONS: CHARGE = Coloboma of the eye, Heart defects, Atresia of the choanae, Retardation of growth and/or development, Genital and/or urinary abnormalities (hypogonadism), Ear anomalies and/or deafness; OB = olfactory bulb; OT = olfactory tract

Olfaction involves recognition of myriad chemicals in various concentrations enabling discrimination among scents. In humans, the olfactory system provides less survival advantage than the other senses and the olfactory apparatus is proportionately much smaller than that in other mammals but is readily identifiable on routine MR imaging.¹

The olfactory system begins to form early in gestation and has multiple origins, including the olfactory placode, cranial neural crest, and the olfactory bulb (OB), which is an extension of the

telencephalon. The olfactory placode develops into the olfactory epithelium and nerves, which migrate toward the developing OB. Olfactory ensheathing cells are likely neural crest derivatives, which serve as a scaffolding for initial migration.² Adjacent to the olfactory placode is the developing adenohypophyseal placode. The OB projection neurons or olfactory tracts (OTs) innervate multiple cortical regions and are collectively referred to as the olfactory cortex. The olfactory cortex comprises the anterior olfactory nucleus, olfactory tubercle, piriform cortex, entorhinal cortex, and septal, habenular, and brain stem nuclei as well as the amygdale, hippocampus, and parahippocampal gyrus.^{2,3}

Thus, anomalies of the primary olfactory system might be associated with diverse and widespread anomalies of the remainder of the brain. Syndromes associated with malformed primary olfactory pathways include Kallmann syndrome; CHARGE syndrome (Coloboma of the eye, Heart defects, Atresia of the choanae, Retardation of growth and/or development, Genital and/or urinary abnormalities [hypogonadism], Ear anomalies and/or deafness); septo-optic dysplasia; and craniotelencephalic dyspla-

Received November 19, 2015; accepted after revision January 14, 2016.

From the Department of Radiology, Children's Medical Center of Dallas, Dallas, Texas; and Department of Radiology, University of Texas Southwestern Medical Center, Dallas, Texas.

Paper previously presented at: Annual Meeting of the American Society of Neuroradiology and the Foundation of the ASNR Symposium, April 25–30, 2015; Chicago, Illinois.

Please address correspondence to Timothy Booth, MD, Children's Medical Center of Dallas, Department of Radiology, 1935 Medical District Dr, Dallas, TX 75235; e-mail: Tim.booth@childrens.com

<http://dx.doi.org/10.3174/ajnr.A4738>

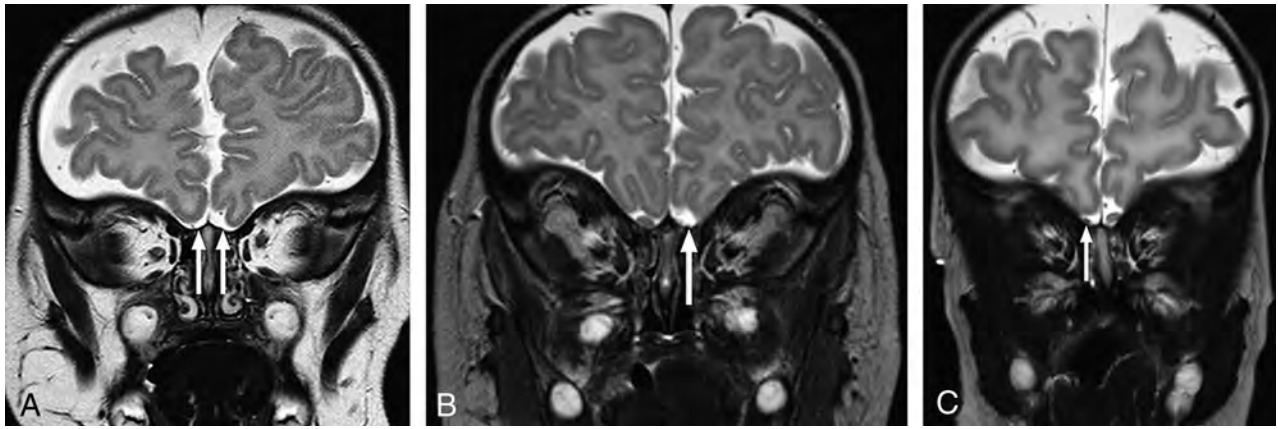


FIG 1. Coronal T2-weighted images at the expected region of the olfactory bulb demonstrating representative examples of olfactory anomalies found. *A*, There is bilateral absence of the OBs (arrows) with absence of the right olfactory sulcus. Small vessels are noted in the expected region of the olfactory OBs. No OTs are present (not shown). *B*, There is unilateral absence of the left OB (arrow) and OT (not shown). The olfactory sulcus is hypoplastic on the left. *C*, Note unilateral hypoplasia of the right OB (arrow) with a normal OT (not shown). The ipsilateral sulcus is hypoplastic.

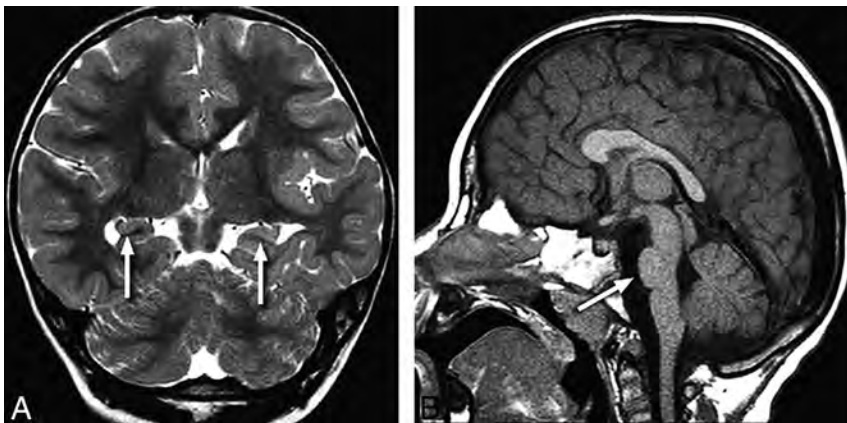


FIG 2. A 2-year-old child with seizures and bilateral absent OBs and OTs. Coronal T2-weighted image (*A*) through the mid-temporal lobes demonstrates abnormal rotation of both hippocampi with laterally positioned fimbria (arrows). Midline sagittal T1-weighted image (*B*) shows hypoplasia of the ventral pons (arrow). Genetic information was not available.

sia, malformations for which the molecular genetics are variably defined.^{3,4} We reviewed a sizable population of patients with abnormalities of the primary olfactory pathways to further categorize the clinical presentation, syndromic associations, and genetic results and expand the range of associated brain malformations and provide correlative diffusion tensor imaging and results of genetic testing.

MATERIALS AND METHODS

The study was approved by the Institutional Internal Review Board (University of Texas Southwestern Medical Center) and is Health Insurance Portability and Accountability Act–compliant. A retrospective search of radiologic reports was performed at a tertiary pediatric hospital by using the keyword “olfactory” with inclusive dates of January 2010 to December 2014. Consensus was reached about findings on MR imaging after review by 2 pediatric neuroradiologists with Certificates of Added Qualification in neuroradiology, each with ≥ 18 years’ experience.

Inclusion criteria were diagnostic-quality coronal T2WI of ≤ 4 -mm section thickness and absence or hypoplasia of the primary olfactory pathways. Patients with regional masses or paren-

chymal destruction were excluded. The medical record was reviewed for clinical presentation, clinical and laboratory evidence of neuroendocrine function, hearing loss, and additional cranial nerve dysfunction. Genetic results including chromosomal microarray, fluorescence in situ hybridization, karyotype, and any potential syndromic associations, were noted.

The OBs and OTs were qualitatively classified as normal, absent, or hypoplastic. Bulbs classified as hypoplastic lacked the typical anterior focal expansion at the level of the posterior crista galli. In cases of asymmetric OB or OT, the small side was considered abnormal.

The olfactory sulci were designated as normal, hypoplastic, absent, or dysplastic. A pattern search of supratentorial content focused on callosal morphology, the septum pellucidum, hippocampus rotation, and malformations of cortical development. The posterior fossa was evaluated for the mid- and hind brain malformations and skull base anomalies. The optic nerves, chiasm, and tracts were evaluated for hypoplasia or absence. The presence and position of the neurohypophysis were documented, along with the presence of the infundibulum. When possible, the structures of the membranous labyrinth and lower cranial nerves were evaluated. The directionally encoded color maps from diffusion imaging were reviewed in a subset of patients for anomalies of major commissural, association, and projection fibers.

RESULTS

Forty-four patients with olfactory anomalies were found by using the specified inclusion criteria. Three patients were excluded due to hydranencephaly, large craniopharyngioma, and a frontal encephalocele, resulting in a cohort of 41 patients. The age range was 0.03–18 years with a mean age of 4.5 years. The male/female ratio was 19:22.

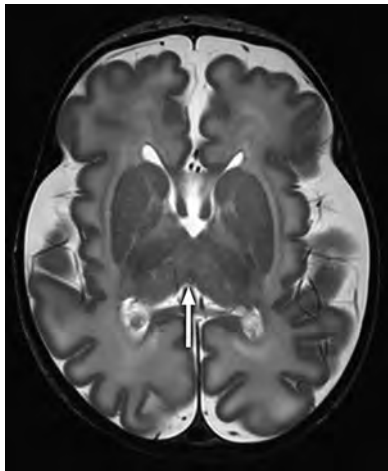


FIG 3. A 1-month-old infant with dysmorphic features and hypothyroidism and absent ONs and OTs. Axial T2-weighted image shows thalamic fusion (*arrow*) and mild diffuse undersulcation. Note multiple chromosomal abnormalities on chromosomal microarray (Table, patient 9).

Olfactory Findings

Of the 41 patients, abnormalities of the primary olfactory apparatus were bilateral in 31 (76%) and unilateral in 10 (24%). Fifty-six of 82 (68%) OBs and OTs were absent. Other olfactory findings included absent OB with OT hypoplasia in 5, hypoplastic OB with a normal OT in 5, absent OB with a normal OT in 2, hypoplastic OB and OT in 3, and a normal OB with a hypoplastic OT in 1. Sixty-one of 82 (74%) olfactory sulci were abnormal, and 38 were classified as hypoplastic. The sulcus was absent in 16 and dysplastic in 7. An abnormal sulcus was consistently associated with an abnormal OB and/or OT (Fig 1).

Associated Imaging Abnormalities

Of the 41 patients, only 2 (5%) had no associated brain anomalies; 1 patient had an absent OB and OT bilaterally, and the other had bilateral OB hypoplasia. Anomalies seen in the other 39 (95%) patients included hippocampal dysplasia in 26/41 (63%), which was bilateral in 22 patients and unilateral in 4 (Fig 2). Fifteen (37%) patients had supratentorial cortical malformations. The most common cortical malformation was polymicrogyria involving the insular cortex and was found in 8 patients. Other malformations included pachygyria in 1, subependymal heterotopias in 4, transmantle heterotopias in 2, and thalamic fusion of varying degrees in 3 patients (Figs 3 and 4). The corpus callosum was dysgenetic in 10 (24%) patients, with complete agenesis in 4 (Fig 5).

Anatomic pituitary abnormalities were present in 11 of 41 (27%) patients, which included ectopic or absent neurohypophysis. The optic nerves, chiasm, and/or tracts were absent, hypoplastic, or dysplastic in 12/41 (29%) patients, with associated septum pellucidum agenesis in 4. Ten of 12 (83%) patients with optic abnormalities had abnormalities of the pituitary gland. Additional intracranial abnormalities were found in 11 of 12 (92%) patients with optic abnormalities, most commonly peri-Sylvian polymicrogyria (Fig 6). Pituitary abnormalities were found in 2 patients without associated optic hypoplasia, both with ectopic neurohypophysis. Pituitary cysts were not considered abnormal.

Five of 6 patients with sensorineural hearing loss had high-

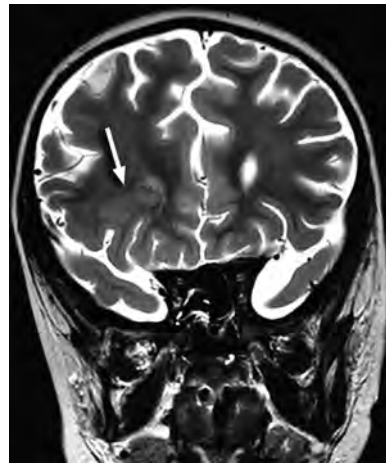


FIG 4. A 5-year-old child with seizures and absent OBs and OTs. Coronal T2-weighted image through the frontal lobes shows right transmantle cortical dysplasia (*arrow*).

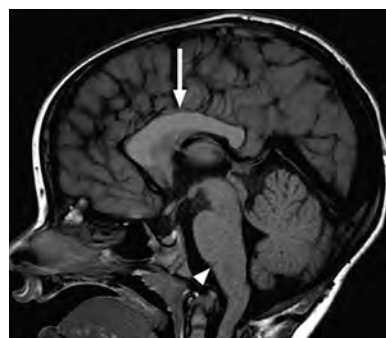


FIG 5. A 3-year-old child with developmental delay and hypoplastic OBs and OTs. Midline sagittal T1-weighted image shows a thickened body of the corpus callosum (*arrow*) and poor definition of the pontomedullary junction (*arrowhead*). The occipital cervical junction is abnormal as well. A directionally encoded fractional anisotropy map confirms anomalous supracallosal fibers (not shown), which result in the enlargement of the callosal body. Trisomy 2p was found on chromosomal microarray.

resolution MR imaging, which showed typical imaging findings of CHARGE syndrome, with absent semicircular canals and small vestibules in 3 (Fig 7). The cochlear nerve was deficient or absent in 4 ears, and the vestibular nerves were absent in 4 ears. One of these patients was found to have unilateral absence of the seventh cranial nerve as well. The 2 other patients had dilated vestibules with incorporation of the lateral semicircular canals, with 1 having enlarged cisternal segments of the fifth cranial nerve. Absent or hypoplastic third and fifth cranial nerves, both demonstrating a hypoplastic pons, were found in 2 children without sensorineural hearing loss.

Anomalies of the posterior fossa were found in 15 (37%) patients and were not usually isolated. Mid- and hind brain abnormalities included ventral pontine hypoplasia in 8 patients and an abnormal pontomedullary junction in 2 (Fig 2). Cerebellar vermal hypoplasia was seen in 3, and hemispheric dysplasia, in 1 (Fig 8). Four patients had a hypoplastic or dysplastic clivus with associated basilar invagination in 1 (Fig 7).

Diffusion tensor imaging was available in 15 patients, and findings were abnormal in 8; 2 had complete callosal agenesis.

Anomalous supracallosal fibers were seen in 1 patient with a thickened body of the corpus callosum (Fig 2). Anomalies of the brain stem on DTI included absence of the dorsal transverse pontine fibers in 3 patients and complete absence of transverse fibers in 1 patient (Fig 9). In this group, 1 patient had a normal pons by routine MR imaging but DTI showed a small corticospinal tract ipsilateral to left-sided basal ganglia hypoplasia and extensive bilateral frontal polymicrogyria.

Clinical Findings

The medical record was available for review in all patients. Twenty-four of 41 (59%) children were found to have developmental delay. Seizures were present in 14 of 41 (34%) patients, with coexisting developmental delay in 9. Neuroendocrine dysfunction was present in 14 of 41 (34%) patients, with 8 having panhypopituitarism; 2, isolated absent gonadotropin-releasing hormones; and 1, isolated growth hormone deficiency. Diabetes insipidus was present in 6 patients and was usually associated with anterior pituitary dysfunction. Pituitary hormone levels were evaluated in 18 of 41 patients. Pituitary function was considered normal in the absence of clinical indicators to suggest hormone deficiency or

normal laboratory values. Eight patients had clinical findings indicating optic pathway pathology, including optic nerve hypoplasia and/or nystagmus, and sensorineural hearing loss was present in 6. Children commonly had multiple presenting symptoms ($n = 25$, 61%). Isolated anosmia or hyposmia was noted in only 3 patients.

Six children had multiple congenital anomalies reported, most commonly congenital heart disease, and 5 had dysmorphic facies. Cleft lip/palate or a bifid crista galli was noted in 4 patients. Syndromic associations were found in 9 (22%) and included CHARGE in 3, Kallmann in 2, as well as DiGeorge, Johanson-Blizzard, Jacobsen, and PHACE (posterior fossa malformations–hemangiomas–arterial anomalies–cardiac defects–eye abnormalities–sternal cleft and supraumbilical raphe) syndrome. A history of fetal alcohol syndrome or maternal drug exposure was present in 2 patients.

Genetic evaluation was performed in 23 (56%) patients, including chromosomal microarray in 19, fluorescence in situ hybridization in 3, and karyotype in 3, with some patients undergoing multiple genetic tests. Abnormal and diverse results were found in 11 (48%) patients (Table).

DISCUSSION

A search of a large radiology report archive in a tertiary children's hospital netted 41 patients with confirmed abnormalities of the primary olfactory apparatus during a 5-year period, indicating that this malformation is uncommon. However, because detection of malformed OBs, OTs, and sulci requires coronal imaging, preferably T2, which may not be routinely performed, this spectrum of malformations is presumably more common than we appreciated. In our cohort, review of the medical records showed that most patients had no clinical symptoms referable to the olfactory pathway and usually presented with developmental delay (59%) and or seizures (34%). Neuroendocrine

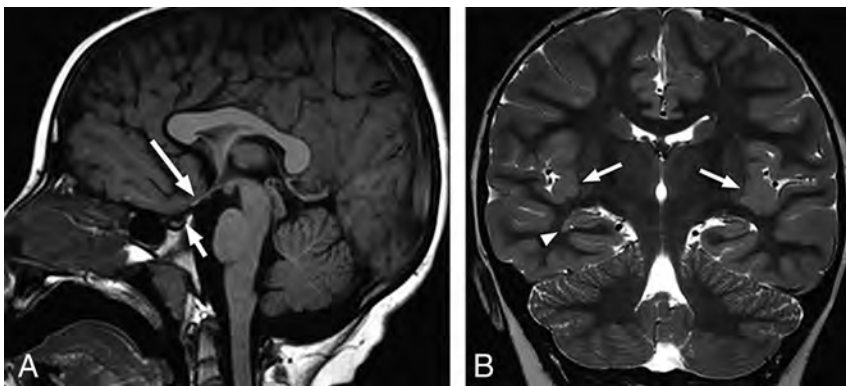


FIG 6. A 6-year-old child with blindness, nystagmus, developmental delay, and absent OBs and OTs. Midline sagittal T1-weighted image (A) demonstrates hypoplasia of the optic chiasm (*long arrow*) and a small anterior pituitary gland with an absent neurohypophysis (*short arrow*). Coronal T2-weighted image (B) through the insular cortex shows subtle nodularity of the insular cortex bilaterally, consistent with polymicrogyria (*arrows*) and a small subependymal heterotopia adjacent to the right temporal horn (*arrowhead*). Imaging and clinical findings are consistent with optic hypoplasia syndrome with the septum pellucidum present. No abnormality was present on chromosomal microarray.

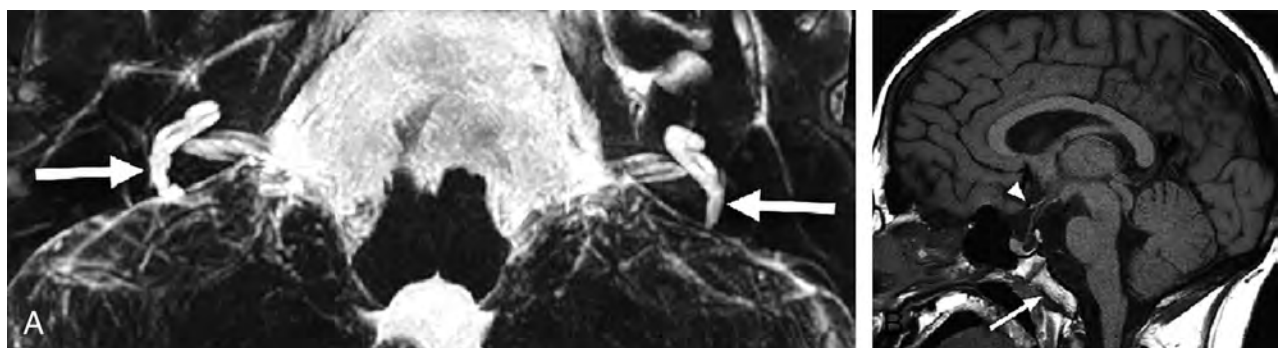


FIG 7. A 17-year-old adolescent with sensorineural hearing loss, panhypopituitarism, and absent OBs and OTs. Axial 3D T2-weighted MIP image (A) shows diminutive vestibules with vestigial posterior semicircular canals (*arrows*). No other semicircular canals are present. The cochlea is dysplastic bilaterally. Sagittal T1-weighted image (B) demonstrates an abnormal brain stem with an accentuated dorsal concavity and poor delineation of the ventral pontomedullary junction and a dysmorphic clivus (*arrow*). The optic chiasm is hypoplastic (*arrowhead*), and an anterior pituitary cyst is present. Imaging and clinical findings met criteria for CHARGE syndrome. Genetics information was not available.

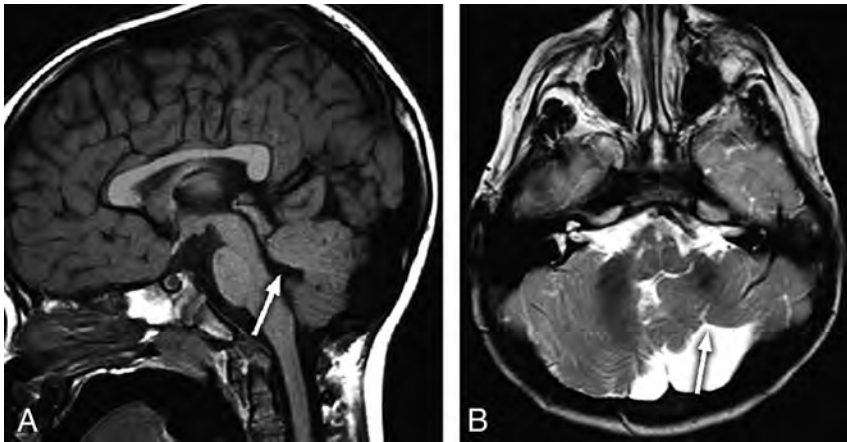


FIG 8. An 18-month-old child with developmental delay and an absent left OB and OT. Midline sagittal T1-weighted image (A) shows hypoplasia of the vermis with disorganization of the superior cerebellar lobules and deformity of the fourth ventricular roof (arrow). There is an incidental anterior pituitary cyst. Axial T2-weighted image (B) demonstrates a hypoplastic left cerebellar hemisphere with gyral disorganization (arrow).

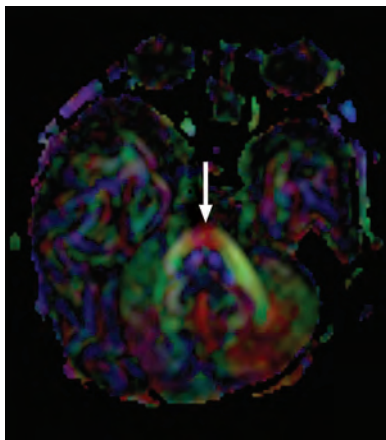


FIG 9. A 2-month-old infant with esotropia, seventh nerve palsy, and absent OBs and OTs. Axial directionally encoded fractional anisotropy map shows a single transverse pontine fiber bundle anterior to the corticospinal tracts (arrow). Anatomic images show only mild ventral pontine hypoplasia (not shown). Genetic information was not available.

dysfunction (34%) was often associated as well. The myriad intracranial malformations associated with anomalies of the OB and/or OT may be explained by the extensive known anatomic and functional connections.³ Pachygyria, polymicrogyria, subependymal heterotopias, transmantle cortical dysplasia, and thalamic fusion were all found in this group of patients. There are multiple case reports and small series of olfactory anomalies either isolated or with associated abnormalities⁵⁻⁸; however, this is largest pediatric cohort reported.

The lateral projections or stria of the OTs extends to the parahippocampal cortex, with the region likely responsible for the characterization and memorization of odors. This feature may explain the high incidence of abnormal hippocampi seen in patients with olfactory anomalies. The presence of abnormalities of the brain stem may be predicted by the anatomic connections of medial projections of the OTs that extend to multiple locations within the brain stem, including the reticular formation, salivary nuclei, dorsal nucleus of cranial nerve X, and the olfacto-hypo-

thalamo-tegmental bundle. Also, the development of the olfactory system occurs very early in gestation, suggesting the potential association with anomalies of phylogenetically older structures such as the posterior fossa.³ Potentially linking the formation of the cerebellar vermis and olfactory apparatus is the transcription factor zinc finger protein 423, which has been shown to be a requirement for patterning the development of precursors in the cerebellar vermis and olfactory apparatus in rats.⁹

In this cohort, agenesis of the corpus callosum was commonly found associated with olfactory anomalies. Abnormalities of the corpus callosum have been linked to OB absence, and this may be related to an absent induction phenomenon, with the olfactory bulbs representing a trigger for callosal development.

In fetal mice, agenesis of the corpus callosum has been shown to result from destruction of the olfactory bulb.¹⁰ *PAX6* mutations may result in agenesis of the OBs and corpus callosum as well as polymicrogyria.⁸ Also, *TUBA1A* mutations have been reported associated with absent OBs and agenesis of the corpus callosum and extensive brain anomalies, including dysplastic basal ganglia/thalami, cerebellar hypoplasia, and lissencephaly.^{11,12}

One of the first reported clinical finding associated with congenital olfactory anomalies was isolated hypogonadotropic hypogonadism with absent or incomplete puberty, usually in males, in the setting of Kallmann syndrome. The gonadotropin receptors migrate along the olfactory tracts in the early fetus, explaining the association between low follicular stimulating and luteinizing hormones and absent olfactory bulbs and tracts.^{5,13} In our cohort, a minority of patients had isolated hypogonadotropic hypogonadism consistent with Kallmann syndrome. Panhypopituitarism was by far the more common pituitary presentation. Multiple genetic loci for Kallmann syndrome have been found, including the X-linked gene *KAL1* and autosomal transmission on *FGFR1* (chromosome 8), *FGF8* (chromosome 10), *PROKR2* (chromosome 3), and *PROK2* (chromosome 20) genes.^{14,15} The *PROKR2* and *PROK2* mutations have also been reported to be the cause of isolated congenital anosmia.¹⁶ The 2 patients with suspected Kallmann syndrome did not have a chromosomal microarray.

Septo-optic dysplasia has been reported associated with olfactory bulb and tract hypoplasia.⁴ Ten of our patients with olfactory anomalies had imaging findings consistent with septo-optic dysplasia, with the entity defined in patients fulfilling 2 of 3 criteria (optic hypoplasia, pituitary dysfunction, and absent septum pellucidum). Two patients had imaging evidence of optic hypoplasia without additional criteria present. Most interesting, 6 of 10 patients with septo-optic dysplasia had a normal septum pellucidum. In the recent literature, the term “optic nerve hypoplasia syndrome” has been proposed as a more appropriate name because the development of the septum pellucidum is likely an in-

Abnormal genetic results

Patient No.	Chromosomal Abnormality	Syndrome
4	6q27 loss, 11q24.1q25 gain	None
7	7q31.32 copy number loss	None
9	10q25.1-q26.3 duplication, 11q23.3-q25 deletion, copy number neutral mosaic, allelic homozygosity 17q13.3-p11	Jacobsen
15	22q11.2 deletion	DiGeorge
18	Partial trisomy 13	None
19	Partial trisomy 18	None
21	<i>CHD7</i> mutation	CHARGE
22	9p24.3p22.3 loss, 17q25.3 gain, unbalanced translocation between chromosomes 9 and 7, trisomy distal 17q segment	None
24	Continuous duplication and terminal deletion of chromosome 6	None
30	13q12.12 gain, <i>UBR1</i> mutation	Johanson-Blizzard
39	Trisomy 2p	None

dependent process. The more consistent association with optic hypoplasia is cortical dysgenesis and hypopituitarism.^{17,18} Pituitary dysfunction was routinely identified (83%) in this subset of patients. Most interesting, a genetic link may be present between Kallmann syndrome and optic hypoplasia syndrome with loss-of-function mutations in *PROKR2* found in both.¹⁹ The association of anterior pituitary dysfunction may relate to the proximity of the developing adenohypophyseal and olfactory placodes.² Brain MR imaging protocols may benefit from the routine addition of coronal T2-weighted imaging, which would be optimal for evaluation of the olfactory apparatus and optic nerves.

Six patients had sensorineural hearing loss associated with olfactory anomalies. CHARGE syndrome was suspected 3 patients with typical inner ear malformations, including a small vestibule and absent semicircular canals. The olfactory nerves should be carefully evaluated in children with sensorineural hearing loss, especially with imaging findings consistent with CHARGE syndrome.⁶ The presence of anosmia in patients with CHARGE syndrome can be predictive of associated pituitary dysfunction; however, this association may be difficult to clinically assess in young patients and the presence of olfactory anomalies should prompt an evaluation of pituitary function.^{20,21} Panhypopituitarism was present in one of the patients with CHARGE. Basioccipital hypoplasia has also been reported to be common in CHARGE syndrome, with the *CHD7* gene thought to have a role in neural crest development.²² Two of the patients with CHARGE syndrome had an abnormal clivus, and all 3 had dysmorphic brain stems. The olfactory nerves, regional facial structures, and skull base are derived from the cranial neural crest, and the association may explain the incidence of facial and skull base abnormalities present in this patient population.² Absent semicircular canals and olfactory anomalies have also been reported in Waardenburg syndrome with *SOX10* mutations, but this syndrome is typically associated with large vestibules. *SOX10* is a regulator of neural crest development, which offers an additional link between normal development of neural crest structures and the olfactory apparatus.^{23,24}

Additional chromosomal abnormalities have been reported associated with olfactory anomalies. In a recent report, a 6q27 microdeletion was present in 2 patients with olfactory bulb aplasia.⁷ One patient in our series had this microdeletion and associated ventral pontine hypoplasia. Partial trisomy (13 and 18) has been reported with olfactory aplasia, and these mutations were found in 2 of our patients.²⁵ A 10q25 duplication was present in 1 patient and is in close proximity to the 10q24.32 gene mutation reported in the *FGF8* type of Kallmann syndrome. DiGeorge syndrome is associated with a 22q11.2 deletion, with the

findings of the fluorescence in situ hybridization analysis positive in our patient. A diverse clinical spectrum has been demonstrated with the syndrome.^{26,27} There are multiple reports linking the DiGeorge genetic abnormality to absent olfactory bulbs.^{28,29}

The patients with Johanson-Blizzard syndrome had a confirmed *UBR1* gene mutation as well as a 13q12.12 gain. The gene encodes for a protein involved in many basic biologic functions including neurogenesis and has been associated with absent OBs.³⁰ The patient with Jacobsen syndrome had an 11q23.3 deletion and additional genetic abnormalities. Patients typically have facial dysmorphism, thrombocytopenia, and multiple malformations that include the CNS. Pachygyria, subependymal heterotopias, ventriculomegaly, and agenesis of the corpus callosum have been reported.^{31,32} Our patient had vermian hypoplasia, thalamic fusion, and optic hypoplasia. More than 40% of the 856 olfactory receptor genes are located along chromosome 11, possibly explaining the association, but to our knowledge, OB absence has not been reported in this syndrome. *TUBA1A* mutations were not found in our cohort but have been reported associated with absent OBs.

Fetal alcohol exposure has been reported to lead to abnormal olfactory development in adult mice, and impaired odor discrimination has been seen in children with heavy prenatal alcohol exposure.^{33,34} Our 2 cases of fetal alcohol and drug exposure may represent an in utero toxic acquired etiology rather than a genetic origin.

Diffusion tensor imaging has been reported to be helpful in evaluating the brain stem to determine the location and integrity of different white matter tracts.³⁵ Diffusion tensor imaging found additional or clarified associated intracranial abnormalities in many of our patients. Morphologically abnormal brain stems were demonstrated in 10 patients, with absence or fusion of the transverse pontine fiber tracts often found in these patients. Asymmetric association tracts were identified, with associated thickened corpus callosum and prominent hippocampal commissures in children with agenesis of the corpus callosum. Diffusion tractography has been shown to be helpful in distinguishing

the white matter connections within the corpus callosum, such as the presence of homo- or heterotopic fiber tracts.^{36,37}

This was a retrospective study with resultant limitations inherently present. We cannot infer the incidence of olfactory anomalies in the pediatric population. The patients did not undergo a uniform clinical evaluation, and genetic evaluation was performed in just over one-half of the patients. All patients were not evaluated by an endocrinologist and did not undergo laboratory evaluation of pituitary function. Imaging was not specifically tailored to visualization of the OBs and OTs; however in our experience, the structures are adequately visualized on standard 4-mm coronal T2-weighted images. Olfactory bulb hypoplasia designation was subjective but was agreed on by consensus.

CONCLUSIONS

Children with OB and OT anomalies rarely present with symptoms referable to diminished smell. While pituitary dysfunction was a typical presentation in patients with olfactory anomalies, panhypopituitarism, not isolated hypogonadotropic hypogonadism, was the most common presentation. A wide spectrum of neurologic presentations was found, with seizures and developmental delay most common. Two distinct known associations of optic nerve hypoplasia syndrome and sensorineural hearing loss were commonly encountered. However, novel syndromic and genetic associations were also found. Anomalies of the olfactory apparatus are indicators of the presence of pituitary dysfunction and additional and often multiple brain malformations, with coronal T2-weighted imaging required for diagnosis. The results of genetic testing in this group are commonly abnormal and are suggested in the evaluation.

REFERENCES

1. Castillo M. **The complicated equation of smell, flavor, and taste.** *AJNR Am J Neuroradiol* 2014;35:1243–45 CrossRef Medline
2. Katoh H, Shibata S, Fukuda K, et al. **The dual origin of the peripheral olfactory system: placode and neural crest.** *Mol Brain* 2011;4:34 CrossRef Medline
3. Leboucq N, Menjot de Champfleury N, Menjot de Champfleury S, et al. **The olfactory system.** *Diagn Interv Imaging* 2013;94:985–91 CrossRef Medline
4. Levine LM, Bhatti MT, Mancuso AA. **Septo-optic dysplasia with olfactory tract and bulb hypoplasia.** *J AAPOS* 2001;5:398–99 CrossRef Medline
5. Truwit CL, Barkovich AJ, Crumbach MM, et al. **MR imaging of Kallmann syndrome, a genetic disorder of neuronal migration affecting the olfactory and genital systems.** *AJNR Am J Neuroradiol* 1993;14:827–38 Medline
6. Blustain J, Kirsch CF, Panigraphy A, et al. **Olfactory anomalies in CHARGE syndrome: imaging findings of a potential major diagnostic criterion.** *AJNR Am J Neuroradiol* 2008;29:1266–69 CrossRef Medline
7. Gerber JC, Neuhann TM, Tyshchenko N, et al. **Expanding the clinical and neuroradiological phenotype of 6q27 microdeletion: olfactory bulb aplasia and anosmia.** *Am J Med Genet* 2011;155:1981–86 CrossRef Medline
8. Mitchell TN, Free SL, Williamson KA, et al. **Polymicrogyria and absence of the pineal gland due to PAX6 mutation.** *Ann Neurol* 2003;53:658–63 CrossRef Medline
9. Alcaraz WA, Gold DA, Raponi E. **Zfp423 controls proliferation and differentiation of neural precursors in cerebellar vermis formation.** *Proc Natl Acad Sci U S A* 2006;103:19424–29 CrossRef Medline
10. Naruse I, Hiromi K. **Induction of agenesis of the corpus callosum by the destruction of anlage of the olfactory bulb using fetal laser surgery exo utero in mice.** *Brain Res Dev Brain Res* 1993;71:69–74 CrossRef Medline
11. Myers KA, Bello-Espinosa LE, Kherani A, et al. **TUBA1A mutation associated with eye abnormalities in addition to brain malformation.** *Pediatr Neurol* 2015;53:442–44 CrossRef Medline
12. Okumura A, Hayashi M, Tsurui H, et al. **Lissencephaly with marked ventricular dilation, agenesis of the corpus callosum, and cerebellar hypoplasia caused by TUBA1A mutation.** *Brain Dev* 2013;35:274–79 CrossRef Medline
13. Schwanzel-Fukuda M, Bick D, Pfaff DW. **Luteinizing hormone releasing hormone (LHRH)-expressing cells do not migrate normally in inherited hypogonadal (Kallmann) syndrome.** *Mol Res Mol Brain Res* 1989;6:311–26 CrossRef Medline
14. Hardelin JP. **Kallmann syndrome: towards molecular pathogenesis.** *Mol Cell Endocrinol* 2001;179:75–81 CrossRef Medline
15. Dodé C, Levilliers J, Dupont JM, et al. **Loss-of-function mutations in FGFR1 cause autosomal dominant Kallmann syndrome.** *Nat Gen* 2003;33:463–65 CrossRef Medline
16. Zenaty D, Bretones P, Lambe C, et al. **Paediatric phenotype of Kallmann syndrome due to mutations of fibroblast growth factor receptor 1 (FGFR1).** *Mol Cell Endocrinol* 2006;254–255:78–83 Medline
17. Borchert M. **Reappraisal of the optic hypoplasia syndrome.** *J Neuroophthalmol* 2012;32:58–67 CrossRef Medline
18. Garcia-Fillon P, Eppert K, Nelson M, et al. **Neuroradiographic, endocrinologic, and ophthalmic correlates of adverse developmental outcomes in children with optic nerve hypoplasia: a prospective study.** *Pediatrics* 2008;121:e653–59 CrossRef Medline
19. McCabe MJ, Gaston-Massuet C, Gregory LC, et al. **Variations in PROKR2, but not PROKR2, are associated with hypopituitarism and septo-optic dysplasia.** *J Clin Endocrinol Metab* 2013;98:E547–57 CrossRef Medline
20. Bergman JE, Bocca G, Hoefsloot LH, et al. **Anosmia predicts hypogonadotropic hypogonadism in CHARGE syndrome.** *J Pediatr* 2011;158:474–79 CrossRef Medline
21. Gregory LC, Gevers EF, Kasia T, et al. **Structural pituitary abnormalities associated with CHARGE syndrome.** *J Clin Endocrinol Metab* 2013;98:E737–43 CrossRef Medline
22. Fujita K, Aida N, Asakura Y, et al. **Abnormal basiocciput development in CHARGE syndrome.** *AJNR Am J Neuroradiol* 2009;30:629–34 CrossRef Medline
23. Elmaleh-Bergès M, Baumann C, Noël-Pétrouff N, et al. **Spectrum of temporal bone abnormalities in patients with Waardenburg syndrome and SOX10 mutations.** *AJNR Am J Neuroradiol* 2013;34:1257–63 CrossRef Medline
24. Barnett CP, Mendoza-Londono R, Blaser S, et al. **Aplasia of cochlear nerves and olfactory bulbs in association with SOX10 mutation.** *Am J Med Genet A* 2009;149A:431–36 CrossRef Medline
25. Teixeira L, Guimont F, Dodé C, et al. **Defective migration of neuroendocrine GnRH cells in human arrhinencephalic conditions.** *J Clin Invest* 2010;120:3668–72 CrossRef Medline
26. Cancrini C, Puliafito P, Digilio MC, et al; Italian Network for Primary Immunodeficiencies. **Clinical features and follow-up in patients with 22q11.2 deletion syndrome.** *J Pediatr* 2014;164:1475–80.e2 CrossRef Medline
27. Maggadottir SM, Sullivan KE. **The diverse clinical features of chromosome 22q11.2 deletion syndrome (DiGeorge syndrome).** *J Allergy Clin Immunol Pract* 2013;1:589–94 CrossRef Medline
28. Sobin C, Kiley-Brabeck K, Dale K, et al. **Olfactory disorder in children with 22q11 deletion syndrome.** *Pediatrics* 2006;118:e697–e703 CrossRef Medline
29. Romanos M, Schecklmann M, Kraus K, et al. **Olfactory deficits in deletion syndrome 22q11.2.** *Schizophr Res* 2011;129:220–21 CrossRef Medline
30. Sukalo M, Fiedler A, Guzmán C, et al. **Mutations in the human UBR1 gene and the associated phenotypic spectrum.** *Hum Mutat* 2014;35:521–31 CrossRef Medline

31. Mattina T, Perrotta CS, Grossfeld P. **Jacobsen syndrome.** *Orphanet J Rare Dis* 2009;4:9 CrossRef Medline
32. So J, Stockley T, Stavropoulos DJ. **Periventricular nodular heterotopias and transverse limb reduction defect in a woman with interstitial 11q24 deletion in the Jacobsen syndrome region.** *Am J Med Genet A* 2014;164A:511–15 CrossRef Medline
33. Akers KG, Kushner SA, Leslie AT, et al. **Fetal alcohol exposure leads to abnormal olfactory bulb development and impaired odor discrimination in adult mice.** *Mol Brain* 2011;4:29 CrossRef Medline
34. Bower E, Szajer J, Mattson SN, et al. **Impaired odor identification in children with histories of heavy prenatal alcohol exposure.** *Alcohol* 2013;47:275–78 CrossRef Medline
35. Briguglio M, Pinelli L, Giordano L, et al. **Pontine tegmental cap dysplasia: developmental and cognitive outcome in three adolescent patients.** *Orphanet J Rare Dis* 2011;6:36 CrossRef Medline
36. Rollins NK. **Diffusion imaging of the congenitally thickened corpus callosum.** *AJNR Am J Neuroradiol* 2013;34:660–65 CrossRef Medline
37. Takahashi T, Sato N, Ota M, et al. **Asymmetrical interhemispheric fiber tracts in patients with hemimegalencephaly on diffusion tensor magnetic resonance imaging.** *J Neuroradiol* 2009;36:249–54 CrossRef Medline

Reduction of Oxygen-Induced CSF Hyperintensity on FLAIR MR Images in Sedated Children: Usefulness of Magnetization-Prepared FLAIR Imaging

H.-K. Jeong, S.W. Oh, J. Kim, S.-K. Lee, and S.J. Ahn



ABSTRACT

BACKGROUND AND PURPOSE: Oxygen-induced CSF hyperintensity on FLAIR MR imaging is often observed in sedated children. This phenomenon can mimic leptomeningeal pathology and lead to a misdiagnosis. The purpose of this study was to investigate whether magnetization-prepared FLAIR MR imaging can reduce oxygen-induced CSF hyperintensity and improve image quality compared with conventional (non-magnetization-prepared) FLAIR MR imaging.

MATERIALS AND METHODS: Bloch simulation for magnetization-prepared and non-magnetization-prepared FLAIR sequences was performed for tissue contrast. We retrospectively reviewed 85 children with epilepsy who underwent MR imaging under general anesthesia with supplemental oxygen (41 with non-magnetization-prepared FLAIR and 44 with magnetization-prepared FLAIR). CSF hyperintensity was scored from 0 to 3 points according to the degree of CSF signal intensity and was compared between the 2 sequences. The contrast-to-noise ratios among GM, WM, and CSF were evaluated to assess general image quality from both sequences. To assess the diagnostic accuracy for hemorrhage, we reviewed an additional 25 patients with hemorrhage.

RESULTS: Bloch simulation demonstrated that CSF hyperintensity can be reduced on magnetization-prepared FLAIR compared with non-magnetization-prepared FLAIR. CSF hyperintensity scores were significantly lower in magnetization-prepared FLAIR than in non-magnetization-prepared FLAIR ($P < .01$). The contrast-to-noise ratios for GM-WM, GM-CSF, and WM-CSF were significantly higher in magnetization-prepared FLAIR than in non-magnetization-prepared FLAIR ($P < .05$). Hemorrhage was clearly demarcated from CSF hyperintensity in the magnetization-prepared group (100%, 12/12) and non-magnetization-prepared group (38%, 5/13).

CONCLUSIONS: Magnetization-prepared 3D-FLAIR MR imaging can significantly reduce oxygen-induced CSF artifacts and increase the tissue contrast-to-noise ratio beyond the levels achieved with conventional non-magnetization-prepared 3D-FLAIR MR imaging.

ABBREVIATIONS: MP = magnetization-prepared; oxy-CSF = oxygenated CSF

MR imaging is the diagnostic tool of choice in pediatric neurologic diseases because it has no ionizing radiation and is noninvasive. However, sedation is unavoidable if suitable MR images are sought because pediatric patients usually do not cooperate during long-duration scans.

CSF hyperintensity on FLAIR MR images is frequently encountered in sedated children.¹⁻⁵ These artifacts cause a diagnostic dilemma because they can mimic hemorrhage, infection, and leptomeningeal seeding metastasis, which are all known to generate hyperintense CSF signals on FLAIR MR images.⁶⁻⁹ Initially, CSF hyperintensity was attributed to anesthetic-induced T1-shortening, protein redistribution due to changes in the intravascular membrane permeability, hyperdynamic CSF pulsation due to altered vascular tone, and supplemental oxygen during anesthesia.^{2-4,10} However, several studies have revealed that the most plausible cause of hyperintense CSF artifacts in FLAIR imaging is the administration of supplemental oxygen during anesthesia.^{1,2,4,5,10}

Oxygen is a weak paramagnetic substance, which has 2 unpaired electrons that can cause a moderate increase in the T1 relaxation rate.^{11,12} Studies have shown that the diffusional transfer of oxygen from blood to CSF and a consequent FLAIR MR signal increase depend on the inhaled oxygen concentration^{1,2,4,13} and oxygen delivery methods.^{3,10}

Received December 16, 2015; accepted after revision January 5, 2016.

From Philips Korea (H.-K.J.), Seoul, Republic of Korea; Korea Basic Science Institute (H.-K.J.), Chungcheongbuk-do, Republic of Korea; Department of Radiology (S.W.O.), Soonchunhyang University Cheonan Hospital, Cheonan, Chungnam, Korea; and Department of Radiology (J.K., S.-K.L., S.J.A.), Yonsei University College of Medicine, Seoul, Korea.

This study was supported by the Dongkook Pharmaceutical Co, Ltd, Korea. The authors have no conflicts of interest that are directly relevant to the contents of this study.

Please address correspondence to Sung Jun Ahn, MD, Department of Radiology, Gangnam Severance Hospital, Yonsei University, College of Medicine, 211 Eonju-ro, Gangnam-gu, Seoul 135-720, Korea; e-mail: aahng77@yuhs.ac

Indicates article with supplemental on-line photo.

<http://dx.doi.org/10.3174/ajnr.A4723>

Table 1: Demographic characteristics and MRI findings

	Non-MP 3D FLAIR (n = 41)	MP 3D FLAIR (n = 44)	P Value
Age (yr)	6.31 ± 4.9	5.18 ± 4.63	.27
Sex	17 girls (41%)	17 girls (39%)	.96
MRI findings (No.)			.94
Normal	23 (56%)	24 (54%)	
Cortical malformation	8 (19%)	11 (25%)	
Ischemia	3 (8%)	4 (9%)	
Tumor	6 (14%)	3 (7%)	
Metabolic disease	1 (3%)	2 (5%)	

3D-FLAIR imaging is based on the 3D TSE imaging technique that modulates a refocusing flip angle at the TSE echo-train to maintain relatively steady signal levels during a long train of echo signals, which can provide improved image sharpness, helpful in detecting small structures. Consequently, the relaxation-induced image blurring, partial volume effect, and specific absorption rate can be reduced allowing high-resolution 3D data acquisition at isotropic voxels during clinically feasible scan durations.¹⁴ 3D-FLAIR also provides increased SNR and reduces CSF pulsation artifacts compared with 2D FLAIR.^{5,15-18} In magnetization-prepared (MP) 3D-FLAIR imaging, a dedicated magnetization preparation is implemented before typical inversion recovery, followed by TSE imaging, which is known to reduce unwanted T1-weighting and image TR.^{19,20} Therefore, the purpose of this study was to compare magnetization-prepared 3D-FLAIR imaging with conventional (non-MP) 3D-FLAIR imaging in terms of the ability to reduce oxygen-induced CSF hyperintensity and improve image quality in sedated pediatric patients.

MATERIALS AND METHODS

Study Population

We retrospectively screened consecutive children with epilepsy who were referred to our pediatric neurology outpatient clinic from June 2014 to June 2015. This retrospective study was approved by the institutional review board of Severance hospital. We included patients who underwent MR imaging by using a routine seizure protocol in the hospital and excluded patients with a history of brain operations due to the possibility of metal artifacts. We identified 85 pediatric patients (51 boys and 34 girls; age range, 0–12 years; mean age, 6 years). Detailed demographic characteristics and MR imaging findings are described in Table 1.

To assess the diagnostic accuracy for hemorrhage, we additionally included in the study 25 patients (17 boys and 8 girls; age range, 0–10 years; mean age, 5 years) who underwent neurosurgery due to epilepsy in our hospital from June 2014 to June 2015. These patients underwent immediate postoperative brain CT and MR imaging sequentially within 3 days after the operation. Hemorrhage was detected on their brain CTs. Patients were excluded if hemorrhage was not detected on the brain CT scan. In most cases, the preoperative MR imaging findings were normal (11/25, 44%); however, cortical malformation (9/25, 36%), ischemia (3/25, 12%), tumor (6/25, 24%), and hippocampal sclerosis (1/25, 4%) were also observed. The most frequent type of operation performed was callosotomy (13/25, 52%), followed by lesionectomy (6/25, 24%), lobectomy (4/25, 16%), and hemispherectomy (2/25, 8%).

Table 2: Imaging and sequence timing parameters for non-MP and MP 3D-FLAIR

Parameter	Non-MP 3D FLAIR	MP 3D FLAIR
FOV (mm)	224	250
TR (ms)	8000	4800
TE (ms)	340	299
TE, effective (ms)	154	128
Acquisition voxel size (RO/PE/SS) (mm)	1.0/1.0/1.0	0.98/0.99/1.0
Matrix (RO/PE)	224 × 223	256 × 253
Sensitivity encoding factor (PE/SS)	2.5/2.0	2.6/2.0
Acquisition time	7 min 44 sec	6 min 10 sec
No. of sections	350	360
TSE factor	110	182
NSA	1	2
Echo-train length (ms) (τ_5)	626	572
Inversion time (ms) (τ_1)	2400	1650
T2 preparation (ms) (τ_2)	N/A	125
Spoiler duration (ms) (τ_3)	N/A	17.23
Sequence dead time ^a (ms) (τ_4)	4974	2435.77

Note:—RO indicates readout; PE, phase-encoding; SS, section-selection; NSA, number of signals averaged.

^a Duration between the end of the echo-train and TR.

MR Imaging

All pediatric patients were examined with 1 of 2 3T MR imaging scanners (Achieva; Philips Medical System, Best, the Netherlands). One MR imaging scanner was operated with the conventional (non-MP) 3D-FLAIR imaging protocol, and the other MR imaging scanner was operated with the MP 3D-FLAIR imaging protocol due to the difference in the MR imaging scanner software versions. Patients were randomly assigned to 1 of the 2 MR imaging scanners according to a patient schedule and the availability of the scanners. The scan parameters for FLAIR imaging were optimal for suppression of CSF signals and are used for non-sedated adult patients in our institution. Detailed imaging and sequence timing parameters are shown in Table 2.

In our pediatric neurology clinic, general anesthesia was recommended to achieve a suitable diagnostic quality in the acquired MR images. Parent consent was obtained by the anesthesiologist before each procedure. Anesthesia was induced at an infusion rate of 125–250 μg of propofol per kilogram of body weight per minute, and all patients breathed spontaneously with supplemental 70%–80% oxygen via a nasal cannula during anesthesia.

Simulation

The magnetization behavior was simulated by using Bloch equations for the current MR imaging sequence and parameters as shown in Fig 1 and Table 2, respectively. The magnetization preparation used in 3D-FLAIR included nonselective radiofrequency pulses that consisted of a 90° block pulse for excitation, followed by 4 hyperbolic secant adiabatic refocusing pulses and a –90° flip-up pulse (FU). This was followed by inversion recovery, fat-saturation, and TSE readout with a variable refocusing flip angle scheme available in the scanner.¹⁹ The longitudinal magnetization after magnetization preparation and inversion recovery before TSE readout can be represented as follows:

$$1) \quad M_z(\tau_1^-) = M_0 \left\langle 1 - \left\{ 2 - \left[1 - \left(1 - e^{-\frac{\tau_1}{T_1}} \right) e^{-\frac{\tau_2}{T_1}} \right] e^{-\frac{\tau_3}{T_1}} \right\} e^{-\frac{\tau_4}{T_1}} \right\rangle,$$

where M_0 is the equilibrium magnetization, M_z is the longitudinal magnetization, and τ_1 , τ_2 , τ_3 , and τ_4 are the sequence timing pa-

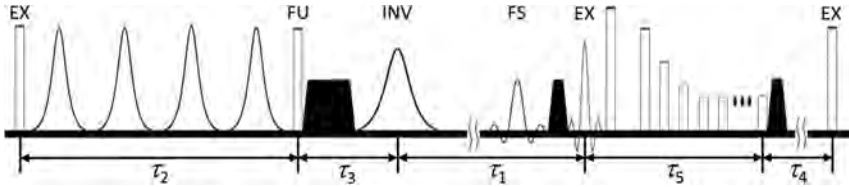


FIG 1. Pulse sequence diagram for MP 3D-FLAIR imaging. Magnetization preparation is implemented during τ_2 with radiofrequency pulses for 90° excitation (EX), followed by T2-preparation and -90° flip-up (FU). FLAIR inversion recovery is achieved during τ_1 with radiofrequency pulses for inversion (INV), followed by spectral fat saturation (FS) and TSE readout with 90° excitation (EX), followed by a train of refocusing pulses during τ_5 . τ_3 and τ_4 are the times for gradient spoiling and to the end of the current TR period, respectively. Black shaded trapezoids represent spoiling gradients to eliminate transverse magnetization.

Table 3: Tissue relaxation parameters

	GM	WM	CSF	Oxy-CSF
T1 (ms)	1820 ^a	1084 ^a	4356.6 ^c	3510 ^e
T2 (ms)	99 ^a	69 ^a	2500 ^d	2500
Proton density	0.81 ^b	0.71 ^b	1.0	1.0

^a Values acquired from Stanisiz et al.²⁴

^b Values acquired from Neeb et al.²²

^c Value estimated from Lu et al.²¹ for the best CSF nulling in FLAIR.

^d Value acquired from Smith et al.²³

^e Value acquired from Zaharchuk et al.¹³ (measured at 1.5T, see "Discussion").

rameters, as shown in Fig 1 and Table 2. The superscript "minus sign" represents the time before radiofrequency irradiation. When τ_3 is negligible, Equation 1 can be reduced to

$$2) \quad M_z(\tau_1^-) = M_0 \left\{ 1 - \left[1 + \left(1 - e^{-\frac{\tau_4}{T_1}} \right) e^{-\frac{\tau_2}{T_2}} \right] e^{-\frac{\tau_1}{T_1}} \right\},$$

and Equation 2 becomes M_z .^{19,20} When magnetization preparation is not used, longitudinal magnetization can be represented as follows:

$$3) \quad M_z(\tau_1^-) = M_0 \left[1 - 2e^{-\frac{\tau_1}{T_1}} + e^{-\frac{(\tau_4 + \tau_1)}{T_1}} \right],$$

and Equation 3 becomes M_z for inversion recovery.^{13,19} The evolution of magnetization with and without magnetization preparation was simulated to determine T1-weighting and signal contrast among brain tissues. In the simulation, the imaging and sequence timing parameters used are shown in Table 2, and the tissue relaxation parameters are demonstrated in Table 3.^{13,21-24} Because there was no significant difference in the T2 relaxation constant between CSF and oxygenated CSF (oxy-CSF),^{10,13} the T2 relaxation constant for oxy-CSF was assumed to be equal to that of the CSF. The simulation was performed with effective TE, where the T2 contrast in the pure T2-weighting sequence was equivalent to the T2 contrast in a sequence with a long refocusing train of radiofrequency with a variable flip angle.^{19,25}

Image Analysis

Two experienced neuroradiologists (S.J.A. with 4 years of experience in neuroimaging and J.K. with 10 years of experience in neuroimaging) were blinded to the patient information and imaging sequences. In the first session, the investigators independently evaluated CSF hyperintensity on non-MP 3D-FLAIR and MP 3D-FLAIR images, modifying a previous method.⁵ Imaging data were randomly assigned to each reader. CSF hyperintensity artifacts were scored from 0 to 3 according to the degree of the CSF signal intensity: 0, no visual CSF signal; 1, homogeneous

diffuse minimal CSF signal; 2, CSF signal similar to that of the pons; 3, CSF signal higher than that of the pons (On-line Fig). The premedullary, prepontine, suprasellar, basal, ambient, quadrigeminal cistern, and sulci regions of the cerebral convex were evaluated. The averaged values of CSF hyperintensity from each neuroradiologist were used for further analysis.

To assess tissue contrast on 2 sequences, a third neuroradiologist (S.W.O. with 2 years of experience in

neuroimaging) independently drew 4 circular ROIs (area = 10 mm²) in the caudate nucleus of the right basal ganglia and averaged the values representing GM. He was blinded to the patient information and sequences. Averaged values for the ROIs from the right frontal subcortical WM and adjacent lateral ventricle at the same plane represent WM and CSF, respectively. To ensure identical placement of the ROIs on both sequences, he carefully positioned the ROIs by hand in the same region of both images. Contrast-to-noise ratios were calculated among the GM, WM, and CSF. A contrast-to-noise ratio was defined on the basis of the signal intensity (SI) and SD in the ROI as follows:

$$4) \quad (SI_i - SI_j) / (SD_i^2 + SD_j^2)^{1/2},$$

where the subscripts i and j for SI and SD represent tissue types, such as GM, WM, or CSF.

Three weeks later, in the second session, the first 2 radiologists assessed whether the intracranial hemorrhage that occurred after neurosurgery could be clearly demarcated from CSF hyperintensity in the second study population. The decision for discrepant cases was established by consensus between the 2 neurologists. The flow chart for image analysis is summarized in Fig 2.

Statistical Analysis

CSF hyperintensity artifact scores for the premedullary, prepontine, suprasellar, basal, ambient, quadrigeminal cistern, and sulci regions of the cerebral convex were compared between non-MP 3D-FLAIR and MP 3D-FLAIR images by using the Student t test. Interobserver agreement for CSF hyperintensity was analyzed by using κ statistics. The contrast-to-noise ratios (GM/WM, GM/CSF, and WM/CSF) were compared between the 2 FLAIR MR imaging sequences. Statistical analyses were performed by using commercial software (MedCalc for Windows, Version 10.1.2.0; MedCalc Software, Mariakerke, Belgium). A P value < .05 was statistically significant.

RESULTS

Figure 3 shows the simulation results for the evolution of steady-state magnetization for the non-MP and MP sequences by using imaging and sequence timing parameters and tissue relaxation constants. Magnetization preparation (τ_2) induced lower T1-weighting than the non-MP sequences. Finally, oxygen-induced CSF hyperintensities were markedly reduced, and the contrast

between GM and WM was enhanced at the TE on MP FLAIR images compared with non-MP FLAIR images (see magnified view in Fig 3).

CSF hyperintensity artifact scores for the premedullary, pre-pontine, suprasellar, basal, ambient, quadrigeminal cistern, and sulci regions of the cerebral convex were significantly lower in MP 3D-FLAIR than in non-MP 3D-FLAIR (Fig 4 and Table 4). The interobserver agreement between the 2 readers was excellent for CSF hyperintensity artifact scores ($\kappa > 0.85$).

The contrast-to-noise ratio values for GM-WM, GM-CSF, and WM-CSF were significantly higher on MP 3D-FLAIR than on non-MP 3D-FLAIR (Table 4).

Hemorrhage was clearly demarcated from CSF hyperintensity in all 12 patients who underwent the MP sequence but in only 5 of 13 patients (38%) who underwent the non-MP sequence (Fig 5). There were no instances of discrepancy between the investigators.

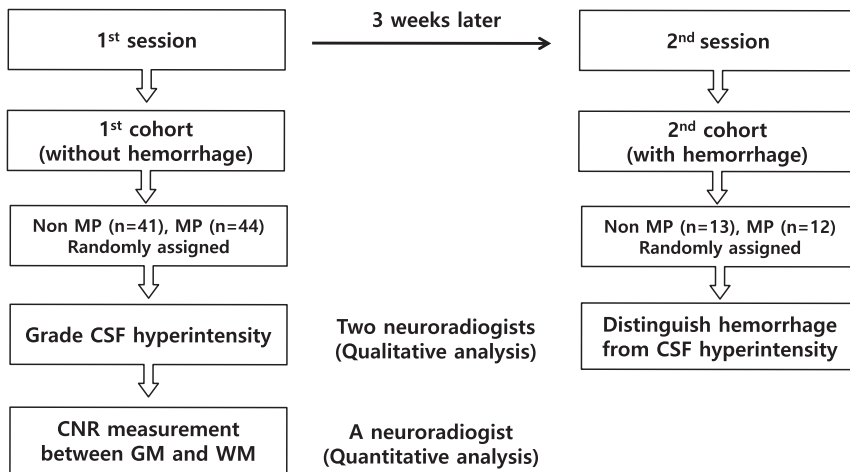


FIG 2. Flow chart for image analysis. CNR indicates contrast-to-noise ratio.

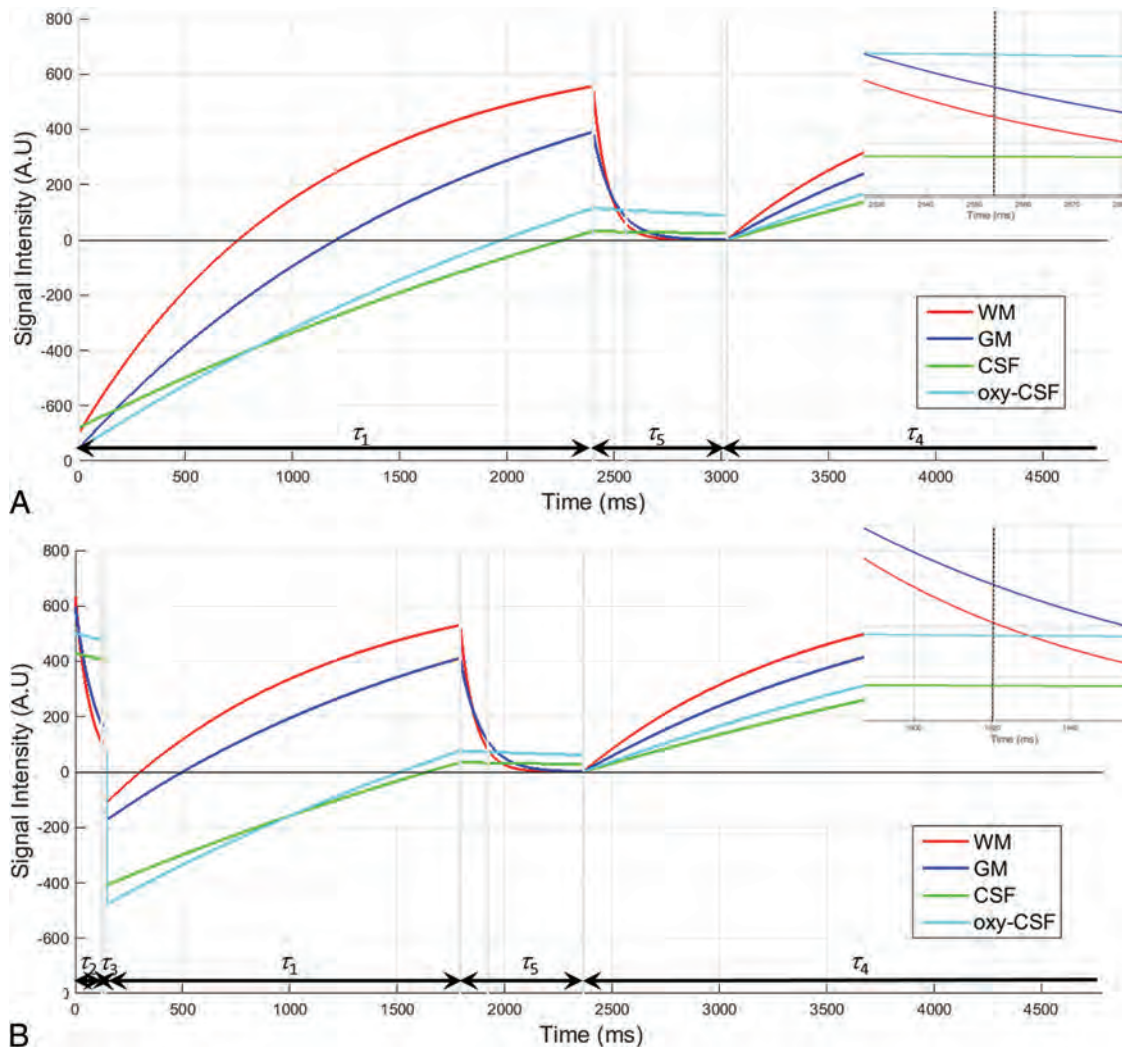


FIG 3. Simulation results for the evolution of steady-state magnetization for each type of tissue (WM, GM, CSF, and oxy-CSF) are presented for non-MP (A) and MP (B) FLAIR sequences. Imaging and sequence timing parameters (Table 2) and tissue relaxation constants (Table 3) were used in simulation. Sequence timing parameters ($\tau_1 \sim \tau_5$) are presented along with the time axis at each figure. An inset within each figure presents a magnified segment of the evolution of magnetization around the TE (dotted black vertical line). A.U. indicates arbitrary unit.

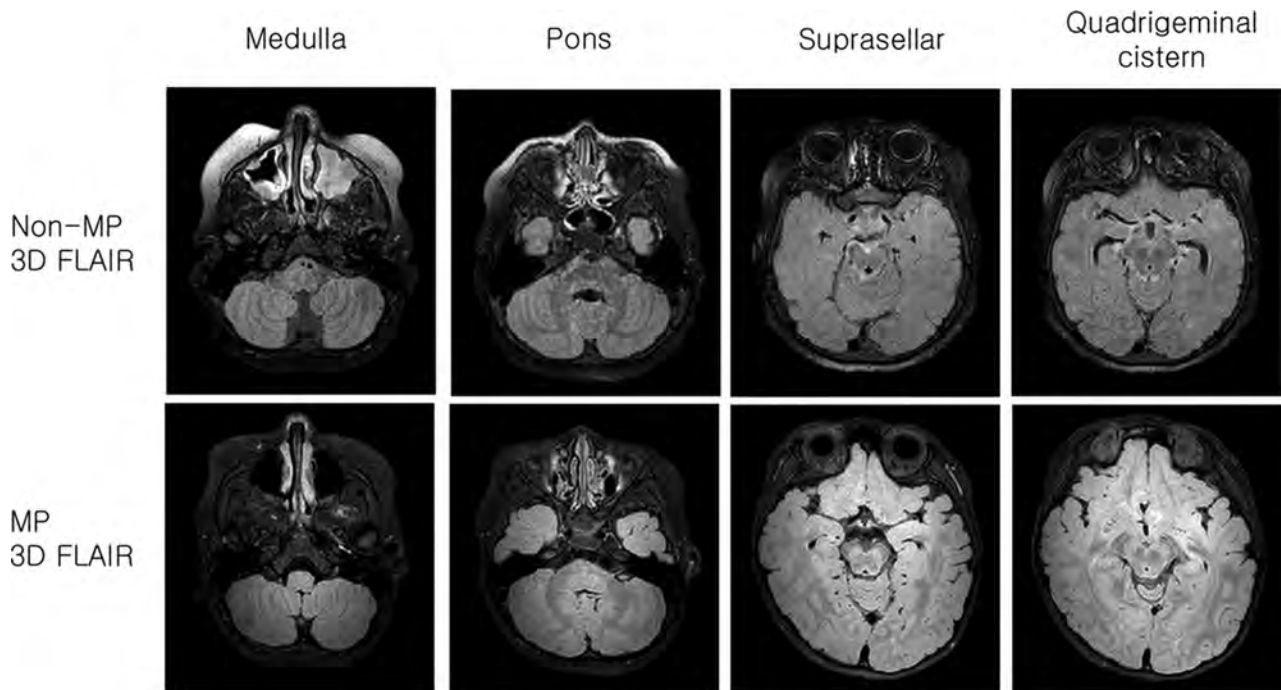


FIG 4. The non-MP 3D-FLAIR sequences of a 3-year-old boy with epilepsy (*upper row*). CSF hyperintensity artifact scores totaled 17 (premedullary cistern, 2; prepontine cistern, 2; suprasellar cistern, 3; basal cistern, 3; ambient cistern, 3; quadrigeminal cistern, 3; sulci of cerebral convex, 1). MP 3D-FLAIR sequences of a 4-year-old boy with epilepsy (*lower row*). CSF hyperintensity artifact scores totaled 4 (premedullary cistern, 0; prepontine cistern, 0; suprasellar cistern, 1; basal cistern, 1; ambient cistern, 1; quadrigeminal cistern, 1; sulci of the cerebral convex, 0).

Table 4: Hyperintense CSF artifact scores and CNR between GM and WM

	Non-MP 3D FLAIR (n = 41)	MP 3D FLAIR (n = 44)	P Value
Hyperintense CSF artifact scores			
Premedullary cistern	1.09 ± 0.58	0.38 ± 0.49	<.01
Prepontine cistern	1.8 ± 0.55	0.77 ± 0.47	<.01
Suprasellar cistern	2.19 ± 0.74	0.86 ± 0.41	<.01
Basal cistern	2.26 ± 0.74	0.88 ± 0.38	<.01
Ambient cistern	2.29 ± 0.87	0.88 ± 0.38	<.01
Quadrigeminal cistern	2.53 ± 0.77	0.86 ± 0.41	<.01
Sulci of cerebral convex	1.19 ± 0.55	0.21 ± 0.46	<.01
CNR			
GM-WM	3.28 ± 1.15	4.14 ± 1.28	.02
GM-CSF	12.85 ± 2.79	16.14 ± 2.43	<.01
WM-CSF	10.67 ± 2.78	13.82 ± 3.16	<.01

Note:—CNR indicates contrast-to-noise ratio.

DISCUSSION

In this study, we found that oxygen-induced CSF hyperintensity was significantly reduced in MP 3D-FLAIR compared with non-MP 3D-FLAIR. Moreover, MP 3D-FLAIR provided higher contrast-to-noise ratios among GM, WM, and CSF than non-MP 3D-FLAIR. The clinical implications of this observation are important because supplemental oxygen-induced hyperintense CSF artifacts can reduce the diagnostic accuracy of CSF pathology in sedated pediatric patients.^{1,10} Therefore, MP 3D-FLAIR can improve the diagnosis rate of CSF abnormalities and provide enhanced contrast among GM, WM, and CSF.

Previous studies hypothesized that CSF hyperintensity is associated with anesthetic-induced T1 shortening or redistribution of proteins due to changes in intravascular membrane permeability. However, subsequent studies have revealed that this hypothesis

might not be valid. For example, Deliganis et al² investigated the impact of the T1 relaxation constant on different anesthetic solutions with varying anesthetic concentrations that ranged from low-to-high clinical dose levels. They found no major differences in T1 over diverse anesthetic concentrations. Anzai et al¹⁰ showed, in a phantom study, that no noticeable FLAIR signal changes were observed over various albumin concentrations, except at a very high concentration (>1250 mg/dL). The normal CSF protein content is 22–52 mg/dL²⁶: 15–45 mg/dL in adults and 20–120 mg/dL in children.³ Vascular pulsation might partially explain CSF hyperintensity, but these effects can be reduced further by using 3D-FLAIR imaging in place of 2D FLAIR imaging.^{15–18} Additionally, pulsation artifacts can be easily distinguished by analyzing the signal-intensity pattern distributions throughout the brain.²

Studies claim that the most reliable explanation for CSF hyperintensity in sedated pediatric patients is attributable to the T1-shortening effect caused by the high concentration of paramagnetic supplemental oxygen administered during anesthesia. Moreover, various experimental factors (eg, inhaled oxygen concentrations and oxygen delivery methods) during supplemental oxygen administration are known to influence CSF hyperintensity. Deliganis et al² found that a patient who received 50% supplemental oxygen did not demonstrate any CSF hyperintensity, whereas patients with 100% supplemental oxygen showed noticeable signal increases in FLAIR images. This finding was confirmed in the study by Frigon et al,⁴ in which CSF hyperintensity was observed in patients with 100% supplemental oxygen but only partial or no CSF hyperintensity was observed in patients with 30% oxygen inhalation. In a study with healthy volunteers, Anzai et al¹⁰ observed CSF hyperintensity with 100% supplemental ox-

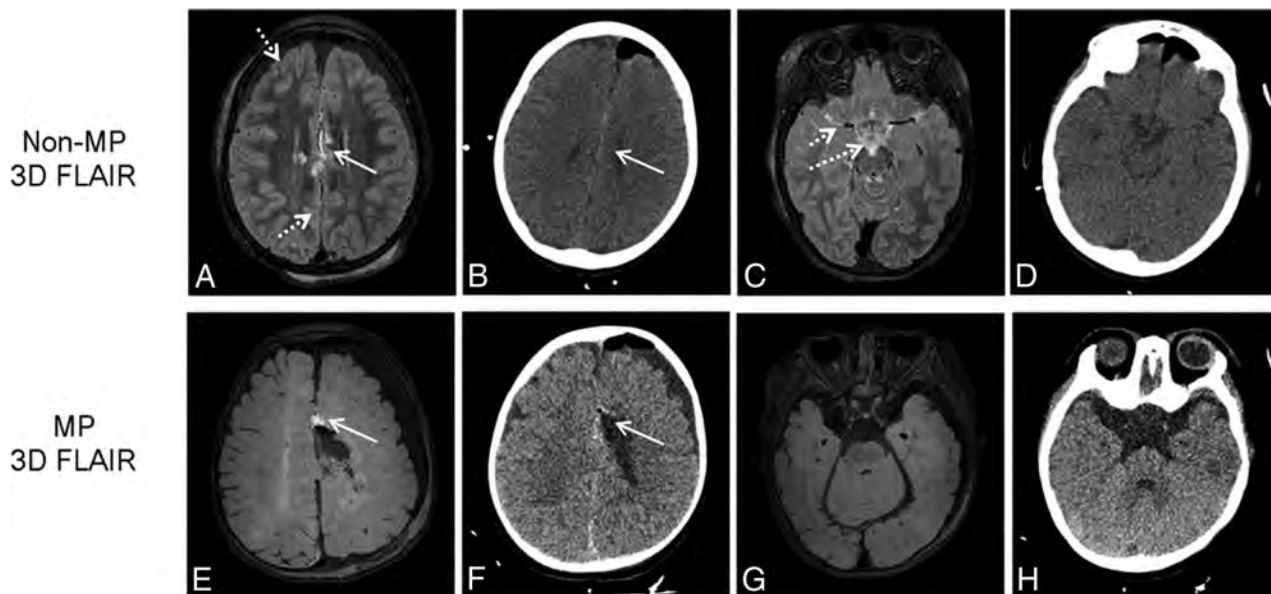


FIG 5. The subdural hemorrhage (solid arrow) is suspected in the non-MP 3D-FLAIR (upper row) of a 5-year-old girl after a callosotomy, which is also observed in the immediate postoperative CT scan. However, it is not clearly demarcated from CSF hyperintensity artifacts (dotted arrow). Hemorrhage (solid arrow) is clearly demarcated in the MP 3D-FLAIR (lower row) of an 8-month-old boy after lesionectomy, which is also observed in the immediate postoperative CT scan because CSF hyperintensity artifacts are suppressed.

xygen but no visible CSF hyperintensity in room air conditions (21% oxygen inhalation). The oxygen delivery method affects the efficiency of oxygen transport from the blood to the CSF. Oxygen delivery methods (eg, loose oxygen mask, nonrebreathing oxygen mask, or nasal cannula) were also reported to be important factors that influence CSF hyperintensity.^{3,10}

Oxygen distribution within the CSF is facilitated by diffusion of dissolved free oxygen from the blood into the CSF because there are no oxygen-carrying molecules such as hemoglobin or myoglobin in the CSF. Although dissolved free oxygen occupies only a small fraction of blood (<0.3%), a relatively large amount of inhaled oxygen can increase the concentration and facilitate oxygen transport into the CSF.^{2,10} The primary locations of oxygen entry into the CSF have been reported to be regions where large arterial vessels are lined with abundant pia-arachnoid surface areas.^{2,10} According to our results, CSF hyperintensity was more prominent in the suprasellar, basal, ambient, and quadrigeminal cistern than in the premedullary, prepontine cistern, and sulci regions of the cerebral convex on both MP and non-MP FLAIR sequences. These regional differences in the appearance of CSF hyperintensity can be explained by the following factors: First, the amount of CSF that surrounds the suprasellar, basal, ambient, and quadrigeminal cisterns is relatively small; therefore, there would be relatively less dilution of dissolved oxygen than in the premedullary and prepontine cisterns, which contain larger CSF pools.¹⁰ Second, the pituitary and pineal glands are circumventricular organs that have leaky blood-brain barriers, and they might facilitate the transport of dissolved oxygen into the CSF in the basal, suprasellar, ambient, and quadrigeminal cisterns.²⁷ However, this regional differential appearance of CSF hyperintensity requires further investigation.

In this study, Bloch simulations were used to compare MP and non-MP FLAIR sequences with previously reported tissue relaxation properties and sequence timing parameters. The behavior of

the simulated FLAIR signals was compatible with that in our *in vivo* observations, in which the magnitude of MR signals was $\text{oxy-CSF} > \text{GM} > \text{WM}$ in non-MP FLAIR and $\text{GM} > \text{WM} > \text{oxy-CSF}$ in MP FLAIR. The tissue magnetizations experienced inversion recovery in non-MP FLAIR, while they behaved more like saturation recovery in MP FLAIR,¹⁹ providing an oxy-CSF MP FLAIR longitudinal magnetization of only 67% to the non-MP FLAIR longitudinal magnetization before excitation (τ_1). Therefore, superior suppression of CSF hyperintensity might be achieved in MP FLAIR compared with non-MP FLAIR. Because magnetization preparation reduces T1 shortening, it is possible that the sensitivity of the detection of leptomeningeal pathology also decreases. However, according to our results, hemorrhage was clearly demarcated from CSF hyperintensity on MP FLAIR, whereas it was difficult to differentiate hemorrhage from CSF hyperintensity on non-MP FLAIR. Reducing T1 shortening might not be enough to suppress the signal intensity of hemorrhage. In addition, suppression of CSF artifacts makes it easier to assess the extent of hemorrhage on MP 3D-FLAIR compared with non-MP FLAIR.

The magnetization preparation provided additional benefits other than reducing CSF hyperintensity. The desired T2 contrast can be compromised because of reducing unwanted T1-weighting. MP 3D-FLAIR imaging provided better T2-weighted contrast among GM, WM, and CSF than non-MP 3D-FLAIR imaging. The improved contrast between GM and WM is crucial for identifying and characterizing epileptogenic lesions.²⁸ Therefore, MP 3D-FLAIR might also be helpful for detecting epileptic foci, which can be verified in a future study.

There were some limitations in this study. First, on FLAIR images, WM progressed from hyperintense to hypointense relative to adjacent GM during the first 2 years of life, which is slightly delayed compared with the observations on T2-weighted images.^{29,30} Therefore, young children with incomplete myelination

may have different GM-MW contrast enhancements from those in older children. Our cohort was heterogeneous, ranging in age from 0 to 12 years, which might have affected the contrast-to-noise ratios. However, our Bloch simulation also supports our GM-WM contrast findings. Therefore, our results might be applicable to patients with complete myelination. Future studies with larger and more homogeneous populations are necessary to validate and extend these results. Second, in the simulation, we used an oxy-CSF T1 constant of 3510 ms on the basis of a study that used 1.5T MR imaging¹³ because the oxy-CSF T1 constant at 3T MR imaging was not available. However, the simulated FLAIR signal was comparable with that our in vivo observations. Accurate measurement of the oxy-CSF T1 constant at 3T MR imaging is required for more effective sequence design and in vivo application.

CONCLUSIONS

MP 3D-FLAIR imaging yields fewer CSF hyperintensity artifacts and provides superior contrast between GM and WM compared with non-MP 3D-FLAIR imaging. Therefore, we propose that MP 3D-FLAIR imaging provides better diagnostic accuracy in CSF pathologies and epileptogenic lesions in sedated pediatric patients who receive supplemental oxygen.

Disclosures: Ha-Kyu Jeong—RELATED: Employment: Philips Korea (regular salary).

REFERENCES

- Braga FT, da Rocha AJ, Hernandez Filho G, et al. Relationship between the concentration of supplemental oxygen and signal intensity of CSF depicted by fluid-attenuated inversion recovery imaging. *AJNR Am J Neuroradiol* 2003;24:1863–68 Medline
- Deliganis AV, Fisher DJ, Lam AM, et al. Cerebrospinal fluid signal intensity increase on FLAIR MR images in patients under general anesthesia: the role of supplemental O₂. *Radiology* 2001;218:152–56 CrossRef Medline
- Filippi CG, Ulug AM, Lin D, et al. Hyperintense signal abnormality in subarachnoid spaces and basal cisterns on MR images of children anesthetized with propofol: new fluid-attenuated inversion recovery finding. *AJNR Am J Neuroradiol* 2001;22:394–99 Medline
- Frigon C, Shaw DW, Heckbert SR, et al. Supplemental oxygen causes increased signal intensity in subarachnoid cerebrospinal fluid on brain FLAIR MR images obtained in children during general anesthesia. *Radiology* 2004;233:51–55 CrossRef Medline
- Ozcan UA, Isik U, Ozpinar A, et al. Assessment of sedated pediatric brain with 3D-FLAIR sequence at 3T MRI. *Brain Dev* 2015;37:495–500 CrossRef Medline
- Mohamed M, Heasley DC, Yagmurlu B, et al. Fluid-attenuated inversion recovery MR imaging and subarachnoid hemorrhage: not a panacea. *AJNR Am J Neuroradiol* 2004;25:545–50 Medline
- Noguchi K, Ogawa T, Seto H, et al. Subacute and chronic subarachnoid hemorrhage: diagnosis with fluid-attenuated inversion-recovery MR imaging. *Radiology* 1997;203:257–62 CrossRef Medline
- Bozzao A, Bastianello S, Bozzao L. Superior sagittal sinus thrombosis with high-signal-intensity CSF mimicking subarachnoid hemorrhage on MR FLAIR images. *AJR Am J Roentgenol* 1997;169:1183–84 CrossRef Medline
- Dechambre SD, Duprez T, Grandin CB, et al. High signal in cerebrospinal fluid mimicking subarachnoid haemorrhage on FLAIR following acute stroke and intravenous contrast medium. *Neuroradiology* 2000;42:608–11 CrossRef Medline
- Anzai Y, Ishikawa M, Shaw DW, et al. Paramagnetic effect of supplemental oxygen on CSF hyperintensity on fluid-attenuated inversion recovery MR images. *AJNR Am J Neuroradiol* 2004;25:274–79 Medline
- Berthezene Y, Tournut P, Turjman F, et al. Inhaled oxygen: a brain MR contrast agent? *AJNR Am J Neuroradiol* 1995;16:2010–12 Medline
- Runge VM, Stewart RG, Clanton JA, et al. Work in progress: potential oral and intravenous paramagnetic NMR contrast agents. *Radiology* 1983;147:789–91 CrossRef Medline
- Zaharchuk G, Martin AJ, Rosenthal G, et al. Measurement of cerebrospinal fluid oxygen partial pressure in humans using MRI. *Magn Reson Med* 2005;54:113–21 CrossRef Medline
- Busse RF, Hariharan H, Vu A, et al. Fast spin echo sequences with very long echo trains: design of variable refocusing flip angle schedules and generation of clinical T2 contrast. *Magn Reson Med* 2006;55:1030–37 CrossRef Medline
- Kallmes DF, Hui FK, Mugler JP 3rd. Suppression of cerebrospinal fluid and blood flow artifacts in FLAIR MR imaging with a single-slab three-dimensional pulse sequence: initial experience. *Radiology* 2001;221:251–55 CrossRef Medline
- Kitajima M, Hirai T, Shigematsu Y, et al. Comparison of 3D FLAIR, 2D FLAIR, and 2D T2-weighted MR imaging of brain stem anatomy. *AJNR Am J Neuroradiol* 2012;33:922–27 CrossRef Medline
- Naganawa S, Koshikawa T, Nakamura T, et al. Comparison of flow artifacts between 2D-FLAIR and 3D-FLAIR sequences at 3 T. *Eur Radiol* 2004;14:1901–08 Medline
- Wu HM, Yousem DM, Chung HW, et al. Influence of imaging parameters on high-intensity cerebrospinal fluid artifacts in fast-FLAIR MR imaging. *AJNR Am J Neuroradiol* 2002;23:393–99 Medline
- Visser F, Zwanenburg JJ, Hoogduin JM, et al. High-resolution magnetization-prepared 3D-FLAIR imaging at 7.0 Tesla. *Magn Reson Med* 2010;64:194–202 CrossRef Medline
- Wong EC, Liu TT, Luh WM, et al. T(1) and T(2) selective method for improved SNR in CSF-attenuated imaging: T(2)-FLAIR. *Magn Reson Med* 2001;45:529–32 Medline
- Lu H, Nagae-Poetscher LM, Golay X, et al. Routine clinical brain MRI sequences for use at 3.0 Tesla. *J Magn Reson Imaging* 2005;22:13–22 CrossRef Medline
- Neeb H, Zilles K, Shah NJ. A new method for fast quantitative mapping of absolute water content in vivo. *Neuroimage* 2006;31:1156–68 CrossRef Medline
- Smith SA, Edden RA, Farrell JA, et al. Measurement of T1 and T2 in the cervical spinal cord at 3 Tesla. *Magn Reson Med* 2008;60:213–19 CrossRef Medline
- Stanisz GJ, Odobina EE, Pun J, et al. T1, T2 relaxation and magnetization transfer in tissue at 3T. *Magn Reson Med* 2005;54:507–12 CrossRef Medline
- Hennig J, Weigel M, Scheffler K. Multiecho sequences with variable refocusing flip angles: optimization of signal behavior using smooth transitions between pseudo steady states (TRAPS). *Magn Reson Med* 2003;49:527–35 CrossRef Medline
- Melhem ER, Jara H, Eustace S. Fluid-attenuated inversion recovery MR imaging: identification of protein concentration thresholds for CSF hyperintensity. *AJR Am J Roentgenol* 1997;169:859–62 CrossRef Medline
- Cottrell GT, Ferguson AV. Sensory circumventricular organs: central roles in integrated autonomic regulation. *Regul Pept* 2004;117:11–23 CrossRef Medline
- Vattipally VR, Bronen RA. MR imaging of epilepsy: strategies for successful interpretation. *Neuroimaging Clin N Am* 2004;14:349–72 CrossRef Medline
- Murakami JW, Weinberger E, Shaw DW. Normal myelination of the pediatric brain imaged with fluid-attenuated inversion-recovery (FLAIR) MR imaging. *AJNR Am J Neuroradiol* 1999;20:1406–11 Medline
- Welker KM, Patton A. Assessment of normal myelination with magnetic resonance imaging. *Semin Neurol* 2012;32:15–28 CrossRef Medline

Effect of the Suboccipital Musculature on Symptom Severity and Recovery after Mild Traumatic Brain Injury

S. Fakhran, C. Qu, and L.M. Alhilali



ABSTRACT

BACKGROUND AND PURPOSE: Neck musculature mass has been suggested as a biomechanical contributor to injury severity in mild traumatic brain injury. We sought to determine how the cross-sectional areas of the suboccipital muscles affect symptom severity, neurocognitive performance, and recovery time in patients with mild traumatic brain injury.

MATERIALS AND METHODS: Sixty-four consecutive patients with mild traumatic brain injury underwent MR imaging and serial neurocognitive testing with the Immediate Post-Concussion Assessment and Cognitive Test. Cross-sectional areas of the rectus capitis posterior musculature were retrospectively obtained at C1, and cross-sectional areas of the remaining 7 suboccipital muscles were measured at C2. Cross-sectional area reproducibility was evaluated. Overall and individual muscle cross-sectional areas were correlated with symptom severity, neuropsychological testing, recovery time, and headache.

RESULTS: Sixty-four patients with mild traumatic brain injury had imaging through C1, and 43 had imaging through C2. Reproducibility of cross-sectional area measurements was substantial (correlation coefficients = 0.9517–0.9891). Lower cross-sectional area of the rectus capitis posterior minor was correlated with greater symptom severity ($r = 0.596, P < .0001$), longer recovery time ($r = 0.387, P = .002$), poor verbal memory performance ($r = 0.285, P = .02$), and headache ($r = 0.39, P = .001$). None of the other cross-sectional areas were associated with symptom severity, recovery time, neurocognitive testing, or headache.

CONCLUSIONS: In mild traumatic brain injury, the rectus capitis posterior minor is the only suboccipital muscle whose cross-sectional area is associated with symptom severity and worse outcome. Given the unique connection of this muscle to the dura, this finding may suggest that pathology of the myodural bridge contributes to symptomatology and prognosis in mild traumatic brain injury.

ABBREVIATIONS: ΔV = change in head velocity; ImPACT = Immediate Post-Concussion Assessment and Cognitive Test; mTBI = mild traumatic brain injury; rectus capitis-PMaj = rectus capitis posterior major; rectus capitis-PMin = rectus capitis posterior minor

Mild traumatic brain injury (mTBI), often referred to as “concussion,” is a common hazard in contact sports, with approximately 3.8 million sports-related injuries documented each year.¹ Despite the outwardly mild nature of these injuries, approximately 15% of patients with mTBI have persistent, often debilitating symptoms beyond 3 months, termed “postconcussion syndrome.”²

The underlying injury in mTBI is theorized to be related to acceleration and deceleration of the brain within the cranial

vault.³ Animal models have shown that the severity of brain injury is correlated with the change in head velocity (ΔV).⁴ Forces from a large ΔV predominantly impact frequent locations of shear injuries associated with postconcussive syndrome.⁵

In computer models of mTBI, early neck resistance is key in decreasing ΔV .^{6,7} As impact forces are proportional to ΔV ,^{4,7} this means that very small reductions in ΔV by the neck musculature can result in a significant reduction in impact forces in regions associated with postconcussive syndrome.

Supporting the finding of increased neck strength and decreased ΔV , studies have shown that increased neck muscle strength results in decreased risk of postconcussion syndrome.^{8,9} However, increased overall neck strength has not resulted in alterations in ΔV during trauma in the experimental setting.¹⁰ This finding raises the question of whether specific muscles rather than overall strength are key to decreasing brain injury. Notably, muscles resisting head movement have been found central in determining outcome after linear acceleration injuries in whiplash.¹¹

Received September 29, 2015; accepted after revision January 13, 2016.

From the Department of Radiology (S.F.), East Valley Diagnostic Imaging/Banner Health and Hospital Systems, Mesa, Arizona; Department of Radiology (C.Q.), Division of Neuroradiology, University of Pittsburgh Medical Center, Pittsburgh, Pennsylvania; and Department of Neuroradiology (L.M.A.), Barrow Neurological Institute, Phoenix, Arizona.

Please address correspondence to Lea Alhilali, MD, Barrow Neurological Institute, Department of Neuroradiology, 350 W Thomas Road, Phoenix, AZ 85013; e-mail: lalhilali@snweb.net

Indicates article with supplemental on-line table.

<http://dx.doi.org/10.3174/ajnr.A4730>

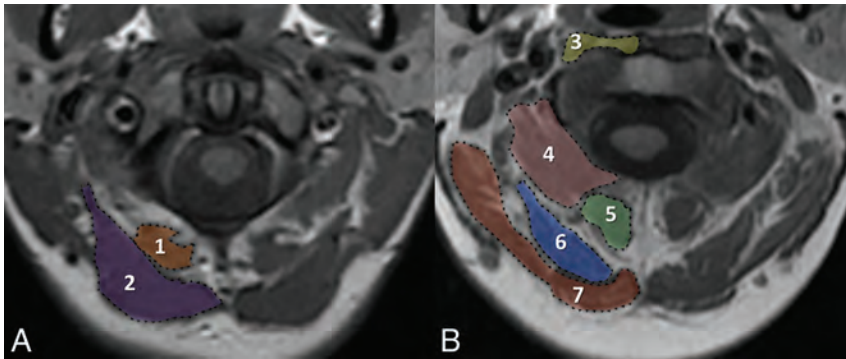


FIG 1. Measurement of cross-sectional areas for the suboccipital muscles. Representative tracing of the cross-sectional areas on T1-weighted imaging of the rectus capitis posterior minor (1) and rectus capitis posterior major (2) muscles at the level of the anterior arch of C1 (A) and the longus colli/capitis (3), inferior oblique capitis (4), semispinalis cervicis/multifidus (5), semispinalis capitis (6), and splenius capitis (7) muscles at the midthoracic level (B).

The suboccipital musculature is central to promoting and resisting head motion, including flexion, extension, and rotation.¹² The rectus capitis posterior major (rectus capitis-PMaj), rectus capitis posterior minor (rectus capitis-PMin), semispinalis cervicis, multifidus, semispinalis capitis, and splenius capitis are head extensors, while the longus colli and longus capitis are head flexors. The rectus capitis-PMaj, inferior oblique capitis, and semispinalis capitis are also involved in rotation. Because the cross-sectional area of muscles has previously been shown to be proportional to muscle strength,^{13,14} we sought to determine how the cross-sectional area of the suboccipital muscles affects symptom severity, neurocognitive performance, and recovery time in patients with mTBI.

MATERIALS AND METHODS

Patient Selection and Image Acquisition

Our institutional review board approved this study with a waiver of informed consent. All MR imaging examinations were performed during the routine care of patients and were retrospectively reviewed.

We searched our electronic medical record to identify MR imaging studies performed for mTBI. Radiology reports from January 1, 2008, to July 31, 2013, were searched by using the keyword “concussion.” Inclusion criteria were 10–50 years of age, English language proficiency, and mild TBI defined as witnessed closed head trauma, no focal neurologic deficit, loss of consciousness of <1 minute, and posttraumatic amnesia of <30 minutes. Exclusion criteria were any abnormality on brain MR imaging as defined by a fellowship-trained neuroradiologist, including microhemorrhage/shear injury on gradient sequence (3 patients), the imaging not extending to C1 (4 patients), unavailable neurocognitive Total Symptom Score (4 patients), the Total Symptom Score being zero (3 patients), or excessive motion precluding accurate measurements (3 patients).

Neurocognitive testing was performed at the time of presentation, and the Immediate Post-Concussion Assessment Cognitive Test (ImPACT), a computerized test measuring cognitive function and postconcussion symptoms, was used. The ImPACT is the most scientifically validated and commonly used computerized neurocognitive evaluation system.¹⁵ It determines a total symptom score by using a 7-point Likert scale over 22 different

categories and measures cognitive performance against normative data gathered on >17,000 athletes who participated in baseline testing as part of their pre-sport participation. The percentile rank for a subject’s performance is determined by using the normative data from the control athletes of the same age group.¹⁶ After the initial neurocognitive testing, serial postconcussion symptom scores were obtained to determine the time to recovery, which was defined as the score being zero or the patient stating that he or she was asymptomatic.

Age and sex were recorded. Data collected included type of trauma, dates of injury and clinical evaluation, neurocognitive results, history of prior concussions, imaging results, clinical management, and any edema of the suboccipital musculature on T2 imaging. A prior concussion was defined as a diagnosis of concussion by an athletic trainer, neuropsychologist, or other medical personnel at any facility; however, documentation of that diagnosis had to be placed in the medical record. Recovery time was defined as when the patient stated that he or she was asymptomatic or the neurocognitive Total Symptom Score was zero.

MR imaging examinations were performed within 3 days of clinical examination on a 1.5T system (Signa; GE Healthcare, Milwaukee, Wisconsin) with a standard head coil and included axial images through C2. During the study period, all patients included in this study underwent the identical postconcussion imaging protocol on the same magnet system as follows: sequences included sagittal and axial T1-weighted imaging (TR, 600 ms; TE, minimum; section thickness, 5 mm; NEX, 1), and T2-weighted imaging (TR, 2000–2500 ms; TE, 84–102 ms; section thickness, 5 mm; NEX, 1). FOV ranged from 200 to 240 mm.

Suboccipital Muscle Cross-Sectional Area Calculations

Neck muscle boundaries were manually outlined along their fascial borders by 2 radiologists on T1-weighted images with an orientation parallel to the foramen magnum with the assistance of a 3D viewer (Vitrea Core; Vital Images, Minnetonka, Minnesota). The cross-sectional area of the following muscles was evaluated at the C1 anterior arch: 1) rectus capitis-PMin, and 2) rectus capitis-PMaj; and the following, at the midthoracic level: 3) longus colli and longus capitis (traced together), 4) inferior oblique capitis, 5) semispinalis cervicis and multifidus (traced together), 6) semispinalis capitis, and 7) splenius capitis musculature (Fig). Individual muscle cross-sectional areas were calculated, and total neck muscle cross-sectional area was determined by summing all of the individual neck musculature cross-sectional areas. Radiologists each reviewed 10 sample cases for training purposes. Reproducibility of muscle cross-sectional area measurements was then assessed on 20 test cases for each muscle group using 2 neuroradiologists, blinded to both the patient’s history and the other observer’s measurements. The Lin concordance correlation coefficient was used to evaluate agreement¹⁷ and was interpreted as

Table 1: Clinical and demographic characteristics of patients with mTBI

	No. (%) or Mean (SD)
Age (yr)	17.7 (5.6)
Male sex	44 (69%)
Prior concussion	15 (23%)
Postconcussive headache	29 (45%)
Injury mechanism:	
Sports injury	40 (63%)
Motor vehicle collision	5 (8%)
Time to presentation (days)	10.1 (10–50) ^a
Initial Total Symptom Score	33.7 (24)
Verbal Memory Score (percentile)	32.5 (29)
Visual Memory Score (percentile)	27.1 (28)
Processing Speed Score (percentile)	36.1 (29)
Reaction Speed Score (percentile)	33.5 (29)
Recovery time (wk)	36.6 (11–74)

^a Time intervals are presented as median (interquartile range).

follows¹⁸: poor agreement (<0.90), moderate agreement (0.90 to <0.95), substantial agreement (0.95–0.99), and almost perfect agreement (>0.99). Following the 20 test cases, a single neuro-radiologist blinded to the patient's history made measurements.

Univariate Data Analysis

Comparison of the demographic data was performed with a Fisher exact test or a 2-tailed *t* test. Comparison of cross-sectional area measurements was performed with an unpaired *t* test. Correlation of the cross-sectional area measurements with clinical metrics was performed with the Pearson correlation coefficient or a point-biserial coefficient. Correlation of clinical variables or muscle cross-sectional areas with recovery time was performed with a Pearson correlation coefficient or point-biserial coefficient. *P* values of < .05 were statistically significant.

Multivariate Data Analysis

Multivariate analysis for variables correlating with recovery time was performed with an ordinary least-squares model, by using variables whose *P* values were <0.10 by univariate analysis. Goodness of fit was evaluated with the Hosmer-Lemeshow statistic. Odds ratios and their 95% confidence intervals were calculated. *P* values < .05 were statistically significant.

RESULTS

Patient Selection and Image Acquisition

Sixty-four patients were included (44 males, 20 females). A summary of the demographic and clinical data is shown in Table 1. No patients had macroscopic edema of the suboccipital musculature on T2-weighted imaging on the included FOV.

Suboccipital Muscle Cross-Sectional Area Calculations

Reproducibility of the cross-sectional areas was substantial for all muscles (Lin correlation coefficients = 0.9517–0.9891) (Table 2). The average cross-sectional area measurements for the rectus capitis-PMin and rectus capitis-PMaj at C1 and the remaining suboccipital musculature at C2 are shown in Table 3.

Univariate Data Analysis

The lower cross-sectional area of the rectus capitis-PMin was correlated with the following outcome measures: 1) greater symptom

Table 2: Lin correlation coefficients for CSA of the muscles of head movement

Muscle	Lin Correlation Coefficient	95% CI
Rectus capitis posterior minor	0.9891	0.9737–0.9955
Rectus capitis posterior major	0.9645	0.9137–0.9856
Longus colli/capitis	0.9531	0.8887–0.9806
Inferior oblique capitis	0.9608	0.9070–0.9837
Semispinalis cervicis/multifidus	0.9517	0.8830–0.9804
Semispinalis capitis	0.9797	0.9497–0.9919
Splenius capitis	0.9586	0.9001–0.9831

Note:—CSA indicates cross-sectional area.

Table 3: Average CSAs of the suboccipital musculature

Muscle	Mean CSA (cm ²)	SD
Rectus capitis posterior minor	2.36	1.20
Rectus capitis posterior major	5.12	1.76
Longus colli/capitis	1.19	0.45
Inferior oblique capitis	3.73	0.54
Semispinalis cervicis/multifidus	1.48	0.45
Semispinalis capitis	4.04	0.61
Splenius capitis	4.98	0.82
Total muscle CSA	19.70	6.80

Note:—CSA indicates cross-sectional area.

Table 4: Variables trending towards correlation with recovery time (*P* < .10) on univariate analysis

Variable	<i>r</i>	<i>P</i>
Rectus capitis posterior minor CSA	−0.387	.002
Longus colli/capitis CSA	0.218	.08
Age	0.423	.005
Male sex	−0.318	.01

Note:—CSA indicates cross-sectional area.

Table 5: Subsequent performance in a multivariate model

Variable	Adjusted Odds Ratio (95% CI)	<i>P</i> Value
Rectus capitis posterior minor CSA	0.22 (0.11–0.43)	.03
Longus colli/capitis CSA	1.66 (1.18–2.34)	.14
Age	1.15 (1.01–1.31)	.27
Male sex	0.78 (0.43–1.37)	.65

Note:—CSA indicates cross-sectional area.

severity ($r = 0.596$; $P < .0001$), 2) longer recovery time ($r = 0.387$; $P = .002$), 3) poorer verbal memory performance ($r = 0.285$; $P = .02$), and 4) postconcussive headache ($r_{pb} = 0.39$; $P = .001$). Neither the overall cross-sectional area nor those for any of the other individual muscles were associated with symptom severity, recovery time, neurocognitive testing, or headache. Among demographic factors, age and male sex correlated with recovery time on univariate analysis ($r = 0.423$ and -0.318 ; $P = .005$ and $.01$, respectively). Correlation results are summarized in the On-line Table.

Multivariate Analysis

Four variables had *P* values < .10 by univariate analysis: the rectus capitis-PMin cross-sectional area, longus coli/capitis cross-sectional area, age, and sex. Multivariate analysis found that the only statistically significant factor for prognosis was the rectus capitis-PMin cross-sectional area. A larger rectus capitis-PMin cross-sectional area was protective against a longer recovery time (adjusted odds ratio, 0.22; $P = .03$). Summary of the multivariate analysis is shown in Tables 4 and 5.

DISCUSSION

In mTBI, a lower cross-sectional area of the rectus capitis-PMin alone among the suboccipital muscles was associated with greater symptom severity, longer recovery time, poor neurocognitive test performance, and postconcussive headache. Overall suboccipital muscle cross-sectional area did not correlate with clinical metrics or symptomatology after mTBI.

Suboccipital muscle atrophy has long been associated with chronic pain.¹⁹ Previous studies have shown greater atrophy in the rectus capitis-PMaj and rectus capitis-PMin among the suboccipital muscles in patients with persistent whiplash symptoms,^{20,21} and atrophy of these muscles has been associated with higher inflammatory biomarkers, hyperalgesia, and worse outcomes in patients with whiplash.²² However, these studies focusing on the effects of the suboccipital musculature on posttraumatic outcomes have focused exclusively on patients with whiplash-associated neck pain.²³ No studies have extended these findings to patients with mTBI, who may not necessarily have an associated neck injury but often have an acceleration-deceleration energy transfer similar to that in whiplash injuries.²⁴

Most interesting, decreased cross-sectional area in the rectus capitis-PMaj and rectus capitis-PMin musculature has also been found in patients with chronic tension-type headaches, in which the lower cross-sectional areas of the rectus capitis-PMaj and rectus capitis-PMin were associated with greater headache intensity, duration, and frequency.²⁵ Tension-type headaches are among the most common headaches experienced after mTBI, with almost 40% of postconcussive headaches reported as tension headaches.²⁶ However, the role of the rectus capitis-PMaj and rectus capitis-PMin in mTBI and their association with posttraumatic headaches have not been investigated, to our knowledge.

In our study, only the rectus capitis-PMin was associated with greater symptomatology, poorer outcome, and posttraumatic headaches after mTBI. Although the rectus capitis-PMaj and rectus capitis-PMin are both head extenders,²⁰ the rectus capitis-PMin experiences the greatest load in low-energy impacts.²⁷ In these low-energy injuries, the proportion of energy absorbed by the suboccipital muscles themselves is decreased relative to the strain on their tendons and connective tissue connections.²⁷ The rectus capitis-PMin has a unique connective tissue bridge to the dura mater,²⁸ which has been noted on both anatomic specimens and MR imaging.²⁹⁻³¹ This connective tissue bridge is responsible for resisting dural enfolding during neck extension. Traumatic injury to this myodural bridge can occur with a weak or atrophic rectus capitis-PMin. A smaller/weaker rectus capitis-PMin can absorb less energy, and as a result, higher energy is deposited in the myodural bridge, increasing the risk of injury.³² Secondary atrophy of the rectus capitis-PMin after trauma can also cause chronic dysfunction of the myodural bridge²⁹ because an atrophic rectus capitis-PMin is less able to resist inward folding of the dura, resulting in abnormal dural movement and tension.³³ This outcome can result in prominent referred pain because the dura itself is highly sensitive to tractional forces.

The dura is innervated by the first 3 cervical nerves, which converge with the trigeminal nerve in the trigeminal nucleus caudalis. Resulting activation of the nociceptors in the trigeminoc-

er nucleus by these cervical nerves produces a cervicogenic headache. It is therefore not surprising that the low cross-sectional area of the rectus capitis-PMin was associated with greater symptom severity and headaches in our cohort. In fact, cervicogenic headache from injury to the rectus capitis-PMin–dural connection is a well-known phenomenon in headaches from suboccipital procedures, where injury to the myodural bridge results in abnormal adhesions between the rectus capitis-PMin and the dura.³⁴ Lysis of these abnormal rectus capitis-PMin–dural adhesions in these patients has been shown to provide symptom relief.³⁵

Additional symptomatology associated with rectus capitis-PMin atrophy could arise from its role as the proprioceptive center of the upper cervical spine.³⁶ The rectus capitis-PMin has the greatest concentration of muscle spindles among the suboccipital musculature,³⁷ with an especially high concentration of large-diameter A- β fibers, which convey proprioceptive information. Transmission of proprioceptive data along these A- β fibers effectively blocks nociceptive signals from muscle C-fibers from reaching the spinal cord and higher order pain centers.³⁶ Atrophy of the rectus capitis-PMin results in a decrease in A- β fibers, which, in turn, causes less inhibitory signals and greater pain impulses to central pain pathways.

Cognitive difficulties are commonly seen in patients with both acute and chronic pain,³⁸ and pain is one of the most significant contributors to neurocognitive performance after mTBI.³⁹ Thus, rectus capitis-PMin atrophy may play a role in both the symptomatology and cognitive deficits after mTBI. Together, these findings may indicate a role for preventive strengthening exercises focused on the rectus capitis-PMin musculature in individuals at high-risk for mTBI.

Our study has limitations. Our evaluation was a retrospective, single-institution study with a moderate sample size. Accordingly, the findings should be corroborated with a larger prospective study. Furthermore, our study included both patients who were thought to warrant imaging clinically and those with prior concussions. Thus, a selection bias may exist toward more seriously injured patients who present with significant symptoms that warrant imaging. Arguably, although a bias exists, it is a bias toward the patients that would most benefit from imaging biomarkers. Additionally, only the suboccipital muscles were evaluated in our study, and further studies evaluating the relationship of the lower neck muscles to symptoms and outcomes in mTBI would help to better understand how the biomechanical and physiologic properties of the neck affect what has often been considered exclusively brain pathology.

CONCLUSIONS

In mild TBI, the rectus capitis-PMin is the only suboccipital muscle whose cross-sectional area is correlated with symptom severity and worse outcome. This may reflect greater strain on the myodural bridge in patients with a smaller rectus capitis-PMin or perhaps decreased inhibition of nociceptive pathways from rectus capitis-PMin spindle atrophy. Understanding how suboccipital muscle loss influences the pathophysiology of mTBI may help develop physical therapy rehabilitation programs to improve outcomes in this population.

REFERENCES

1. Langlois JA, Rutland-Brown W, Wald MM. **The epidemiology and impact of traumatic brain injury: a brief overview.** *J Head Trauma Rehabil* 2006;21:375–78 CrossRef Medline
2. Shenton ME, Hamoda HM, Schneiderman JS, et al. **A review of magnetic resonance imaging and diffusion tensor imaging findings in mild traumatic brain injury.** *Brain Imaging Behav* 2012;6:137–92 CrossRef Medline
3. Gennarelli TA, Seggawa H, Wald U, et al. **Physiological response to angular acceleration of the head.** In: Grossman RG, Gildenberg PL, eds. *Head Injury: Basic and Clinical Aspects.* New York: Raven Press; 1982:129–40
4. Denny-Brown D, Russell R. **Experimental cerebral concussion.** *Brain* 1941;64:93–164 CrossRef
5. Niogi SN, Mukherjee P. **Diffusion tensor imaging of mild traumatic brain injury.** *J Head Trauma Rehabil* 2010;25:241–55 CrossRef Medline
6. Viano DC, Casson IR, Pellman EJ, et al. **Concussion in professional football: brain responses by finite element analysis, part 9.** *Neurosurgery* 2005;57:891–916; discussion 891–916 CrossRef Medline
7. Viano DC, Casson IR, Pellman EJ, et al. **Concussion in professional football: comparison with boxing head impacts, part 10.** *Neurosurgery* 2005;57:1154–72; discussion 1154–72 CrossRef Medline
8. Reid SE, Raviv G, Reid SE Jr. **Neck muscle resistance to head impact.** *Aviat Space Environ Med* 1981;52:78–84 Medline
9. Tierney RT, Sitler MR, Swanik CB, et al. **Gender differences in head-neck segment dynamic stabilization during head acceleration.** *Med Sci Sports Exerc* 2005;37:272–79 CrossRef Medline
10. Mansell J, Tierney RT, Sitler MR, et al. **Resistance training and head-neck segment dynamic stabilization in male and female collegiate soccer players.** *J Athl Train* 2005;40:310–19 Medline
11. Vibert N, MacDougall HG, de Waele C, et al. **Variability in the control of head movements in seated humans: a link with whiplash injuries?** *J Physiol* 2001;532(pt 3):851–68 CrossRef Medline
12. Plagenhoeff S, Evans FG, Abedelnour T. **Anatomical data for analyzing human motion.** *Res Q Exerc Sport* 1983;54:169–78 CrossRef
13. Maughan RJ, Watson JS, Weir J. **Muscle strength and cross-sectional area in man: a comparison of strength-trained and untrained subjects.** *Br J Sports Med* 1984;18:149–57 CrossRef Medline
14. Schantz P, Randall-Fox E, Hutchison W, et al. **Muscle fibre type distribution, muscle cross-sectional area and maximal voluntary strength in humans.** *Acta Physiol Scand* 1983;117:219–26 CrossRef Medline
15. Mayers LB, Redick TS. **Clinical utility of ImpACT assessment for postconcussion return-to-play counseling: psychometric issues.** *J Clin Exp Neuropsychol* 2012;34:235–42 CrossRef Medline
16. Maelender A, Flashman L, Kessler A, et al. **Examination of the construct validity of ImpACT™ computerized test, traditional, and experimental neuropsychological measures.** *Clin Neuropsychol* 2010;24:1309–25 CrossRef Medline
17. Lin LI. **A concordance correlation coefficient to evaluate reproducibility.** *Biometrics* 1989;45:255–68 Medline
18. McBride GB. **A proposal for strength-of-agreement criteria for Lin's Concordance Correlation Coefficient.** *NIWA Client Report* 2005;HAM2005–062
19. Hallgren RC, Greenman PE, Rechten JJ. **Atrophy of suboccipital muscles in patients with chronic pain: a pilot study.** *J Am Osteopath Assoc* 1994;94:1032–38 Medline
20. Elliott J, Jull G, Noteboom JT, et al. **Fatty infiltration in the cervical extensor muscles in persistent whiplash-associated disorders: a magnetic resonance imaging analysis.** *Spine (Phila Pa 1976)* 2006;31:E847–55 CrossRef Medline
21. McPartland JM, Brodeur RR, Hallgren RC. **Chronic neck pain, standing balance, and suboccipital muscle atrophy: a pilot study.** *J Manipulative Physiol Ther* 1997;20:24–29 Medline
22. Sterling M, Elliott JM, Cabot PJ. **The course of serum inflammatory biomarkers following whiplash injury and their relationship to sensory and muscle measures: a longitudinal cohort study.** *PLoS One* 2013;8:e77903 CrossRef Medline
23. Elliott JM. **Are there implications for morphological changes in neck muscles after whiplash injury?** *Spine (Phila Pa 1976)* 2011;36(25 suppl):S205–10 CrossRef Medline
24. Evans RW. **Persistent post-traumatic headache, postconcussion syndrome, and whiplash injuries: the evidence for a non-traumatic basis with an historical review.** *Headache* 2010;50:716–24 CrossRef Medline
25. Fernández-de-Las-Peñas C, Bueno A, Ferrando J, et al. **Magnetic resonance imaging study of the morphometry of cervical extensor muscles in chronic tension-type headache.** *Cephalalgia* 2007;27:355–62 CrossRef Medline
26. D'Onofrio F, Russo A, Conte F, et al. **Post-traumatic headaches: an epidemiological overview.** *Neurol Sci* 2014;35(suppl 1):203–06 CrossRef Medline
27. Hedenstierna S, Halldin P, Siegmund GP. **Neck muscle load distribution in lateral, frontal, and rear-end impacts: a three-dimensional finite element analysis.** *Spine (Phila Pa 1976)* 2009;34:2626–33 CrossRef Medline
28. Gray H, Williams PL, Bannister LH. *Gray's Anatomy: The Anatomical Basis of Medicine and Surgery.* 38th ed. New York: Churchill Livingstone; 1995:806
29. Alix ME, Bates DK. **A proposed etiology of cervicogenic headache: the neurophysiologic basis and anatomic relationship between the dura mater and the rectus posterior capitis minor muscle.** *J Manipulative Physiol Ther* 1999;22:534–39 CrossRef Medline
30. Humphreys BK, Kenin S, Hubbard BB, et al. **Investigation of connective tissue attachments to the cervical spinal dura mater.** *Clin Anat* 2003;16:152–59 CrossRef Medline
31. Demetrius J. **Post-traumatic upper cervical subluxation visualized by MRI: a case report.** *Chiropr Osteopat* 2007;15:20 CrossRef Medline
32. Hallgren RC, Greenman PE, Rechten JJ. **MRI of normal and atrophic muscles of the upper cervical spine.** *J Clin Engineering* 1993;18:433–39
33. Hack GD, Koritzer RT, Robinson WL, et al. **Anatomic relation between the rectus capitis posterior minor muscle and the dura mater.** *Spine (Phila Pa 1976)* 1995;20:2484–86 CrossRef Medline
34. Soumekh B, Levine SC, Haines SJ, et al. **Retrospective study of post-craniotomy headaches in suboccipital approach: diagnosis and management.** *Am J Otol* 1996;17:617–19 Medline
35. Hack GD, Hallgren RC. **Chronic headache relief after section of suboccipital muscle dural connections: a case report.** *Headache* 2004;44:84–89 CrossRef Medline
36. Wall PD. **The dorsal horn.** In: Wall PD; McMahon SB, Koltzenburg M, eds. *Wall and Melzack's Textbook of Pain.* 2nd ed. Philadelphia: Elsevier/Churchill Livingstone; 2006:102–11
37. Peck D, Buxton DF, Nitz A. **A comparison of spindle concentrations in large and small muscles acting in parallel combinations.** *J Morphol* 1984;180:243–52 CrossRef Medline
38. Moriarty O, McGuire BE, Finn DP. **The effect of pain on cognitive function: a review of clinical and preclinical research.** *Prog Neurobiol* 2011;93:385–404 CrossRef Medline
39. Cooper DB, Vanderploeg RD, Armistead-Jehle P, et al. **Factors associated with neurocognitive performance in OIF/OEF service members with postconcussive complaints in postdeployment clinical settings.** *J Rehabil Res Dev* 2014;51:1023–34 CrossRef Medline

Evaluation of Focal Cervical Spinal Cord Lesions in Multiple Sclerosis: Comparison of White Matter–Suppressed T1 Inversion Recovery Sequence versus Conventional STIR and Proton Density–Weighted Turbo Spin-Echo Sequences

D.K. Sundarakumar, C.M. Smith, W.D. Hwang, M. Mossa-Basha, and K.R. Maravilla



ABSTRACT

BACKGROUND AND PURPOSE: Conventional MR imaging of the cervical spinal cord in MS is challenged by numerous artifacts and interreader variability in lesion counts. This study compares the relatively novel WM-suppressed T1 inversion recovery sequence with STIR and proton density–weighted TSE sequences in the evaluation of cervical cord lesions in patients with MS.

MATERIALS AND METHODS: Retrospective blinded analysis of cervical cord MR imaging examinations of 50 patients with MS was performed by 2 neuroradiologists. In each patient, the number of focal lesions and overall lesion conspicuity were measured in the STIR/proton density–weighted TSE and WM-suppressed T1 inversion recovery sequence groups. Independent side-by-side comparison was performed to categorize the discrepant lesions as either “definite” or “spurious.” Lesion contrast ratio and edge sharpness were independently calculated in each sequence.

RESULTS: Substantial interreader agreement was noted on the WM-suppressed T1 inversion recovery sequence ($\kappa = 0.82$) compared with STIR/proton density–weighted TSE ($\kappa = 0.52$). Average lesion conspicuity was better on the WM-suppressed T1 inversion recovery sequence (conspicuity of 3.1/5.0 versus 3.7/5.0, $P < .01$, in the WM-suppressed T1 inversion recovery sequence versus STIR/proton density–weighted TSE, respectively). Spurious lesions were more common on STIR/proton density–weighted TSE than on the WM-suppressed T1 inversion recovery sequence (23 and 30 versus 3 and 4 by readers 1 and 2, respectively; $P < .01$). More “definite” lesions were missed on STIR/proton density–weighted TSE compared with the WM-suppressed T1 inversion recovery sequence (37 and 38 versus 3 and 6 by readers 1 and 2, respectively). Lesion contrast ratio and edge sharpness were highest on the WM-suppressed T1 inversion recovery sequence.

CONCLUSIONS: There is better interreader consistency in the lesion count on the WM-suppressed T1 inversion recovery sequence compared with STIR/proton density–weighted TSE sequences. The focal cord lesions are visualized with better conspicuity due to better contrast ratio and edge sharpness. There are fewer spurious lesions on the WM-suppressed T1 inversion recovery sequence compared with STIR/proton density–weighted TSE. The WM-suppressed T1 inversion recovery sequence could potentially be substituted for either STIR or proton density–weighted TSE sequences in routine clinical protocols.

ABBREVIATIONS: LES = lesion edge sharpness; PDWTSE = proton density–weighted TSE; WMS = WM-suppressed T1 inversion recovery

The cervical spinal cord is commonly affected in multiple sclerosis, which is often associated with an increase in clinical disability.^{1–3} A focal form of involvement is more common in the relapsing–remitting variant of MS compared with the other less common MS subtypes.⁴ MS lesions undergo complex cycles of inflammation, followed by variable extent of repair and, there-

fore, have heterogeneity in the prolongation of T1 and T2 relaxation times, which influence their conspicuity on the standard MR imaging sequences such as STIR and proton density–weighted TSE (PDWTSE).

The PDWTSE sequence with a lower TE is better than the longer TE T2-weighted sequences in the detection of focal MS lesions in the spinal cord.^{5,6} STIR has intrinsic sensitivity to T1 shortening effects in addition to T2 prolongation effects and improves the lesion contrast compared with T2-weighted sequences, translating to a better interreader agreement in the assessment of the extent of disease.⁷ Nevertheless, artifacts and lower lesion conspicuity prevalent on these sequences may cause variability in the clinical evaluation of lesion burden, which is difficult to resolve in the absence of a true reference standard.⁸ Reliable characteriza-

Received October 1, 2015; accepted after revision February 2, 2016.

From the Department of Radiology, University of Washington, Seattle, Washington.

Please address correspondence to Dinesh K. Sundarakumar, MD, Department of Radiology, University of Washington Medical Center, 1959 NE Pacific St, BB308, Seattle, WA 98195; e-mail: dineshs@uw.edu

<http://dx.doi.org/10.3174/ajnr.A4761>

tion of the lesion burden on follow-up examinations is therefore important for assessing treatment efficacy and optimizing treatment strategies.

Many novel sequences have been devised attempting to improve imaging quality and lesion conspicuity with fewer artifacts and with a reasonable acquisition time. In a smaller study population, the WM-suppressed T1 inversion recovery (WMS) sequence has shown improvement in lesion conspicuity over STIR and dual-echo fast spin-echo.⁹ While the principles of the contrast mechanism on WMS are similar to those on STIR, the sequence parameters of WMS are optimized for better intramedullary imaging. In WMS, the section-selective inversion pulse is applied at 385 ms to suppress the background signal from white matter, whereas in STIR, it is applied at 160 ms to optimize fat suppression.¹⁰ A shorter TE is used in WMS compared with STIR or PDWTSE, which further increases the T1-weighting of the sequence, which acts as the main contrast mechanism in this long TR/short TE sequence.^{11,12} MS lesions have increased T1 relaxation times and thus are not suppressed with a white matter selective inversion recovery suppression pulse. There is a need for larger scale evaluation of WMS for clinical utility in routine practice against the standard sequences (STIR and PDWTSE) in the detection of MS cord lesions. The purpose of this retrospective study was to compare the utility of WMS compared with routinely used STIR and PDWTSE sequences in the evaluation of focal cervical cord lesions in MS.

MATERIALS AND METHODS

Subjects

This retrospective study was approved by the institutional review board and was conducted in compliance with the Health Insurance Portability and Accountability Act. Following earlier implementation of the WMS sequence, cervical spinal cord MR imaging examinations of 50 consecutive patients with multiple sclerosis (14 men and 36 women; average age, 43.1 years; range, 19–64 years; median age, 43.5 years; disease duration range, 3–20 years; Expanded Disability Status Scale range, 1.0–5.5) with known or suspected involvement of the spinal cord, scanned between August 2013 and June 2014, were retrospectively reviewed. There were 40 relapsing-remitting, 5 primary-progressive, and 5 secondary-progressive subtypes of MS in the study population. These patients were being treated by using various regimens, including immunomodulatory therapy, as clinically appropriate.

MR Image Acquisition

The images were acquired on a 3T MR imaging scanner (Ingenia; Philips Healthcare, Best, the Netherlands), by using an integrated head and neck coil (18-channel maximum). Sagittal STIR (TR/TE/TI, 2700/50/250 ms; FOV, 250 mm; echo-train length, 15; NEX, 1), sagittal PDWTSE (TR/TE, 2700/45 ms; FOV, 250 mm; echo-train length, 15; NEX, 1), and axial PDWTSE (TR/TE, 2700/45 ms; FOV, 140 mm; echo-train length, 15; NEX, 1) sequences were compared with sagittal WMS (TR/TE/TI, 3600/11/385 ms; FOV, 240 mm; echo-train length, 8; NEX, 2) and axial WMS (TR/TE/TI, 3600/11/380 ms; FOV, 250 mm; echo-train length, 19; NEX, 1), acquired in the same corresponding geometric planes. The TIs and TEs in WMS were chosen from a pilot trial

performed by us (data not presented here). The sagittal images were acquired with a section thickness of 3 mm; and axial images, with 5-mm thickness with a 10% intersection gap. The in-plane acquired pixel size was 0.89×0.89 mm for sagittal STIR and sagittal PDWTSE sequences, and it was 0.54×0.61 mm for the axial PDWTSE sequences. The in-plane acquired pixel sizes for sagittal and axial WMS sequences were 0.68×0.95 mm and 0.69×0.92 mm, respectively. The average combined scan time for both sagittal and axial WMS imaging was 7 minutes 30 seconds. WMS images were reconstructed in both magnitude and phase-sensitive modes. On magnitude reconstruction, there is the possibility of suppressing signal from lesions having a null point very close to that of normal white matter. Phase-sensitive reconstruction overcomes this “blind-spot” by using the directional information of the longitudinal magnetization, thereby improving the dynamic range of contrast near the TI.⁵ To maintain uniformity between imaging sequences, we used only the magnitude images for analysis and statistical comparison. Postcontrast sagittal and axial imaging was performed after IV injection of 0.1 mL/kg of gadoteridol (ProHance; Bracco Diagnostics, Princeton, New Jersey).

Image Analysis

The image series of the patients were segregated and randomized with the conventional sequences (sagittal STIR/sagittal PDWTSE/axial PDWTSE) in 1 anonymized folder, and the WMS sequences (sagittal WMS/axial WMS), in a separate folder. The 2 image groups were independently examined by 2 blinded fellowship-trained neuroradiologists having 3 and 7 years' experience, respectively. The axial images were cross-referenced to the sagittal sequences in each group. The cervical spine was arbitrarily divided into 2 levels: C1–C4 and C5–C7. The lesion count and the overall lesion conspicuity were reported for the 2 cervical levels in each sequence group. We decided to divide the cervical spine into upper and lower levels during evaluation due to imaging heterogeneity between these 2 regions that arises from field inhomogeneity artifacts and dielectric effects. These factors affect the image quality of the lower cervical region more than the upper region, due to increased body thickness at the shoulders, which can potentially confound evaluation.¹³ Thus, we thought that separate comparison of upper and lower cervical lesions would be a more accurate assessment. This separation also allowed minimizing variation of measurements by limiting the region of cord being evaluated at one time. To assess the overall burden of focal abnormalities, we initially asked the readers to count all visualized focal abnormalities, including those later determined to be spurious. Overall conspicuity for focal findings in each cervical level was then graded on the following scale: 1, image quality was nondiagnostic; 2, >50% of lesions were uncertain; 3, 25%–50% of lesions were uncertain; 4, <25% of lesions were uncertain; and 5, all the lesions were well-visualized and certain.

In a second reading session, each reader individually compared both sequence groups side-by-side and noted each discrepant finding. “True” lesions were selected and distinguished from spurious findings on the basis of the following criteria: biplanar visualization of a lesion and lesion presence on 2 consecutive MR imaging studies or the presence of enhancement on postcontrast sequences. Further discrepancies in the lesion characterization

were resolved by consensus. Then, within the STIR/PDWTSE group, each reader was asked the following question: On which sagittal sequence—STIR (A), PDWTSE (B), or similar on both (A = B)—were the lesions better visualized?

Quantitative contrast (lesion-to-cord) ratios for 82 selected focal lesions, visualized in all 3 sagittal sequences (up to 4 lesions in each patient), were calculated by D.K.S. by using following formula:

$$\text{Contrast Ratio}_{\text{Lesion}} = \frac{(\text{Signal Lesion} - \text{Signal Normal Cord})}{\text{Signal Normal Cord}}$$

The lesion edge sharpness (LES) of 25 selected lesions (measuring ≥ 1 cm, up to 1 lesion per patient) was measured on the sagittal STIR, WMS, and PDWTSE sequences by D.K.S. A line was drawn along the length of these lesions and was extended slightly to include normal-appearing cord at both ends. An intensity profile was obtained along this length (Fig 1). The lesion-margin sharpness was defined as the average of the distance for a 20%–80% difference in signal intensity on the line-intensity profile at the cranial and caudal margins of the lesion.¹⁴

Statistical Analysis

Weighted κ statistics were used to analyze the interreader variability in the lesion count in each group at each cervical level. The Wilcoxon signed rank test was used to compare the lesion conspicuity

between the 2 groups. The difference in lesion count per patient between sequence groups and the LES was analyzed by using a paired Student *t* test. A linear regression model based on a generalized estimation equation was used to analyze the difference in lesion contrast ratios among STIR, PDWTSE, and WMS. The comparison of reader preference between STIR and PDWTSE was analyzed by a χ^2 test. The threshold for statistical significance was set at $P < .05$.

RESULTS

The number of lesions detected on STIR/PDWTSE by readers 1 and 2, respectively, was 177 (average lesions per patient, 4.2 ± 3.0) and 183 (average lesions per patient, 4.3 ± 3.4). The total number of lesions detected was marginally higher on WMS for both readers (reader 1: 191; average lesions per patient, 4.5 ± 3.5 ; and reader 2: 189; average lesions per patient, 4.5 ± 3.5). There was no statistically significant difference in the lesion count per patient between STIR/PDWTSE and WMS ($P = .64$) (Table 1). No lesions were identified in 8 patients in both sequence groups by both readers.

Qualitative Analysis

Interreader agreement on lesion count per cervical level on STIR/PDWTSE was fair ($\kappa = 0.49$ and 0.52 at C1–C4 and C5–C7 levels, respectively; overall agreement, $\kappa = 0.52$). On the other hand, the interreader agreement for lesion count was substantial on WMS ($\kappa = 0.82$ and 0.84 at C1–C4 and C5–C7 levels, respectively; overall agreement, $\kappa = 0.82$).

The average score of both reviewers for overall subjective lesion conspicuity at the C1–C4 and C5–C7 levels was better on WMS (3.7/5 and 3.8/5) than on STIR/PDWTSE (3.1/5 and 3.1/5), respectively ($P < .01$) (Fig 2 and Table 2). Within the STIR/PDWTSE group, the lesions were better visualized on STIR in 21 and 17 patients and better seen on PDWTSE in 10 and 12 patients. They were equal in 11 and 13 patients by readers 1 and 2, respectively ($P = .1$).

On a side-by-side comparison of the 2 sequence groups, 191 true lesions were identified. More spurious findings were

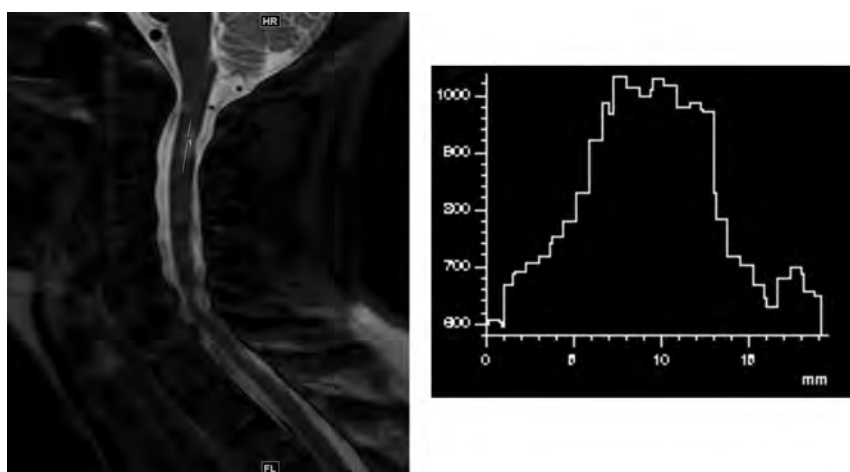


FIG 1. Measurement of lesion edge sharpness on a sagittal WMS image in a 39-year-old woman with a relapsing-remitting subtype of multiple sclerosis. A line is drawn along the long axis of the lesion located at the C2–C3 level, which includes the adjoining normal-appearing cord. The histogram derived represents the signal-intensity profile along the line. Lesion edge sharpness is determined by the average of distance required for a 20%–80% change in the signal intensity at the upper and lower margins of the lesion.

Table 1: Lesion counts in STIR/PDWTSE and WMS

Independent Analysis	STIR/PDWTSE		WMS	
	TL, MPL (SD)	Interreader Agreement (κ)	TL, MPL (SD)	Interreader Agreement (κ)
Total lesion count in 42 patients				
Reader 1	177, 4.2 (3.0)		191, 4.5 (3.5)	
Reader 2	183, 4.3 (3.4)		189, 4.5 (3.5)	
C1–C4 lesion count				
Reader 1	101, 2.4 (1.6)	0.49	104, 2.5 (1.9)	0.82
Reader 2	108, 2.6 (2.0)		104, 2.5 (2.0)	
C5–C7 lesion count				
Reader 1	76, 1.8 (1.7)	0.52	87, 2.1 (1.9)	0.84
Reader 2	79, 1.9 (1.8)		85, 2.0 (1.8)	

Note:—TL indicates total lesion count; MPL, mean lesions per patient.

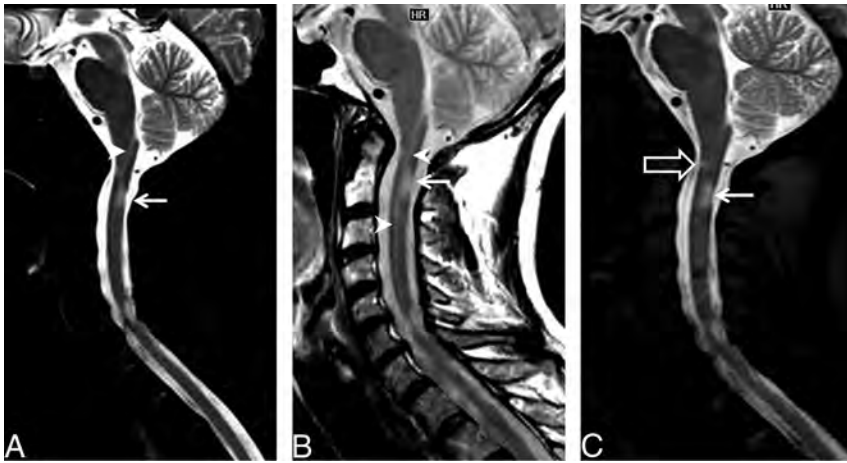


FIG 2. Example of improved lesion conspicuity in a 45-year-old woman with a relapsing-remitting subtype of multiple sclerosis. Sagittal STIR (A) and PDWTSE (B) images show a focal lesion in the dorsum of the cord at the lower C2 level (arrow). Anterior to this lesion, there is linear hyperintensity in the center of the cord usually noted on the STIR/PDWTSE sequence group (arrowhead). The central canal is more homogeneous in signal intensity on sagittal WMS image (C); this feature improves the definition of the superior margin of the dorsal lesion. An additional focal lesion is noted in the ventral cord at the upper C2 level (open arrow), better identified on the WMS sequence (C).

Table 2: Qualitative analysis of focal lesions

	STIR/PDWTSE	WMS	P Value
Independent analysis			
Overall subjective lesion conspicuity, C1–C4 ($M_{1,2}$, M_1 , M_2)	3.1, 3.1, 3.0	3.7, 3.8, 3.7	<.01
Overall subjective lesion conspicuity, C5–C7 ($M_{1,2}$, M_1 , M_2)	3.1, 3.2, 3.0	3.8, 4.1, 3.5	<.01
Side-by-side analysis			
Spurious discrepant lesions			
Reader 1 (DL, M_{DL})	23, 0.5	3, 0.1	<.01
Reader 2 (DL, M_{DL})	30, 0.7	4, 0.1	<.01
True missed discrepant lesions			
Reader 1 (DL, M_{DL})	37, 0.9	3, 0.1	<.01
Reader 2 (DL, M_{DL})	38, 0.9	6, 0.1	<.01

Note:— $M_{1,2}$ indicates mean lesions per level for reviewers 1 and 2; M_1 , mean lesions per level for reviewer 1; M_2 , mean lesions per level for reviewer 2; DL, total discrepant lesion; M_{DL} , average mean discrepant lesion.

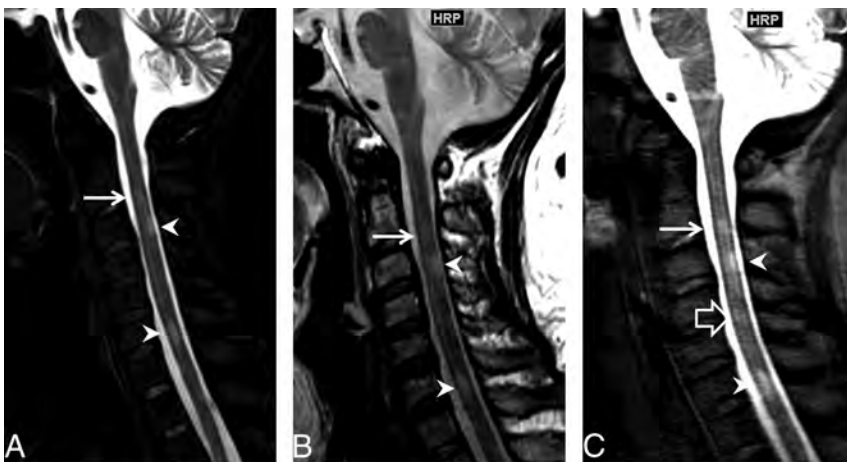


FIG 3. An example of a definite lesion missed on STIR/PDWTSE in a 40-year-old woman with multiple sclerosis. Sagittal STIR (A) and PDWTSE (B) images show focal lesions at the C3 and C6 levels (arrowheads). Another lesion at the C2 level (arrow) is less conspicuous due to central cord high signal in STIR/PDWTSE. On WMS (C), the lesion at C2 is better visualized. An additional focal lesion is noted on WMS at the C4 level (open arrow), which is identified on PDWTSE as a faint hyperintensity on the side-by-side comparison.

noted on STIR/PDWTSE than on WMS by readers 1 and 2 in the cervical cord (23, 30 and 3, 4 on STIR/PDWTSE and WMS, respectively, $P < .01$). Of 53 spurious lesions noted by both readers in the STIR/PDWTSE group, 32 of 53 spurious lesions (60.4%) were noted on PDWTSE and 21 of 53 were noted on STIR (39.6%). Readers 1 and 2 missed 37 and 38 definite lesions on STIR/PDWTSE, whereas 3 and 6 such lesions were missed on WMS ($P < .01$) (Fig 3 and Table 2).

Quantitative Analysis

The average contrast ratio and lesion sharpness were measured on the sagittal STIR, PDWTSE, and WMS sequences. Analysis was done on 82 lesions using all 3 sagittal sequences. Average length of the lesions was 1.0 ± 0.5 cm. The contrast ratio of these analyzed lesions was higher in WMS (0.8) compared with STIR (0.4) and PDWTSE (0.2) ($P < .01$). The contrast ratio was higher in STIR (0.4) compared with PDWTSE (0.2) ($P < .01$). The lesion edge sharpness was measured in a subset of 25 selected lesions by using a line-intensity profile tool. LES was higher on WMS (2.3 mm) than in the other group (3.1 mm on STIR and 2.9 mm on PDWTSE, $P < .01$). Furthermore, within the STIR/PDWTSE group, the LES was marginally better for PDWTSE (2.9) than on STIR (3.1), though this finding was not statistically significant ($P = .11$) (Table 3).

DISCUSSION

Detection of the focal spinal cord lesions may increase confidence in the clinical diagnosis of MS or can predict conversion of a clinically isolated syndrome into definite MS.¹⁵⁻¹⁷ In diagnosed cases of MS, quantification of disease activity is important for monitoring treatment efficacy.¹⁸ The purpose of this study was to compare the WMS sequence with a short TE with the conventional sequences of STIR and PDWTSE in imaging the cervical spinal cord in MS. Because there are no studies that detail the optimal TE used in the inversion recovery sequence for imaging MS lesions, we chose a WMS TE of 11 ms after comparing the signal-to-noise ratio and lesion contrast with TE = 5 ms, TE = 11 ms, and TE = 25 ms in a pilot study (data

Table 3: Quantitative analysis of focal lesions

	STIR (Mean) (SD)	PDWTSE (Mean) (SD)	WMS (Mean) (SD)	P Value		
				STIR vs PDWTSE	STIR vs WMS	PDWTSE vs WMS
Contrast ratio (<i>n</i> = 82)	0.4 (0.2)	0.2 (0.2)	0.8 (0.5)	<.01	<.01	<.01
LES in mm (<i>n</i> = 25)	3.1 (0.9)	2.9 (0.5)	2.3 (0.6)	.11	<.01	<.01

not shown). A shorter TE in WMS (11 ms) compared with STIR or PDWTSE (50 and 45 ms, respectively) is advantageous for MS imaging. T1 prolongation is a manifestation of myelin loss in MS, which acts as a dominant contrast mechanism in long TR/shorter TE sequences such as WMS. Additionally, the dephasing effects of CSF pulsation artifacts are less pronounced at lower TEs.¹⁹ On the other hand, T2 prolongation is less specific for MS and occurs due to edema in active lesions and gliosis in chronic lesions.²⁰ Also, as discussed earlier, there is a loss of contrast between the MS plaques and spinal cord on T2-weighted sequences with longer TEs.

The combined acquisition time of the axial and sagittal WMS sequence used in the current study (7.5 minutes) is similar or less compared with the sagittal and axial 2D single-inversion WMS (10.5 minutes) described in a prior study⁹ and compared with previous descriptions using 3D double inversion recovery or T1WI magnetization-prepared rapid acquisition of gradient echo sequences (7–7.5 minutes).^{21,22} While separate axial and sagittal acquisitions do not have the advantage of the isotropic resolution needed for multiplanar evaluation, they are less prone to image degradation due to shorter acquisition times compared with the 3D techniques.²²

By implementing the WMS sequence in a routine MS cervical cord imaging protocol, we were able to increase interreader agreement in level-by-level focal lesion counts, improve lesion conspicuity, and decrease artifacts compared with standard STIR/PDWTSE, without a serious time penalty.

The average number of lesions per patient detected on WMS was similar to that in STIR/PDWTSE. However, the lesion counts per patient at each cervical level varied between these techniques and had only fair intersequence group agreement. This finding signifies an underlying difference in the perception and interpretation of focal findings between the techniques (ie, in terms of what constitutes a lesion versus artifacts). The interreader agreement on the lesion count per each level and overall on WMS was significantly better compared with STIR/PDWTSE. Higher interreader agreement in WMS was probably related to better lesion contrast and margin delineation of lesions compared with STIR/PDWTSE, a feature vital for maintaining consistency in monitoring MS disease activity across different radiologists on follow-up imaging.

The contrast ratio on WMS was 2-fold better than that on STIR and approximately 4 times better than that on PDWTSE. However, the extent of improvement in the contrast ratio on the WMS sequence we used was less than that reported by Poonawalla et al.⁹ This difference may be due to variations in sequence parameters, such as the TE used in this study. Previous studies have demonstrated that STIR provided a superior contrast ratio and better lesion depiction over PDWTSE.⁵ In this study, although the contrast ratio on STIR was 2 times better than that on PDWTSE,

the LES was not significantly different; therefore, there was no reader preference toward either of these sequences in terms of lesion delineation. The low interreader agreement on lesion count on STIR is comparable with findings described in an earlier study.⁷ Traditionally, STIR and PDWTSE have been used

in combination to overcome each other's shortcomings.^{10,23} The LES in WMS was marginally but statistically better than that on STIR and PDWTSE; this finding may be due to better background suppression of the normal white matter. Better LES could also be a result of a shorter TE, which, in addition to improving lesion contrast by decreasing T2-weighting, also limited the dephasing effects of CSF pulsation, which could result in blurring of the tissue interfaces.⁵

The number of missed definite lesions was higher on STIR/PDWTSE sequences. All these lesions could be retrospectively visualized on STIR/PDWTSE by side-by-side comparison with WMS. The higher chance of missing true lesions on STIR/PDWTSE could be explained on the basis of the lower contrast ratio of the definite lesions, higher number of artifacts, and decreased margin sharpness that was essential to resolve closely situated multiple lesions in the STIR/PDWTSE group.

Artifacts related to CSF pulsations are known to produce focal T2WI signal changes on the STIR sequence, which can be mistaken for real abnormalities.²⁴ Similarly, the higher T2WI signal of gray matter and the central canal on STIR and PDWTSE can cause spurious T2WI hyperintense foci or can obscure the central lesions, which have a signal intensity similar to that of gray matter.²⁵ WMS provided a more homogeneous background, in which the centrally located lesions were better appreciated than in the STIR/PDWTSE group. Nelson et al²⁶ have demonstrated improved visualization of cortical and juxtacortical MS lesions on WMS over FLAIR and dual FSE in the cerebral cortex. Later, Poonawalla et al⁹ described the advantage of phase-sensitive inversion recovery over STIR and dual-echo T2 sequences in the delineation of gray matter involvement in the cervical spinal cord. Another study found that phase-sensitive inversion recovery retains this advantage over high-resolution axial 3D proton density-weighted gradient-echo (fast-field echo) imaging as well, though the latter sequence was better in detecting focal abnormalities.²⁷ Studies specifically evaluating the utility of WMS in depicting lesions within the spinal cord gray matter will be needed in the future.

The study has a few limitations. Undersampling in the phase-encoding direction in WMS resulted in lower spatial resolution along the phase-encoding direction, manifesting as mild blurring. Further work is needed to overcome this shortcoming while limiting the image-acquisition time. While WMS was better than STIR and PDWTSE in the evaluation of focal cord lesions, the extra-axial structures such as disc, spine, and paraspinal tissues were not as well-visualized on WMS. Therefore, inclusion of either STIR or PDWTSE is still necessary for complete evaluation of extramedullary structures in the cervical spine MR imaging examination. In this limited study, WMS was not advantageous over STIR or PDWTSE in evaluating diffuse lesions and cord atrophy in progressive subtypes of MS. In these patients, cord-volume assessment, magnetization transfer, and diffusion tensor imaging

may be better for the quantification of disease activity.¹⁸ Finally, there is no reference standard for identification of “true” lesions in the spinal cord. Instead, we relied on follow-up imaging and 2-plane visualization to select lesions deemed most likely to represent actual spinal cord lesions. With this classification system, WMS imaging outperformed STIR and PDWTSE sequences in our analysis.

CONCLUSIONS

WMS could potentially be substituted for either STIR or PDWTSE sequences in routine clinical protocols. There is better interreader consistency in the lesion count on WMS compared with STIR/PDWTSE sequences. The focal cord lesions are visualized with better conspicuity due to better contrast ratio and edge sharpness. There are fewer spurious lesions on WMS compared with STIR/PDWTSE. The WMS techniques can allow better lesion delineation and confidence in lesion counts.

Disclosures: Kenneth R. Maravilla—UNRELATED: Consultancy: Guerbet; Grants/Grants Pending: Bayer,*Bracco,*Guerbet,*Comments: clinical trial grants; Payment for Lectures (including service on Speakers Bureaus): Bracco. *Money paid to the institution.

REFERENCES

- Bergers E, Bot JC, De Groot CJ, et al. Axonal damage in the spinal cord of MS patients occurs largely independent of T2 MRI lesions. *Neurology* 2002;59:1766–71 CrossRef Medline
- Bergers E, Bot JC, van der Valk P, et al. Diffuse signal abnormalities in the spinal cord in multiple sclerosis: direct postmortem in situ magnetic resonance imaging correlated with in vitro high-resolution magnetic resonance imaging and histopathology. *Ann Neurol* 2002;51:652–56 CrossRef Medline
- Lycklama G, Thompson A, Filippi M, et al. Spinal-cord MRI in multiple sclerosis. *Lancet Neurol* 2003;2:555–62 CrossRef Medline
- Bot JC, Barkhof F, Polman CH, et al. Spinal cord abnormalities in recently diagnosed MS patients: added value of spinal MRI examination. *Neurology* 2004;62:226–33 CrossRef Medline
- Hittmair K, Mallek R, Prayer D, et al. Spinal cord lesions in patients with multiple sclerosis: comparison of MR pulse sequences. *AJNR Am J Neuroradiol* 1996;17:1555–65 Medline
- Chong AL, Chandra RV, Chuah KC, et al. Proton density MRI increases detection of cervical spinal cord multiple sclerosis lesions compared with T2-weighted fast spin-echo. *AJNR Am J Neuroradiol* 2016;37:180–84 CrossRef Medline
- Nayak NB, Salah R, Huang JC, et al. A comparison of sagittal short T1 inversion recovery and T2-weighted FSE sequences for detection of multiple sclerosis spinal cord lesions. *Acta Neurol Scand* 2014;129:198–203 CrossRef Medline
- Vargas MI, Delavelle J, Kohler R, et al. Brain and spine MRI artifacts at 3Tesla. *J Neuroradiol* 2009;36:74–81 CrossRef Medline
- Poonawalla AH, Hou P, Nelson FA, et al. Cervical spinal cord lesions in multiple sclerosis: T1-weighted inversion-recovery MR imaging with phase-sensitive reconstruction. *Radiology* 2008;246:258–64 CrossRef Medline
- Philpott C, Brotchie P. Comparison of MRI sequences for evaluation of multiple sclerosis of the cervical spinal cord at 3 T. *Eur J Radiol* 2011;80:780–85 CrossRef Medline
- Vaithianathar L, Tench CR, Morgan PS, et al. Magnetic resonance imaging of the cervical spinal cord in multiple sclerosis—a quantitative T1 relaxation time mapping approach. *J Neurol* 2003;250:307–15 CrossRef Medline
- Smith SA, Edden RA, Farrell JA, et al. Measurement of T1 and T2 in the cervical spinal cord at 3 Tesla. *Magn Reson Med* 2008;60:213–19 CrossRef Medline
- Fries P, Runge VM, Kirchin MA, et al. Magnetic resonance imaging of the spine at 3 Tesla. *Semin Musculoskelet Radiol* 2008;12:238–52 CrossRef Medline
- Camren GP, Wilson GJ, Bamra VR, et al. A comparison between gadofosveset trisodium and gadobenate dimeglumine for steady state MRA of the thoracic vasculature. *Biomed Res Int* 2014;2014:625614 CrossRef Medline
- Bot JC, Barkhof F. Spinal-cord MRI in multiple sclerosis: conventional and nonconventional MR techniques. *Neuroimaging Clin N Am* 2009;19:81–99 CrossRef Medline
- Polman CH, Reingold SC, Banwell B, et al. Diagnostic criteria for multiple sclerosis: 2010 revisions to the McDonald criteria. *Ann Neurol* 2011;69:292–302 CrossRef Medline
- Sombekke MH, Wattjes MP, Balk LJ, et al. Spinal cord lesions in patients with clinically isolated syndrome: a powerful tool in diagnosis and prognosis. *Neurology* 2013;80:69–75 CrossRef Medline
- Gass A, Rocca MA, Agosta F, et al; MAGNIMS Study Group. MRI monitoring of pathological changes in the spinal cord in patients with multiple sclerosis. *Lancet Neurol* 2015;14:443–54 CrossRef Medline
- Melhem ER, Benson ML, Beauchamp NJ, et al. Cervical spondylosis: three-dimensional gradient-echo MR with magnetization transfer. *AJNR Am J Neuroradiol* 1996;17:705–11 Medline
- Brück W, Bitsch A, Kolenda H, et al. Inflammatory central nervous system demyelination: correlation of magnetic resonance imaging findings with lesion pathology. *Ann Neurol* 1997;42:783–93 CrossRef Medline
- Riederer I, Karampinos DC, Settles M, et al. Double inversion recovery sequence of the cervical spinal cord in multiple sclerosis and related inflammatory diseases. *AJNR Am J Neuroradiol* 2015;36:219–25 CrossRef Medline
- Nair G, Absinta M, Reich DS. Optimized T1-MPRAGE sequence for better visualization of spinal cord multiple sclerosis lesions at 3T. *AJNR Am J Neuroradiol* 2013;34:2215–22 CrossRef Medline
- Rovira A, Wattjes MP, Miller D, et al; MAGNIMS study group. Evidence-based guidelines: MAGNIMS consensus guidelines on the use of MRI in multiple sclerosis—establishing disease prognosis and monitoring patients. *Nat Rev Neurol* 2015;11:597–606 CrossRef Medline
- Bot JC, Barkhof F, Lycklama à Nijeholt GJ, et al. Comparison of a conventional cardiac-triggered dual spin-echo and a fast STIR sequence in detection of spinal cord lesions in multiple sclerosis. *Eur Radiol* 2000;10:753–58 CrossRef Medline
- Yiannakas MC, Kearney H, Samson RS, et al. Feasibility of grey matter and white matter segmentation of the upper cervical cord in vivo: a pilot study with application to magnetisation transfer measurements. *Neuroimage* 2012;63:1054–59 CrossRef Medline
- Nelson F, Poonawalla AH, Hou P, et al. Improved identification of intracortical lesions in multiple sclerosis with phase-sensitive inversion recovery in combination with fast double inversion recovery MR imaging. *AJNR Am J Neuroradiol* 2007;28:1645–49 CrossRef Medline
- Kearney H, Altmann DR, Samson RS, et al. Cervical cord lesion load is associated with disability independently from atrophy in MS. *Neurology* 2015;84:367–73 CrossRef Medline

SAPHO Syndrome: Imaging Findings of Vertebral Involvement

 A.M. McGauvran,  A.L. Kotsenas,  F.E. Diehn,  J.T. Wald,  C.M. Carr, and  J.M. Morris

ABSTRACT

BACKGROUND AND PURPOSE: Imaging findings in patients with a combination of synovitis, acne, pustulosis, hyperostosis, and osteitis (SAPHO) are often misinterpreted as discitis/osteomyelitis or metastases, resulting in multiple biopsies and delayed diagnosis. We have incidentally noted a semicircular morphology in vertebral body imaging in several cases of SAPHO syndrome with vertebral involvement. Our goal was to evaluate the prevalence of this distinctive morphology in these patients.

MATERIALS AND METHODS: A retrospective review of patients with SAPHO syndrome diagnosed between July 1998 and August 2013 was conducted. A descriptive analysis of MR imaging, CT, radiography, bone scanning, and PET imaging was performed for the presence and distribution of vertebral body signal intensity or attenuation changes and/or enhancement; contiguous vertebral body involvement; vertebral body collapse; endplate irregularity; disc space, facet, and spinous process involvement; subligamentous thickening; and paraspinal soft-tissue involvement.

RESULTS: Eighteen patients (16 women [89%]; mean age, 52.9 years) with SAPHO and spine involvement were included. Contiguous involvement of ≥ 2 vertebral bodies was found in 16 patients (89%), with a curvilinear or “semicircular” pattern involving portions of adjacent vertebral bodies in 10 (63%, $P = .14$). Most intervertebral discs demonstrated absence of abnormal T2 hyperintensity (73%) and enhancement (89%). Subligamentous thickening was present in 12 (67%). Paraspinal soft-tissue involvement was present in 6 (33%).

CONCLUSIONS: SAPHO syndrome should be included in the differential diagnosis in a patient with a curvilinear or semicircular pattern of vertebral involvement, contiguous vertebral body involvement, and absence of intervertebral disc edema and enhancement.

ABBREVIATION: SAPHO = combination of synovitis, acne, pustulosis, hyperostosis, and osteitis

The association of bone disease and chronic cutaneous pustular lesions has been observed since the 1960s, but it was not until 1987 that Chamot et al¹ first used the acronym SAPHO to describe this rare group of chronic, relapsing, inflammatory osteoarticular disorders commonly associated with skin manifestations. SAPHO was proposed to refer to a combination of synovitis, acne, pustulosis, hyperostosis, and osteitis as a heading for these syndromes. Cutaneous lesions are characterized by palmo-plantar pustulosis, acne conglobata, and/or hidradenitis suppurativa. A wide variety of bone and joint manifestations has been described.

SAPHO syndrome shares some overlapping features with other spondyloarthropathies, including reactive arthritis, psoriatic arthritis, spondyloarthropathy associated with inflammatory bowel disease, and idiopathic ankylosing spondylitis. In children, the disease most commonly presents as a recurrent multifocal osteomyelitis, favoring the long bone metaphysis. This presentation is in contradistinction to that in adults in whom the anterior chest wall, including the sternoclavicular and manubriosternal junctions, is most commonly affected.¹⁻⁴ The spine is also frequently involved in adults. Findings of spinal involvement on conventional radiographic imaging have been reported to include vertebral body osteosclerosis, paravertebral ligament ossification, hyperostosis, and discovertebral junction lesions. Although plain radiographic findings of vertebral involvement have been well-described, the radiology literature has only a limited number of case reports and small case series describing imaging findings in detail with other modalities, specifically MR imaging.⁵⁻¹⁰ These advanced imaging findings are often misinterpreted as discitis/osteomyelitis or metastases.^{11,12} In our experience, this misinter-

Received October 9, 2015; accepted after revision January 14, 2016.

From the Department of Radiology, Mayo Clinic, Rochester, Minnesota.

Paper previously presented at: Annual Meeting of the American Society of Neuroradiology and the Foundation of the ASNR Symposium, May 17–22, 2014; Montreal, Quebec, Canada.

Please address correspondence to Amy L. Kotsenas, MD, Department of Radiology, Mayo Clinic, 200 First St SW, Rochester, MN 55905; e-mail: Kotsenas.amy@mayo.edu; @AmyKotsenas

<http://dx.doi.org/10.3174/ajnr.A4736>

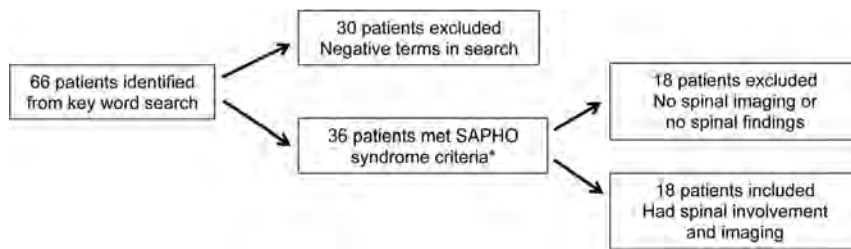


FIG 1. Flow chart demonstrating how patients were narrowed from a large subset to 18 patients with SAPHO syndrome and spinal involvement. *SAPHO criteria were based on Benhamou et al.¹⁴

pretation can lead to unnecessary biopsies, other invasive procedures, and, ultimately, delayed diagnosis.

Anecdotally, we have commonly observed a “semicircular” pattern of contiguous vertebral body involvement localized to either the anterior or posterior vertebral bodies of the middle segments and adjacent anterior or posterior endplates of the surrounding vertebral bodies. This was first reported by Peffers et al.¹³ The goal of the study was to evaluate the imaging findings in a series of patients with vertebral involvement as part of SAPHO syndrome, with specific attention paid to the prevalence of this unique semicircular morphology in the vertebral bodies.

MATERIALS AND METHODS

Patients

Institutional review board approval was obtained, and informed consent was waived for this retrospective review. This study complied with all Health Insurance Portability and Accountability Act requirements. A search of clinical notes and the radiology information management system for patients with the possible diagnosis of SAPHO or any combination of the terms “synovitis,” “acne,” “pustulosis,” “hyperostosis,” and “osteitis” between July 1998 and August 2013 identified 66 patients (Fig 1). Of these, 36 patients had a final clinical diagnosis of SAPHO meeting at least 1 of the 4 criteria proposed by Benhamou et al¹⁴: 1) osteoarticular manifestations of acne conglobata, acne fulminans, or hidradenitis suppurativa; 2) osteoarticular manifestations of palmar plantar pustulosis; 3) hyperostosis involving either the anterior chest wall, spine, or limbs with or without dermatosis; and 4) chronic recurrent multifocal osteomyelitis with or without dermatosis. Eighteen patients were further excluded because they did not have imaging of the spine.

Imaging and Analysis

We retrospectively reviewed the radiographic imaging findings, including MR imaging, CT, bone scintigraphy, and PET/CT. The images were evaluated by 2 experienced neuroradiologists in consensus (A.L.K. with 15 years, J.M.M. with 7 years). Biopsies, including location, number, and histopathologic and microbiologic culture results, were also recorded.

MR imaging was evaluated for vertebral body signal-intensity changes and/or enhancement; contiguous vertebral body involvement; the presence of vertebral body collapse; endplate irregularity; disc space involvement including enhancement; facet and spinous process involvement; subligamentous thickening; and paraspinal soft-tissue involvement. MR imaging sequences, imag-

ing parameters, and magnet strength varied because many of the scans came from outside facilities. Vertebral body signal intensity was evaluated on T1- and T2-weighted MR images and on gadolinium-enhanced T1-weighted images when available. The semicircular pattern of enhancement was recorded if present. The intervertebral discs were evaluated for enhancement, irregularity, associated fluid, and narrowing or widening.

The number and laterality of the facet joints with signal abnormalities and/or enhancement and the presence of spinous process signal changes were recorded. We looked for ligamentous thickening of the anterior or posterior longitudinal ligaments and ligamenta flava, including thickening that extended to uninvolved vertebral bodies. When there was masslike soft-tissue involvement, the location, maximal diameter (in millimeters), and longitudinal extent of the abnormal tissues were recorded.

CT was evaluated for vertebral body sclerosis or lysis. Radiotracer uptake, if present, was recorded for bone scintigraphy and PET/CT examinations.

Statistical Analysis

Statistical analysis was performed by using the JMP software package (Version 9.0; SAS Institute, Cary, North Carolina). The Fisher exact test was used to determine the association between the presence of vertebral involvement and sex, the semicircular pattern of involvement, disc space narrowing, and endplate irregularities. Only 2-tailed tests were used. A *P* value of < .05 was significant.

RESULTS

Demographics

Of the 36 patients with SAPHO who were identified (Fig 1), 26 (72%) were female with an age range of 11–76 years (mean, 44 years; median, 47.5 years). Eighteen patients had spinal imaging available for review, and all demonstrated spinal involvement (50%; 16 women [89%; *P* = .06]; age range, 23–69 years).

Vertebral Lesions

A total of 104 vertebral bodies were involved in 18 patients (Table). One patient had a single level of involvement (6%), while the remaining 17 patients had a median of 5 vertebral levels involved (range, 2–13 levels; mean, 5.8 ± 3.4 levels). The thoracic spine was most commonly involved ($n = 14$, 78%), with ≥ 2 separate thoracic segments involved in 57% of patients ($n = 8/14$). The lumbosacral spine was the next most commonly involved ($n = 7$, 39%), followed by the cervical spine ($n = 3$, 17%). Multiple regions of the spine were involved in 7 patients (39%). Contiguous involvement of ≥ 2 vertebral bodies was found in 16 patients (89%), with a curvilinear or semicircular pattern involving the anterior or posterior portions of adjacent vertebral bodies in 10 of these patients (63%, *P* = .14) (Fig 2A, -B).

Vertebral body findings per imaging modality

Imaging Modality	Vertebral Body Finding	No. of Patients
MRI (n = 16)		
T1-weighted images (n = 16)	T1 hypointensity	15
	T1 hypointensity → T1 hyperintensity	1
T2-weighted images (n = 15)	T2 hyperintensity	12
	Mixed T2 hypo- and hyperintensity	3
Gadolinium-enhanced images (n = 9)	Enhancement corresponding to areas of T1 hypointensity/T2 hyperintensity	9
CT (n = 14)	Sclerosis corresponding to MR signal abnormalities	14
Technetium Tc99m methylene diphosphonate 3-phase bone scan (n = 10)	Increased radiotracer uptake	10
Whole-body FDG-PET/CT (n = 2)	No abnormal FDG uptake	2



FIG 2. MR imaging, CT, and bone scan of the thoracic spine in a 74-year-old woman with back pain. Sagittal T1-weighted (A) and STIR (B) images demonstrate hypo- and hyperintensity, respectively, in a curvilinear or semicircular pattern (*dashed line*) in contiguous vertebral body segments. Note the absence of abnormal signal within the intervertebral disc spaces. C, Sagittal CT image shows associated sclerosis (*arrows*) corresponding to levels of abnormal increased signal on MR imaging. D, Bone scan, posteroanterior view, demonstrates focal areas of increased radiotracer uptake within thoracic vertebral bodies and the right sternoclavicular joint (*arrow*). E, Previously undiagnosed plantar pustulosis was evident on physical examination.

MR imaging was available for 16 patients (89%). Many patients came to our institution with imaging from other facilities. Therefore, there was variation in the MR imaging field strength, sequences, and imaging parameters. T1-weighted images were available in all cases; 1 patient (6%) did not have T2-weighted imaging. Vertebral body low-signal intensity on T1-weighted images was seen in 15/16 patients (93%) with corresponding high-signal intensity on T2-weighted images in 12 patients (75%), compatible with bone marrow edema (Fig 2A, -B). One patient (6%) had mixed hypo-/hyperintensity on T1-weighted images, while 3 patients (18%) had mixed hypo-/hyperintensity on T2-weighted images, suggestive of concomitant bone marrow edema and cancellous bone sclerosis. Gadolinium-based contrast was administered in 9 patients in whom MR imaging was available (56%), with 100% of patients demonstrating enhancement in the same distribution as the signal changes described above. Vertebral body corner erosions were not observed in any patient.

Corresponding noncontrast CT imaging was available in 14 of the 16 patients in whom MR imaging was available. CT demonstrated sclerosis in the areas of MR signal abnormality in 100% of patients, regardless of the pattern of the MR imaging signal changes (Fig 2C). No lytic lesions were identified.

Nine patients had technetium Tc99m methylene diphosphonate 3-phase whole-body bone scans to correlate with the spinal MR imaging. All 9 patients demonstrated increased radiotracer on MR imaging in the vertebral bodies affected (Fig 2D). There were no discordant areas of vertebral body uptake between the 2 modalities. Extravertebral findings on bone scans are described in further detail below.

In 2 of the 18 (11%) patients with spinal involvement who did not have an MR imaging, the number, level, and contiguity of vertebral lesions were determined solely by nuclear medicine bone scanning in 1 patient and with lumbar spine radiographs in the second. In the first patient, the bone scan demonstrated radiotracer uptake in the non-contiguous T5, T9, T11, and L1 vertebral bodies and right sacroiliac joint. In the second, lumbar spine radiographs demonstrated attenuated vertebral body sclerosis from L3 to the sacrum and partial fusion of the left sacroiliac joint.

Thirteen of 18 patients (72%) had plain radiographs. One patient had normal findings on plain radiographic imaging (8%). Twelve patients had vertebral body sclerotic changes, including shiny corners (92%). Despite abnormal findings on MR imaging, no abnormal FDG uptake was seen in the 2 patients with whole-body FDG-PET/CT.

Facet Joints/Spinous Processes

There were 34 facet joints involved with T2 hyperintensity and/or enhancement in 7 patients (39%), with unilateral involvement at 6 levels (3 patients, 17%) and bilateral involvement at 14 levels (4 patients, 22%). Spinous process T2 hyperintensity or enhancement or both was observed at 15 levels in 5 patients (28%), all with concurrent uni- or bilateral facet joint involvement at the same levels (Fig 3).

Disc Spaces

MR imaging demonstrated at least 1 intervening or adjacent disc space that was narrowed in 8 of 16 (50%) patients, with irregular endplates observed in 7 patients (43%). The combination of disc space narrowing with endplate irregularity was noted in 5 patients who had MR imaging (62%; $P = .11$). High signal on T2-weighted images in the disc was seen in 5 patients (31%). Disc space enhancement on gadolinium-enhanced T1-weighted images was observed in 2 of 9 patients receiving gadolinium (22%). The combination of disc space narrowing, abnormal T2 hyperintensity, and endplate irregularity was observed in 3 patients (18%), while only 1 patient (11%) had all 4 findings: disc space narrowing, abnormal T2 hyperintensity, endplate irregularity, and disc space enhancement.



FIG 3. MR images in a 32-year-old woman with back pain. Sagittal T1-weighted fat-saturated images of the thoracic spine following administration of gadolinium demonstrate multilevel enhancement (arrows) of the spinous processes (B) and bilateral facet joints (A and C).

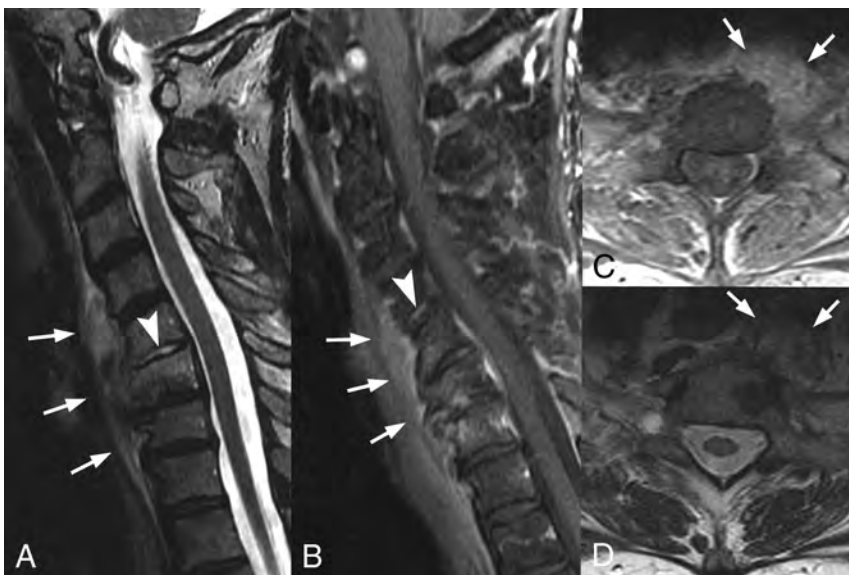


FIG 4. MR images in a 69-year-old woman with cervical and thoracic back pain. A, Sagittal T2-weighted fat-suppressed image of the cervical spine demonstrates paravertebral soft-tissue thickening (arrows), extending from the C3–C4 interspace to T3. Note the abnormally high T2-weighted signal within the C5–C6 disc (arrowhead). B, Sagittal T1-weighted gadolinium-enhanced fat-suppressed image demonstrates corresponding enhancement of the paravertebral soft tissue (arrows) with disc space enhancement (arrowhead). C, Axial T1-weighted gadolinium-enhanced fat-suppressed image demonstrates enhancement of the thickened paravertebral soft tissues (arrows). D, Axial T2-weighted fat-suppressed image further demonstrates the extent of the paravertebral soft-tissue thickening (arrows).

Soft Tissues

Thickening of the anterior longitudinal ligament was present in 12 patients (80%) and extended to otherwise uninvolved vertebral bodies in 3 patients (25%). No other spinal ligaments were involved. Paraspinal soft-tissue involvement consisted of mass-like soft-tissue thickening with enhancement (Fig 4). This was observed in 6 patients (37%), with a range of 1–6 vertebral levels involved. Masslike paraspinal soft-tissue involvement did not exceed 15 mm in maximal diameter in any case (range, 2–15 mm).

Extraspinal Involvement

Seventeen of 18 patients (94%) had typical skin manifestations. Ten (59%) of the 17 patients had palmoplantar pustulo-

sis (Fig 2E), 2 patients (12%) had acne conglobata, 1 patient (6%) had hidradenitis suppurativa, and 6 patients (35%) had nonspecific dermatoses. Two patients (12%) had >1 skin manifestation, with 1 patient having both palmoplantar pustulosis and acne conglobata, while the other patient had both palmoplantar pustulosis and hidradenitis suppurativa. Seven of the 18 patients (39%) with SAPHO syndrome and spinal involvement also had concurrent sternoclavicular involvement (Fig 2), while 4 patients (22%) had involvement of the first costovertebral joint. Four of the 18 patients (22%) had plain radiographs of the sacroiliac joints, with 1 patient (25%) demonstrating sclerosis and the remaining 3 patients demonstrating no involvement of the sacroiliac joint.

Pathology/Microbiology

Twelve patients (67%) underwent biopsy; 7 patients had a single biopsy, 3 patients had 2 biopsies, and 2 patients had 3 biopsies, totaling 19 biopsies. The vertebral body was the most commonly biopsied location ($n = 11$), followed by the paravertebral soft tissues ($n = 5$) and disc interspace ($n = 1$). In 2 patients with spinal involvement, a concomitant sternal lesion was biopsied. Pathology was negative for malignancy in all biopsy specimens ($n = 19$), including 2 patients (11%) with a known history of malignancy. Microbiologic cultures were also negative for infection in all 8 patients who had microbiologic testing performed.

Inflammatory/Infectious Markers

C-reactive protein levels were available in 13 of 18 patients (72%), with elevated levels in 8 patients (62%). Sedimentation rate levels were available in 16 of 18 patients (89%), with elevated levels in 6 patients (38%). White blood cell counts were available in 17 of 18 patients (94%), with all patients having normal levels.

DISCUSSION

A curvilinear or a semicircular pattern of contiguous vertebral body involvement localized to either the anterior or posterior vertebral bodies of the middle segments and adjacent anterior or posterior endplates of the surrounding vertebral bodies was found in most of our patients (63%) with SAPHO and spinal involvement. The high prevalence of this semicircular pattern of vertebral body signal alteration and enhancement may help to

differentiate SAPHO syndrome from metastases, which tend to be randomly distributed throughout the spine. When combined with a relatively low prevalence of abnormal disc space T2-signal and enhancement, the high prevalence of the semicircular pattern may also be helpful to radiologists in cases in which spinal infection is being considered. Correlation with CT may be beneficial because sclerosis in the areas of MR signal abnormality was present in 100% of our patients, regardless of the pattern of the MR signal changes. Recognition of these findings by radiologists should prompt clinical consultation with dermatology and/or rheumatology to assess typical skin and other musculoskeletal manifestations.

Osteosclerosis of the vertebral bodies in SAPHO syndrome has been described by Leone et al¹⁵ and may progress to produce diffuse and generalized sclerosis with development of hyperostosis in more chronic cases. Prior case reports¹⁶⁻¹⁸ have shown the utility of [¹⁸F] FDG-PET/CT to differentiate active from healed chronic inflammatory lesions because PET/CT shows increased uptake only in lesions with active inflammation. The chronic osteosclerotic changes seen in our patients are hypothesized to represent a quiescent phase of the disease, which likely accounts for the normal FDG uptake in the 2 patients who had PET/CT scans in our series.

In contrast to a study performed by Laredo et al,⁶ our patients were more likely to have involvement at contiguous levels. In addition, while our patients had frequent involvement of vertebral body corners, we did not identify erosion in any case. Because we are a tertiary referral center, our patients may have presented at a later clinical stage. In fact, nearly all our patients presented after other manifestations such as skin lesions or sternoclavicular involvement, both of which are considered highly specific, were evident.

The frequency of spondylodiscitis in SAPHO syndrome has been reported to be 9%–32%.¹⁰ Prior studies have shown chronic sterile nonspecific inflammation from intervertebral disc biopsies in patients with SAPHO syndrome, equivalent to the Andersson lesion, which has been identified in 4.5% of patients with ankylosing spondylitis.^{5,10} Others have suggested that spondylodiscitis is due to *Propionibacterium acnes*.¹⁹ Although disc space involvement with fluidlike signal on T2-weighted images and disc space enhancement have been previously described in patients with SAPHO syndrome,^{5,7} our study showed that most intervertebral discs in patients with SAPHO syndrome demonstrated the absence of both fluidlike signal on T2-weighted images (69%) and disc space enhancement (78%). The absence of these findings may be helpful in distinguishing SAPHO involvement from spinal infection.

We found single-level vertebral involvement rare, with contiguous involvement of ≥ 2 levels in nearly 90%, often with ≥ 5 levels involved. This finding is in contrast to cases of spondyloarthropathy, in which it is uncommon to see contiguous involvement.⁶

Nachtigal et al⁷ previously described the paravertebral soft tissues in patients with SAPHO involvement of the spine possibly

showing abnormal signal intensity. We found similar results, with thickening and enhancement of the anterior longitudinal ligament present in 37% of patients with SAPHO syndrome. These findings further complicate the differential diagnosis of SAPHO syndrome versus infection but may help to differentiate it from spondyloarthropathies, which, to our knowledge, have only been reported to affect the supraspinous ligament, interspinous ligaments, and ligamenta flava.²⁰ Additionally, in the 2 patients with vertebral body involvement determined solely on nuclear medicine bone scans or plain radiographs, both demonstrated unilateral sacroiliac joint involvement. Depasquale et al¹¹ and Leone et al¹⁵ have both described increased sclerosis and hyperostosis, particularly at the iliac side of the joint, in patients with SAPHO. When seen in patients with features of moderate sacroiliitis, this presentation was thought to be highly suggestive of SAPHO syndrome and helped to differentiate it from other spondyloarthropathies.

Peffer et al¹³ first described a subset of patients with nonbacterial osteitis involving the thoracic spine. Spinal involvement in our study had a strong female predominance and preferentially affected the thoracic spine. This is in contrast to osteomyelitis and discitis, in which males are affected twice as often as females and the lumbar spine is most commonly affected.²¹

MR imaging of the spine and sacroiliac joints has played a key role in patients with spondyloarthropathies and has led to improved understanding of the course of the disease and to an earlier diagnosis.²⁰ We suggest an imaging protocol consisting of at least a sagittal T1-weighted turbo spin-echo sequence, sagittal fat-saturated T2-weighted turbo spin-echo sequence or STIR sequence with high resolution, and a sagittal fat-saturated gadolinium-enhanced T1-weighted sequence for evaluation of patients with suspected SAPHO syndrome, spondyloarthropathy, or osteomyelitis/discitis.

Our study had a number of limitations. This was a retrospective review without a control group, and images were reviewed in consensus rather than independently by the 2 neuroradiologists, which might limit the reproducibility. Additionally, the number of patients was small; however, SAPHO syndrome is an uncommon entity, and ours is one of the largest studies to date. The MR imaging protocols were not standardized. For example, not every patient had a fat-saturated sequence, 1 patient lacked a T2-weighted sequence, and 7 of 16 patients (44%) did not receive intravenous contrast material. Variation in MR imaging field strength and imaging protocols was a relatively minor limitation because signal change was noted on precontrast T1-weighted images in all patients. Finally, biopsy and microbiologic results were not available in half of the patients, perhaps due to the presence of other highly specific anterior chest wall and/or skin manifestations.

Additional studies involving larger numbers of patients with SAPHO syndrome and comparison groups of other infectious and noninfectious spinal inflammatory conditions are needed to

determine whether this semicircular pattern is a unique spinal finding in patients with SAPHO syndrome.

CONCLUSIONS

In a patient with a curvilinear or semicircular pattern of contiguous vertebral involvement, sclerosis along ligamentous attachment sites, and the absence of intervertebral disc abnormal T2 hyperintensity and enhancement, SAPHO syndrome should be included in the differential diagnosis and clinical consultation with dermatology and/or rheumatology should be considered. This may prevent the imaging findings from being misinterpreted as discitis/osteomyelitis or metastases, with subsequent potential reduction in the number of unnecessary biopsies and delayed diagnoses.

ACKNOWLEDGMENTS

We thank Sonia Watson, PhD, for her assistance in editing the manuscript.

REFERENCES

1. Chamot AM, Benhamou CL, Kahn MF, et al. **Acne-pustulosis-hyperostosis-osteitis syndrome: results of a national survey—85 cases [in French].** *Rev Rhum Mal Osteoartic* 1987;54:187–96 Medline
2. Boutin RD, Resnick D. **The SAPHO syndrome: an evolving concept for unifying several idiopathic disorders of bone and skin.** *AJR Am J Roentgenol* 1998;170:585–91 CrossRef Medline
3. Kahn MF, Chamot AM. **SAPHO syndrome.** *Rheum Dis Clin North Am* 1992;18:225–46 Medline
4. Maugars Y, Berthelot JM, Ducloux JM, et al. **SAPHO syndrome: a followup study of 19 cases with special emphasis on enthesitis involvement.** *J Rheumatol* 1995;22:2135–41 Medline
5. Akisue T, Yamamoto T, Marui T, et al. **Lumbar spondylodiscitis in SAPHO syndrome: multimodality imaging findings.** *J Rheumatol* 2002;29:1100–01 Medline
6. Laredo JD, Vuillemin-Bodaghi V, Boutry N, et al. **SAPHO syndrome: MR appearance of vertebral involvement.** *Radiology* 2007;242:825–31 CrossRef Medline
7. Nachtigal A, Cardinal E, Bureau NJ, et al. **Vertebral involvement in SAPHO syndrome: MRI findings.** *Skeletal Radiol* 1999;28:163–68 CrossRef Medline
8. Perez C, Hidalgo A, Olier J, et al. **MR imaging of multifocal spondylodiscitis as the initial manifestations of SAPHO syndrome.** *AJR Am J Roentgenol* 1998;171:1431–32 Medline
9. Tohme-Noun C, Feydy A, Belmatoug N, et al. **Cervical involvement in SAPHO syndrome: imaging findings with a 10-year follow-up.** *Skeletal Radiol* 2003;32:103–06 CrossRef Medline
10. Toussiroit E, Dupond JL, Wendling D. **Spondylodiscitis in SAPHO syndrome: a series of eight cases.** *Ann Rheum Dis* 1997;56:52–58 CrossRef Medline
11. Depasquale R, Kumar N, Lalam RK, et al. **SAPHO: what radiologists should know.** *Clin Radiol* 2012;67:195–206 CrossRef Medline
12. Hong SH, Choi JY, Lee JW, et al. **MR imaging assessment of the spine: infection or an imitation?** *Radiographics* 2009;29:599–612 CrossRef Medline
13. Peffers G, James SL, Stirling A, et al. **Thoracic spine osteitis: a distinct clinical entity, a variant of SAPHO or late-onset non-bacterial osteitis?** *Rheumatology (Oxford)* 2012;51:191–93 CrossRef Medline
14. Benhamou CL, Chamot AM, Kahn MF. **Synovitis-acne-pustulosis hyperostosis-osteomyelitis syndrome (SAPHO): a new syndrome among the spondyloarthropathies?** *Clin Exp Rheumatol* 1988;6:109–12 Medline
15. Leone A, Cassar-Pullicino VN, Casale R, et al. **The SAPHO syndrome revisited with an emphasis on spinal manifestations.** *Skeletal Radiol* 2015;44:9–24 CrossRef Medline
16. Inoue K, Yamaguchi T, Ozawa H, et al. **Diagnosing active inflammation in the SAPHO syndrome using 18FDG-PET/CT in suspected metastatic vertebral bone tumors.** *Ann Nucl Med* 2007;21:477–80 CrossRef Medline
17. Patel CN, Smith JT, Rankine JJ, et al. **F-18 FDG PET/CT can help differentiate SAPHO syndrome from suspected metastatic bone disease.** *Clin Nucl Med* 2009;34:254–57 CrossRef Medline
18. Takeuchi K, Matsusita M, Takagishi K. **A case of SAPHO (synovitis-acne-pustulosis-hyperostosis-osteomyelitis) syndrome in which [18F]fluorodeoxyglucose positron emission tomography was useful for differentiating from multiple metastatic bone tumors.** *Mod Rheumatol* 2007;17:67–71 CrossRef Medline
19. Gerster JC, Lagier R, Livio JJ. **Propionibacterium acnes in a spondylitis with palmoplantar pustulosis.** *Ann Rheum Dis* 1990;49:337–38 Medline
20. Sieper J, Rudwaleit M, Baraliakos X, et al. **The Assessment of SpondyloArthritis international Society (ASAS) handbook: a guide to assess spondyloarthritis.** *Ann Rheum Dis* 2009;68(suppl 2):ii1–44 Medline
21. Chen WH, Jiang LS, Dai LY. **Surgical treatment of pyogenic vertebral osteomyelitis with spinal instrumentation.** *Eur Spine J* 2007;16:1307–16 CrossRef Medline